The University of Nottingham

School of Chemical & Environmental Engineering

Investigation of Periodic Structures in Gas-Liquid Flow

By

Mhunir Bayonle Alamu, *BSc, MSc*

Thesis submitted to The University of Nottingham

for the degree of Doctor of Philosophy

October 2010

ABSTRACT

Three different experimental campaigns had been launched to investigate the periodicity of the two-phase flow structures like the void waves in bubbly flow, liquid slugs and Taylor bubbles in slug flow, huge waves in churn flow, disturbance waves in annular flow and wisps in wispy-annular flow. The three experiments and data analysis had been considered in increasing order of complexity. Time varying data were acquired in all the three campaigns. At the simplest level of analysis statistical measures were extracted from the time series, presented, discussed and conclusions drawn.

In the first campaign, time varying void fraction has been measured using a stack of five flush mounted ring-type conductance probes fitted with a 0.005 m internal diameter pipe, 3 m long. The test section was located 390 pipe diameters from the two-phase mixer. Three liquids of different physical properties with viscosity values of 1, 10 and 12 mPa s were mixed with air to establish two-phase flow. Pressure drop measurement was carried out using two pressure taps separated by a distance of 100 pipe diameters. Upstream tap was positioned 290 pipe diameters from the mixer. Structure frequency was determined from Power Spectrum Density (PSD) of auto-covariance function; structure velocity was estimated by cross-correlating two signals separated 0.002 m apart. It is shown that flow structure becomes more periodic as liquid viscosity increases. Air/more viscous liquid two-phase flow exhibits higher structure frequency than air/water two-phase flow maintained at similar conditions. On the other hand, structure velocity decreases with increase in liquid viscosity due to lower liquid phase momentum. Analyzing the time series by considering the variations

in amplitude and frequency space to generate Probability Density Function (PDF) provides additional detail. The plot of PDF against void fraction for air/water and air/12 mPa s viscous liquid at same liquid and gas superficial velocities of 0.64 m/s and 0.27 m/s shows a marked shift between the void fractions as liquid viscosity increases. For air/12 mPa s two-phase flow, the PDF is characterized by a single, serrated, taller, narrower peak, with void fraction varies from 0.18 to 0.40, finger-printing bubbly flow. In the case of air/water, the PDF displays a twin peak distribution typical of slug flow, with an average void fraction of 0.80 and a long tail that extends to zero void fraction. Next, activity in the second campaign is summarized.

In the second campaign, dynamic drop concentration, Sauter Mean Diameter (SMD) and Mass Median Diameter (MMD) were measured in annular two-phase flow for the first time employing a new generation instrumentation based laser diffraction technique. The measurement was conducted with air/water flow on a 0.019 m internal diameter vertical special test section. The gas superficial velocity was varied systematically from 13 m/s to 43 m/s at fixed liquid superficial velocities of 0.05 and 0.15 m/s. Additional tests were carried out with the gas velocity fixed at 14 m/s for liquid superficial velocities range between 0.03 and 0.20 m/s.

Conductance probes were used to log the void fraction and the film hold-up. Spraytec was used to measure the drop concentration and the characteristic drop diameters (SMD & MMD). Pressure drop was investigated and measured between two pressure taps separated 1.55 m apart in the vertical direction. All instruments were linked and synchronized to achieve simultaneous data acquisitions such that one-to-one correspondence was established between the time varying film hold-up, drop

concentration and the system pressure drop. The time averaged values extracted from the dynamic signals were compared with data from previous measurements. They were found to be in good agreement. Sauter Mean Diameter (SMD) and entrained fraction display an obvious similar signature characterized by inflection points at the transition to co-current annular flow when gas superficial velocity is 21 m/s. Mass Median Diameter (MMD) on the other hand detected the transition to mist annular flow which occurs at a gas superficial velocity of 30 m/s. Additional detail is revealed when the variation in the time series of the Mass Median Diameter (MMD) is considered in amplitude and frequency space to generate Probability Density Function (PDF). The PDF of the MMD changed from multiple maxima/peaks to single maximum/peak signifying transition from heterogeneous/ multi-modal to homogeneous/mono-modal drop size distribution at a gas superficial velocity of 30 m/s. This change has been linked to transition from co-current to mist annular flow. Beyond the transition, momentum of drops produced from thinner film start decreasing as the drop size decreases as gas superficial velocity increases. However, an exact opposite trend is observed in the case of drop momentum produced from thicker film. The entrained drops within this regime exhibit higher mass density, momentum and drop concentration/ entrained fraction as a result of greater interaction with the gas core.

A relationship between pressure drop and entrained fraction is observed to follow a power law having minimum at a point where pressure drop is minimum marking transition to mist flow at gas superficial velocity of 30 m/s and entrained fraction of 0.20. Visualization studies of the high speed videos recorded during the experiment show that at a fixed gas superficial gas velocity of 14 m/s, below liquid superficial velocity of 1.2 m/s, wisps are seen in region classified as churn flow regime by

existing flow pattern transition models. The observed wisps have been linked to the incomplete atomization of liquid film principally caused by dominance of gravity over drag force. Huge waves dominate with high amplitude and high standard deviation the film hold-up.

At another level of analysis, fluctuation of film hold-up and drop concentration with time is considered. Both show evidence of periodicity, film thickness being more periodic than drop concentration. Thus, frequency analysis is carried out to establish the relationship between drop and wave frequency. Surprisingly, wave frequency is seen to be higher than drop frequency most cases examined. This is due to the rate of drop coalescence and turbulent diffusion in the dispersed phase. Traditional Strouhal number-Lockhart-Martinelli parameter provides a good correlation for the wave frequency. However, correlating drop frequency using same approach proves inadequate. Second campaign, therefore, concludes that the subtle changes in Sauter Mean Diameter (SMD), entrained fraction and the Mass Median Diameter (MMD) make the evidences of flow pattern transition within annular flow more compelling.

In the third and the last campaign, flow structures were investigated in the most complex flow geometry used. The test section is made up of a 0.005 m internal diameter vertical dividing junction; located 1.3 m vertically downstream of the two-phase mixer constitutes the test section. The junction splits and mal-distributes the incoming two-phase flow into the vertical run and the horizontal side arm. The fraction of gas and liquid taken off at the horizontal side arm determines the measured flow splits.

Effect of liquid viscosity on partial separation of phases between the outlets of the junction has been investigated by testing with air/water and air/viscous liquids. The

liquid phase viscosity has been increased systematically from 1 to 36 mPa s. Test matrix implemented varied between 0 - 32 m/s and 0.003 - 1.3 m/s for gas and liquid phase superficial velocities respectively.

Plotting corresponding liquid hold-up against gas superficial velocity for each take off point elucidates churn – annular transition boundary at gas superficial velocity of 15 m/s. Liquid hold-up is seen to increase as liquid viscosity and fraction of gas taken off increases suggesting corresponding increase in partial separation of phases. However, effect of liquid viscosity does not become significant until a threshold is exceeded when fraction of gas taken off equals 0.40. In all cases examined, periodicity of flow structures is observed to increase as liquid viscosity increases.

Considering the results of the three investigations carried out, it can be concluded that periodicity of two-phase flow structure increases as liquid viscosity increases and transition to co-current annular flow occurs at gas superficial velocity of 21 m/s.

LIST OF PUBLICATIONS

Alamu, M.B., G. P. Van der Meulen, Azzopardi, B.J. ,2010. Dynamic Drop Size Measurement in Vertical Annular Two-Phase Flow. 7th International Conference on Multiphase Flow ICMF 2010, Tampa, FL USA, May 30-June 4, 2010.

Alamu, M.B., G. P. Van der Meulen,Hernandez Perez, V., Azzopardi, B.J. (2010). Investigation of Liquid Loading in Gas Well: Simultaneous Measurements of Drop Size, Film Thickness and Pressure Drop. Proceedings of the ASME 2010 29th International Conference on Ocean, Offshore and Arctic Engineering, OMAE2010, June 6-11, 2010, Shanghai, China.

Alamu, M.B., Khiang. N., Azzopardi, B.J.,2007:"Effects of Liquid Viscosity on Two-Phase flow Split at a T-Junction with Vertical inlet Pipe," paper 294, Int.Conf.Multiphase Flow 2007, Leipzig, Germany, 9-13 July

Alamu, M.B., G. P. , Azzopardi, B.J. ,2010. Effect of Entrained Fraction, Annular Film thickness and Pressure Drop on Gas & Condensate Production J.Energy Res. Tech. (Submitted).

Alamu, M.B., Azzopardi, B.J. ,2010. Dynamic Drop Concentration Measurement in Annular Two-Phase Flow. Int. J.Heat & F.Flow. (Submitted).

ACKNOWLEDGEMENTS

All praises due to almighty, the beneficent, the merciful. My profound appreciation goes to Prof. B. J. Azzopardi for his supervision, guidance and patience and supportive roles in played throughout the programme. His constructive suggestions and ideas contributed immensely to the successful completion of this PhD thesis. Special gratitude to Amanda for making available some of her data used on T-junction experiment Babatunde Oloro and Simisola Oniru are gratefully acknowledged for providing air-sugar solution data. Dr. Ryuhei Kaji support is gratefully acknowledged. Supports received from the School of Chemical & Environmental Engineering and the International Office, The University of Nottingham are gratefully acknowledged.

Special acknowledgement goes to Dr.Paul Kippax and Dr. Ann Virden of Malvern Instruments, UK, for loan of the Spraytec used in the drop size measurement and for providing quality technical support throughout the experiments. Support received from Cal Gavin Ltd. (Process Intensification Engineering) is also gratefully acknowledged.

This work has been undertaken within the Joint Project on Transient Multiphase Flows and Flow Assurance. I wish to acknowledge the contributions made to this project by the UK Engineering and Physical Sciences Research Council (EPSRC) and the following: - Advantica; BP Exploration; CD-adapco; Chevron; ConocoPhillips; ENI; ExxonMobil; FEESA; IFP; Institutt for Energiteknikk; PDVSA (INTEVEP); Petrobras; PETRONAS; Scandpower PT; Shell; SINTEF; StatoilHydro and TOTAL. I sincerely express my gratitude for this support."

I like to thank Prof Cem Sarica for providing the opportunity to visit Tulsa University Fluid Flow Project (TUFFP). The placement at Tulsa University Fluid Flow Project, Tulsa, Oklahoma, USA was made possible through the Business-Engineering and Science Travel Scholarship (BESTS), Roberts Money of the Graduate School, University of Nottingham. This sponsorship is gratefully acknowledged. I also like to thank Prof Ovadia Shoham, head of Tulsa University Technology Separation Projects (TUSTP) for his exciting discussion during my stay in Tulsa.

Special thank goes to the laboratory technicians - Phil, Fred, Mick, Reg, Paul, Vikki and Marion for their supportive roles in the laboratory. Paul your effort in aligning the laser is gratefully appreciated.

My profound gratitude to Valente for his wonderful support. Peter, Safa, Muktar, Nasir, Lokman, Seun and Mayowa have all been wonderful colleagues. They have all contributed immensely to make this programme a success.

Finally, I like to express my sincere appreciation for the supportive role of Dr. Nasiru Idowu and other brothers during the programme.

This work is dedicated to my family: my dad for visionary suggestion, my grand mother for her passionate love and care, my mum for her support and encouragement, my brothers and sisters for their kindness and support and to Kudroh for her love and support throughout the programme.

Table of contents

List of figures

List of tables

Chapter 1

Introduction

1.1 Flow Assurance

With ever growing world population having improving quality of life, energy consumption is projected to increase year after year. The situation implies that hydrocarbon stocks, including both commercial and strategic reserves of lighter oils are running out. We are left therefore, with no robust alternative but to harness heavy oil resources which present themselves as inevitable option to meet the future energy demand. Unfortunately, exploration and production of heavy oil and their associated gas poses a lot of environmental and flow assurance challenges.

Flow is only assured when the energy driving the flow is greater than the resistance to flow. Flow assurance is a term which encapsulates a number of fluid flow, heat transfer, production, and chemistry issues that have important implications for the transportation of hydrocarbons from reservoirs to processing facilities, Pickering et al. (2001).

In oil and gas production, deepwater fields present similar flow assurance challenges to those encountered in the traditional shallow water developments. Many of the problems encountered during the development of reservoirs located in deep waters, stem from the characteristics of the reservoirs as some of them are located in turbidite sandstone formations with vast water depth. The depth of the formation below the seabed is often quite small. Usually, extraction requires intelligent completion and Floating Production, Storage and offloading Vessels (FPSO) as shown in Figure 1.1. These reservoirs are

characterised by low-energy having relatively low pressures and temperatures compared to conventional reservoirs. Elf's Girassol and Dalia reservoirs in deepwater offshore Angola are good examples where development posed great flow assurance implications because not only is pressure for driving the flow limited, the low temperature implies greater difficulties with heat conservation and the avoidance of solid formation especially hydrates and waxes, Pickering et al. (2001).

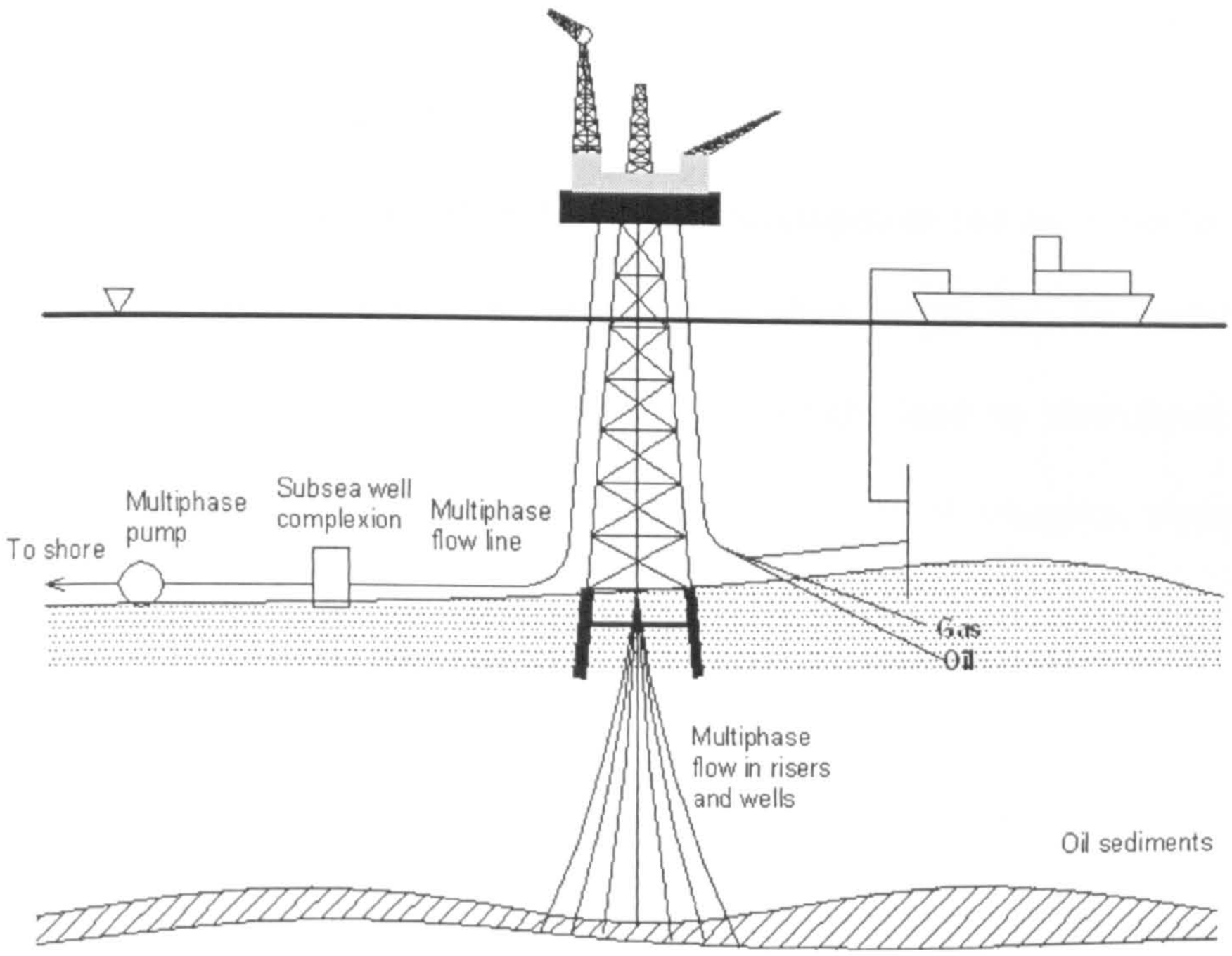

Figure 1.1: Schematic diagram of offshore operation with Floating Production, Storage and offloading Vessels (FPSO) and Dry Completion Unit (DCU).

Strand et al. (2000) reported some of the physical properties of heavy oil produced from the British North sea production facilities. Average samples have 19°API Gravity and a viscosity ranging typically from 200 mPa s at processing conditions of 90° C to close to 2000 mPa s at a temperature of 5°C (sea water temperature). The viscosity can be as high as 10 000 mPa s at reservoir temperature especially in the deepwater environment.

In this hostile environment, design of production tubing and transportation system for the production of oil demands special consideration on account of high fluid viscosity with special attention given to slug flow. This is primarily because of the liquid phase intermittency along the pipe during production. The piping system (e.g. as in Figure 1.1) must be able to withstand the fluctuating nature of the slug flow and at the same time be able to accommodate the pressure drop associated with fluid movement in the pipe. Unmitigated and increasing pressure drop may cause frequent shut-ins and inevitable loss of revenue from production.

The increase in riser height in deepwater development has an important implication for system stability. In particular, increases in riser height can be destabilizing, causing multiphase slugging which in some cases might lead to shut-down of the facility. Increasing the riser height also increases the severity of slugging, measured in terms of the magnitude of pressure fluctuations and slug sizes.

1.2 Periodic Structures in Gas-Liquid Flow

Interaction between gas and liquid phases in two-phase flow provokes complex, highly deformable interface and configurations usually difficult to describe. The simultaneous flow of gas and liquid in a pipe for instance can produce a large number of spatial configurations of the phases due to the deformable interface between them. These spatial configurations give rise can become periodic over time leading to chains of interrelated flow structures. The chain of these interrelated flow structures is usually referred to as phase distribution in flow assurance.

Examples of these periodic structures are void waves in bubbly flow, liquid slugs and

Taylor bubbles in slug flow, huge waves in churn flow, disturbance waves in annular flow and wisps in wispy annular flow. The void waves, slugs, huge waves, disturbance waves and wisps, have unique characteristic velocities and frequencies which can be used to classify them into flow patterns. Thus, information about this periodic structure is valuable to reconstruct the overall pressure drop in any multiphase flow system.

The focus of this thesis is on these periodic structures. This thesis also examines dependence of flow structures dependence on flow rates, fluid physical properties and flow channel geometry.

In practice, phase distribution in a pipe is usually determined from periodic structure extracted from dynamic data logged by the sensor, when the sensor sc ans the flow structures during the passage of two-phase flow. From very detailed measurements, Sekoguchi and Mori (1997) have shown that more than one of these structures can occur simultaneously. The void waves, slugs, huge waves, disturbance waves and wisps, have unique characteristic velocities and frequencies which can be used to classify them into flow patterns. Flow pattern maps are generated based on information from two-phase flow periodic structures. Dependence of the structure velocities and frequencies on flow rates and methods which link them with flow pattern transitions have been reported, Azzopardi (2004). This valuable information can be used to reconstruct the overall pressure drop in any multiphase flow system. Based on the uniqueness of the flow structure, flow patterns and flow pattern maps are discussed next.

1.3 Flow Patterns in Vertical Pipes

Gas-liquid two-phase flow is widely encountered in petroleum, chemical, nuclear, space, and geothermal industries. Two-phase flow is encountered in a wide range of engineering applications. For instance, in the petroleum industries, the common problems associated with gas-liquid two-phase flow include: calculation of flow rate, pressure loss, and liquid holdup in the pipeline. These parameters are essential in design of production tubing, gathering and separation system, sizing of gas lines, heat exchanger design and gas condensate line design, Brown (1977). It has been the design methods for these applications that have stimulated extensive two-phase flow research since 1950s.

In vertical pipes, two-phase flows can be classified into five major flow regimes:

- Bubble flow
- Slug flow
- Churn flow and
- Annular flow
- Dispersed-bubble flow

Figure 1.2 shows common vertical gas-liquid two-phase flow normally encountered in pipes in the industry. Stratified flows do not occur in vertical gas-liquid two-phase flow. For horizontal flow, the patterns encountered are shown in Figure 1.3 while Figure 1.4 indicates flow patterns for the entire pipe inclinations.

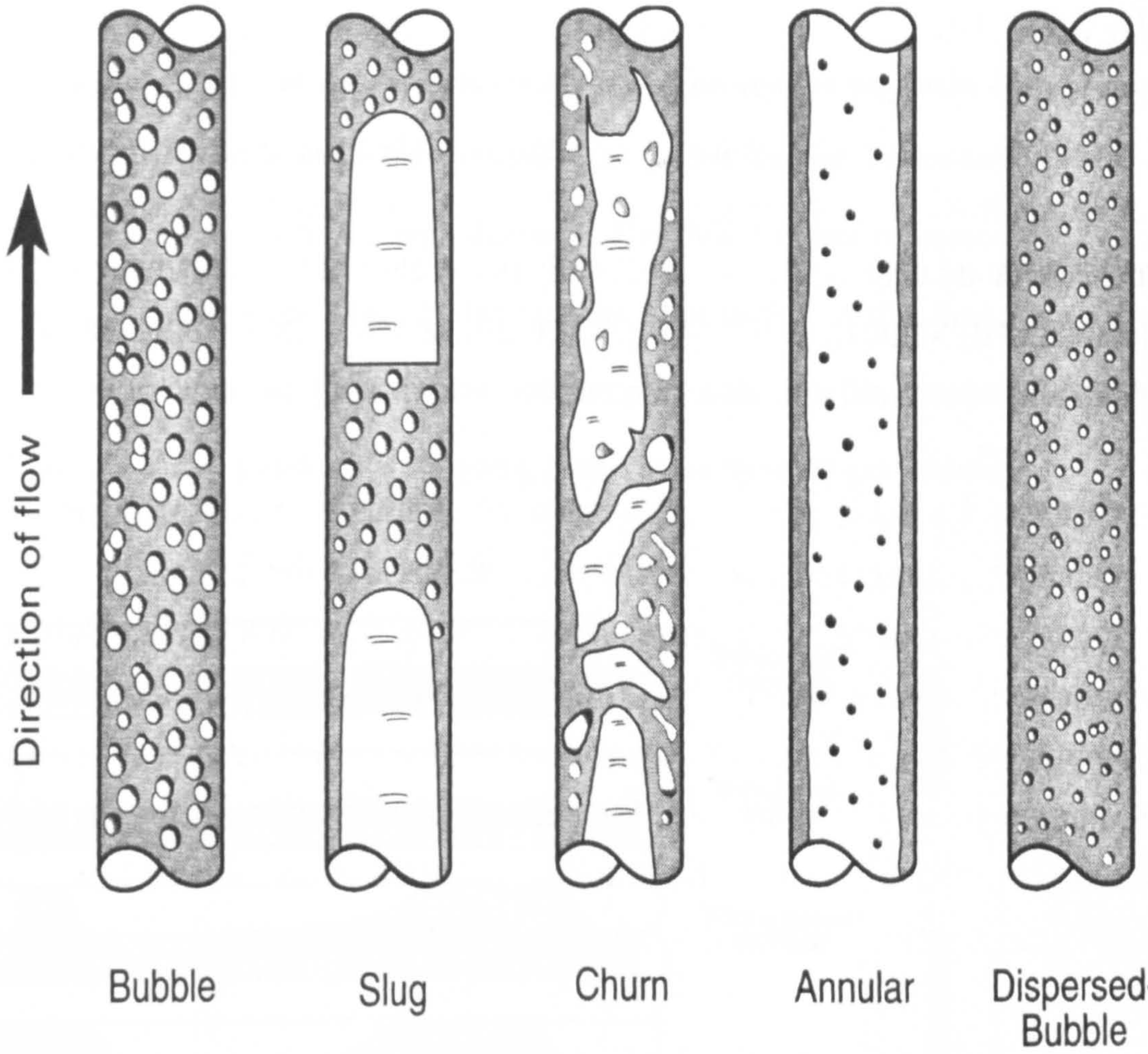

Figure 1.2: Flow Patterns in vertical and inclined pipes, Shoham (2006).

1.3.1 Bubble Flow

In bubble flow, the gas phase is dispersed into small discrete bubbles, moving upward in a zigzag motion, in a continuous liquid-phase. In vertical flow, the bubble distribution is approximately homogeneous through the pipe cross section. Bubble flow occurs at relatively low liquid rates, with low turbulence, and is characterized by slippage between the gas-and the liquid-phases, resulting in large values of liquid holdup.

1.3.2 Slug Flow

The slug flow regime in vertical pipes is symmetric around the pipe axis. Most of gas-phase is located in a large bullet-shaped gas pocket termed Taylor-bubble with a diameter almost equal to the pipe diameter. The flow consists of successive Taylor bubbles and liquid slugs, which bridge the pipe cross section. A thin liquid film flows downward between the Taylor-bubble and the pipe wall. The film penetrates into the following liquid slug and creates a mixing zone aerated by small gas bubbles.

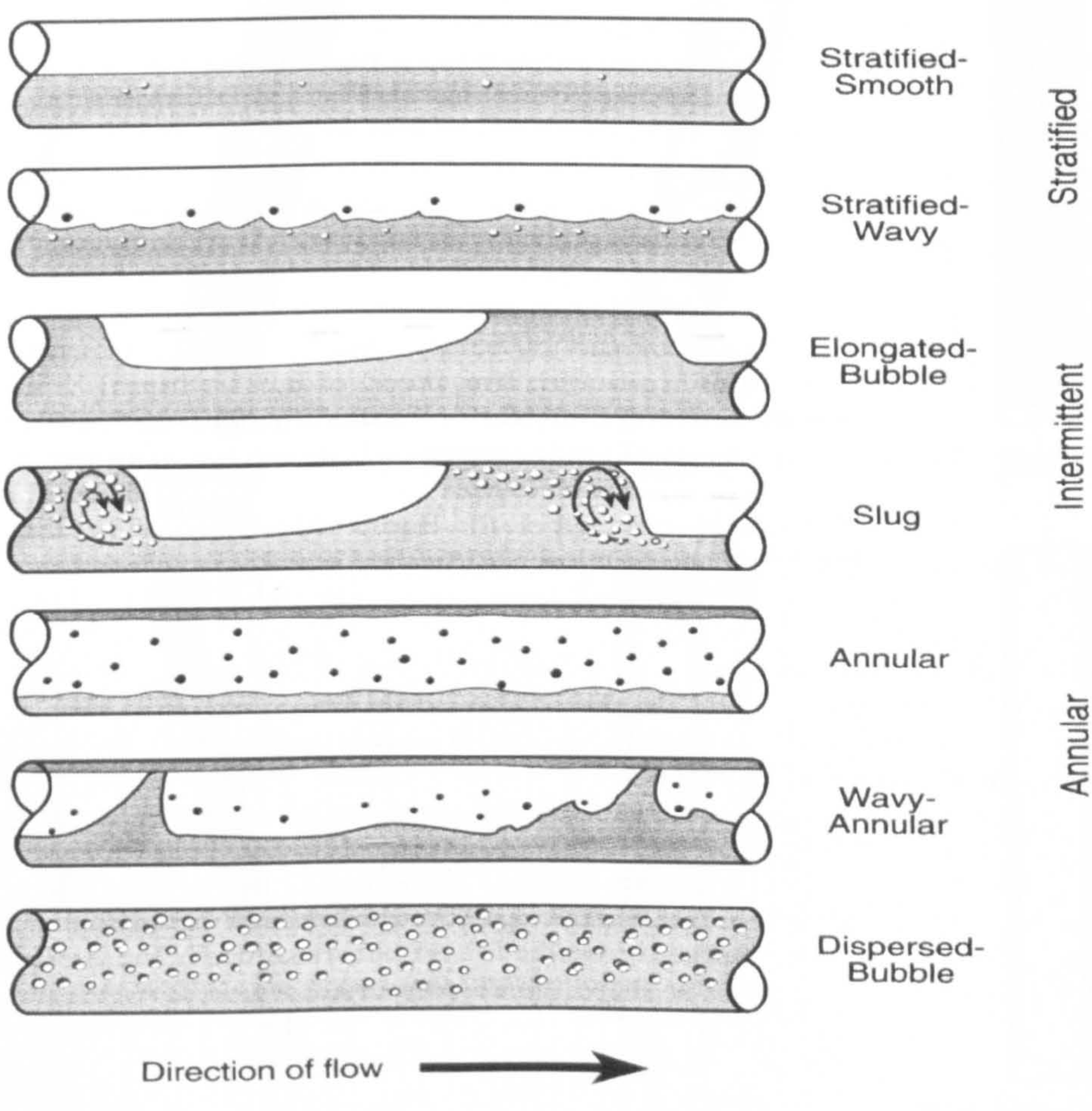

Figure 1.3: Flow Patterns in horizontal and near horizontal pipes

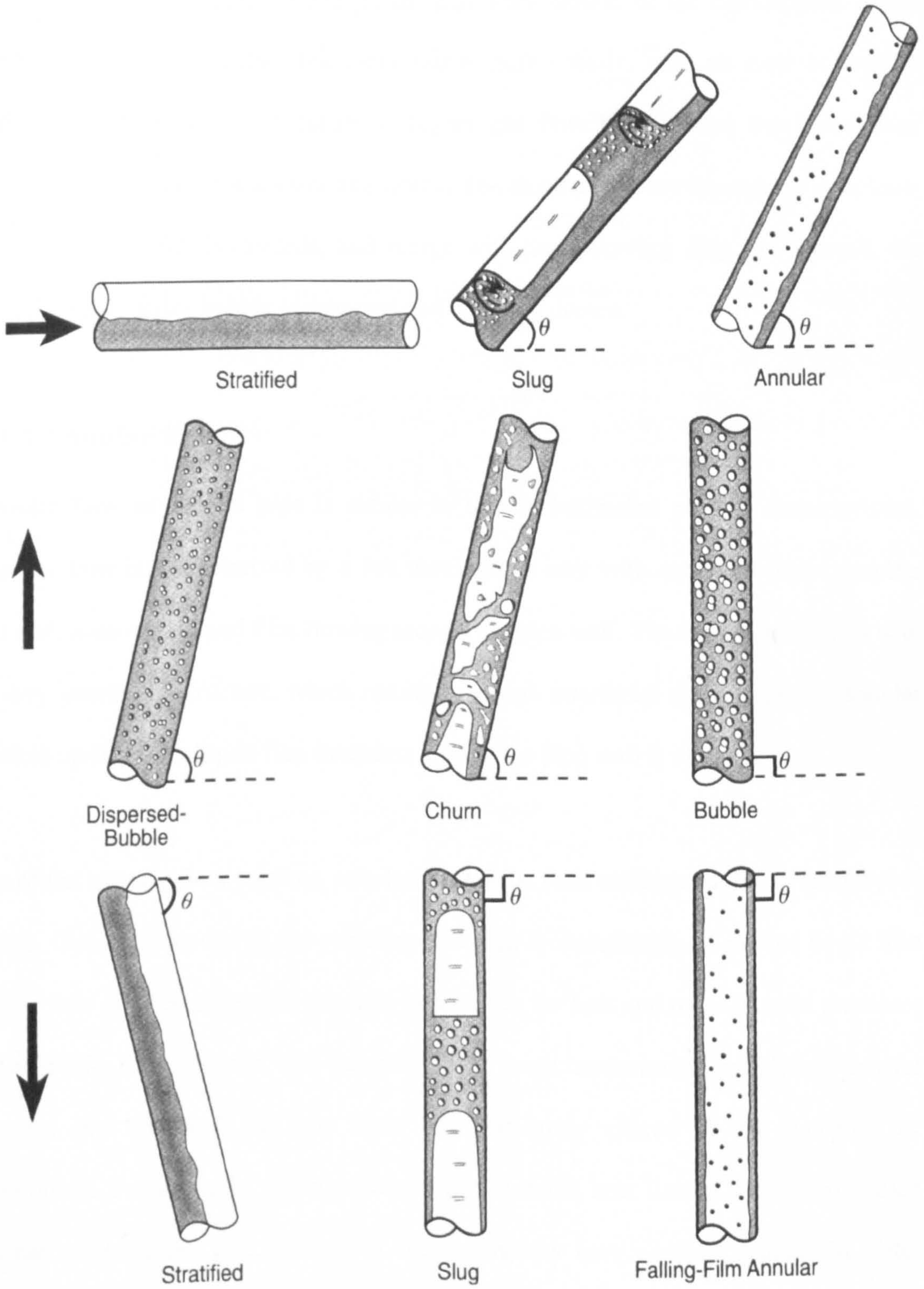

Figure 1.4: Flow Patterns in entire range of inclinations, Shoham, (2006).

1.3.3 Churn Flow

This flow pattern is characterized by an oscillatory motion of the liquid-phase. Churn flow is similar to slug flow but looks much more chaotic, with no clear boundaries between the two phases. It occurs at higher gas flow rates, where the liquid slugs bridging the pipe become shorter and frothy. The slugs are blown through by gas-phase, and then break, fall backwards, and merge with the following slug. As a result, the bullet-shaped Taylor bubble is distorted and churning occurs.

1.3.4 Annular Flow

Annular flow in vertical pipe is similar to that in horizontal pipe in characteristics. Annular flow is characterized by a fast moving gas core with entrained liquid droplets and a slow-moving liquid film flowing around the pipe wall. The flow is associated with a wavy interfacial structure, which results in a high interfacial shear stress. In annular vertical up-flow, the liquid film thickness around the pipe wall is uniform.

Out of the existing flow patterns, annular flow is the least understood due to its complex nature. Good knowledge of the conditions leading to atomization of part of liquid film by gas flow is of considerable practical importance for heat and mass transfer processes in two-phase flow systems. The mechanisms of mass, momentum, and energy transfer between the film and gas core flow is significantly altered by the inception of entrainment. For example, the burnout and post-burnout heat flux in light-water cooled nuclear reactors, the effectiveness of the emergency core cooling systems in water reactors, and the performance of the film cooling of jet and rocket engines can be

significantly affected by the entrainment of the liquid film into the gas core flow. Numerous other examples where the atomization and entrainment of the liquid film imposes operational and performance limitations could be found in various chemical engineering systems.

In the petroleum industry, gas well operates in annular flow. However, liquid loading into the gas well and in the gas condensate lines has been identified as a common problem that lowers productivity of nearly all the gas wells in the world. Again the problem persists because of poor understanding of annular flow mechanisms. Design of process equipment requires knowledge of first-order parameters such as pressure drop. Unfortunately, pressure drop can only be modeled successfully if and only if the behavior of entrained droplet in the gas core is understood. Annular flow forms the central theme of this thesis. Contribution has been made to the existing annular flow literature as detailed in Chapter Four.

1.3.5 Dispersed-Bubble Flow

Another flow pattern which is common to both vertical and horizontal flow is Dispersed-Bubble flow. Similar to horizontal flow characteristics, Dispersed-Bubble flow in vertical and sharply inclined pipes occurs at relatively high liquid-flow rates, under which conditions the gas-phase is dispersed as discrete bubbles into the continuous liquid-phase. For this flow pattern, the dominant liquid-phase carries the gas bubbles, and no slippage takes place between the phases. Hence, the flow is considered

homogenous no-slip. Figure 1.5 shows Dispersed-Bubble Flow as encountered in concentric annulus, among other flow patterns.

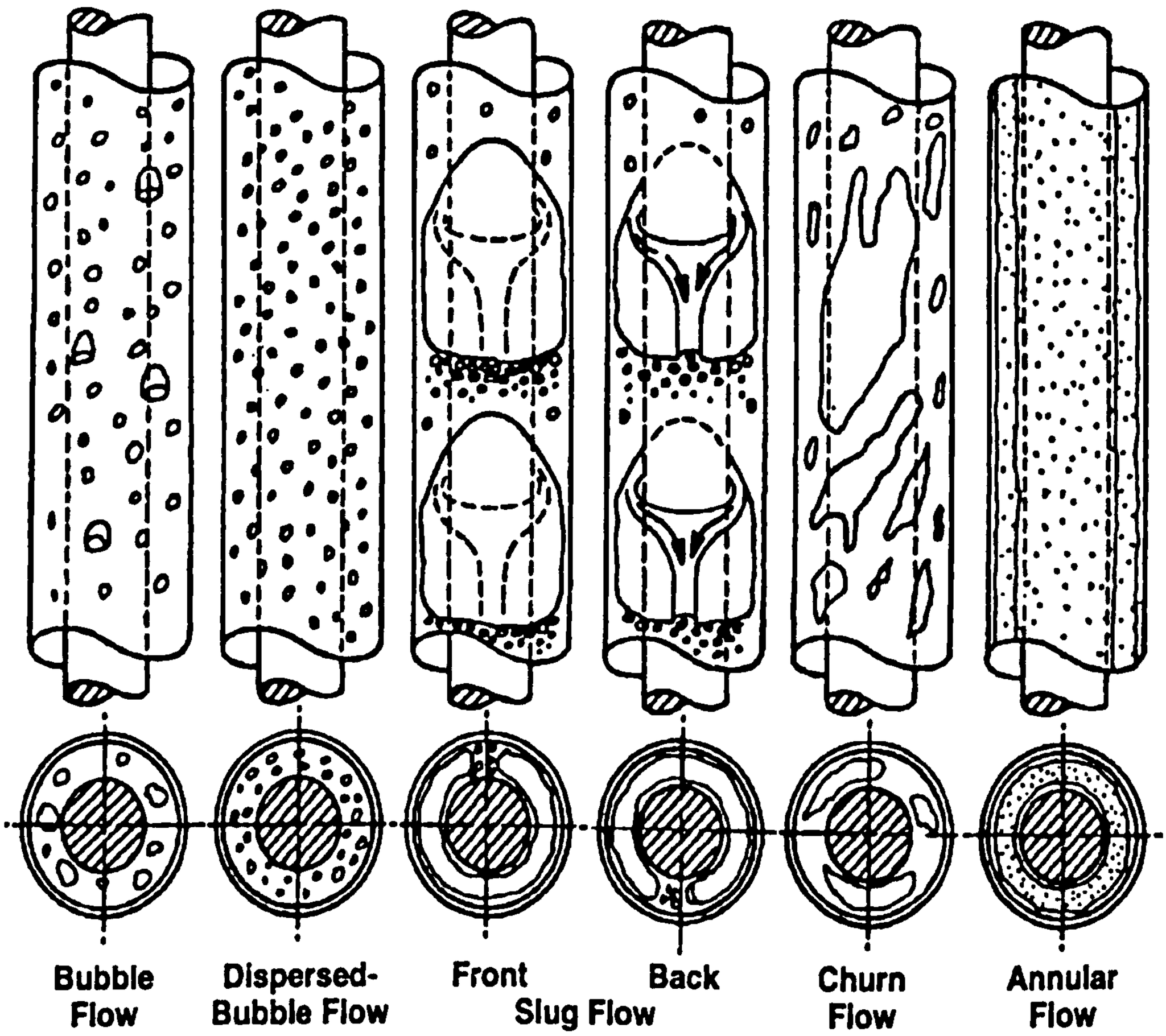

Figure 1.5: Upward Vertical through a concentric annulus

1.4 Flow Pattern Maps

A Flow-Pattern Map is generated when flow parameters (i.e. superficial phase velocities of fluids) are mapped on a 2-D plot, and the transition boundaries between the different flow patterns are clearly demarcated. The Flow-Pattern Map is an earlier empirical approach adopted by researchers for predicting flow pattern. The approach is purely

empirical and determinations of flow pattern are carried out by visual observations. Therefore, their applications are limited and they are only reliable in the range of conditions similar to those under which the data were acquired. Their extension to other flow conditions is highly uncertain. Figures 1.6, 1.7, 1.8, 1.9 and 1.10 show typical flow pattern maps for vertical and horizontal flows.

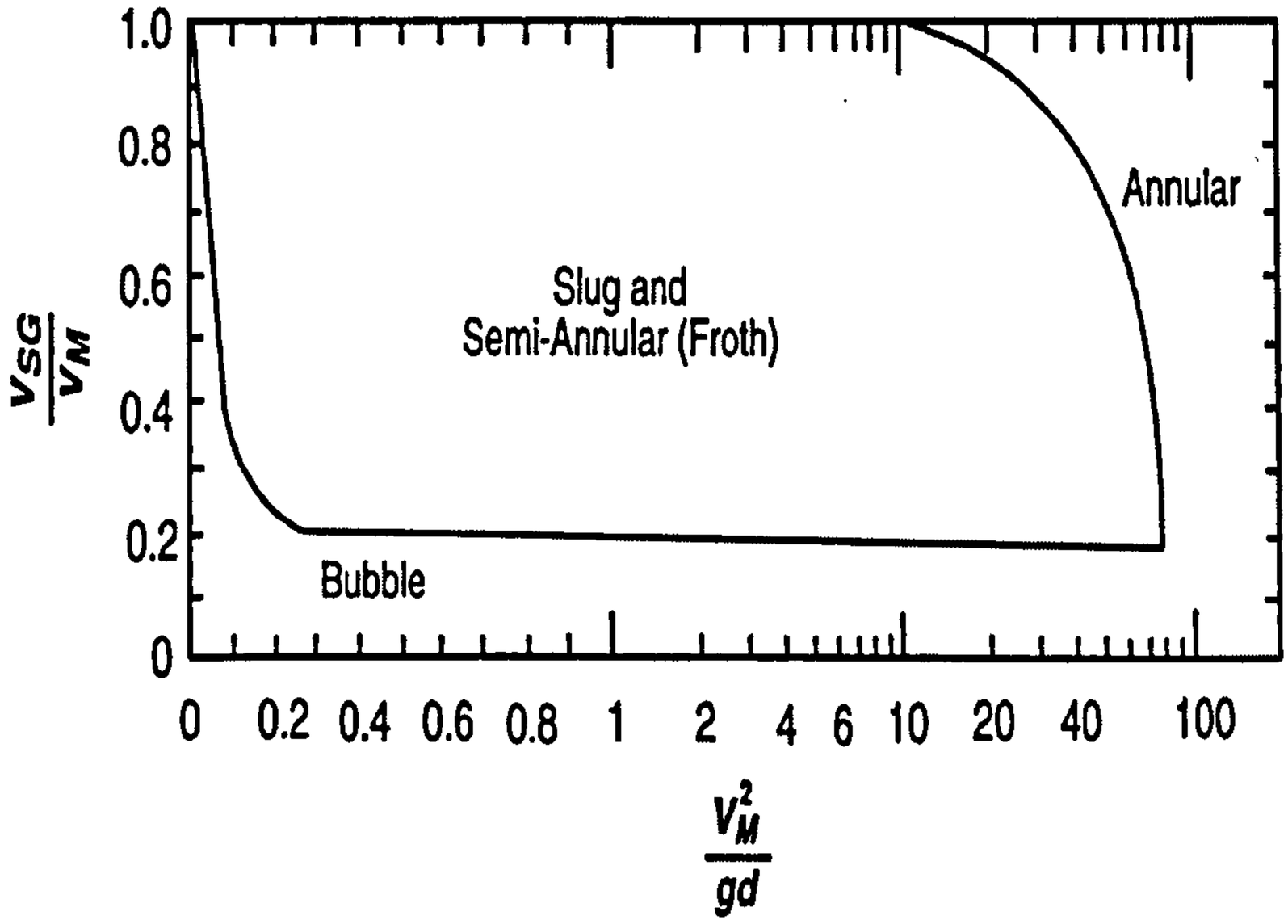

Figure 1.6: Flow Pattern Map Vertical Flow (Griffith and Wallis, 1961)

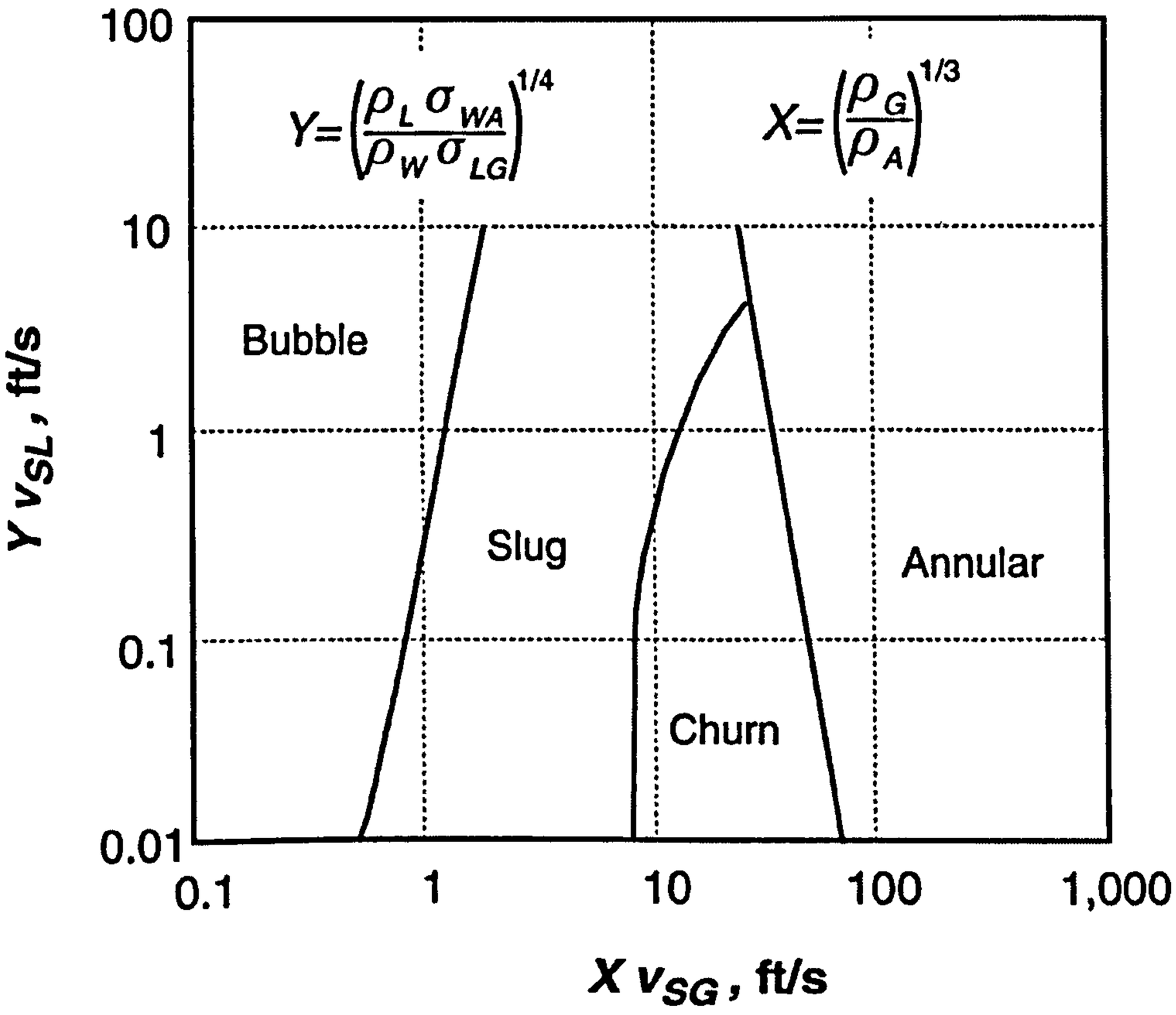

Figure 1.7: Flow Pattern Map for Vertical Flow (Govier and Aziz, 1972)

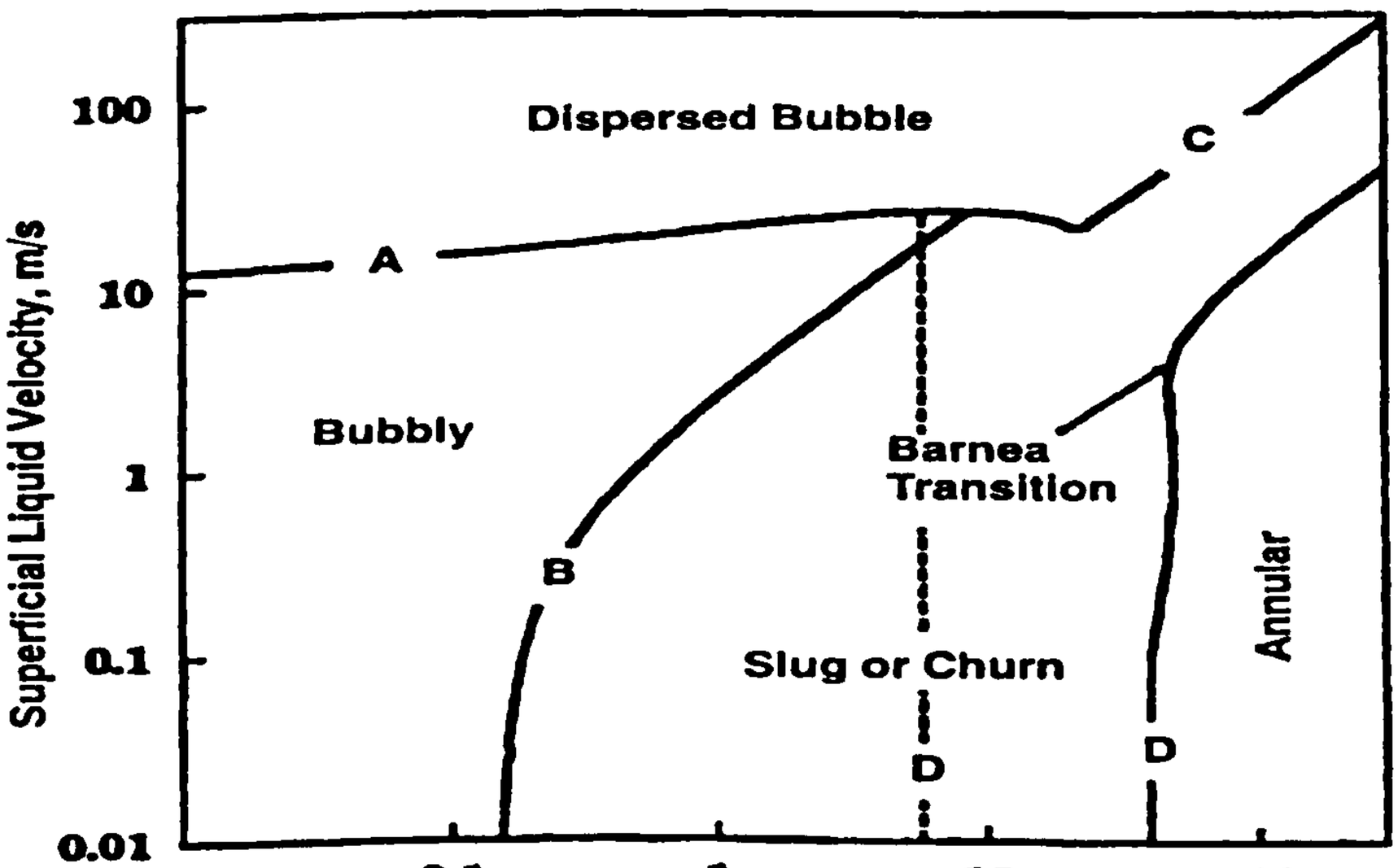

Figure 1.8: Flow Pattern Map Vertical Flow (Taitel – Barnea - Dukler (1980)).

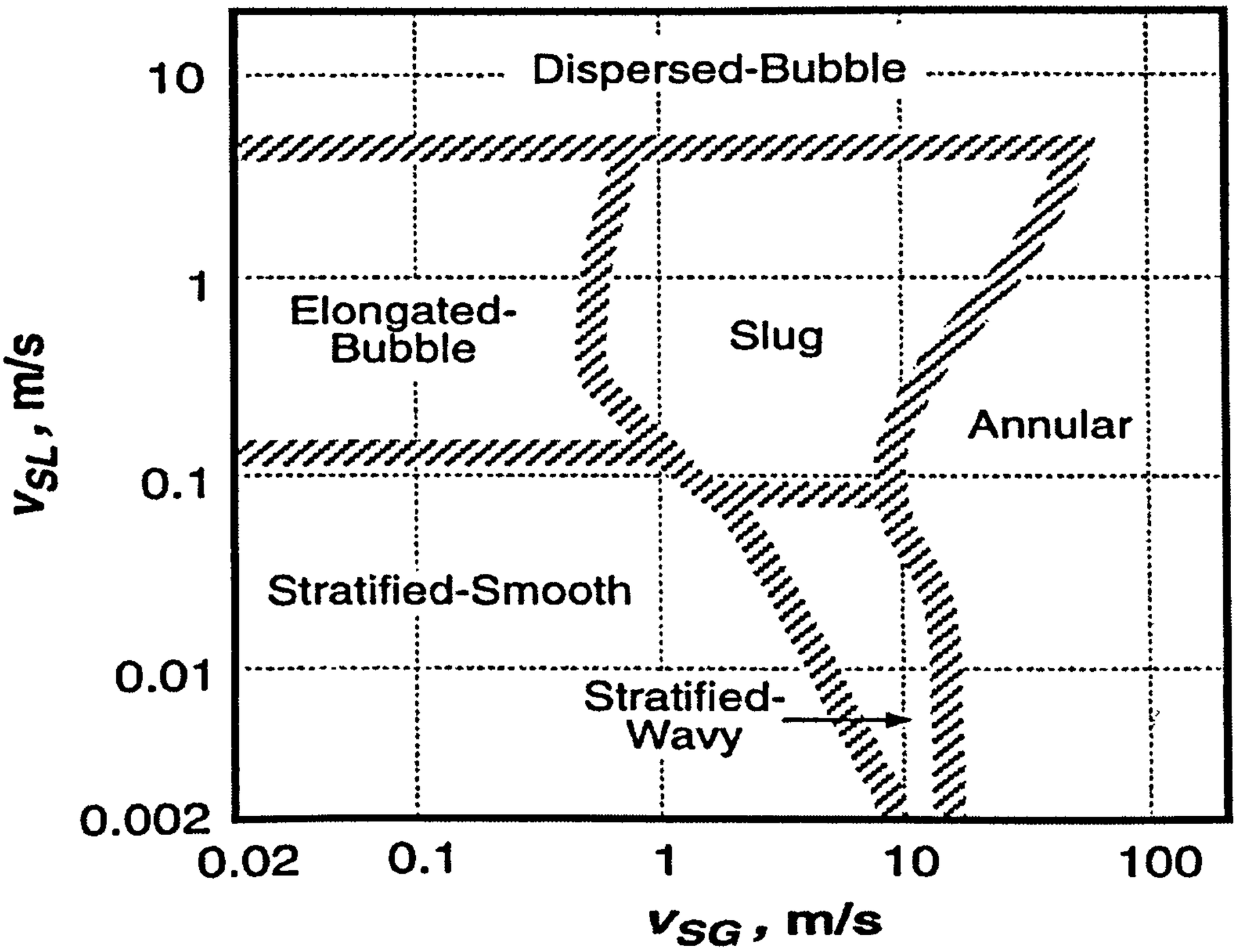

Figure 1.9: Flow-pattern map for horizontal flow (Mandhane et al., 1974)

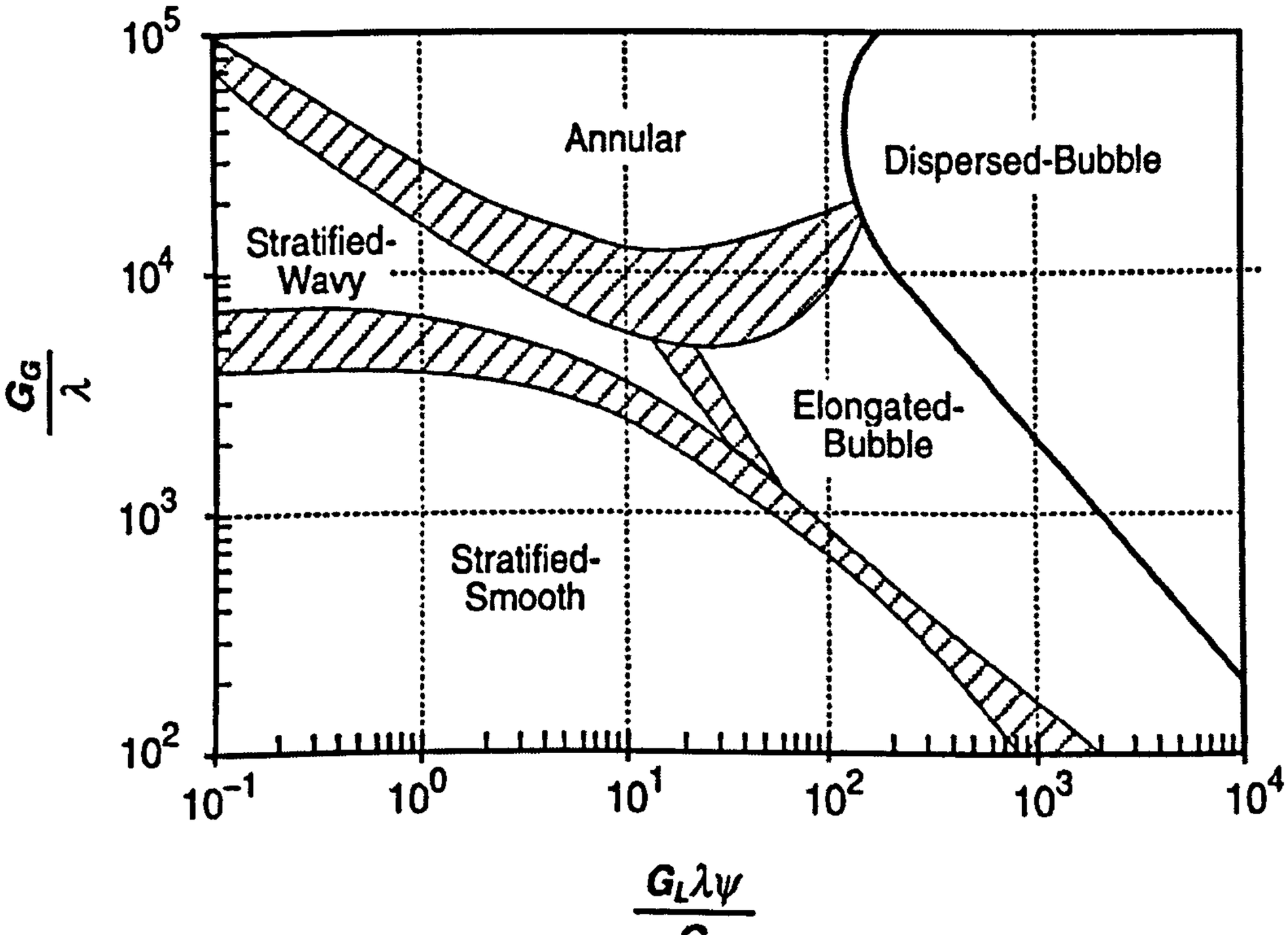

Figure 1.10: Flow-pattern map for horizontal flow (Baker, 1954).

1.5 Aims and Objectives

Three different experimental campaigns were implemented and reported in this thesis:

1. 5mm pipe flow experiments were carried out with air/water, air-glycerol solution and air-sugar solution. Focus is on bubbly, churn and slug flows.

2. 19mm pipe flow experiments which focuses only on measurement of periodic structures in annular flow. Dynamic and time-resolved measurements of drop size and entrained liquid fraction were carried out and reported for the first time using diffraction-based instrument.

3. 5mm T-junction experiments, these involve partial separation of two-phase flow at a vertical T-junction. Air/water, and air-glycerol solutions of various concentrations were used to investigate effect of liquid viscosity on the gas and the liquid take-offs.

The aims of these studies are stated as follows:

1. To use conductance probe technique to acquire void fraction data in order to identify the effect of liquid viscosity on periodic flow structures in pipe flows (5mm and 19mm ID pipes) and T-junction experiments.

2. To use laser diffraction principle to obtain time-resolved drop sizes and entrained fraction in annular two-phase flow.

The objectives for undertaking these studies can be stated as follows:

1. To investigate the effects of liquid viscosity periodic structures on gas-liquid pipe flow and phase splitting at vertical T-junction.

2. To use characteristics of periodic structures to identify and classify flow patterns.

3. To establish relationship between wave (liquid film) and drop frequency by taking simultaneous measurements of film and drop concentration.

4. To use drop size/entrained fraction information to identify and classify flow pattern transition boundaries in annular flow regimes

5. To establish relationship between pressure drop and entrained liquid fraction

1.6 Structure of the Thesis

In order to achieve the objectives stated above this thesis has been structured into eight different Chapters. Chapter One is the introduction emphasising the importance of flow assurance. Chapter Two of this report addresses state-of-the-art of two-phase flow literature review of relevant publications. Chapter Three focuses on 5 mm ID pipe flow experiment. Chapter Four discusses experimental methodologies adopted including detailed description of test section for simultaneous measurements of void fraction, pressure drop and drop size/entrained fraction on 19 mm ID facility. Chapter Five presents the wave dynamics in annular two-phase flow. Chapter Six focuses on wave amplitude modelling. Chapter Seven gives detailed description of T-junction experiments. Chapter Eight summarises the conclusions drawn from this study and recommendations for further work.

Chapter 2

Literature Review

Slug and annular flow literature are predominantly reviewed in this section. Slug flow is discussed first and then review of relevant work on annular flow follows. As set out earlier in the objective of this study, more effort is directed to annular flow in order to better understand complex nature of the dispersed phase periodic structures.

Slug flow hydrodynamics is complex with characteristic unsteady flow behaviour, structure velocity, hold-up and pressure distributions. There has been no consensus yet on a unified correlation for predicting frequency of the periodic structure that occurs in slug flow. One of the identified causes of the divergent views on slug frequency model is the paucity of air-viscous liquid data. Most of the existing correlations are based on air/water data whereas periodic structures in slug flow behave differently when experiments are carried out with liquids more viscous than water.

Although the literature is awash with publications on disturbance waves and its evolution in gas-liquid two-phase flow the mechanism of atomization of part of the liquid film to form drops in annular two-phase flow is still not entirely understood. It has been observed that drop creation only occurs when there are large disturbance waves present on the film interface. Woodmansee and Hanratty (1969) observed that ripples on these waves were a precursor to drops. Though it has been reported that drops occur in bursts Azzopardi (2006) all previous drop size or concentration measurements have been

time integrated. In subsequent subsections relevant literatures are reviewed along with descriptions of flow patterns based on the periodic structures associated with them.

2.1 Flow pattern description

Gas-liquid two-phase periodic structures have been used to identify and classify flow pattern. Flows observed in vertical pipe are discussed in detail as follows:

2.1.1 Slug Flow

Slug flow can be related to other flow patterns. It could be said that every flow pattern is represented in slug flow, e.g., the film zone of slug flow resembles stratified or annular flow, and the slug body resembles bubbly or dispersed bubble flow. Schematic of a slug unit in horizontal flow is shown in Figure 2.1. Slug flow is always found in the central part of a flow pattern map, surrounded by the other flow patterns. Therefore, significant progress can be made if the gas-liquid two phase flow of viscous liquid is investigated based on slug dynamics as the starting point.

In production tubing and casing design for an oil well, consideration is always given to slug flow because of the liquid phase intermittency along the pipe. Piping system must therefore be able to safely withstand the fluctuating nature of the slug flow whilst accommodating pressure drop associated with fluid movement in the pipe. Uncontrolled and increasing pressure drop may make a well economically unproductive. Therefore, for effective and optimal design performance, it is important to obtain accurate system properties based on the understanding of mechanism responsible for slug flow as this is the basis for any detailed heat-transfer analysis.

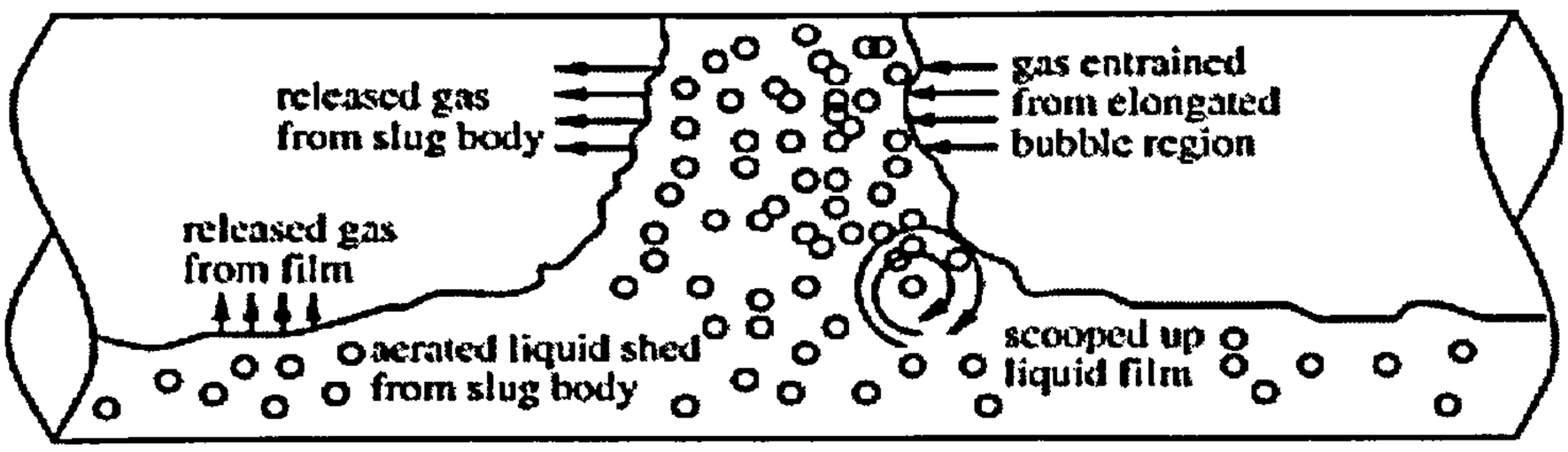

Figure 2.1: Schematics of slug unit in horizontal slug flow.

Xiaodong (2005) used a numerical approach to simulate the flowing field around Taylor bubble with a view to determining Taylor bubble configuration in vertical slug flow. He modified the mechanistic model of Zhang et al.(2003) to obtain the liquid hold-up in wake region, in which the average diameter of small bubbles is estimated by the correlation of Hinze (1955).The length of wake region is set at value which can give the average void fraction of 0.37 in the slug region. This value comes from the assumptions that the highest void fraction is 0.52 and the empirical value is 0.22 when the wake region gets fully developed. He recommended for further studies that surface tension and viscosity effects be included for the determination of configuration of Taylor bubble.

Bonizzi and Issa (2003) investigated gas bubble entrainment in two-phase horizontal slug flow. A model of gas bubble entrainment into slug was proposed in order to improve the accuracy of prediction of slug characteristics. It was found that more studies are necessary for different pipe configurations and flow conditions to improve an important factor in determining characteristics of slug flow. Issa et al. (2006) proposed two improved closure models for gas entrainment and interfacial shear for slug flow in horizontal pipes. The models were validated against experimental data. They however, suggested more detailed studies on high pressure and high gas velocities.

Van Hout et al. (2002) investigated experimentally the translational velocities of elongated bubbles in continuous liquid slug for various flow rates, pipe inclinations and pipe diameters. Measurements were carried out by cross-correlating the output signals of consecutive optical fibre probes and by image process technique.

The velocities of single elongated bubbles in a stagnant and a flowing liquid were measured for comparison with experimental results of elongated bubbles in continuous slug flow case. The results show that measured velocities of single elongated bubbles were in all cases predicted quite well by correlations while the velocities in continuous slug flow, for certain cases, were considerably under predicted. This discrepancy is ascribed to the presence of dispersed bubbles in the liquid slug. They therefore proposed a model to account for this discrepancy.

2.1.1.1 Structure Velocity, V_T

Slug flow in gas-liquid two-phase flow can be described by Taylor (elongated) bubble separated by liquid slugs which in most cases may contain dispersed bubbles. A complete model for slug flow requires information about this Taylor bubble with respect to their propagation or translational velocity (V_T) as shown in Figure 2.2.

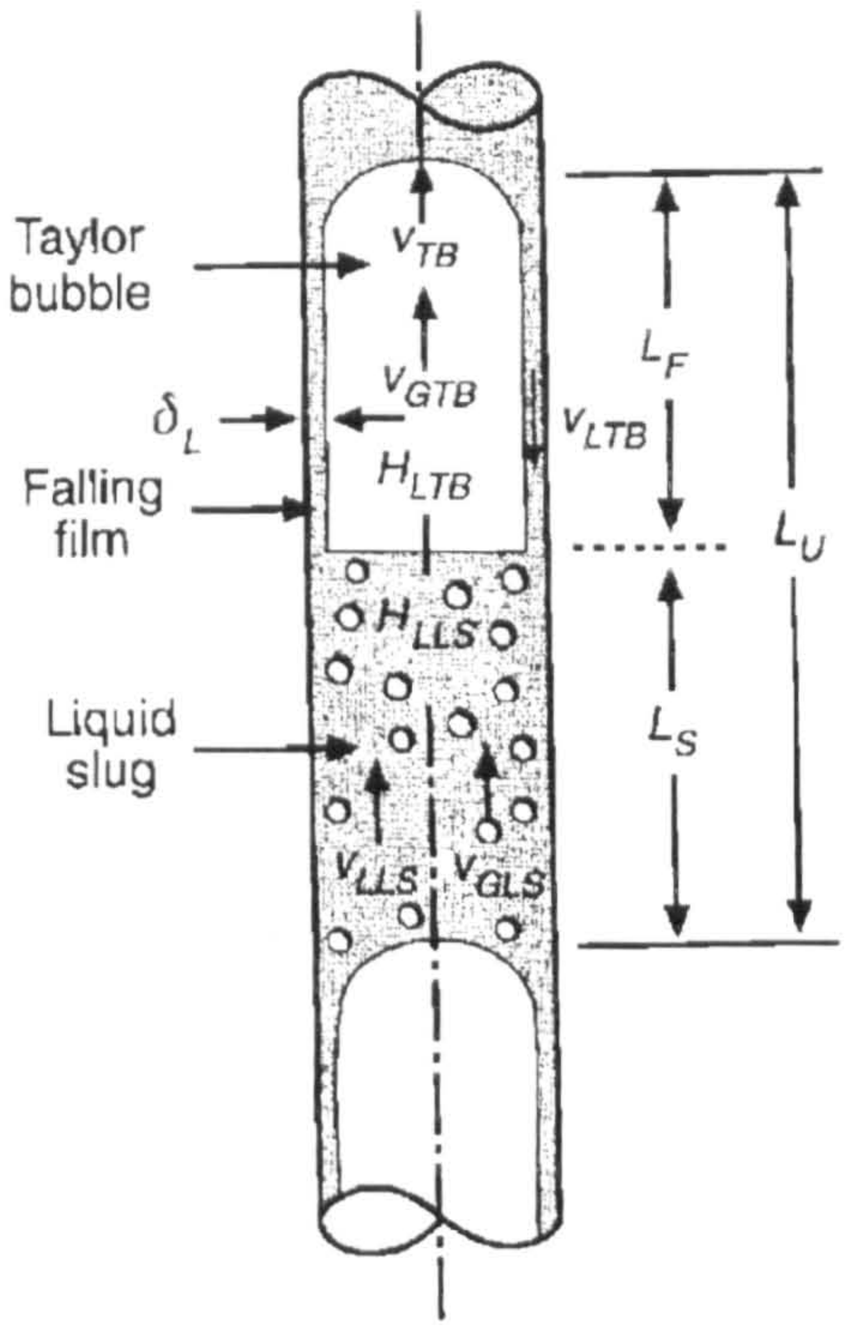

Figure 2.2: Schematic Diagram of slug flow parameters, Shoham(2006).

Nicklin et al. (1962) performed an experiment to determine translational slug velocity with a pipe 25.4 mm ID using water/air as test fluid. They concluded that absolute velocity of a slug can be represented by the expression:

$$V_{TB} = 1.2\,V_{SL} + 0.35(gD)^{1/2} \qquad (2.1)$$

Where:

V_{SL} = average liquid velocity, [m/s]; D = pipe diameter, [m]; g = acceleration due to gravity, [m/s^2].

and proposed the expression for the translational velocity of Taylor bubble as:

$$V_{TB} = C_o V_M + C_1 V_D \qquad (2.2)$$

Or

$$V_{TB} = C_o V_M + V_{Drift} \quad (2.3)$$

The value of the coefficient C_o, of the mixture velocity V_M; and C_1, of the drift velocity, V_D can be determined experimentally. It is generally assumed theoretically that translational velocity is a linear function of mixture (slug) velocity as expressed by Equation (2.3).

For laminar flow the ratio V_{max}/V_{mean} approaches 2.0 and indeed there is strong indication that C_0 increases as the Reynolds number decreases and reaches a value of about 2.0. A more precise theory shows that C_0, for laminar flow, equals 2.27 as reported in Taylor (1961); Collins et al. (1978), for the case where the surface tension is neglected. The exact value of C_0 for turbulent flow, and in particular for laminar flow, is inconclusive.

2.1.1.2 Coefficient of Drift Velocity, C_1

Taitel & Barnea (1990) stated that drift velocity is expected to depend on the liquid viscosity, or the bubble Reynolds number. Zukoski (1966) however, shows that the dependence of the drift velocity on viscosity is negligible for Reynolds number Re > 300 where:

$$Re = \frac{D\, V_{SG}\, \rho_L}{\mu_L} \quad (2.4)$$

Where:

Re = Reynolds number, [-], V_{SG} = superficial gas velocity, [m/s], D = pipe diameter, [m] , μ_L = dynamic liquid viscosity , [kg/m-s], ρ_L = liquid phase density, [kg/m^3]

Davies and Taylor (1950) performed a potential flow analysis around the nose of the elongated bubble and obtained the following expression:

$$V_D = C_1\sqrt{gD} \tag{2.5}$$

The drift velocity of long bubbles moving in a liquid at rest depends primarily on the force that creates the drift, i.e. gravity. However other forces such viscous or surface tension may have secondary effect; therefore many authors have studied the influence of the physical properties of the operating fluids and the pipe inclination to the drift coefficient C_1.

The dependency found is expressed through the general relationship given by Zukoski (1996) as:

$$V_D = C_1\left(N_f, E_o, \beta\right)\sqrt{gD} \tag{2.6}$$

Where:

$$g = \frac{g\Delta\rho}{\rho_L} \tag{2.7}$$

$$N_f = D^{\frac{3}{2}}\sqrt{\frac{\rho\Delta\rho g}{\mu_L}} \tag{2.8}$$

Where N_f is the dimensionless inverse viscosity number. μ_L is the liquid viscosity,

[mPa s or kg/m-s], ρ_L is the liquid phase density, [kg/m^3].β is the pipe inclination, and

E_o is the Eotvos number, which is the ratio of gravitational to the surface tension forces

:

$$E_o = \frac{\Delta\rho g D^2}{\sigma} \tag{2.9}$$

For small diameter pipes, Weber (1981) showed that the surface tension is important as its increase considerably decrease the drift velocity. He proposed a correlation based on Zukoski (1966) data using the following relation:

$$C_1 = 0.54 - \frac{1.76}{E_o^{0.56}} \tag{2.10}$$

Bendiksen (1984) investigated large bubbles in inclined pipes and suggested two different regimes of bubble motion, and therefore confirmed the existence of Ferre (1979) first transition criteria in horizontal pipes. He suggested liquid based Froude number to track the transitions between these two bubble regimes. The Froude number can be expressed as:

$$Fr_L = \frac{V_{SL}}{\sqrt{gD}} \tag{2.11}$$

Where: J_L = superficial liquid velocity, [m/s], Fr_L = liquid Froude number, [-],

g = acceleration due gravity, [m/s^2], D = pipe diameter, [m].

He suggested further this transition might occur at a critical value of 3.5 and validated his model for all pipe inclinations as expressed below:

$$C_1 = \begin{cases} 0.54\cos\beta + 0.35\sin\beta, \ldots\ldots\ldots Fr_L < 3.5 \\ 0.35\sin\beta, \ldots\ldots\ldots\ldots\ldots\ldots\ldots Fr_L > 3.5 \end{cases} \quad (2.12)$$

Theron (1989) proposed a continuous form of Equation (2.12) from Bendiksen (1984). This is particularly useful to avoid problem of discontinuity at translational Froude number during numerical calculations.

Theron's idea can be expressed as:

$$C_1 = \left(-0.5 + \frac{0.8}{\Gamma}\right)\cos\beta + 0.35\sin\beta \quad (2.13)$$

β is the pipe inclination from horizontal and

$$\Gamma = 1.0 + \left(\frac{Fr_M}{Fr_C}\cos\beta\right)^{10} \quad \text{And} \quad Fr_c = 3.5 \quad (2.14)$$

while:

$$Fr_M = \frac{V_M}{\sqrt{gD}} \quad (2.15)$$

2.1.1.3 Mean Bubble Motion Coefficient/Flow distribution Coefficient, C_o

The parameter C_o in the bubble translational velocity equation is a distribution coefficient related to the velocity profiles in dispersed systems. It may be closely

approximated by the ratio of the maximum to the mean velocity in the liquid ahead of the bubble. The exact value of C_o is not clear for all flow conditions and reported experimental values spread considerably from 1.02 to 1.35. Hale (1994) attributed this to the fact that the plot of translational velocity V_T versus the mixture velocity V_M is not perfectly linear, but instead bends very slightly upwards, Bendiksen (1984).

Nicklin et al. (1962) suggested a constant of 1.2 for fully developed turbulent flow, but noticed the variation of this coefficient at low Reynolds numbers (< 8000).

From various expressions found in the literature, the parameter C_o can be expressed through the following general expression:

$$C_o = C_o\left(Fr_M, \mathrm{Re}_s, \beta\right) \tag{2.16}$$

Where:

β is the pipe inclination from horizontal.

$$Fr_M = \frac{V_M}{\sqrt{gD}} \tag{2.17}$$

And:

$$\mathrm{Re}_s = \frac{\rho_L V_M D}{\mu_L}$$, is the slug Reynolds number (2.18)

Experimental result of Ferre (1979) suggested that the discrepancies in the coefficient C_o might be due to the occurrence of a flow transition. He found two different critical

Froude numbers at which the values of the drift velocity change, and proposed the following expression:

$$C_0 = \begin{cases} 1.10, \ldots\ldots\ldots Fr_L \leq 3.5 \\ 1.30, \ldots\ldots\ldots 2.26 < Fr_M < 8.28 \\ 1.02, \ldots\ldots\ldots Fr_M \geq 8.28 \end{cases} \qquad (2.19)$$

Similarly, Bendiksen (1984) while investigating motion of a single bubble in pipes noticed that there was a critical Froude number at which the values suddenly changed. As a result, he suggested that the following criteria should be used for all pipe inclinations:

$$C_0 = \begin{cases} 1.05 + 0.15\sin^2(\beta), \ldots\ldots\ldots Fr_L < 3.5 \\ 1.20, \ldots\ldots\ldots\ldots\ldots\ldots\ldots Fr_L \geq 3.5 \end{cases} \qquad (2.20)$$

Theron (1989) included the effect of the Froude number on the distribution coefficient C_0, and presented a simple continuous form of the correlation which is valid for pipes of all inclinations. This is particularly useful to avoid problem of discontinuity at translational Froude number during numerical calculations.

$$C_0 = 1.3 - \frac{0.23}{\Gamma} + 0.13\sin^2\beta \qquad (2.21)$$

β is the pipe inclination from horizontal and :

$$\Gamma = 1.0 + \left(\frac{Fr_M}{Fr_C}\cos\beta\right)^{10} \quad \text{and} \quad \mathrm{Fr_c} = 3.5 \qquad (2.22)$$

while:

$$Fr_M = \frac{V_M}{\sqrt{gD}} \tag{2.23}$$

Recently, Petalas & Aziz (1998) used the Stanford Multiphase Flow Database to account for the effect of the slug Reynolds number on the coefficient C_o, and empirically derived the following correlation:

$$C_0 = \frac{1.64 + 0.12\sin\beta}{\mathrm{Re}_s^{0.031}} \tag{2.24}$$

Taitel and Barnea (1990) proposed a unified model considering the slug hydrodynamics for vertical, horizontal and inclined pipes. Several approaches for hydrodynamics of liquid film were investigated. Two methods were developed to predict pressure drop across a slug unit. The pressure drop can be calculated using a force balance along a slug unit or only for the liquid slug zone.

Zhang et al. (2003) developed a mechanistic model for slug flow based on a balance between turbulent and kinetic energy of the liquid phase and the surface free energy of the dispersed gas bubbles. The model predicts transition boundary between slug and dispersed bubble flows for all inclinations.

2.1.1.4 Velocity of Dispersed Bubbles in the Liquid Slug

Bubbles with a chord length larger than the pipe diameter D are considered Taylor bubbles while bubbles with smaller than this are referred to as dispersed bubbles.

In similar manner, the translational velocity for dispersed bubbles in the liquid slug V_B is a linear combination of the bubble drift velocity V_{Drift} and the mixture velocity in the slug zone V_M.

$$V_B = C_o V_M + V_{Drift} \tag{2.25}$$

Unlike the case of Taylor bubbles, the translational velocity and the gas velocity are the same for small bubbles. For vertical case V_{Drift} is the drift velocity of a bubble in the pipeline. For very small bubbles the bubbles behave as rigid spheres and the free rise is governed by Stokes law. For larger bubble a boundary layer solution is applicable. When the bubble size exceeds some critical value, d_{CD}, the rise velocity of the dispersed bubble tends to be constant and independent of the bubble diameter.

The bubbles in the slug zone are usually larger than d_{CD} . For a relatively large and deformable bubble, the equation proposed by Harmathy (1960) for the bubble rise velocity is considered to be sufficiently accurate:

$$V_{Drift} = 1.53 \left[\frac{\sigma g (\rho_L - \rho_G)}{\rho_L^2}\right]^{0.25} \tag{2.26}$$

This equation shows that free rise velocity is independent of the bubble size. The free rise velocity of a bubble within a swarm of bubbles is lower than the free rise of a single

bubble. This can be viewed as the decrease of buoyancy that acts on a single bubble in a gas-liquid mixture.

This decrease is correlated in the form:

$$V_o = V_{Drift}\,(1.0 - \varepsilon_S)^n \qquad (2.27)$$

For relatively large bubbles, Wallis (1969); and Govier & Aziz (1972) suggested the use of n = 1.5. Fernandes et al. (1983) used n = 0.5. A value of n = 0 was recommended by Wallis (1969) for a region termed churn-turbulent. This is very close to the flow of bubbles in the slug region and, thus, the value n = 0 is recommended.

The value of C_o depends on the concentration distribution of bubbles in the liquid slug as demonstrated by the method of Zuber and Findlay (1965). Wallis (1969) points out that C_o for vertical dispersed flow ''usually lies between 1.0 and 1.5 with a most probable value of about 1.2''.

2.1.2 Transition criteria to Dispersed-Bubble Flow

Barnea (1986) suggested a combined criterion for transition to dispersed-bubble flow to occur by the expression:

$$d_{\max} \le d_{CD}\,, \quad d_{\max} \le d_{CB} \qquad (2.28)$$

Where:

$$d_{max} = \left(0.75 + 4.15\sqrt{\alpha}\right)\left(\frac{\sigma}{\rho_L}\right)^{0.6}(\varepsilon)^{-0.4} \quad (2.29)$$

ε = rate of energy dissipation per unit mass, [m^2/s^3]

α = void fraction, [-]

$$d_{CD} = 2\left[\frac{0.4\sigma}{(\rho_L - \rho_G)g}\right]^{0.5} \quad (2.30)$$

$$d_{CB} = \frac{3}{8}\frac{\rho_L}{(\rho_L - \rho_G)}\frac{f_M V_M^2}{g\cos\theta} \quad (2.31)$$

d_{max} = the maximum stable diameter of the dispersed bubbles ,[m]

d_{CD} = the critical bubble diameter, above which bubbles start to deform and coalesce, [m]

d_{CB} = critical bubble diameter, [m]

The combined criterion ensures that neither agglomeration of bubbles nor 'creaming' will occur and that the dispersed-bubble flow exists. The model of Barnea (1986) is only valid for gas void fraction of 0.52. The value of α = 0.52 represent the maximum possible packing of bubbles above which bubble is not possible, yielding a transition to slug flow.

In conclusion, based on the extensive literature review on modeling of the velocity of the periodic structure in slug flow, no consensus has been reached on the value of flow distribution coefficient, C_o, and the coefficient of drift velocity term, C_1, in estimating flow structure velocity.

The gap identified in the review above forms the basis for experimental campaign described in Chapter Three using air/water, air/10 mPa s and air/12 mPa s viscous liquids with a view to determining experimentally the value of C_o and C_1.

2.1.3 Annular Flow

Annular flow is dominated by high gas flow rates. The gas phase moves fast at the center of the pipe (gas core), while the liquid phase flows as an annular film around the pipe wall. Annular flow is characterized by high interfacial shear stress, caused by high shear velocities introduced by the high gas rates and the continuous processes of droplet entrainment (out of the liquid film) and droplet deposition (into the liquid film).

At steady state conditions, the rates of deposition and entrainment are equal, resulting in an equilibrium entrainment fraction of droplets in the gas core.

Shoham (2006) has identified deep understanding of the following flow parameters as the key to modeling annular two-phase flow. The parameters are:

- Interfacial shear stress.
- Fraction of liquid entrained as droplets in gas core.
- Liquid film thickness

- Heat transfer coefficient at the pipe wall.

- Slippage between droplets and the gas core.

In this study our investigations are limited to the first three parameters. Since the thrust of this work is directed towards annular flow, it is therefore imperative to review pertinent literature on annular flow. Fortunately, Shoham (2006) and Mantilla (2008) have published detailed and excellent literature review including past and recent efforts which would be referred to in the next discussion.

2.1.3.1 Interfacial Waves in annular flow

Interfacial waves are very important in two-phase flows as they play a central role in the mass and momentum transfer between the gas and liquid phases. Waves are recognized as the source of entrained droplets, Woodmansee (1968). Most of the studies published on interfacial waves have been performed in horizontal channels where the curvature of the pipes is eliminated, providing better conditions for observations and measurements. Wave studies have dealt with identification of wave types and the prediction of the transition between them, Andritsos (1986). Also, the predictions of the conditions at which the interfacial waves are unstable leading to slug flow or atomization have been considered.

Several studies on annular flow for both vertical and horizontal pipes have been presented. The main characteristics of interfacial waves, such as the velocity (celerity), frequency and wavelength and also geometrical parameters including the height,

amplitude and wave base length have been presented in various studies including Chopra (1982), Martin and Azzopardi (1984), Azzopardi (1986), Azzopardi (1997), Wolf et al. (2001), Fukano et al. (1983), Jayanti et al. (1990), Paras and Karabelas (1991b), Andritsos (1986), Paras et al. (1994)) etc. More recently, studies have presented wave characteristics obtained under normal and microgravity conditions (Han et al. (2006)). Waves in stratified two-phase flow have also been studied extensively, dealing mainly with the predictions of the conditions at which the waves become unstable through linear stability theory (Hanratty and Hershman (1961), Lin (1985), Bruno and McCready (1988), Andreussi et al. (1985), Uphold (1997), Kuru et al. (1995) among others).

Models published in the literature attempt to predict wave characteristics utilizing non linear theory especially for roll waves. These models predict the wave celerity, wavelength and wave geometrical parameters based on the Two-Fluid Model equations (Dressler (1949), Miya et al. (1971), Watson (1989), Johnson et al. (2005)). Another approach used is the "shallow water" theory, which aims at reducing the Two-Fluid Model equations, based on the fact that the film thickness is small as compared to the axial characteristic length (wavelength). Most of the models are 1-D, but a 3-D model has been published by Pols (1998), based on shallow water theory for the prediction of roll or disturbance wave characteristics in horizontal pipes. The use of 1-D models for horizontal annular two-phase flow should be based on the determination of average conditions for the wave characteristics, since the film could be asymmetric with respect to the pipe circumference. In 2-inch pipes the film becomes symmetric for superficial gas velocities above 50 m/s at nearly atmospheric conditions.

For lower gas velocities, the asymmetry of the film can be easily observed because the disturbance waves (rings) exhibit an angle with the vertical plane.

In the following a summary of the important publications in the literature regarding experimental techniques, entrainment correlations, stratified, annular flow and wave modeling.

2.1.3.2 Relevant Literature

Important studies in annular flow have documented and presented in Azzopardi (2006) and Shoham (2006). Some of these detailed documentations are repeated here to identify where knowledge is deficient. In their respective books, Wallis (1969), Hewitt & Hall-Taylor (1970) presented general discussions on annular flow. The early study by Dukler (1960) attempted to develop a model for annular falling–film in vertical pipes. Later Hewitt (1961) extended that work to cover upward vertical flow. More recently, other models for vertical annular flow have been published by Oliemans et al.(1986), Yao and Sylvester(1987), Hassan and Kabir(1988), and Alves et al.(1991). Hassan and Kabir (1988) developed a comprehensive model for predicting two phase flow behavior in wellbores. The model includes analysis of annular flow using previously established methods. Yao and Sylvester (1987) presented a simple annular flow model for prediction of the film thickness and pressure drop. The Oliemans et al. (1986) and Alves et al. (1991) models are based on the two- fluid model, with closure relationship correlations for the interfacial friction factor and entrainment fraction. Finally, Caetano et al. (1992) presented a model for annular flow in an annulus configuration.

Extensive studies have been carried out on the physical phenomena associated with annular flow. Turner et al. (1969), Ilobi and Ikoku (1981) studied the minimum gas velocity required for liquid removal in vertical pipes. Taitel et al.(1980) adopted this concept to predict the transition boundary to annular flow. Several investigators developed correlations for the interfacial friction factor, including Wallis (1969), Henstock and Hanratty (1976), Whalley and Hewitt (1978), and Asali et al.(1985). Others such as Wallis (1969), Hanratty and Asali (1983), and Ishii and Mishima (1989) have studied the entrainment process. Oliemans et al. (1986) presented a comprehensive review of both interfacial shear and entrainment and developed their own correlations for three parameters.

Because of the physical nature of Alves et al. (1991) annular flow model, it will be used frequently in subsequent Chapters to validate experimental results of this study.

2.2 Mechanistic model of Alves et al. (1991)

The model is based on physical phenomena. The Alves et al. (1991) mechanistic model for annular flow in vertical and off-vertical pipes is a 1D two fluid model. The flow is schematically described in Figure 2.3. The two fluids are the core fluid (gas and entrained droplets) and the liquid film. In this respect, the approach is similar to the approach used in development of stratified flow model. However, the annular model is on the basis of different geometry and different physical phenomena. The model enables detailed prediction of the annular- flow- pattern characteristics, including the velocity distribution, liquid- film thickness, gas void fraction, and pressure gradient.

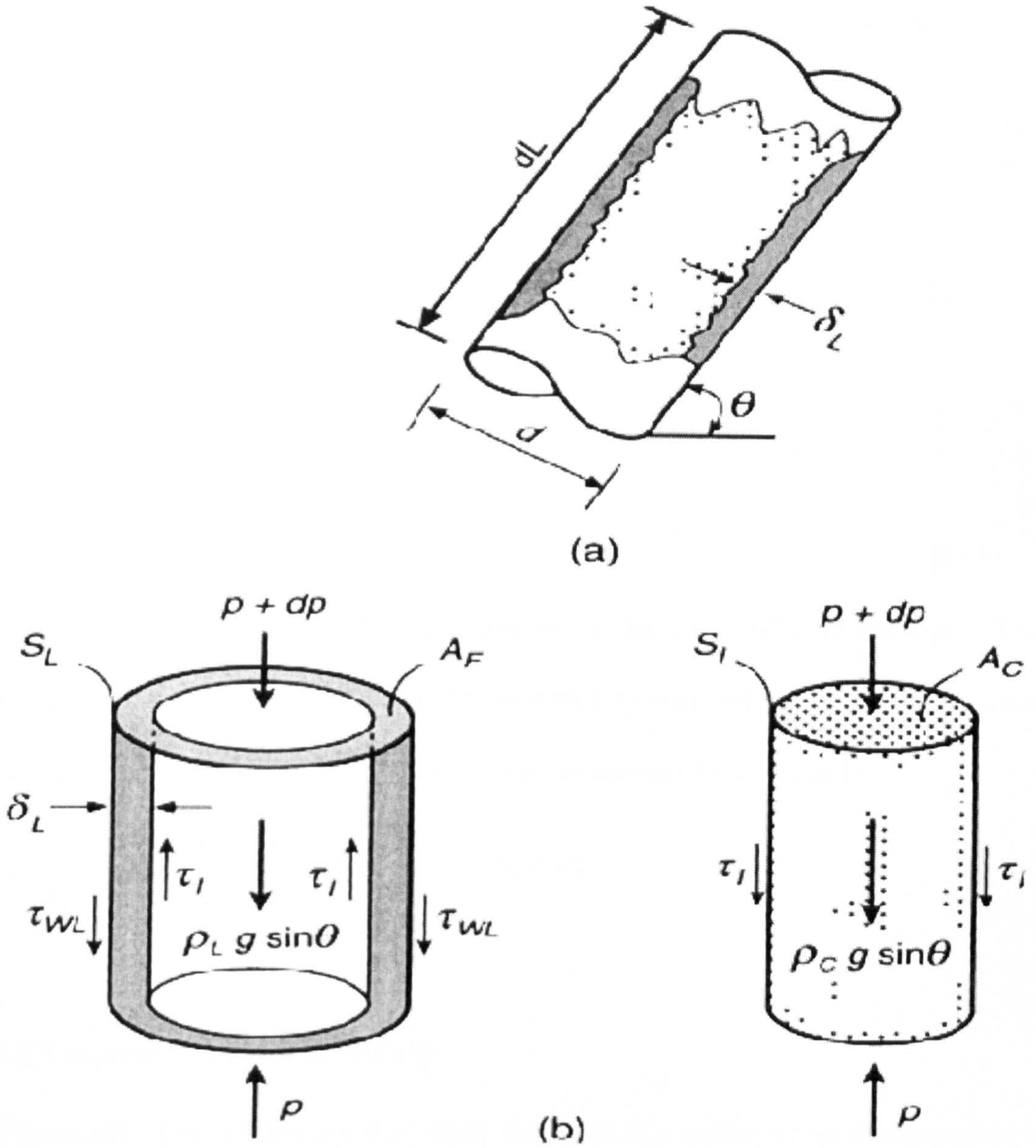

Figure 2.3: Schematics of annular flow two fluid model approach, Alves et al. (1991).

2.2.1 Momentum Equations

The model is derived by applying the momentum balances to the liquid film and the core, respectively. Note that because the flow is considered incompressible at a given location, the rate of change if momentum is neglected, resulting in reduction of the

momentum balances to force balances. The momentum (force) balances for the liquid film and core are given, respectively, by:

$$-\tau_{wL}\frac{S_L}{A_F}+\tau_I\frac{S_I}{A_F}-\left(\frac{dP}{dL}\right)_F-\rho_L g\sin\theta\ =0 \tag{2.32}$$

And

$$-\tau_I\frac{S_I}{A_C}-\left(\frac{dP}{dL}\right)_C-\rho_L g\sin\theta\ =0 \tag{2.33}$$

For fully developed flow, the pressure gradient in the film and core are equal. Thus, Equation 2.32 and Equation 2.33 can be combined by eliminating the pressure gradient, resulting in the combined momentum equation for annular flow, given by:

$$-\tau_{WL}\frac{S_L}{A_F}+\tau_I S_I\left(\frac{1}{A_F}+\frac{1}{A_C}\right)-(\rho_L-\rho_C)g\sin\theta=0. \tag{2.34}$$

2.2.2 Geometrical Relationship

The geometrical parameters are derived on the basis of a uniform film thickness and are expressed as follows:

$$A_C=\pi(d-2\delta_L)^2/4$$

$$A_F=\pi\delta_L(d-\delta_L)$$

$$S_I=\pi(d-2\delta_L)$$

And $S_L=\pi d.$ (2.35)

The hydraulic diameters of the liquid film and core are given, respectively, by:

$$d_F = 4\delta_L(d-\delta_L)/d, \quad and\ d_C = (d-2\delta_l) \tag{2.36}$$

2.2.3 Mass Balances

Mass balances are carried out to determine the film and core velocities, core average physical properties, and the gas void fraction. The liquid flow rate in the film can be determined from the total liquid flow rate on the basis of the entrainment fraction as

$$q_F = q_L(1-f_E) = A_p v_{SL}(1-f_E) = v_F A_F \tag{2.37}$$

Where

AP = cross-sectional area of pipe, [m^2]

The different correlations for determining the entrainment fraction, f_E, are discussed in the subsequent section.

Film velocity is determined is expressed as

$$v_F = v_{SL}\frac{(1-f_E)d^2}{4\delta_L(d-\delta_L)} \tag{2.38}$$

The core velocity is determined in a similar manner. The flow rate in the core is given by

$$q_C = q_G + q_L f_E = A_P(v_{SG} + v_{SL} f_E) = A_C v_C \tag{2.39}$$

and the core superficial velocity and actual velocity are, respectively,

$$v_{sc} = v_{SG} + v_{SL} f_E \tag{2.40}$$

$$\text{and } v_C = \frac{(v_{SG} + v_{SL} f_E)d^2}{(d-2\delta_L)^2} \tag{2.41}$$

Assuming homogeneous no slip mixture of the gas- phase and the entrained droplets in the core, the core void fraction is determined as

$$\alpha_C = \frac{v_{SG}}{v_{SG} + v_{SL} f_E} \tag{2.42}$$

and the core density and viscosity are given, respectively, by

$$\rho_C = \rho_G \alpha_C + \rho_L(1-\alpha_C)\,;\ \mu_C = \mu_G \alpha_C + \mu_L(1-\alpha_C) \tag{2.43}$$

As the flow in the core is homogeneous no- slip flow, the gas velocity is equal to the core velocity i.e. $v_G = v_C$

Thus, the total void fraction of the flow can be determined from the relationship $\alpha_T = v_{SG}/v_G$, or also from geometrical consideration, either of which yield the same result.

$$\alpha_T = \alpha_C(1-2\frac{\delta_L}{d})^2 \tag{2.44}$$

2.2.4 Reynolds numbers

It is possible now to determine the core and film Reynolds number given, respectively, by

$$\mathrm{Re}_C = \frac{\rho_C v_C d_C}{\mu_C},\ and\quad \mathrm{Re}_F = \frac{\rho_L v_F d_F}{\mu_L}. \tag{2.45}$$

Note that the liquid – film wall shear stress, τ_{WL}, is determined on the basis of Re_F. The core superficial Reynolds number is defined as

$$\mathrm{Re}_{SC} = \frac{\rho_C v_{SC} d}{\mu_C} \tag{2.46}$$

2.2.5 Shear Stress

The liquid film wall shear stress is given by the following expression as

$$\tau_{WL} = f_F \frac{\rho_L v_F^2}{2} \tag{2.47}$$

Where f_F is the film friction factor. For a smooth pipe, the Blasius equation can be used, as given by:

$$f_F = C_F \, \mathrm{Re}_F^{-n} \tag{2.48}$$

Where $C_F = 16$ for laminar flow and 0.046 for turbulent flow, and the exponent n is 1 for laminar flow, and 0.2 for turbulent flow.

The interfacial shear stress is determined from

$$\tau_I = f_I \frac{\rho_C (v_C - v_F)^2}{2} \tag{2.49}$$

where the interfacial friction factor is expressed in terms of a dimensionless parameter I,

$$I = \frac{f_I}{f_{SC}} \tag{2.50}$$

The Wallis (1969) correlation may be given by

$$I = 1 + 300 \frac{\delta_L}{d} \tag{2.51}$$

2.3 Entrained fraction

Experimental evidences have shown that entrained liquid fraction is responsible for pressure drop in annular two-phase flow. Gas and gas condensate lines operate in annular flow regime. Poor understanding of the system pressure drop can lead to

frequent operational shut-ins and re-starts to carry out remedial or intervention assignments on the well and production lines alike. This can lead to loss of revenue due to production impairment.

Liquid film extraction technique based on mass balance appears to be the commonest and most reliable way to determine entrained liquid fraction in annular two-phase flow. The practicability of this approach is rather doubtful in field application as a result of operational constraints. Therefore, producers are compelled to base the determination of entrained liquid fraction in natural gas stream on the available empirical correlations. Some of these correlations lack physical basis because their derivations were not mechanistic. Sometimes their predictions can be misleading.

Measurement of entrained liquid fraction employing laser diffraction techniques using Spraytec presents itself as a robust, cost effective alternative to close the gaps and deficiencies in knowledge caused by the traditional empirical models. Another advantage of the present arrangement is that it can be incorporated into the well head in offshore platforms as part of intelligent completion.

2.3.1 Liquid loading in gas production

Entrained fraction and liquid loading in gas production are related topical issues. It is not very clear if the reported liquid loading mechanisms consider drop concentration in the gas core of annular flow as an important parameter. However, annular flow transition models have drop size as dependent variable. In vertical annular flow, fully developed flow occurs when drag force from the gas phase overcomes the gravity force on liquid droplet suspended in the gas core. Therefore, agglomeration and packing of liquid

droplets in the core as well as drop concentration should not be detached from liquid loading as the following discussion presents.

Liquid loading is a common operating problem in gas production. The producer is forced to shut down production after the liquid content of the gas has exceeded a permissible limit as a result of liquid loading. Revenue is lost as liquid loading continues to impair production. The problem can be conceptualized as follows.

In a producing gas and gas condensate well, as reservoir pressure decreases, entrained liquid forms an increasing restriction on gas production because liquid (water, oil, and condensate) is usually produced simultaneously with the gas production, the flow pattern inside the production tubing being annular dispersed two-phase flow. The liquid phase flows partly as a wavy film along the pipe circumference, and partly as entrained droplets in the turbulent gas core. At the end of the lifetime of gas wells, the gas production rate decreases strongly. Due to this decrease, the drag force of the gas phase exerted on the liquid phase may not be sufficient anymore to bring all the liquid to the surface. Liquid starts to drain downward (flow reversal). In such a situation, depending on the gas reservoir conditions, the liquid could accumulate down hole, block the inflow into the production tubing and gas production could cease. This phenomenon called liquid loading, occurs at a gas rate below the minimum in the pressure gradient curve, and is closely related to flooding, Westende et al. (2007).

In the gas producing industry, the onset of liquid loading is commonly predicted using a correlation developed by Turner et al. (1969). The idea behind this correlation is to estimate the minimum gas velocity that can elutriate the largest droplet, present in the gas core. When the gas velocity in the production tubing gets below this minimum

velocity, liquid loading occurs. It is, thus, implicitly assumed that the dispersed phase is causing liquid loading, although direct evidence for this is not available, Westende et al. (2007).

Belfroid et al. (2008) analyzed behavior of different natural gas wells based on both production data collected over a period of time and the numerical simulations results using both commercially available software and dedicated dynamic models. The study and many others confirmed many wells start liquid loading at gas rates well above the values predicted by classic steady state models such as Turner while the liquid loading point is strongly dependent on inclination angle, flow regime transitions and the interaction between tubing outflow behavior and the reservoir Inflow Performance Relationship (IPR).

Westende et al. (2007) performed detailed Phase Doppler Anemometry (PDA) measurements in annular flow with air/water in a 50mm internal diameter vertical pipe to understand the role of dispersion in an annular flow close to liquid loading. Probability Density Function (PDF) of the drop diameter, drop concentration, pressure gradient and amount of entrained fraction were determined from time varying measurements in order to establish distribution of dispersed phase hydrodynamic properties. In that study, drop size and entrained fraction data were not time resolved. Other differences between the present study and the work of Westende et al. (2007) are discussed as follows. Some of the liquid superficial velocities tested in the present study are higher than in the work of Westende et al. (2007). Whilst we employ laser diffraction

technique to size liquid droplets and entrained fraction only; Westende et al. (2007) utilized PDA to determine liquid film thickness, drop sizes and pressure drop.

2.3.2 Time resolved measurements

Nearly all the world's gas wells are at risk of or suffering from liquid loading, Belfroid et al. (2008). The prediction of the minimum stable gas rate using the existing models could be misleading because of their non-physical basis. For instance, almost all existing models do not include entrained liquid fraction in determining the onset of liquid loading. This probably may be due to lack of drop concentration/entrained fraction data. This study reports for the first time dynamic, time-resolved drop concentration and drop size measurements.

One importance of time resolved drop concentration measurement is the determination of the dispersed phase periodic structure distribution using Probability Density Function (PDF). This will be discussed in the subsequent sub-sections.

2.3.3 Entrainment fraction correlations

Entrainment fraction in annular flow is defined as a fraction of the total liquid flow flowing in the form of droplets through the central gas core. Its prediction is important for the estimation of pressure drop and dry-out in annular flow. In gas production it is important to determine liquid content of the natural gas stream. The most widely used entrained fraction correlations for vertical annular two-phase flow include Wallis (1969), Oliemans et al. (1986), Ishii and Mishima (1989) , Pan and Hanratty (2002a) and recently Sawant et al.(2009). These correlations are presented as follows:

2.3.4 Wallis (1969)

This entrained fraction correlation is a modification of the method proposed by Paleev and Filippovich (1966).

The correlation is given by

$$E_F = 1.0 - \exp[-0.125(\phi - 1.5)] \tag{2.52}$$

Where:

$$\phi = 10^4 \frac{V_{SG}\mu_G}{\sigma}\left(\frac{\rho_L}{\rho_G}\right)^{1/2} \tag{2.53}$$

One limitations of this correlation according to Wallis is that the correlation give errors for entrainment fractions greater than 0.5. It is also not valid for low liquid Reynolds numbers, where thin films are more stable. The model has been observed to over predict entrained fraction for this case.

2.3.5 Oliemans et al. (1986)

The Oliemans et al. (1986) correlation has been developed from a regression analysis of the Harwell data bank including air/water, air-Ethanol, air-Genklene (trichloroethane) and water-steam fluid systems. The data base covers pipe diameters of 0.6 to 32 mm, gas Froude numbers of 1 to 10, liquid Reynolds numbers in laminar and turbulent flow, gas densities of 56 kg/m^3 and surface tensions of 0.012 to 0.073 N/m.

The model is expressed as follows:

$$\frac{E_F}{1-E_F} = 10^{\beta_0}\rho_L^{\beta_1}\rho_G^{\beta_2}\mu_L^{\beta_3}\mu_G^{\beta_4}\sigma^{\beta_5}D^{\beta_6}V_{SL}^{\beta_7}V_{SG}^{\beta_8}g^{\beta_9} \tag{2.54}$$

The values of the coefficients are given in Table .2.1

Table 2.1: coefficients for entrained fraction correlation of Oliemans et al. (1986)

Coefficient	β_0	β_1	β_2	β_3	β_4	β_5	β_6	β_7	β_8	β_9
Value	-2.52	1.08	0.18	0.27	0.28	-1.80	1.72	0.70	1.44	0.46

2.3.6 Ishii and Mishima (1989)

This correlation was developed based on a force balance on the wave where the drag force is opposed by the surface tension force. Two dimensionless numbers are used, namely, a modified gas Weber number and a liquid Reynolds number. The functional form of the correlation (hyperbolic tangent) was chosen from the fact that the entrainment fraction goes from zero (low gas velocities) to one (high gas velocities). The database utilized for developing the correlation includes air/water systems, pipe diameters of 0.95 to 3.2 cm, superficial gas velocities of up to100 m/s, and liquid Reynolds numbers of 370 to 6400 and gas densities of 1.2 to 4.8 kg /m^3. The entrainment fraction correlation can be calculated from

$$E_F = \tanh[7.25\times10^{-7} We^{1.25} \mathrm{Re}_{SL}^{0.25}] \tag{2.55}$$

where the modified Weber number is given by

$$We = \frac{\rho_G V_{SG}^2 D}{\sigma}\left(\frac{\rho_L - \rho_G}{\rho_G}\right)^{1/3} \tag{2.56}$$

and the superficial liquid Reynolds number is

$$\mathrm{Re}_{SL} = \frac{\rho_L V_{SL} D}{\mu_L} \tag{2.57}$$

Since the criterion for the entrainment fraction calculation is based on a force balance on a wave, the correlation is limited to liquid Reynolds numbers greater than 2 for vertical

downward flow, and 160 for vertical upward and horizontal flow for low viscosity liquids. These limits mark the initiation of roll waves. The correlation is limited to air/water systems.

2.3.7 Pan and Hanratty (2002a)

The authors presented a correlation for vertical annular flow based on the balance of the rate of atomization of the liquid film and the rate of deposition of drops. The development of the correlation considers data bases with pipe diameters of 1.06 to 5.72 cm, superficial gas velocities of 20 to 119 m/s, superficial liquid velocities of 0.012 to 1.35 m/s, gas densities of 0.27 to 35 kg/m^3 and surface tensions of 0.01 to 0.073 N/m.

Correlations are presented for entrainment fraction, critical superficial gas velocity at onset of entrainment and deposition rate flux. It is reported that the entrainment fraction increased by increasing the liquid and gas rate, gas density and pipe diameter.

The entrainment fraction also increases as surface tension decreases. No big differences are observed between downward and upward flow data. Pan and Hanratty (2002a) entrainment correlation is presented by:

$$\frac{E_F}{1-E_F} = 6\times10^{-5}\left(\frac{(V_{SG}-V_{Gcr})^2 D\sqrt{\rho_L\rho_G}}{\sigma}\right) \tag{2.58}$$

The term V_{Gcr} is the critical gas velocity at the onset of atomization, given by

$$V_{Gcr} = 40\sqrt{\frac{\sigma}{D\sqrt{\rho_L\rho_G}}} \tag{2.59}$$

2.3.8 Sawant et al. (2009)

Sawant et al. (2009) entrained fraction correlation is an improved version of Sawant et al. (2008). The new correlation accounts for the existence of critical gas and liquid velocities below which no entrainment is possible. Measurements were carried out for entrained fraction, droplet entrainment rate, and droplet deposition using the liquid film extraction technique in a pipe diameter of 9.4mm and 10.2mm. The test fluids are air/water and organic fluid (Freon-133).

Sawant et al. (2009) is expressed as follows:

$$E_F = \left(1 - \frac{13N_{\mu L}^{-0.5} + 0.3\left(\mathrm{Re}_L - 13N_{\mu L}^{-0.5}\right)^{0.95}}{\mathrm{Re}_L}\right) \times \tanh\left(2.31\times10^{-4}\,\mathrm{Re}_L^{-0.35}\left(We - We_{cr}\right)^{1.25}\right) \tag{2.60}$$

According to the authors the correlation is only valid for mist annular flow regime.

Sawant et al. (2008) is given by the following expression:

$$E_F = E_{MAX}\tanh\left(aWe^{1.25}\right) \tag{2.61}$$

Where :

$$E_{Max} = 1 - \frac{\mathrm{Re}_{LMin}}{\mathrm{Re}_L}; \qquad \mathrm{a} = 2.31\times10^{-4}\,\mathrm{Re}_L^{-0.35}; \qquad Re_{LMin} = 250\ln(Re_L) - 1265$$

$$We = \frac{\rho_G V_{SG}^2 D}{\sigma}\left(\frac{\Delta\rho}{\rho_G}\right)^{0.25}; \qquad \mathrm{Re}_L = \frac{\rho_L V_{SL} D}{\mu_L}$$

2.4 Drop size correlation

The most popular correlation for Sauter Mean Diameter (D_{32}) is the correlation of Azzopardi (1997). The correlation is given by the following expression:

$$\frac{d_{32}}{D} = 1.91 \mathrm{Re}_{SG}^{0.1} We_{SG}^{-0.6} \left(\frac{\rho_G}{\rho_L}\right)^{0.6} + 0.4E\frac{V_{SL}}{V_{SG}} \tag{2.62}$$

Where, $We = \frac{\rho_G V_{SG}^2 D}{\sigma}$,[-]; $\mathrm{Re}_{SG} = \frac{\rho_G V_{SG} D}{\mu_G}$, [-]; $E = \frac{\dot{M}_{LE}}{\rho_L V_{SL}}$,[-].

The first term in the RHS of the Equation (4.11) is the contribution from drop break-up while the second term represents contribution from drop coalescence.

Another simple model was suggested by Azzopardi (2006) for vertical annular two-phase flow. It is expressed as follows:

$$D_{32} = \left[0.069V_{SG} + 0.0187\left(\frac{\rho_L V_{SL}}{\rho_{SG} V_{SG}}\right)^2\right]\frac{\sigma}{\rho_{SG} V_{SG}^2} \tag{2.63}$$

In conclusion, a lot of work has been carried out in annular flow on entrained fraction prediction, drop size prediction including information about the disturbance waves that create drops. So far, there is no reliable information on the inter-relationship between drop concentration fluctuation and disturbance wave frequency. This is partly due to scarcity of data and non-existence of time resolved drop data.

2.5 T-junction relevant literature

Works related to T-junction and its application has been reviewed by Mak et al. (2006). Based on the equation of mass, momentum and energy balance, Dionissios (2007) studied the dynamic separation of gas and liquid inside a T-junction with a horizontal run and a vertical branch. He proposed a mathematical model which predicts phase distribution and pressure drop across the T-junction of different orientations and pipe diameters taking into account the flow pattern before the junction. The model was validated by good agreement between measured and predicted data. Adechy et al. (2004) used CFD to simulate dispersed core flow simultaneously with the flow of liquid film along the walls in which the core is represented as a dispersed two-phase mixture and the liquid film modelled as a thin boundary layer. They reported predictions data which agreed very well with measurements for a certain range of phase split. Wang (2008) published data on oil-water split across T-junction. They applied CFD and validated numerical data with experimental. They reported a reasonable agreement between the two methods.

Gas-liquid two-phase flow experiments where liquid phase viscosity is varied systematically in order to study the influence of liquid viscosity across the T-junction is scarce in horizontal flow and very rare in vertical flow with a tee to divert part of the flow to a side-arm. Hong (1978) worked with different liquid viscosities in his experiment with a T-junction ID = 0.0095 m in order to investigate flow split across the junction. He reported a distinct difference in phase split between water and liquid viscosity of 5mPa s. However, he concluded that a further increase in viscosity to 10 mPa s has a little effect on the phase split.These experiments are of particular relevance

to the current study, since the pipe diameter employed (ID = 0.0095 m) is the closest to that utilized in the present work. Hong (1978) varied the liquid and gas flow rates as well as the liquid viscosity, and found that increasing the inlet liquid superficial velocity decreased the fraction of liquid taken off in the side arm. He also found that increasing the gas flow rate increased the fraction of liquid taken off. Hong suggested a mechanism for this splitting phenomenon, which is similar to that originally proposed by Oranje (1973). Hong argued that an abrupt change in the direction of gas entering the side arm produced a centripetal force, which creates an under pressure inside the 90^0 be nd, drawing liquid into the side arm. When the gas intake is small, the centripetal force and hence the under pressure is small compared with the inertial force of the liquid stream, so the liquid flows straight through the junction. Under these circumstances, liquid only enters the side arm after a higher portion of the gas is diverted into the branch. Mak et al. (2006) used same facility as used in this study but only tested with air/water.

Viscosity is an important property because of its overall implication on flow assurance in a multiphase flow system. Liquid viscosity influences flow assurance such that flow is only assured when transport energy is greater than resistance to flow by liquid viscosity. In oil and gas industry most of the existing flow models and pattern maps are largely derived based on liquid with lower viscosity, in most cases water, with viscosity of 1 mPa s. Some oil wells flow oil as viscous as 10,000 mPa s at reservoir condition. This creates a big gap between laboratory and field analysis.

A common characteristic of two-phase flows through T-junctions is the maldistribution of the phases between the outlets. The occurrence of this maldistribution in equipment downstream of the junction can constitute a major problem in operation and control of the process and power industries as well as in oil and gas production.

Stacey et al. (2000) gives a good example taken from natural gas distribution networks during winter. Observations have shown that small quantities of the heavier components condensing out of the gas flow could arrive in appreciable amounts at any one of the delivery stations. This is caused by liquid emerging preferentially from an outlet in one of the junctions used to split the flow between delivery stations. Another example given by Azzopardi (1994 c) describes pipe work supplying two-phase feed to exchangers operating as condensers mounted in parallel. Maldistribution of the phases will have a direct effect on the performance of the heat exchangers. Those exchangers receiving mainly liquid will underperform significantly because the in-tube heat transfer coefficients during sub-cooling will be much lower than the corresponding condensation coefficient. In contrast, those exchangers receiving mainly vapor will perform slightly better than expected. However, the entire bank could operate below specification as this would not normally be sufficient to compensate for poor performers. On a more positive note, the maldistribution of phases that occurs at a T-junction can be used for phase separation in the processing industry.

Currently, the large thick-walled vessels being used as separators are expensive to build and the large inventory of flammable material that is contained in such vessels present some challenges to safe operation. Hence, the partial separation of gas–liquid mixtures possible by using a T-junction will help reduce the load on the main separator, possibly

leading to smaller units. Azzopardi et al. (2002) have reported the successful application of a T-junction within the chemical industry. The T-junction was used to partially separate the flashed products from a reactor. The output gas and liquid phase streams were then introduced at different points of a distillation column to improve its efficiency.

A survey of the existing literature shows that most of the previous work on dividing two-phase flow at a T-junction has been for sizes greater than 30mm in hydraulic diameter. Although Stacey et al. (2000), Lee and Lee (2001, 2004), Das et al. (2005) and Wren et al. (2005) have worked with pipe diameters ranging from 5 to 10 mm, these experimental studies were performed using either rectangular channels or horizontal T-junctions. Lee and Lee (2004) provide further motivation for research in this area when reporting that the flow distribution from a header to a parallel channel which is important for predicting the transfer performance of compact heat exchangers can be simulated as an accumulation of small T-junctions.

Various models have been developed for predicting the flow behavior at a T-junction. The model by Azzopardi (1987) for predicting the phase split for annular flow approaching a vertical T-junction was modified by Azzopardi (1988) to give better predictions by assuming the total deposition of drops. The use of a geometrical model to describe phase split was suggested by Azzopardi and Whalley (1982). Shoham et al. (1987) later developed a flow pattern-dependent geometrical model by assuming constant film thickness, no entrainment and uniform mass flux distribution. The flow regimes considered were annular and stratified flow. Under annular flow conditions, Shoham et al. (1987) ascribes the preferential liquid take off at high gas flow rates to

centripetal forces. This gives reasonable agreement with their experiments. Sliwicki and Mikielewicz (1988) considered the local forces at the front corner of the T-junction and ignored the effects of gravity in analyzing the diversion of the liquid film for annular flow. The fraction of drops diverted into the side arm was also calculated. Using the data of Azzopardi and Whalley (1982), they optimized the constants in their equations.

The model by Sliwicki and Mikielewicz (1988) is only valid for smooth films and is expected to be more accurate at lower gas velocities for which the film is less wavy.

The main aim of this study therefore, is to conduct an experimental investigation on the phase split occurring at a 5mm diameter vertical T-junction and compare the results with relevant models by Azzopardi (1988), Shoham et al. (1987) and Sliwicki and Mikielewicz (1988). Furthermore, time varying, void fraction data obtained using ring-type conductance probes, have been analyzed to give valuable information about the flow periodic structures around the junction.

2.6 Justification

As reported by Belfroid et al. (2008) virtually all of the world's gas wells are either at risk of or suffering from liquid loading and that the modeling of liquid loading behavior is still quite immature. The prediction of the minimum stable gas rate using the existing models could be misleading because of their non-physical basis. For instance, almost all existing models do not include entrained liquid fraction in determining the onset of liquid loading. This probably may be due to lack of drop size and entrained fraction data.

Vital information from time resolved drop concentration can help in formulating a good mechanistic model with a sound physical basis.

Drop size data has been measured in vertical annular two-phase flow using optical techniques. Azzopardi et al. (1980, 1991) have used the angular scattering of light into small forward angles. The same approach has been used by Simmons and Hanratty (2001) and Al-Sarkhi and Hanrratty (2002) for horizontal annular flow. The instruments employed used the assumption that the scattering was dominated by Fraunhofer diffraction and time averaging was almost inevitably employed to improve measurement accuracy. The method provides average values over a finite volume. Drops size distributions are extracted from the angular variation of scattered light. In addition, information of the time averaged concentrations was also determined (by integration).

In practice, drop size data are usually time integrated. This integration in time may compromise the quality of the data because of the complex mathematics and the assumptions made in time and space. Hence, analyzing data this way in amplitude and frequency space with respect to time to yield Probability Density Functions and or to identify the dominant structure frequency using Power Spectrum Density may often give misleading interpretations.

Azzopardi and Teixeira (1994 a) and van't Westende (2007) have used Phase Doppler anemometry to measure drop size in the past. This provides data at one point in space. The sampling position has to be traversed about the pipe cross section to obtain fully representative data. This approach also provides drop velocity information. Azzopardi &

Teixeira (1994 a) have shown that the drop size distribution from the diffraction and Phase Doppler anemometry instruments are the same if they are both converted to the same basis.

The pertinent issue is non-existence of time resolved drop-size data before this study. Literature is awash with time resolved void fraction, film thickness and pressure drop data in annular two-phase flow, the whole idea of dynamic, timed averaged drop concentration data is entirely inchoate.

This study presents new, time resolved drop size and drop concentration data for the first time. They were simultaneously acquired alongside time resolved film thickness and pressure drop data. This work, therefore, contributes to the on-going discussions on liquid loading problem in natural gas production and transportation by providing new and novel information from experiments to better understand the behavior of the periodic structures in annular two-phase flow as well as the mechanisms governing exchange and transfer of momentum between film and the gas core in vertical annular two-phase flow.

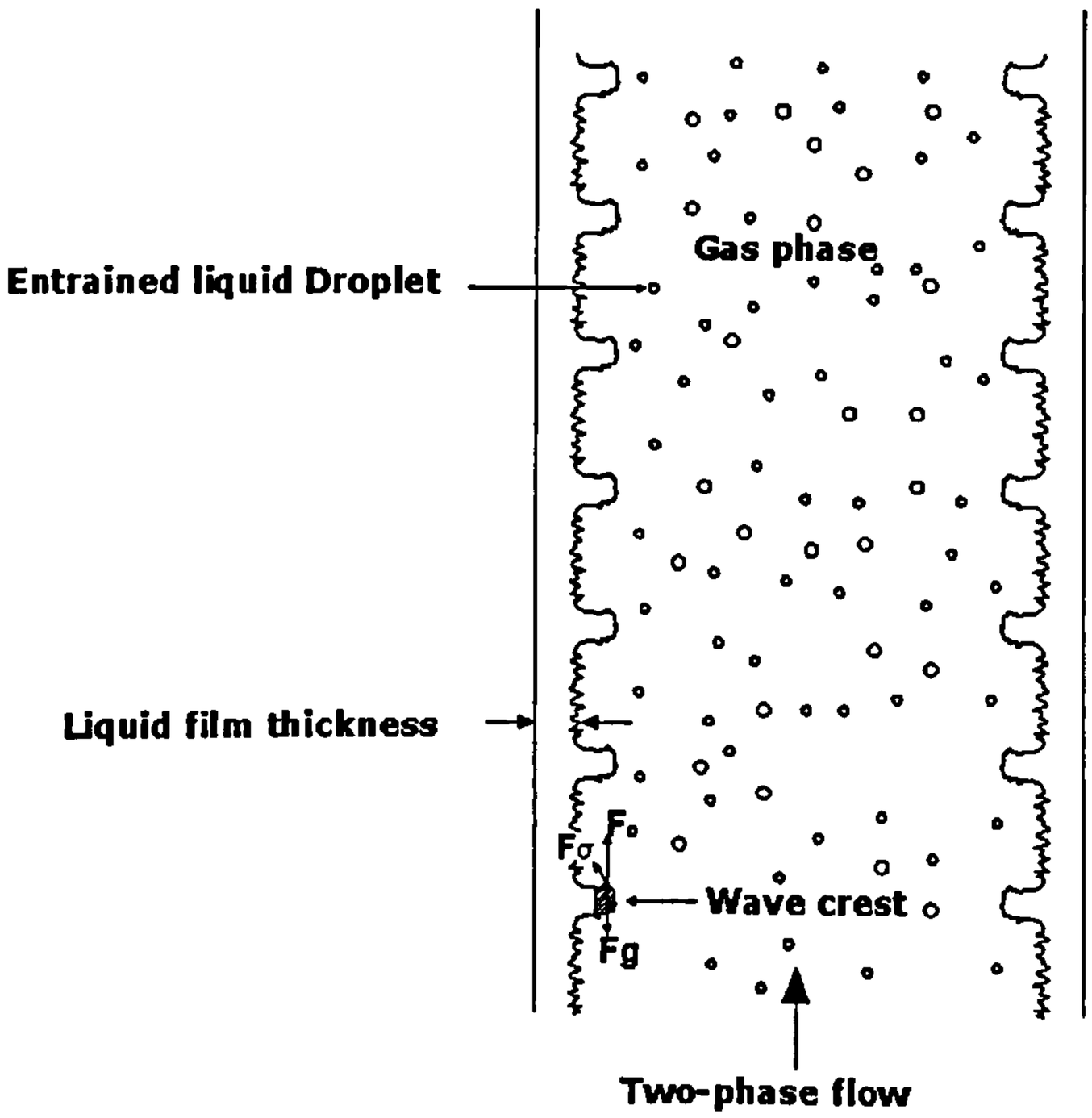

Figure 2.4: Schematics of vertical annular two-phase flow

Woodmansee and Hanratty (1969) showed evidence that the creation of drops from the film on the channel walls did not take place from of the film but specifically from periodic structures, usually called disturbance waves, Figure 2.4, which travel over the film at velocities of a few metres per second. Azzopardi (2006) presents more evidence of this. Therefore, it might be expected that there would be an interrelationship between the fluctuations of drop concentration and the frequency of disturbance waves. Unfortunately, hitherto there has been hardly any work presenting information about the way in which the drop concentration varies with time. The most useful study is that of Azzopardi & Whalley (1980 a) who used a camera looking axially up the pipe to record drops passing up the pipe. To ensure that it was known which waves the drops came from, a method of injecting artificial waves was employed. The liquid flow rate was set

at the value just before disturbance waves appeared. A small volume of liquid was then injected rapidly into the film. This produced a single wave which travelled up the vertical pipe. The cine films taken with this technique were analyzed manually. It was found that before liquid injection there were no drops. Whilst the wave was in the pipe there were an increasing number of drops as the wave approached the camera at the end of the pipe. However, the increase was not monotonic; drops came in bursts or waves. Once the disturbance wave had exited the pipe no more drops were seen.

2.7 Statement of the problem

Drop concentration, entrained liquid fraction, droplet diameters are all characteristic, periodic flow structures in the gas core of the annular two-phase flow. In flow assurance, modeling and prediction of entrained liquid entrained fraction in annular flow is still not well understood. Common reason is the lack of good understanding of the mechanisms of atomization of part of the liquid film to form droplets in the fast moving gas core. Flow assurance engineers in the oil & gas, power generation and nuclear industries all reply on commercial software to carry out flow assurance study. These commercial codes have been proven to be of excellent performance in predicting slug flow parameters for instance in many pipelines and production oil wells. However, their extensions to annular flow (wet gas transportation) have been unsuccessful. The primary reason responsible for this failure has been traced to lack of understanding of the mechanisms responsible for exchange of momentum between the liquid film and the gas core couple with paucity of data from which reliable correlations can be generated.

There is also supporting evidence that drops are created from periodic structures, usually called disturbance waves which travel over the film at velocities of a few metres per second. Therefore, it might be expected that there would be an interrelationship between the fluctuations of drop concentration and the frequency of disturbance waves where they are sourced.

Unfortunately, there has been hardly any work presenting quality information about the way in which the drop concentration varies with time. The interrelationship between fluctuations of drop concentration and the frequency of disturbance waves has never been reported.

All previous drop size and drop concentration measurements have always been time integrated. This integration in time may compromise the quality of the data. Hence, analyzing data in amplitude and frequency space with respect to time to yield Probability Density Functions and or to identify the dominant structure frequency using Power Spectrum Density may often give misleading interpretations of actual dominating flow mechanism.

Chapter 3

Effect of Liquid Viscosity on Gas-Liquid Flow Structures

3.1 Introduction

Viscosity is an important fluid property which has been found to be significant in two-phase gas-liquid flow. Flow pattern characteristics, including flow pattern transition boundaries, have been observed to behave differently when the viscosity of the liquid is increased over and above that for water. Analysis is carried out with liquid of different viscosities.

There are many important practical situations where effect of liquid viscosity on two-phase flow regime has been a source of concern to both academia and flow assurance engineers. Typical among these is the petroleum industry where the existing flow pattern maps and correlations are based on liquid with lower viscosity, in most cases water with viscosity of 1.0 mPa s. Mandil (2002) reported some oil wells flowing oil up to 10 000 mPa s viscosity. Therefore, a wide gap exists between laboratory and field data.

The approach of some authors has been to assume that all vertical two-phase flow occurs in a highly turbulent manner which made them often assume viscous effects are negligible. This has been a logical approach, for instance, most practical oil-well flow problems have liquid flow rates and gas-liquid ratios of such magnitudes that both phases will be in the turbulent flow. It has been noted, however, that in case where this assumption has been made serious discrepancies occur when the resulting correlation is

applied to low production wells or wells producing very viscous crude as stated in Hagendoorn et al. (1964). Both conditions suggest that perhaps viscous effects may be the cause of these discrepancies. In the first case, the increased energy losses have been observed to be responsible for the increased slippage between the gas and liquid phases as the liquid viscosity increases. This is contrary to what one might expect from Stokes law of friction, but the same observations were made by Ros et al. (1961) that attributed this behaviour to the velocity distribution in the liquid as affected by the presence of the pipe wall.

3.2 Experimental Description

Solutions of different viscosity are obtained by combining glycerine with water at various proportions. The viscosities of these solutions were determined using a Brookfield Dial Viscometer (Model LVT).The pump used is a jet pump with the following details: (Grundfos JP5-CEA-CVBP, 6 Bars Max, 40^0C), liquid viscosity of 60 centistokes (i.e. kinematic viscosity multiply by liquid density = Dynamic viscosity, in this case of glycerol, dynamic viscosity = 75.6 mPa s) at full capacity. Liquid viscosity tested was limited to the maximum liquid viscosity the jet pump can handle which is 70 mPa s. Schematic diagram of the flow facility is shown in Figure 3.1.

Air was drawn from the compressed gas mains and supplied to the mixing unit where it mixes with glycerol-solution pumped from the liquid tank by means of a centrifugal pump. Inflow of air and glycerol/water mixture was controlled by using separate banks of calibrated rotameters. The mixing unit consists of an annular section surrounding a

porous wall. Downstream of the mixer are probes 1, 2 and 3 before pressure tap 1, Figure 3.1. The probes calibration curves are given in Figure 3.2. The pressure taps are separated 0.5 m apart to allow flow develop before the test section. The pressure taps were connected to a Rosemount differential pressure transducer (Model 305) to measure the pressure drop between taps 1 and 2.

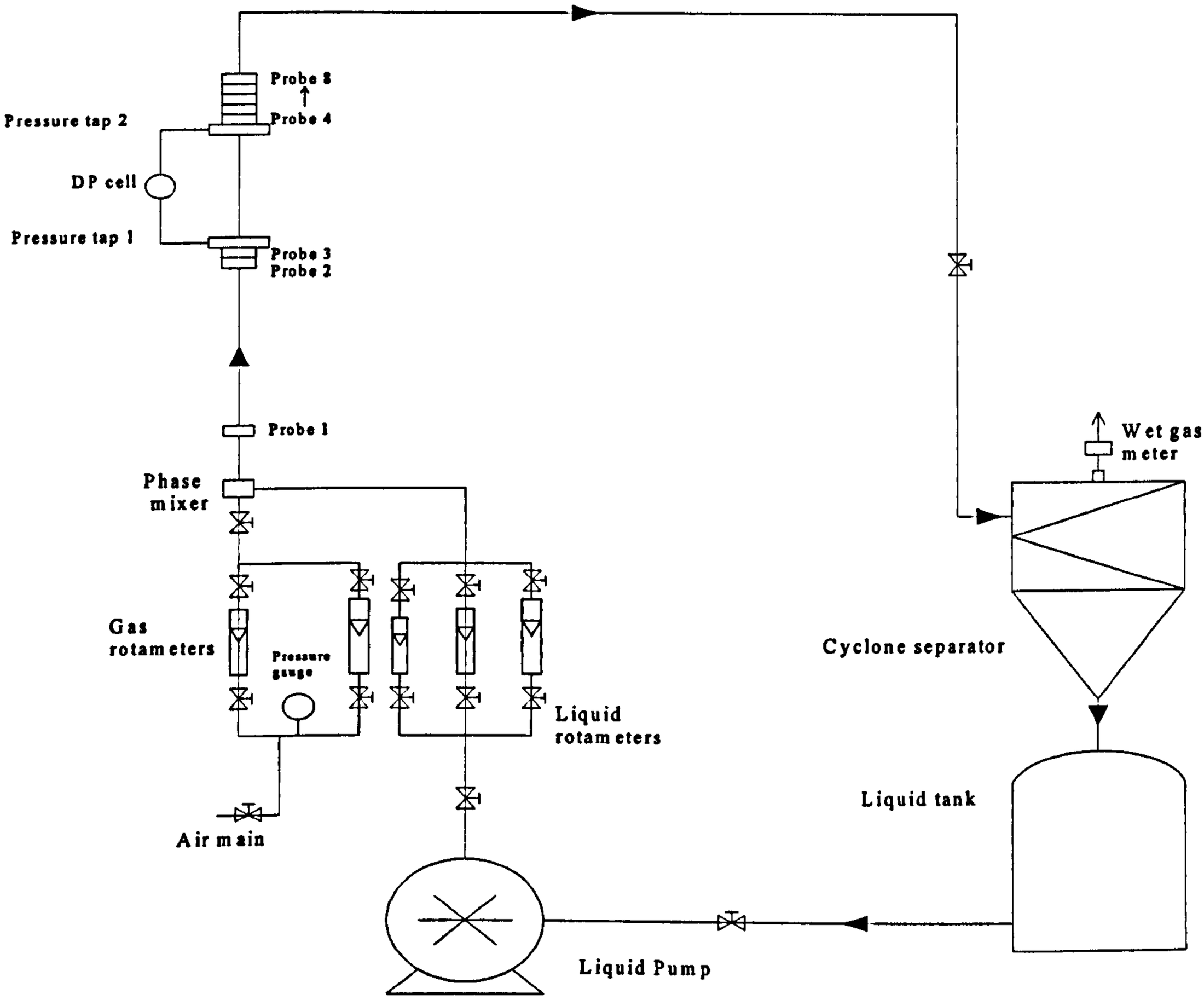

Figure 3.1: Schematic flow diagram of the 5.0 - mm internal diameter rig.

The two phases travel upward along 150 mm length, 5 mm internal diameter stainless steel, v ertical pipe, where time varying, cross-section averaged void fractions were measured using a stack of five identical conductance probes 4, 5, 6, 7, and 8 placed along the flow path shown in Figure 3.3.

Beyond the test section, the two-phase flow travels further upward and then horizontally for 1.07 m and finally vertically downwards for 3.12 m. The outlet streams were collected in a cylindrical cyclone 1000 mm internal diameter where the phases were separated. After separation, the liquid was collected and returned to the tank. Air was vented to the atmosphere. Volumetric flow rate of liquid was determined by timing an effluent from the cyclone separator over a lengthy period of time to minimize measurement uncertainties.

Air was metered using a calibrated wet gas meter which allowed the flow rates to be measured over a period of time. The liquid level in the separator was kept constant such that all measurements were carried out with reference to that datum. The datum served as a baseline to ensure accuracy.

3.3 Instrumentation

The electronic circuitry employed for the conductance probe is similar to that of Fossa (1998) and Fossa and Guglielmini (1998). The conductance technique has been chosen to measure void fraction because water is an electrical conductor, while air is essentially resistive. Tap water was used to calibrate the conductance probes.

Glycerol in its raw form is not conductive. Sodium Chloride solution was added to the glycerol solution to raise the conductivity of the solution to that of water. Andreussi et al. (1988) and Tsochatzidis et al. (1992) are some of the researchers to have used conductance probe successfully. In this technique, a cross-sectional averaged void fraction can be determined once the relationship between the electrical impedance and

the phase distribution has been established. For the ring conductance probes used in the present experiments, the distance between the electrode plates and width of each plate are 1.7 and 0.5 mm, respectively. This gives electrode spacing to pipe diameter ratio *(De/D)* of 0.34 and electrode width to pipe diameter ratio (*s/D)* of 0.1. The probes give a voltage output which is proportional to the resistance of the two-phase mixture. This response is converted to dimensionless conductance by referring to the value obtainable when the pipe is full of liquid.

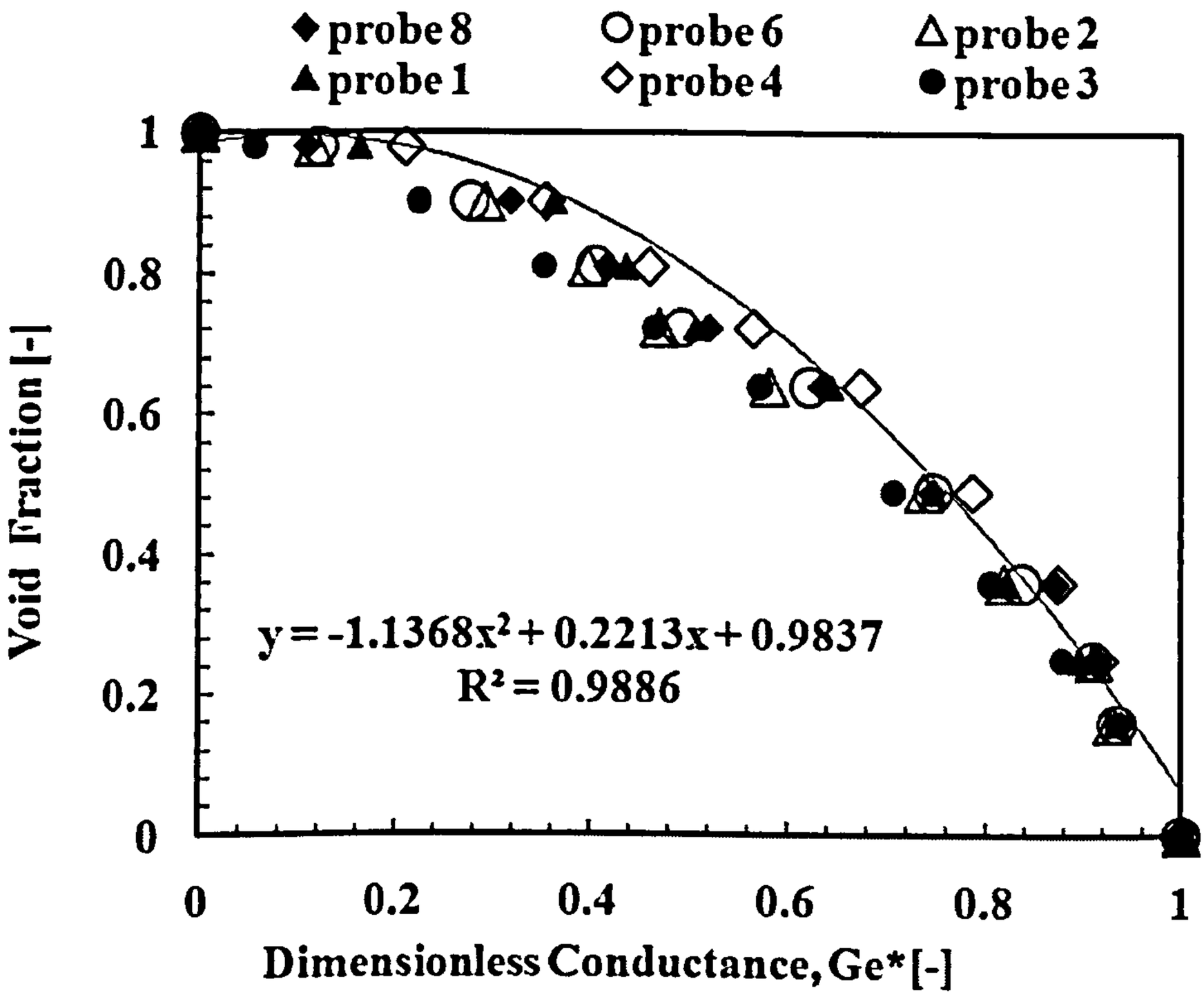

Figure 3.2: Conductance probe calibration curves, Omebere-Iyari et al. (2006).

The probe calibration equation used is the same as that of Omebere-Iyari et al. (2006). Omebere-Iyari artificially created instantaneous void fractions using plastic plugs with cylindrical rods of known diameters and relating this to the dimensionless conductance. One of the calibration equations used in the data acquisition is shown in Figure 3.2 for Probe 4.

The output from the conductance probes and the differential pressure cell were fed into a PC via a National Instruments acquisition card and processed using a LabView programme.

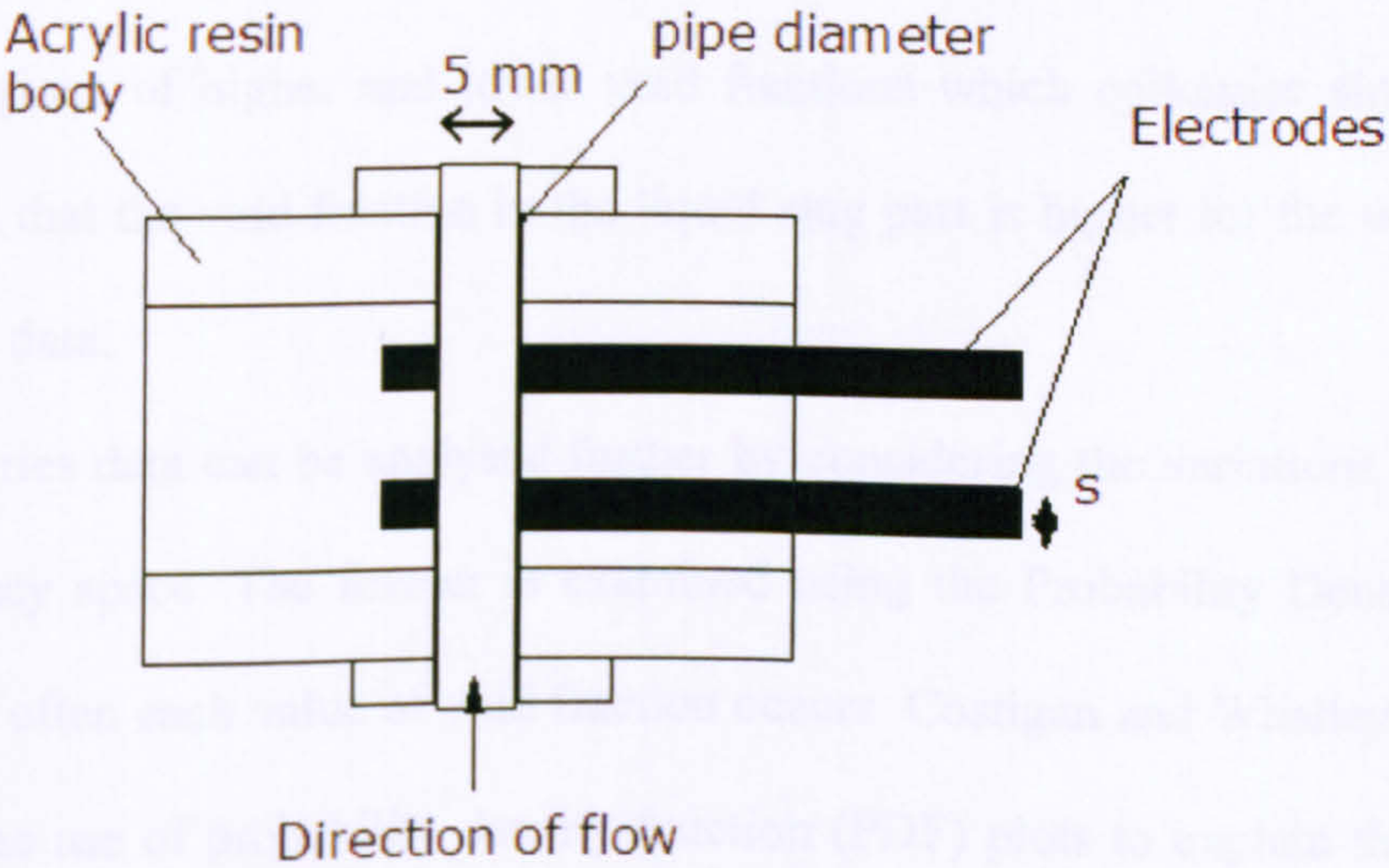

Figure 3.3: Top- a stack of conductance probes which constitute the test section (150 mm long). Bottom- cross section of a ring conductance probe.

3.4 Results and Discussion

Liquid hold-up/void fraction measured in various flow regimes are presented and discussed. Air/water, air/10 mPa s and air/12 mPa s two-phase flows were examined. The results are considered in increasing levels of complexity. At the simplest level, the time series of cross-sectionally averaged void fraction were examined. Next, simple statistical measures were extracted.

3.4.1 Time Resolved Measurement and Probability Density Function (PDF)

Time varying/time resolved void fraction data for air/water and air/12 mPa s are presented in Figure 3.4. Time-resolved information can be examined at a number of levels. A great deal of information can be obtained by considering the time series of the cross-sectionally averaged void fraction. An example of this for the two liquids studied is shown in Figure 3.4. These are taken at gas superficial velocity of 0.27 m/s and a liquid superficial velocity of 0.64 m/s. In both cases the results show the characteristic alternate regions of higher and lower void fractions which epitomise slug flow. It is clearly seen that the void fraction in the liquid slug part is higher for the water than for the glycerol data.

The time series data can be analysed further by considering the variations in amplitude and frequency space. The former is examined using the Probability Density Function (PDF), how often each value of void fraction occurs. Costigan and Whalley (1997) have suggested the use of probability density function (PDF) plots to explain the features of

two-phase flow. PDF plots of air/water and air/glycerol data are compared at same inlet condition as in Figure 3.4. Figure 3.5 presents the finding.

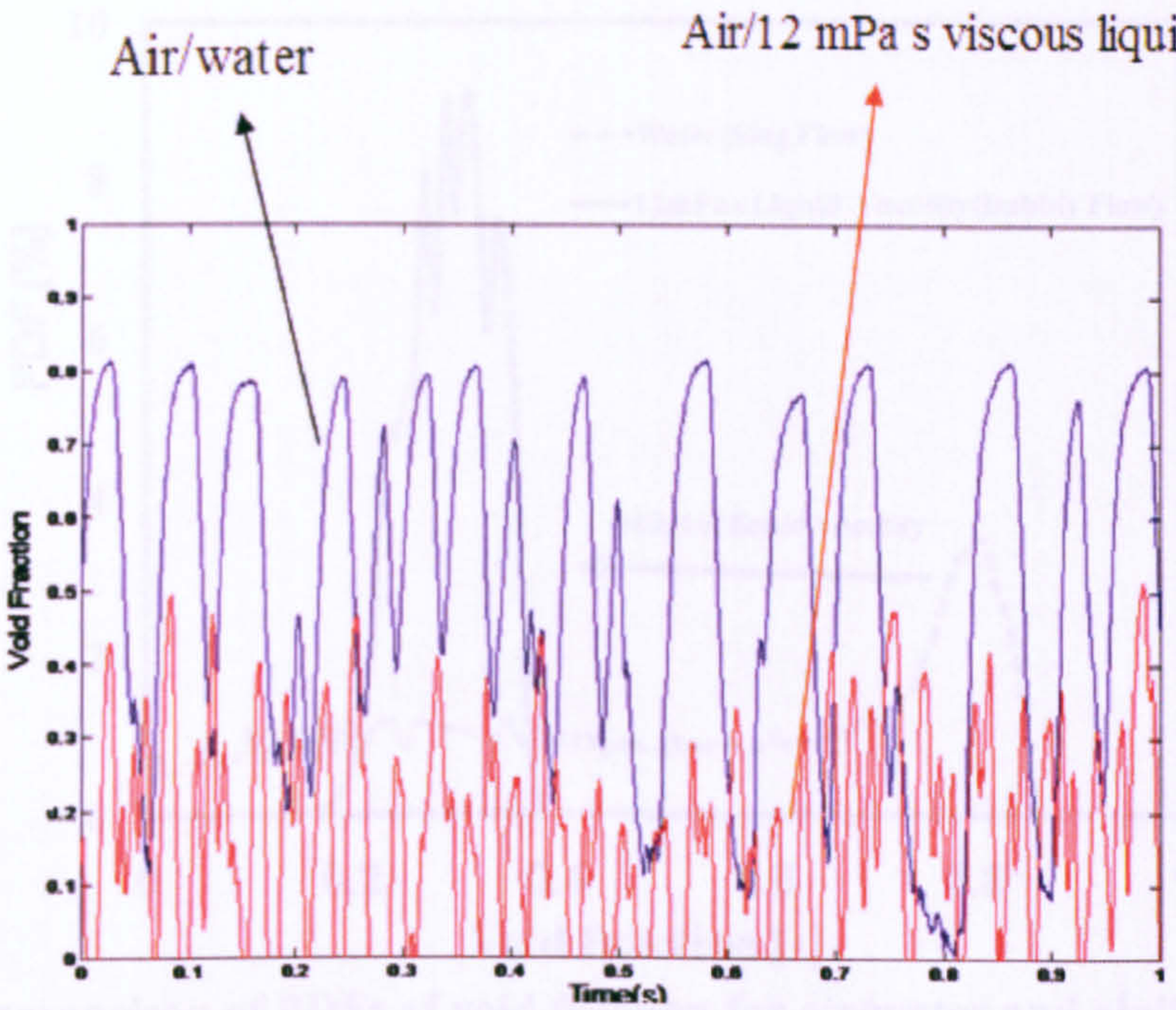

Figure 3.4: Comparison of time resolved void fraction data for r air/water and air/12 mPa s viscous liquid at same inlet conditions where superficial gas and liquid velocities are 0.27 m/s and 0.64 m/s respectively.

As can be seen in Figure 3.5, there are typical shapes or signatures which are obvious in these plots. Generally, a narrow single peak at low void fraction is typical of bubbly flow. A double peak is usually found in slug flow. The low void fraction peak corresponds to the liquid slug whilst peak at the higher void fraction is associated with the Taylor bubble region. The third type, a single peak at high void fraction with a long tail down to lower void fractions is recognised as the signature for churn flow. The last one, annular flow is characterised by a single peak at very high void fraction. The PDF of air/water and air/glycerol solution are plotted in Figure 3.5 to elucidate any effect of liquid physical properties and to identify flow pattern within the system based on the

void fraction distribution. According to Figure 3.5, the signature displays by air/water indicates slug flow whilst the typical shape displays by air/glycerol data fits the description of bubbly flow.

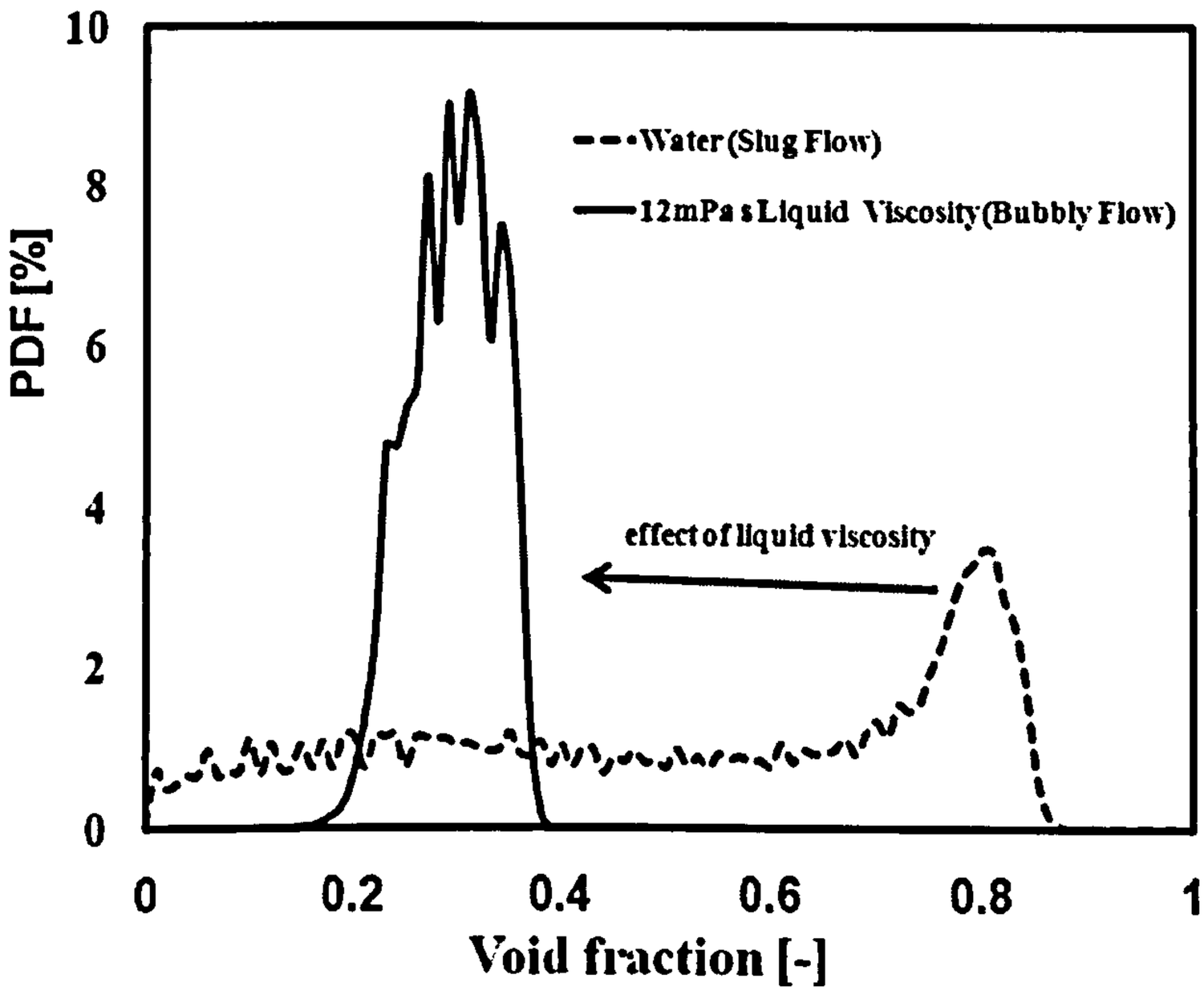

Figure 3.5: Comparison of PDFs of void fraction for air/water and air/12 mPa s viscous liquid for $V_{SG} = 0.27$ m/s, $V_{SL} = 0.64$ m/s.

There is a marked shift to the left towards decreasing void fraction when liquid viscosity increased from 1 mPa s (water) to 12 mPa s at the same inlet conditions. This can be supported by time varying signal in Figure 3.4 where the average void fraction for air/glycerol can be seen to be around 0.30 and that of air/water 0.65. This reduction in cross-sectional void fraction, shown as lateral displacement in Figure 3.5 is a direct effect of increase in liquid viscosity.

3.4.2 Void fraction

Mean values of void fraction for the three liquids are extracted from their time series and plotted against superficial mixture velocity as shown in Figure 3.6. Generally, Figure 3.6 shows that void fraction increases with mixture velocity. Effect liquid viscosity is however obvious as mean void fraction becomes smaller as liquid viscosity increases.

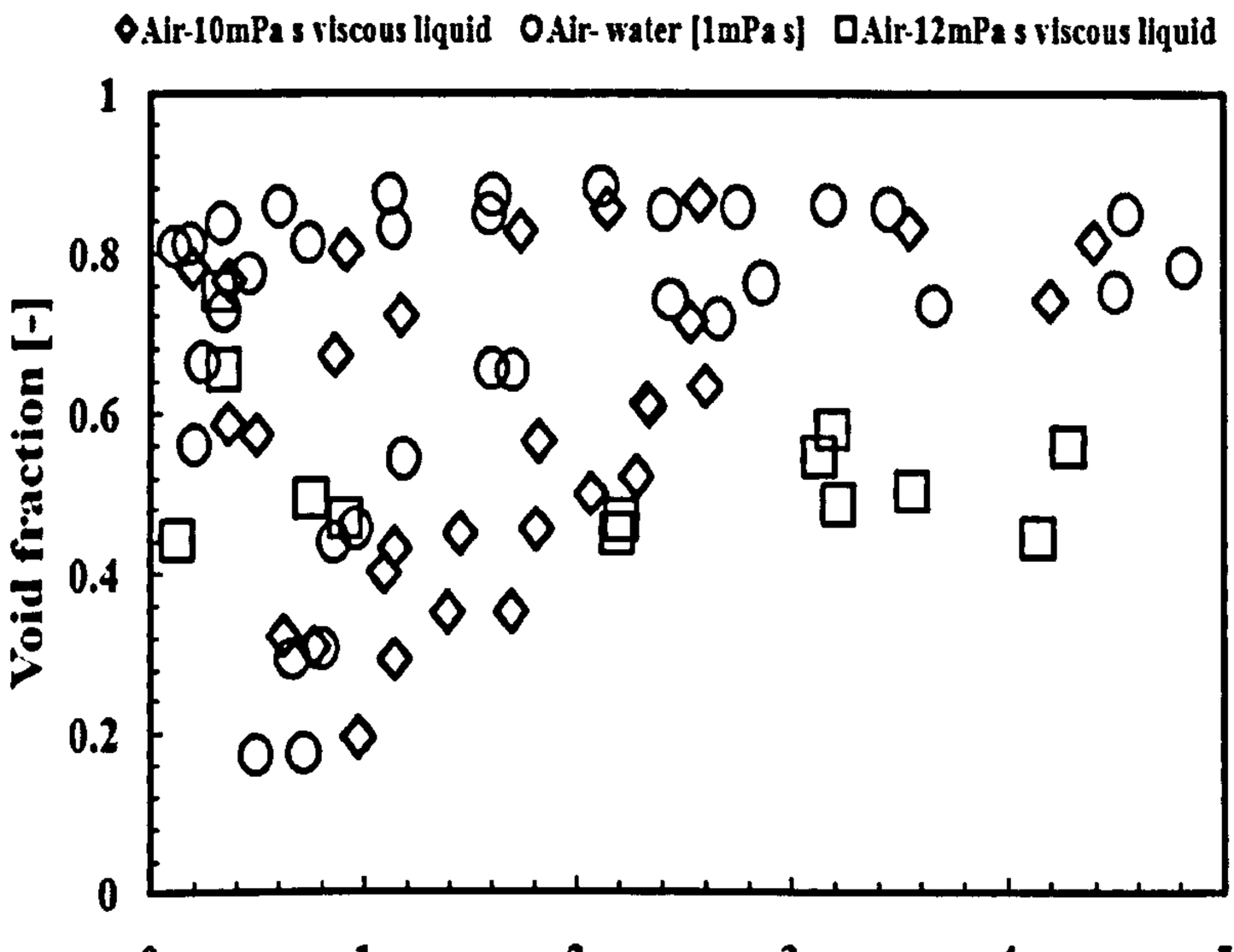

Figure 3.6: Void fraction as a function of mixture velocity at different viscosity.

In order to investigate effect of liquid viscosity further on phase distribution, liquid superficial velocity was fixed at V_{SL} = 0.03 m/s for mixture varied between 0 and 2.5 m/s for both air/water and air/10 mPa s sugar solutions. Results of the comparison are shown in Figure 3.7. The plot shows significant decrease in void fraction at higher liquid viscosity. The possible reason for decrease in void fraction as liquid viscosity increases may be due to decrease in liquid film velocity of the viscous phase adjacent to the wall which causes higher liquid hold-up and less void distribution across the cross section of the pipe.

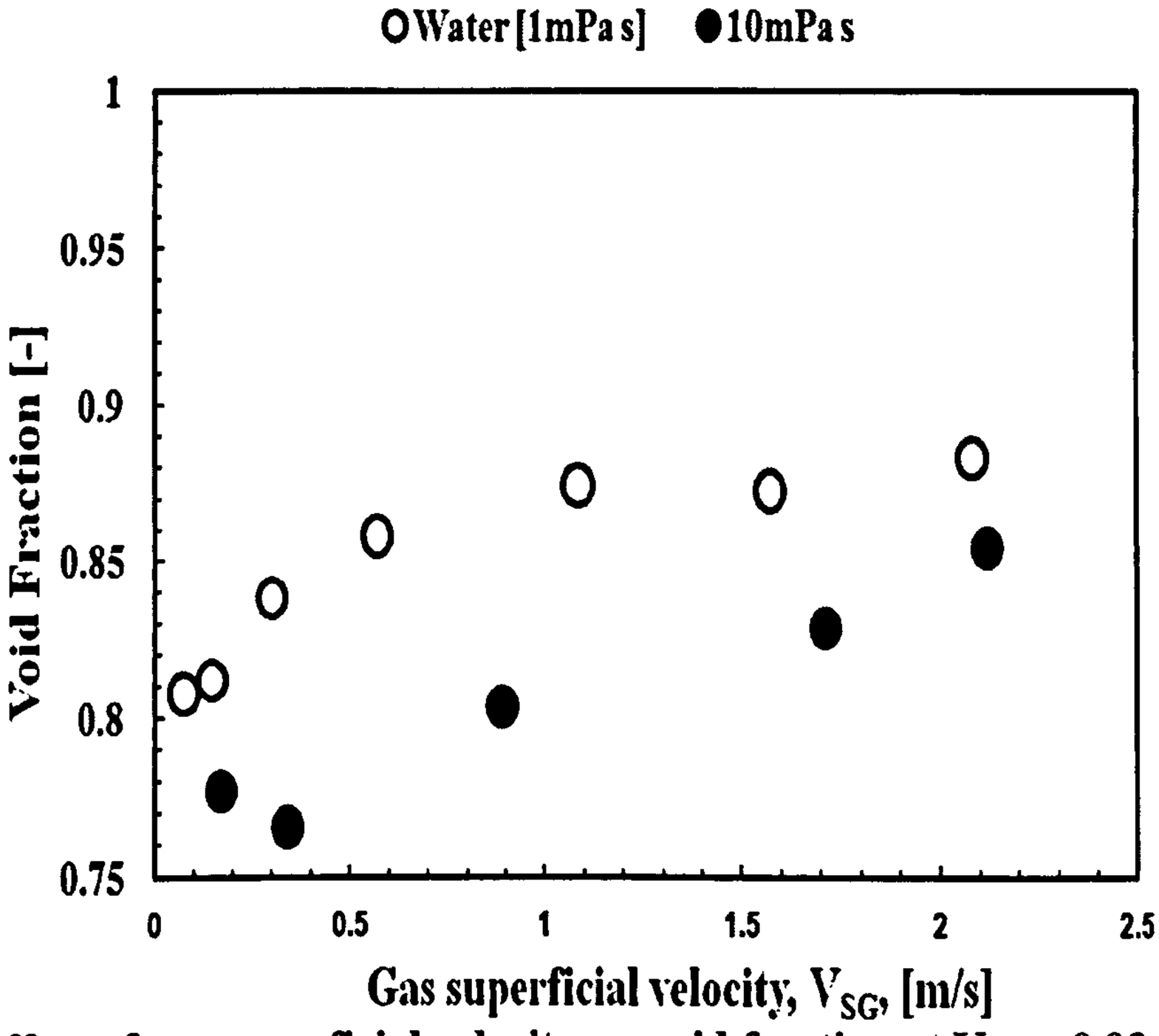

Figure 3.7: Effect of gas superficial velocity on void fraction at V_{SL} = 0.03 m/s for air/water and air-10mPa s liquid.

3.4.3 Structure frequency

The frequency characteristics of the times series can be obtained using Power Spectrum analysis. Here, Power Spectrum Densities (PSD) has been obtained by using the Fourier transform of the auto covariance functions generated from the time series. The detail of this procedure has been explained in Chapter FIve, section 5.2.

Obviously, Figure 3.8 shows increase in structure frequency with increase in gas superficial velocity. The figure also shows that liquid of higher viscosity produces higher structure frequency than lower viscosity liquid. Bubble, slug, churn and annular flow are all analogous because of the similarities between the flow patterns and their characteristic periodic structures. Azzopardi (2004) showed that bubbly and slug flow

regime frequency data could be correlated using Strouhal number and Lockhart-Martinelli parameter.

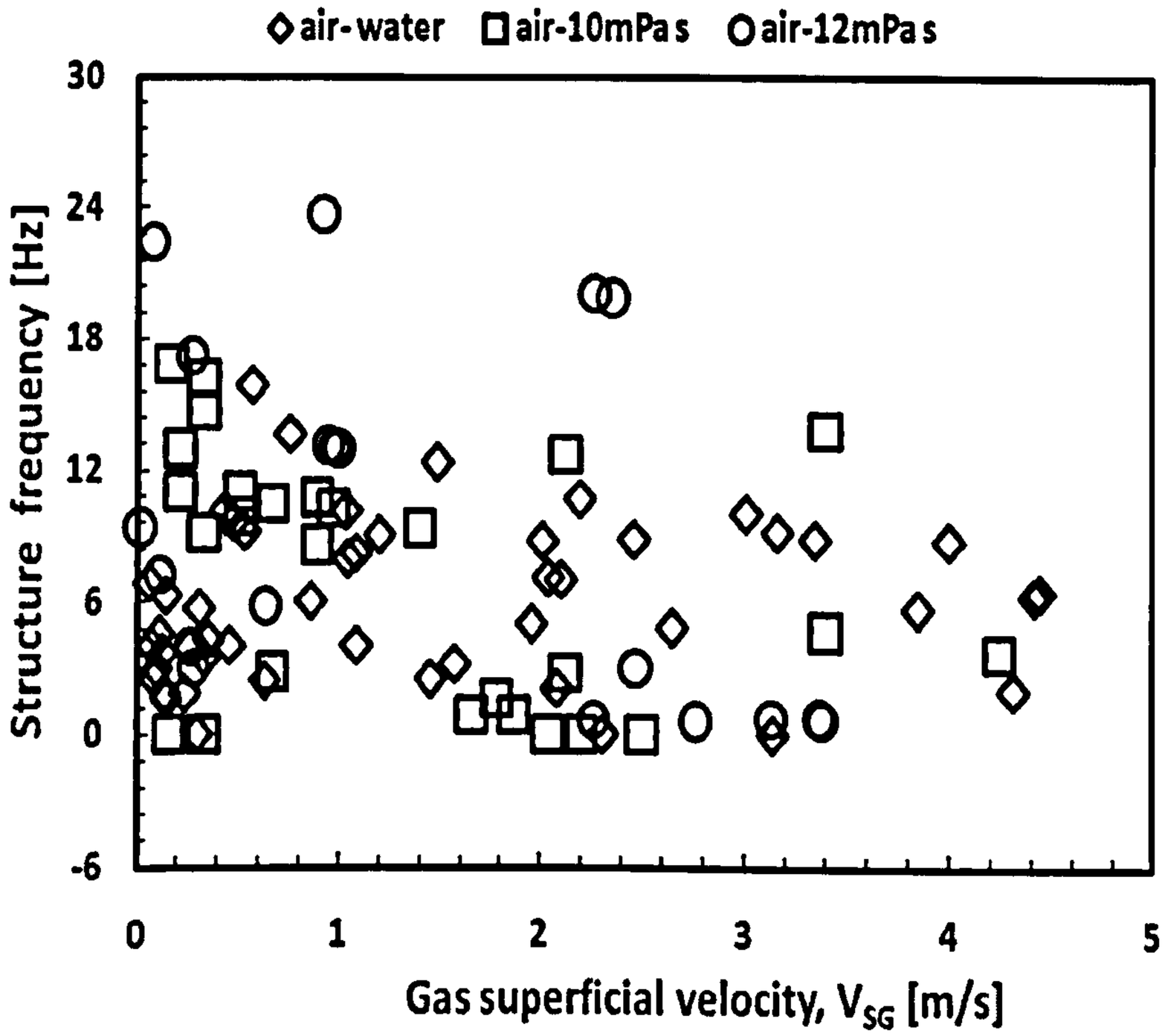

Figure 3.8: Effect of gas superficial velocity on periodic structure frequency for air/water, air/10 mPa s and air/12 mPa s viscous liquid.

The frequency of periodic structure in this case, void wave in all flow patterns encountered has been correlated using gas based Strouhal number and Lockhart-Martinelli parameter. Strouhal number and Lockerhart-Martinelli parameter are dimensionless numbers given by Equation (3.1) and Equation (3.2) respectively:

$$St_G = \frac{f_w d}{V_{SG}}, \text{[-]} \qquad (3.1)$$

$$X = \left[\frac{\rho_L V_{SL}^2}{\rho_L V_{SG}^2}\right]^{0.5}, \quad \text{[-]} \qquad (3.2)$$

The result is shown in Figure 3.9. The figure shows Strouhal number increases with increase in Lockhart-Martinelli parameter. The scatter noticed in the figure may be as a result of significant variation in gas density.

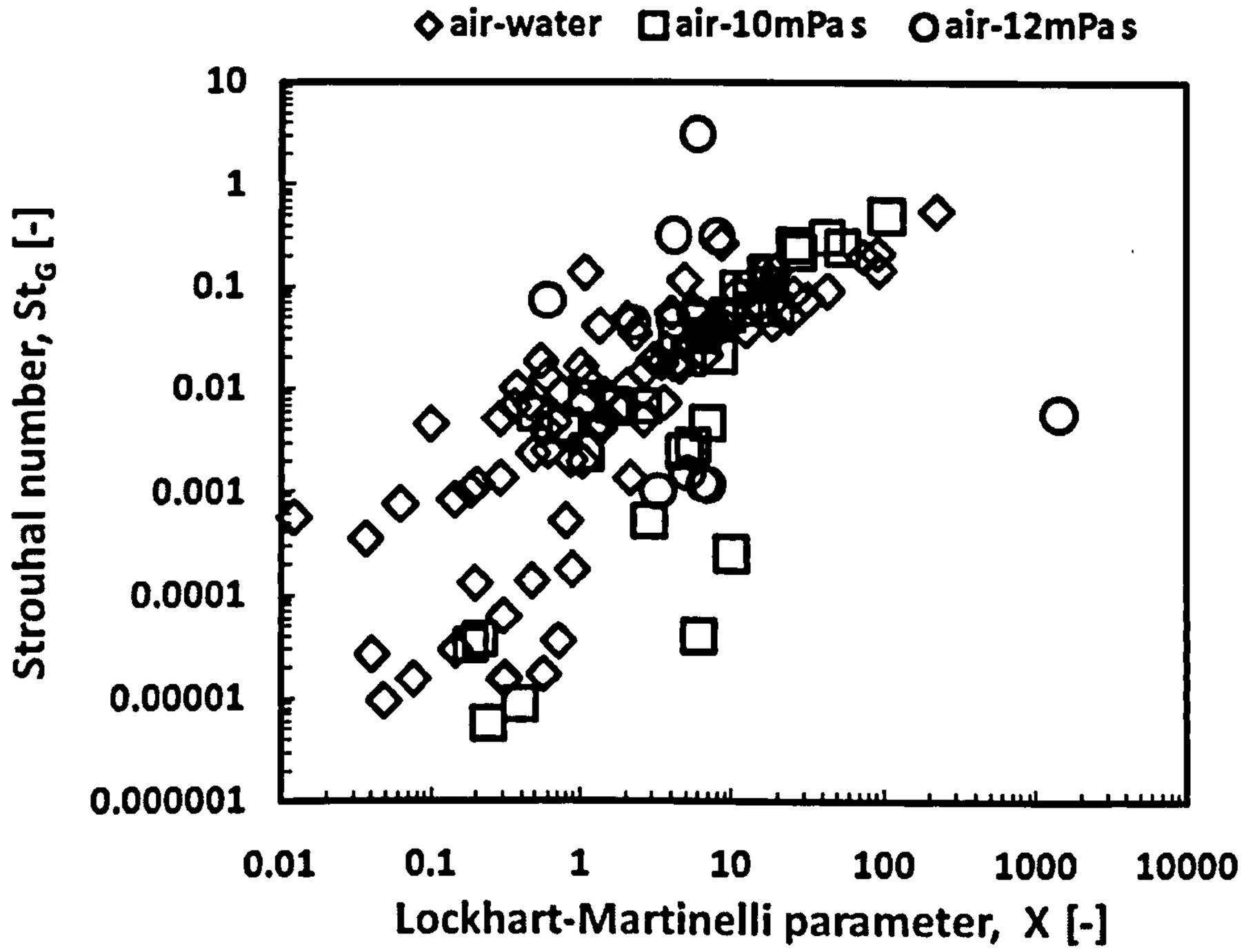

Figure 3.9: correlation of structure frequency using gas based Strouhal number with Lockerhart-Martinelli parameter.

In this analysis, a constant and unique value was used in each of the cases considered. These data follow same trend as the trend observed in Figure 5.15 and will fall on the same line if plotted together. The dependence of structure frequency on superficial gas and liquid velocities is clearly demonstrated in Figure 3.9.

The best linear equation fitting the experimental data points in Figure 3.9 takes the form:

$$St_G = 0.009\, V_{SG} \sqrt{\frac{\rho_L}{\rho_G}} \qquad (3.3)$$

Combining Equations (3.1) and (3.2) yields the following expression for slug frequency:

$$f_{slug} = 0.009\, V_{SG} \sqrt{\frac{\rho_L}{\rho_G}} \qquad (3.4)$$

Provided inlet condition is known, slug frequency can be estimated from Equation (3.4).

3.4.4 Structure velocity

Time series of the void fraction can be examined further to extract velocity of periodic structure by cross-correlating two signals from conductance probes separated 20 mm apart. Cross-correlation produces transit time in seconds. Structure velocity is obtained by dividing the separation distance between the probes by the transit time. Cross-correlation technique has been discussed in detailed by Omebere-Iyari (2006).

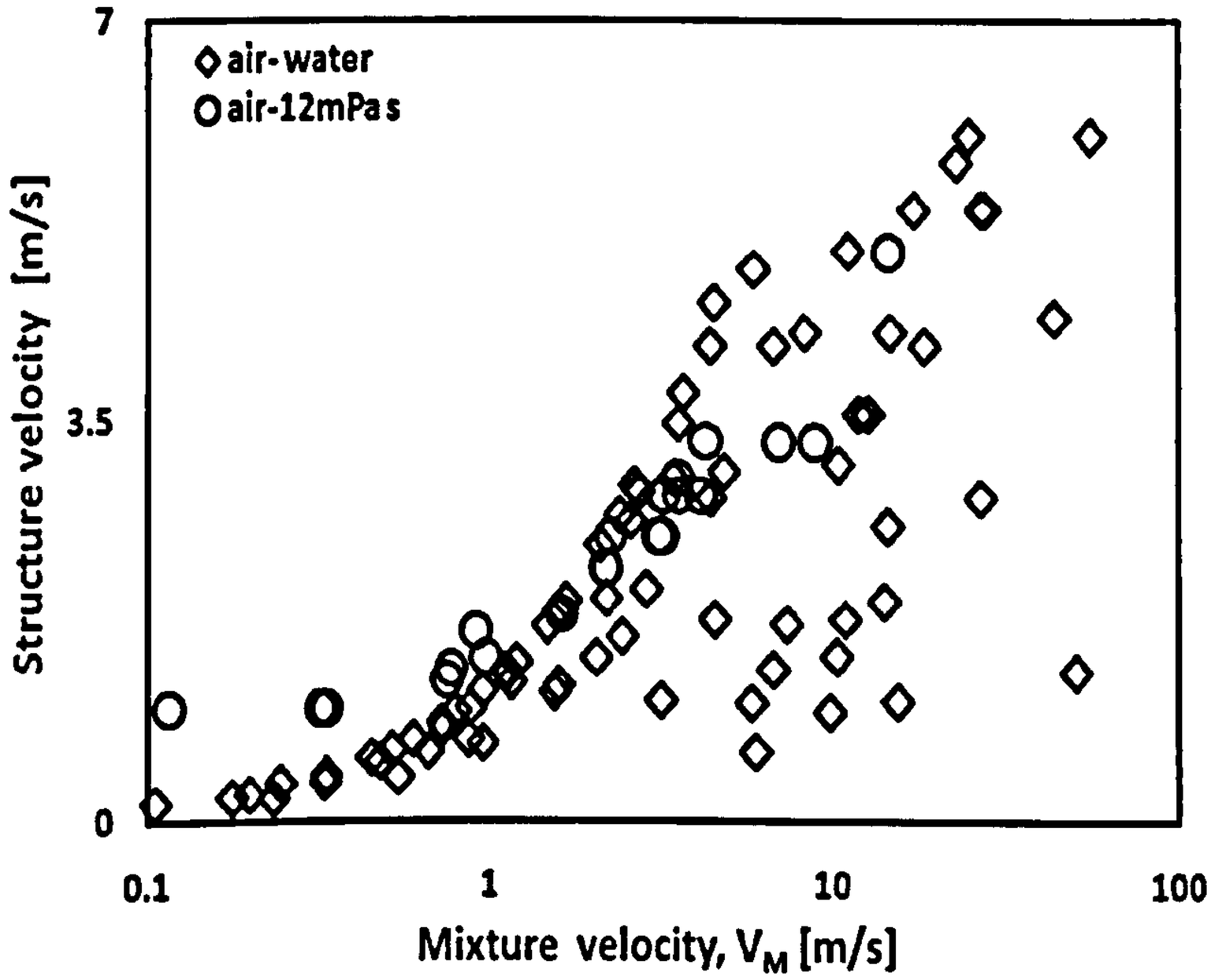

Figure 3.10: Structure velocity as a function of mixture velocity for air/water and air/12 mPa s viscous liquid.

Figure 3.10 shows how structure velocity varies with mixture velocity for air/water and air/12 mPa s viscous liquid respectively. The figure shows that at low superficial velocities, there exists a noticeable difference in structure velocity between air/water and

air/12 mPa s viscous liquid. However, at higher mixture velocities, both structure velocities become indistinguishable Figure 3.10.

Further analysis to determine the drift velocity of the flow structure is carried out on data in Figure 3.10. The data were re-plotted on a log-normal plot as shown in Figure 3.11. The intercept on the vertical in Figure 3.10 and Figure 3.11 gives an indication of drift velocity of the flow structure velocity according Nicklin et al. (1962).

Flow structure in air-glycerol mixture exhibits higher drift velocity as shown in Figure 3.10 and Figure 3. The reason for this behavior can be attributed to the effect of surface tension on structure velocity. Water has a surface tension of 0.073 N/m that of glycerol being 0.046 N/m at the test condition. Surface tension forces hold the flow structure together. The higher the surface tension acting between the interface, the lesser the structure frequency Figure 3.8.

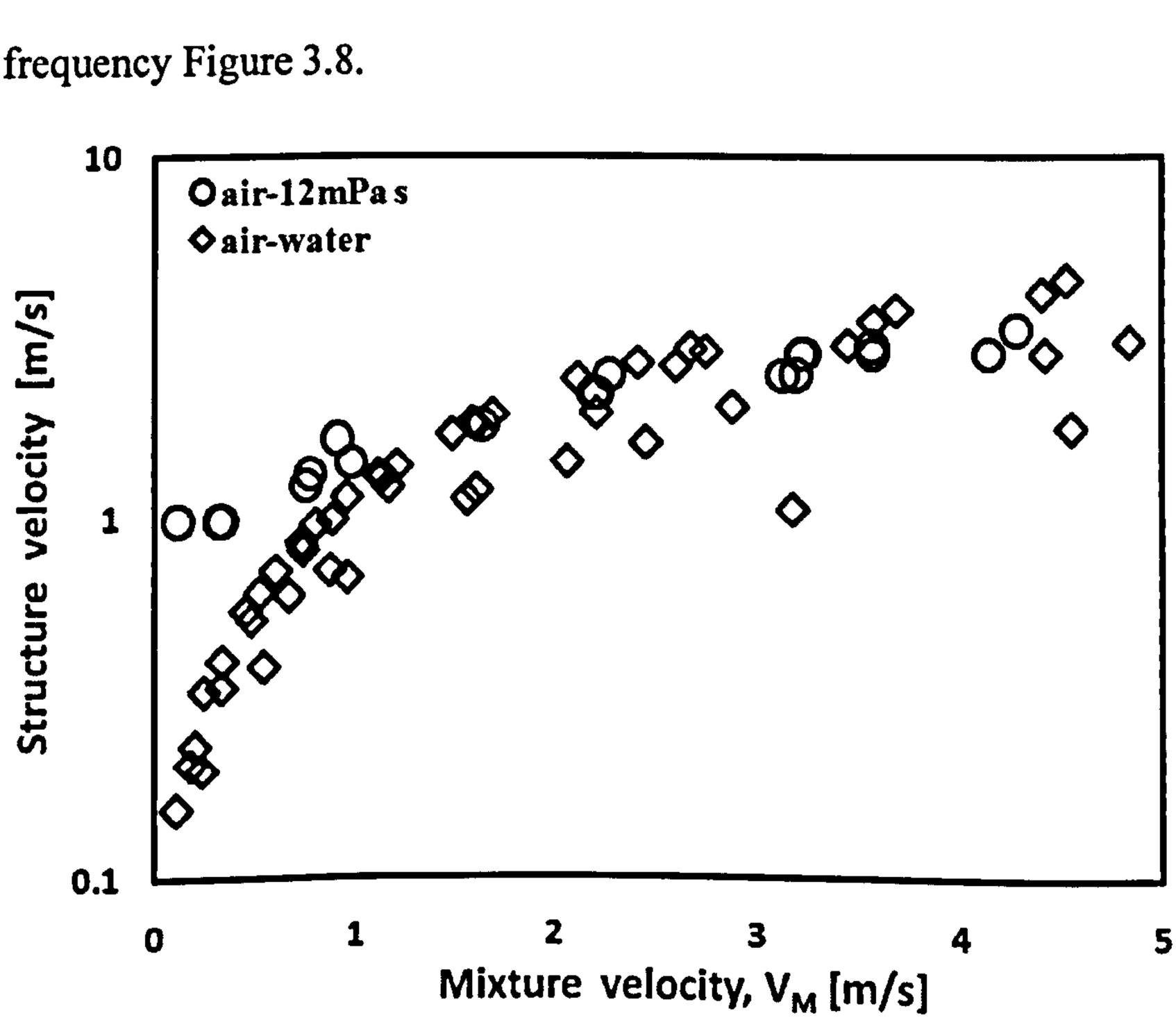

Figure 3.11: Effect of physical properties on structure velocity in the slug flow regime for air/water and air-12mPa s viscous liquid.

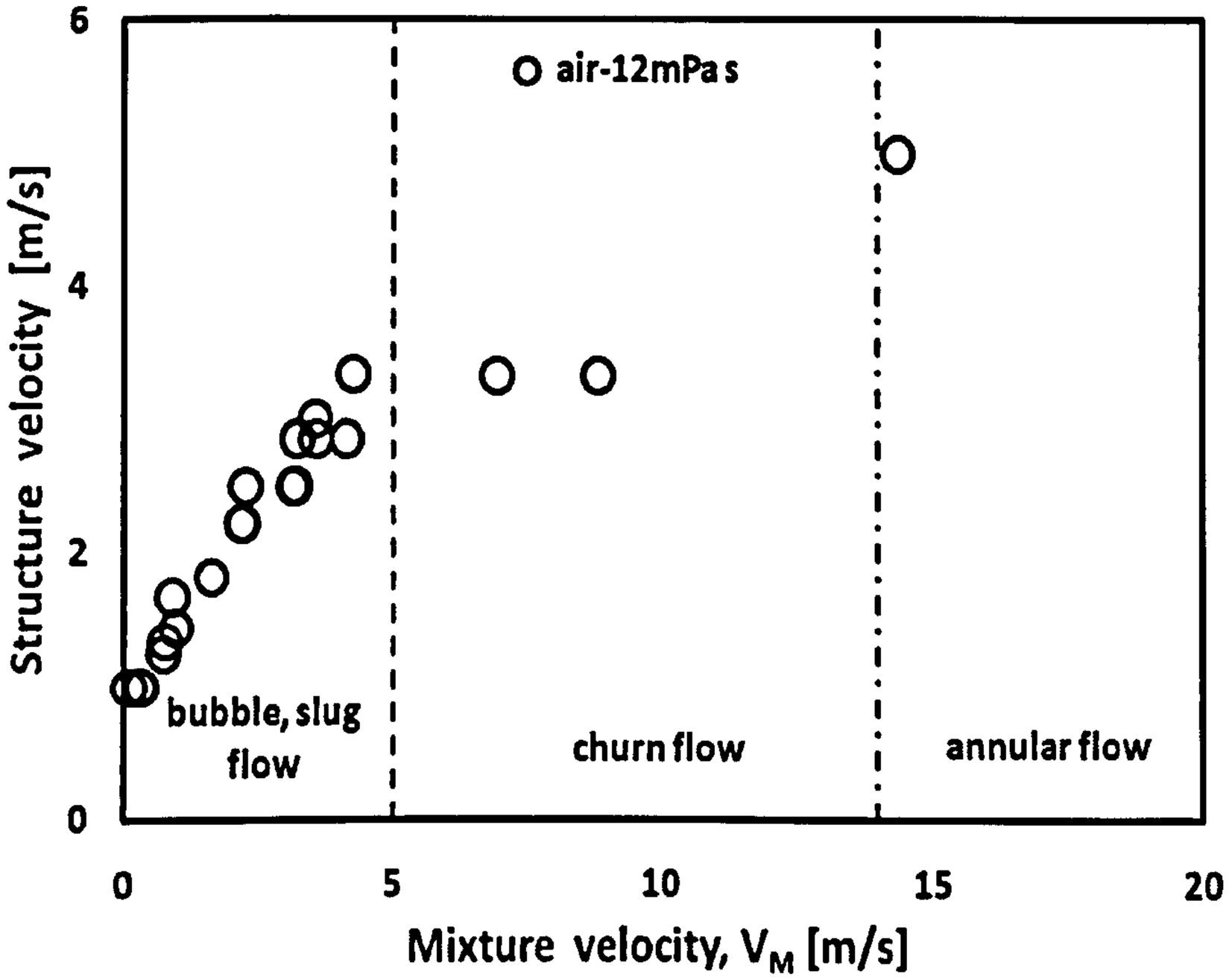

Figure 3.12: Identification of flow regimes using structure velocity variation with mixture velocity for air/12 mPa s.

Analysing the data further, structure velocity variation with mixture velocity for air/12 mPa s viscous liquid is presented in Figure 3.12 to extend the analysis to cover churn and annular flow regimes. Figure 3.12 reveals that in the bubble and slug flow regimes, structure velocity increases monotonically with mixture velocity. However, a point of inflection is reached around V_M = 5 m/s. This point marks beginning of churn flow regime. After this point, the structure velocity remains constant with increase in mixture velocity. Another transition is boundary is crossed around V_M = 14 m/s where the structure velocity becomes higher than in churn flow. This point marks the beginning of annular flow.

In bubble/slug flow dominated regime, bubble coalescence takes place. In the slug flow, Taylor bubbles may coalesce to form bigger bubbles until a critical bubble diameter is reached when gas stream shear overcomes the surface tension and the gravity forces.

Churning of liquid film, flow reversal, flooding and liquid loading may occurs. At this point, bubble collapse and break-up occurs. Net momentum transfer across the phases is zero as bubble coalescence and collapse compensate each other. Hence, the existence of plateau as noticed in Figure 3.12. In churn flow, huge waves dominate the surface of the liquid film. The liquid flows as film around the pipe wall whilst the continuous phase gas flows in the centre transporting the entrained droplets as core flow.

Transition to annular flow occurs around V_M = 14 m/s according to Figure 3.12. This is particularly interesting as the value agrees with V_{SG} = 15 m/s at the transition to annular in a pipe of similar diameter with T-junction to divert part of the flow reported in Chapter 7. Although the controlling mechanism is different for T-junction and pipe flow, this link in transition to annular flow between the two systems suggests there is interrelationship between the flow pattern transitions even when geometry is different.

At the beginning of annular flow the gas velocity is sufficient to lift the entrained liquid up as the drag from the gas phase overcomes the gravity force acting downward forcing the droplet down.

In conclusion, the mechanism governing the flow from one flow pattern to another is different as discussed using information from dynamics of flow structure in two-phase flow. A common area exists in flow pattern transition between pipe flow and dividing junction as demonstrated by transition to annular flow.

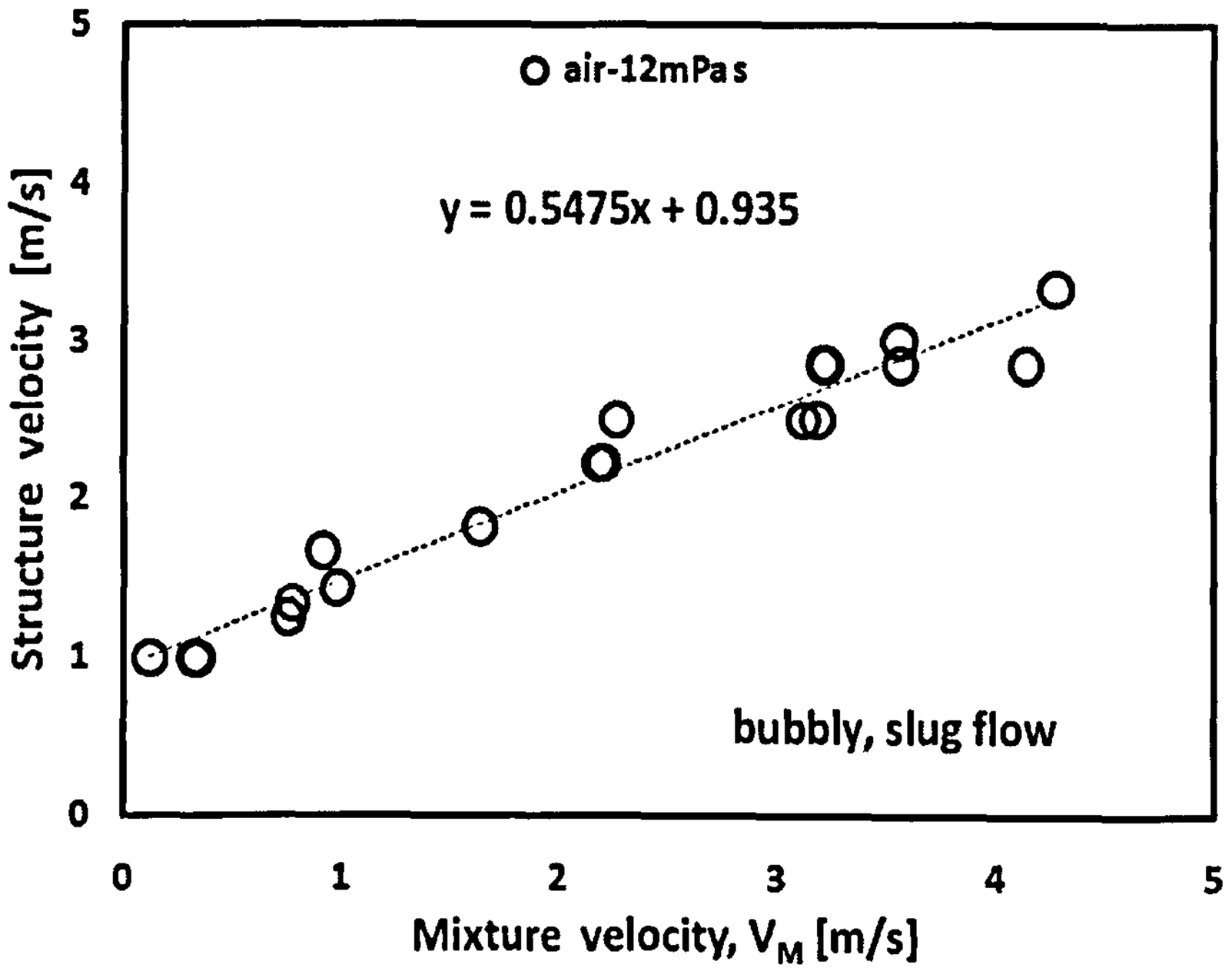

Figure 3.13: Effect of physical properties on structure velocity in the slug flow regime for air-12mPa s viscous liquid.

Flow distribution coefficient, C_o and drift velocity, V_D can be determined experimentally especially in slug flow regime when structure velocity is plotted against mixture velocity as shown in Figure 3.13 for air-glycerol solution based on the idea of Nicklin et al. (1962).

According to Azzopardi (2004), one interesting finding is that the velocities of void waves, Taylor bubbles and wisps all lay on the curve proposed by Nicklin et al. (1962) for slug flow. Following this, it is seen that a deviation from the Nicklin's curve occurs when the flow changes to churn. According to Figure 3.13, based on the idea of Nicklin, it is observed that $C_o = 0.5475$, the slope of the straight line representing the data. This is much lower than the value of 1.2 reported by Nicklin et al. (1962) from air/water experiments. The possible reason may be that the bubbles entrained in the liquid are wall-peaking. It is well known that small bubbles tend to flow in the near wall region and present a wall-peaking profile of the gas holdup, whereas large bubbles tend to

migrate to the core region forming a core-peaking profile. Based on the definition of C_o, velocity of the bubble travelling at the centre-line is lower than that at the wall for a core-peaking behaviour. The likely cause of this phenomenon may be the presence of tiny bubbles dispersed in the liquid slug. This was observed during the experiment. What actually started as slug flow turned bubbly flow when colour of the liquid turned milky after few minutes of start-up. This can be supported by the PDF plot in Figure 3.7. Therefore, it is not surprising that Nicklin's equation fails to capture C_o as expected for air/12 mPa s viscous liquid flow because it was formulated based on on slug flow mechanism.

The C_o value of 0.5475 is too low compared to C_o = 1.2 for air/water. This is the limitation of this method. The C_o should clearly be more than or equal to 1.2 at least. Again, it is also evident from time resolved void fraction plot Figure 3.5 that air/12 mPa s viscous liquid displays a lower value of void fraction when it is compared with air/water data at same inlet condition.

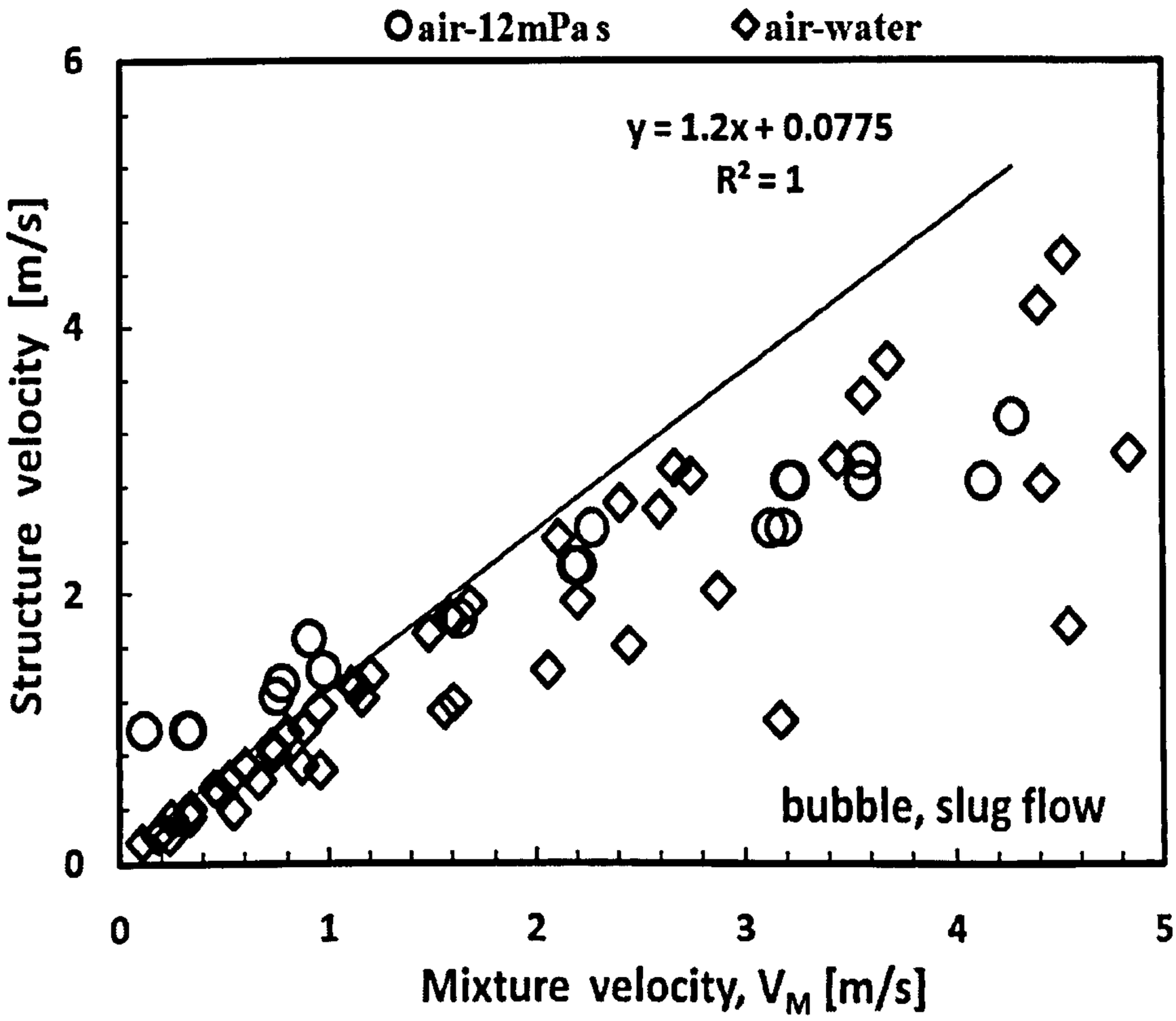

Figure 3.14: Determination of distribution coefficient from Nicklin/Davison line.

Figure 3.14 shows a good agreement between air/water data and Nicklin et al. (1962) line. The slope of the air/water line, that is the flow distribution coefficient, C_o equals 1.20 and the drift velocity, V_D, which is the intercept on the structure velocity line, being equal 0.0775 m/s. The value of C_o agrees with C_o =1.17 reported by Omebere-Iyari (2006). The reason for this good agreement may be due to the nature of the formulation of the Nicklin's equation. The derivation was based on potential flow analysis according to Davies and Taylor (1950). Effect of surface tension and liquid viscosity was not taken into account. Therefore, it is not surprising it works well for air/water.

Air/12 mPa s viscous liquid shows a departure from Nicklin's line before V_M = 1 m/s and after V_M = 2 m/s. This may be as a result of the effect of physical properties, surface

tension and liquid viscosity. It seems liquid viscosity has a stronger effect on flow distribution coefficient, C_o while drift velocity is surface tension dependent.

As earlier reviewed in Chapter 2 sub-sections 2.1.2, 2.1.3 and 2.1.4, for laminar flow the ratio v_{max}/v_{mean} approaches 2.0 and indeed there is strong indication that C_0 increases as the Reynolds number decreases and reaches a value of about 2.0. A more precise theory shows that C_0 for laminar flow equals 2.27 as reported by Taylor (1961); Collins et al. (1978) for the case where the surface tension is neglected. The exact value of C_0 for both turbulent flow and laminar flows is inconclusive.

Hale (1994) has attributed the non-uniqueness of value of C_o to the nature of the plot of structure velocity or bubble translational velocity against mixture velocity plot. The plot is not perfectly linear, but instead bends very slightly upwards (Bendiksen, 1984). The exact value of C_o is not clear for all flow conditions and reported experimental values spread considerably from 1.02 to 1.35, Xiaodong (2005). Nicklin et al. (1962) suggested a constant of 1.2 for fully developed turbulent flow, but noticed the variation of this coefficient at low Reynolds numbers (< 8000).

Again, refer to the classical work of Weber (1981) for small diameter pipes, Weber showed that the surface tension is important as its increase considerably decrease the drift velocity. This statement agrees with recent observations in Figure 3.13. Using air/water as a reference, air/12 mPa s glycerol solution has a lower surface tension of 0.046 N/m and a higher V_D = 0.935 m/s compares to air/water with V_D = 0.0775 m/s from Figure 3.14.

Next, calculating C_o from measured void fraction using drift flux approach is considered.

3.4.5 Flow Distribution Coefficient, C_o

Flow distribution coefficient is the ratio of centre-line to mean velocity in turbulent flow as suggested by Nicklin et al (1962). It is suitable to model liquid slugs in fully developed flow. Nicklin Equation for the velocity of Taylor bubbles in fully developed slug flow is given by the following expression:

$$\underbrace{V_T}_{Structure\ velocity} = 1.2\ \underbrace{(V_{SG} + V_{SL})}_{Mixture\ velocity} + \underbrace{0.35\sqrt{gD}}_{Drift\ velocity} \qquad (3.5)$$

Where:

Drift velocity = rise velocity of Taylor bubble in liquid slug, m/s.

Recently, Taitel & Barnea (1990) has emphasised that drift velocity is expected to depend on liquid viscosity based on observation from their experimental work.

Next, using similar approach flow distribution coefficient and coefficient of second term in Equation (3.5) will be determined from measured void fraction.

3.4.6 Drift flux approach

Zuber & Findlay (1965) proposed a drift flux model which relates inlet condition, void fraction and flow distribution coefficient as given by the following expression:

$$V_G = \frac{V_{SG}}{\epsilon_g} = C_O V_M + V_D \qquad (3.6)$$

Woldesemayat and Ghajar (2007) carried out comparison of the performance of 68 void fraction correlations based on unbiased data set of 2845 data points covering wide range of parameters than any previous assessments made. The duo engaged on comprehensive

literature search for the available void fraction correlations and experimental void fraction data. After systematically refining the data, the performance of the correlations in correctly predicting the diverse data sets was evaluated. The analysis showed that most of the correlations developed are very restricted in terms of handling a wide variety of data sets. Based on the observations made, an improved void fraction correlation which could acceptably handle all data sets regardless of flow patterns and inclination angles was developed. The inclination angle and the system pressure effect on the measured void fraction data were closely analyzed a nd accounted for in their n ew correlation.

Bankoff (1960) has shown that the non-uniformity in phase distribution is a function of pressure while Zuber and Findlay (1965) emphasized the importance drift velocity. The latter claimed drift velocity is a function of the concentration profile and that it is also dependent on momentum transfer between the phases. The concentration profiles across the pipe for a given inclination are generally assumed constant for flows without mass transfer along the pipe length.

Integrating these observations and noting that this effect is normal to the pipe inclination, a correction factor of the form $[1 + \cosh]^{0.25}$ was introduced . The functional dependency of drift velocity on the momentum transfer between the phases assuming one dimensional force interaction would be a maximum for pipes with very high inclination angles operating near atmospheric pressure. This effect could conveniently be captured by the factor, $[1 + \sin\theta]^{\left(P_{atm}/P_{sys}\right)}$. where P_{atm} and P_{sys} are the atmospheric and system pressures respectively.

These two correction factors have been introduced into the drift velocity expression of Dix (Coddington and Macian, 2002) correlation. Hence, the modified correlation of Woldesemayat and Ghajar (2007) becomes:

$$\varepsilon_g = \frac{V_{SG}}{C_O V_{SG} + V_{Drift}} \quad ; \; C_O = 1 + \left(\frac{V_{SL}}{V_{SG}}\right)^n ; \; n = 1 + \left(\frac{\rho_g}{\rho_L}\right)^{0.1} \tag{3.7}$$

Where:

$$V_{Drift} = 2.9\left[\frac{gd\sigma(1+Cos\theta)(\rho_L - \rho_g)}{\rho_L^2}\right]^{0.25}(1.22 + 1.22Sin\theta)^{\frac{P_{atm}}{P}} \tag{3.8}$$

V_D = drift velocity, m/s; V_m = superficial mixture velocity, m/s; V_G = gas velocity, m/s, C_o = flow distribution coefficient, [-]

Therefore, C_o can be estimated from the measured void fraction by calculating drift velocity from Equation (3.8) and substitute the value in Equation (3.7). The results are presented in Table 3.1 , Figure 3.15 and Figure 3.16 respectively.

From Figure 3.15 and Figure 3.16, C_o is varying with mixture velocity (liquid superficial velocity) probably because as liquid superficial velocity goes to zero, the Reynolds number for the liquid ($Re_L = \frac{\rho V_{SL} d}{\mu_L}$) becomes more laminar. For instance, if V_{SL} = 0.8 m/s, the Re = 400. Nicklin et al.(1962) reported C_o can go to 2.0. This explains why the distribution of Co for air/12 mPa s in Figure 3.15 clusters around 2.0. Basically, the figure shows that air/12 mPa s glycerol solution C_o concentrated around 2.0 while that of air/10 mPa s concentrated around 1.60 Figure 3.16.

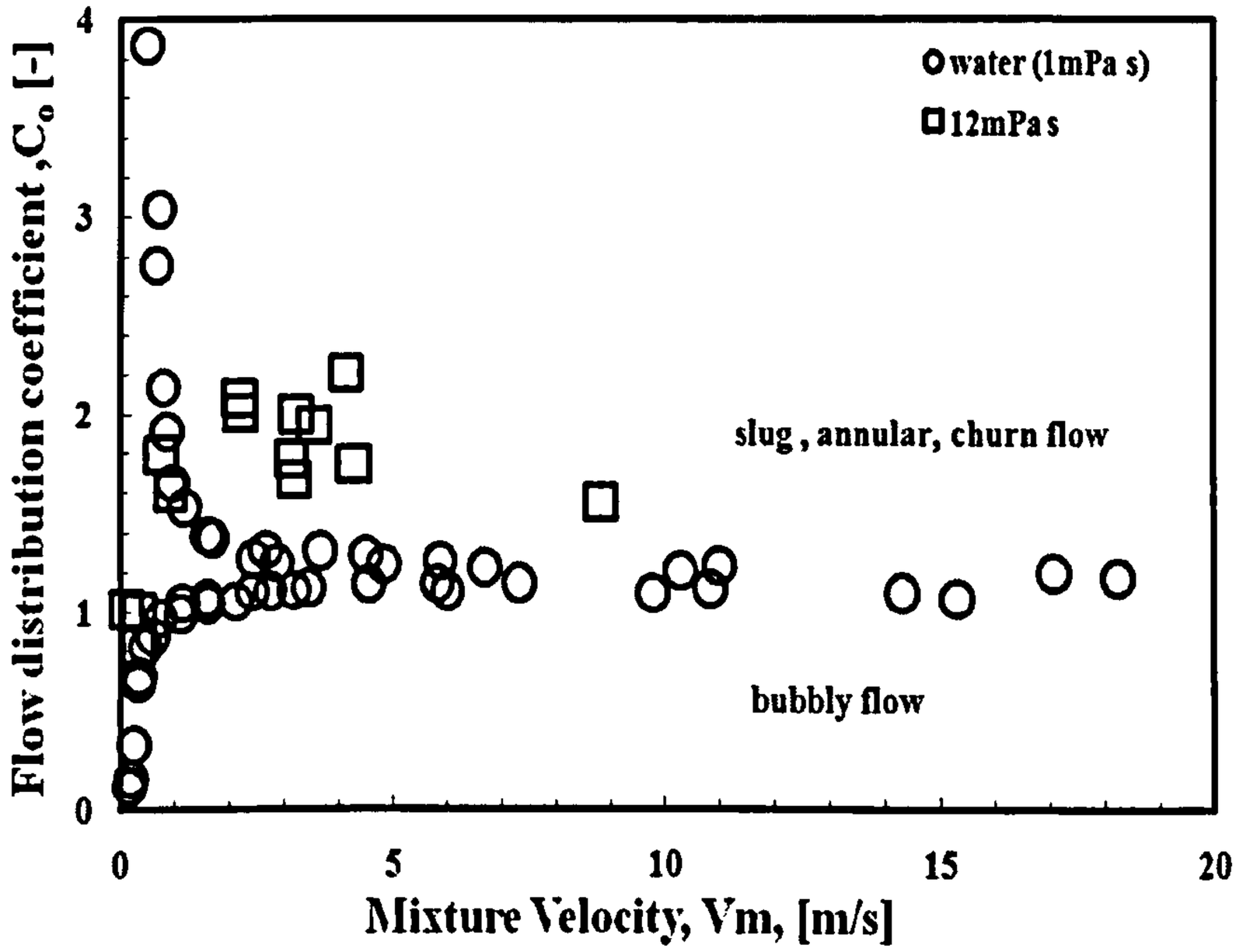

Figure 3.15: Flow parameter as function of superficial mixture velocity.

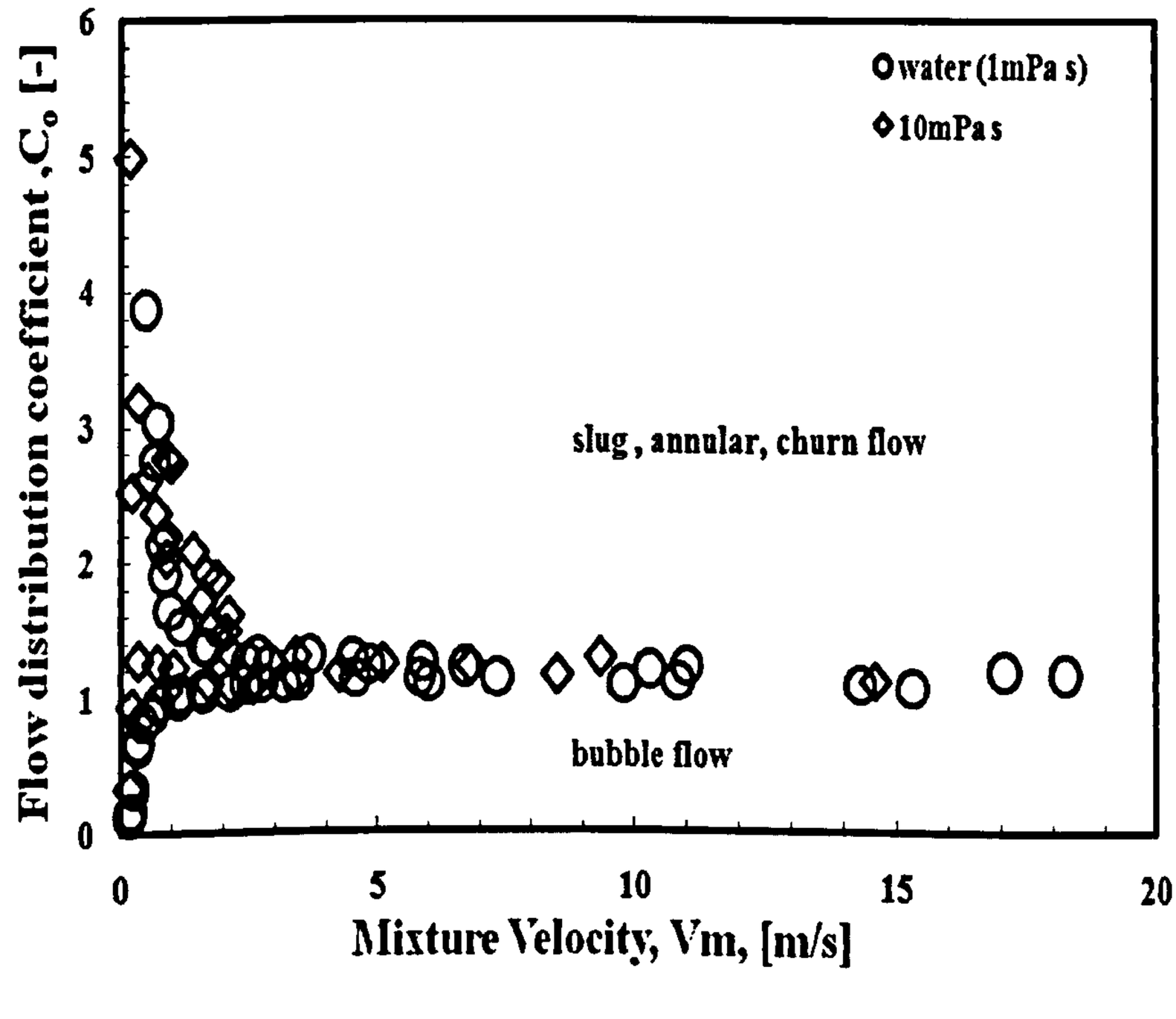

Figure 3.16: Flow parameter as function of superficial mixture velocity.

This implies that flow structure, Taylor bubble in case of slug flow, travel faster at the centre-line with air/12 mPa s glycerol solution two-phase flow than in air/water at the same inlet condition.

Table 3.1: Table of physical properties, C_o and C_1 for the test fluids

Fluid	Liquid density [kg/m^3]	Surface tension [mN/m]	Drift velocity [m/s]	C_o [-]	C_1 [-]
Air/water	999	0.073	0.1651	1.2	0.7455
Air/10mPa s	1177	0.078	0.1612	1.6	0.7279
Air/12mPa s	1200	0.046	0.1405	1.6	0.6347

Omebere-Iyari (2006) using air/water with the same experimental facility reported a value of 1.17 for Co and -0.16 m/s for drift velocity when he plotted structure velocity against mixture velocity under intermittent flow conditions (Slug & Churn). This is in good agreement with the average value of 1.20 for C_o obtained using present approach. Also, the drift velocity calculated using Equation (3.8) yields V_D = 0.16 m/s which agrees 100% with the Omebere-Iyari (2006) value of V_D = -0.16m/s in slug and churn flow regimes. The only difference is in the flow direction as indicated by the negative sign which signified reverse flow possibly due to dominance of churn flow.

Flow distribution coefficient appears to be higher for the larger liquid viscosities used as indicated in Figure 3.15 and Figure 3.16 respectively. Both figures have same C_o of about 1.60 if the statistical average is determined from the distribution C_o. This is not surprising as the difference in viscosity is very small about 2 mPa s. In the case of 10

mPa s, C_o decreases from a value of about 5.0 with increasing mixture velocity to a value of 1.6; for air/water, C_o decreases from 4.0 to a value of about 1.2. This ties in with the findings of Schmidt et al. (2008).

The bifurcation along the average C_o line is another interesting feature noticed in the trend displayed by C_o for Bubbly flow as highlighted by Figure 3.15 and Figure 3.16 respectively. The bifurcation delineates churn, slug and annular flow from bubbly flow. This can also be supported by visual observation during the experiment. Based on this division, flow pattern above the average C_o line is characterized by periodic structures travelling faster than the mixture velocity at the centre-line. This is characteristic of slug, churn and annular flow. They are often dominated by huge waves which travel faster than disturbance. Another possible reason to support the former statement may be core-peaking effect whereby the flow structures travel along the centre-line couple with the influence of centripetal acceleration on the flow structure.

In the case where C_o is less than unity for instance the flow was observed to be bubbly where wall-peaking effect dominates, with bubble velocity in the liquid stream less than the mixture velocity. All values of C_o below 1.0 for air/water, air/10mPa s and air/12 mPa s viscous liquids may be a direct result of wall-peaking effect in bubbly flow regime where the centre-line velocity is less than the total superficial velocities. Therefore, if Nicklin's expression is suitable for slug flow then the expression has to be modified to reflect changes in C_o as liquid physical properties change. Before the modification to Nicklin's expression, drift velocity will be discussed first.

Drift velocity is the velocity of gas phase relative to the gas-liquid mixture velocity. Drift velocity of 0.07752 m/s is obtained if it is calculated from expression of Nicklin's expression ($0.35\sqrt{gD}$) for the present case where pipe internal diameter equals 0.005 m. However, a different value of drift velocity, V_D = -0.16 m/s was reported by Omebere-Iyari (2006) which agrees very well with the value V_D = 0.16 m/s using the proposed drift velocity correlation by Woldesemayat and Ghajar (2007) except in the flow direction. These values are an order of magnitude higher than the value obtained from Equation (3.5). The difference in value obtained is due to the inclusion of physical properties in the calculation of drift velocity using Equation (3.8). Using the value of drift velocity to determine the drift velocity coefficient, C_1 (Equation 2.5), the results are reported in Table 3.1. The value of C_1 = 0.7455 obtained for air/water is more than twice a value of C_1 = 0.35 using Nicklin's equation.

Modification to the Nicklin's expression to reflect new C_o and C_1 is necessary in order to predict structure velocity with upmost accuracy in the slug flow regime. Therefore, an improved version of Nicklin 's expression is proposed for slug translational velocity for air/water and air viscous liquid two-phase flows as follows:

$$V_{Slug} = C_0 V_M + C_1\sqrt{gD} \qquad (3.9)$$

Where $V_M = V_{SG} + V_{SL}$

The coefficients of the LHS of Equation (3.9) are available in Table 3.2 for different correlations.

3.4.7 Slippage between gas and liquid phases

As an alternative to the drift flux model, the slip S, between the phases, by definition equal to the ratio of gas velocity, V_G, to liquid velocity, V_L, may be used to calculate the void fraction. Both slip and drift flux models have been used extensively in the literature to correlate experimental pressure drop and void fraction data.

Schmidt et al. (2008) define slip ratio, S, by the following expression:

$$S = \frac{\varphi(1-\varepsilon_g)}{\varepsilon_g} \quad ; \; \varepsilon_g = S.\left(\frac{V_{SG}}{V_{SL}}\right) + V_{SG} = \left(\frac{\varphi}{S+\varphi}\right) \tag{3.10}$$

Where:

$$\varphi = \frac{V_{SG}}{V_{SL}} \tag{3.11}$$

S = Slip velocity ratio, [-]

In order to investigate effect of liquid viscosity on slip ratio Equation (3.10) and Equation (3.11) were utilized using the measured value of void waves obtained during the experiment with air and liquid of different liquid viscosities. The results are shown in Figure 3.17.

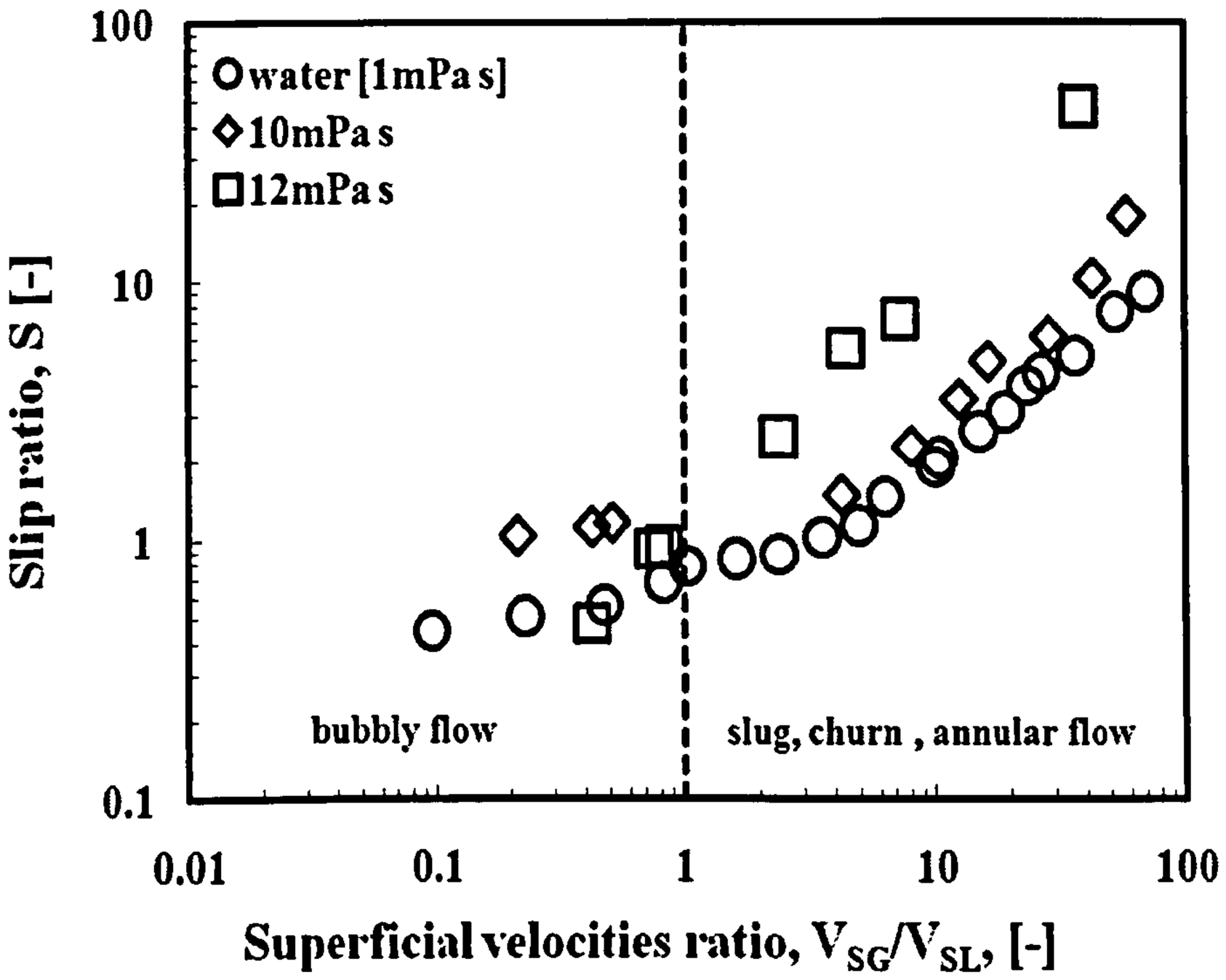

Figure 3.17: Slip ratio, S, as a function of superficial velocities ratio

In Figure 3.17, slip ratio is almost unity for superficial velocities ratio less than 1.0. However, for values of φ above 1.0, effects of liquid viscosity can be seen as the line for air-10mPa s and air-12mPa s shift towards higher slip ratio with air-12mPa s tending towards highest slip ratio.

Another comparison was carried out for V_{SL} = 0.4 m/s for air/water and air-10mPa s as in Figure 3.18. Again, higher slippage is experienced by the fluid because of the resistance of the liquid phase. The lateral separation distance between the water and 10mPa s sugar solution is a direct effect of liquid viscosity as the flow experience higher slippage between gas and liquid phases when liquid viscosity increases from 1 mPa s (water) to 10 mPa s for sugar solution.

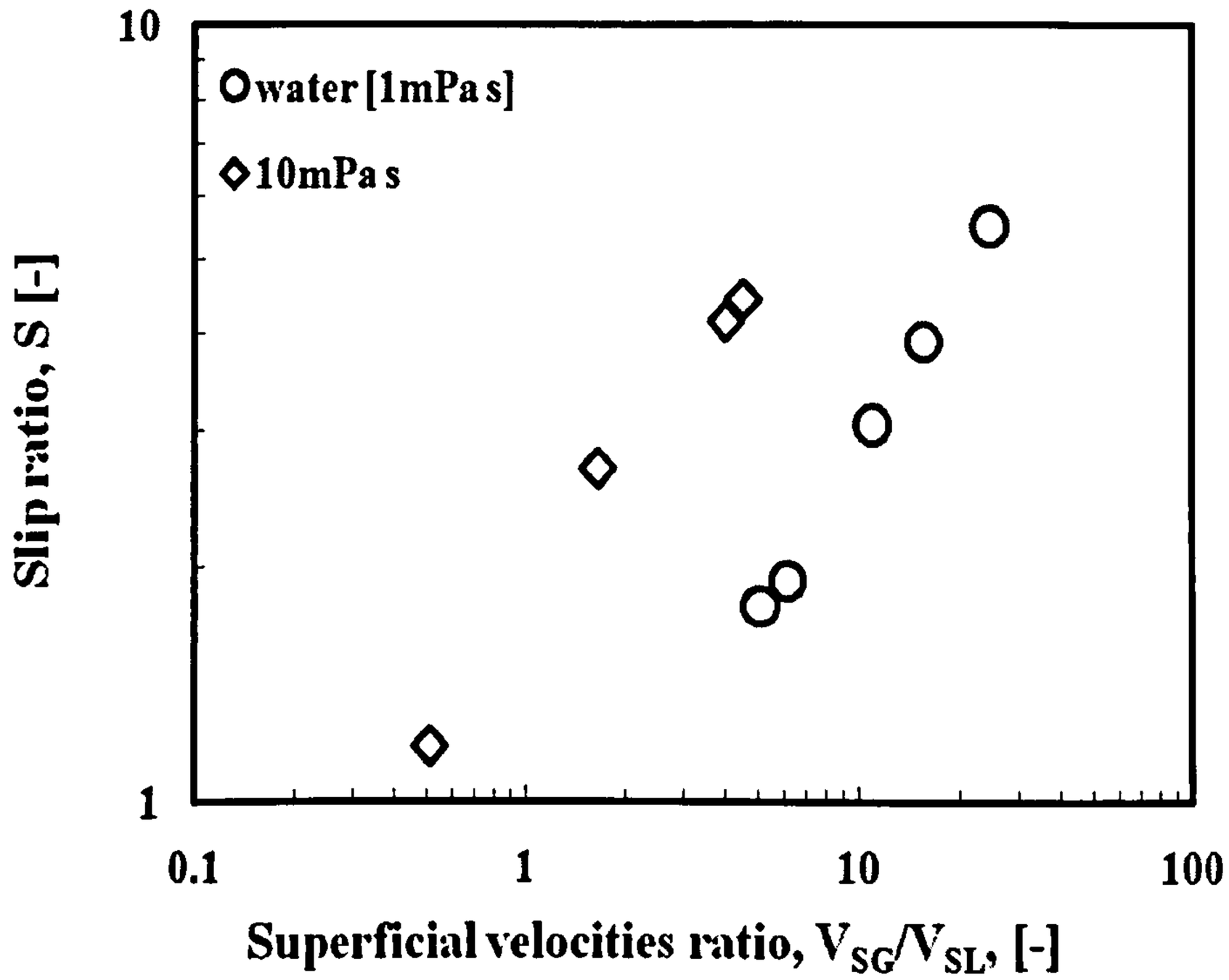

Figure 3.18: Slip ratio, S, as a function of superficial velocities ratio, V_{SL} = 0.4 m/s.

3.4.8 Flow pattern map

Effect of physical properties has been investigated by plotting the present data on the flow map of Taitel et al. (1980) as shown in Figure 3.19. At the same inlet condition V_{SG} = 0.27 m/s, V_{SL} = 0.64 m/s, effect of liquid viscosity and surface tension are observed in Figure 3.19. The operating point shifts from slug flow with air/water towards bubble flow (transition line) when the test fluids physical properties are changed to air/12 mPa s viscous liquid. This agrees with previous findings of Nan Da Hlaing et al. (2007) and Schmidt et al. (2008) for vertical upward flow that liquid viscosity causes flow pattern transition boundary to shift to the left on flow pattern map.

A similar behaviour has been reported by Taitel et al. (1980) for experiment with natural gas and crude oil. They reported transition to annular flow generally shifted towards lower gas superficial velocities due to effect of liquid viscosity. They also reported the

presence of micro-bubbles in the liquid tank which were difficult to remove without heating the liquid or complete evacuation from the tank.

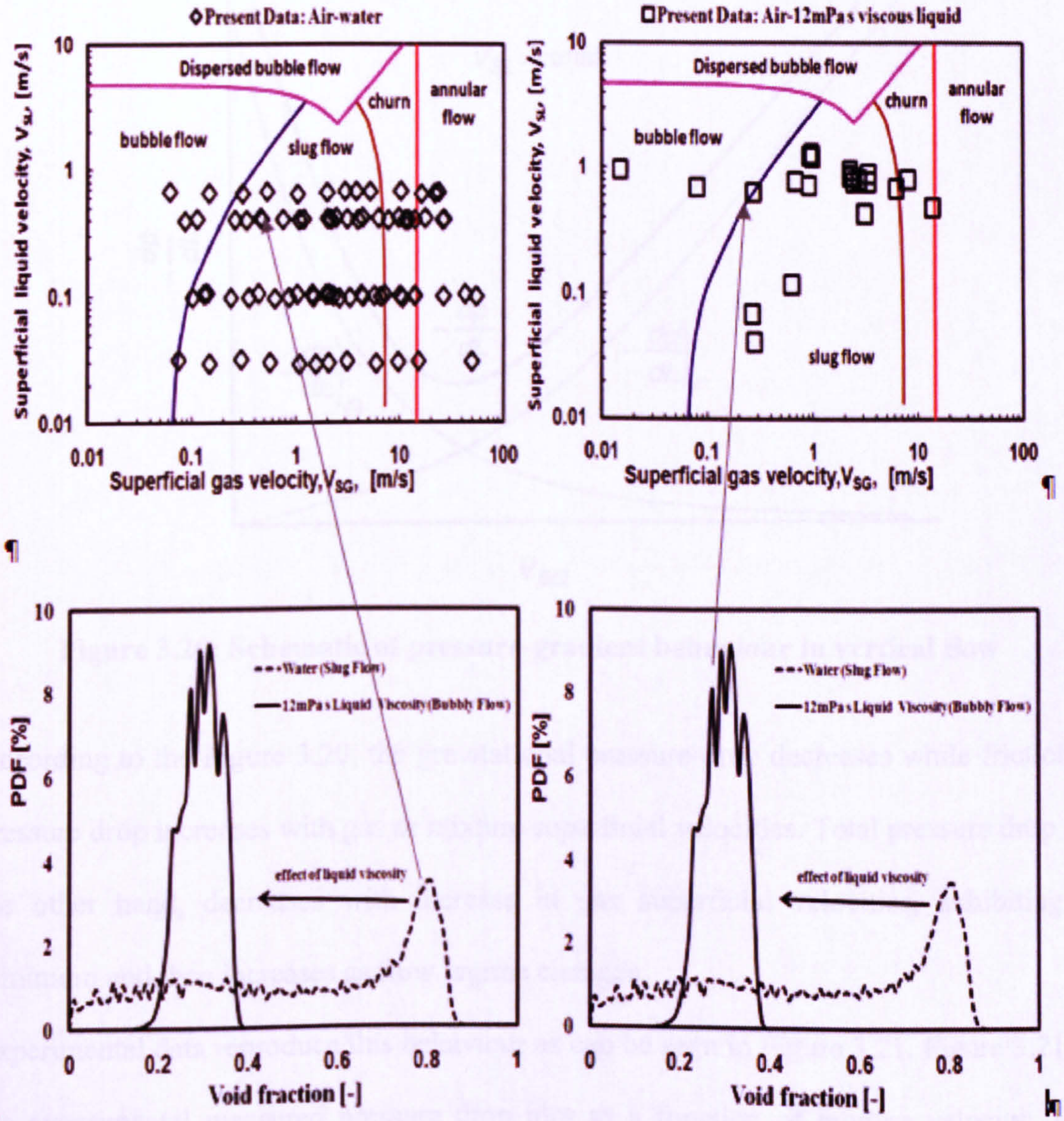

Figure 3.19: Top - Test matrix for air/water and air-12mPa s viscosity liquid represented on flow Pattern map of Taitel et al. (1980). Bottom – PDF of void fraction corresponding to air/water and air/12 mPa sviscous liquid. Inlet condition V_{SG} = 0.27 m/s, V_{SL} = 0.64 m/s.

3.4.9 Pressure Drop

The total pressure drop behaviour for vertical flow is shown schematically below in Figure 3.20. $(-dp/dL)_G$, $(-dp/dL)_F$ and $(-dp/dL)$ represents gravitational, frictional and total pressure drop respectively.

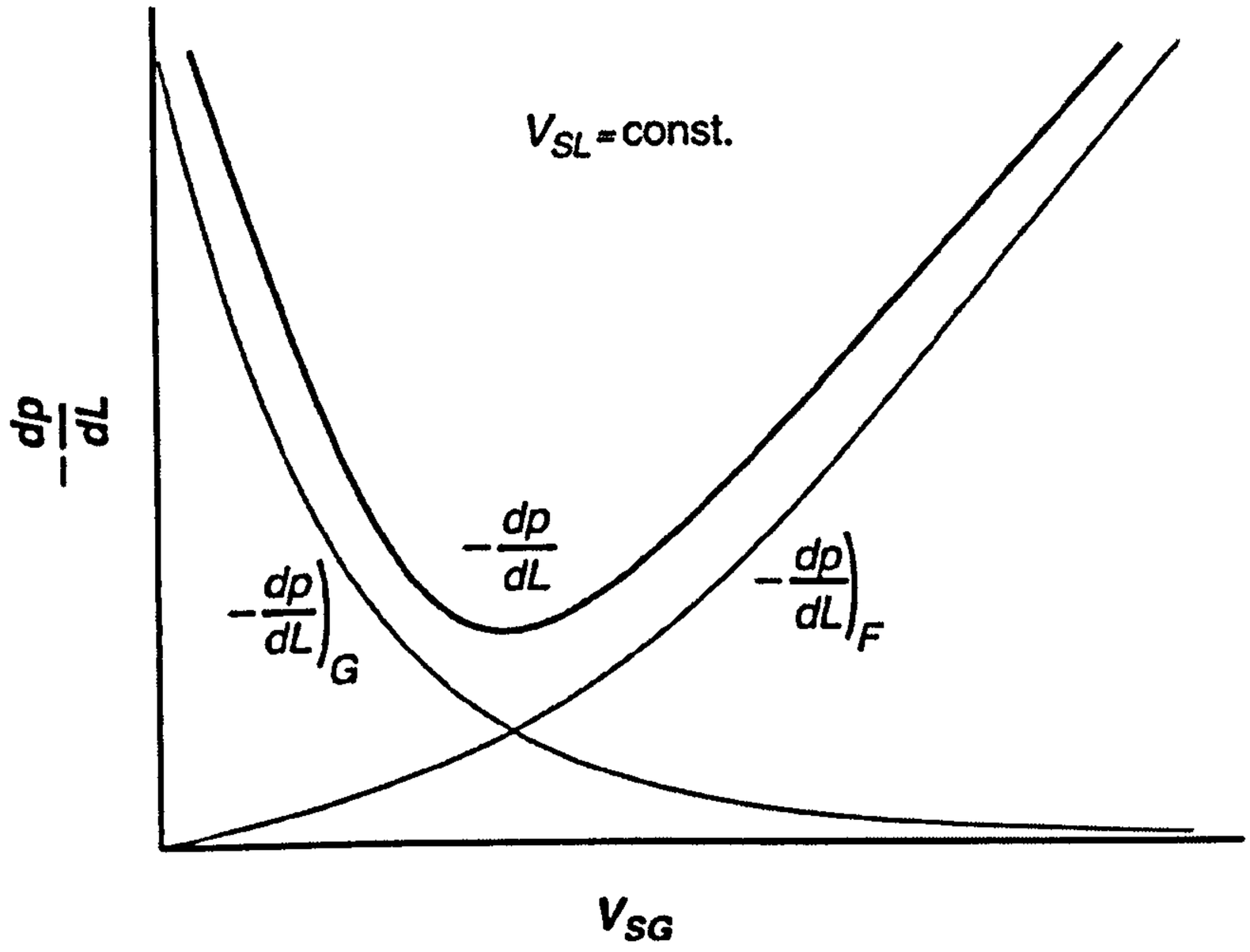

Figure 3.20: Schematic of pressure-gradient behaviour in vertical flow

According to the Figure 3.20, the gravitational pressure drop decreases while frictional pressure drop increases with gas or mixture superficial velocities. Total pressure drop on the other hand, decreases with increase in gas superficial velocities, exhibiting a minimum and then increases as flow regime changes.

Experimental data reproduce this behaviour as can be seen in Figure 3.21. Figure 3.21 is the experimental measured pressure drop plot as a function of mixture velocity. The pressure drop was measured across two pressure taps separated a distance 0.50 m apart. Pressure drop is noticed to decrease from 12410 [Pa/m] from Bubble/Slug flow

characterised by high liquid hold-up associated with high gravitational pressure gradient exhibiting a minimum during slug/Intermittent flow at 12330 [Pa/m].

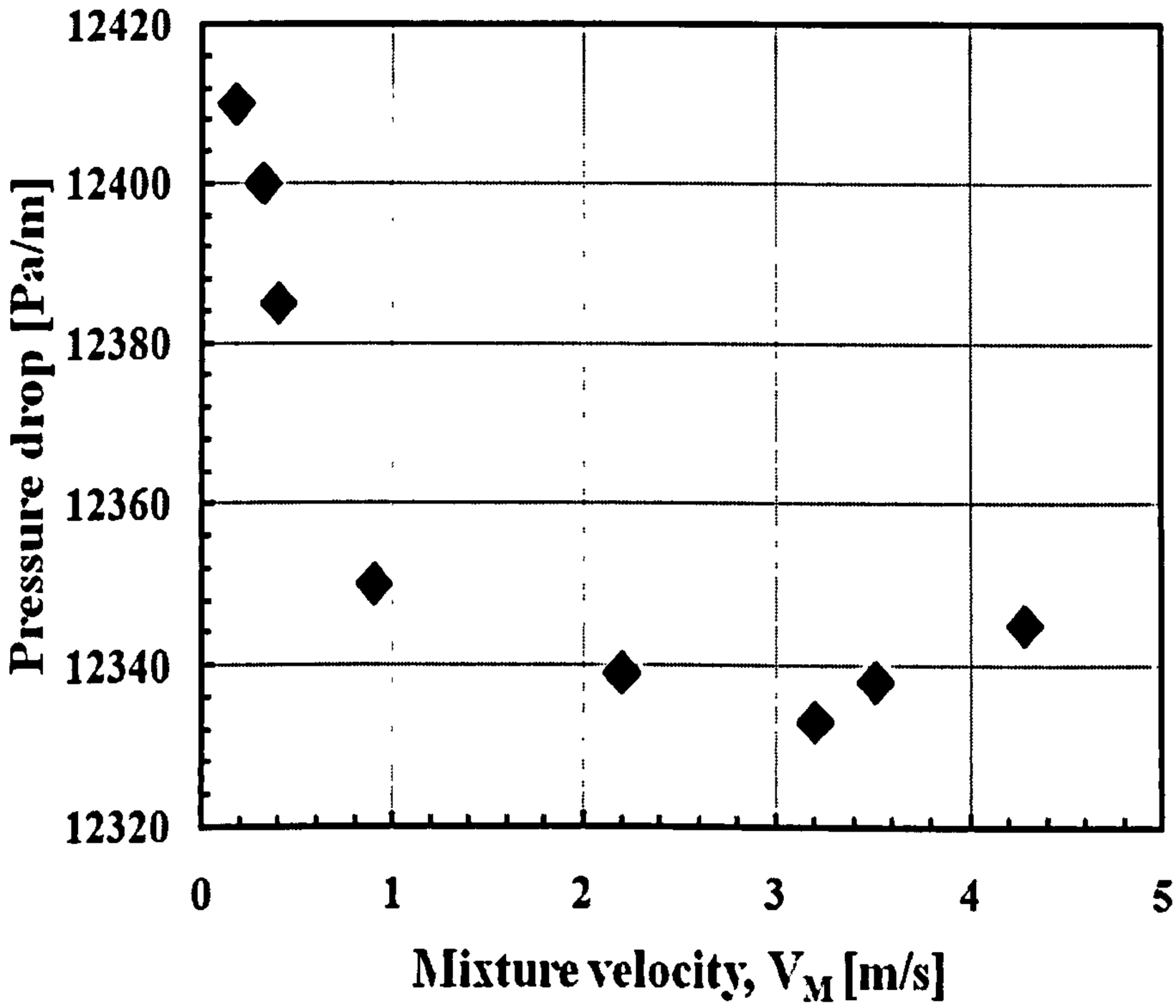

Figure 3.21: Pressure gradient as a function of mixture velocity. Liquid phase viscosity = 12 mPa s.

This is because the superficial gas velocity is not high enough to cause high frictional pressure drop. Gravitational pressure drop dominates because of high liquid hold-up across the pipe cross-section. As a result, the total pressure gradient decreases exhibiting a minimum. The pressure drop behaviour reported here agrees with the result of Nan Da Hlaing et al (2007) which examined effect of liquid viscosity on flow regimes and pressure gradients. Nan Da Hlaing et al. (2007) reported that in the Bubble, the slug and the slug-churn flow regimes, the pressure gradients decreased with increasing mixture Reynolds number while in annular and mist flow regimes, pressure gradients increased with mixture Reynolds number.

In order to minimise pressure-drop and losses during two-phase flow operators more often than not will like to operate in the Intermittent/Slug flow regime. This practice is typical and is preferred in the production of oil and gas in vertical wells, Shoham (2006).

3.4.10 Performance of structure velocity correlation

Performance of existing structure velocity correlations has been tested using present data for air/water and air/12 mPa s viscous liquid. The statistical parameters used in this assessment are Average Percentage relative Error (APE), Average Absolute Percentage relative Error (AAPE) and Standard Deviation (STDEV). The Average Percentage relative Error (APE) is a measure of the relative deviation of the predicted values from the experimental values in percentage. The smaller the APE the more evenly distributed the positive and negative difference between predicted and measures values. APE is expressed as:

$$APE = \frac{1}{n}\sum_{i=1}^{n}\left[100\left(\frac{(Y_{predicted} - Y_{Measured})}{Y_{Measured}}\right)_i\right] \tag{3.12}$$

The Average Absolute Percentage relative Error (AAPE) is defined as:

$$AAPE = \frac{1}{n}\sum_{i=1}^{n}\left[100\left|\frac{(Y_{Predicted} - Y_{Measured})}{Y_{Measured}}\right|_i\right] \tag{3.13}$$

The smaller the AAPE the better the correlation. For similar value of AAPE, the lowest standard deviation value defines the best correlation.

Given that relative error is:

$$RE = \left(\frac{Y_{Predicted} - Y_{measured}}{Y_{Measured}}\right)100 \tag{3.14}$$

The Standard Deviation STDEV can be calculated using:

$$STDEV = \sqrt{\frac{n\sum_{i=0}^{n} RE_i^2 - \sum_{i=0}^{n} RE_i}{n^2}} \tag{3.15}$$

Figure 3.22 presents the results when the predicted structure velocity by various correlations and the experimental data are plotted against mixture velocity.

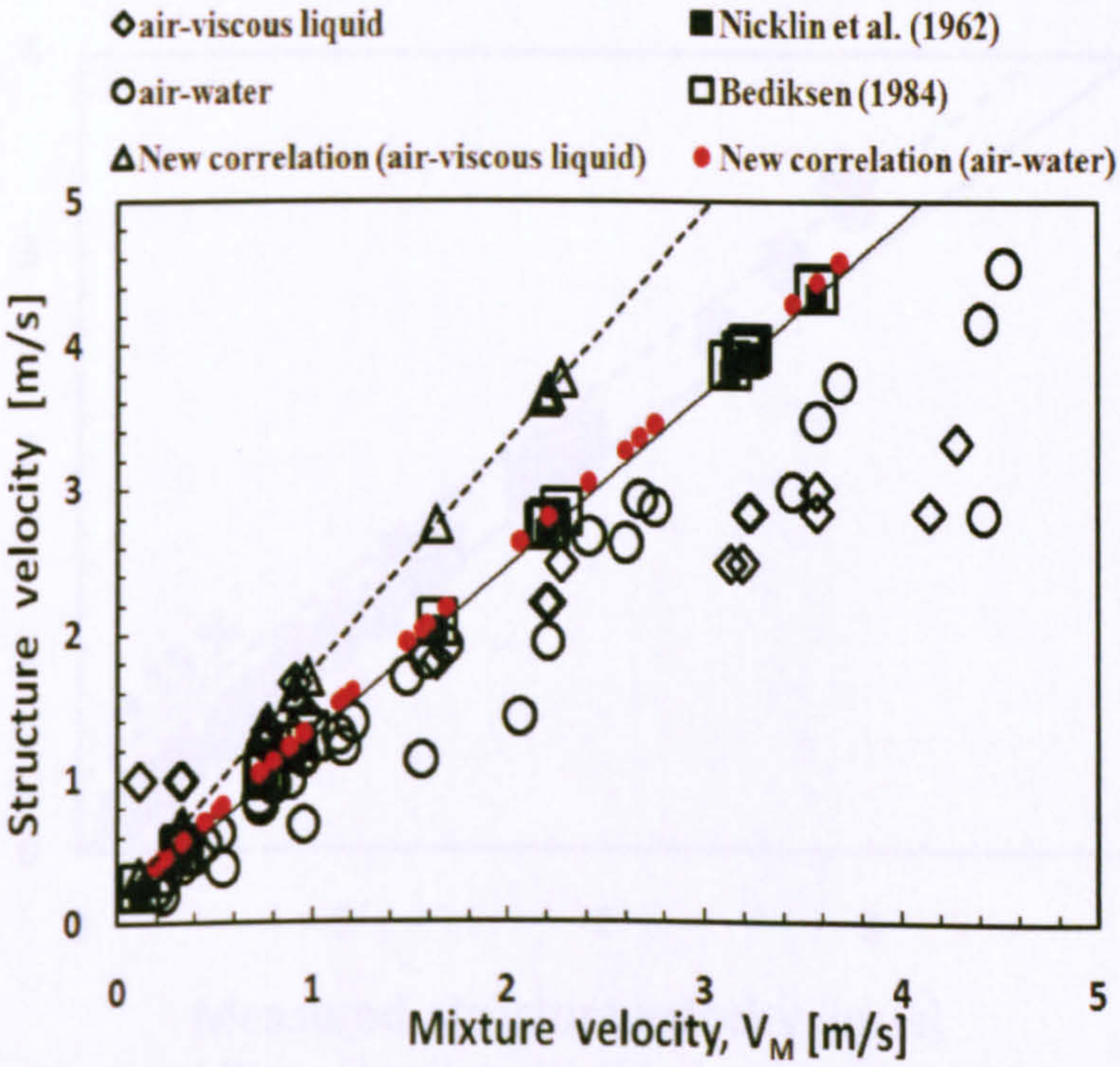

Figure 3.22: Comparison of various structure velocity correlations against experimental data.

The new correlations for air/water and air/viscous liquid are the results of changes in the coefficients of Equation (3.9). Equation (3.9) is the Nicklin's expression for translational velocity of Taylor bubble in slug flow.

Bediksen (1984) correlation for structure velocity in slug flow is given as:

$$\underbrace{V_T}_{Structure\ velocity} = 1.20\ \underbrace{(V_{SG} + V_{SL})}_{Mixture\ velocity} + \underbrace{0.54\sqrt{gD}}_{Drift\ velocity} \qquad (3.15)$$

The coefficients and the results of statistical assessment carried out on the existing correlations and the proposed new correlations are tabulated in Table 3.2.

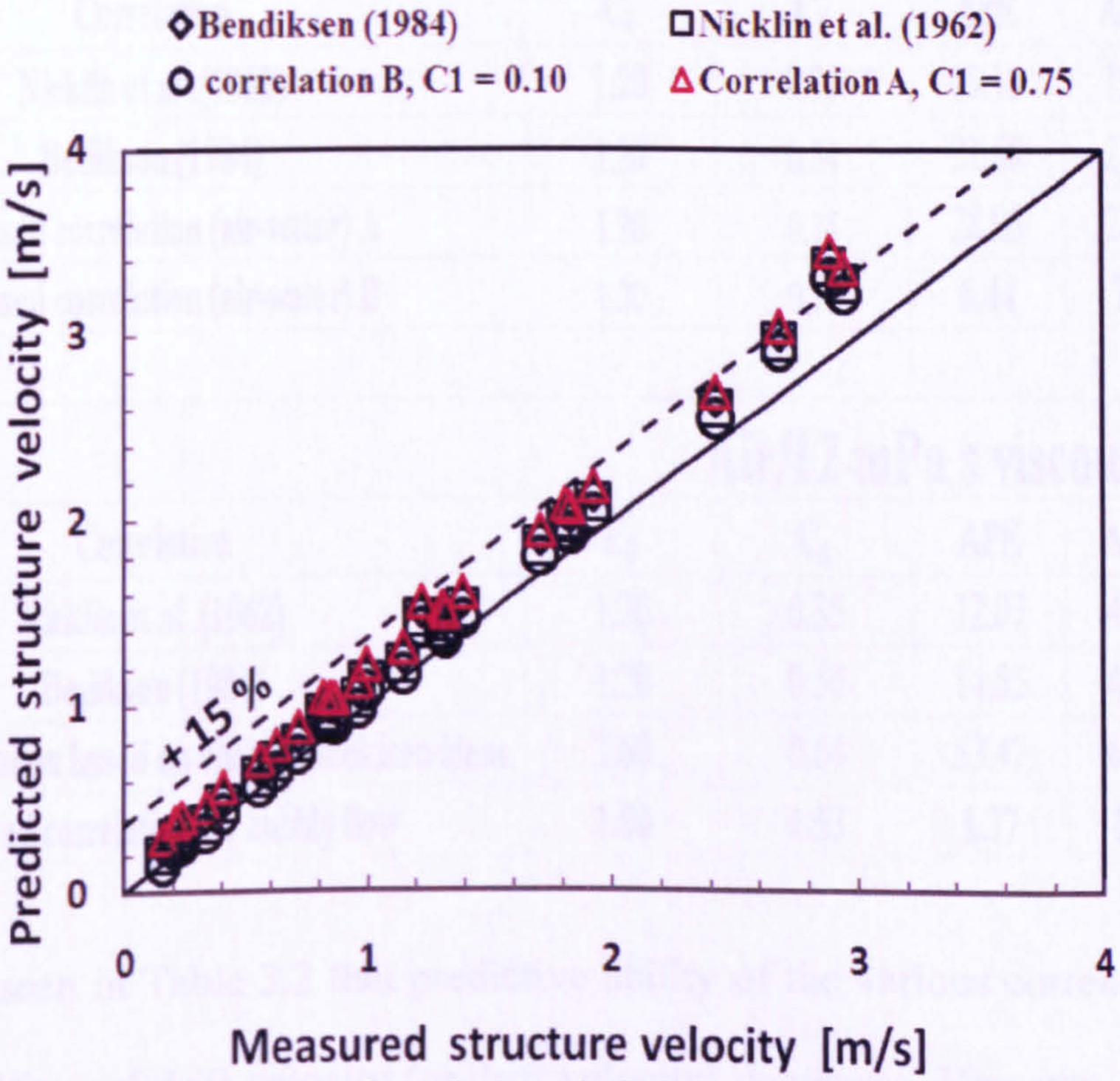

Figure 3.23: Predictive ability of various existing correlations and the proposed correlation for air/water data.

For air/water flow, the proposed correlation B, with $C_1 = 0.10$, gives the best performance with the least AAPE (Absolute Average Percentage Relative Error). The correlation B can predict the experimental data within $\pm 15\ \%$ Figure 3.23.

Unfortunately, the proposed correlation A, whose coefficients were obtained from the experimental data based on Nicklin's idea, could not re-produce original experimental data. However, correlation B gives better prediction of structure velocity when the coefficient of drift velocity was tuned until a better match was achieved between experimental and predicted structure velocity. In this case, the predicted structure velocity was accurate within ± 15 % when the coefficient of drift velocity term was reduced 0.10.

Table 3.2: Table of coefficients C_o and C_1 for different correlations.

		Air/Water			
Correlation	C_0	C_1	APE	AAPE	STDEV
Nicklin et al .(1962)	1.20	0.35	15.10	15.10	8.16
Bediksen (1984)	1.20	0.54	21.68	21.68	13.84
Proposed correlation (air-water) A	1.20	0.75	28.95	28.95	20.55
Proposed correlation (air-water) B	1.20	0.10	**6.44**	**7.15**	**4.80**
		Air/12 mPa s viscous liquid			
Correlation	C_0	C_1	APE	AAPE	STDEV
Nicklin et al .(1962)	1.20	0.35	12.07	42.10	44.25
Bediksen (1984)	1.20	0.54	14.55	41.82	43.22
Modified corelation based on Nicklin/Bedkisen ideas	1.60	0.64	53.47	68.64	56.94
Proposed correlation for bubbly flow	**1.00**	**1.53**	**1.77**	**29.4**	**33.26**

It is clearly seen in Table 3.2 that predictive ability of the various correlation increases as the coefficient of drift velocity (or drift velocity) decreases. However, this is not the case in air/12 mPa s viscous liquid analysis, Table 3.2. In the case of air/12 mPa s viscous liquid, Nicklin's/Bediksen idea was used by adjusting the value of distribution coefficient and the coefficient of the drift velocity in the structure velocity Equation

(3.9). The modified correlation based on Nicklin/Bediksen ideas produces drift velocity coefficient of 0.64 and a C_o of 1.60 was used in the calculation based on observation in Figure 3.15. This correlation performs gives worst performance with highest AAPE of 68.64. Nicklin's correlation with the drift velocity coefficient of 0.35 performs better than the modified correlation with a lesser AAPE of 42.10. Bediksen (1984) correlation performs better than the modified correlation and the Nicklin's with lesser AAPE of 41.82.

The reason why the modified correlation fails to predict experimental data may be that the modification of Nicklin/Bediksen's expression is not suitable to model bubbly flow. It may be that the integrity of the liquid slug has been affected by numerous tiny bubble entrained in the liquid as observed during the experiments. Therefore, another model is proposed for estimating structure velocity in the bubbly flow regime. Going by the observation in Figure 3.15 and Figure 3.16, it is reasonable to assume that in bubbly flow, the flow distribution coefficient does not exceed 1.0. Harmathy (1960) suggested Equation 2.26 for calculating drift velocity in bubbly. Again, the Equation is expressed as:

$$1.53\left[\frac{\sigma g\,(\rho_L - \rho_G)}{\rho_L^2}\right]^{0.25} \tag{3.16}$$

Replacing drift velocity term in Equation (3.9) with the expression in Equation (3.16) and substituting 1.0 for Co in the same equation yields Equation (3.17). Equation (3.17) is the proposed correlation for structure velocity in bubbly flow regime.

$$\underbrace{V_T}_{Structure\ velocity} = 1.0\ \underbrace{(V_{SG} + V_{SL})}_{Mixture\ velocity} + \underbrace{1.53\left[\frac{\sigma g\,(\rho_L - \rho_G)}{\rho_L^2}\right]^{0.25}}_{Drift\ velocity} \quad (3.17)$$

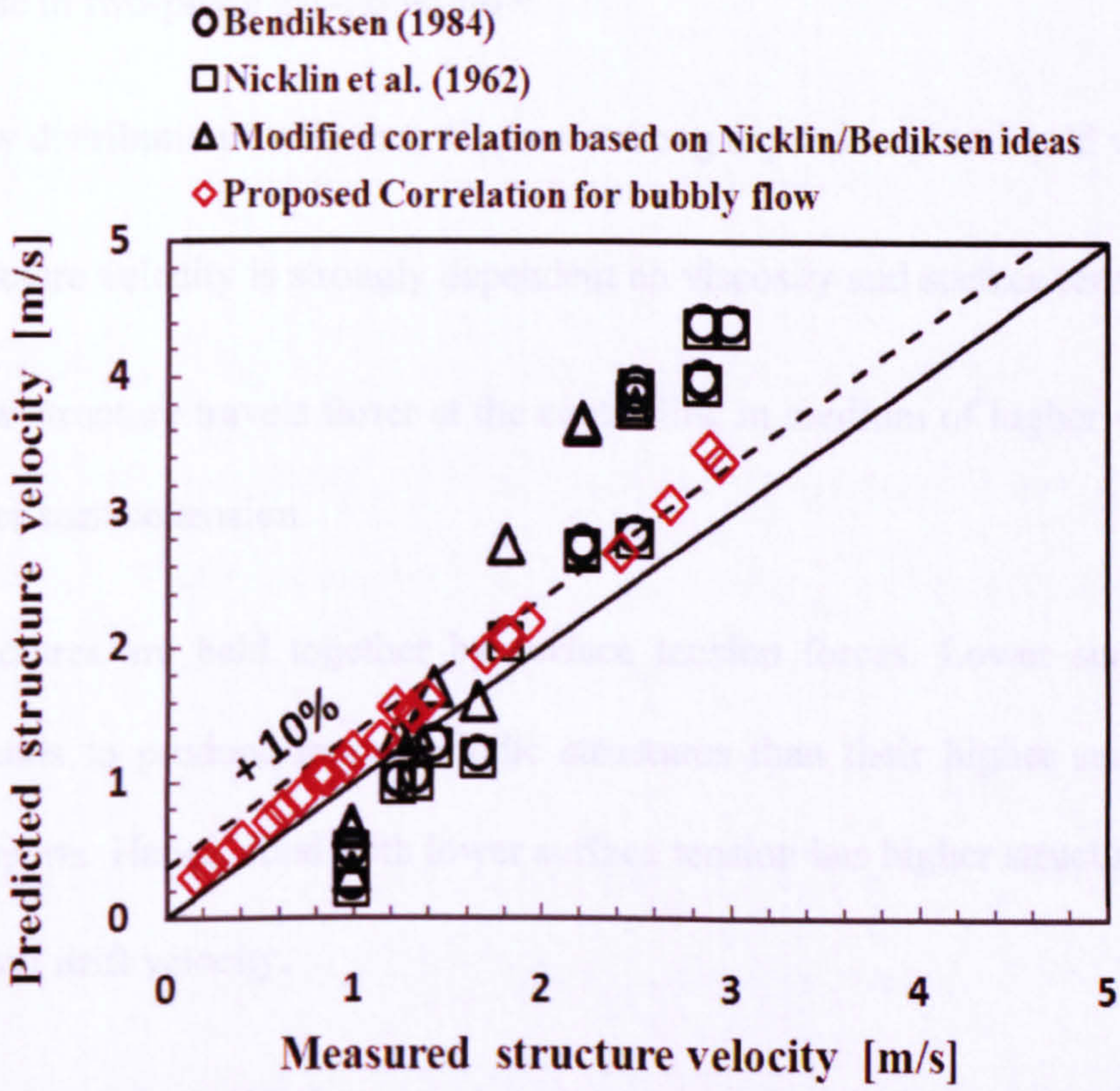

Figure 3.23: Predictive ability of various existing correlations and the proposed correlation for bubbly flow.

The proposed correlation for bubbly flow gives best performance with the least AAPE = 29.40, Table 3.2 and Figure 3.23.

3.5 Conclusions

The following conclusions can be drawn from the study of effect of liquid viscosity and surface tension on periodic structures in vertical two-phase flow:

1. Void fraction decreases with increase in liquid viscosity.

2. Structure frequency increases with increased liquid viscosity.

3. Both liquid viscosity and surface tension causes shift to transition boundary.

4. Higher viscosity liquid phase induces higher slippage between gas and liquid phase in two-phase gas-liquid flow.

5. Flow distribution coefficient, C_o, has a strong dependence on liquid viscosity.

6. Structure velocity is strongly dependent on viscosity and surface tension.

7. Flow structure travels faster at the centre-line in medium of higher viscosity and lower surface tension.

8. Structures are held together by surface tension forces. Lower surface tension fluid tends to produce more periodic structures than their higher surface tension counterparts. Hence, fluid with lower surface tension has higher structure frequency and lower drift velocity.

9. Structure velocity has been used to characterise flow into various regimes.

10. Slip between gas and liquid phases has been used to dermacate bubbly, churn, slug and annular flow.

11. Increase in liquid phase viscosity shifts transition boundary to left on flow pattern map.

12. A new model has been proposed to calculate structure velocity in bubbly flow. It predict the experimental structure velocity within $\pm$ 15 %.

Chapter 4

Dynamic Drop Size Measurement in Vertical Annular Two-Phase Flow

4.1 Introduction

Drop size data has been measured in vertical annular two-phase flow using optical techniques. Azzopardi et al. (1980, 1991) have used the small forward angle light scattering. The same approach has been used by Simmons and Hanratty (2001) and Al-Sarhki and Hanratty (2002) for horizontal annular flow. The instruments employed used the assumption that the scattering was dominated by Fraunhofer diffraction and time averaging was almost inevitably employed to improve measurement accuracy. The method provides average values over a finite volume. Drop size distributions were extracted from the angular variation of scattered light. In addition, information on the time averaged concentration was also determined. The other approach used utilized Phase Doppler Anemometry; Azzopardi and Teixeira (1994 a), van't Westende (2007). This provides data at one point in space. The sampling position has to be traversed about the pipe cross section to obtain fully representative data. This approach also provides information about drop velocity. Azzopardi & Teixeira (1994 a) have shown that the drop size distribution from the diffraction and Phase Doppler anemometry instruments are the same if they are both converted to the same basis.

Though it has been reported that drops occur in bursts Azzopardi (2006), almost all previous drop size or concentration measurements have been time integrated. This integration over time may compromise the quality of the data because of the complex

mathematics and the assumptions made in time and space. Hence, analyzing data this way in amplitude and frequency space with respect to time to yield Probability Density Functions and or to identify the dominant structure frequency using Power Spectrum Density may often give misleading interpretations.

Dynamic time averaged drop-size measurements are reported for the first time for annular two-phase flow. They were carried out on a 19 mm internal diameter vertical pipe with air and water as fluids. A laser light scattering technique was employed to obtain the drop size and concentration variations in time. Simultaneously, time-resolved measurements were made of film thickness using conductance probes employing a pair of flush mounted rings as electrodes and of pressure gradient. The gas superficial velocities ranged from 13-43 m/s at liquid superficial velocities of 0.05 and 0.15 m/s. Additional tests were carried out at a fixed gas velocity of 14 m/s for liquid superficial velocities of 0.03-0.18 m/s. Though structures are not clearly visible in the signals acquired they have been analyzed in amplitude and frequency space to yield Probability Density Function (PDF) and to identify the dominant frequencies. Cross-correlation between two film thickness probes provides the wave velocities. Characteristic frequencies for both waves on the film interface and drop concentration have been reported.

Therefore, this work contributes experimentally to provide information on mechanisms responsible for liquid entrainment in annular two-phase flow by providing new data

taken simultaneously for film thickness (waves), drop sizes/concentration and pressure drop measurements.

For the sake of clarity, drop size is presented here in Chapter Four while and results and discussions on wave measurements are deliberately deferred till Chapter Five. Chapter Six extends Chapter Five by discussing wave amplitude and modeling in greater detail. Because of the link between these consecutive chapters, sometimes presentation and discussions of results are carried in way that references are inevitably made to them.

4.2 Experimental Arrangements

The experiments were carried out on a vertical 19 mm diameter 7 m long pipe using air and water as the fluids at with an operating pressure of 1.5 bar absolute. The flow facility is shown schematically in Figure 4.1. Drop size and drop concentration data (entrained fraction) were taken with a light scattering technique using a Malvern Spraytec instrument. Film thickness was measured using conductance probe employing a pair of flush mounted rings as electrodes. Pressure drop across the system was monitored with a differential pressure cell. The output from the conductance probes and the differential pressure cell were fed into a PC via a National Instruments acquisition card and processed using a LabView programme.

In the first series of experiments the gas superficial velocity was varied between 13 and 43 m/s at liquid superficial velocities of 0.05 and 0.15 m/s. The second series kept the

gas velocity at 14 m/s for liquid superficial velocities of 0.03-0.18 m/s. Pressure difference over a length of the pipe has also been measured.

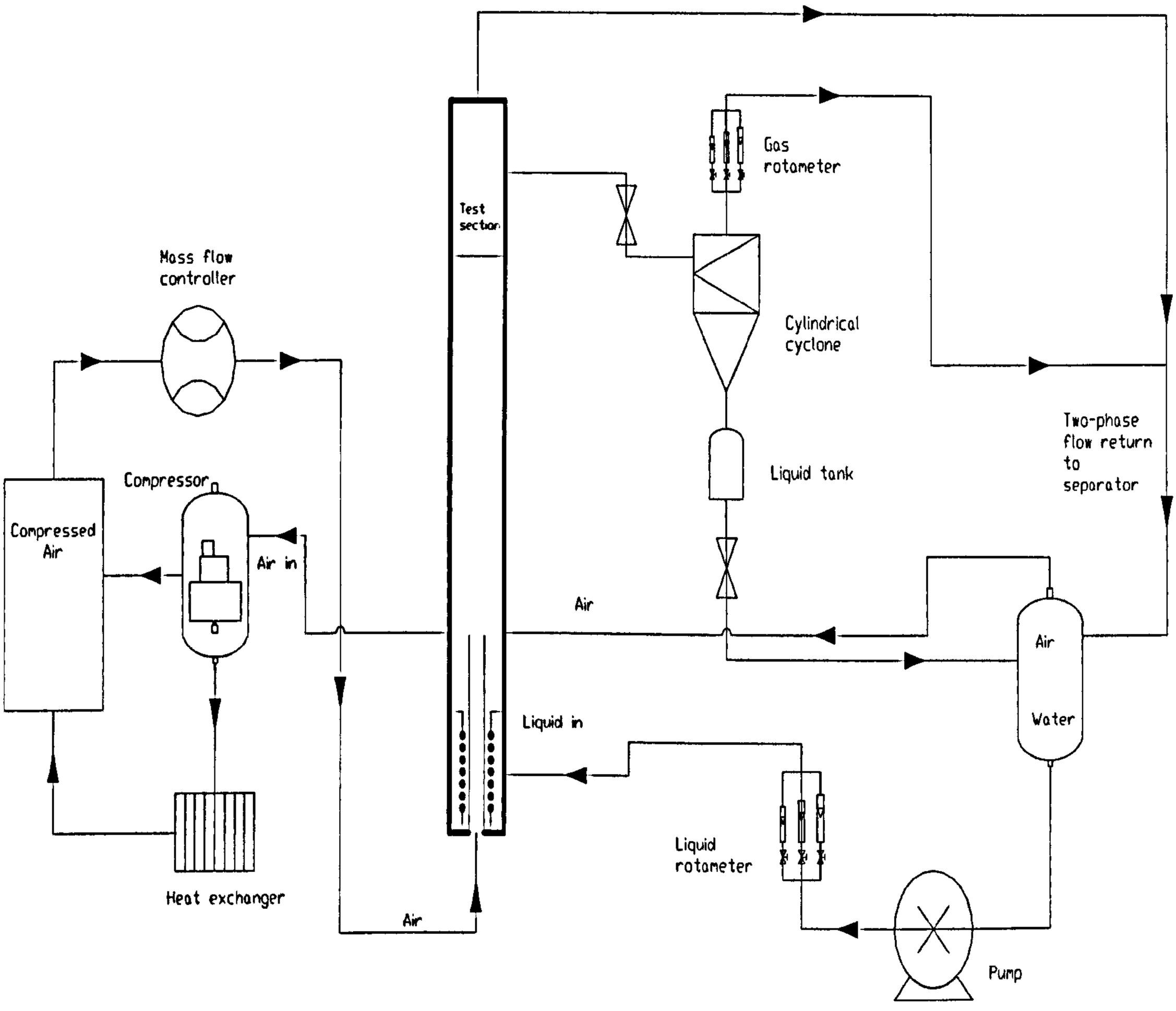

Figure 4.1: Schematic flow diagram of the rig used in the present study

4.2.1 Flow Rig

The experiments were carried out in an experimental facility used by Kaji (2008) with an internal diameter of 19 mm. The schematic of the flow facility is shown in Figure 4.2. It had been modified to accommodate a special test section which houses drop size test section as shown in Figure 4.2.

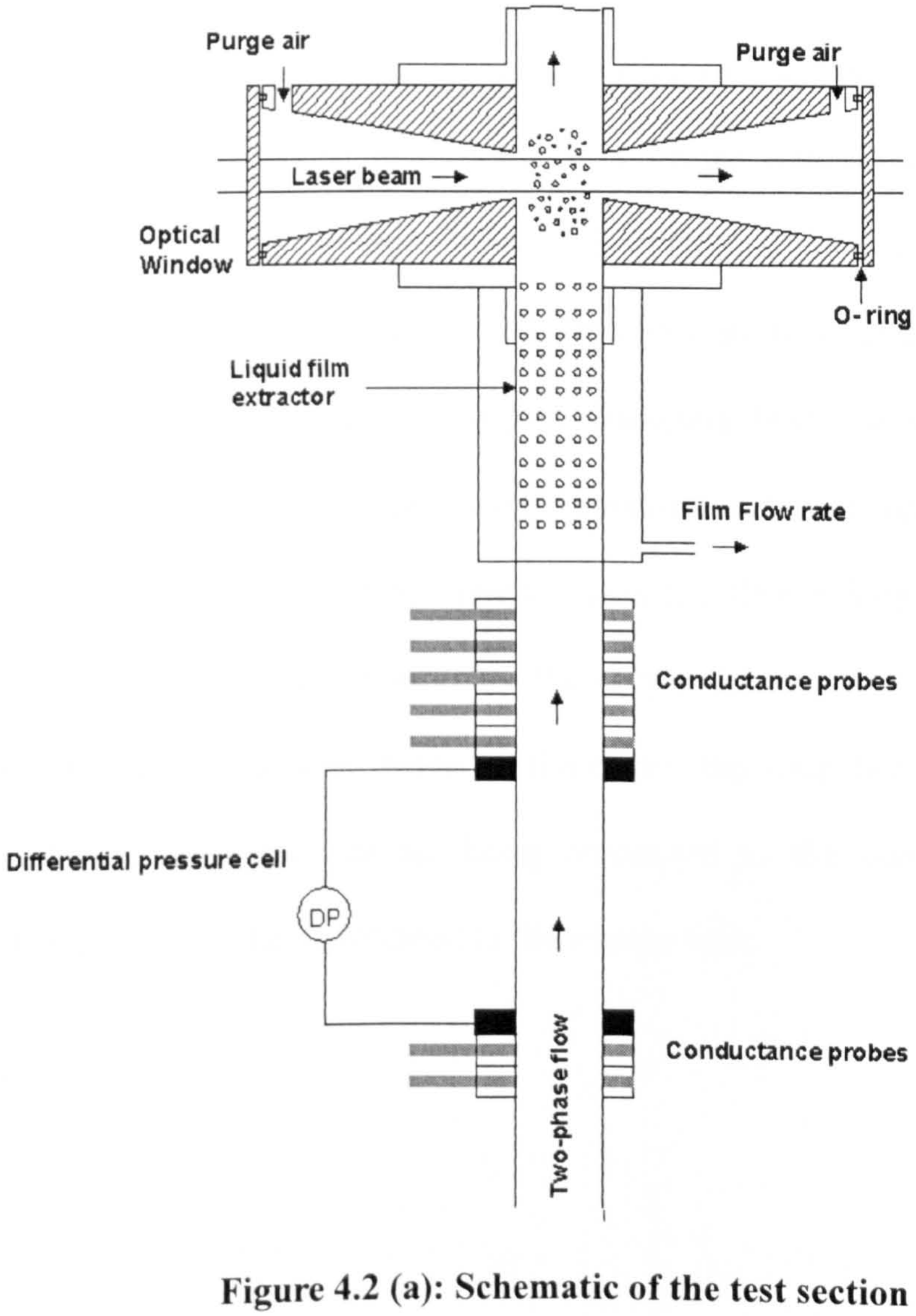

Figure 4.2 (a): Schematic of the test section

The special test section comprises the new drop size unit, liquid film extractor and a stack of conductance probes. Figure 4.2 displayed the schematics of the combined special test section showing the optical access to the drop size unit from the laser beam.

The fluids used were water and air. Water is taken from a storage tank and pumped through a bank of calibrated rotameters to monitor the flow rate into mixer.

Bronkhorst EL-Flow, a dynamic mass flow controller was used for some inlet conditions to regulate gas flux. The schematic of instrument is available in Appendix A. A bank of calibrated air rotameters was used in other category of experiments to monitor air into two-phase mixer.

The mixer consisted of an annular section into which air was introduced. Water emerged into the annulus through a series of 5 mm holes on the wall of the capped central pipe. This mixer was mounted at the bottom of the pipe 310 pipe diameters from section where the conductance probes are located. Two pressure taps connected to a Rosemount differential pressure cell, located 230 pipe diameters from the mixer, separated by a distance of 82 pipe diameters were used to monitor the pressure drop in the system. The liquid film is extracted via a 19mm internal diameter, 350mm long, 0.80 porosity acrylic pipe. Beyond the liquid extractor, only the droplet-laden gas core flows through the chamber which admits laser beam to illuminate the core flow. The pipe outlet is connected to a separator, the air being connected to the compressor, vented into atmosphere, the liquid being returned to the storage tank.

4.3 Instrumentation

The instrumentation in this study consists of the Spraytec instrument, conductance probes and differential pressure cell.

4.3.1 Spraytec

Laser diffraction instrument such as Spraytec measure changes in light scattering as a function of drop concentration and characteristic drop diameter. Spraytec provides time resolved volume-based, drop size distribution from the analysis of a diffraction pattern resulting from the interaction between a drop and a laser beam. Power from Helium-Neon laser illuminates drop saturated gas core. The measurement volume is the intersection of a droplet field and the laser beam. Entrained droplets scatter the beam principally by diffraction, Figure 4.2 (b). Un-diffracted light are recorded as obscuration of the measurement, obscuration [%], being 100% minus transmission [%].

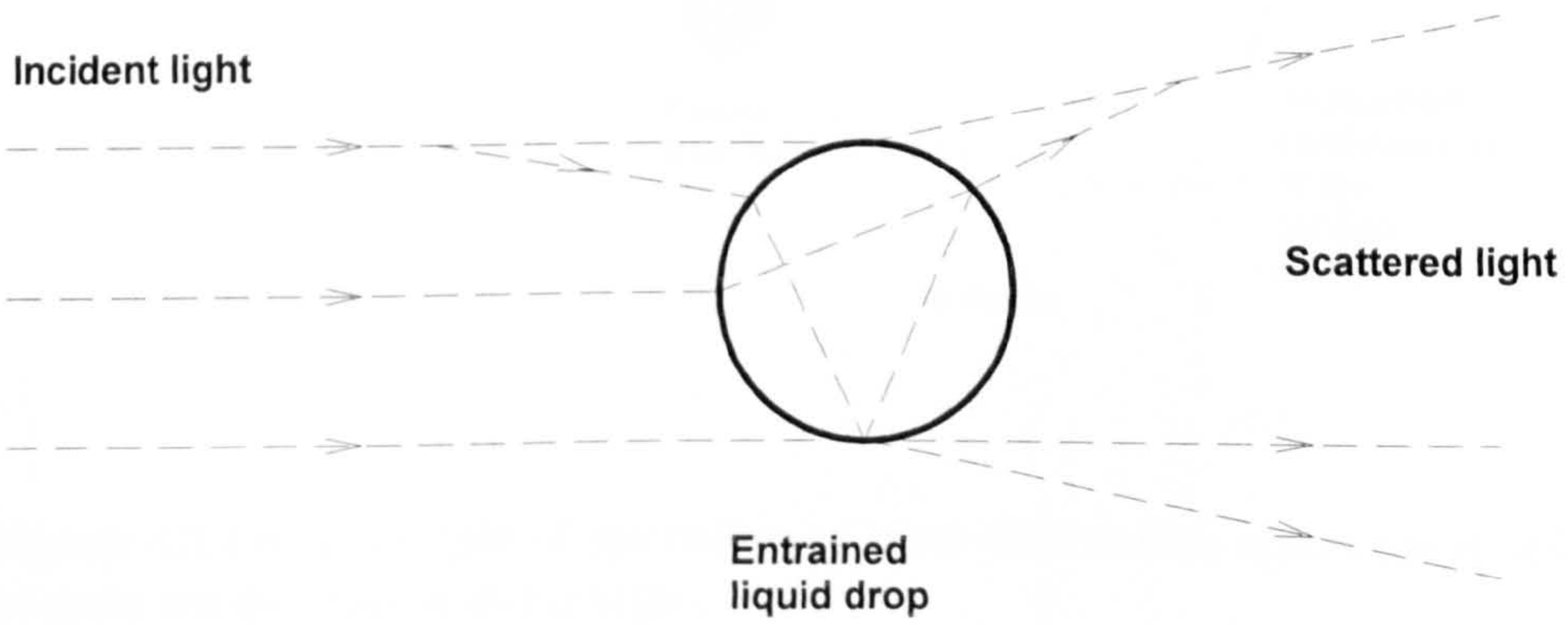

Figure 4.2 (b): Incident light scattering by a single drop within the measurement volume.

In line with the beam and beyond the drops, the receiving optics is placed which uses a Fourier transform lens to collect the diffracted light in the forward direction. The Fourier

lens converts the scattered light into a far field diffraction pattern. This diffraction pattern is then focused onto a multi-element photoelectric detector composed of: one main detector ring (ring 0) and thirty one other concentric annular rings which produce analogue signal proportional to the incident light intensity, Figure 4.2 (c). Once the diffraction pattern is read, a volume based, drop concentration and size distribution is then derived employing a non-linear least square analysis which gives the most closely fitted diffraction pattern.

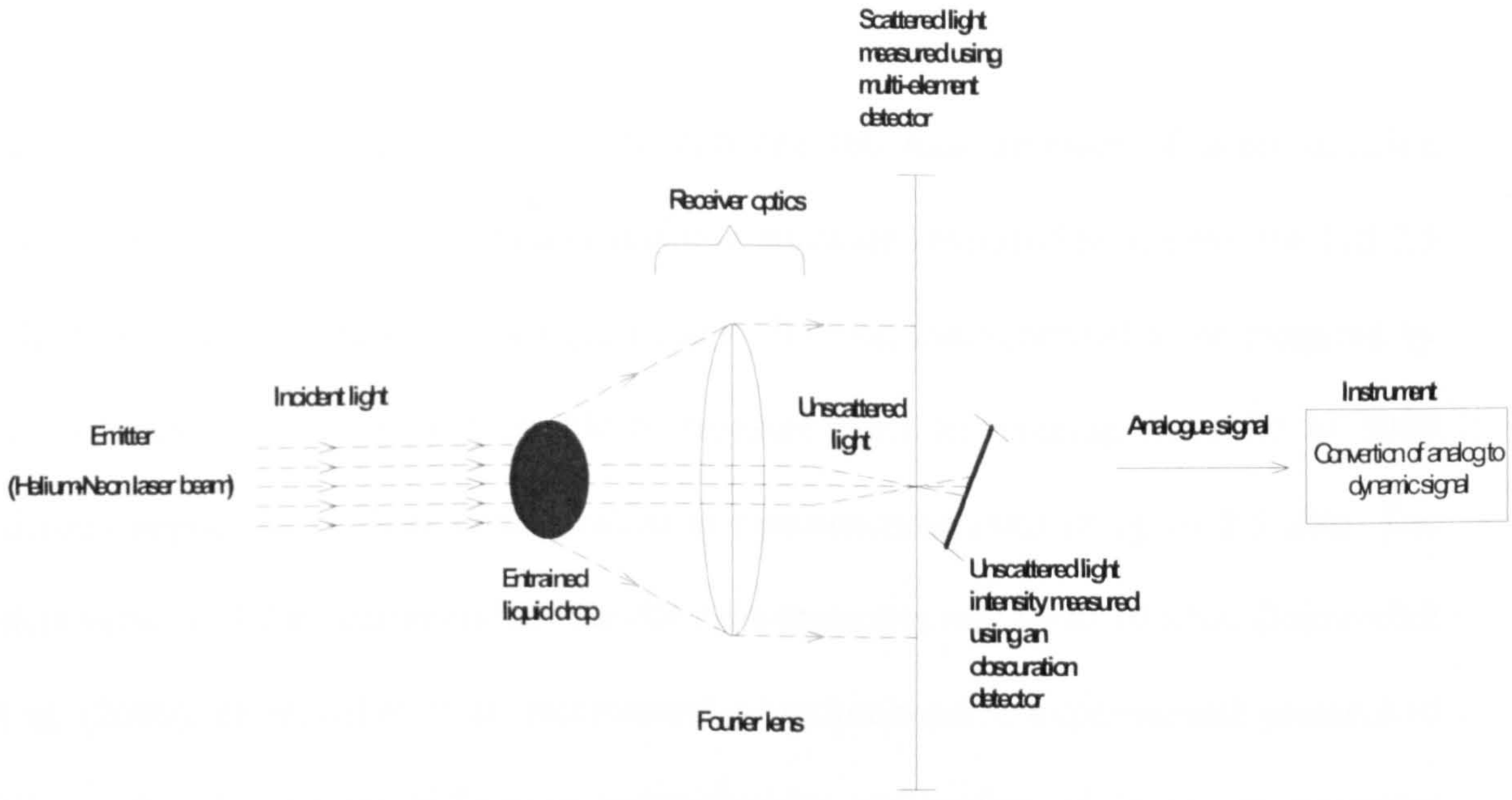

Figure 4.2 (c): Principle of operation of laser diffraction instrument utilized in present experimental campaign.

The instrument is factory calibrated with a repeatability of ±1% .The instrument mathematical inversion process employs both patented Lorenz-Mie algorithms (an improvement over Fraunhofer's principle) and a multiple scattering algorithm to reconstruct scattered light profile to generate drop size distribution with improved accuracy. Lorenz–Mie theory accounts for the contribution of the angular light energy

based on the Fraunhofer diffraction theory interpreted this portion of light energy as diffracted light and overestimated the small particle population. These features enable the instrument to provide accurate size distribution information in environments that other laser-diffraction systems can not. Corcoran et al., (2000) reported use of the Lorenz–Mie theory considerably improves the instrument performances when measuring very small drops. Time resolved drop-size measurement is possible with the special in-built Insitec card. The Insitec card records cycle-to-cycle temporal variations of the drop - rich gas core as the instrument scans the detector.

Spraytec includes features designed to enhance the measurement of short duration events, including Flash Mode data acquisition software (required to achieve the full 2.5 kHz data acquisition rate), and a trigger input allowing measurement to be triggered by external devices. The system is able to measure particles ranging from 0.5 to 1000 microns depending on lens configuration at measurement rates of up to 2.5 kHz. The latest version of the instrument can handle measurements rate up to 10 kHz, Dumuochel et al. (2009). Dumuochel et al. recommend a comprehensive experimental protocol to follow when laser light diffraction measurements are performed in severe operating conditions. Dumuochel et al. (2009) presented beam steering, the vignetting and the light multiple scattering effects as the measurement phenomena which can affect laser diffraction data quality. Although their work is not hydro dynamically related to the present study the recommendation was used in this work as a guide to check the quality of our data.

Beam steering effect is the manifestation of light scattered because of a refractive index gradient in the gas phase. A refractive index gradient in the surrounded gas flow can be caused by temperature gradients or by the presence of liquid vapor. The mathematical inversion procedure mistaken and interprets this supplementary scattered light to the presence of drops and calculates the drop size distribution accordingly. Beam steering deviates light at small angles and mainly affects the proportion of light detected by the first inner diodes, i.e., those sensitive to the big drops. In consequence, the drop-size distribution overestimates the big drop population and may exhibit a supplementary peak in this range of droplets. A characteristic feature of the presence of beam steering is a peak of light intensity detected by the first diode Dumuochel et al. (2009). The data were carefully checked against the bias of beam steering effect, beam steering does not affect the quality of the present study.

Vignetting is avoided by setting the separation distance between the emitter and receiver to 300 mm i.e. 1.5 times focal length of lens used which was 200 mm. Drop-size test sections in Figure 4.2 (a) was designed such that the width of the box is not up to 300mm.Recommended vignetting distance from the lens to the test section by the instrument manufacturer is available in appendix B. Vignetting is a phenomenon where scattered light escapes from the collection angle i.e. the drop do not diffract light at such a high angle that the light does not illuminate the Fourier lens. The effect is underestimation of small drop population because they have greatest diffracted light angle.

Multiple light scattering occurs when the measuring volume contains a high number of drops either because the drop density is high or because the measuring volume is large. The reduction of the mean diameter is a consequence of the overestimation of the small drop population. It has widely reported that light multiple scattering affects the measurement when the transmission is less than 40% and introduces a bias that depends on the transmission and on drop characteristics.

The ratio of the diffracted light intensity to the incident light intensity provides the obscuration of the measurement. Unscattered light intensity is measured by the instrument using obscuration detector. The experiments were carefully controlled such that light obscuration did not greater than 20% i.e. transmission = 100%-obscuration. The Spraytec multiple light algorithms helped correct multiple scattering effects.

Finally, background checks are carried out at no flow condition in order to check instrument response quality. The background is a measure of stray light in the optical system and, most importantly, particulate contamination of the windows. A good background measurement is critical to ensure accurate and precise particle size distribution measurements. The raw detector signal should have a beam power reading (ring 0) of at least 1000 and a smooth, inverse bell-shaped curve for the remaining rings. The data reduction verification settings contain threshold values for the transmission and average signal levels allowed for a valid background. If an error threshold is reached, the system produces an error message and the background measurement is terminated.

RTSizer uses the background to compensate for any particulate contamination by using the background as a baseline that is subtracted from all particle size distribution scattering measurements. It is therefore, a good practice to carry out background measurements before each test. Background measurement was a routine experimental protocol throughout the experimental campaign.

Spraytec can be synchronized with other instrumentation using a trigger system which allows simultaneous data acquisition with other instrumentation. In the present arrangement, Spraytec was operated in external trigger mode. This mode allows the instrument to link electronically with other instrumentation like conductance probes and differential pressure cell such that data acquisition can be carried out in a simultaneous manner. In order to achieve simultaneous data acquisition, a pulse generator subroutine is written using LabView command to control the execution of the three data acquisition programmes associated with the three different electronics.

Spraytec was operated in flash mode in order to impose a sampling frequency and sampling time respectively for the measurement. The dynamic range of the instrument is capable to size drops between 0.5 - 460 microns based on the focal length used for collection of the scattered light. The instrument model is RTS 5114, with maximum power 1.004 mW and characteristic wavelength range between 400 – 670 nm. Table 4.1 gives some technical information about the Spraytec.

Table 4.1: Spraytec technical specifications

Model	RTS 5114
Maximum Power	1.004mW
Wavelength Range	400 – 670nm

4.3.2 Conductance probe

A Cross-sectional view of the conductance probe is shown in Figure 4.3. The thickness of each electrode is 0.5mm while the distance of separation between them equals 1.7 mm. The Probes are connected to electric circuit. The voltage response, that is, electrical impedance or resistance, has a unique relationship with phase distribution as already established by calibration equation. Void fraction or film thickness is then estimated from this resistance-phase distribution relationship as the two-phase flow structures pass the sensor.

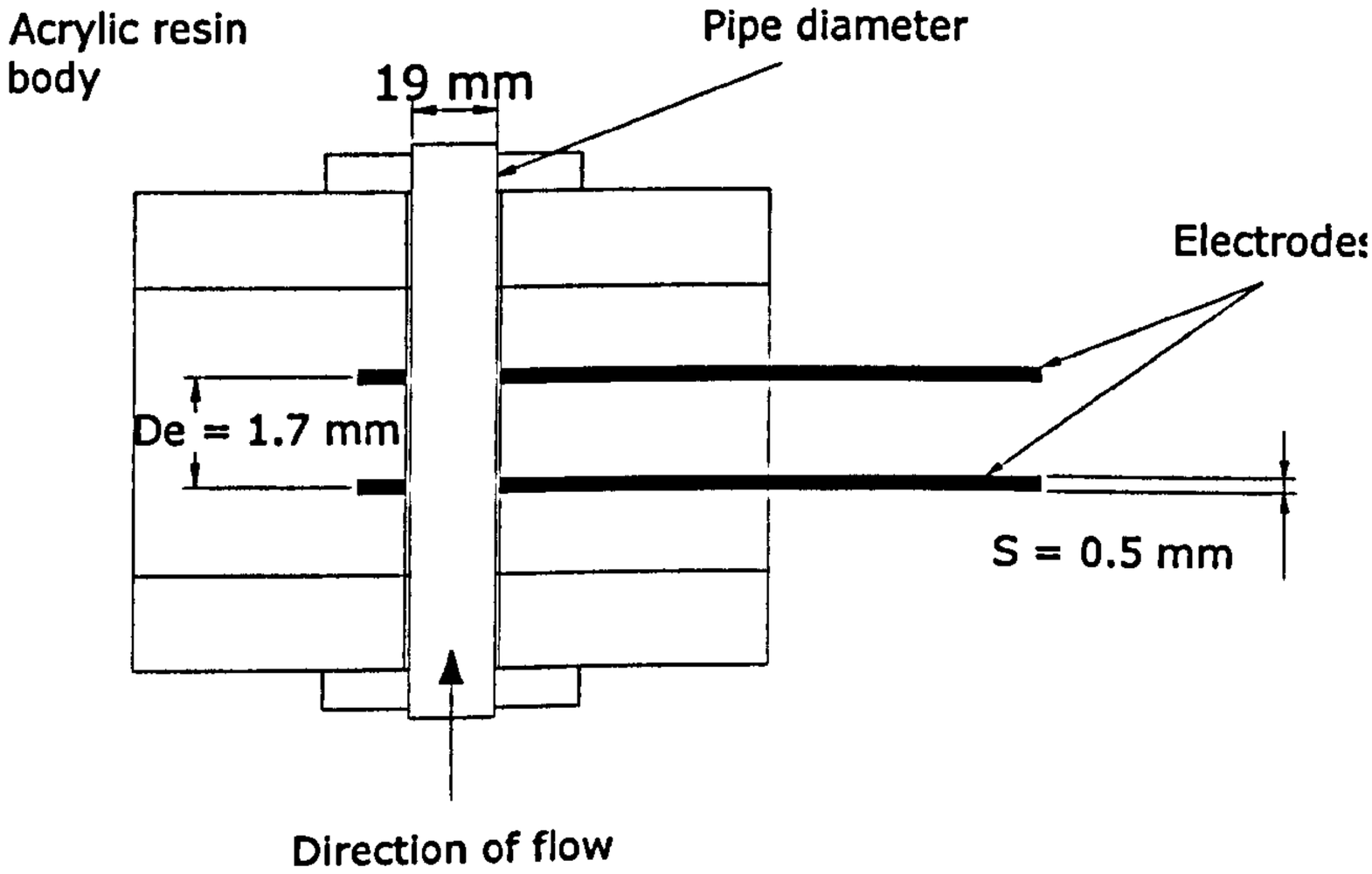

Figure 4.3: Cross sectional view of ring-type conductance probes used to measure void fraction.

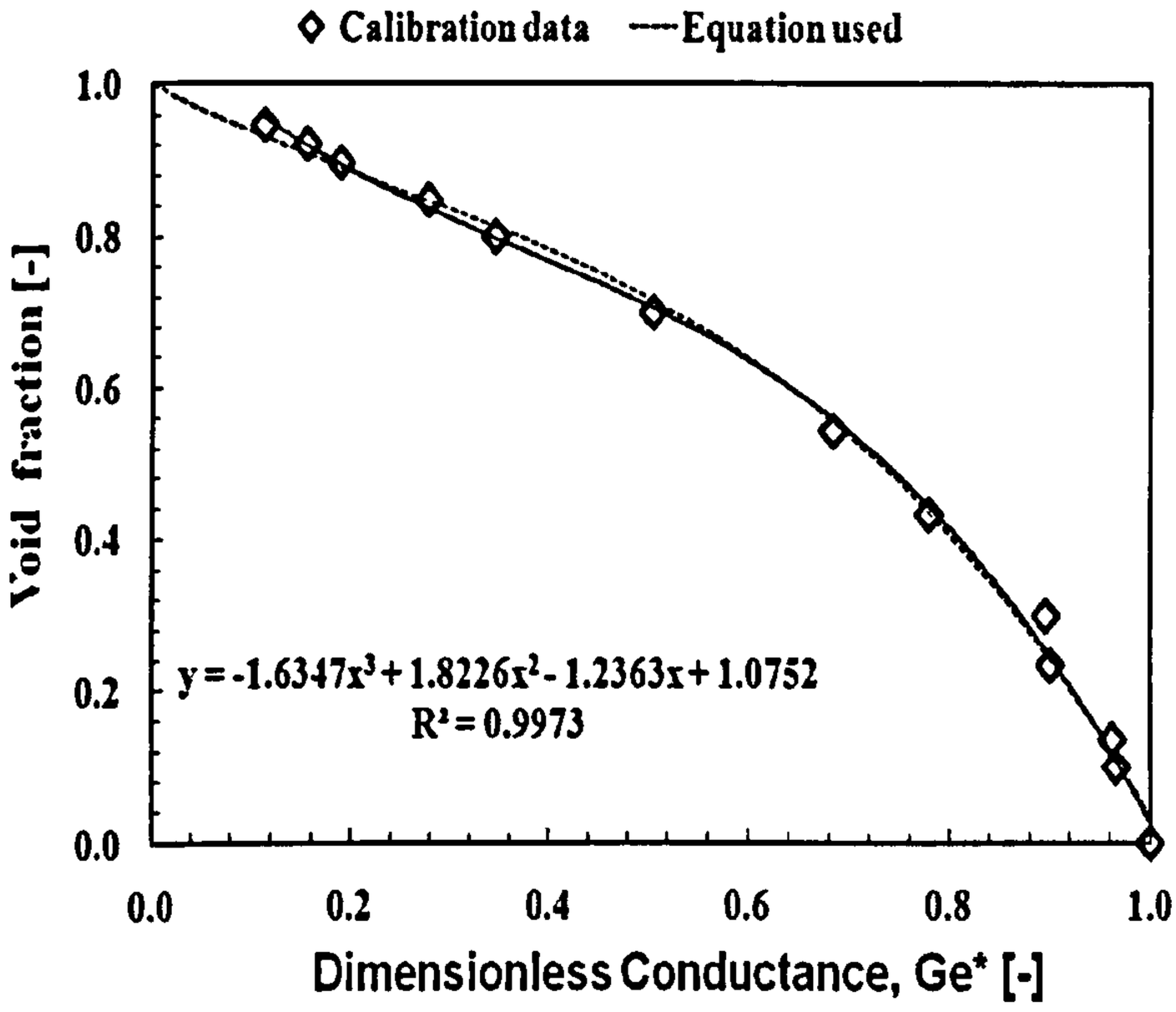

Figure 4.4: One of the calibration curves for the conductance probes used in the present study.

A unique mathematical relationship has been established between voltage response from the electrical circuitry (electrical impedance/resistance) and the phase distribution during calibration of the probe Kaji (2008).The calibration curves used in this study are shown in Figure 4.4. This equation is programmed into LabView software to generate void fraction during the experiment. The measurements from the probes and the DP cell were acquired using a PC installed with NI DAQ card. The details of the DP cell and conductance probe calibrations are available in Kaji (2008).

The pressure difference between a pair of tappings 1.55 m apart was measured by a differential pressure cell, Kent Taylor Smart Deltapi K series. In order to ensure that there is only one phase in the tapping lines a liquid purging technique was used. This prevented bubbles from entering the tapping lines. Before the measurement a high

purging rate was applied to clear any bubbles from the lines. It was then reduced to an optimum flow rate which is low enough that the measured pressure gradient is not affected by the purged flow.

The data acquisition pad consists of two data acquisition boxes. One for Spraytec and the other for conductance probes and the differential pressure meter. The measurements from the probes and the differential pressure cell were acquired using a PC installed with NI DAQ card with nine channels. Eight channels for conductance probes and one for differential pressure meter. Calibration procedures for the differential meter and conductance probe are detailed in Kaji (2008).

Sampling frequency was set at 1000Hz to achieve 6 seconds data acquisition time for 6000 data points for each element of the test matrix investigated LabView programme controls data acquisition for conductance probe and DP cell whilst RTSizer serves as the graphic user's interface for Spraytec.

4.4 Measurement Accuracy

Bronkhorst EL-Flow mass controller was factory calibrated and measured the air flow rate to within 1 percent. Air rotameters were accurate within 5 percent. Water flow rate were measured by rotameters, which were calibrated by weighing a timed efflux. They could be read within 5 percent. Spraytec was factory calibrated. The accuracy of the calibration was checked using recticle reference. It was accurate within 3 percent.

Conductance probes measures void fraction within the accuracy of 10 percent. The range of the differential pressure cell was 0 –70 kPa of which the resolution was ±45 Pa.

4.5 Results

First, flow pattern map is discussed with respect to transition to annular flow. Various transition models are considered and discussed. Next, statistical measures were extracted from the time varying signals acquired simultaneously during the experimental campaigns and measurements. Statistical average of principal flow variables were generated from their respective time series and plotted against superficial gas velocity in a systematic manner. Results are then considered, presented and discussed in increasing level of complexity.

4.5.1 Flow Pattern Map

Vertical annular two-phase flow can be classified into several flow regimes. Figure 4.5 (a) presents the present study flow conditions on the flow regime map plotted for the air–water flow in 9.4 mm diameter tube at 1.2 bar similar to the one used in Sawant et al. (2009) except for the inclusion of Taitel et al. (1980) annular flow transition boundary.

It is obtained from the flow regime transition criteria proposed by Mishima and Ishii (1984). The map also includes an onset of entrainment boundary (dashed line) obtained from Ishii and Grolmes's (1975) onset of entrainment criterion. The onset of entrainment boundary divides annular flow regime into two sub-regimes; annular flow with entrained droplets and annular flow without entrained droplets. They also observed that the onset of entrainment

boundary shows two limiting conditions, a critical gas velocity below which no entrainment is possible at any liquid flow rate and a critical liquid velocity below which no entrainment is possible at any gas velocity.

In a transition region between these two limiting conditions, the critical gas velocity at the onset of entrainment increases with the decrease in liquid velocity. Ishii and Grolmes (1975) developed this criterion based on a mechanism of shearing off the crest of disturbance waves. They assumed that the onset of entrainment takes place when the drag force on the tip of disturbance waves exceeds the retaining force of surface tension. Also it can be observed that the gas velocity required for the onset of entrainment increases very sharply at the critical liquid velocity.

Based on mechanism governing vertical annular flow, Taitel et al. (1980) proposed a transition criterion (red dashed line) from churn to annular flow Figure 5. The idea was based on Turner et al. (1969) droplet's model. In order to establish co-current vertical annular flow the drag force on gas phase must overcome the resultant effect of gravity and surface tension forces such that a liquid droplet entrained in the gas core can be sufficiently levitated without falling back. Thus the criterion for the transition boundary is given by the expression in Equation (4.1):

$$F_D = F_G \tag{4.1}$$

Where

F_D = drag force, F_G = gravity force;

In Equation (4.1), F_D and F_G can be substituted by defining the terms on the left hand side and right hand side of the equation respectively as follows:

$$C_D \frac{\pi d_D^2}{4} \frac{\rho_G V_G^2}{2} = \frac{\pi d_D^3}{6} g(\rho_L - \rho_G) \tag{4.2}$$

C_D = drag coefficient, [-]

d_D = drop diameter, [m]

g = gravitational acceleration, [m/s^2]

Solving for V_G from above expression yields the gas velocity on the transition boundary, which corresponds to the minimum gas velocity required to lift the droplets in the core and maintain annular flow.

The droplet diameter is determined from a balance of surface tension forces that promote larger droplets and the impact of forces of the gas-phase that tend to break the droplets into smaller ones. Taitel et al. quantified this phenomenon by Weber number given by the following expression:

$$We = \frac{d_D \rho_G V_G^2}{\sigma} \tag{4.3}$$

Very small particles (droplets or bubbles) correspond to conditions where We = 8.0, Shoham (2008). At the transition to annular flow, the larger droplets occur, where it is assumed that

the Weber number is between 20 and 30. Thus, once the We is given, the droplet diameter can be determined as:

$$d_D = \frac{\sigma We}{\rho_G V_G^2} \tag{4.4}$$

Turner at al. (1969) suggested a value of $C_D = 0.44$ for fully developed turbulent flow and We = 30 for large droplets. Based on the fact that annular flow is associated with small liquid hold-up they approximated $V_G = V_{SG}$.

When various substitutions are made final expression for transition to annular flow is obtained as given in Table 4.2. It can also be expressed in dimensionless form as in Equation (5). The dimensionless number, 3.1, on right side of Equation (4.5) is called Kutateladze number.

$$3.1 = \frac{V_{SG}\rho_G^{0.5}}{[\sigma g(\rho_L - \rho_G)]^{0.25}} \tag{4.5}$$

When the experimental data are substituted into this transition model, a value of gas superficial velocity of 12.67 m/s is obtained. This is different from a value of gas superficial velocity of 21 m/s observed based on observation of subtle changes in entrained fraction and SMD measured as liquid and gas superficial velocities increase in the present study. The difference in result of the transition model of Taitel et al. (1980) and present study may be as a result of assumption made in arriving at the final form of the transition model.

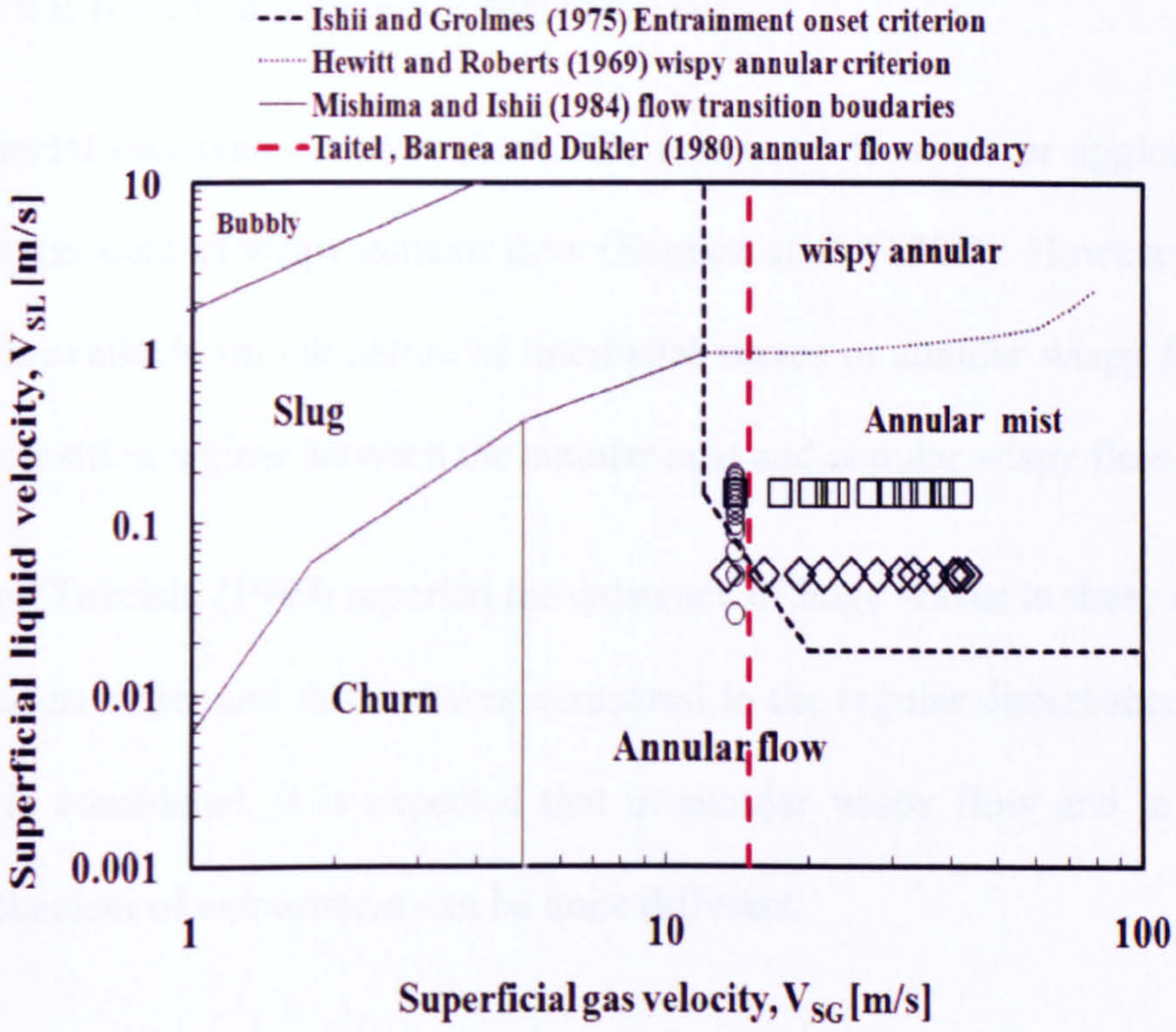

Figure 4. 5 (a): Flow pattern map for vertical two-phase flow. The open symbols represent the conditions at which present study were carried out.

Recently, Pan and Hanratty (2002) proposed an empirical correlation for the critical gas velocity based on the experimental data. The authors presented a correlation for vertical annular flow based on the balance of the rate of atomization of the liquid film and the rate of deposition of drops. The development of the correlation considers data bases with pipe diameters of 1.06 to 5.72 cm, superficial gas velocities of 20 to 119 m/s, superficial liquid velocities of 0.012 to 1.35 m/s, gas densities of 0.27 to 35 kg/m^3 and surface tensions of 0.01 to 0.073 N/m. The critical superficial velocity marks the onset of atomization of liquid film in to liquid droplet in the gas stream. The correlation is given in Table 4.2.

In annular with entrained droplets, as liquid velocity is increased for a given gas velocity, a flow regime transition from annular mist to annular wispy flow is observed (Hawkes et al.,

(2000)). An empirical transition criteria proposed by Hewitt and Roberts (1969) for the prediction of this transition is shown in Figure 4.5 (a).

The experimental observations have shown the existence of wisps or agglomerated liquid structure in a gas core of wispy annular flow (Bennett et al. (1965)). However, very limited information is available on the nature of interfacial waves in annular wispy flow regime as well as in a transition regime between the annular mist and annular wispy flow.

Sekoguchi and Takeishi (1989) reported the existence of huge waves in these regimes which they described as larger and faster waves compared to the regular disturbance waves. If the flow physic is considered, it is expected that in annular wispy flow and in the transition regimes, mechanism of entrainment can be quite different.

In the present study, efforts were to visualize the flow. Flow visualization studies were carried out by studying the cine movies recorded by high speed camera in slow motion mode to study the interaction of entrained structures in the gas core. Vision Research, Phantom, high speed camera version V7.1, equipped with SR-CMOS sensors was used to acquire cine information which was fed into a PC installed with Phantom software version 606. The PC controls the video processor via 10/100 Ethernet (1Gbit 2Q03). The recording was carried out at 1000 frames per minute with a resolution of 800 x 600 pixels. In order to enhance the image quality, a Nikon 24 – 85 mm F2.8 macro zoom lens was used to direct the sensor focus on to the pipe section where the cine movies were recorded.

Table 4.2 : Annular flow transition models, their respective superficial gas velocity at the beginning of annular flow and experimental evidences of transition to co-current annular flow.

Author	Equation	V_{SG} [m/s]	Remarks
Taitel et al. (1980)	$V_{SG} = \frac{3.1[\sigma g(\rho_L - \rho_G)]^{0.25}}{\rho_G^{0.5}}$	12.67	This model shows that transition to annular flow is independent of liquid superficial velocity
Pan and Hanratty (2002)	$V_{Gcr} = 40\sqrt{\frac{\sigma}{D\sqrt{\rho_L \rho_G}}}$	12.39	V_{Gcr} is the critical gas velocity at the onset of atomization
Wallis parameter	$V_G^* = \frac{V_{SG}\rho_G^{0.5}}{\sqrt{\sigma g(\Delta\rho)}} \approx 1.0$	10.78	Commonly referred to as flow reversal point criterion. Transition independent of liquid superficial velocity
Barbosa et al. (2002)	Experimental	20.00	Investigated churn - - annular transition in 31.8 mm vertical pipe
van Westende et al. (2007)	Experimental	20.00	Reported churn - - annular transition in 50 mm vertical pipe
Mantilla (2008)	Experimental	20.00	Evidence based on entrained fraction profile in152.4mm horizontal pipe. Drop size was not measured.
Present study	Experimental	21.00	Subtle changes in SMD profile at transition to co-current annular flow.

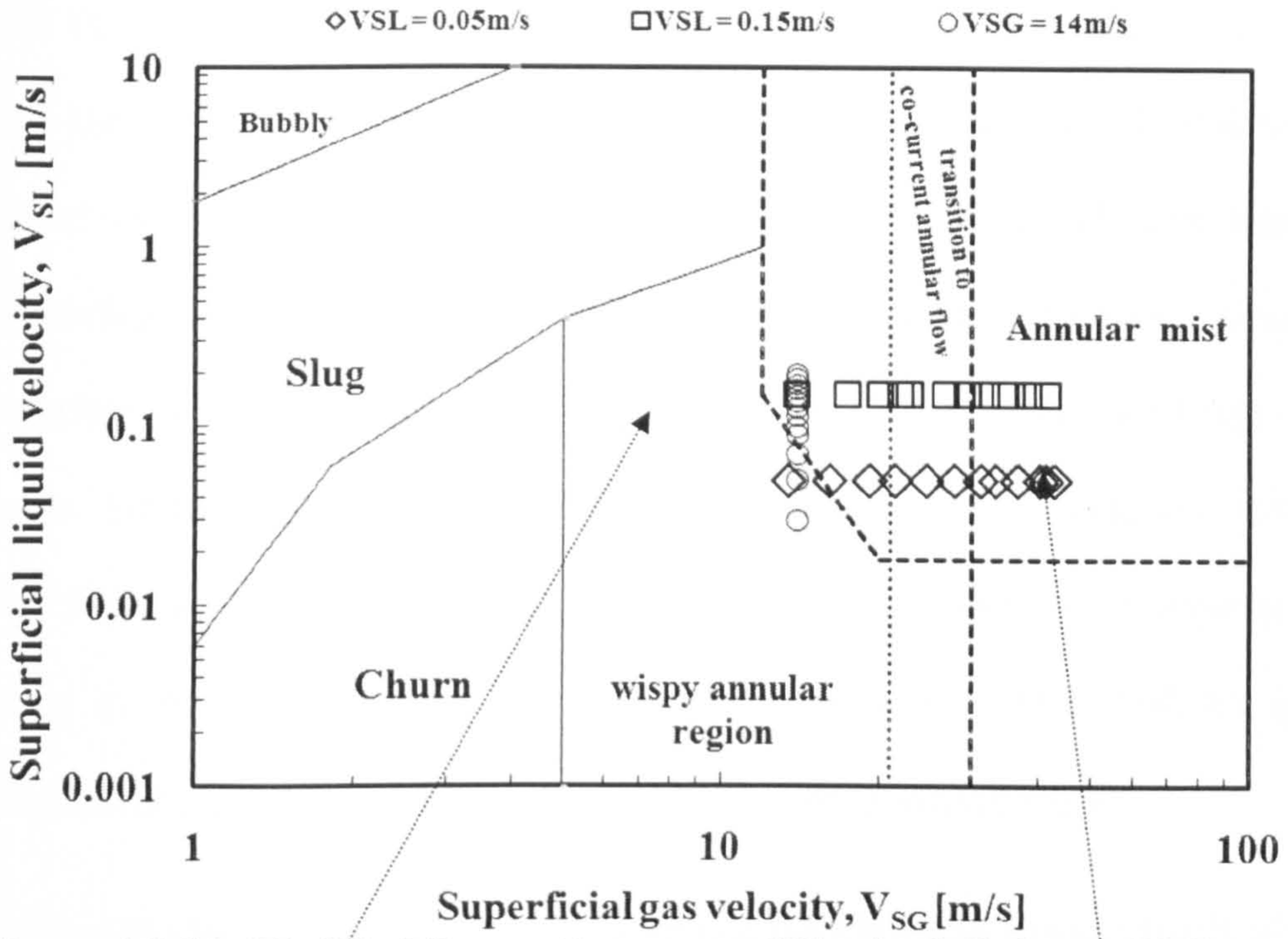

Figure 4.5 (b): Modified flow pattern map of Hewitt & Roberts (1969) based on new information from drop concentration measurement in vertical annular two-phase flow.

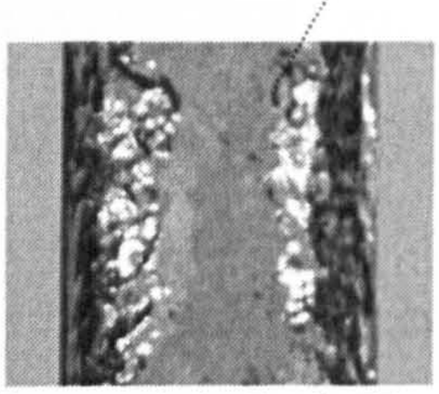

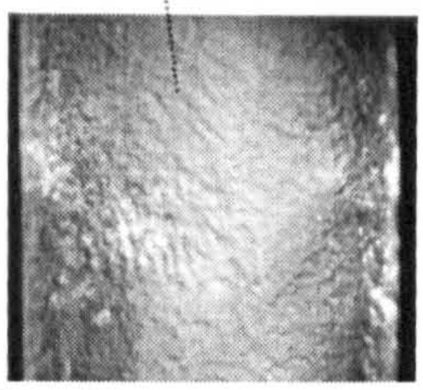

Figure 4.6: Left Hand Side (LHS) – image of wispy annular flow at gas superficial velocity of 14 m/s and liquid superficial velocity of 0.19 m/s. Right Hand Side (RHS) – image showing evolution of 'ring' disturbance wave around transition to mist annular after gas superficial velocity of 30 m/s.

Wisps or fractal of liquid structures entrained in the gas core were observed at conditions where they are not expected. This is supported by the high speed images recorded during the experiments. In Figure 4.5 (b), one of the images extracted from the cine movie recorded during the flow , Figure 4.6 LHS , where wisps were seen at gas superficial velocity , V_{SG} = 14 m/s and at liquid superficial velocity V_{SL} = 0.19 m/s, was attached to the flow map in the (wispy annular regime). This image demonstrates incompatibility of the present observation

with the popular flow map, Figure 4.5 (b). This visualization evidence, however, conforms with the recent finding by Azzopardi et al. (2008). Azzopardi et al. observed wisps in the region usually identified as churn flow regime by published flow transition models. According to Hewitt and Roberts (1969) transition criterion to wispy annular, the critical superficial liquid velocity value, V_{SL} = 1.2 m/s must be exceeded for wispy annular flow to occur. However, wisps are seen in the present study at conditions below the critical superficial liquid velocity value, V_{SL} = 1.2 m/s. Further evidences in support of existence of wisps in region where they are not expected in annular flow will be provided in the subsequent discussion using the Probability Density Function (PDF).

Other video footages recorded for flow around the transition to mist annular flow and beyond are presented in Table 4.3 column (a) and (c) respectively. A similar image recorded by Mantilla (2008) was presented in column (b) Table 4.3 to show similarity of the entrainment mechanism after transition to mist annular flow.

At relatively low gas superficial velocity, fractal of liquid film resembles sausage in shape are seen in the gas core description of which fits into wispy annular described by Sekoguchi and Takeishi (1989). The possible explanation for presence of wisps at these conditions of relatively lower gas and liquid superficial velocities can be attributed to incomplete atomization of liquid torn off the wave crest by the shear influence of the gas phase not enough to completely break down the bag of liquid due to gravity pull in the opposite direction.

Another interesting structure was observed around gas superficial velocity of 30 m/s and beyond. The wave structure captured under the high speed cine movie was shown in column

(c) Table 4.3. The wave was referred to as ring disturbance wave according to Mantilla (2008) who observed similar wave (Table 4.3 column (b)) in his experiment with a pipe diameter of 152.4mm, horizontal annular flow. The wave was characterized by higher amplitude and frequency. Wave properties associated with the various entrainment processes is discussed in detailed in Chapter Five.

Table 4.3: High speed cine movies/images recorded during the experimental for conditions around transition to mist flow at gas superficial velocity of 30 m/s and beyond.

Present study	Mantilla (2008)	Present study
	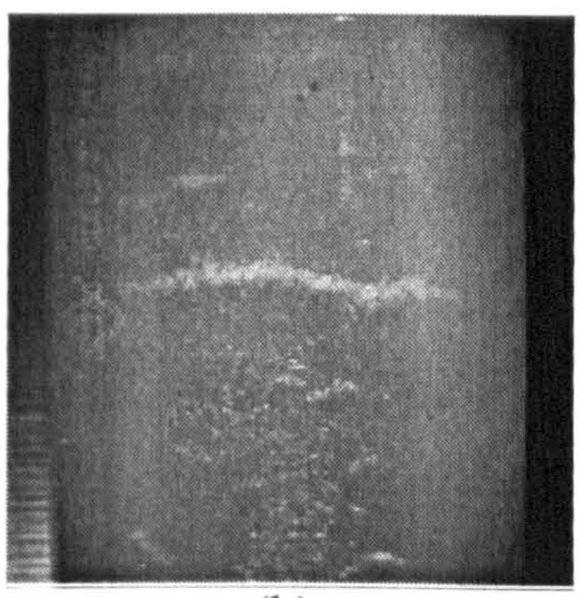	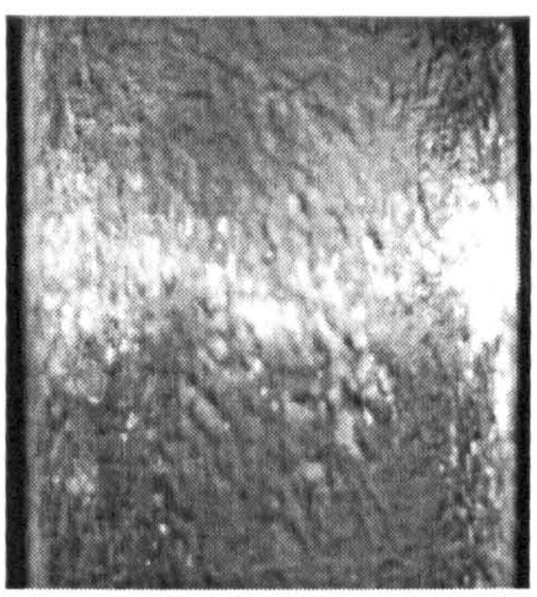
(a)	(b)	(c)

4.5.2 Void Fraction

Mean void fraction is plotted against gas superficial velocity at fixed liquid superficial velocities as shown in Figure 4.7 (a). Conductance probe next to the liquid extractor was chosen for this analysis. An interesting phenomenon occurs in the case of V_{SL} = 0.05 m/s. The data behaves unexpectedly and there is an abrupt increase in void fraction before V_{SG} = 21 m/s. This behavior is non-linear. However, void fraction returns to linearity after V_{SG} = 21 m/s where it continues to increase linearly with increase in gas superficial velocity at constant liquid flow rate. Also, in the case of V_{SL} = 0.15 m/s, a change of gradient occurs around V_{SG} = 21 m/s. The changes to void fraction in order of magnitude in the case of V_{SL} = 0.15 m/s is far less compared to the case of V_{SL} = 0.05m/s. Figure 4.7 (a) displayed how measured mean void fraction varies with inlet conditions. In Figure 4.7 (c), this behavior is not readily obvious.

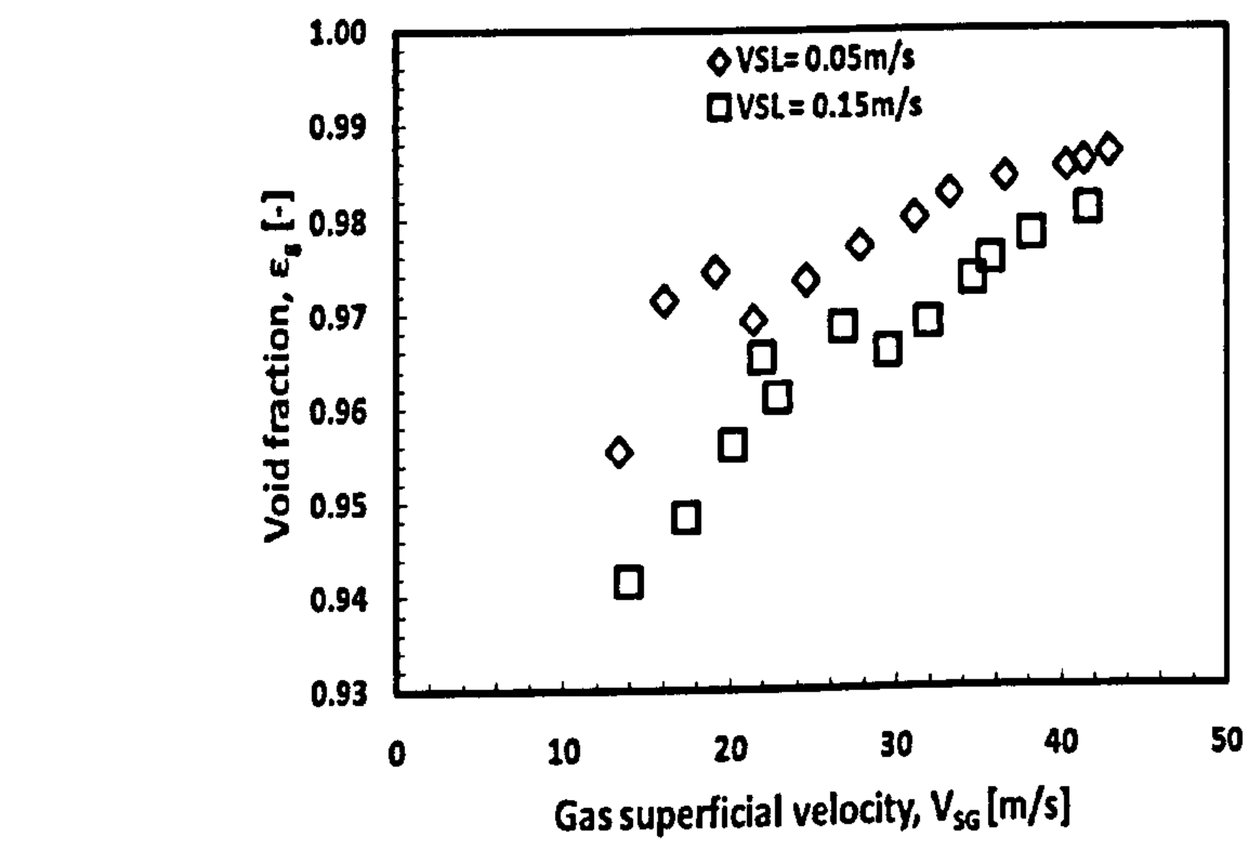

Figure 4.7: (a) **(b)**

Figure 4.7(a) Void fraction variation with increase gas superficial velocity.
Figure 4.7 (b) Measured void fraction validated with the model of Alves et al. (1991).

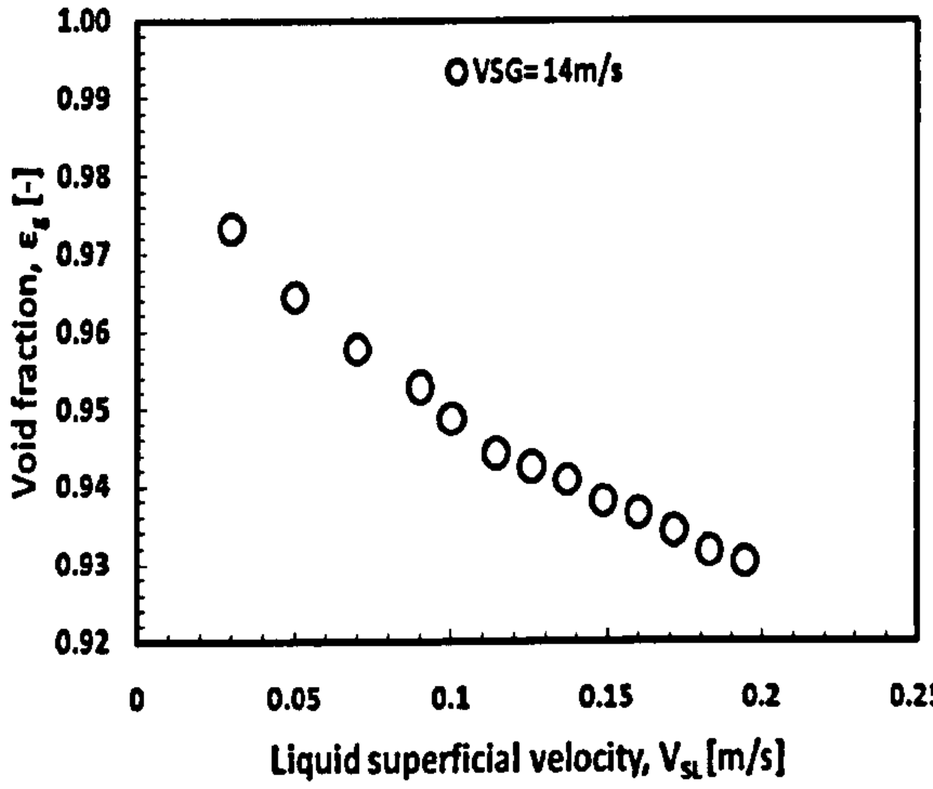

Figure 4.7: (c)

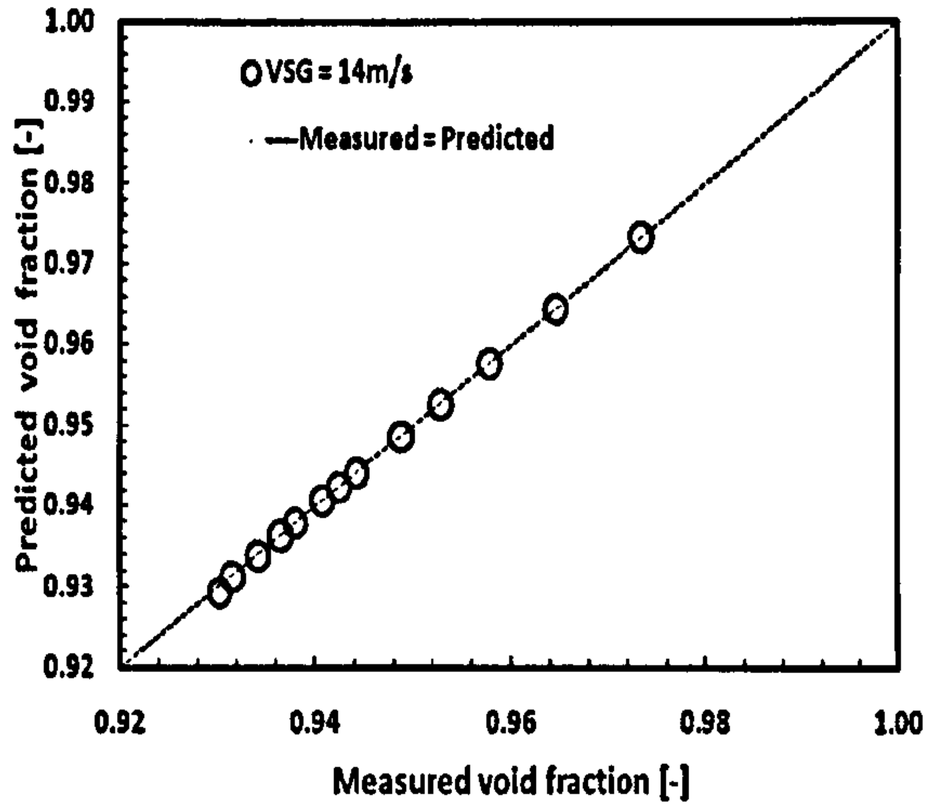

Figure 4.7: (d)

Figure 4.7 (c) Void fraction variations with increase liquid superficial velocity.
Figure 4.7 (d) Validation of measured void fraction with mechanistic model of Alves et al. (1991).

The measured void fraction was validated with the mechanistic model of Alves et al. (1991) as shown in Figure 4.7 (b) and Figure 4.7 (d) respectively. Excellent match is observed between the measured and the predicted values.

The possible reason for the unexpected behavior noticed in Figure 4.7 (a) can be attributed to the dispersed phase turbulence intensity. Below V_{SG} = 21m/s, gravity influence dominates (this statement will be supported with facts from other data in the subsequent chapters). In the case of V_{SL} = 0.05 m/s, thinner film produces relatively bigger drops. Bigger drops move at relatively slower velocity and do not follow gas phase turbulence closely. Increase concentration of such bigger droplets enhances turbulence intensity, Sawant et al. (2009), therefore, the fluctuation in the void fraction gradient. It is this fluctuating gradient that is responsible for the higher voidage noticed before V_{SG} = 21 m/s. After this boundary, void fraction increases asymptotically with increase in gas superficial velocity.

The distribution in the case of V_{SL} = 0.05 m/s is bi-modal according to the PDF of D_{50} which is characterized by droplet diameters of 100μm and 165μm up to 30 m/s superficial gas velocity, Figure 4.29. Beyond V_{SG} = 30 m/s, the distribution becomes mono-modal with droplets size decreases to around 100 μm. It may be that turbulent intensity decreases with after V_{SG} = 30 m/s as drop size decreases. Another reason may be that smaller droplets dominates the gas core because they follow gas phase turbulence more closely Sawant et al. (2009). This allows for bigger voidage as picked up by all instrumentation used in the data acquisition.

Weihong et al. (2001) first reported the behavior while during their experimental study of low-liquid-loading gas-liquid flow in near horizontal pipes. The phenomenon was noticed when liquid superficial velocity was increased from V_{SL} = 0.03 m/s to V_{SL} = 0.05m/s at constant V_{SG} = 25m/s, the liquid-film flow rate, hold-up, and pressure gradient all decreased, and the droplet entrained fraction increased significantly. They did not give any reason nor explain what was responsible for the behavior but rather emphasized the significance this will have on the development of predictive models for low-liquid-loading wet gas pipe lines. Their experiment was conducted on 50.1mm internal diameter pipe with inclination angles from horizontal of -2^0, -1^0, 0^0, 1^0 and 2^0. They reported that this unexpected behavior occurred at gas superficial velocity of 25m/s which falls within the range of V_{SG} = 21m/s suggesting similar mechanisms governing horizontal and vertical annular two-phase flow.

4.5.3 Drop size

Two characteristic mean diameters are used in this analysis, Mass Median drop Diameter (MMD or D_{50}) and Sauter Mean Diameter (SMD or D_{32}). Mass Median drop Diameter (MMD or D_{50}) is the drop diameter that divides the frequency distribution in half; fifty percent of the gas core mass has droplet with a larger diameter, and fifty percent of the gas core mass has droplet with a smaller diameter. Sauter Mean Diameter (SMD or D_{32}) is often referred to as volume-surface mean drop size. It is the average size of the drop based on the specific surface per unit volume. Or the diameter of a drop having the same volume/surface ratio as the entire drop.

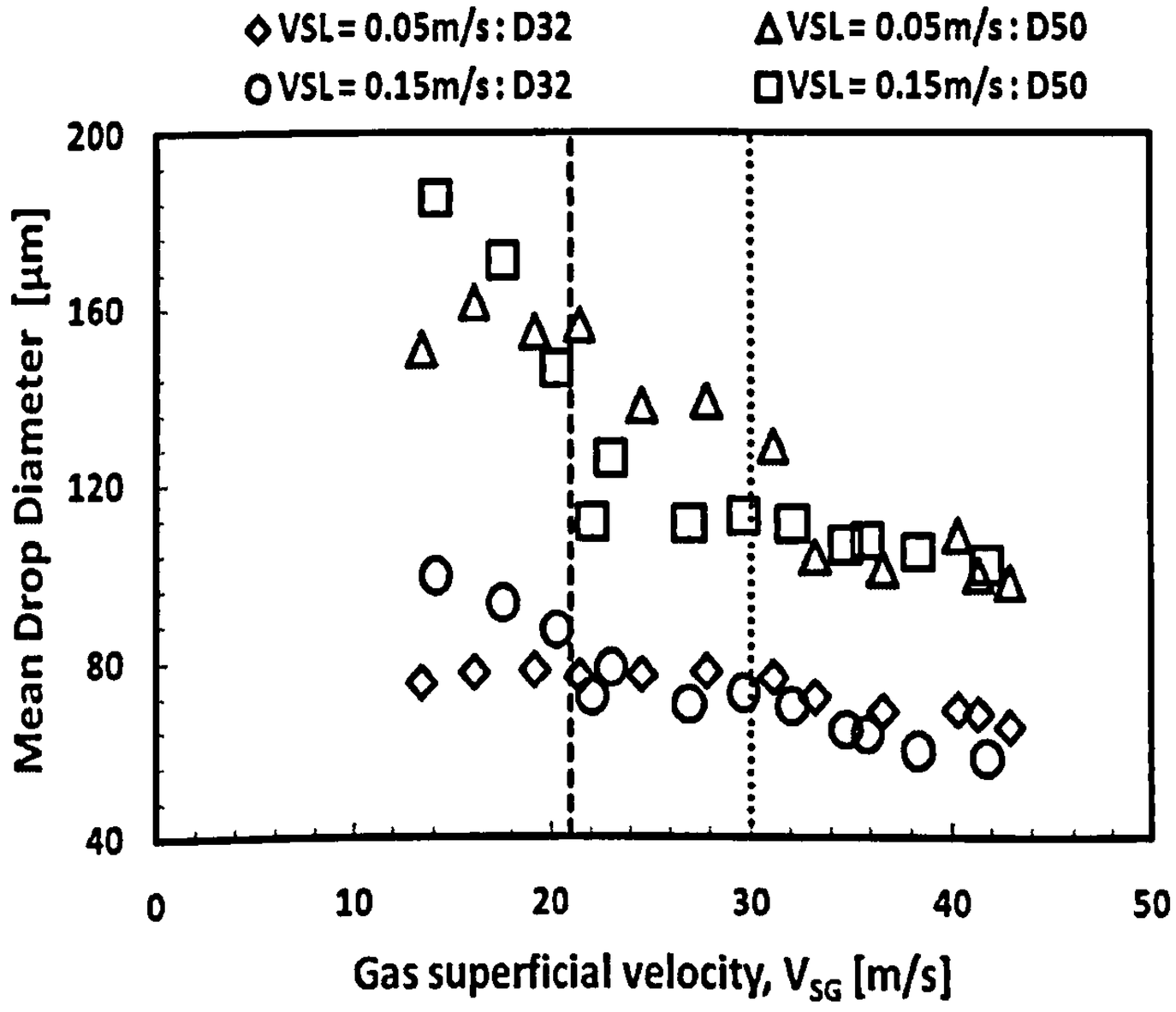

Figure 4.8: Mean drop diameter variation with increase gas superficial velocity.

In Figure 4.8, Sauter Mean Diameter (D_{32}) and Mass Median Diameter (D_{50}) decrease asymptotically with increasing gas superficial velocity at constant liquid superficial

velocity. D_{50} is seen to be greater than D_{32} in all cases tested. D_{50} for V_{SL} = 0.15 m/s is higher than D_{50} for V_{SL} = 0.05 m/s before the transition boundary at V_{SG} = 21 m/s. After the transition, the trend reverses itself. This trend continues until another transition boundary is crossed at V_{SG} = 30 m/s. After the transition to mist flow at V_{SG} = 30 m/s D_{50} for V_{SL} = 0.15 m/s again peaks up crossing-over D_{50} for V_{SL} = 0.05 m/s at V_{SG} = 30 m/s.

4.5.3.1 Identification of Flow Transitions within Annular Flow based on Drop Size Measurement

Subtle changes at transitions within annular flow have been elucidated by the information from characteristic mean diameters measured during the experiment. The conditions at which these changes occurred marked flow regime transitions within annular flow. The drop measurements were logged at constant liquid superficial velocities of 0.05 m/s and 0.15 m/s respectively with gas superficial velocities systematically increased from 13 m/s to 43 m/s. Several fluctuations were seen in the results of MMD. In order to average out effect of this fluctuation MMD was normalized by SMD, Figure 4.9.

Two flow regimes transitions have elucidated in Figure 4.9 using subtle changes in SMD and MMD. First transition occurs at V_{SG} = 21 m/s .This is marked as dotted discontinuous line in Figure 4.9. This transition is captured by SMD profile as drop created from thinner film crosses-over drop from thicker film as gas superficial velocity increases. Gravity influence on thinner film is suppressed as drop from thinner film

crosses the transition boundary at V_{SG} = 21 m/s. This transition is picked up as point of inflection according to MMD profile in Figure 4.9.

The transition marks the beginning of co-current annular two-phase flow. In general, co-current annular flow occurs when drag force on the gas phase is sufficient enough to levitate the liquid drops in the gas core. In terms of waves traversing the gas-liquid interface, before this transition, huge wave dominates although it co-exists with the disturbance wave. After this transition and before gas superficial velocity of V_{SG} = 30 m/s, disturbance wave dominates the gas-liquid interface. However, after gas superficial velocity V_{SG} = 30 m/s huge wave vanishes.

Mass of a drop is directly proportional to its size according to this relationship, Ceylan et al. (2003):

$$m = \frac{\pi \rho_d a^3}{6} \tag{4.6}$$

Where, a = drop size (SMD or MMD).

Therefore, drop mass densities increases as film becomes thinner after the transition. This transition is only detected by SMD profile Figure 4.9. The phenomena presented here by this information from SMD will have significant effect in design of process equipment and in the formulation of mechanistic model to predict drop size distribution in terms of SMD.

In Figure 4.9, MMD was moralized by SMD (secondary axis) and a plot of MMD/SMD against gas superficial velocity reveals two additional details. First, the mean indices of MMD/SMD as superficial gas velocity increases indicate drop size distributions are self-

similar. Self-similarity nature of the profile suggests explicitly that drop coalescence is dominant mechanism although it is believed drop break-up occurs simultaneously but on a scale which can be tacitly neglected in the analysis of result.

Second revelation was the detection of transition boundary to mist annular flow around gas superficial velocity of 30 m/s based on the profile of MMD/SMD. This transition boundary is marked by dashed discontinuous line in Figure 11 at V_{SG} = 30 m/s. According to Figure 4.9, the drop mass density increases with thickness of the liquid film which produces the droplet. This behavior is an exact opposite of the trend observed with the SMD profile. Before this transition, thinner film produces drop of higher mass density in terms of MMD.

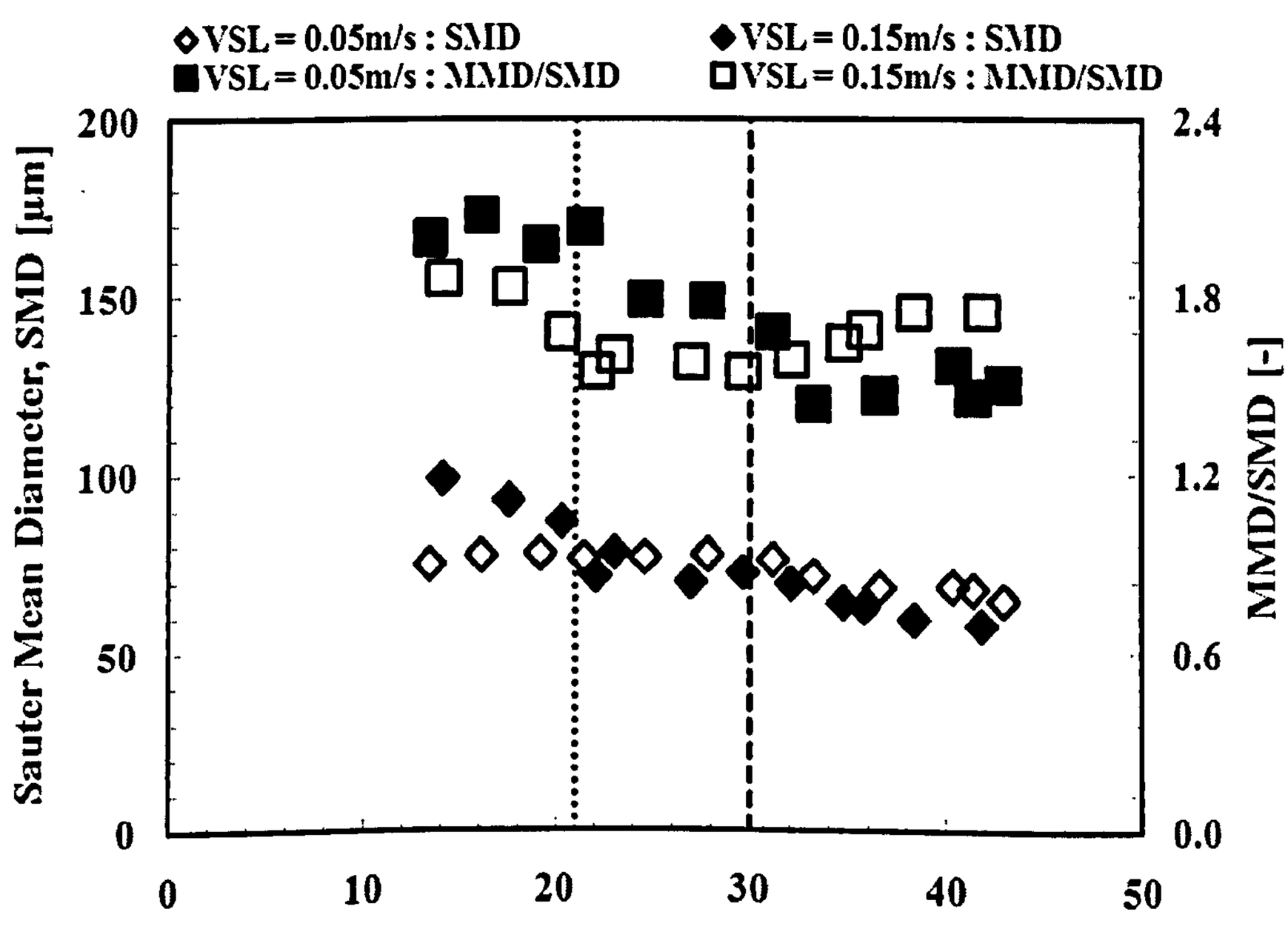

Figure 4.9: Effect of gas superficial velocity on SMD and normalized drop size.

The occurrences at V_{SG} = 21 m/s and V_{SG} = 30 m/s can be linked with change of liquid entrainment mechanisms. Evidences from video footage of the flow recorded using high speed camera suggest that although bag break-up and ligament break-up may co-exist bag break-up dominates before gas superficial velocity ,V_{SG} = 30 m/s while ligament break-up mechanism presents dominant mechanism after gas superficial velocity ,V_{SG} = 30 m/s.

Generally, the droplet creation from film can be explained as follows. As gas velocity increases the flow structures increases. Wave traversing the gas-liquid interface traps gas bubbles into the liquid film. Density difference causes the bubbles to migrate and agglomerate near the wave crest causing increase in interfacial shear stress. Gravity drainage, gas-stream shear and bubble expansion causes liquid membrane to gets thinner. Eventually, bubble bursts forming numerous droplets and develops vortices. The newly formed droplets cause the gas core density to increase and expand. This process continues until liquid film lacks momentum to shed further droplet.

First transition describe transition to co-current upward annular flow at V_{SG} = 21 m/s. For fully developed annular flow to occur, the drag or shear force being exerted by the gas phase must overcome the gravity force in order to keep the entrained drop flow co-currently with the gas phase. Before the transition, the mechanism of entrainment is suggested to be dominated by bag break-up from the video footage of the flow.

From measurements of drop sizes and from flow visualization experiments, Azzopardi (1983) identified two mechanisms by which droplet entrainment takes place. In the first

mechanism (bag break-up), the gas apparently 'undercuts' a large wave forming and open-ended bubble with a thick filament rim. When this bubble bursts, a rapid transient acceleration of the gas phase accelerates the droplets. In the second mechanism, the ligament break-up, the wave crests are pulled forward in the gas core in the form of ligaments. Oscillation within continue to grow until a point is reached when the frequency of oscillation within the ligament becomes equal to the turbulent frequency from the gas phase. At this point resonant effect breaks up the ligament into numerous liquid droplets noticed in the gas core. The second transition marks the flow transition from annular to mist flow at V_{SG} = 30 m/s. This probably reflects a change in the liquid entrainment mechanism from the 'bag break-up' mechanism to the 'ligament tearing' mechanism.

Bag break-up is characterized by shearing of large liquid packets from the film to the gas core. At low gas velocities the droplets are generated from the large flooding-type waves (huge wave) through the undercutting (bag break-up) mechanism. The driving force is the turbulent fluctuation in the gas phase. As the gas flow rate is increased and the occurrence of large flooding-type waves subsides, disturbance waves start to dominates although both mechanisms coexist (V_{SG} = 21 m/s). With further and continuous increase of the gas flow rate (after V_{SG} = 30 m/s) the ligament break-up mechanism becoming dominant atomization mechanism. Based on the foregoing analysis of atomization or entrainment mechanism is controlled by bag break up before the transition co-current annular flow at V_{SG} = 21 m/s. The dominant entrainment mechanism becomes ligament break-up after .V_{SG} = 21 m/s.

The usual expectation is that under low gas velocity condition, droplets are relatively large. As the gas velocity increases, more and more liquid gets entrained into the gas core and liquid film flow rate gradually decreases resulting in decrease of disturbance wave amplitude. Consequently the average size of droplets also decreases with the increase in gas velocity. This is obviously not the case from the observation of present study after V_{SG} = 30 m/s and seems to be only valid for D_{32}.

Wispy annular shown in Figure 4.9 are characterized by incomplete atomization of the liquid film. It may be that droplet inertial is the driving force of droplet dispersion when film undergoes complete atomization. The normalized MMD in Figure 4.9 for V_{SL} = 0.15 m/s, crossed-over the normalized V_{SL} = 0.05 m/s at V_{SG} = 30 m/s. Additional possible explanation for this behavior in the mist annular regime is offered as follows.

Ring disturbance waves were identified in this study around $V_{SG} \geq 30$ m/s. The evolution of this wave influences drop size (MMD) distribution at this transition boundary where V_{SG} = 30m/s and beyond. This is because ring disturbance wave appears to dominate and control the creation and dispersion of entrained liquid droplets in the gas phases after $V_{SG} \geq 30$m/s. If this wave could be thought of as an elastic material then explanation as to why D_{50} of V_{SL} = 0.15m/s is greater than D_{50} at V_{SL} = 0.05m/s can be provided. Then the degree of springiness seems to be higher the higher the liquid flow rate when gas flow rate is maintained at a constant value. Therefore, more elastic D_{50} of V_{SL} = 0.15m/s tends to offer less resistance to the driving force of the dispersed phase

resulting in greater amplitude, greater drop size than in the case of D_{50} of V_{SL} = 0.05m/s which appears to be more rigid.

Another possible reason goes as follows. Thinner film produces bigger drop because of the greater interaction between it and the turbulent gas core. Thicker film on the other hand experiences less interaction with the gas core due to conservation of momentum. However, in mist flow ($V_{SG} \geq 30$ m/s) where the droplets size are smaller and approximately homogeneously distributed, atomization of liquid film is complete. Dispersed phase distribution is inertial-driven. Flow at higher liquid superficial velocity will produce more structures at constant gas superficial velocity. This may explain why normalized drop-size is higher for V_{SL} = 0.15 m/s after $V_{SG} \geq 30$ m/s.

Another reason why drop size of V_{SL} = 0.15m/s is greater than that V_{SL} = 0.05m/s may be explained by expansion of the core as liquid superficial velocity increases. Increases in liquid superficial velocity increases film burst which in turn increases drop size and drop concentration.

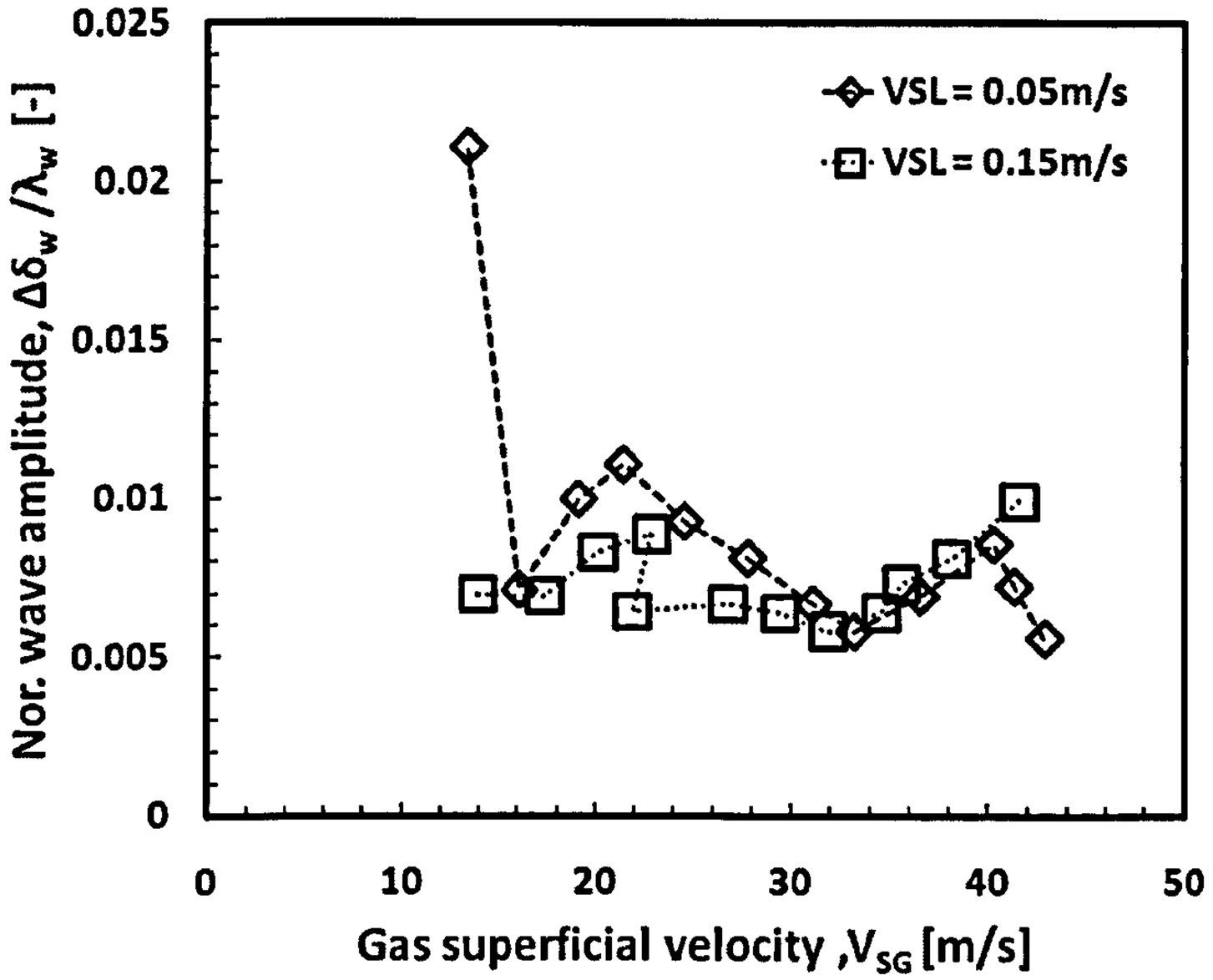

Figure 4.10: Normalized wave amplitude as function of superficial liquid and gas velocities.

When D_{50} is normalized by D_{32} as shown in Figure 4.9, an exception to the rule of thumb that thinner film produces bigger drops is observed. This exception occurs at V_{SG} ≥ 30 m/s according to Figure 4.9 as thicker film produces bigger drops.

When wave amplitude is normalized by wave spacing and plotted against gas superficial velocity, a similar trend observed in the drop size profile is also noticed, Figure 4.10. The wave amplitude data use in Figure 4.10 and their detailed discussions are available in Chapter Six. Therefore, this observation confirms that droplet size (D_{50}) distribution is dependent on the disturbance wave amplitude.

4.5.4 Drop concentration

Measured drop concentration increases in the gas core as gas superficial velocity increases at two fixed liquid superficial velocities as presented in Figure 4.11. Figure 4.11 shows a trend which suggests drop concentration increases monotonically with increasing gas superficial velocity at constant liquid superficial velocity.

Generally, drop concentration is seen to increase with increase in gas and liquid superficial velocities. It is higher the higher the liquid superficial velocity. The thicker film from V_{SL} = 0.15 m/s produces droplets of higher concentration and hence higher entrained fraction. Drop concentration was also observed to be a strong function of gas velocity and gas phase density .This statement can be explained as follows. As gas velocity increases the flow structure increases. Wave traversing the gas-liquid interface traps gas bubbles into the liquid film. Density difference causes the bubbles to migrate and agglomerate near the wave crest causing increase in interfacial shear stress. Gravity drainage, gas stream shear and bubble expansion cause liquid membrane to get thinner. Eventually, bubble bursts forming numerous droplets and develops vortices. The newly formed droplets cause the gas core density to increase and expand. This continues until film becomes thinner and can no longer produce droplet.

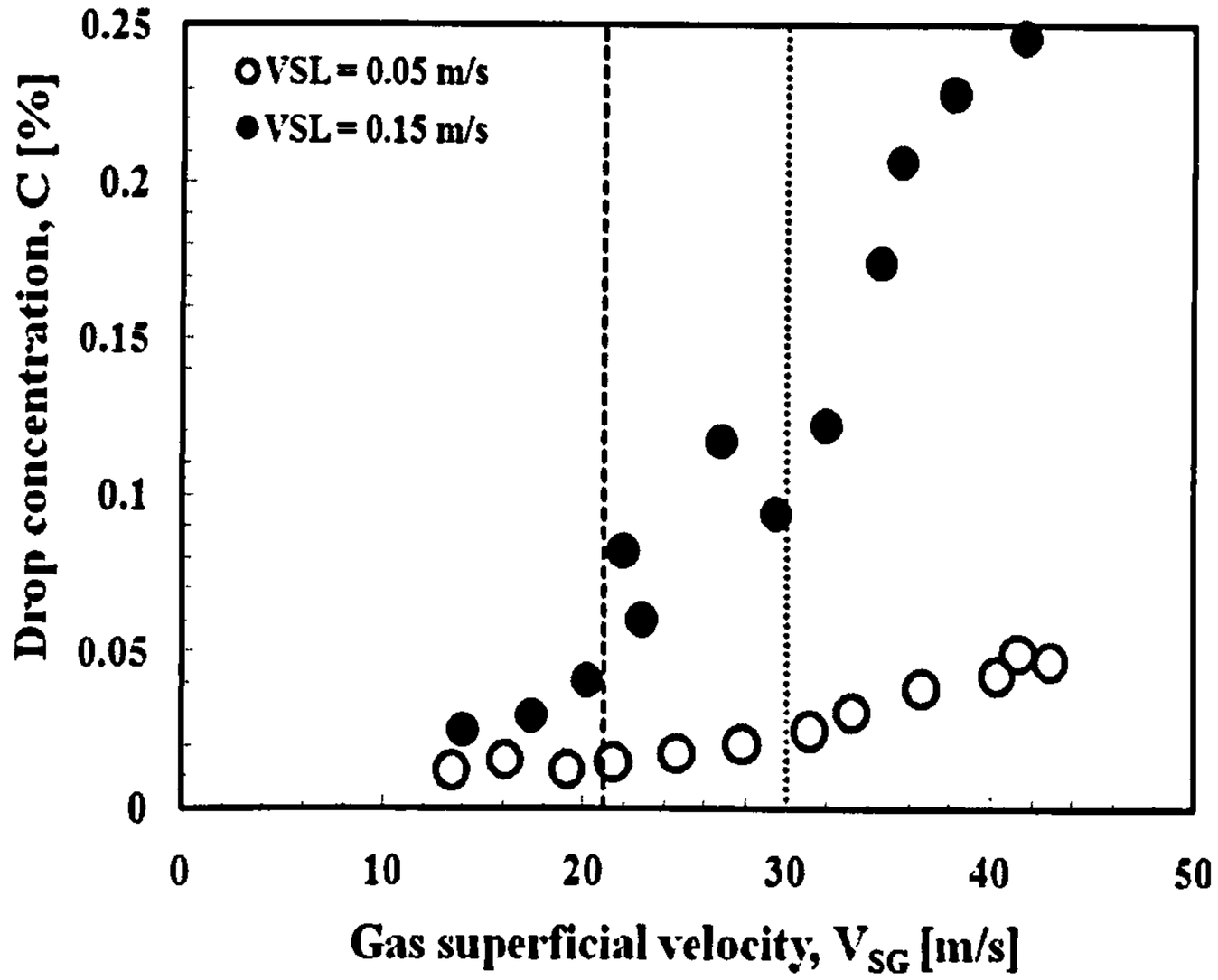

Figure 4.11: Effect of gas and liquid superficial velocities on drop concentration.

The trend shown by liquid superficial velocity, V_{SL} = 0.15 m/s reveals additional details. The transitions at 21 m/s and 30 m/s to co-current annular and mist annular flow respectively. These transitions, however, appear as point of inflections. Though, it can be concluded in terms of drop concentration that thicker film has greater interaction with the gas core.

4.5.5 Entrained Fraction

The concentrations measured with the laser diffraction instruments can be converted to entrained fraction by Equation (4.7):

$$E_F = \frac{\rho_L V_D C}{\dot{m}_{LE}} \tag{4.7}$$

Where V_D is the drop velocity, ρ_L is the liquid density; *c* is the volumetric drop concentration

and $\dot{m}_{LE}$ is the total liquid mass flux.

From the available measurements, Azzopardi & Teixeira (1994 b), Fore & Dukler (1995), Zaidi et al. (1998), van't Westende et al. (2007), it can be seen that the gas superficial velocity is a good approximation to the drop velocity at centre-line while the product of liquid density and superficial liquid velocity approximates the total liquid mass flux. The gas superficial velocity can therefore be used in place of drop velocity in Equation (6). Hence, entrained fraction can be estimated from inlet condition by multiplying drop concentration by superficial velocities ratio (V_{SG}/V_{SL}).

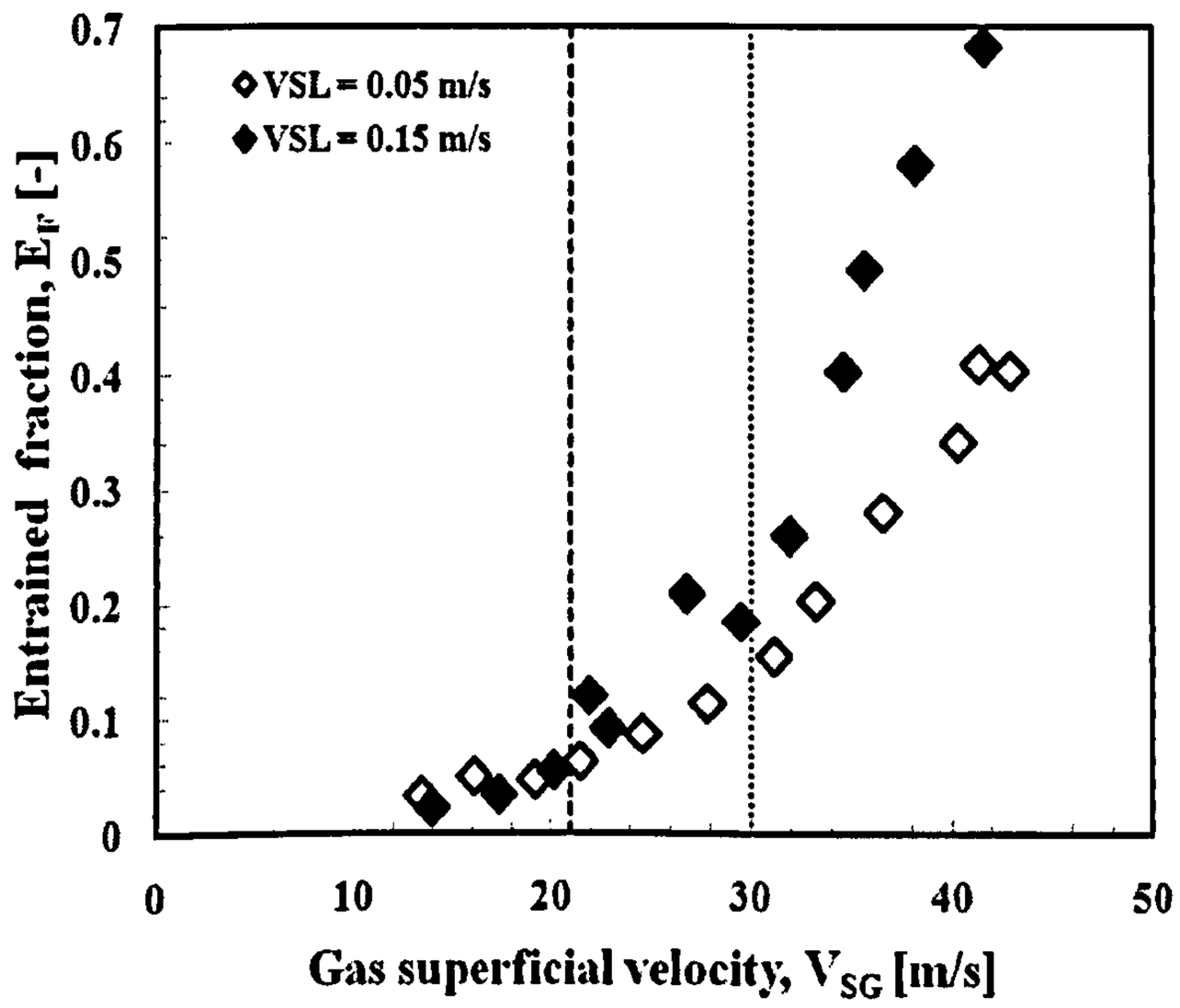

Figure 4.12: Effect of gas and liquid superficial velocities on entrained fraction.

Therefore, Figure 4.12 is obtained when drop concentration is converted to entrained fraction. The figure relates entrained fraction variation with gas superficial velocity at constant liquid superficial velocities. The general trend shows that entrained fraction is higher for thinner film where $V_{SL} = 0.05$ m/s than the case of thicker film where liquid superficial velocity, $V_{SL} = 0.15$ m/s before $V_{SG} \geq 21$ m/s. After $V_{SG} \geq 21$ m/s, the trend

reverses. Entrained fraction becomes higher the higher the liquid superficial velocity.

At the next level of analysis entrainment fraction was normalized with minimum entrained fraction Equation (4.8) by Barbosa et al. (2002) and plotted against increasing superficial gas velocity, Figure 4.13.

$$E_{FMIN} = 0.95 + 342.55\sqrt{\frac{\rho_L \dot{m}_L}{\rho_G \dot{m}_G}}\, d_p^2 \qquad (4.8)$$

Where E_{FMIN} = minimum entrained fraction, [%]; d_p = pipe diameter , [m], ρ_L and ρ_G are liquid and gas densities; [kg/m^3] and $\dot{m}_L$ *and* $\dot{m}_G$ are the liquid and gas mass fluxes respectively in [kg/m-s^2].

Figure 4.13 share similar features with Figure 4.12. This shows good agreement between present study and the model of Barbosa et al. (2002). Figure 4.13 shows entrained fraction profile with three distinct flow transitions: one, wispy annular, characterized by dominance of huge waves; two, transition to annular flow characterized by co-existence of huge and disturbance wave; and three, mist annular flow where disturbance wave dominates. This classification is supported by measured wave properties (see Chapter Five). Wave frequency, wave length and wave velocity have been taken into consideration in categorizing waves into huge and disturbance waves.

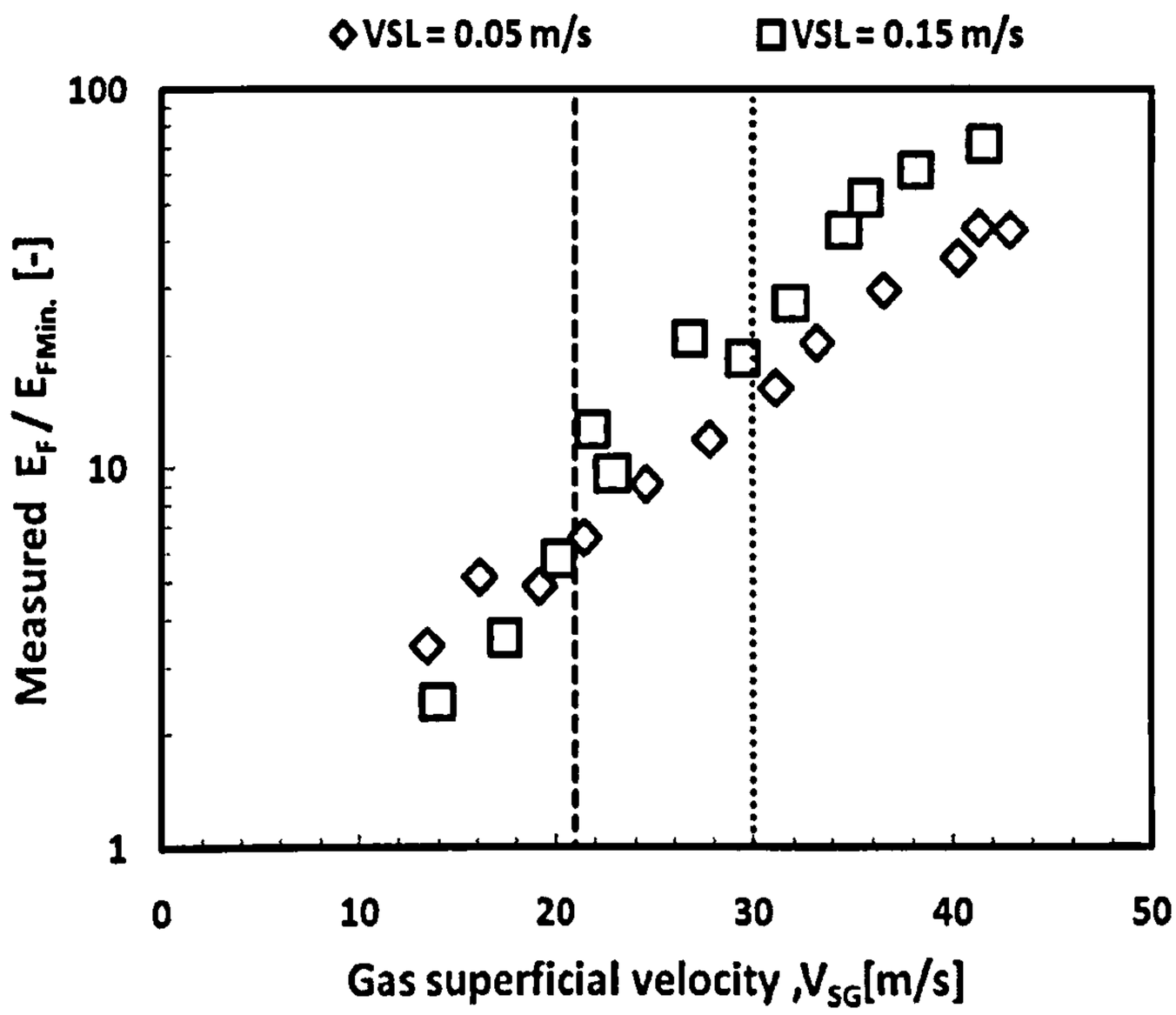

Figure 4.13: Effect of gas and liquid superficial velocities on normalized entrained fraction. Measured entrained fraction normalized by the minimum entrained fraction model of Barbosa et al. (2002).

Figure 4.13 indicates that entrained fraction for the case where V_{SL} = 0.05 m/s is greater than the case where V_{SL} = 0.15 m/s before $V_{SG} \geq 21$ m/s. After $V_{SG} \geq 21$ m/s, the trend reverses, entrained fraction increases with increased liquid superficial velocity at constant gas superficial velocity.

Therefore, it could be concluded that the subtle changes that occurs in entrained fraction profile around gas superficial velocity of 21 m/s is another evidence of transition to co-current annular flow.

4.5.6. Film hold-up

Film hold-up or the liquid film thickness can be estimated from void fraction using geometrical analysis. Geometrical analysis assumes that the interface is not wavy and that liquid film is symmetrically uniformly distributed around the pipe circumference.

Therefore, using the schematic in Figure 4.14, liquid film hold-up on the wall can be estimated from the cross-sectional averaged void fraction logged with the conductance probes using Equation (4.9).

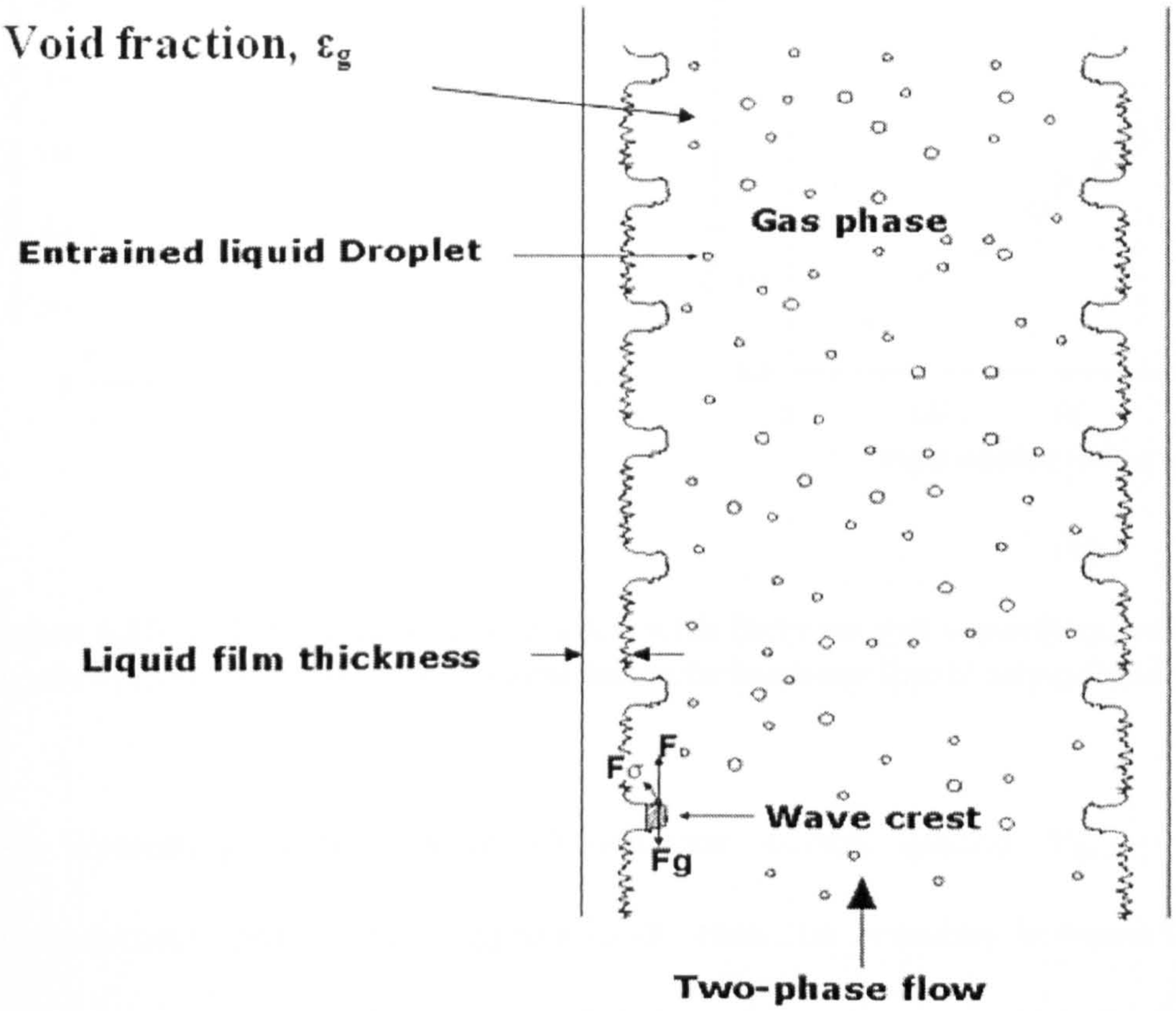

Figure 4.14: Schematic of vertical annular two-phase flow.

$$\delta_L = \frac{d}{2}\left(1 - \sqrt{\varepsilon_g}\right) \tag{4.9}$$

Where:

δ_F = film thickness, [mm]; d = pipe diameter; ε_g = cross sectional average void fraction, [-].

Figure 4.15 (a) shows that if the liquid superficial velocity is kept constant and the gas superficial velocity is increased, the average film thickness decreases monotonically. On

the other hand, Figure 4.15 (b) shows that when gas superficial velocity is kept constant and liquid superficial velocity is varied, the average film thickness increases.

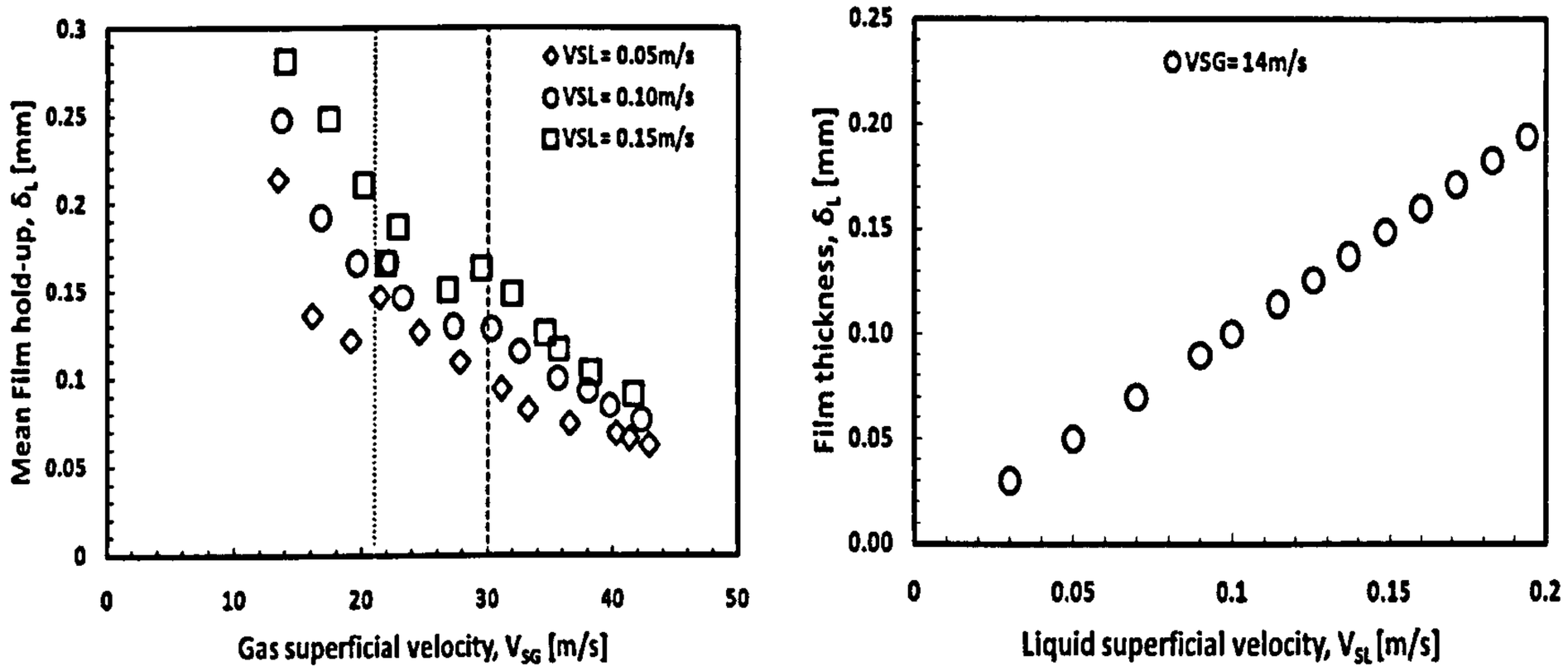

Figure 4.15 (a) Film thickness variation with increase gas superficial velocity.
Figure 4.15 (b) Film thickness variation with increase liquid superficial velocity.

An interesting hydrodynamic phenomenon occurs around V_{SG} = 21m/s. The hydrodynamic phenomenon appears to be transition boundary between wispy annular and co-current annular flow regime. This transition appears as point of inflection around V_{SG} = 21 m/s in Figure 4.15 (a). After V_{SG} = 21 m/s, the film is believed to become more stable and axi-symmetrical. This boundary was picked up by all instrumentation used in the data acquisition. This will be discussed further in subsequent analysis.

The following discussion attempts to offer explanation for this occurrence. It is believed that gravitational acceleration influences annular flow regime Geraci (2005). The influence of gravity increases disturbance waves due to the acceleration of the liquid phase in the opposite direction to the fluid motion McGillivray et al. (2002). The influence of gravity creates an unstable and chaotic film. As noticed previously in the

void fraction profile Figure 4.15: (a), the dominant effect of gravity ceases after V_{SG} = 21 m/s. Under the influence of gravity film is less stable and chaotic. Gravity effect is more pronounced for V_{SL} = 0.05 m/s because the film is thinner, less stable and more chaotic. Thinner film of V_{SL} = 0.05 m/s promotes greater interaction with the gas core and therefore experiences more turbulence than in the case of V_{SL} = 0.10 and 0.15m/s. Values for V_{SL} = 0.10 m/s was interpolated between V_{SL} = 0.05 m/s and 0.15 m/s. In the case of V_{SL} = 0.10 m/s and 0.15 m/s the film are less affected by turbulence. Film thickness decreases at the transition boundary around V_{SG} = 21 m/s. After the transition, it recovers behaving linearly increase with increasing in gas superficial velocity for both V_{SL} = 0.10 m/s and 0.15 m/s.

The trend in the average film thickness behavior with increasing gas and liquid superficial velocity is in good agreement with previous studies on air/water annular flow. Kaji (2008) reported the chaotic nature of the film in the gravity dominated regime to be as a result of change in film thickness with axial distance. Kaji claimed for V_{SG} > 12 m/s, film thickness increases with axial distance up to about 100 pipe diameters then decreases asymptotically.

Film hold-up data, according to the foregoing, therefore, seems to capture the transition to co-current annular flow which occurs at a superficial gas velocity of 21 m/s.

4.5.6.1 Film hold-up and Drop Size

In this sub-section, film hold-up and drop size data are analyzed to establish a relationship between film hold-up (wave) which produces the droplets and the entrained droplets. Standard deviation of the film hold-up presents the most interesting finding of all the statistical analysis carried out. The standard deviation of the film thickness when plotted against superficial gas velocity as shown in Figure 4.16 shows that Mass Median Diameter (MMD) is directly proportional to the standard deviation of the film hold-up. There is a strong relationship between Figure 4.8 and Figure 4.16. The two figures display similar trend for V_{SL} = 0.05 m/s and V_{SL} = 0.15 m/s. This is another interesting observation because data in Figure 4.8 was acquired from Spraytec whilst film thickness data in Figure 4.16 was logged using conductance probes.

It is interesting to see in Figure 4.16 that drop size distribution is directly proportional to the standard deviation of film hold-up from which the drops are produced. By employing the right statistical model instantaneous film thickness can be determined from drop size distribution (MMD).Thus; dynamic film hold-up can be generated from drop size information and vice-versa. In nuclear engineering and multiphase Computational Fluid Dynamics, this valuable information can be used to model and quantify the amount of liquid present in the gas core by carrying out mass balance analysis.

At next level of analysis, standard deviation has been used to distinguish between huge and disturbance waves in annular two-phase flow. In Figure 4.16, the standard deviation of the film thickness is seen to decrease with increasing gas superficial velocity. McGillivray &

Gabriel (2002) used standard deviation of the liquid film thickness to categorize waves in annular two-phase flow into huge and disturbance waves. They characterized huge wave as having large standard deviation. In the present data the standard deviation decreases as film thickness decreases with increase gas superficial velocity. Figure 4.16 shows fluctuations around transition boundaries at gas superficial velocities of 21 m/s and 30m/s respectively. After gas superficial velocity of 30 m/s, the thicker film displays a higher standard deviation similar to the trend observe in drop size distribution Figure 4.16.

McGillivray & Gabriel (2002) did not specify boundary conditions for the huge and disturbance waves based on deviation of the film thickness from the mean. Therefore, using the findings in this study we can conclude that huge wave transverses the gas liquid interface under gravity influence and this dominance ceases after gas superficial velocity = 21 m/s. This is reasonable as the wave is characterized by large amplitude typical of huge wave before transition to co-current annular regime after gas superficial velocity = 21 m/s. After gas superficial velocity = 21 m/s, wave amplitude becomes smaller, decreasing with increasing gas superficial velocity.

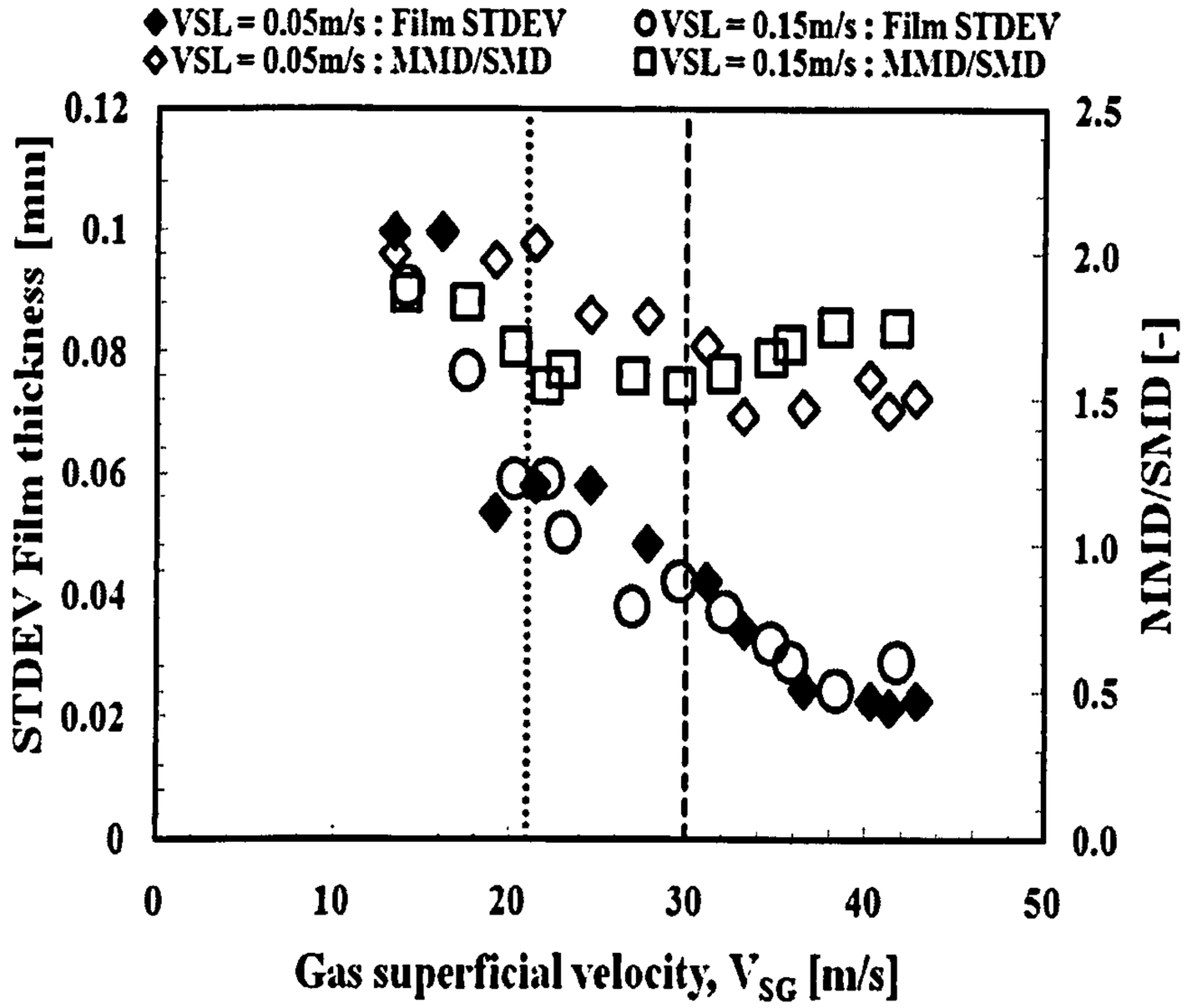

Figure 4.16: Comparison of Standard Deviation of Film hold-up and Drop size (MMD) showing similar trends as gas and liquid superficial velocities increase.

4.5.7 Pressure Drop

Pressure drop is observed to increase with the liquid superficial velocity at constant gas superficial velocity. Figure 4.17 (a) shows how pressure drop measured varies with gas superficial velocity at constant liquid superficial velocity. The transition is very obvious at V_{SG} = 21 m/s. In the case of V_{SL} = 0.15 m/s the linearity of the pressure drop is maintained after the transition. The effect of the transition is ephemeral. However, in the case of V_{SL} = 0.05 m/s, the pressure gradient decreases after the transition.

Pressure drop was normalized by dividing the measured pressure drop by wall shear stress. Wall shear stress was calculated from the model of Alves et al. (1991). Figure 4.17 (b) displays the result obtained when normalized pressure drop is plotted against gas superficial velocity at constant liquid superficial velocity. The Figure shows that contribution of the gravitational pressure drop is dominant over frictional before $V_{SG} \leq$

21 m/s. In the case of V_{SL} = 0.05 m/s, unexpected behavior was noticed. After V_{SG} = 21 m/s when the pressure drop is expected to recover, it did not rather it decreases further until V_{SG} = 36 m/s where it starts to recover.It is not very clear if frictional pressure drop has over-taken gravity at this point.

Result of another experimental campaign where gas superficial velocity was fixed at V_{SG} = 14 m/s whilst the liquid superficial velocity was varied systematically between 0.03 - 0.19 m/s is shown in Figure 4.17 (c). The pressure drop is observed to increase with increase liquid superficial velocity. It reaches a maximum then decreases. Pressure drop maximum corresponds to maximum drop size recorded, Figure 4.21.

Normalized pressure drop for this case is plotted against liquid superficial velocity as shown in Figure 4.17 (d). It is observed that pressure continues to decline with superficial liquid velocity.

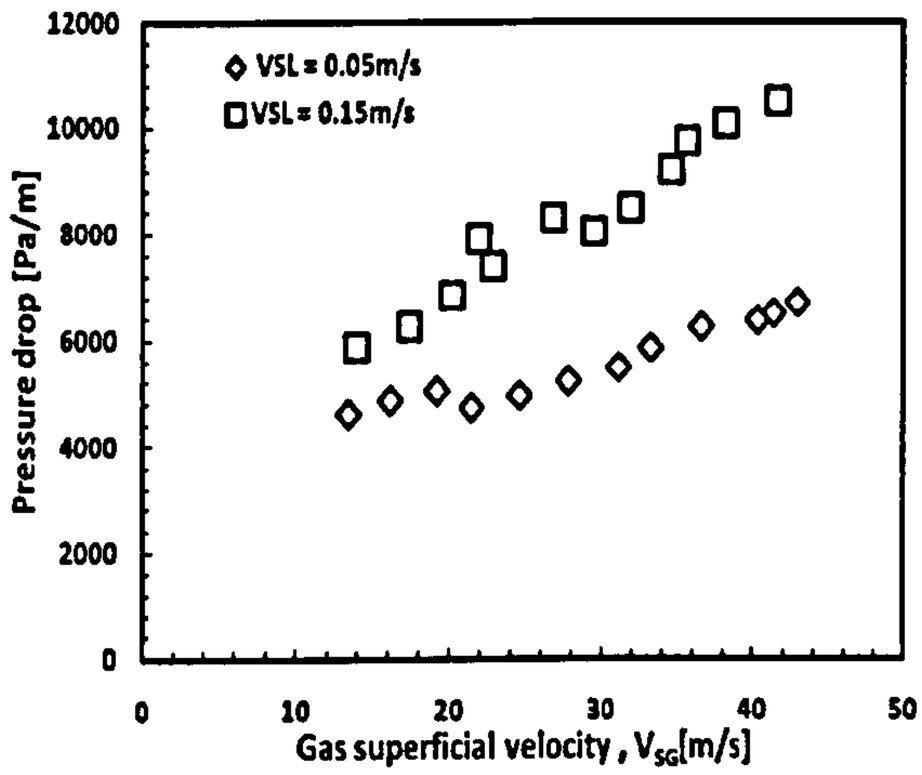

(a)

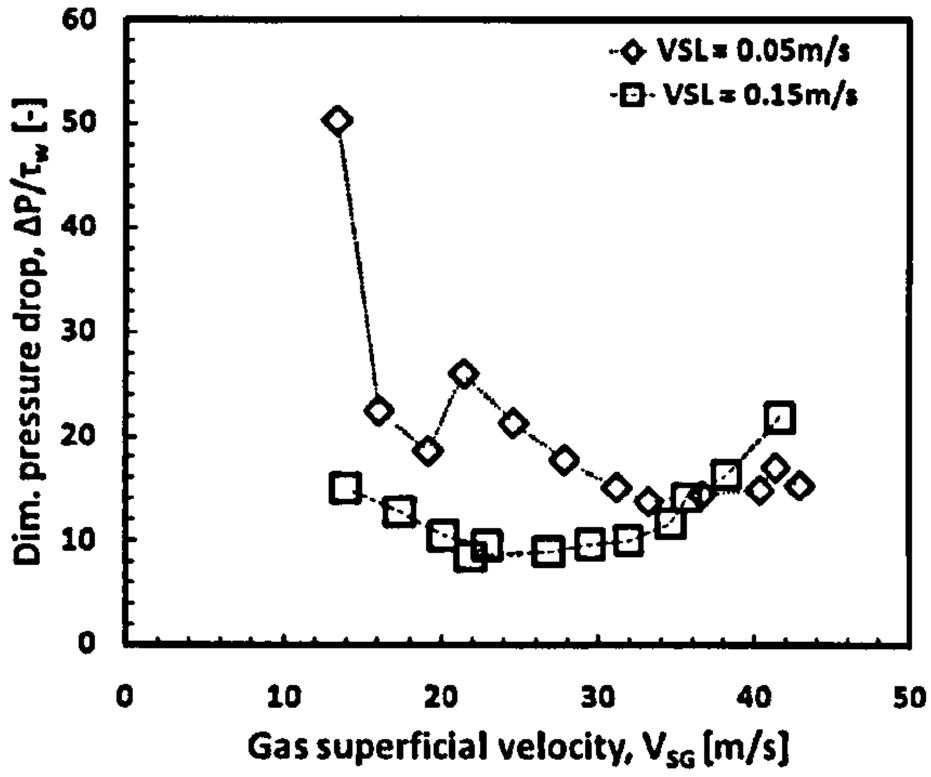

(b)

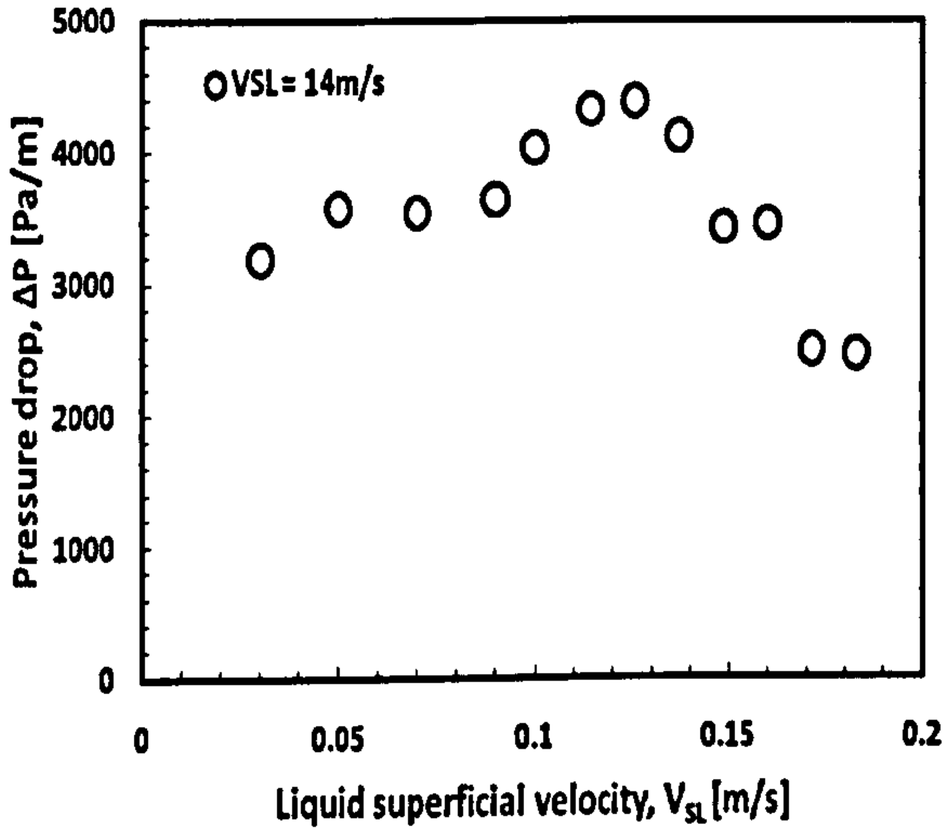

(c)

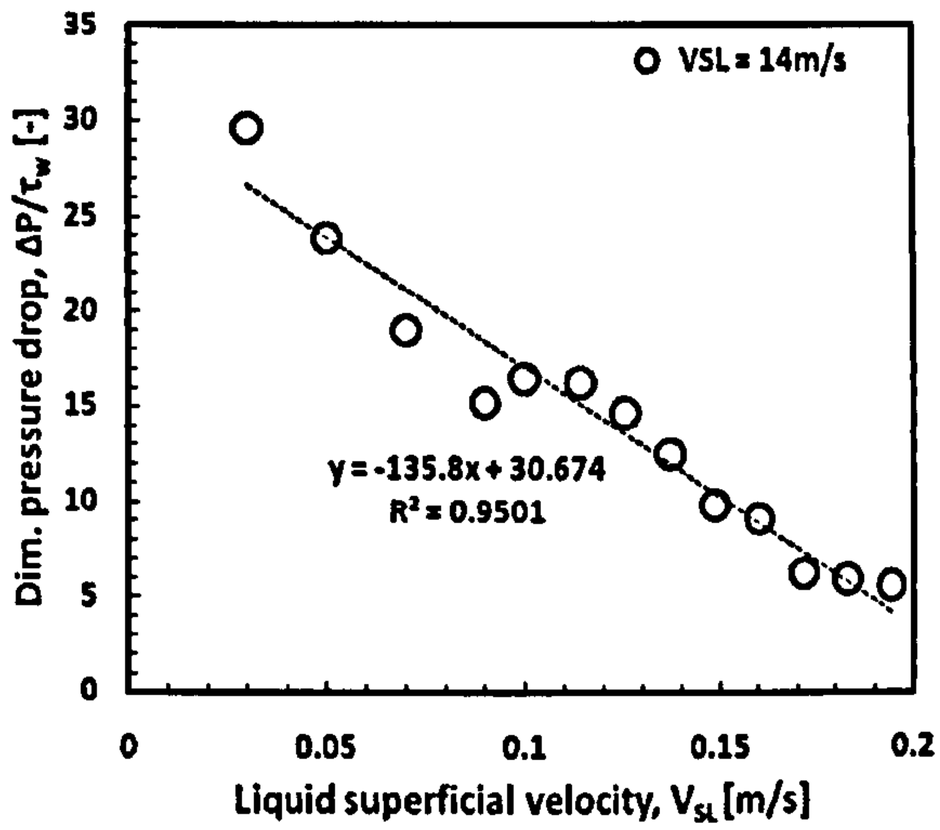

(d)

Figure 4.17 (a) Pressure drop variation with increase gas superficial velocity.
Figure 4.17 (b) Dimensionless pressure drop variation with increase gas superficial velocity.
Figure 4.17 (c) Pressure drop variation with increase liquid superficial velocity.
Figure 4.17 (d) Dimensionless pressure drop variation with increase liquid superficial velocity.

Because the pressure drop data were acquired simultaneously with drop concentration and liquid hold-up a direct comparison is possible among the three data set. Liquid hold-up has been utilized in calculating gas core density. Core density is plotted against gas superficial velocity as shown in Figure 4.17 (e).

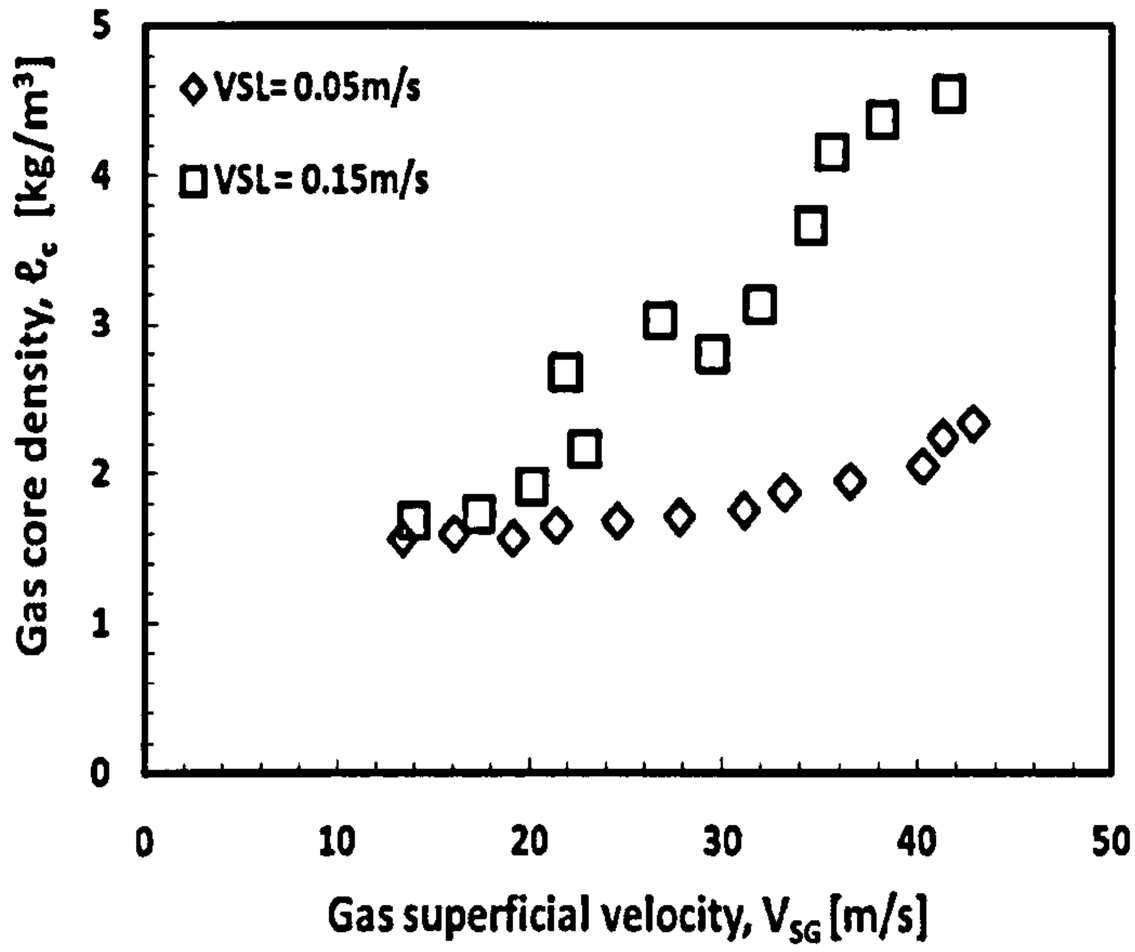

Figure 4.17 (e): Variation of gas core density with inlet conditions.

It can therefore be concluded that entrained liquid fraction comes from the film burst. Film burst produces droplets which cause the expansion of the gas core and subsequent increase in gas core density. This continues until film becomes very thin and can no longer shed droplet.

The physic can also be explained as follows. An increase in gas superficial velocity at constant liquid superficial velocity results in an increase in the interfacial velocity at the liquid-gas interface. Momentum is transferred from the highly energetic gas core to the liquid film, resulting in an increase in the film velocity in the base area of the film. This increases interfacial shear stress and the friction factor which cause an increase in the pressure drop.

Direct similarity has been found between pressure drop and wave amplitude as shown in Figure 4.17 (f) and Figure 4.17 (g) when pressure data are qualitatively compared with wave amplitude profile.

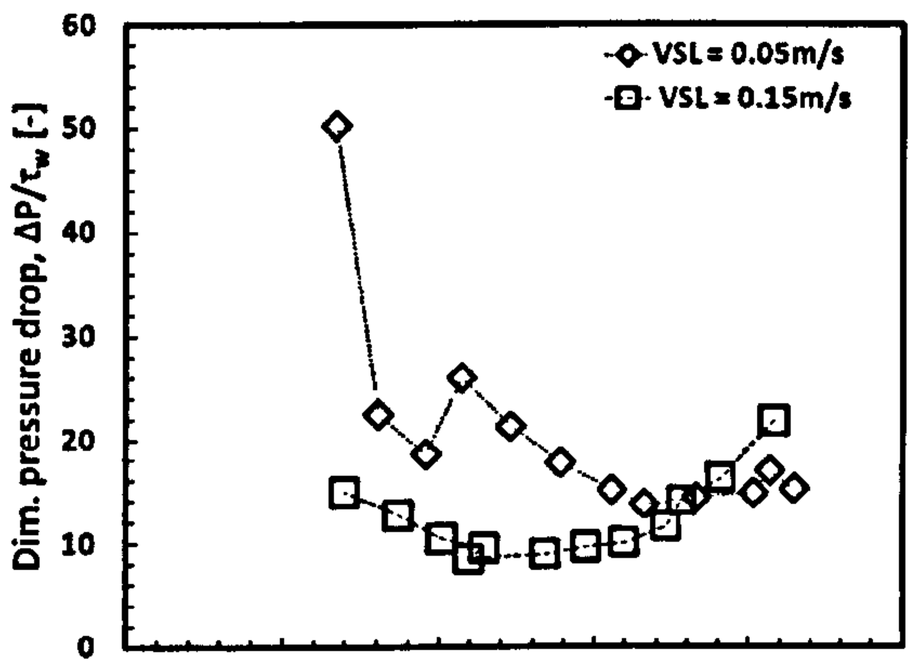

(f)

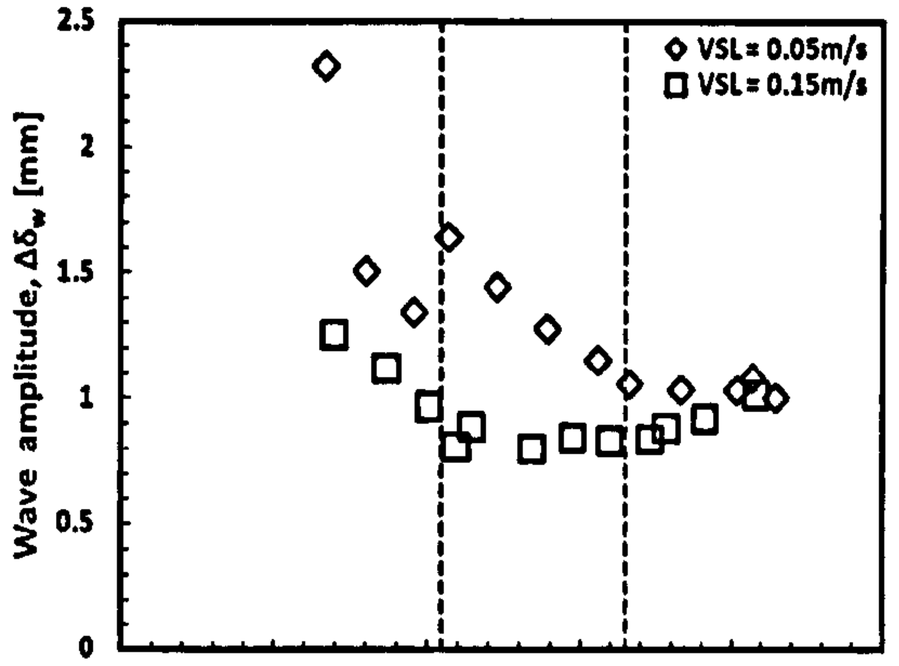

(g)

Figure 4.17 :(f) Normalized pressure drop vs. gas superficial velocity.
Figure 4.17 :(g) Wave amplitude vs. gas superficial velocity.

4.5.7.1 Pressure Drop and Entrained Fraction

One of the questions that have not been addressed satisfactorily in annular two-phase flow is whether or not the pressure drop increases with entrained fraction. An attempt is made in this subsection to provide original observations from the experiments which might answer this question. Since pressure drop, film thickness and entrained fraction data were acquired simultaneously, comparison between one variable and another can be made.

Figure 4.18 (a) shows how the system pressure drop performs with respect to the entrained fraction. It is clear from the plot that pressure drop in the system increases monotonically with entrained fraction and is higher with increased liquid superficial velocity. The relationship was curve-fitted and was observed to follow power law.

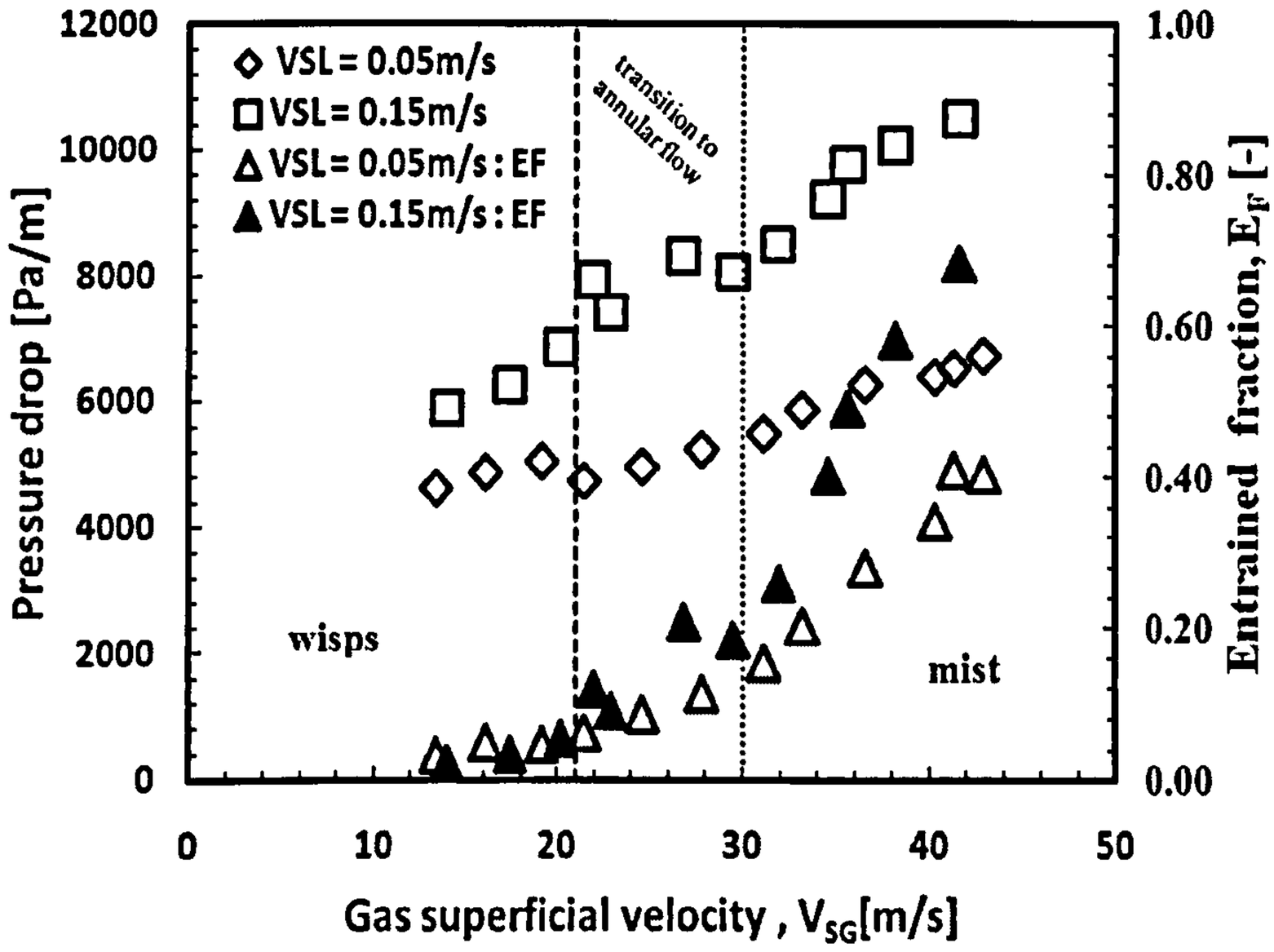

Figure 4.18 (a): Pressure drop-entrained fraction profile.

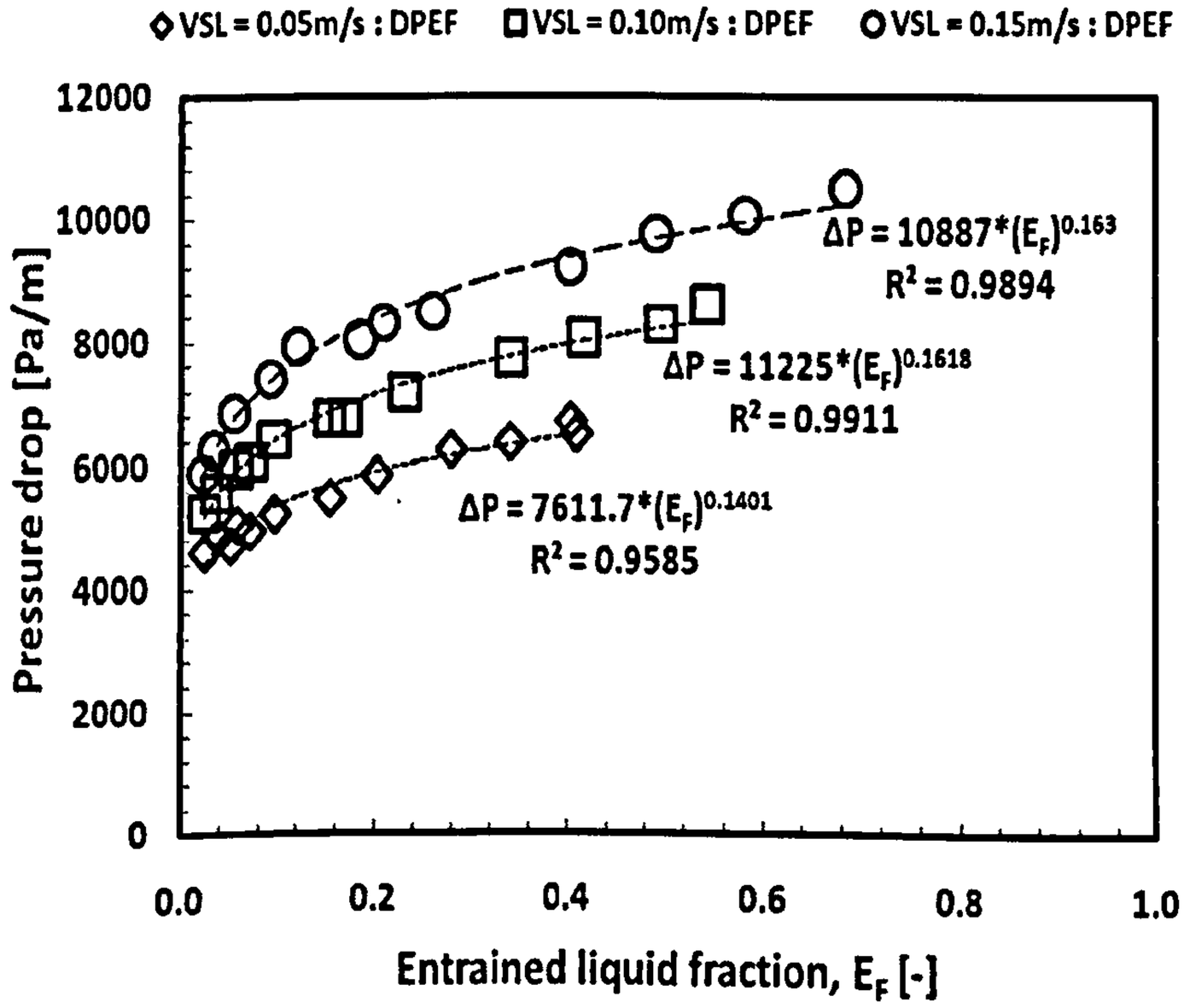

Figure 4.18 (b): Relationship between pressure drop and entrained fraction.

The following empirical correlations were derived based on line of best fit:

$$\Delta P = 10887(E_F)^{0.163}\ ;\ V_{SL} = 0.15\text{m/s}$$

$$\Delta P = 11225(E_F)^{0.1618}\ ;\ V_{SL} = 0.10\text{m/s}$$

$$\Delta P = 76117(E_F)^{0.1401};V_{SL}=0.05\text{m/s} \qquad (4.10)$$

Where ΔP = pressure drop, [Pa/m]; and E_F = entrained fraction, [-].

Normalized pressure drop variation with entrained fraction is presented in Figure 4.18(c). In Figure 4.18(d), present data is compared with the data of Mantilla (2008) who carried out similar work in a bigger diameter pipe. Mantilla calculated entrained fraction from mass balance approach using film extraction technique. The work was carried out on horizontal and inclined pipe.

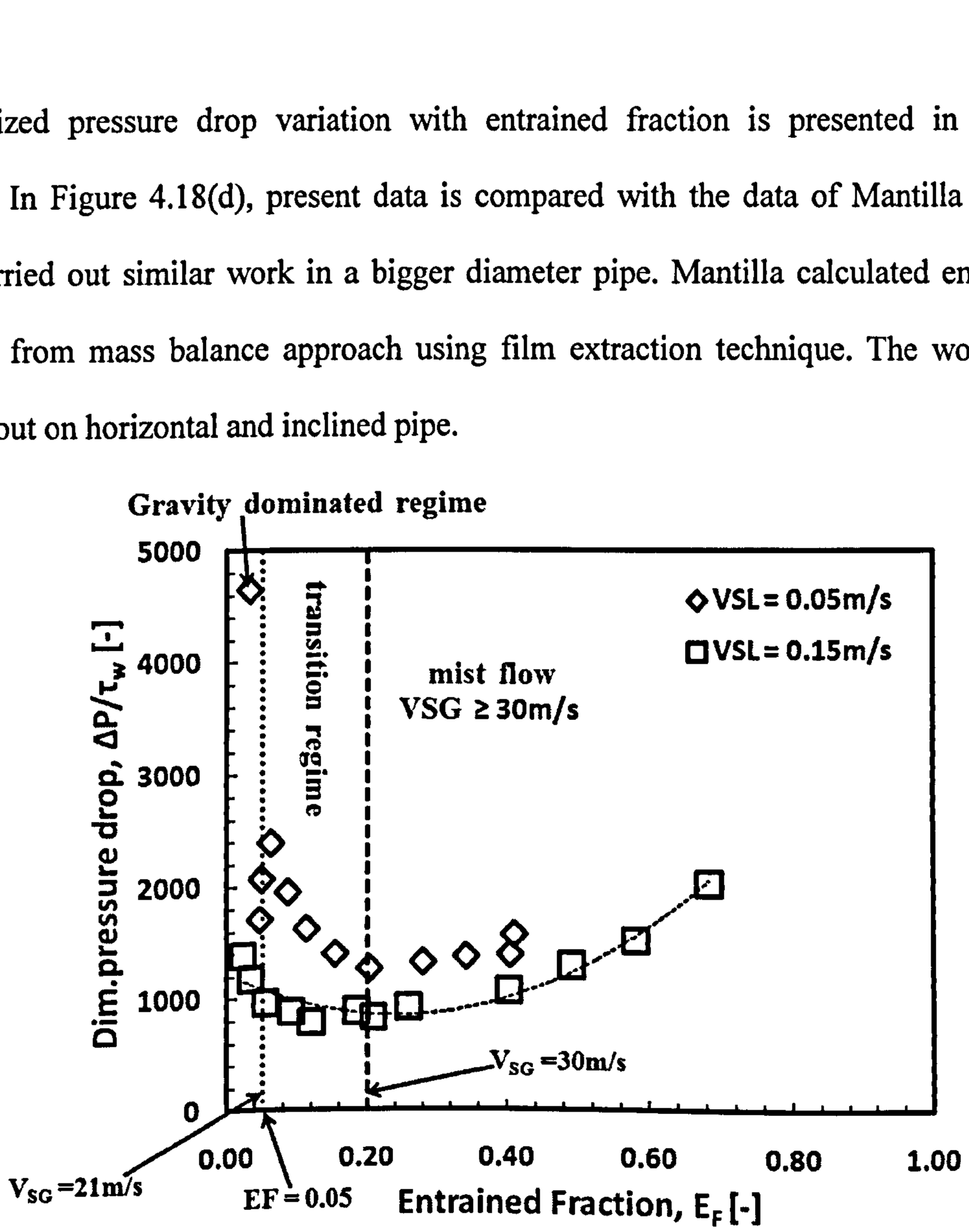

Figure 4.18 (c): Relationship between pressure drop and entrained fraction.

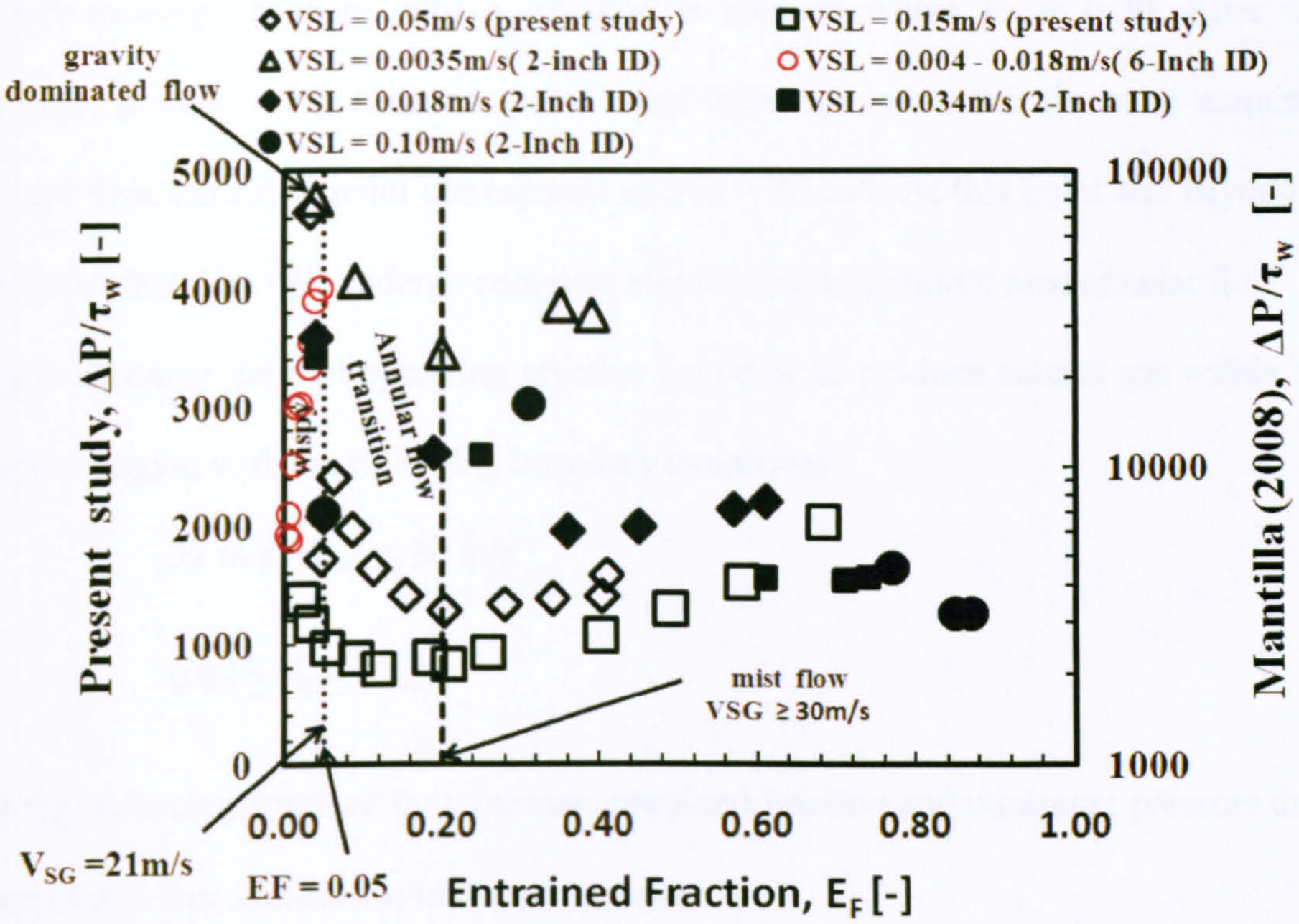

Figure 4.18 (d): Similarities between present study and work of Mantilla (2008).

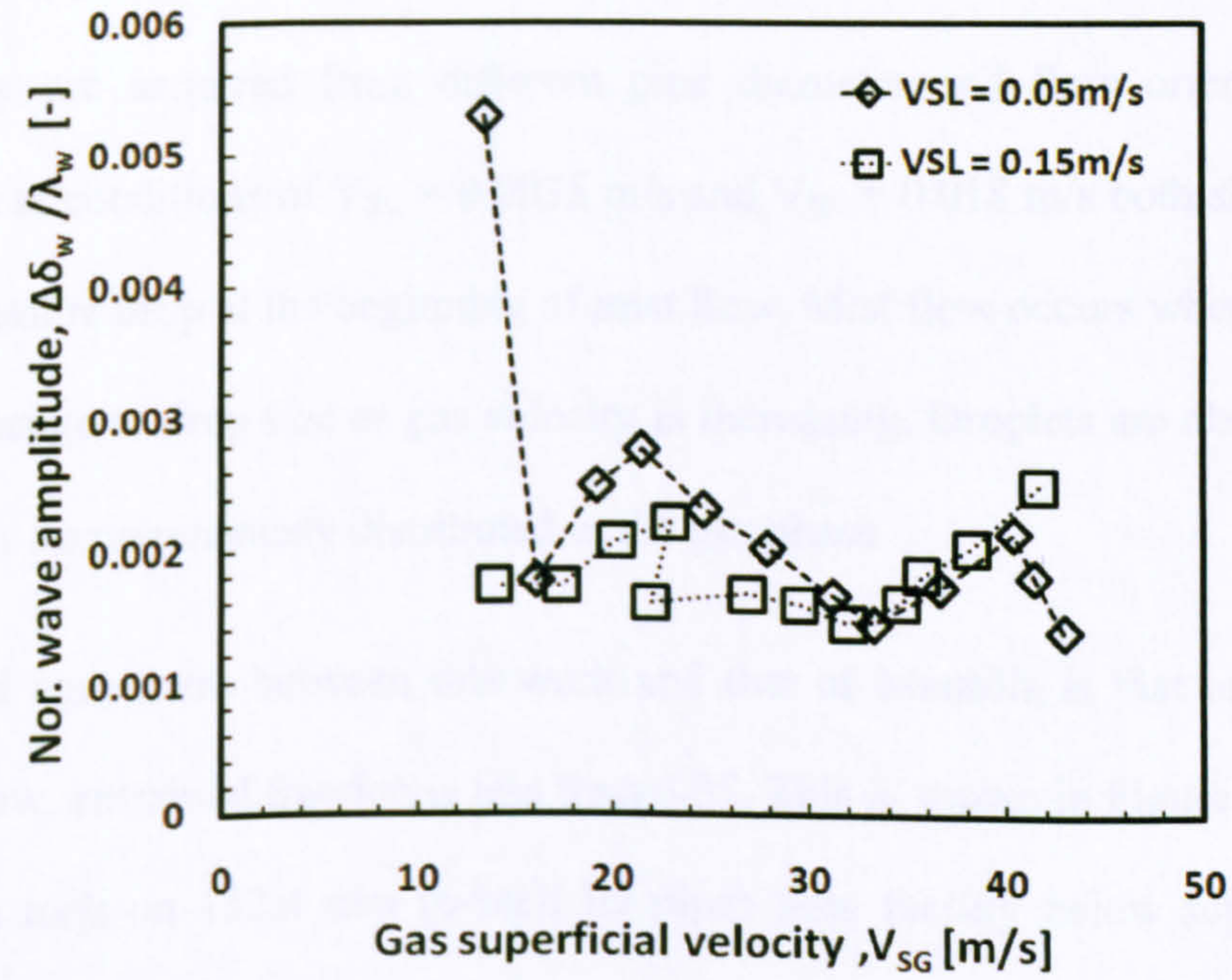

Figure 4.18 (e): Normalized wave amplitude as a function of entrained fraction

In Figure 4.18 (c), pressure drop falls as more droplets are torn off the wave crest into the fast moving gas core until a situation is reached where E_F = 0.20. After this transition, pressure drop starts to recover and increases monotonically with entrained fraction. This transition point corresponds to V_{SG} = 30 m/s. At this point and beyond, it is believed that film will undergo complete atomization to promote mist annular flow.

For gas producer the best operating practice would be to produce natural gas within the transition region with the following boundary conditions:

$$21 \text{ m/s} \geq V_{SG} \leq 30 \text{ m/s}$$

$$0.05 \geq E_F \leq 0.20.$$

This region is characterized by minimum entrained fraction and minimum pressure drop which means less shut-downs and more revenue.

In Figure 4.18(d), the trend in the present study and that of Mantilla is very similar although they are acquired from different pipe diameter and flow orientation. The Mantilla data at conditions of V_{SL} = 0.0035 m/s and V_{SL} = 0.018 m/s both show a slight minimum pressure drop at the beginning of mist flow. Mist flow occurs when there is no significant change to drop size as gas velocity is increasing. Droplets are observed to be approximately homogeneously distributed in the gas phase.

Another good agreement between this work and that of Mantilla is that under gravity dominated flow, entrained fraction is less than 0.05. This is shown in Figure 4.18 (d) for data Mantilla took on 152.4 mm (6-Inch ID pipe) flow facility below superficial gas velocity of 21 m/s. Mantilla reported transition to annular flow occurs at a superficial gas velocity of 20 m/s. This is an excellent agreement with present study value of 21

m/s. At $V_{SG} = 21$ m/s, drag from the gas phase is just sufficient enough to lift the droplet after it overcomes the force of gravity.

Another interesting observation is in Figure 4.18(e) where normalized wave amplitude (discuss in Chapter Six) was plotted against entrained fraction. Figure 4.18(c) and Figure 4.18(e) show that pressure drop and wave amplitude behavior are analogous and similar. The trend is similar in both cases.

4.5.7.2 Pressure Drop and Drop Size - Drop coalescence and break-up

Majority of particle transportation essentially takes place due to the turbulent diffusion in the turbulent flow. In the case of viscous liquids or in viscous sub-layer, on the other hand, when the length scale of turbulence is less than the kolmogorov scale of turbulence , i.e. $\lambda_D < \lambda_k$, and molecular diffusion dominates. Typically, drops with a size comparable to the length scale of turbulence may collide. The collision occur, in general, when the length scale of turbulence is greater than the Kolmogorov scale of turbulence (i.e. $\lambda_D > \lambda_k$) which is observed in the fully developed turbulent flow.

Where:

$$\lambda_k = \left[\frac{\eta_c^3}{\varepsilon_R}\right]^{0.25} \tag{4.11}$$

η_c = kinematic viscosity of the medium, $\eta_c = {}^{\mu}/_{\rho}$, [$m^2/s$]

μ = dynamic viscosity of the medium, [kg/m-s]

ρ = density of the medium, [kg/m^3]

ε_R = dissipation energy per unit mass, [m^2/s^3]

Dissipation energy per unit mass, ε_R, for turbulent flow in a pipe can be calculated from pressure gradient using the following expression , Shoham (2006):

$$\varepsilon_R = \left|\frac{dP}{dL}\right| \frac{V_M}{\rho_M} \tag{4.12}$$

In pipe flows the turbulence length scale can be estimated from the hydraulic diameter. In fully developed pipe flow the turbulence length scale is 7% of the hydraulic diameter i.e. $\lambda_D = 0.07D$, where D is the pipe hydraulic diameter. In this study length scale of turbulence is estimated to be 1.3 mm.

Kolmogorov scale of turbulence was estimated using Equation (4.12) from experimental data and plotted against superficial gas velocity and compared with SMD as shown in Figure 4.20. SMD is used in Figure 4.20 because it is smaller compared to MMD at same condition. Figure 4.20 reveals that the scale of turbulence is higher for the thinner the liquid film; however, it decays generally with increasing gas superficial velocity.

Since length scale of turbulence and the drop diameter (SMD or MMD) are both greater than Kolmogorov length scale of turbulence, it is expected that drop coalescence will dominate over break–up. Therefore, Kolmogorov scale of turbulence in Figure 4.20 will be used in the model to estimate drop collision frequency in Chapter Five.

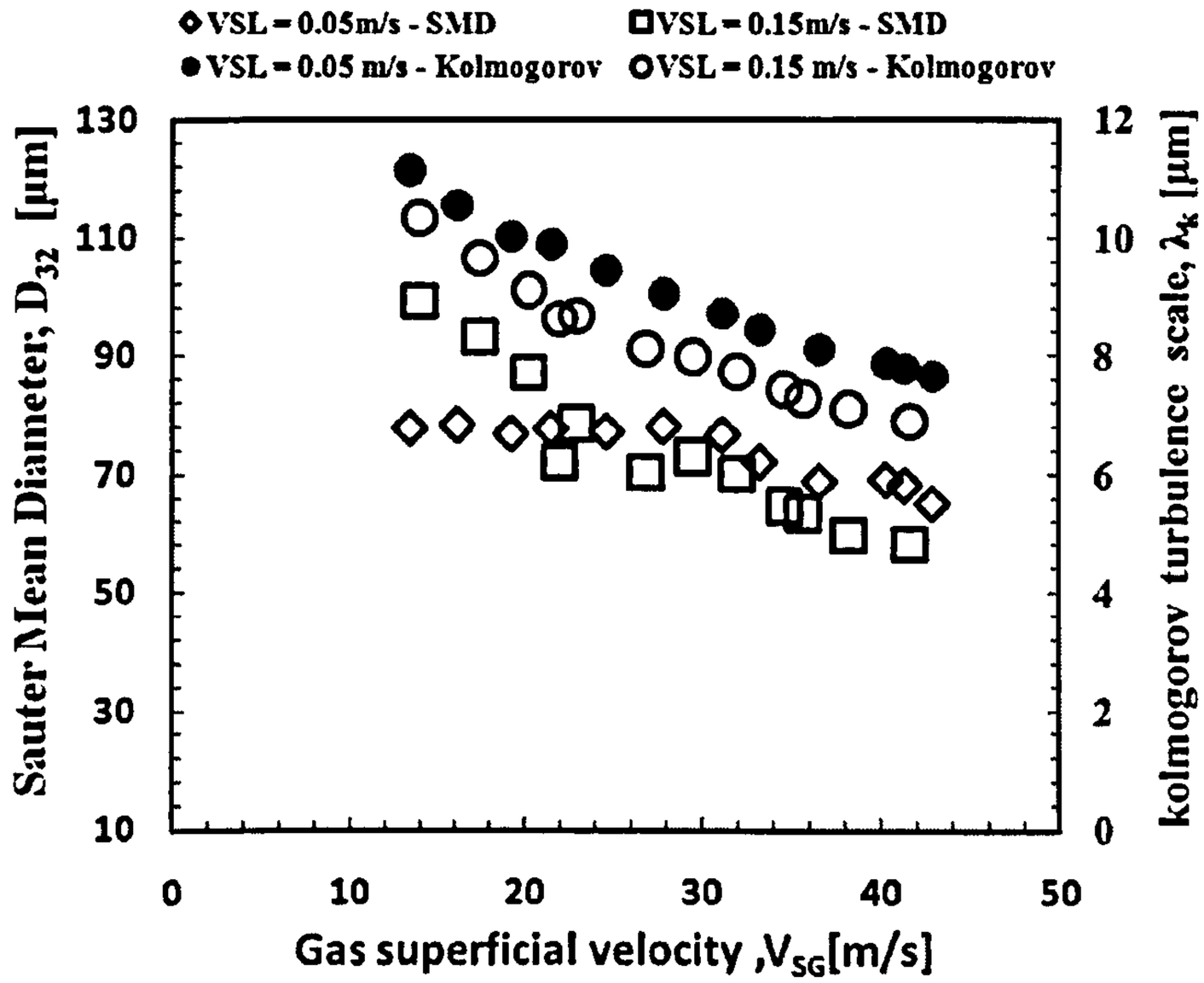

Figure 4.20: Comparison between drop size and Kolmogorov scale of turbulence.

An experimental campaign was conducted to investigate how pressure drop varies with drop size at constant gas superficial velocity. The results of the revels additional details about drop break-up and coalescence. For a constant gas superficial velocity of $V_{SG} = 14$ m/s, liquid superficial velocity were varied systematically between 0.03 m/s and 0.19 m/s corresponding pressure drop monitored by differential pressure cell drop is displayed in Figure 4.21. The figure shows an interesting feature with a maximum pressure drop at $V_{SL} = 0.13$ m/s after which the pressure drop start to decline with further increase in liquid superficial velocity.

Two distinct events can be deduced from plot – drop coalescence and drop break-up. Drop break-up occurs when shear stresses (disruptive force) acting on the drop overcomes the restoring force (surface tension) .When two drops collide, they interact for some time forming dump-bell. The liquid film between the drops starts to drain. If

drainage continues to the critical film thickness within the interaction time, coalescence will take place.

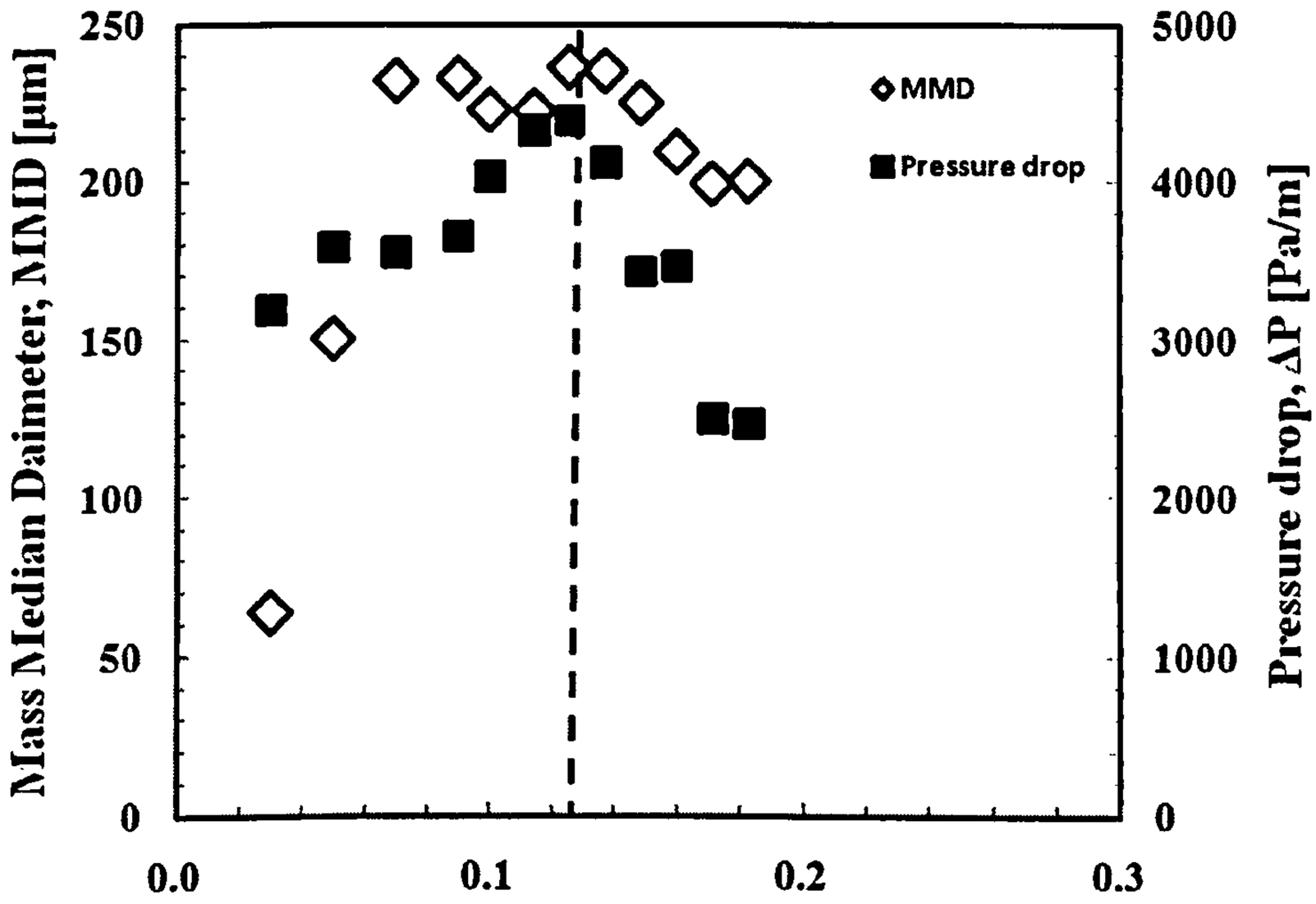

Figure 4.21: Pressure drop and MMD as a function of superficial liquid velocity. V_{SG} = 14 m/s.

The drops with a size larger than a characteristic maximum stable drop size have a tendency to breakup, but smaller drops show a tendency to coalesce. Both coalescence and break-up of drops seems to occur simultaneously. Since the data were acquired simultaneously, comparison of drop size and pressure drop profiles by superimposing the two profiles reveals additional information as shown in Figure 4.21. The plot displays one-to-one correspondence between the two data as Figure 4.21 depicts an unbreakable link between the system pressure drop and the size of the droplet entrained in the gas core. The positive pressure drop gradient represents drop coalescence events as drop continue to increase in size as a result collision with another drop. However, the negative gradient indicates dominance of drop break-up events.

Under coalescence dominated event, drop size grows with liquid superficial velocity. A critical drop diameter (MMD = 248 μm) is attained where further increase in liquid flow rate at constant gas superficial velocity leads to decrease in drop size and the entrained fraction. This diameter can also be referred to as the maximum stable drop size. Drop break-up occurs when the characteristic maximum stable diameter is exceeded. After the point of inflection, the event in the dispersed phase becomes drop break-up dominated. A corresponding decrease in entrained fraction was also observed for this condition. It is noteworthy to see that SMD do not behave in a similar manner to MMD. SMD continue increase with increasing liquid superficial velocity.

James et al. (1980) carried out experimental and analytical studies on the motion of droplets in two-phase flow. As a result of their visualization work (using a laser axial view technique), James et al. found that larger droplets (>200 μm), formed mainly from bag break-up, tend to travel in straight lines at velocities similar to those at the time of their formation. Droplets formed by ligament break-up tend to stay in the core for much longer due to turbulent eddy interactions within the gas core.

Various explanations have been sought for pressure drop maxima behavior. Owen and Hewitt (1987) attributed it to suppression of turbulence in the gas core by very large flux of entrained droplets which they observed under this condition. According to them, increasing the entrained droplet concentration reduces the turbulence, and hence the interfacial friction factor and the pressure gradient decreases with increasing gas mass flux. Another reason given by Owen and Hewitt (1987) responsible for this behavior is the change in interfacial structure.

However, the augmentation of turbulence intensity reported by Azzopardi and Teixeira (1994 b) appears to disagree with the suppression of turbulence reported by Owen and Hewitt (1987). It is noted that Hewitt and Owen based their statement purely on the analysis of mean velocity profiles for the gas as measured by, e.g., Gill et al. (1964). These profiles they fitted to a log law Equation. Using a friction velocity obtained from the two-phase pressure drop, they determined a `two-phase von Karman constant' which they found differed from the classical single-phase value and which correlated with the ratio of gas superficial momentum to that for the gas-drop mixture. They related the change in the von Karman constant to suppression of turbulence. Azzopardi (1999) later reported that the value of turbulence intensity increases with rate of entrainment and therefore entrained fraction. Hence, Azzopardi further proved that increase in turbulence intensity was due to newly created drops.

Summarizing opinions by previous workers, Sawant et al. (2009) concluded that in annular flow smaller droplets which can follow the gas phase turbulence more closely have small slip velocity and increase of concentration of such droplets attenuate the turbulence intensity. On the other hand larger droplets move at relatively slow velocity and do not follow the turbulence very closely. Accordingly the increase of concentration of such droplets enhances the turbulence intensity.

In conclusion of this aspect, the onset of suppression of turbulence at maximum pressure drop suggested by Owen and Hewitt (1987) and the claim by Azzopardi and Teixeira (1994 b) that newly created droplet increases turbulence intensity are both correct and

in line with the observation of the present study according to Figure 4.21. In Figure 4.21, the positive slope correspond coalescence event with resultant effect of creation of more new drops. The newly formed drop generates turbulence eddy causing increase in interfacial shear stress and hence increase in pressure drop. This trend continues until a maximum point is reached. At the maximum point, Figure 4.21, turbulence intensity is observed to be maximum. Therefore, the claim by Azzopardi and Teixeira (1994 b) that newly created drops aggravate turbulence intensity is justified.

In the same vein, at the maximum point in Figure 4.21, the pressure drop is also maximum. Beyond this point suppression of turbulence begins because bigger drops responsible for turbulence generation start undergoing atomizing break-up. As the break-up continues, drop size and entrained fraction decreases and hence decrease in pressure drop. Again, the claim of Owen and Hewitt (1987) is justified.

Therefore, it can be concluded from the foregoing discussion that dispersed phase turbulence increases as new drops are created into the gas stream core of annular flow. The new drops may undergo coalescence to form bigger drops. As the concentration of these drops increases, the entrained fraction systematically increases and therefore pressure drop increases. On the other hand, dispersed phase turbulence subsides when the dominating event is controlled by drop break-up causing drop size, entrained liquid fraction and pressure drop to decrease.

4.6 Validation of Results

Figure 4.22 and Figure 4.23 present comparisons between Spraytec and Particle sizer reported by Azzopardi et al. (1991). Drop concentration results have been validated using the data of Azzopardi et al. (1991) taken with less advanced instrumentation in Figure 4.22. The comparison of Spraytec results with Particle-sizer were carried out at same liquid superficial velocity V_{SL} = 0.05 m/s. The data shows excellent agreement.

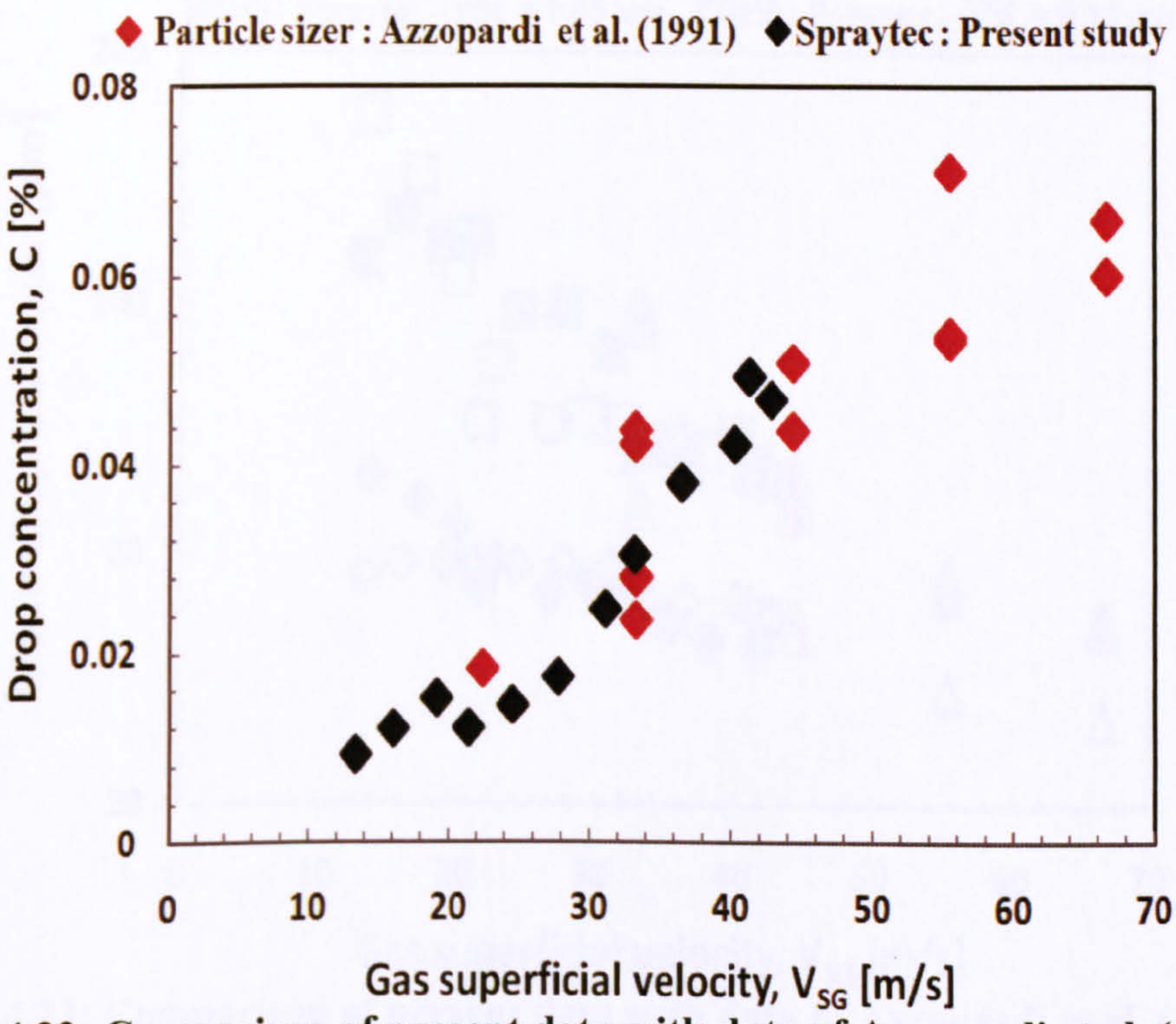

Figure 4.22: Comparison of present data with data of Azzopardi et al. (1991).

Measured mean diameters are compared with the result of less advance instrumentation (particle sizer) at very similar flow conditions as in Figure 4.23. From the results it looks like the systems agree at high gas superficial velocities, but not at low flow rate. When V_{SG} > 30m/s the value of D_{32} and D_{50} are almost identical for the two systems.

In terms of drop sizes (MMD & SMD) , in Figure 4.23, generally both data agree very

well. However, excellent agreement was observed after gas superficial velocity, V_{SG} > 30 m/s. Assuming the two systems have similar dynamic ranges measurements, then it appears that Spraytec under-estimates the particle size when it encounters a very big drop which implies that there were particles outside of the dynamic range of the system. The dynamic range of this version of Spraytec is: 0.5 μm – 460 μm.

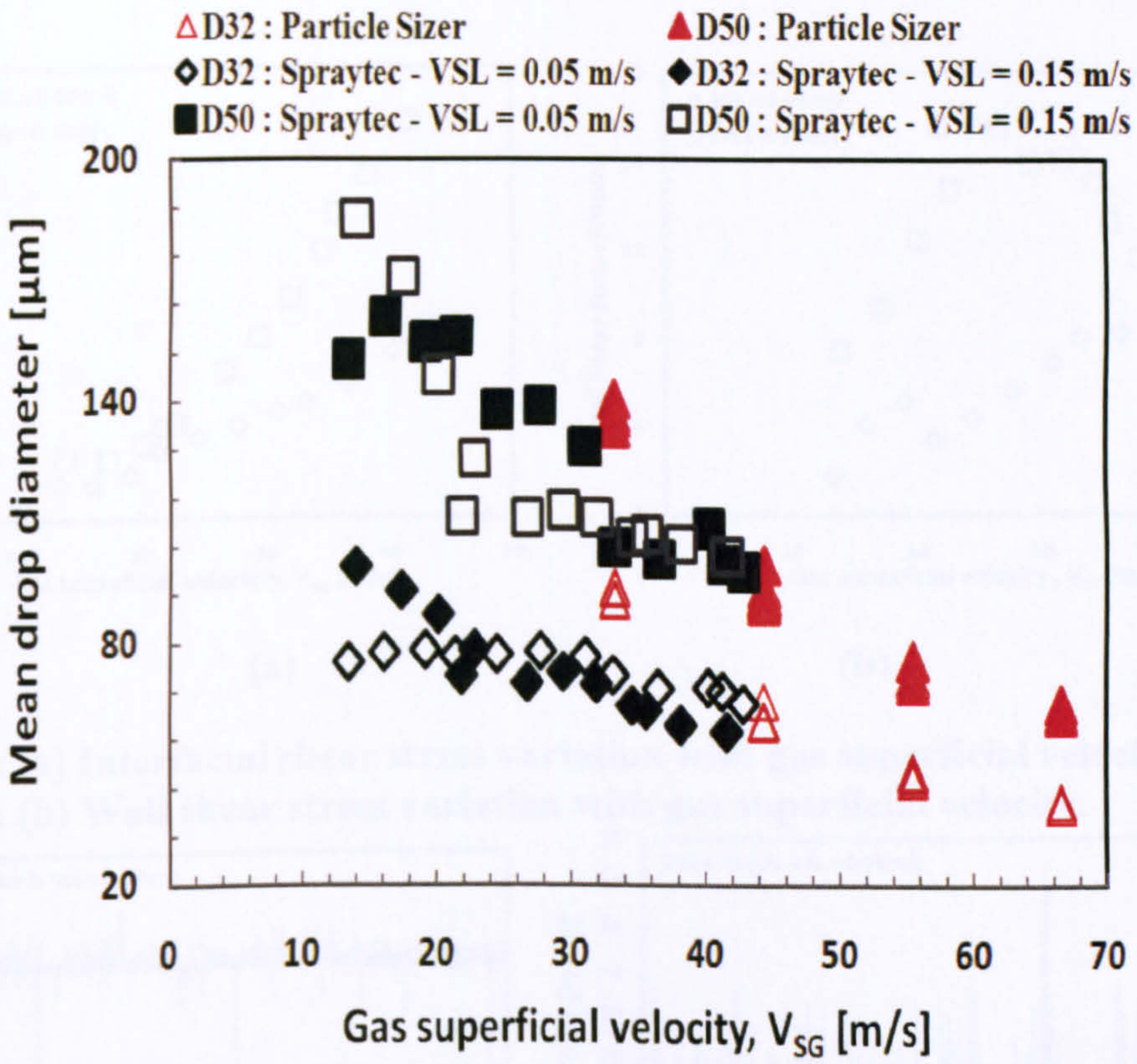

Figure 4.23: Comparison of present data with data of Azzopardi et al. (1991).

Another possible source of conflict in Figure 4.23 is the distance from injection point to the measurements volume or the drop test section in the two experiments. While distance from the probe volume was set at 6.25 metres in the present study, it was 3.0 meter in the work with particle sizer, Azzopardi et al. (1991). It may be that flow was not fully developed at the point where droplet sizes etc. was measured for the work with particle sizer. It may be that drop coalescence and drop break-up events are functions of

the distances from injection points to the probe volumes in the two measurements. It has been established from this study that drop coalescence and drop break-up contributes to hugely in determining size of the drop.

4.7 Shear Stresses

Wall shear stress and interfacial shear stress have been calculated using the mechanistic model of Alves et al. (1991). The results are shown in Figure 4.24 (a) and Figure 4.24 (b).

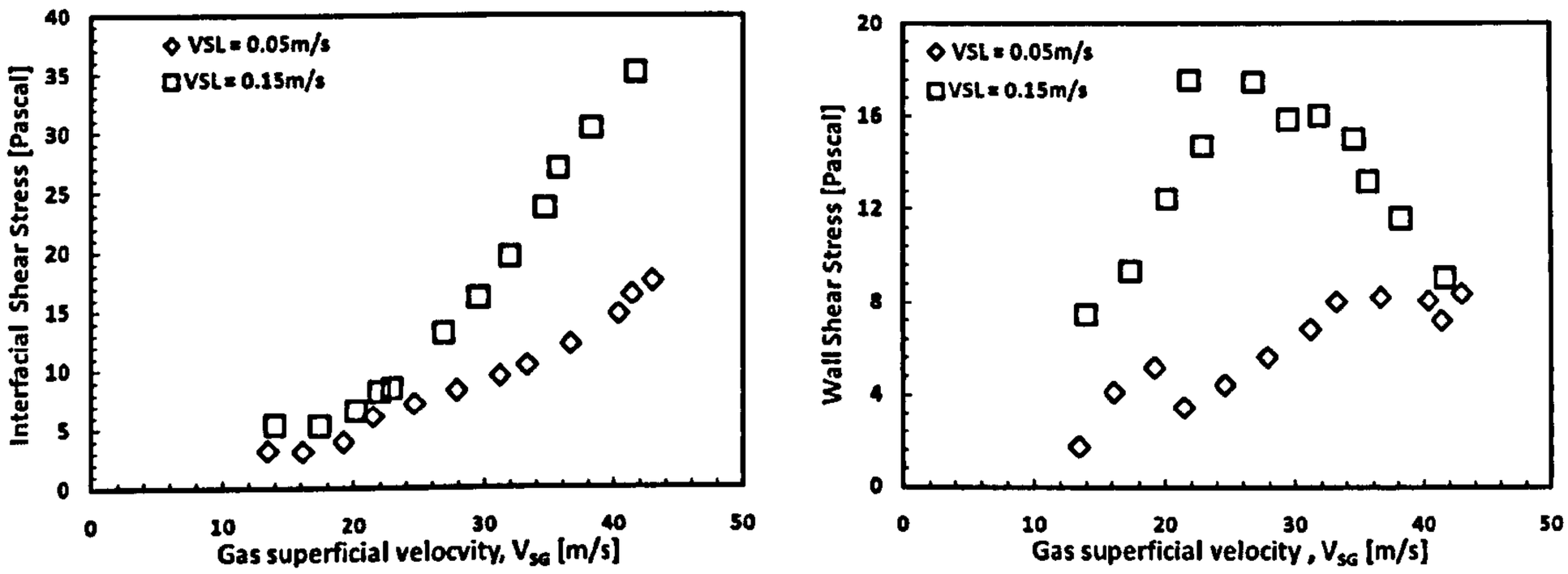

(a) **(b)**

Figure 4.24: (a) Interfacial shear stress variation with gas superficial velocity.
Figure 4.24: (b) Wall shear stress variation with gas superficial velocity.

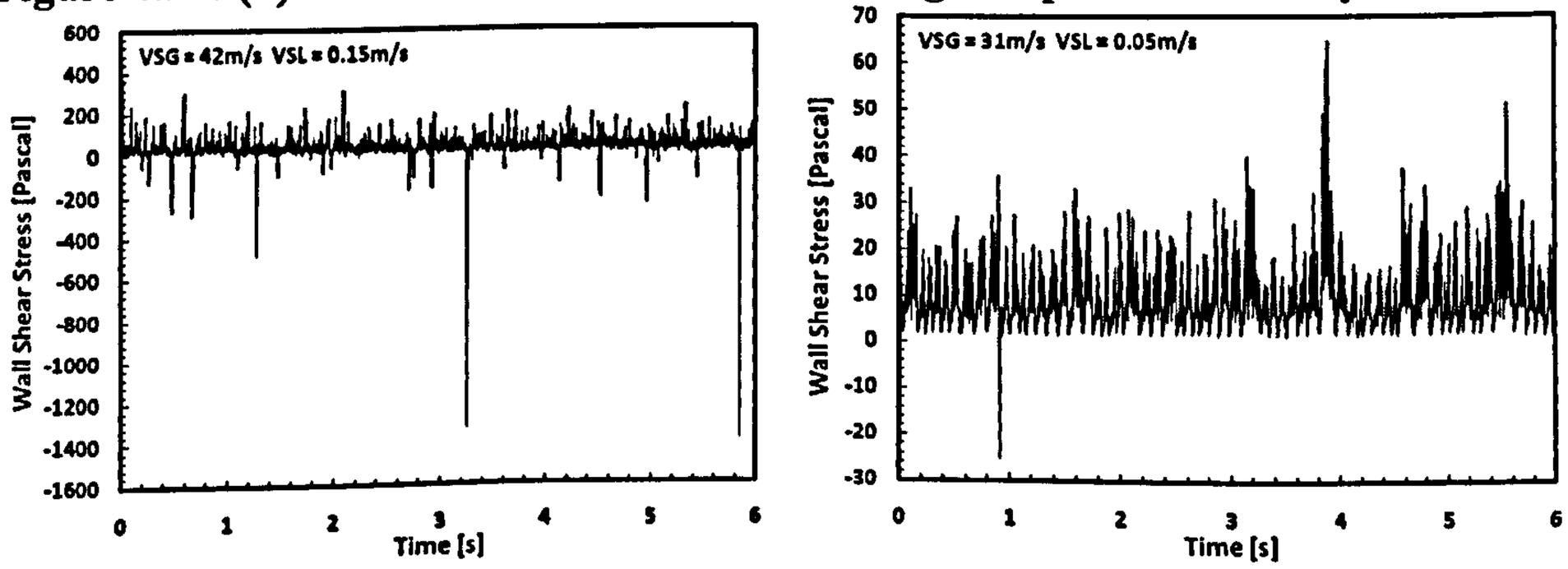

(c) **(d)**

:

Figure 4.24: (c) Wall shear stress time series V_{SG} = 42m/s, V_{SL} = 0.15m/s.
Figure 4.24: (d) Wall shear stress time series V_{SG} = 31m/s, V_{SL} = 0.05m/s.

The interfacial shear stress generally increases with increase in liquid and gas superficial velocities Figure 4.24 (a). Wall shear stress on the other hand, Figure 4.24 (b), displays a different characteristic from interfacial shear stress.

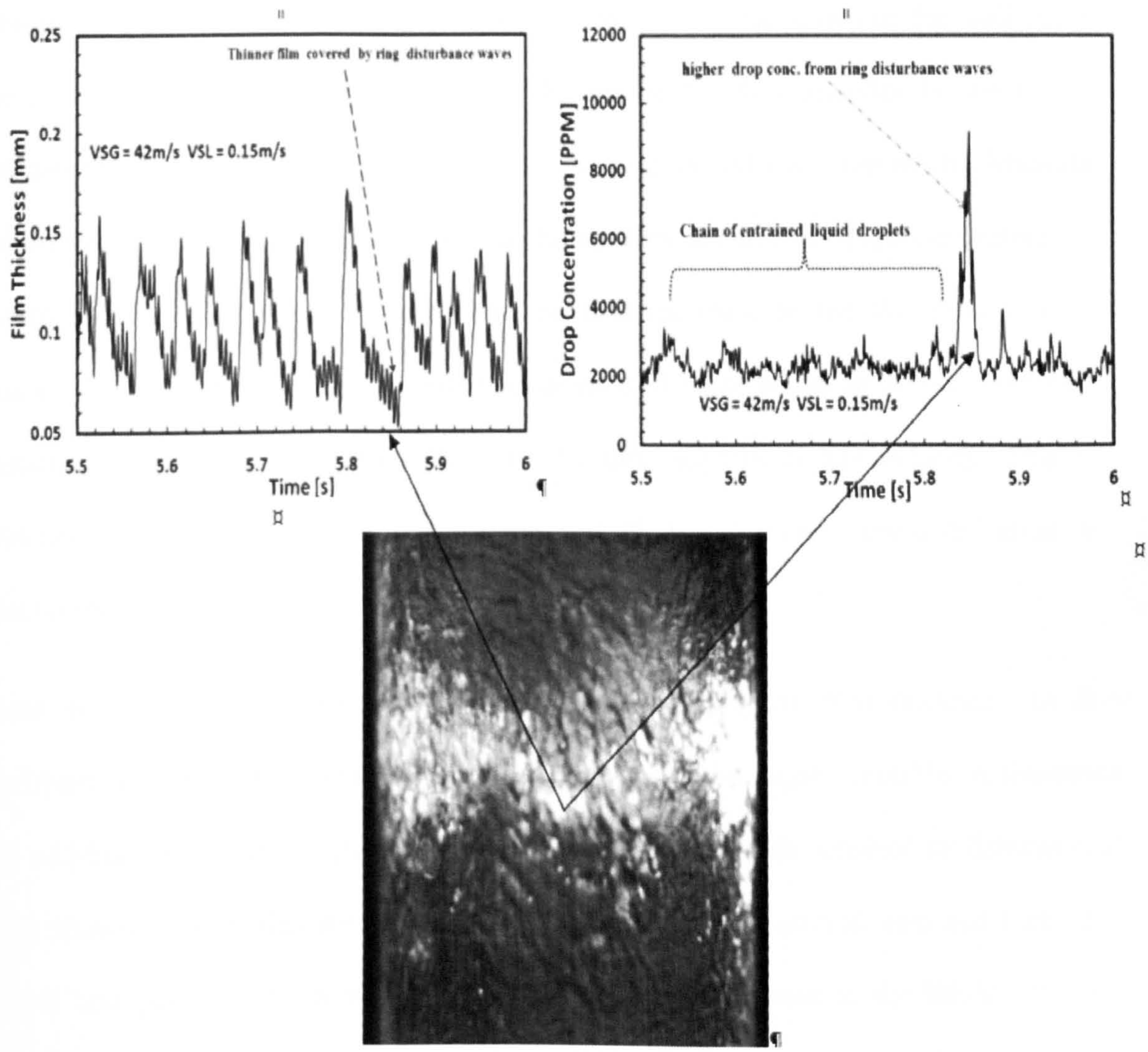

Figure 4.24 (e): Photo evidence of packets of ring disturbance waves occurring when gas superficial velocity exceeds 30 m/s. The corresponding time varying film thickness/ disturbance waves (top left) where the corresponding higher drop concentration at time = 5.85 seconds (top right) are sourced.

Wall shear stress is seen to increase with liquid and gas superficial velocities. However, at the transition to co-current annular flow, it is peaked and then decreases. For thicker

film it continues to decreases while for thinner film it recovers and continues to increase with increasing gas superficial velocity.

Close to V_{SG} = 30 m/s, time-resolved wall shear stress begins to fluctuate from positive to negative value. The negativity becomes stronger with increasing gas superficial velocity. Figure 4.24 (c) and Figure 4.24 (d) display the time series of the wall shear stress for some of the conditions tested. The reason for this behavior is due to the emergence of packets of waves referred to as 'ring disturbance waves' by Mantilla (2008) which covered thinner part of the liquid film around the pipe circumference Figure 4.24 (e). These waves were observed to form close to the transition to mist around V_{SG} = 30 m/s. Mantilla reported occurrence of these waves in 2-inch (50.8mm) diameter horizontal pipe within $30\,m/s - 50$ m/s superficial gas velocity. This is evidence suggesting same mechanism governing dispersed phase flow distribution in annular two-phase flow.

Sawant et al. (2008) attributed this behavior to instability of film thickness. In their experiment flow was visualized and film was observed to be highly unstable. A theoretical study of Moalem Maron and Dukler (1984) and experimental data obtained by Zabaras et al. (1986) showed that in this region wall shear stress fluctuates around zero and takes both negative and positive values which results in an internal recycle in the liquid film. The experiment was carried out at low gas velocity and close to the churn-annular flow regime transition boundary. However, the conditions at which these behaviors were observed in present study are further away from transition boundary and well into annular flow regime as predicted by existing transition models. In fact, the negativity/fluctuation becomes stronger as gas superficial velocity increases.

Another possible explanation for this retrograde flow behavior may be as a result of internal vibration of liquid droplets in the gas core as explained by Sleicher (1962).When drops are created some of them travel in axial direction. Some pinch off and rebounce on hitting the liquid film creates disturbance waves. In some cases the disruption causes internal recycling of liquid film or retrograde flow. The retrograde flow lowers the interfacial shear stress and hence pressure drop. Sleicher's argument contradicts observation in the present study. In the present study pressure increases as gas superficial velocity. Therefore, Sleicher's argument does not explain our experimental observation.

4.8 Flow Structures

In Figure 4.24 (e) structures of the disturbance waves are revealed from time varying information of the liquid film. Droplets in the gas core are sourced from these waves which covered the surface of the liquid film. The corresponding droplet structures dominating the dispersed phase are also very obvious from the time varying drop concentration in Figure 4.24 (e). Interestingly, at time, t = 5.85 Seconds thinner film covered by disturbance waves around the pipe circumference produces a corresponding higher drop concentration according to the characteristic signature displayed by drop concentration time series in Figure 4.24 (e). The time series of drop concentration further shows a chain of smaller droplets almost of same sizes corresponding to the section of liquid film where film is uniformly fairly distributed around the pipe circumference. It is therefore reasonable to suggest that thinner film produces higher drop concentration and hence higher entrained fraction. Structures of other flow variables in the dispersed are considered next.

Figure 4.25 (a) displays typical time varying plots of principal flow variables in annular flow. Flow structures are not clear in the film thickness signal. However, when measured film thickness is used to generate interfacial shear stress the flow structures become very obvious as indicated in Figure 4.25(a). The time series of drop concentration, Mass Median Diameter all display similar signatures with similar peaks and troughs at the same time interval in space.

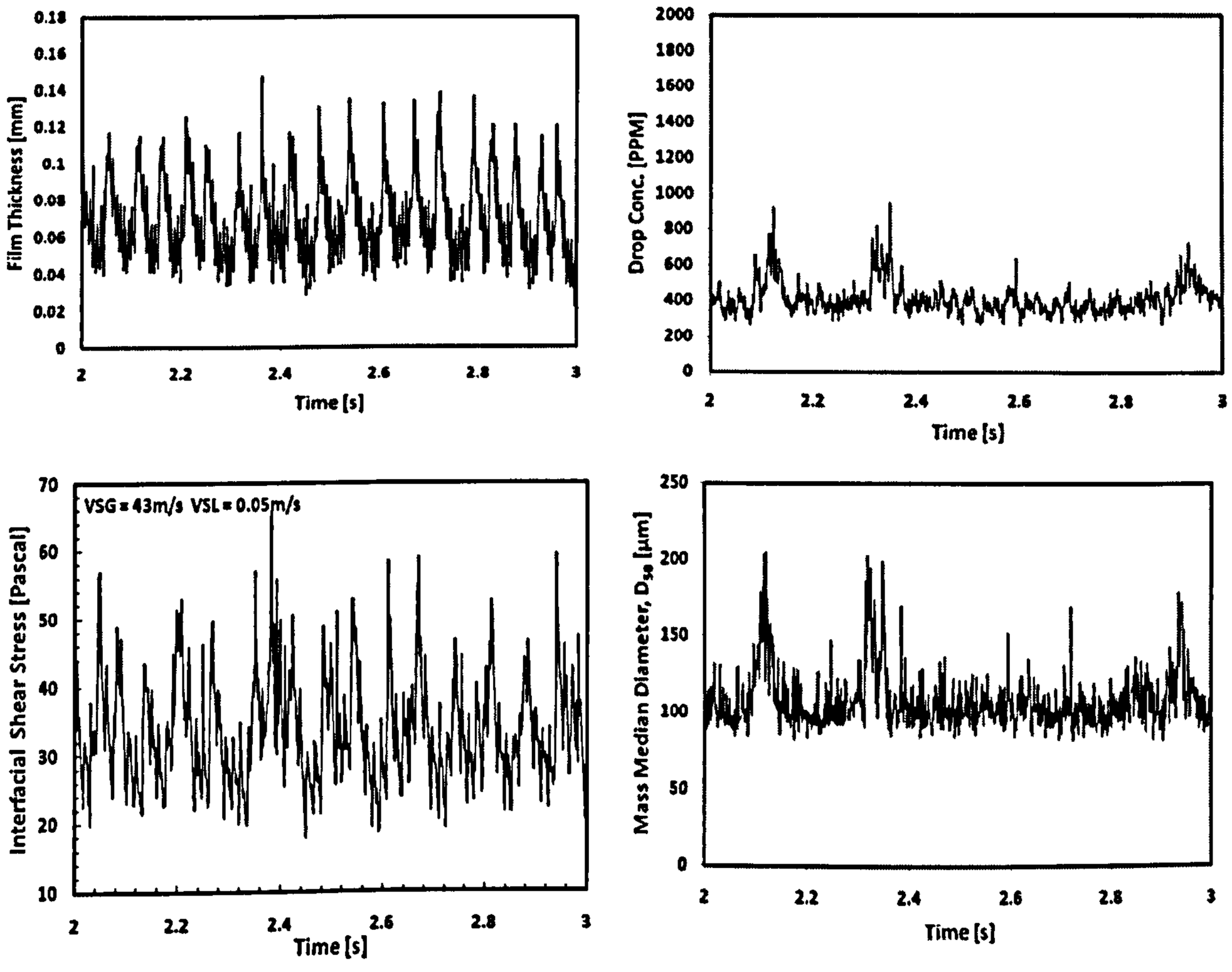

Figure 4.25 (a):Time series of flow variable showing flow structures.

In Figure 4.25 (b) the thinner film covered by disturbance waves around the pipe circumference where the film thickness is close to zero produced a corresponding bigger

structure of liquid droplet entrained in the gas core as shown in the drop concentration time series.

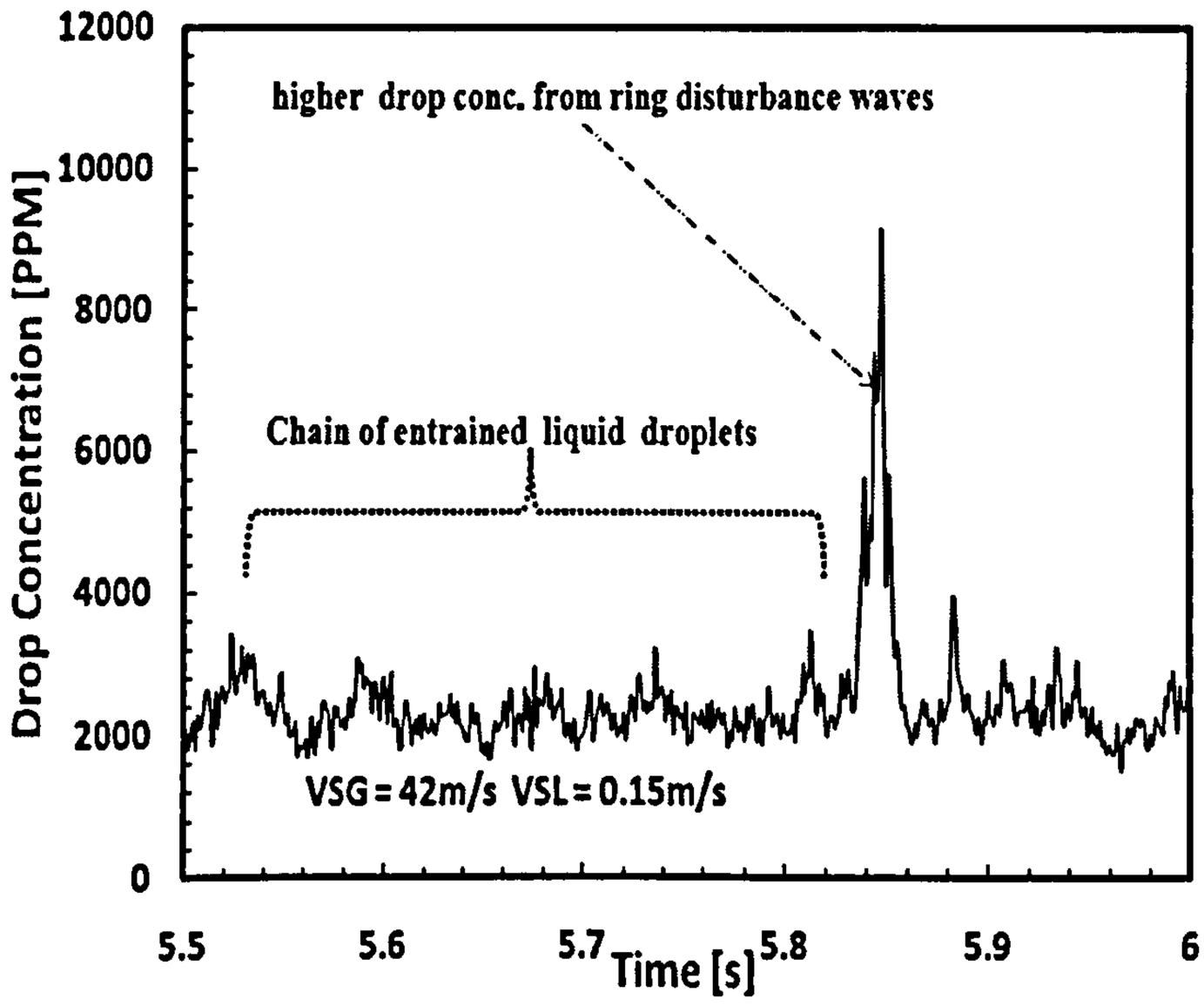

Figure 4.25 (b): Time series of drop concentration showing flow structures

The time series further shows a chain of smaller droplets almost of same size where the film is uniformly distributed around the pipe circumference.

Figure 4.25 (c) shows that this structure created from disturbance waves generate a positive interfacial shear stress and a negative wall shear stress.

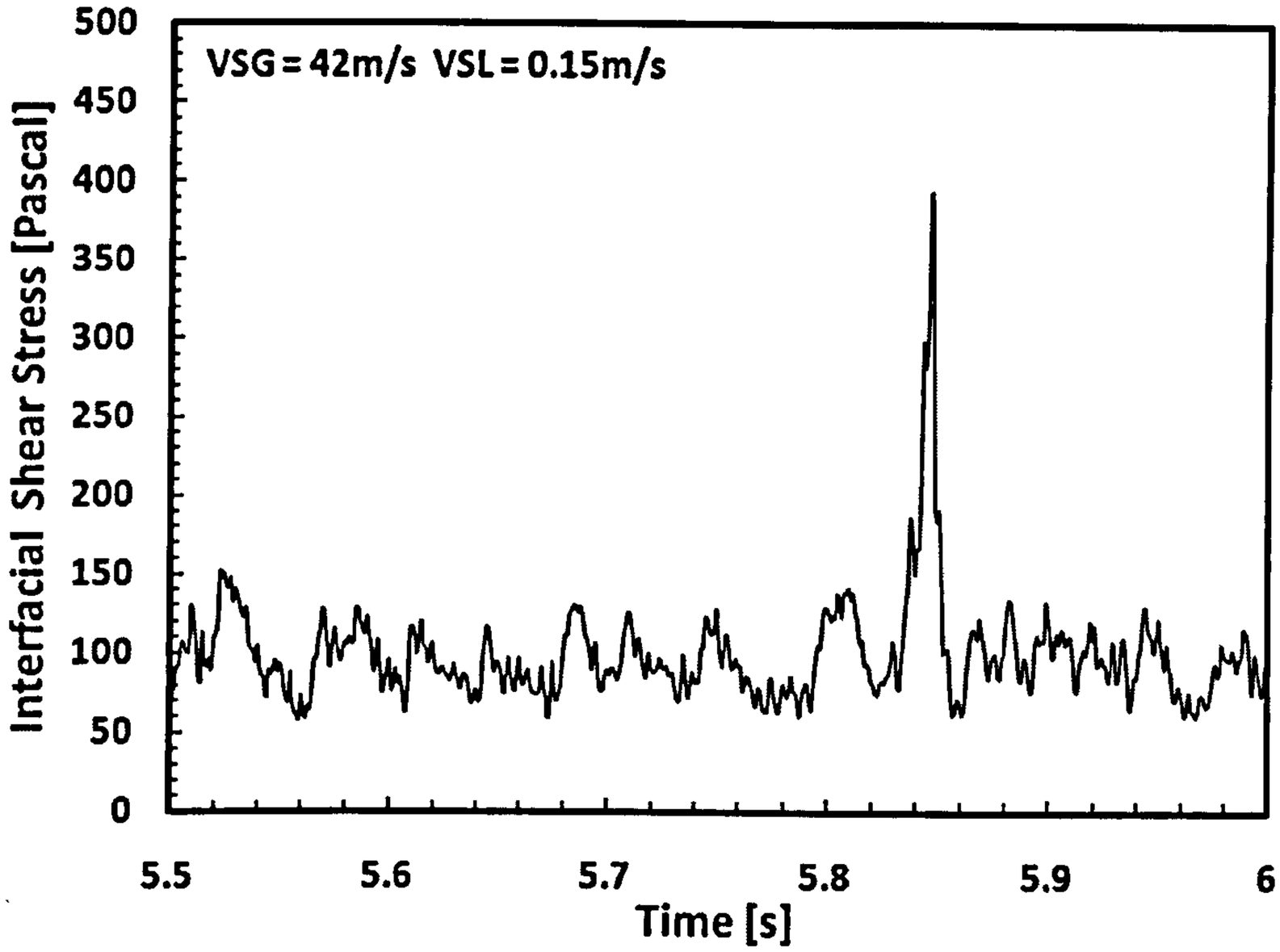

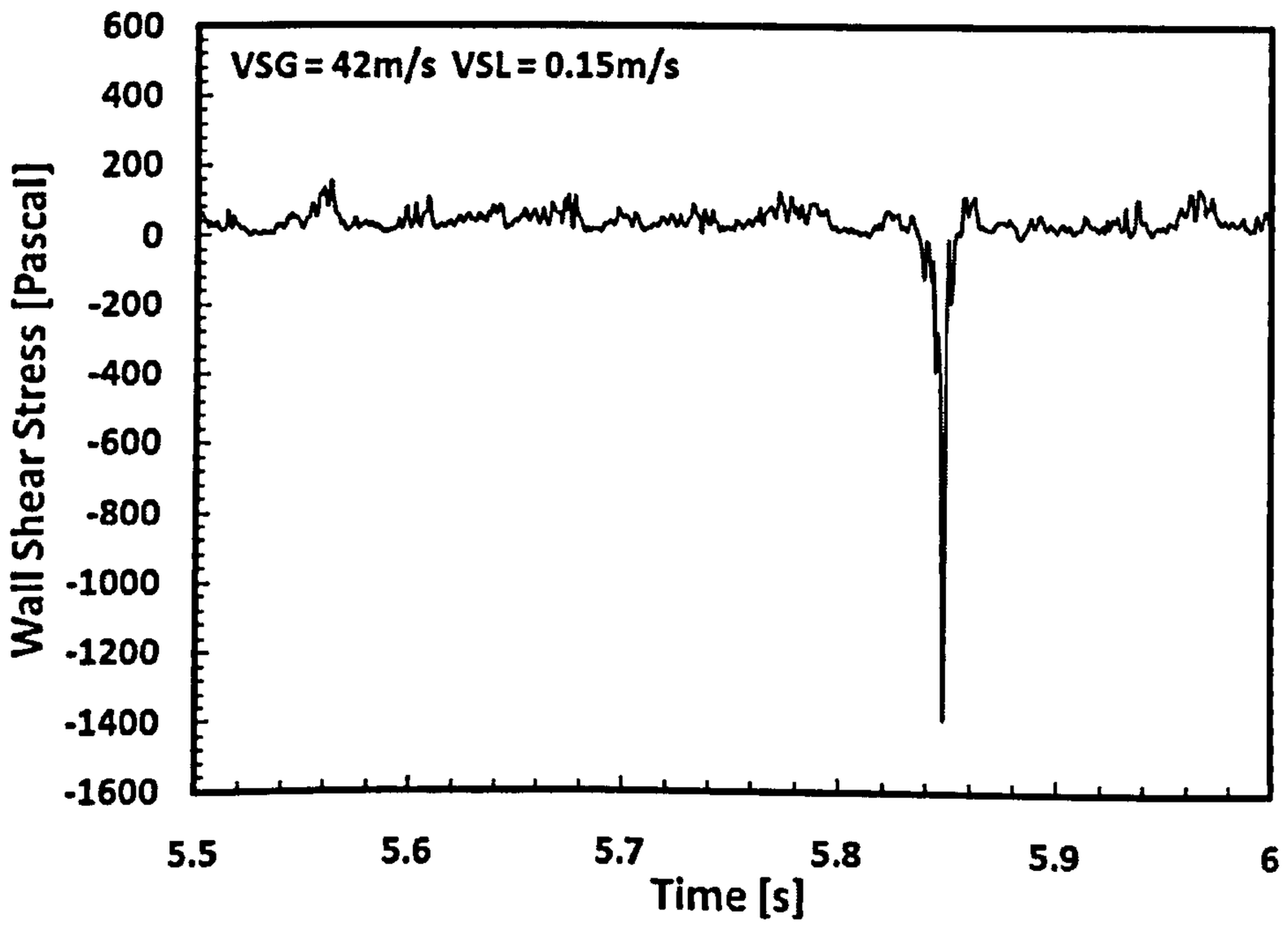

Figure 4.25 (c): Time series of Interfacial and wall shear stress

4.9 Drop velocity

Drop velocity is estimated from the entrained mass flux using Equation (4.13):

$$\dot{M}_{LE} = \rho_L V_D C \qquad (4.13)$$

Where V_D is the drop velocity, ρ_L is the liquid density; c is the volumetric drop concentration and $\dot{M}_{LE}$ is the entrained mass flux. Because film thickness and film velocity is known, film flow rate can be estimated using Equation (2.37).

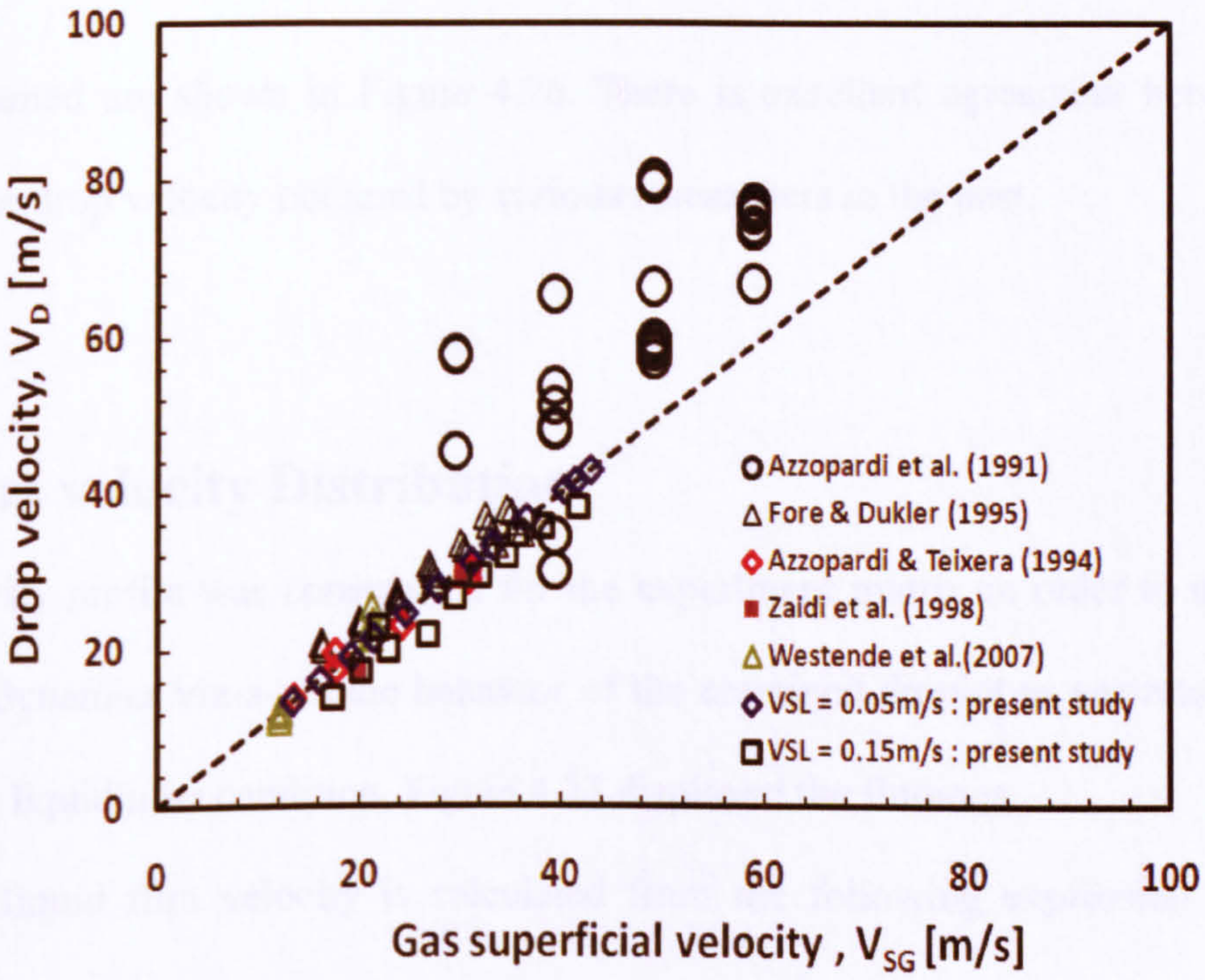

Figure 4.26: Comparison of drop velocity data base and present study

Multiplying Equation (2.37) by film density and divide by area of the pipe produces film mass flux, i. e. $\dot{m}_{LF} = \frac{4q_F \rho_L}{\pi D^2}$, where $q_F = A_p V_{SL}(1 - f_E)$. Total liquid mass flux can be estimated from the product of liquid phase density and the superficial liquid velocity i.e. $\dot{m}_L = \rho_L V_{SL}$. Therefore, entrained mass flux, Equation (4.13) can be estimated by

$\dot{m}_{LE} = \dot{m}_L - \dot{m}_{LF}$. Expressed in terms of drop concentration $\dot{m}_{LE} = \rho_L V_D C$ Therefore, drop velocity can be expressed as $V_D = \frac{\dot{m}_L - \dot{m}_{LF}}{\rho_L C}$, where V_D is the drop velocity, ρ_L is the liquid density; c is the volumetric drop concentration and $\dot{m}_{LE}$ is the entrained mass flux.

Alternatively, entrained mass flux can be obtained from film withdrawal technique by carrying out mass balance. Drop velocity at the centre-line can therefore, be approximated from Equation (4.13) by dividing entrained mass flux by liquid density and drop concentration.

Results obtained are shown in Figure 4.26. There is excellent agreement between present study and the drop velocity obtained by various researchers in the past.

4.10 Film velocity Distribution

Film velocity profile was constructed for the experiment matrix in order to understand film flow dynamics viz-a-viz the behavior of the entrained droplet as gas rate increases at constant liquid inlet condition. Figure 4.27 displayed the findings.

Measured liquid film velocity is calculated from the following expression of Pearce (1979):

$$V_F = \frac{V_{SL} d(1 - E_F)}{4\delta_L} \qquad (4.14)$$

Where

d= pipe diameter, [m]

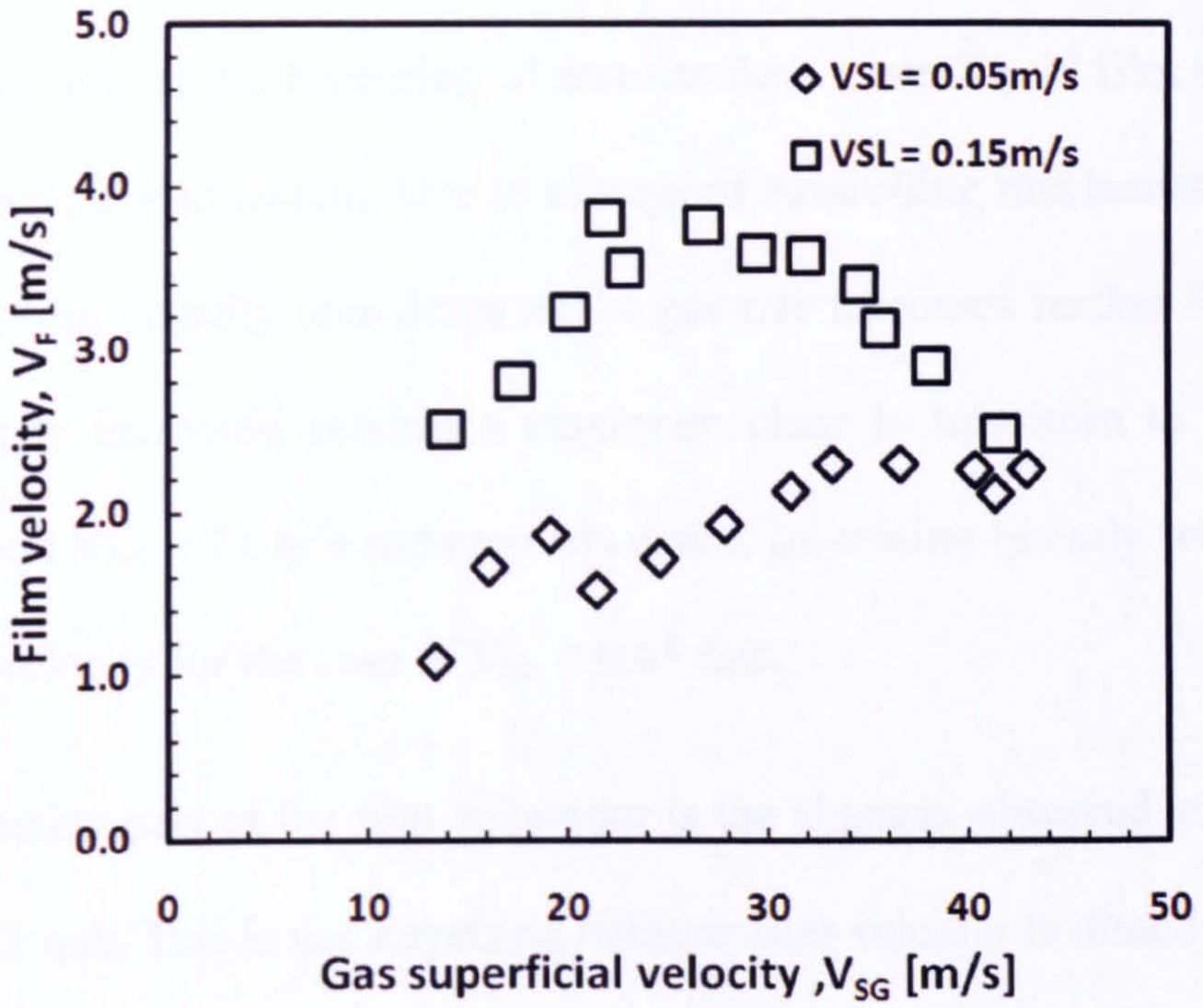

Figure 4.27: Film velocity as a function gas superficial velocity.

Predicted film velocity using the mechanistic model of Alves et al. (1991) is in excellent agreement well with the measured film velocity as shown in Figure 4.28.

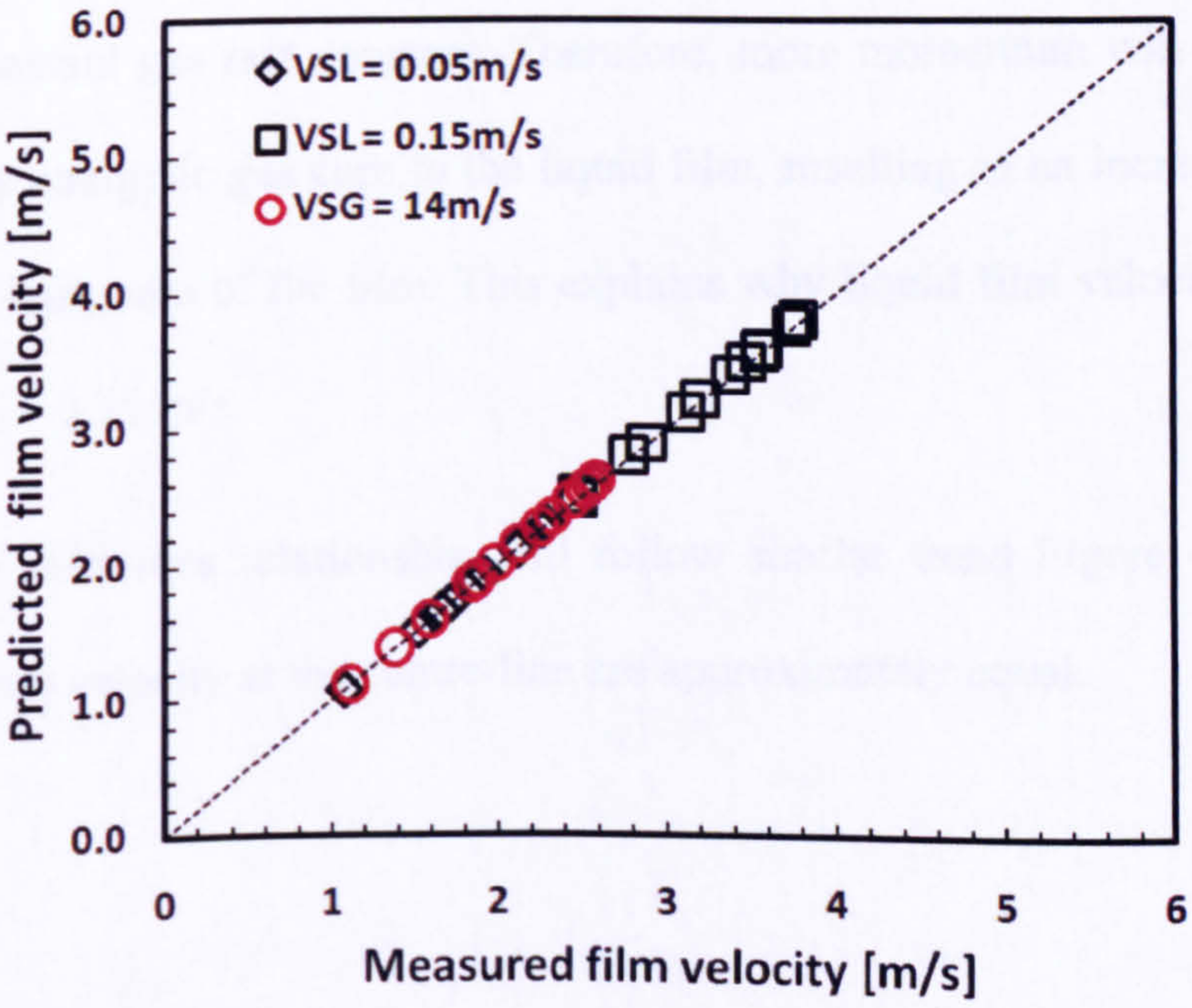

Figure 4.26: Comparison of film velocity with the model of Alves et al. (1991).

Figure 4.27 shows that film velocity increases as gas rate increases, reaches a maximum around V_{SG} = 21 m/s, at the beginning of annular flow when liquid film seems to start undergoing complete atomization. Due to change of controlling mechanism (huge wave to disturbance), film velocity then drops as the gas rate increases further for V_{SL} = 0.15 m/s. Film velocity increases, reaches a maximum close to transition to annular flow, then drops around V_{SG} = 21 m/s and recovers again, increasing linearly with increase in gas superficial velocity for the case of V_{SL} = 0.05 m/s.

The most interesting part of the film behaviour is the changes observed at the transition around V_{SG} = 21 m/s. This is not surprising because film velocity is directly proportional to entrained fraction according to Equation (4.14).

According to Figure 4.27, the liquid film at V_{SL} = 0.15 m/s film has a higher velocity than the liquid film at V_{SL} = 0.05 m/s. This implies that the film has more energy and is richer in momentum and will exhibit more flow structures as liquid superficial velocity increases at constant gas rate constant. Therefore, more momentum will be transferred from the highly energetic gas core to the liquid film, resulting in an increase in the film velocity in the base area of the film. This explains why liquid film velocity is higher in the case of V_{SL} = 0.15 m/s.

Film and drop velocities relationship will follow similar trend Figure 4.27 since gas velocity and drop velocity at the centre-line are approximately equal.

4.11 Probability Density Function (PDF)

Time varying drop size can be examined further in both amplitude and frequency space. The amplitude variation can be carried out using the Probability Density Function (PDF). This is the probability of occurrence of each drop size as instrument scans the detector. In the present study, drop size distribution was tracked using Probability Density Function. It was generated from time-series of MMD for a series of gas superficial velocities at a liquid superficial velocity, V_{SL} = 0.05m/s as shown in Figure 4.29. The shape of the distribution function describes the extent of the homogeneity or heterogeneity of the particle size in the distribution. The Probability Density Function shows marked shifts to the right with increasing time, an indication of dominance of coalescence events. The PDF is characterized by multiple peaks and series of maximums which clearly finger-prints multi-modal distribution before gas superficial velocity of 30 m/s.

An interesting feature is however, noticed after V_{SG} = 30m/s when the drop size distribution changes from multiple peaks to single peak with only one maximum.

The possible explanation for this behaviour is that after superficial velocity of 30 m/s, the drop size distribution becomes uniform as pressure drop starts to recover as flow regime changes from annular to mist annular flow. The peak becomes narrower and taller as superficial gas velocities increase suggesting more uniform distribution. Analysis carried out using modified Rosin-Rammler (1963) model fails to predict MMD before V_{SG} = 30m/s. This is an indication that the model in its original form performs best for mono-modal distribution, and the experimental data was multimodal. Rosin Rammler analysis is treated in the subsequent sub-section.

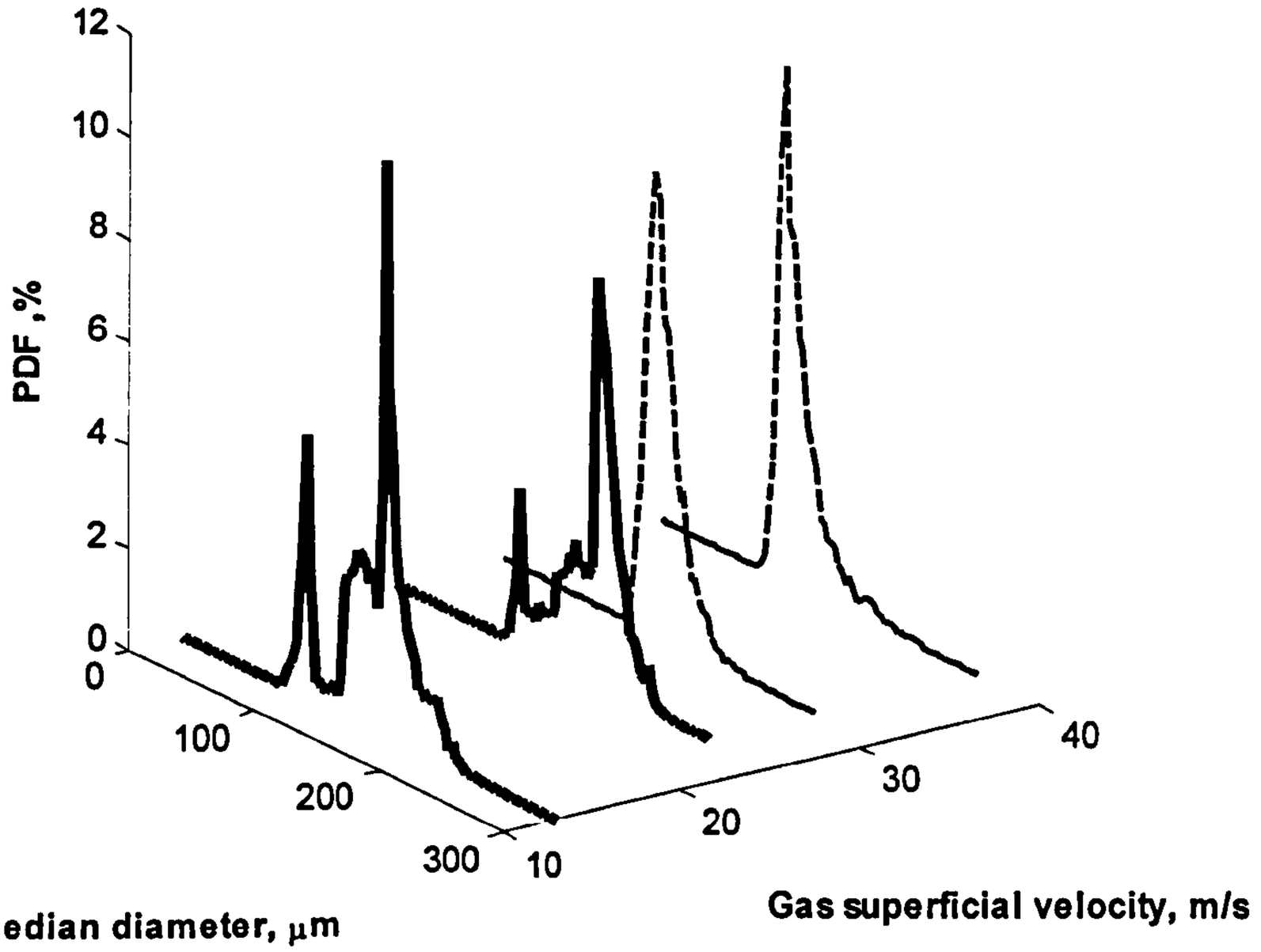

Figure 4.29: Changes in drop size distribution tracked by the Probability Density Function. There is a change from multiple to single peak after gas superficial velocity of 30 m/s marked transition to annular mist flow as D_{50} (MMD) decreases. V_{SL} = 0.05 m/s.

Figure 4.30 shows the time series and the corresponding PDF of dynamic data taken close to the beginning of annular flow as predicted by the transition model of Turner et al. (1969). The figures show how PDF can be used to determine the modality of the drop concentration distribution and the pressure drop in the system. The multiple peak-distribution noticed at this inlet condition V_{SG} = 14.08 m/s and V_{SL} = 0.19 m/s , which is supposed to be in fully developed annular flow according to the droplet model of Turner suggests the presence , in the gas core, of partially atomized fractal of liquid film, otherwise referred to as wisps or agglomerate of liquid body carried by huge wave.

The only explanation for the presence of wisps in this region is the incomplete atomization process promoted by chaotic and unstable nature of liquid film. The presence of wisps in churn region has been reported by Azzopardi et al. (2008). The

PDF of the drop concentration, Mass Median Diameter (MMD) and the pressure drop all show twin peak suggesting bi-modality and heterogeneous nature of the distribution, Figure 4.30. Each peak signifies a different event.

The surface of the liquid film can be covered by disturbance and huge waves when they co-exist in annular flow. Depending on the mechanism of drop entrainment, either huge or disturbance wave could dominate. Surprisingly, the PDF of the wall film which produced the drops displays a single peak implying homogenous and dominance nature of huge wave over disturbance wave. According to Figure 4.30, the PDF of the time averaged film thickness is characterized by a broader and serrated peak. Thus, the wave on the liquid film appears to be a product of meeting or merger of two independent waves traversing the gas-liquid interface. The resultant wave has higher amplitude and hence produces higher drop size Figure 4.30, Appendix D.

Logged time varying signals

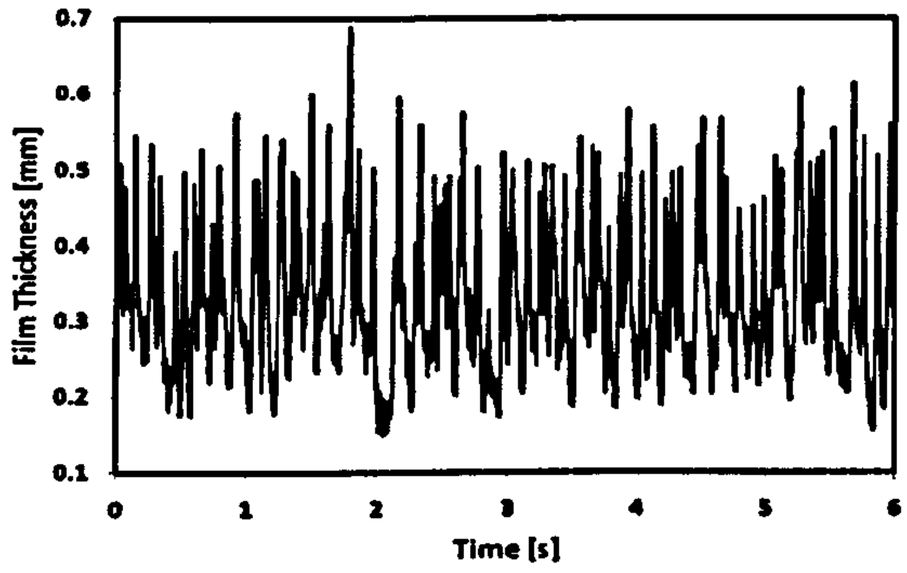

Corresponding PDF Curves

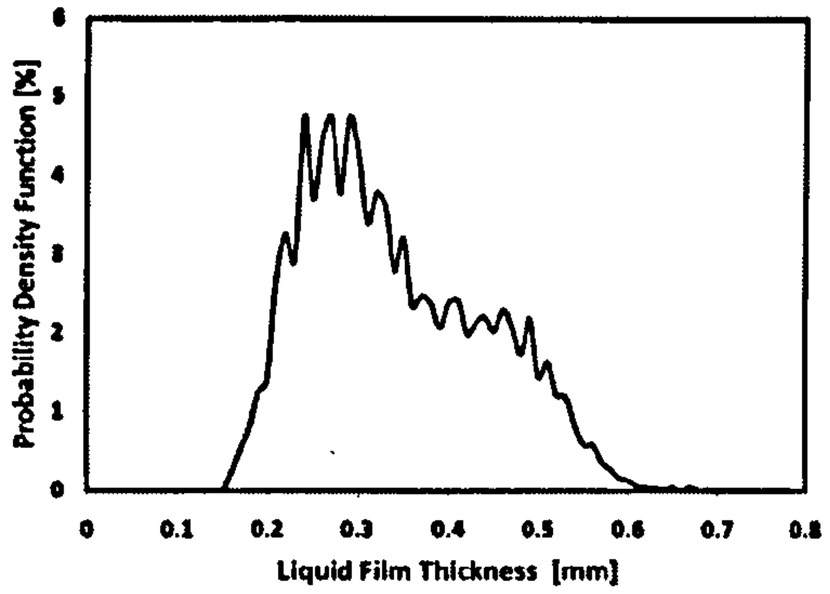

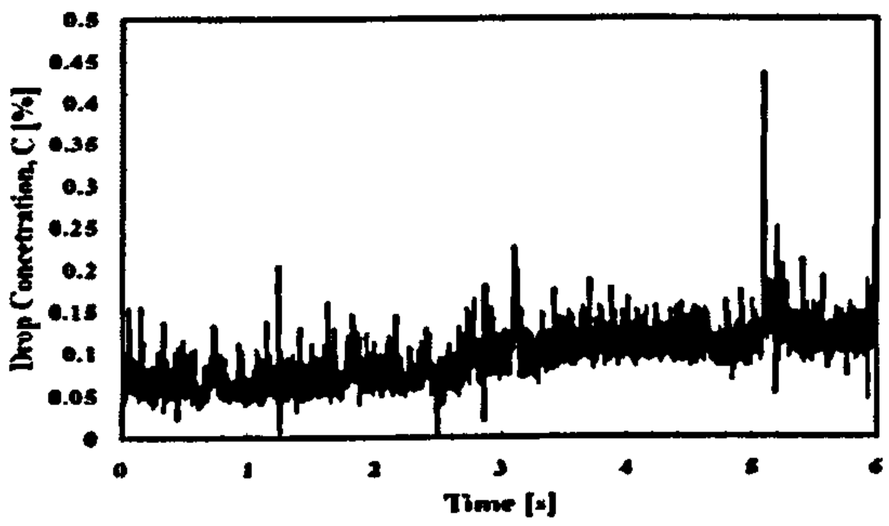

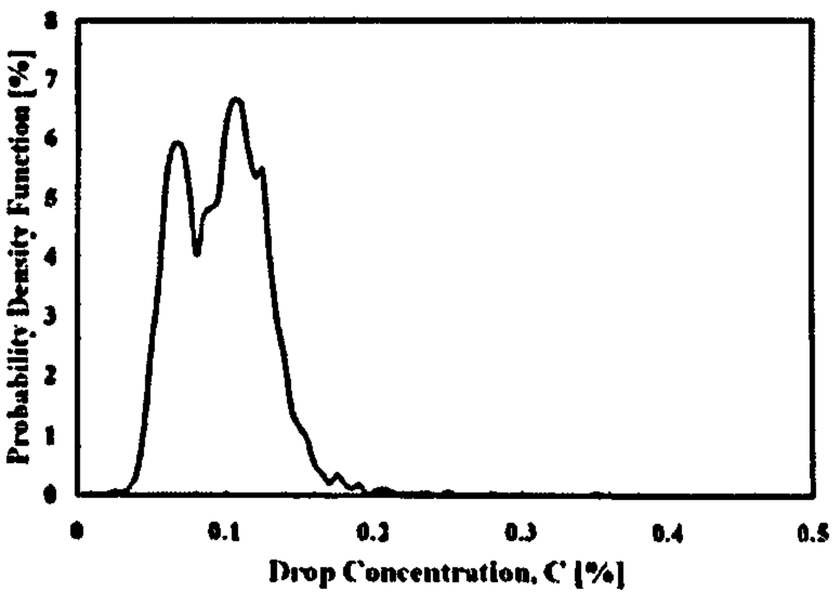

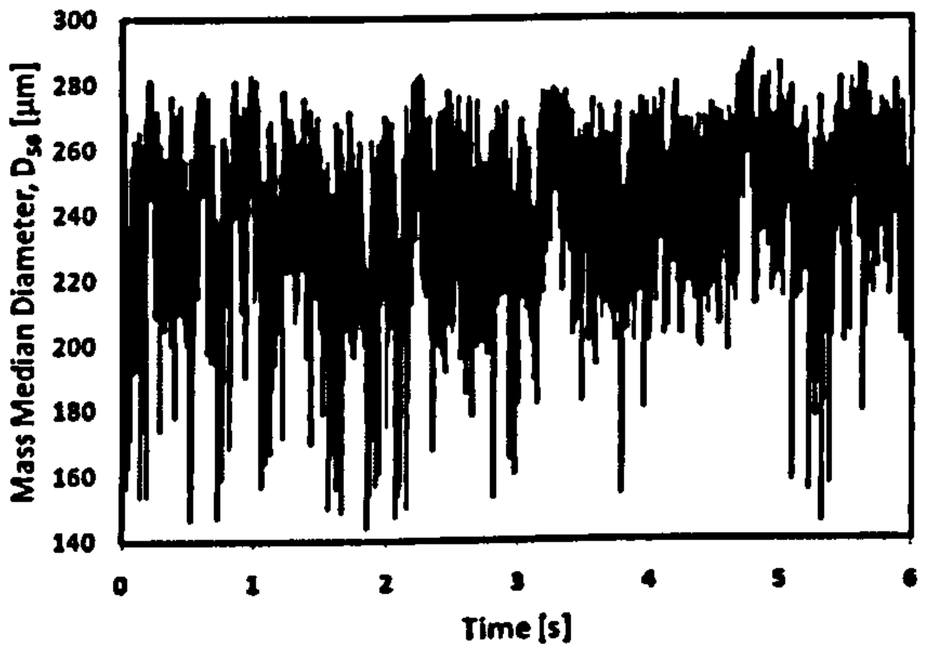

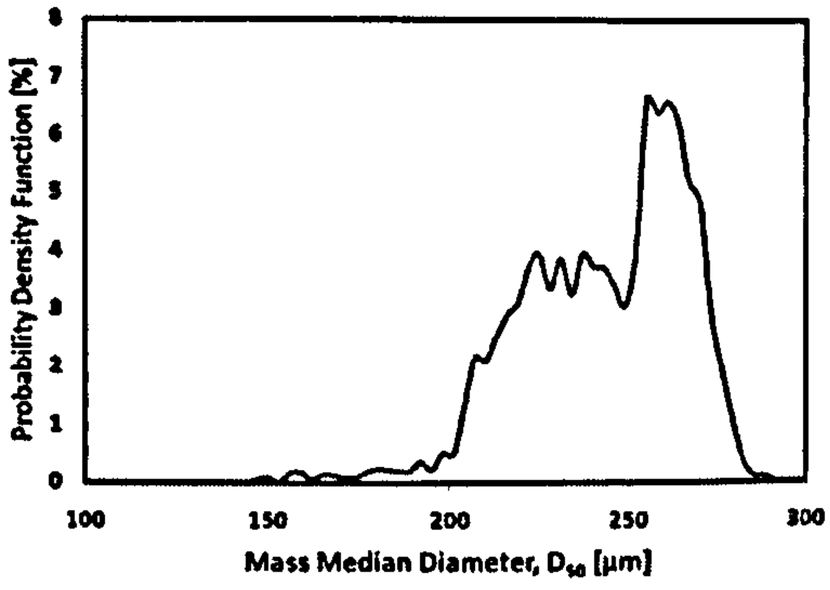

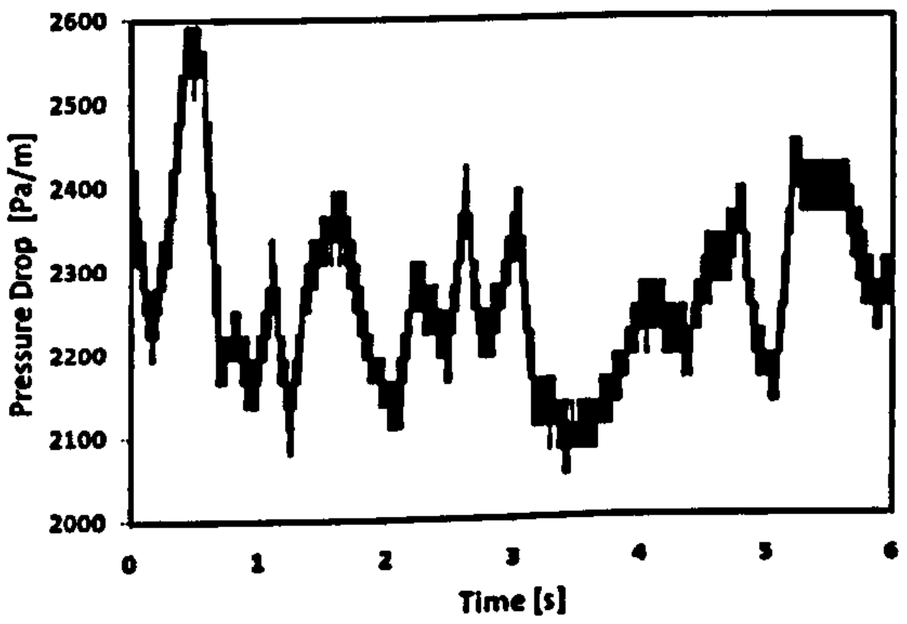

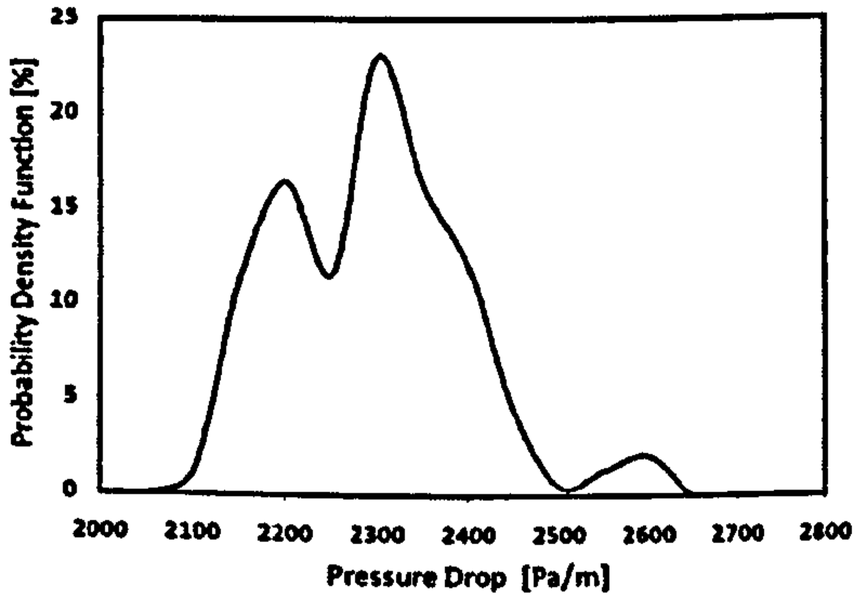

Figure 4.30: Time series and PDF of data showing bi-modality at V_{SG} = 14.08 m/s, V_{SL} = 0.19 m/s. Film thickness was acquired from conductance probes, drop concentration from Spraytec and pressure drop form differential pressures cell.

The new wave is characterized by velocity observed to be greater than the velocity of the parent wave and thus, appears to fit description of huge wave reported by Sekoguchi and Takeishi (1989). The inlet condition at which the PDF in Figure 4.30 was generated falls within the wispy annular regime in Figure 4.31, same flow regime where Sekoguchi and Takeishi spotted wisps in the gas core.

The classification of mist annular flow region on flow pattern map Figure 4.31 is based partly on drop size collected after V_{SG} = 30m/s. Mist flow is characterized by gas phase as a continuous phase where liquid condensate, oil or water exists as very small approximately homogeneously distributed droplets.

4.12 Proposed Flow Pattern Map

Alterations to the transition boundaries have provoked a proposition to amend the existing flow map. This proposition is based on the evidences from void fraction, film hold-up, standard deviation of film thickness, entrained fraction, drop sizes and pressure drop data from measured in the series of experimental campaign of the present study. Evidences from data analysis are strengthened with intensive visualization studies using high speed camera to record the video footage of various flow regimes. The proposed map is a modified version of the Hewitt & Roberts (1969) flow map reported in Sawant et al. (2009) where transitions to wispy annular and annular mist flow have been adjusted to reflect findings and observations in the present study.

Based on the video evidence, it can be concluded that wispy annular flow occurs below V_{SL} = 1.2 m/s. The drop sizes and the video evidences contradict Hewitt & Roberts

(1969) and Sawant et al. (2009) statements that the transition to annular wispy flow takes place at higher liquid phase Reynolds number.

According the present findings, wispy annular prevails in annular flow until gas superficial velocity of 21 m/s is exceeded. This agrees with previous studies i.e. Mantilla (2008), where measurements of drop size and drop concentration were not carried out.

Also, the existing mechanistic models, Table 4.3, have established the non-dependence of this transition on superficial liquid velocity. It is therefore, proposed that this transition in the new map should be independent of liquid superficial velocity. The proposed line is represented by dotted line in Figure 4.31 at superficial gas velocity of 21 m/s. This marks the new transition to co-current annular flow. Wave characteristic associated with this transition will be detailed in Chapter Five.

Transition to mist annular flow occurs when gas superficial velocity exceeds 30 m/s. There are convincing evidence from PDF, MMD and flow visualization studies. This transition is also not dependent on liquid superficial velocity. Therefore, the discontinuous line in Figure 4.31 at gas superficial velocity, $V_{SG} = 30$ m/s represents the new transition boundary to mist annular flow.

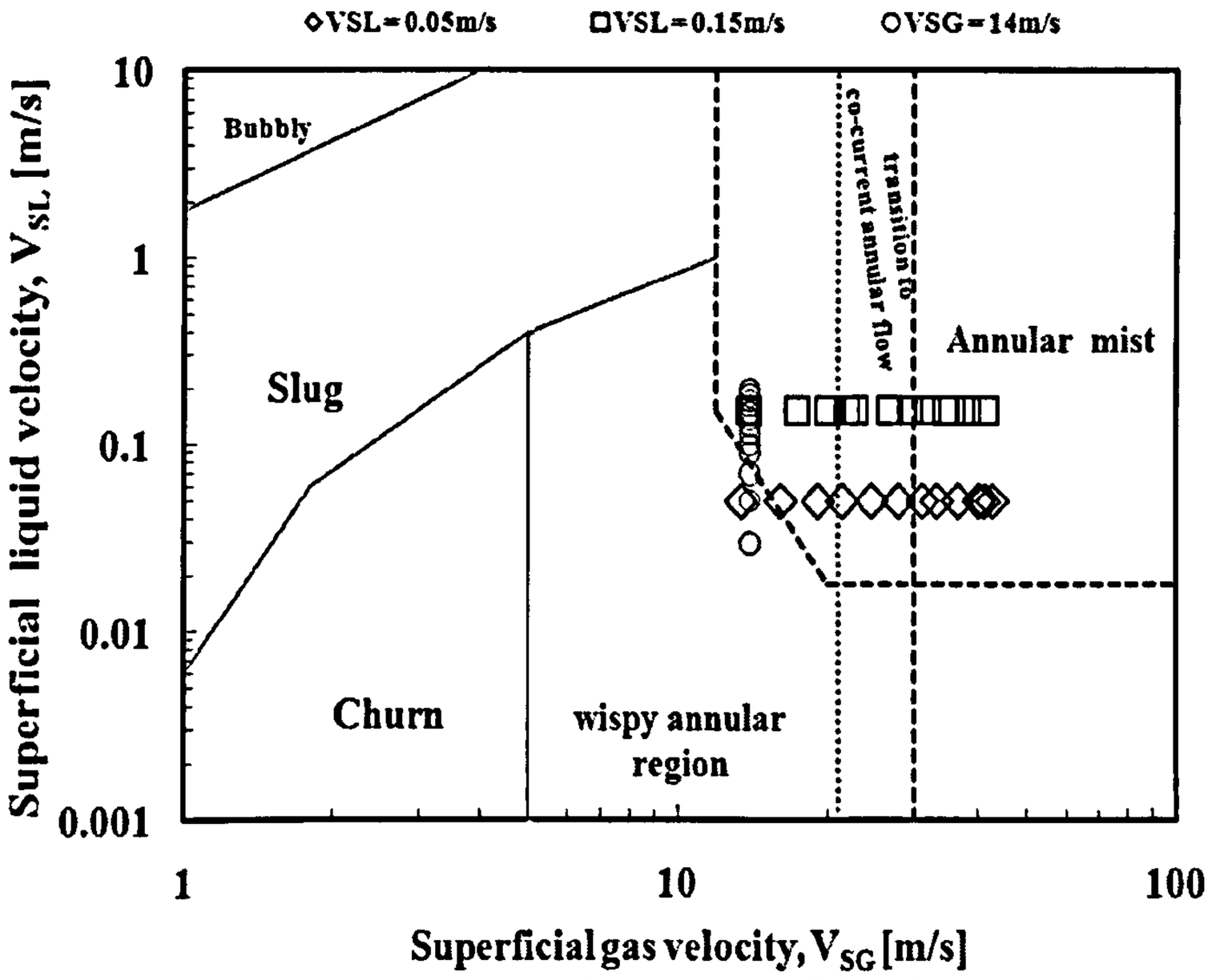

Figure 4.31: Proposed flow pattern map showing modification to wispy annular transition boundary of Hewitt & Roberts (1969) and the new transition boundary to mist annular flow. The open symbols represent the position of the present study on the new flow map.

4.13 Rosin Rammler Analysis

The Rosin-Rammler distribution is frequently used to describe the particle size distribution of powers of various types and sizes. The function has been used in the past to representing drop size distribution in gas-liquid and liquid-liquid flows. The conventional Rosin-Rammler function is described by the expression:

$$R = e^{-\left(\frac{D}{N}\right)^n} \qquad (4.15)$$

The Cumulative Distribution Function (CDF) takes the form:

$$R = 1 - e^{-\left(\frac{D}{N}\right)^n} \qquad (4.16)$$

The Probability Density Function (PDF) is given by:

$$R = -\frac{n}{D}\left(\frac{D}{N}\right)^{n} e^{\left[-\left(\frac{D}{N}\right)\right]^{n}} \qquad (4.17)$$

where R is the retained weight fraction of particles with a diameter greater than D, D is the particle size and N is the mean particle size, and n is a measure of the spread of particle sizes.

Re-writing Equation (4.16) yields:

$$1 - R = e^{-\left(\frac{D}{N}\right)^{n}} \qquad (4.18)$$

Taking natural logarithm on both sides of Equation (4.18) produces:

$$\log_e(1 - R) = \log_e e^{-\left(\frac{D}{N}\right)^{n}} \qquad (4.19)$$

Equation (4.19) can be simplifies further to give:

$$0 - \log_e(1 - R) = \left(\frac{D}{N}\right)^{n} \qquad (4.20)$$

Substituting for 0, on LHS and expanding Equation (4.20) generates:

$$\log_e[0 - \log_e(1 - \mathrm{R})] = n\log_e D - n\log_e N \qquad (4.21)$$

Recall, $0 = \log_e 1$ (4.22)

Putting Equation (4.22) into Equation (4.21) gives:

$$\log_e[\log_e 1 - \log_e(1 - \mathrm{R})] = n\log_e D - n\log_e N \qquad (4.23)$$

Further simplification of Equation (4.23) yields the final form of Rosin Rammler:

$$\log_e\left[\log_e\left(\frac{1}{1-R}\right)\right] = n\log_e D - n\log_e N \quad (4.24)$$

Equation (4.24) is then in a straight-line form:

$$y = mx + c \quad (4.25)$$

Where:

$$y = \log_e\left[\log_e\left(\frac{1}{1-R}\right)\right] \quad (4.26)$$

$$x = \log_e D \quad (4.27)$$

$$m = n \quad (4.28)$$

C = intercept on vertical axis

$$C = -n\log_e N \quad (4.29)$$

Therefore, N can be estimated from Equation (4.29) as follows:

$$N = e^{\left[-\left(\frac{C}{n}\right)\right]} \quad (4.30)$$

D and n are the fitting parameters.

Therefore, plotting Equation (4.26) against Equation (4.27) will produce a straight line, Figure 4.32, with a slope m and intercept C on the vertical axis.

The approach above has been used to represent the present data. A good straight line was generated with a clear intercept on the vertical axis. However, it was found that the model prediction of the drop sizes was poor especially at low superficial gas velocity where the distribution are characterized by several maximums or multiple peaks.

Table 4.4: Particle Size Distribution table for gas superficial velocity, V_{SG} = 14.08 m/s and liquid superficial velocity, V_{SL} = 0.19 m/s.

Size (µm)	% <	% In	Size (µm)	% <	% In	Size (µm)	% <	% In
0.001	0.00	0.00	0.126	0.00	0.00	12.59	0.58	0.17
0.002	0.00	0.00	0.158	0.00	0.00	15.85	0.87	0.29
0.002	0.00	0.00	0.200	0.00	0.00	19.95	1.25	0.38
0.003	0.00	0.00	0.251	0.00	0.00	25.12	1.65	0.40
0.003	0.00	0.00	0.316	0.00	0.00	31.62	2.50	0.85
0.004	0.00	0.00	0.398	0.00	0.00	39.81	4.48	1.97
0.005	0.00	0.00	0.501	0.00	0.00	50.12	5.24	0.76
0.006	0.00	0.00	0.631	0.01	0.00	63.10	5.27	0.03
0.008	0.00	0.00	0.794	0.01	0.00	79.43	5.27	0.00
0.010	0.00	0.00	1.00	0.02	0.01	100.00	5.85	0.58
0.013	0.00	0.00	1.26	0.02	0.01	125.89	21.87	16.01
0.016	0.00	0.00	1.58	0.03	0.01	158.49	32.63	10.77
0.020	0.00	0.00	2.00	0.04	0.01	199.53	32.82	0.18
0.025	0.00	0.00	2.51	0.06	0.02	251.19	33.93	1.12
0.032	0.00	0.00	3.16	0.08	0.02	316.23	80.84	46.91
0.040	0.00	0.00	3.98	0.12	0.03	398.11	100.00	19.16
0.050	0.00	0.00	5.01	0.17	0.05	501.19	100.00	0.00
0.063	0.00	0.00	6.31	0.23	0.06	630.96	100.00	0.00
0.079	0.00	0.00	7.94	0.31	0.08	794.33	100.00	0.00
0.100	0.00	0.00	10.00	0.41	0.10	1000.00	100.00	0.00

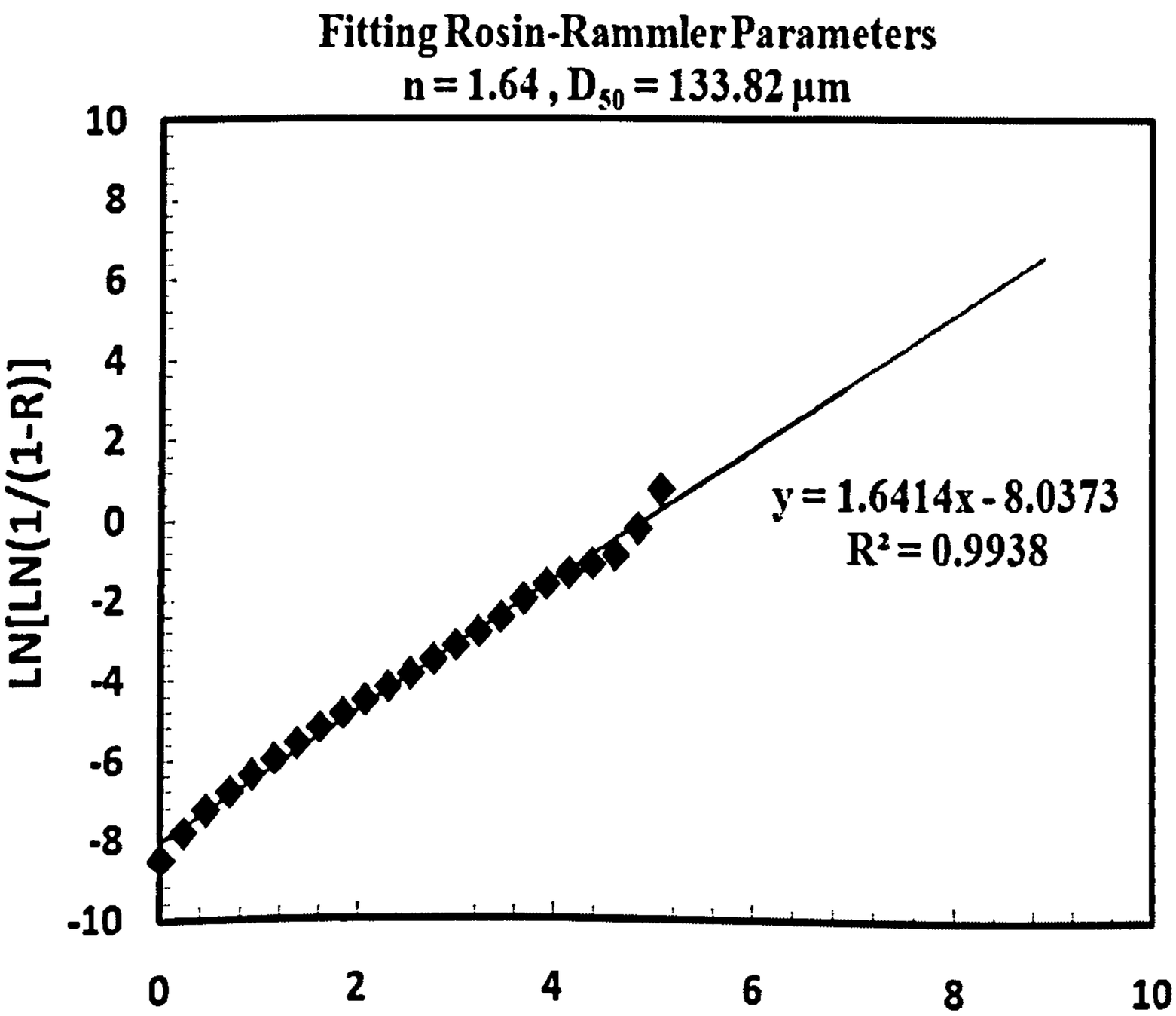

Figure 4.32: Predicting of mean drop diameter using Rosin Rammler model.

The particle size distribution in Table 4.4 was generated from RTSizer, Spraytec software. The predicted MMD by Rosin Rammler approach gave MMD = 133.82 μm while the measured MMD = 241.7μm, Appendix D. This is an indication that the model in its original form cannot satisfactorily predict drop size characterize by multiple peak distribution. Going by the present argument of this study, Rosin-Rammler (1963) model will fail to predict MMD before gas superficial velocity of 30 m/s but will perform better in the single distribution, mist annular flow regime.

4.14. Assessment of entrained fraction correlations

Figure 4.33 shows the comparison between the predicted and measured entrained fraction data. According to Table 4.5, Sawant et al. (2009) entrained fraction model gives lowest statistical parameters, AAPE and STDEV, in the case of 24 data points considered therefore, demonstrating superior performance over other models considered. However, in the case of 36 data points, Ishii & Mishima (1989) correlation gives the best performance according to Table 4.6 with the least AAPE and STDEV. The correlation of Ishii & Mishima is most suitable for predicting entrained fraction at low superficial gas velocities i.e. V_{SG} = 14 m/s.

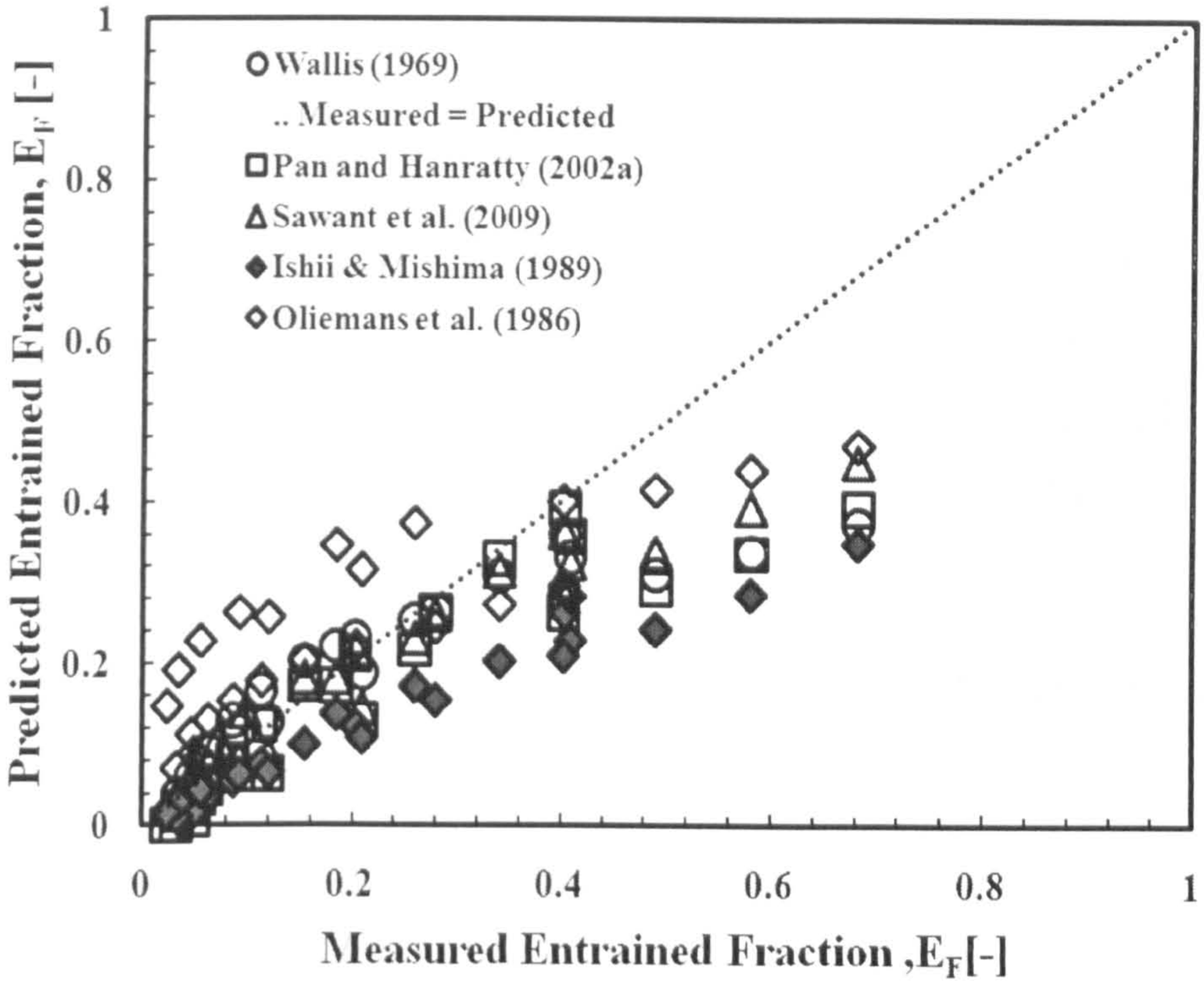

Figure 4.33: Prediction of measured entrained fraction data using existing correlations.

It observable from Figure 4.33 that all models under predict entrained fraction after entrained fraction of 0.4. This is an inadequacy of the existing correlations in predicting entrained fraction accurately in vertical co-current annular two-phase flow. Therefore, a mechanistic model with sound physical basis is advocated for predicting entrained fraction in vertical annular two-phase flow.

Table 4.5: Statistical results of models performance (24 data points)

Models	APE	AAPE	STDEV
Sawant et al. (2009)	-8.72	18.26	19.1
Wallis (1969)	-8.95	35.63	48.17
Ishii & Mishima (1989)	-39.29	39.3	12.05
Pan & Hanratty (2002a)	-31.98	33.96	30.58
Oliemans et al.(1986)	94.48	107.86	147.01

Table 4.6: Statistical results of models performance (36 data points)

Models	APE	AAPE	STDEV
Sawant et al. (2009)	36	54.57	153.77
Wallis (1969)	-17.38	70.19	122.3
Ishii & Mishima (1989)	-11.85	48.92	82.5
Pan & Hanratty (2002a)	-47.99	54.98	43.93
Oliemans et al.(1986)	352.56	361.48	442.97

The statistical parameters used in Tables 4.5 and 4.6 respectively are defined as follows:

APE = Average Percentage Error

AAPE = Absolute Average Percentage Error

STDEV = Standard Deviation

4.15 Drop size correlation

In Figure 4.34(a) the measured Sauter Mean Diameter (D_{32}) is compared with the popular correlation of Azzopardi (1997). The correlation is given by the following expression:

$$\frac{d_{32}}{D} = 1.91 \mathrm{Re}_{SG}^{0.1} We_{SG}^{-0.6} \left(\frac{\rho_G}{\rho_L} \right)^{0.6} + 0.4E \frac{V_{SL}}{V_{SG}} \qquad (4.31)$$

Where, $We = \frac{\rho_G V_{SG}^2 D}{\sigma}$,[-]; $\mathrm{Re}_{SG} = \frac{\rho_G V_{SG} D}{\mu_G}$, [-]; $E = \frac{\dot{M}_{LE}}{\rho_L V_{SL}}$,[-].

The first term in the RHS of the Equation (4.31) is the contribution from drop break-up while the second term represents contribution from drop coalescence.

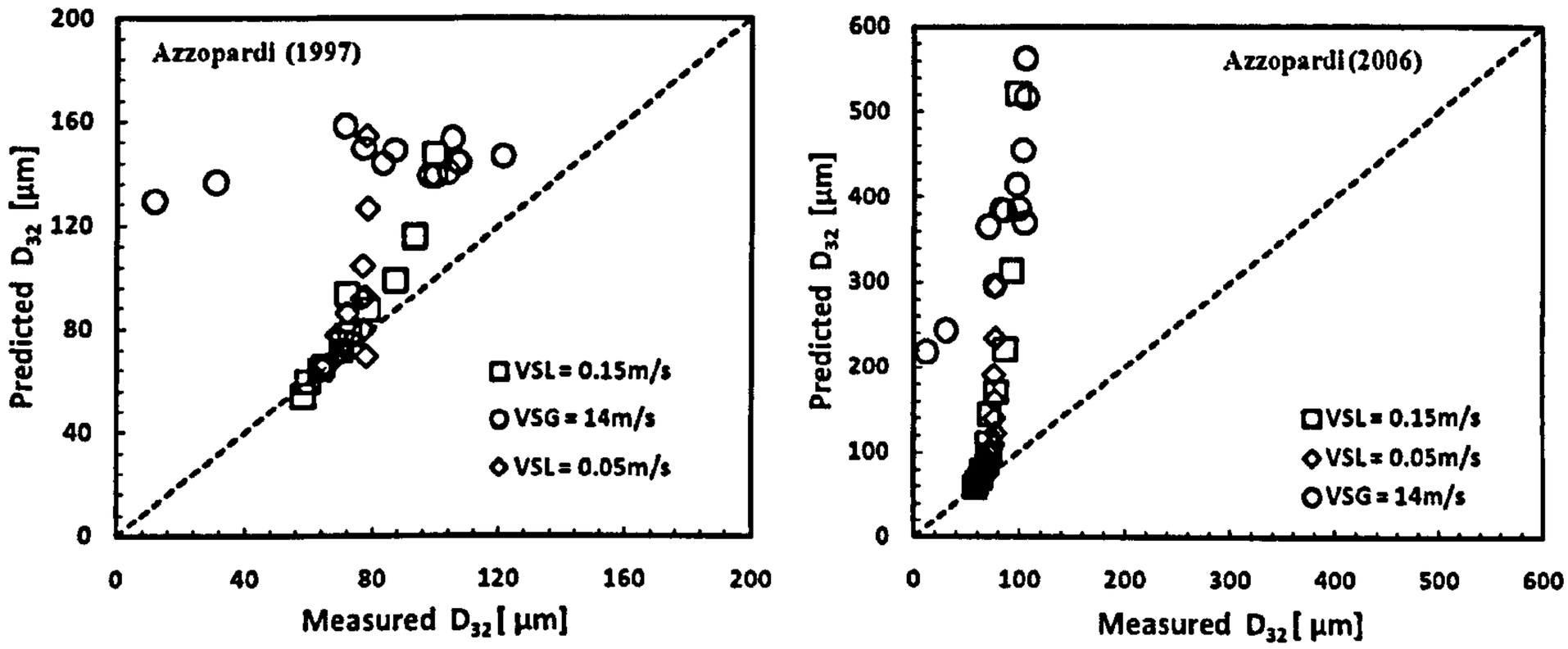

(a) (b)

Figure 4.34: Comparison of predicted and measured SMD using the model of Azzopardi (1997, 2006).

Another simple model was suggested by Azzopardi (2006) for vertical annular two-phase flow. It is expressed as follows:

$$D_{32} = \left[0.069V_{SG} + 0.0187\left(\frac{\rho_L V_{SL}}{\rho_{SG} V_{SG}}\right)^2\right]\frac{\sigma}{\rho_{SG} V_{SG}^2} \qquad (4.32)$$

The model prediction against the measured data is shown in Figure 4.34 (b). The model performance was very poor compared to that of Equation (4.31) as shown in Figure 4.34 (a).

Tuning parameter E in the coalescence term of Equation (4.16) was varied systematically between 1 and 3 at various flow regimes within annular flow to determine influence of drop coalescence on the predictive nature of the model. For instance, in the mist annular flow in the case of V_{SL} = 0.05 m/s and V_{SG}> 30 m/s, best fit was obtained when E = 2.5 (M_{LE} = 125 kg/m^2-s) with maximum relative error of 20%. Between 21 m/s ≥ V_{SG} ≤ 30 m/s, using E = 2.5 over-predicts drop sizes and gives values which are

unrealistic. However, when we use E = 0.001 (M_{LE} = 0.05 kg/m^2-s) the model over-predicts drop size with relative error of up to 100%. Value of E = 0.001 means that coalescence is almost zero. This obviously contradicts the physical reasoning of the model. In the case of V_{SL} = 0.15 m/s, best match with measured data was got when E = 0.3 (M_{LE} = 45 kg/m^2-s) in the mist flow regime where V_{SG}> 30 m/s. The maximum relative error recorded is less than -10%.

Between 21 m/s ≥ V_{SG} ≤ 30 m/s, using E = 0.025 (M_{LE} = 3.75 kg/m^2-s) the model predicts drop size with maximum relative error of -30%. For the case of V_{SG} < 21 m/s, using E = 0.0000125 (M_{LE} = 0.01875 kg/m^2-s) gives best result with maximum relative error of - 48%.

Overall the model does not give good result at low superficial gas velocity. For the case of V_{SG} = 14 m/s, the model over-predicted drop sizes and the values are unrealistic.

4.16 Discussions

Pressure drop was normalized with wall shear stress calculated using the model of Alves et al. (1991). The result was shown in Figure 4.35. For the thicker film where superficial liquid velocity, V_{SL} = 0.15 m/s, pressure minimum occurs at gas superficial velocity, V_{SG} = 21 m/s. This agrees very well with previous studies on churn - annular transition boundary of Barbosa et al. (2002) and van Westende et al. (2007). Both reported gas superficial velocity of 21 m/s for transition from churn to annular in vertical pipe, Table 4.2. For the thinner film, the minimum is not clear, Figure 4.35.

In term of drop size, thicker film produces higher Sauter Mean Diameter (SMD) before transition to annular flow. At the transition boundary and beyond, thinner film overtakes thicker film curve producing higher Sauter Mean Diameter (SMD) as gas superficial velocity continues to increase, Figures 4.8, 4.9 and 4.35.

In Figure 4.9, normalized MMD curve for thicker film (V_{SL} = 0.15 m/s), crossed-over thinner film (V_{SL} = 0.05 m/s) curve at V_{SG} = 30 m/s. The cross-over point marks the transition to mist annular flow. Beyond this transition, thinner film produces bigger drop because of the greater interaction it enjoys with the gas core. Thicker film on the other hand experiences less interaction with the gas core due to conservation of momentum. However, in mist flow ($V_{SG} \geq$ 30 m/s) where the droplets size are smaller and approximately homogeneously distributed, flow at higher liquid rate will produce more structures at constant gas rate. This explains why normalized drop-size is higher for V_{SL} = 0.15 m/s after $V_{SG} \geq$ 30 m/s.

In relation to entrained fraction, pressure continues to drop as more droplets are entrained in the gas core until a minimum is reached where E_F = 0.20. After this transition, pressure drop starts to recover and increases monotonically with entrained fraction. This transition and point of recovery corresponds to V_{SG} = 30 m/s. At this point and beyond, it is believed that liquid film has undergone complete atomization. Liquid entrainment into the gas core and droplet deposition on the liquid film is steady, resulting flow pattern being mist annular. The drag force of the gas phase must overcome the surface tension and gravity forces for a fully developed annular flow to occur. Under the influence of gravity film is less stable and chaotic.

Figure 4.35 shows combined normalized flow variables as a function of superficial gas velocity at constant liquid rates. From the present data gravity dominates flow before transition to co-current annular flow at gas superficial velocity, $V_{SG} = 21$ m/s.

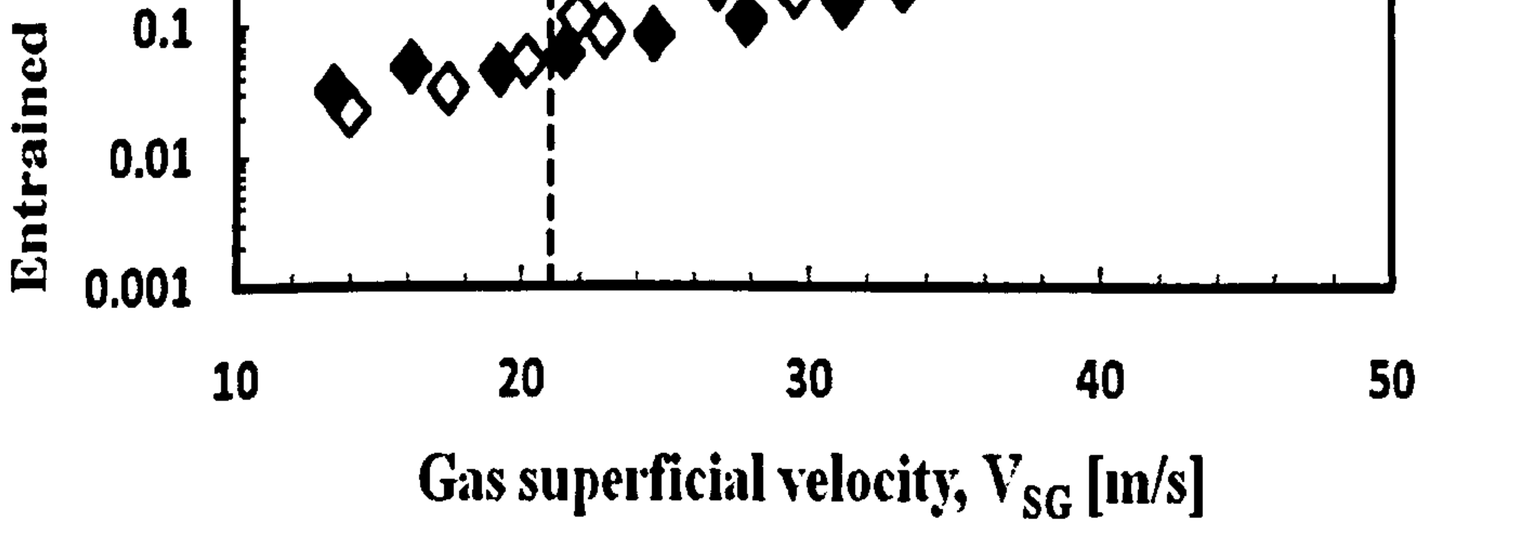

Figure 4.35: Normalized flow variables vs. gas superficial velocity.

At lower gas superficial velocity and before transition to co-current annular flow, thinner film produces higher entrained fraction. However, the entrained fraction curve for thicker film ($V_{SL} = 0.15$ m/s) overtakes entrained fraction curve for thinner film ($V_{SL} = 0.05$ m/s) at transition to co-current annular flow at gas superficial velocity, $V_{SG} = 21$ m/s. After crossing the transition boundary, the thicker film produces higher entrained

fraction than the thinner film, both continue to increase monotonically as gas superficial velocity increases. Liquid film before the transition boundary is believed to be covered principally by huge waves although it co-exists disturbance wave. The dominance of huge wave has been established based on the standard deviation of the film thickness. However, Disturbance waves dominates the flow after V_{SG} = 21 m/s and coexisted with huge wave until gas superficial velocity of 30 m/s. After gas superficial velocity of 30 m/s annular mist flow begins, huge wave disappears; disturbance wave then co-exists with ripple waves.

As gas superficial velocity increases at fixed liquid superficial velocity, the slip within the gas–liquid interface increases, leading to a higher interfacial shear, and hence the total pressure-gradient increases. However, when pressure drop is normalized the behavior changes as in Figure 4.35. Pressure drop is characterized by a minimum suggesting the dominance of gravity forces. It recovers after transition to annular flow as gas superficial velocity continues to increase. The amount of entrained liquid fraction increases as gas flux increases.

Westende et al. (2007) working with air/water at inlet conditions similar to the present study in a 50mm diameter pipe also reported that pressure-gradient and amount of entrained fraction experienced a minimum around V_{SG} = 20 m/s corresponding with a densimetric Froude number = 1.When gas superficial velocity is less than 20 m/s i.e. Fr_g < 1, they said liquid film thickness and the wave height become much larger. At this transition, however, according to Zabaras et al. (1986), wall shear stress fluctuates, occasionally directed upward, and film churning occurs. Below the transition point, they

also reported the presence of large interfacial waves which are propelled fast with the gas flow, which was recognized as huge waves reported by Sekoguchi and Takeishi (1989). Zabaras et al. (1986) referred to the onset of liquid down-flow as flow reversal point and in general occur at a gas velocity below the minimum in the pressure gradient curve.

An interesting phenomenon occurs at a superficial velocity of 21 m/s for thinner film (liquid superficial velocity of 0.05 m/s). The liquid film velocity, pressure gradient, wall shear stress, liquid hold-up, wave frequency and wave length all decrease while drop concentration (entrained fraction) , D_{32} (Sauter Mean Diameter) and wave amplitude all increase significantly. This behavior was first reported by Weihong et al. (2001) who emphasized the impact this behavior might have on the development of predictive models for low-liquid-loading wet gas pipelines. Weihong et al. did not give any reason nor explained the mechanism that was responsible for this behavior. They carried out their experimental investigation on 50.1mm internal diameter pipe with inclination angles from horizontal of -2^0, -1^0, 0^0, 1^0 and 2^0. The superficial gas velocity at which this unusual phenomenon occurred was reported as 25 m/s.

4.17 Conclusions

From the results and discussions presented , dynamic drop size including drop concentration, void fraction/film hold-up and pressure drop information have been used in vertical annular two-phase flow to accomplish the following:

1. New, time-resolved drop size and drop concentration data have been obtained simultaneously with film hold-up and pressure drop information. All these parameters show fluctuations with time. Some, such as film hold-up, are more obviously periodic than others.

2. The time averaged values are in agreement with prior data. Both measured SMD and entrained fraction captured transition to co-current annular flow at gas superficial velocity of 21 m/s. MMD profile on the other hand detected transition to mist annular flow at a gas superficial velocity of 30 m/s.

3. Considering MMD (D_{50}), thinner film produces bigger drops only at this boundary condition: 21 m/s ≥ V_{SG} ≤ 30 m/s. Before V_{SG} = 21 m/s, and after V_{SG} = 30 m/s, thicker film produces bigger droplets.

4. In terms of SMD (D_{32}), thicker film produces bigger drop up to V_{SG} = 21 m/s. After V_{SG} = 21 m/s, thinner film produces bigger drop.

5. Below V_{SG} = 21 m/s, thinner film (V_{SL} = 0.05 m/s) produces higher entrained fraction. After transition to co-current annular flow at gas superficial velocity, V_{SG} = 21 m/s, entrained fraction becomes higher the higher the film thickness or film hold-up (i.e. V_{SL} = 0.15 m/s).

6. Below entrained fraction of 0.05 (E_F = 0.05) and V_{SG} ≤ 21 m/s droplet flow is inertial-driven and gravity appears to have significant effect on entrained fraction. The flow is chaotic and huge waves dominate the gas-liquid interface.

Drop size or MMD is large under gravity-dominated flow. Effects of gravity diminish beyond entrained fraction of 0.05 (i.e. $E_F > 0.05$). After $E_F = 0.05$ pressure drops uniformly with entrained fraction until a minimum is reached where $E_F = 0.20$, $V_{SG} = 30$ m/s.

7. Pressure drop recovers after $E_F = 0.20$, increases with increase entrained fraction as gas superficial velocity increases. Mist flow occurs as a result of complete atomization of liquid film.

8. In mist flow regime droplet size do not change significantly with increase gas superficial velocity.

9. Examination of the time series in amplitude and frequency space reveals interesting features. PDF of MMD displays multiple peaks (multi-modal distributions) before gas superficial velocity, $V_{SG} = 30$m/s, suggesting heterogeneous nature of the drop sizes. This marks transition to mist annular flow earlier detected by MMD profile. In mist annular flow, after $V_{SG} = 30$m/s, PDF changes to single peak (mono-modal distribution) characterize by homogenous uniformly distributed drop size.

10. Wispy annular was observed where they were not expected. This is confirmed with video footage of the flow. Transition from wispy to mist annular has been modified to reflect this observation as well as transition to mist annular flow on the proposed, new flow pattern map.

11. In terms of entrained fraction, transition to mist annular when this boundary condition is satisfied: $V_{SG} \geq 30$m/s, $E_F \geq 0.20$. After this transition, normalized pressure drop increases with entrained fraction as gas superficial velocity increases.

12. For gas producer the best operating practice would be to produce natural gas within the transition region with the following boundary conditions:

$$21 \text{ m/s} \geq V_{SG} \leq 30 \text{m/s}$$

$$0.05 \geq E_F \leq 0.20$$

This region is characterized by minimum entrained fraction and pressure drop which means less shut-downs and more revenue.

13. Entrained fraction is a strong function of gas superficial velocity in two-phase vertical annular flow.

14. A new flow pattern map is proposed based on subtle changes in drop sizes and entrained fraction measurement.

15. The standard deviation of average film thickness is directly proportional to the drop size distribution.

16. At superficial gas velocity of 30 m/s, the following interesting phenomena occur:

(i) Standard deviation of mean film thickness becomes inertial dependent

(ii) Mean drop size (MMD) becomes dependent on superficial liquid velocity.

(iii) PDF of drop size distribution changes from heterogeneous to homogeneous distribution.

Chapter 5

Wave Dynamics in Vertical Annular Two-Phase Flow

5.1 Introduction

The mechanisms of atomization of part of the liquid film to form drops in annular two-phase flow are not entirely understood. It has been observed that drop creation only occurs when there are large disturbance waves present on the film interface. Woodmansee and Hanratty (1969) observed that ripples on these waves were a precursor to drops.

Woodmansee & Hanratty (1969) showed evidence that the creation of drops from the film on the channel walls did not take place from of the film but specifically from periodic structures, usually called disturbance waves which travel over the film at velocities of a few meters per second. Azzopardi (2006) presents more evidence of this. Therefore, it might be expected that there would be an interrelationship between the fluctuations of drop concentration and the frequency of disturbance waves. Unfortunately, hitherto there has been hardly any work presenting information about the way in which the drop concentration varies with time. The most useful study is that of Azzopardi & Whalley (1980 a) who used a camera looking axially up the pipe to record drops passing up the pipe.

At a deeper level there is need to understand interfacial hydrodynamics, exchange and transfer of momentum between the liquid film and the gas core in annular two-phase

flow because a lot of topical issues associated with the flow are still unresolved.

One of the ways in which the problem can be addressed is to measure and report simultaneously the wave properties, film hold-up, drop concentration and the system pressure drop.

Understanding wave properties is a starting point to developing a physically based, mechanistic model from which entrained liquid fraction can be predicted in vertical annular two-phase flow.

Results from present study shows that characteristic drop sizes, entrained fraction and the waves that created them are closely related. In this Chapter, measured wave properties are presented.

Wave properties can be classified into two: - primary and secondary properties, based on the findings of this work. First, the primary properties are the properties inherent in the wave and fundamental to its description. Primary wave properties are dynamic properties which can be used to describe the wave. These properties are stated below:

- Wave frequency
- Wave velocity
- Wave spacing and
- Wave amplitude

The secondary properties are regarded as those properties that are not directly used to describe the wave but are important to its evolution and dynamics. Secondary wave properties are listed below:

- Wall shear stress and
- Interfacial shear stress

Some of these properties are schematically described in Figure 5.1 and Figure 5.2 respectively. Next, some of the measured wave properties are discussed.

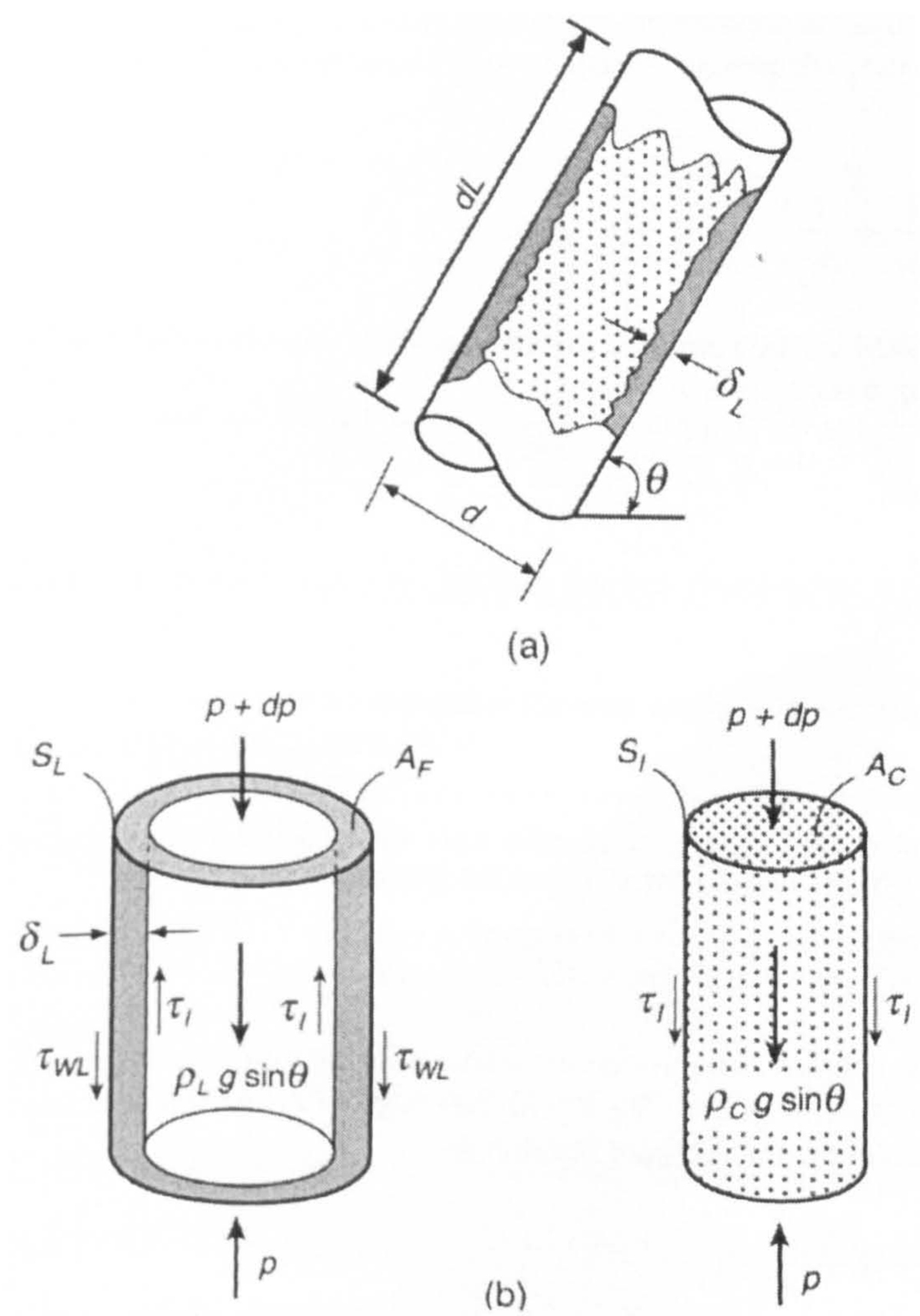

Figure 5.1: Annular flow schematics showing primary and secondary wave properties, Alves et al. (1991).

- Wall shear stress and
- Interfacial shear stress

Some of these properties are schematically described in Figure 5.1 and Figure 5.2 respectively. Next, some of the measured wave properties are discussed.

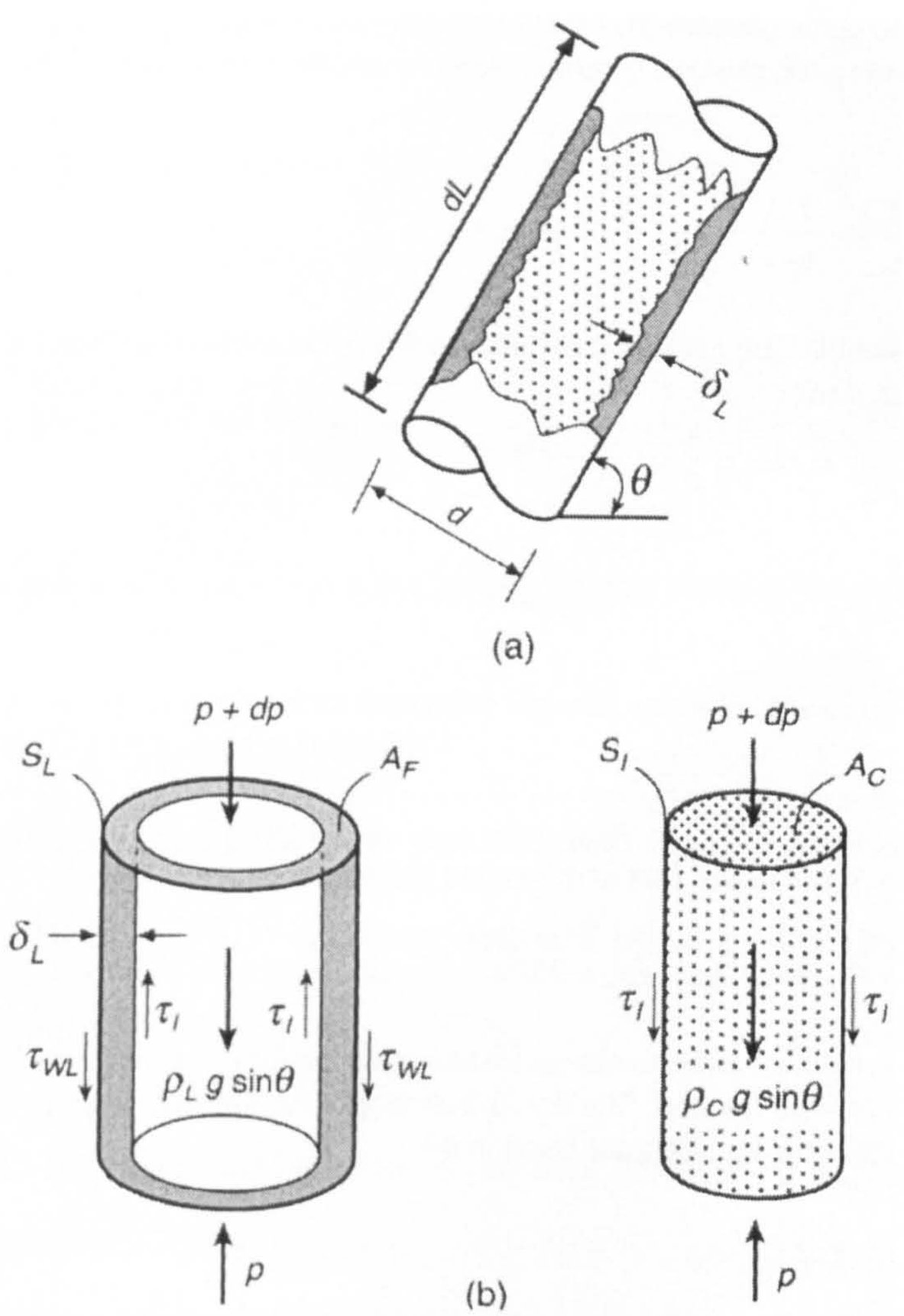

Figure 5.1: Annular flow schematics showing primary and secondary wave properties, Alves et al. (1991).

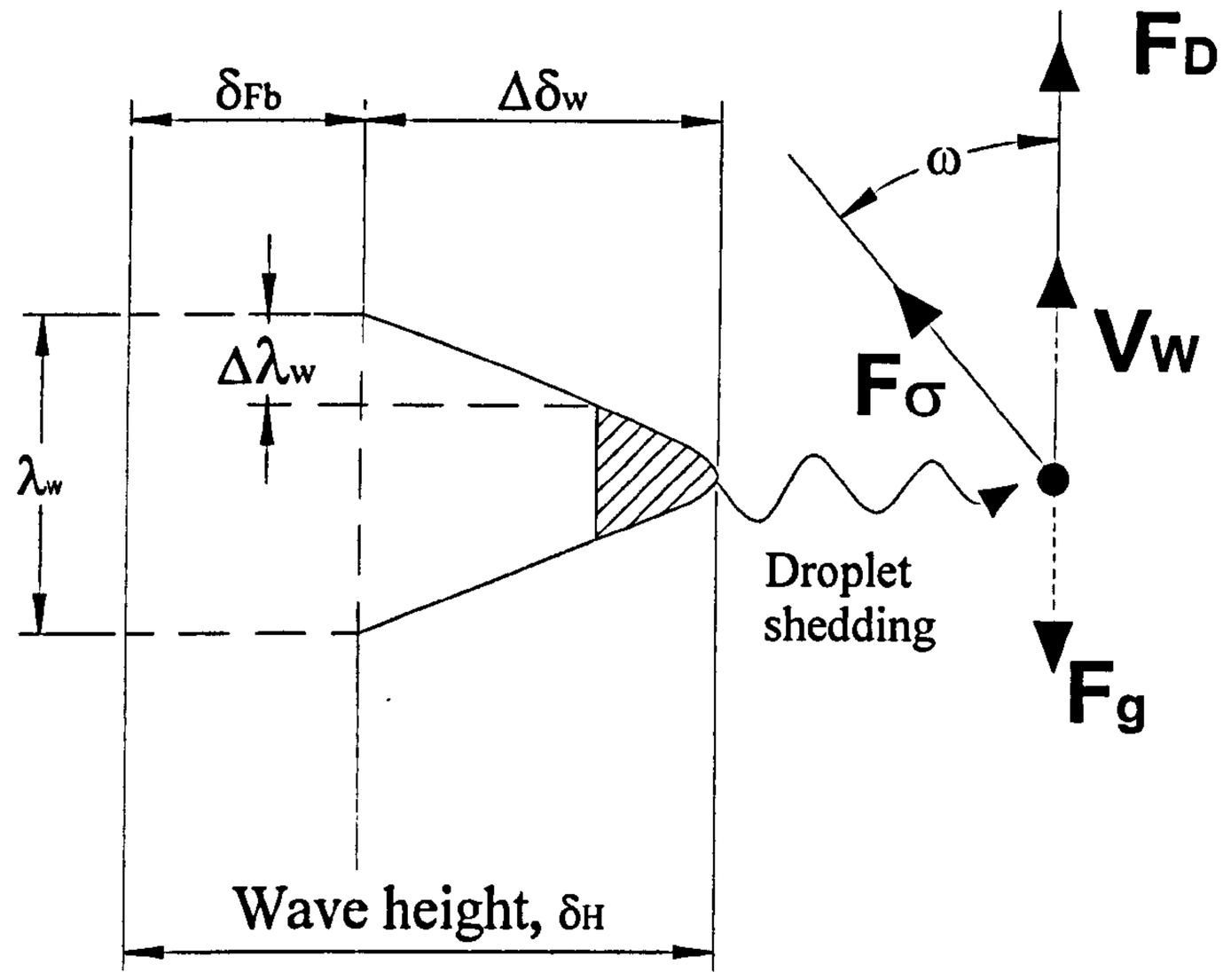

Figure 5.2: Schematic of a unit wave including forces resolution around a droplet.

5.2 Wave and Drop Frequency

The frequency characteristic of the flow was obtained using Power Spectrum analysis. Power Spectrum Densities (PSD) has been obtained by using Fourier transform of the auto-covariance function.

Azzopardi et al. (2008) expressed the auto-covariance function of a signal x (t) as:

$$R_{xx}(k\Delta\tau) = \frac{1}{T-\tau}\int_0^{T-\tau}\left[x(t)-\bar{x}\right]*\left[x(t+k\Delta\tau)-\bar{x}\right]dt\ ;\tau\angle T \qquad (5.1)$$

Where:

T = sampling time, s

$K\Delta\tau$ = time delay, s

τ = interrogating time delay and;

$$\bar{x} = \frac{1}{T}\int_0^T x(t)dt$$

The Power Spectrum Density is then obtained from:

$$P_{xx}(f) = \Delta\tau\left(\frac{1}{2}R_{xx}(0) + \sum_{k=1}^{\tau/(\Delta\tau-1)} R_{xx}(k\Delta\tau)w(k\Delta\tau)\cos(2\pi fk\Delta\tau)\right) \quad (5.2)$$

Where w(kΔτ) is a windowing function.

In this analysis basic Cosine windowing function was used as used in Azzopardi et al. (2008). It is expressed as:

$$w(k\Delta\tau) = Cos\left(\frac{\pi k\Delta\tau}{2\tau}\right) \quad (5.3)$$

In order to obtain frequency of two-phase flow structure we adopted the procedure above to the time-resolved drop concentration and wave (film) data shown in Figures 5.2 (a) and 5.2 (b) in calculating autocorrelations and Power Spectrum Densities displayed in Figures 5.3 (a) and Figures 5.3 (b).

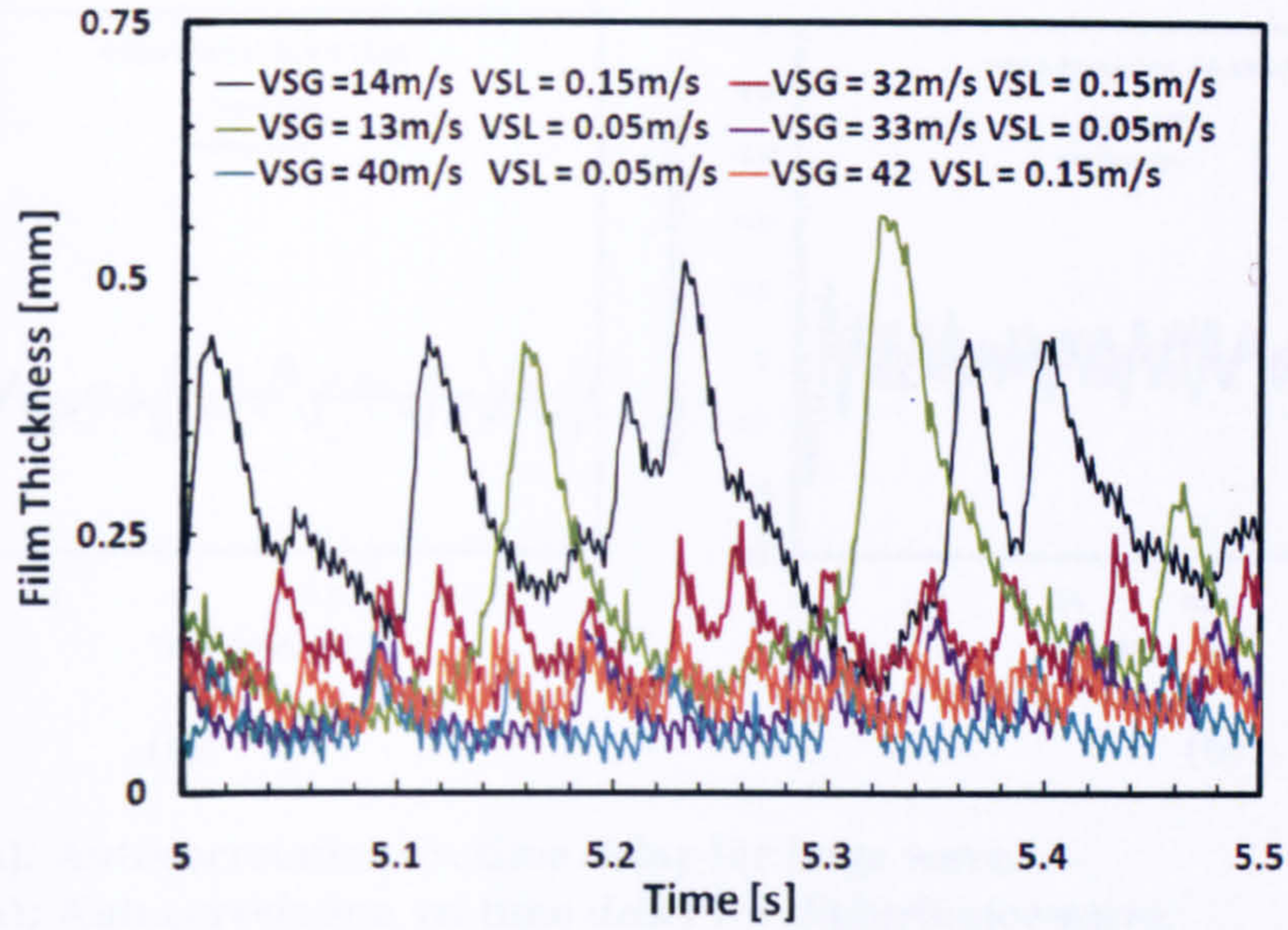

Figure 5.3 (a): Time-averaged film thickness information

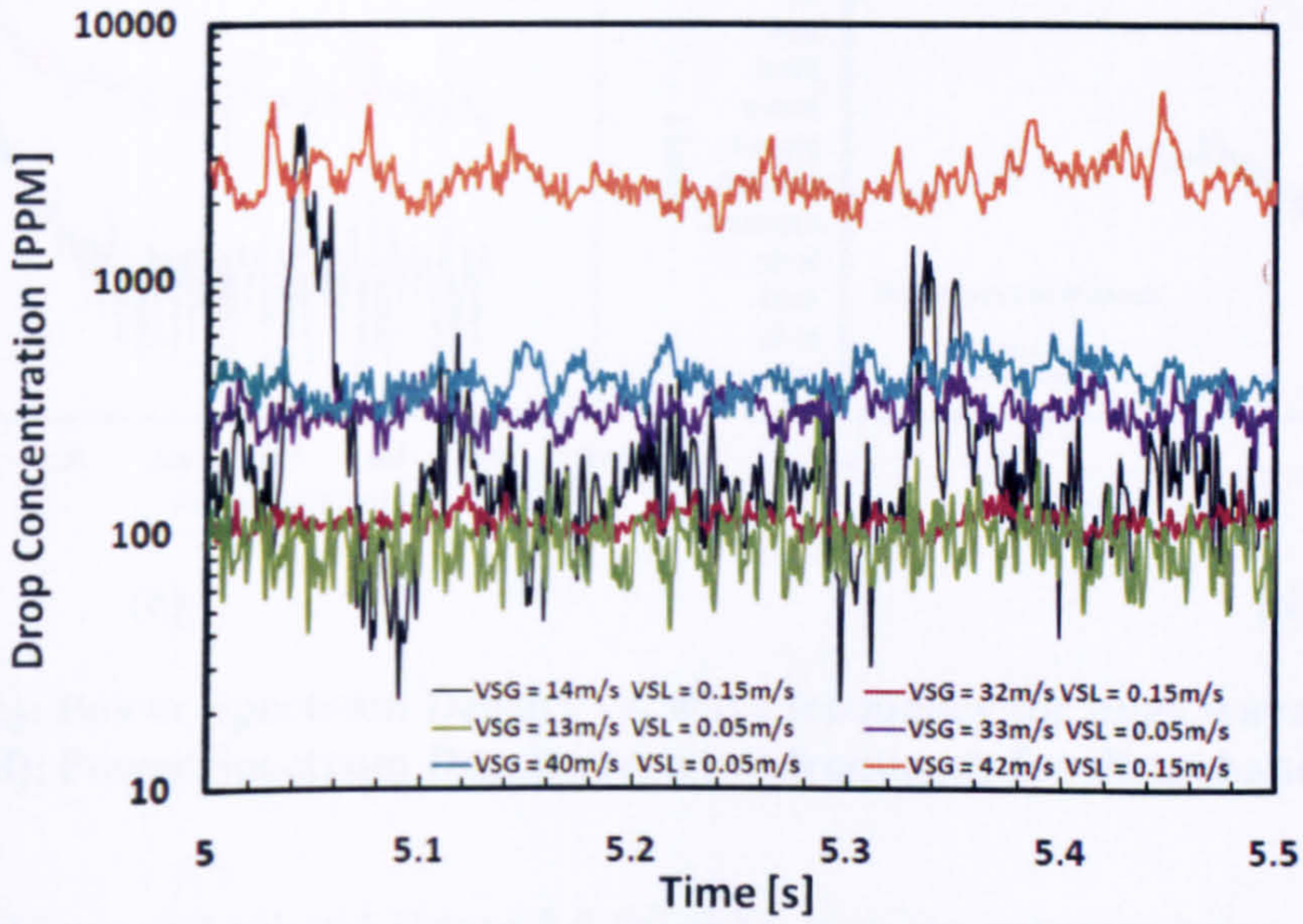

Figure 5.3 (b): Time averaged drop concentration information.

Time-resolved drop concentration was logged during the experiments with Malvern Spraytec equipped with Insitec card and time-averaged film thickness was acquired employing a pair of flush-mounted ring conductance probes.

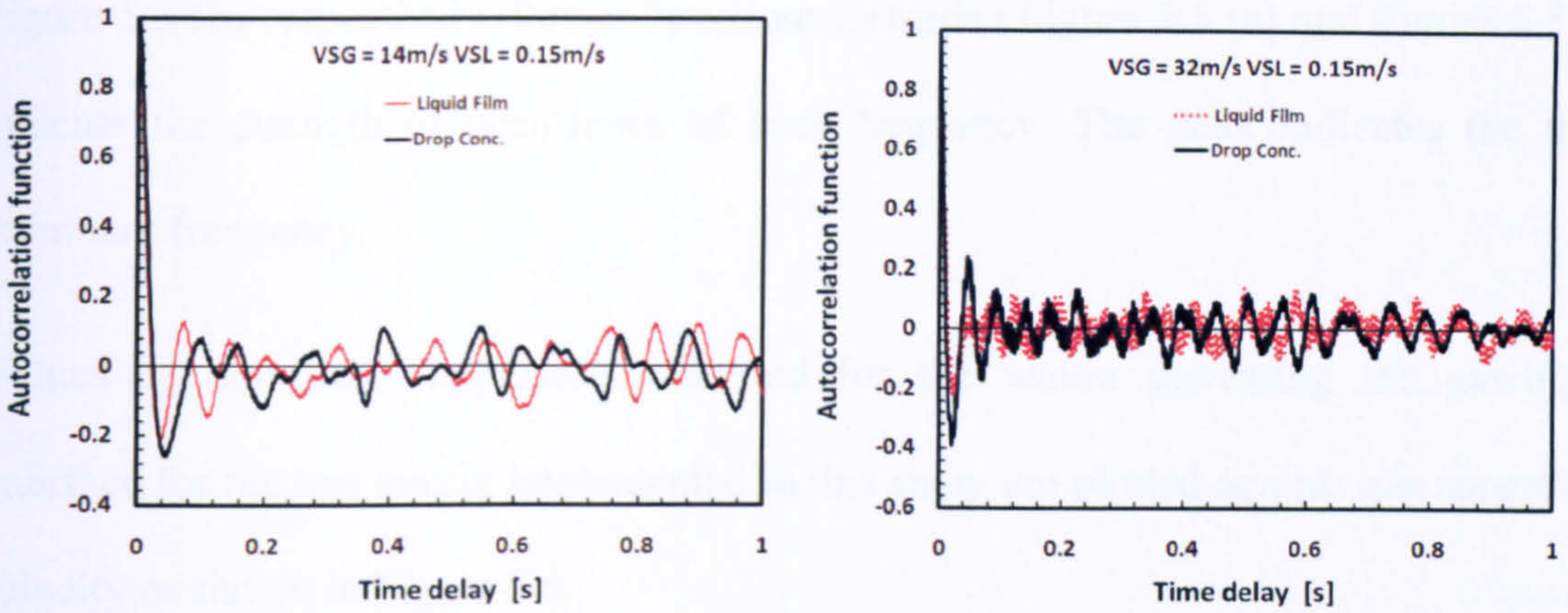

(a): (b)

Figure 5.4 (a): Autocorrelation vs. time delay for huge wave.
Figure 5.4 (b): Autocorrelation vs. time delay for disturbance wave.

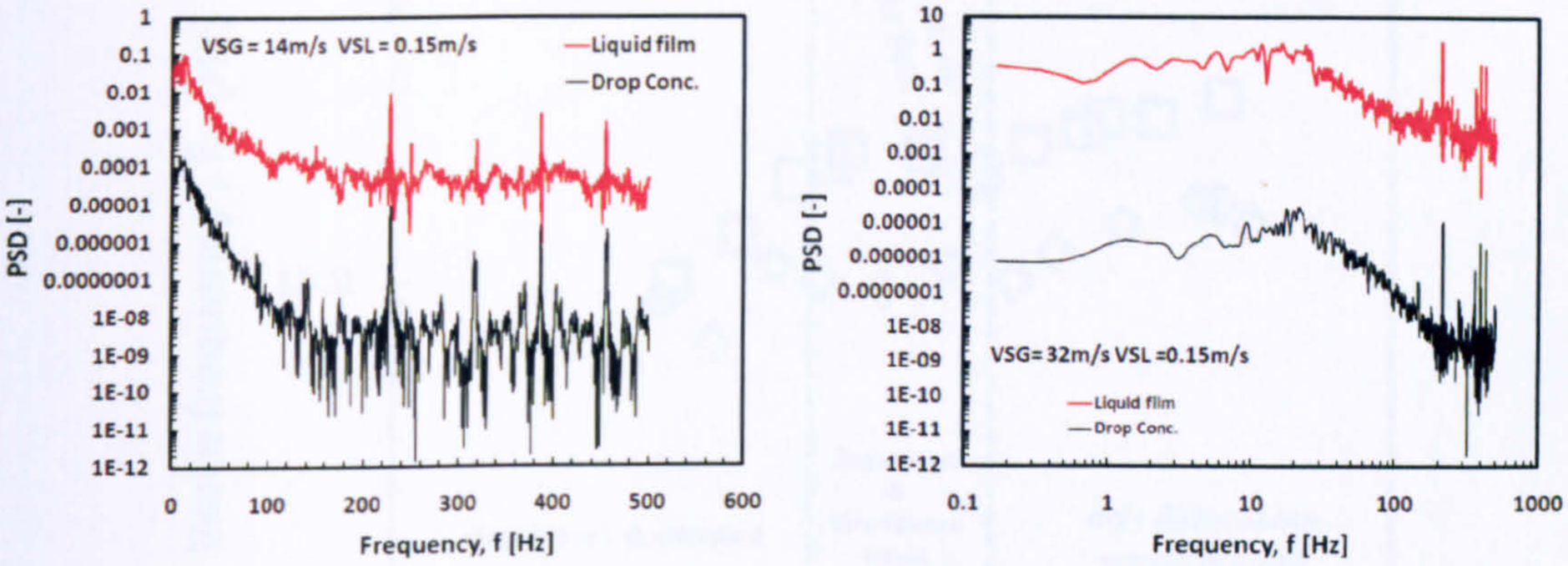

(c) (d)

Figure 5.5 (c): Power Spectrum Density vs. wave frequency for huge wave.
Figure 5.5 (d): Power Spectrum Density vs. wave frequency for disturbance wave.

The data in Figure 5.4 (a) and Figure 5.4 (b) show how the autocorrelation decays with time. There is less correlation at finite time than at time, t = 0 s. The position of a trough after the peak at delay time = 0 s gives the time interval between liquid droplet in the case of time varying drop concentration and time varying film hold-up in the case of disturbance. The inverse of the time delay at the trough indicates approximately half the dominant frequency.

Power Spectrum Densities of these autocorrelations are displayed in Figure 5.5 (a) and Figure 5.5 (b) respectively. Power Spectrum Densities Figure 5.5 (a) and Figure 5.5 (b) indicate the strength of occurrence of each frequency. The peak indicates the most dominant frequency.

Values of dominant frequencies obtained for the waves traversing the gas-liquid interface for the test matrix implemented in this study are plotted against gas superficial velocity as shown in Figure 5.6.

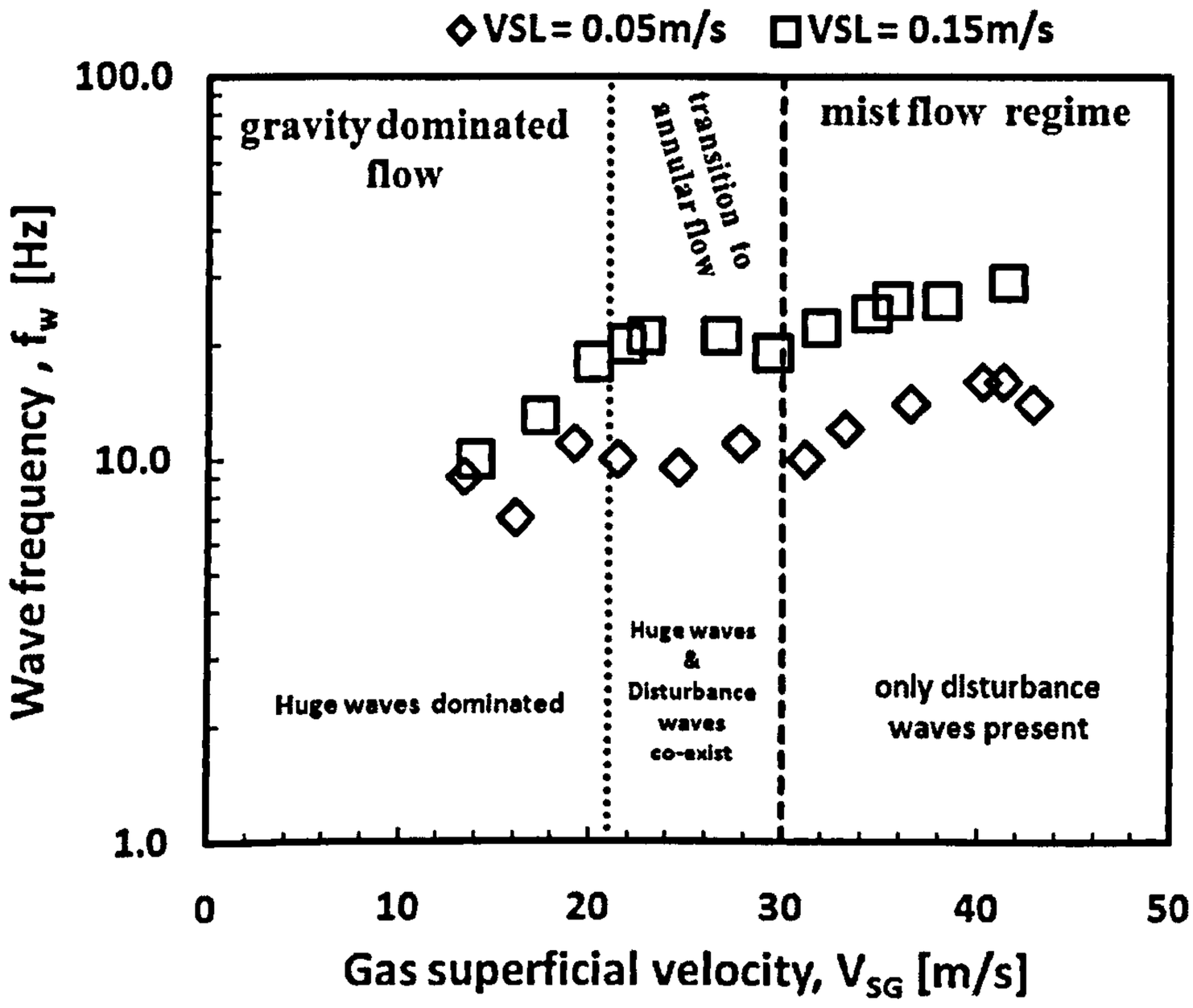

Figure 5.6: Wave frequency as a function of gas superficial velocity.

Observations from Figure 5.6 show that at constant superficial gas velocity, the frequency increases with increase in superficial liquid velocity. The possible reason for this behaviour may be due to the fact that at lower liquid superficial velocity, less energy is required from the gas to keep the waves moving. However, at higher liquid flow rate more energy is required from the energetic gas core to keep the wave in motion.

Therefore, more flow structures are created as a result of the higher momentum transfer which translates to higher structure frequency as observed in Figure 5.6 as liquid superficial velocity increases as in the case of V_{SL} = 0.15 m/s.

Frequency attributes of the wave can be explained further in terms of wave velocity. Wave frequency is directly proportional to wave velocity (i.e. $f = v/\lambda$). Since the wave velocity is also higher as liquid superficial velocity increases, Figure 5.4 (a). Therefore, it is not surprising that frequency is higher as liquid superficial velocity increases. Again, for a fixed gas rate, as liquid flow rate increases more waves occur due to energy creation as a result of exchange and transfer of momentum between the film and the gas core, resulting in higher frequency.

In Figure 5.6 three waves have been identified namely: huge, disturbance and ripple waves. The waves traversing the liquid film interface in annular flow have been classified into two main categories by several researchers Sawant et al. (2008); ripple and disturbance waves (Hewitt and Hall-Taylor, 1970; Azzopardi, 1997).

Ripple waves are relatively small wavelength and small amplitude dynamic waves traveling at much lower velocity compared to the velocity of disturbance waves and gas phase. These waves are also non-coherent and lose their identity after traveling a short distance. On the other hand, disturbance waves are large amplitude kinematic waves and travel at velocity much higher than the velocity of liquid film and ripple waves.

They are coherent and dominate the interfacial transfer of mass, momentum and energy. Disturbance waves also act as a roughness to the central gas flow and contribute to the frictional pressure drop in annular flow.

Ring disturbance waves were identified in this study around $V_{SG} \geq 30$ m/s. The evolution of this wave influences drop size (MMD) distribution at this transition boundary where $V_{SG} = 30$ m/s and beyond. This is because ring disturbance wave appears to dominate and control the creation and dispersion of entrained liquid droplets in the gas phases after $V_{SG} \geq 30$ m/s. If this wave could be thought of as an elastic material then explanation as to why D_{50} of $V_{SL} = 0.15$ m/s is greater than D_{50} of $V_{SL} = 0.05$ m/s can be provided. Then the degree of springiness seems to be higher as the superficial liquid velocity increases at fixed superficial gas velocity. Therefore, more elastic D_{50} of $V_{SL} = 0.15$ m/s tends to offer less resistance to the driving force of the dispersed phase resulting in greater amplitude, greater drop size than in the case of D_{50} of $V_{SL} = 0.05$ m/s which appears to be more rigid.

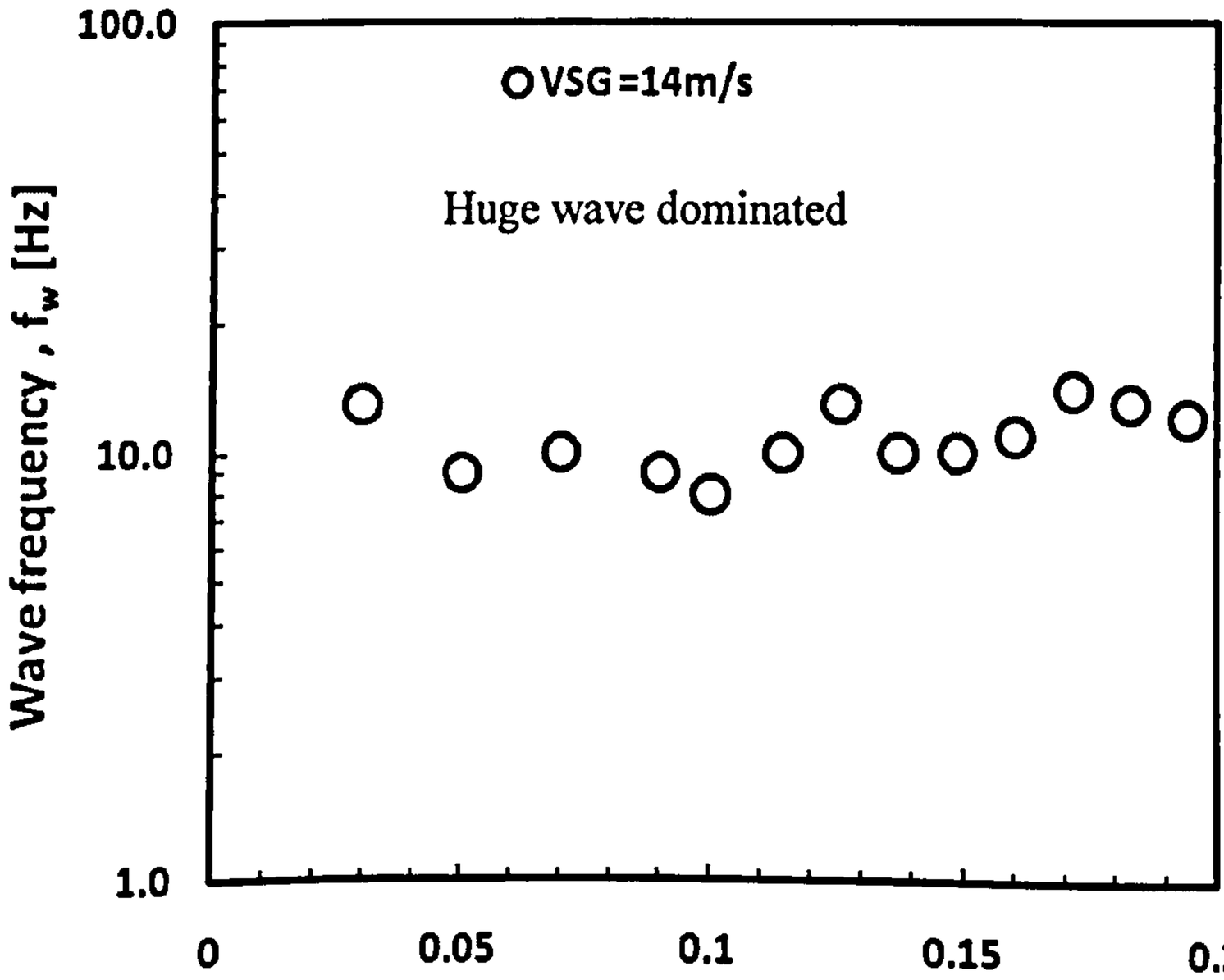

Figure 5.7: Wave frequency as a function liquid superficial velocity.

Figure 5.7 shows fluctuation in wave frequency around 10 Hz. The fluctuation is caused by chaotic nature of the liquid film. The Figure gives an indication that wave frequency is a strong function superficial gas velocity. The wave frequency remains constant because gas flow rate is fixed.

The liquid film is covered by huge wave and the entrained fraction is less than 0.05. Wave frequency reaches a maximum and then drops as liquid superficial velocity increases from 0.03 to 0.20 m/s. This is an attribute of huge wave with frequency attaining a maximum and then drops as the wave propagates. Huge waves are characterized by large amplitude waves as shown on Figure 5.8 and hence high energy. In this case, wave amplitude reduces as liquid flow rate increases at nearly similar gas mass flux, Figure 5.9.

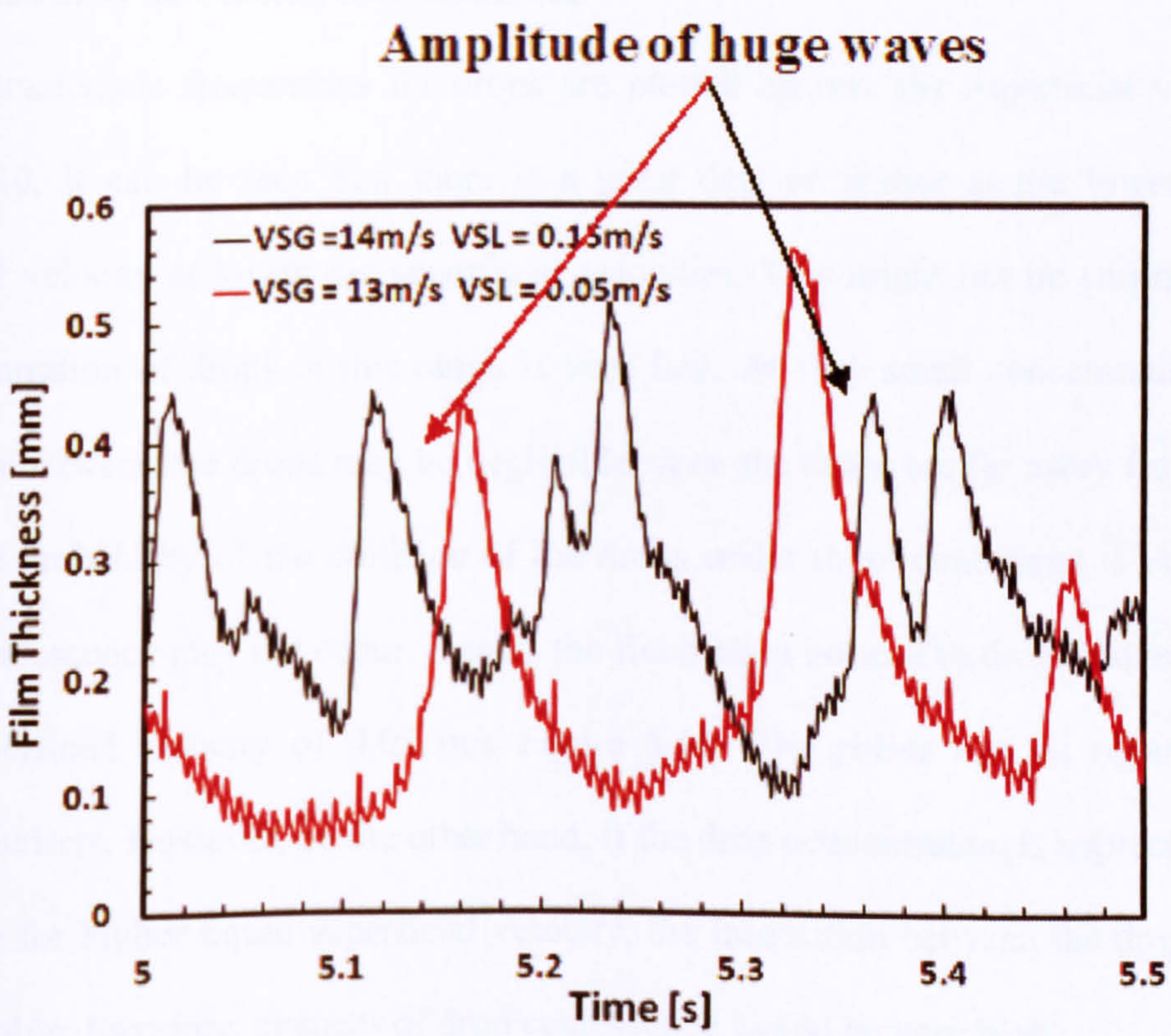

Figure 5.8: Time averaged film thickness characteristic of huge waves.

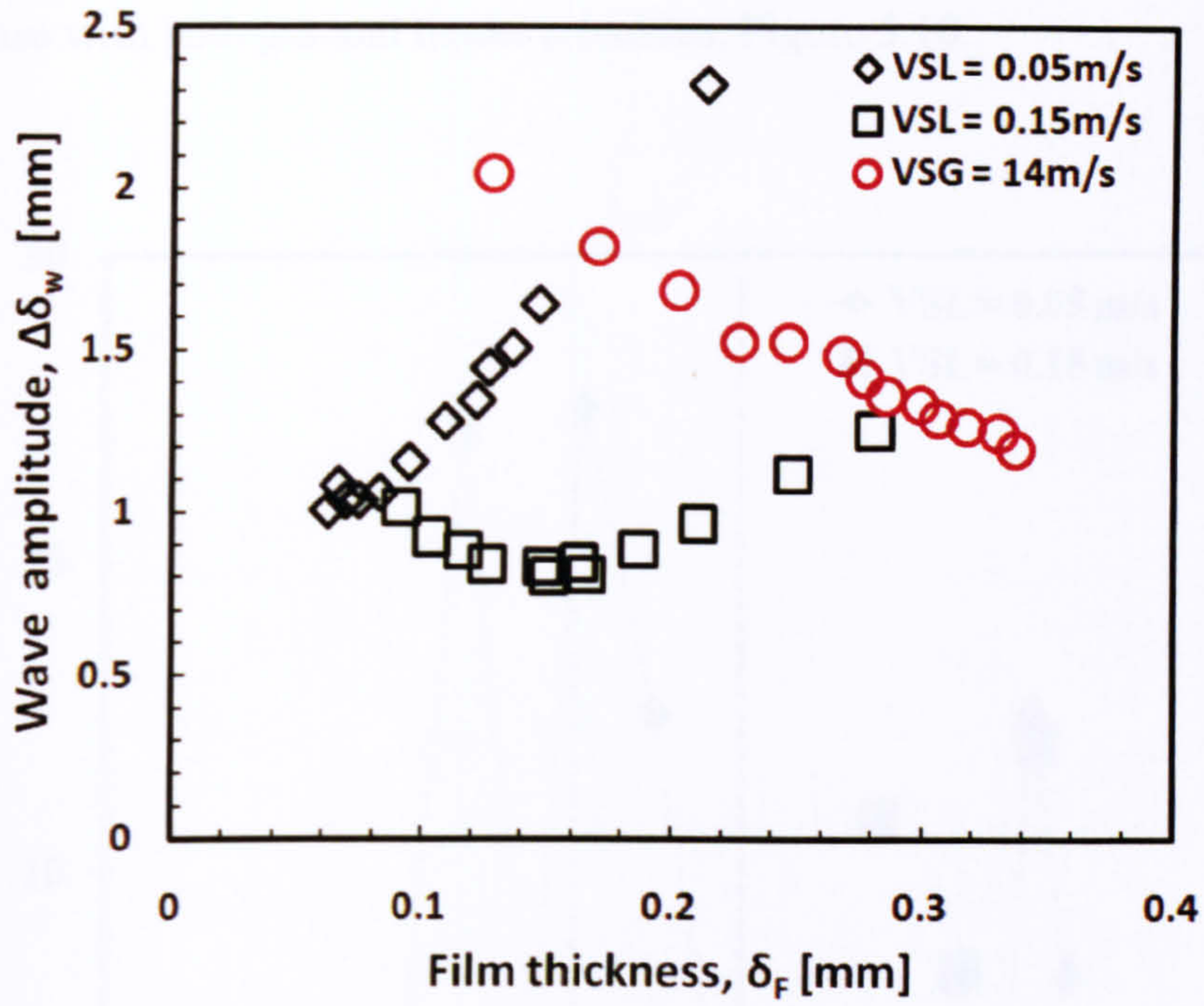

Figure 5.9: Wave amplitude–Film thickness relationship. Superficial gas velocity increases towards decreasing film thickness.

If the characteristic frequencies for drops are plotted against gas superficial velocity, Figure 5.10, it can be seen that there is a great deal of scatter at the lower liquid superficial velocity at lower gas superficial velocities. This might not be surprising as the concentration of drops in this range is very low. At very small concentrations the interaction between the drops may be negligible since the drops are far away from each other. The probability of the collision of the drops under these conditions is very low and the coalescence may not occur. Hence, the fluctuation noticed in drop frequency for liquid superficial velocity of 0.05 m/s Figure 5.10. The points can be regarded as potential outliers. However, on the other hand, if the drop concentration is appreciable as in the case for higher liquid superficial velocity, the interaction between the drops may be appreciable; therefore, chances of drop coalescence would be very high.

Nevertheless, the characteristic frequencies of the fluctuations in drop concentration are seen to increase with both gas and liquid velocities, Figure 5.10.

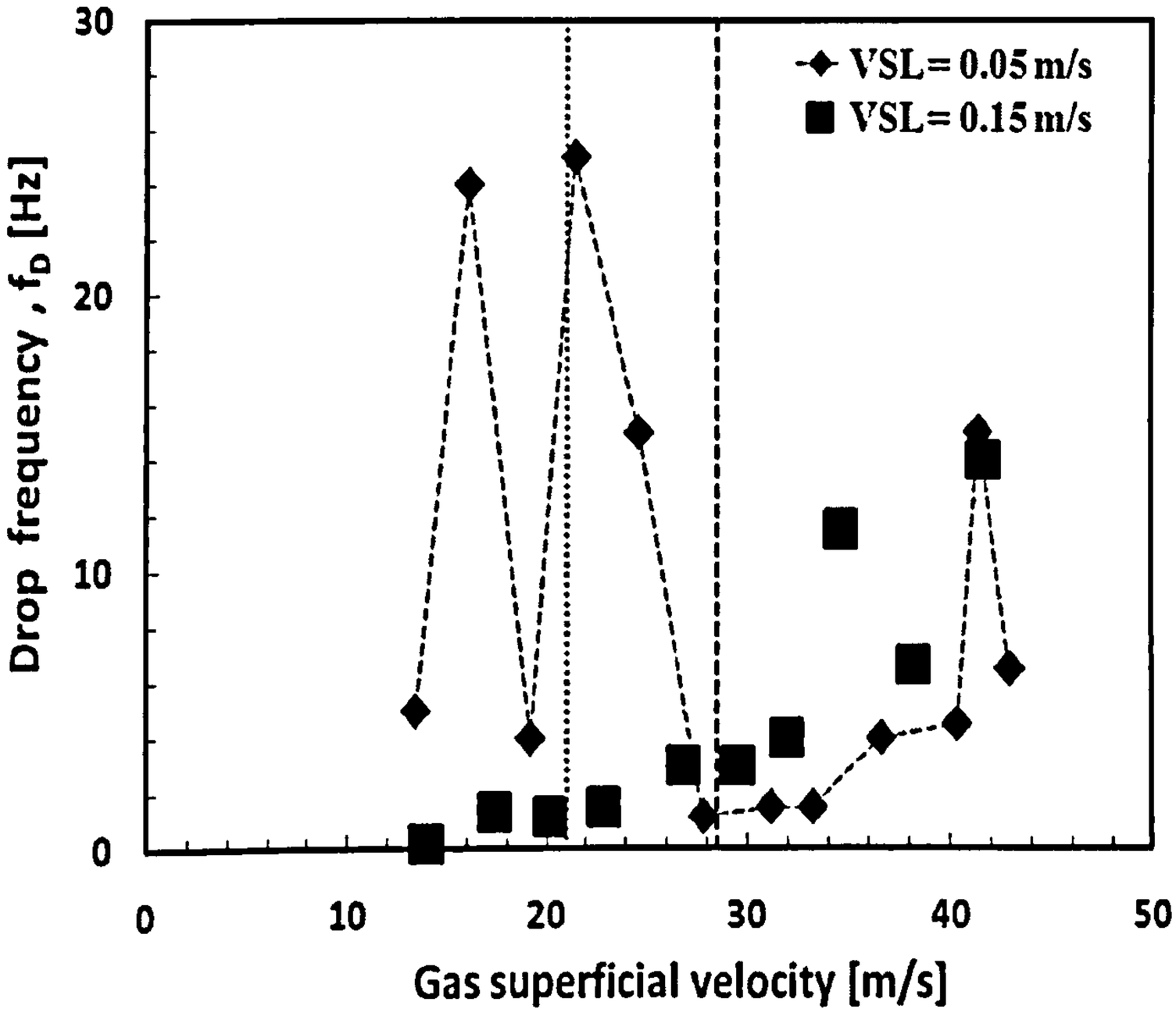

Figure 5.10: Effect of gas superficial velocity on drop frequency.

Referring to the wave frequency values extracted from the film hold-up data, Figure 5.6, it is more obvious that this frequency is that of disturbance waves travelling on the film surface. Again, this wave frequency increases with increase in both gas and liquid superficial velocities.

Plotting drop frequency and wave frequencies as a function of gas and liquid superficial velocities as in Figure 5.11, it is seen that the wave frequencies are higher than the drop frequencies in most cases. This ties in with the limited prior datum reported by

Azzopardi and Whalley (1980 a). Howe ver, at some low drop concentrations drop frequencies are seen to be higher than their corresponding wave frequencies. Generally, one would expect that in every atomization event, that the drop concentration frequency would be greater than the disturbance wave frequency.

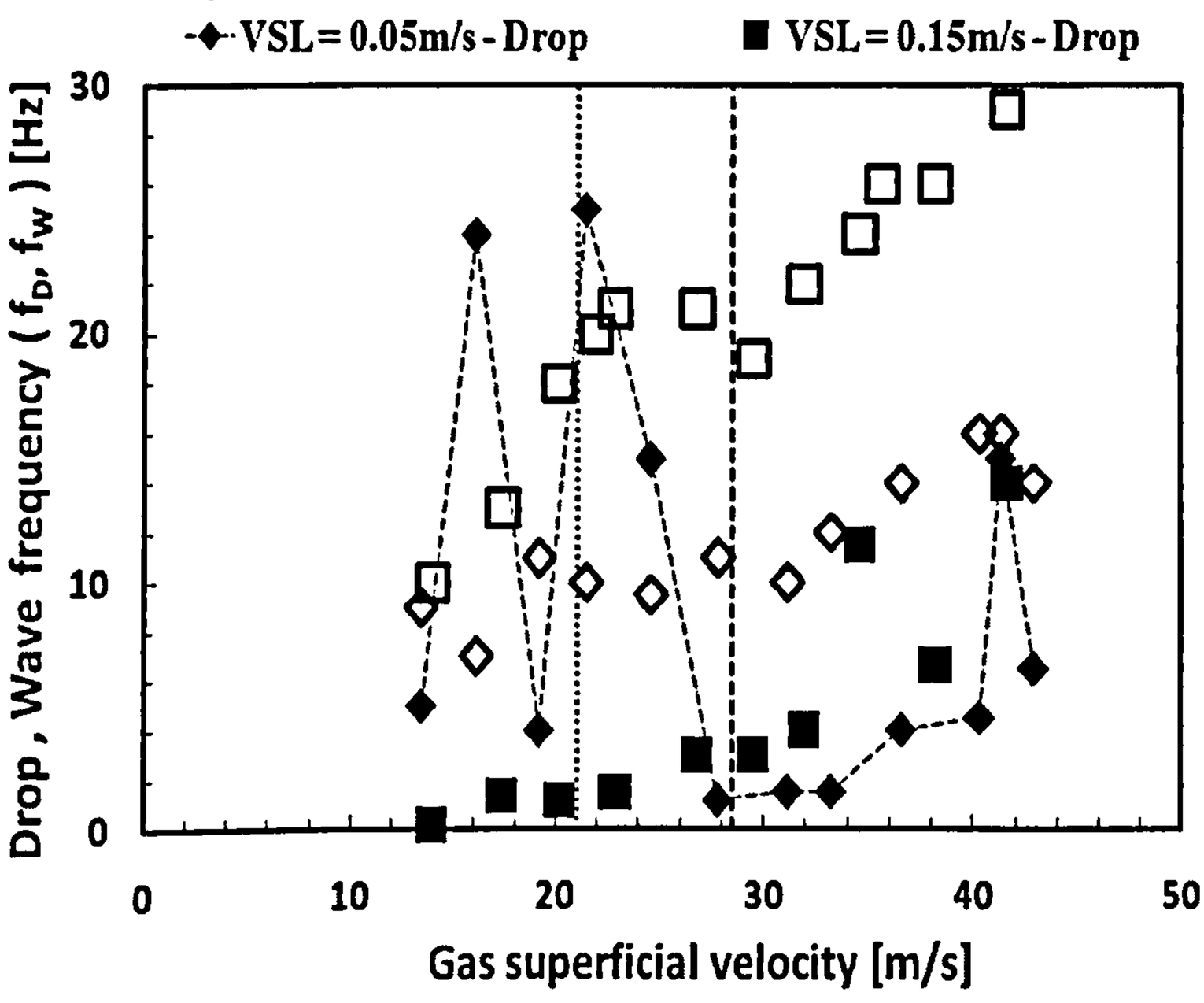

Figure 5.11: Effect of gas and liquid superficial velocities on the frequencies of disturbance waves on the film interface.

That the frequency of fluctuations in drop concentration, f_D, is less than the frequency of disturbance waves, f_W, is surprising as one would expect the contrary. Examination of high speed cine/video footage taken looking axially down the pipe would lead one to expect several drop creation events per wave, i.e., $f_D > f_W$. A possible explanation for the lower than expected frequency of drops is that drops from one atomization event become diffused into those from other events as they pass along the pipe. Each event probably

produces a distribution of sizes. Small drops are accelerated more rapidly and so arrive at the measuring position earlier that the larger drops that are harder to accelerate. Therefore, the faster drops could catch up with slower drops from a previous event and then undergo coalescence in a different event to form new drops. It is also possible that there is dynamic equilibrium between drop formation and coalescence.

It is noted that there is another type of event which might be being picked up in the frequency analysis. It had been reported by Hall Taylor et al. (1963), Hall Taylor and Nedderman (1968), Wilkes et al. (1983) that the frequency of disturbance waves falls from an initially high value to a lower one higher up the vertical pipe. This was attributed to the meeting and merging of waves. Though the waves had a characteristic (mean) velocity, there was a distribution about this mean and faster waves could catch up with slower waves in front of them. The combined wave would be much bigger than normal and so more likely to be broken up to create drops. Wilkes et al. (1983) estimated that the amount of entrainment from these wave coalescence events could be half the total entrainment. Perhaps it is the frequency of coalescence events that is being reported as drop concentration frequency, f_D.

5.3 Drop size and Drop Frequency

Comparison of drop size and drop frequency curves is presented in Figure 5.11 (b). The Figure shows drop concentration is directly proportional to the drop frequency. This is another interesting observation because the two data being compared were logged by

different instrument. The collision frequency increases with the increasing drop concentration and dissipation energies.

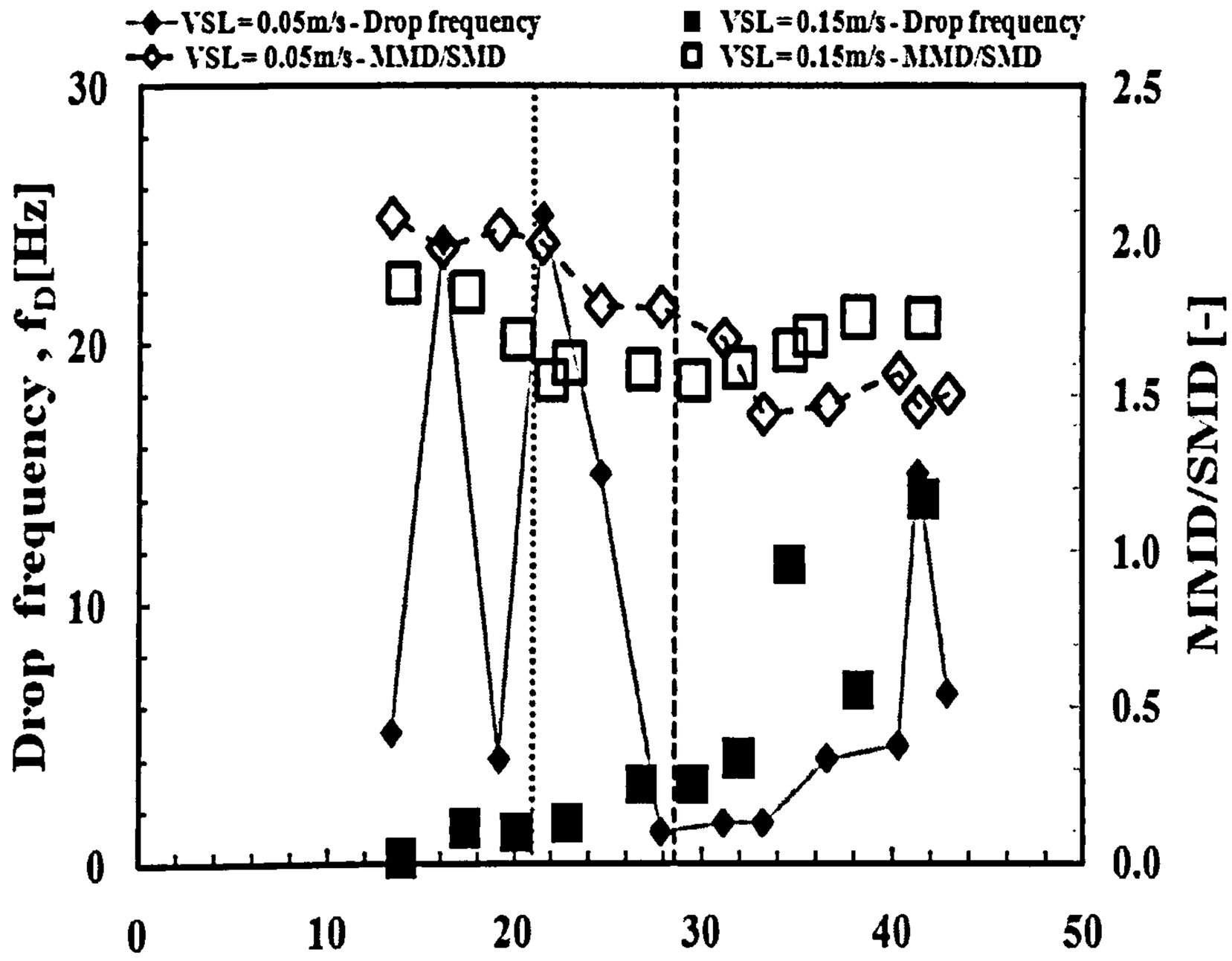

Figure 5.12: Similarity between drop frequency and drop size distribution.

5.4 Wave and Drop Frequency Correlation

The frequency of the disturbance wave in annular flow like any other periodic structures in bubbly and slug flows can be correlated in terms of Strouhal number because of the similarities between the flow patterns. Unlike the characteristic frequencies of the fluctuations in drop concentration, there is a significant data base of the frequencies of disturbance waves, Azzopardi (1997, 2006). It has been shown that data from a number of very different fluid pairs – helium/water, steam water at 70 bar as well as air/water – are well correlated by use of a dimensionless frequency. The Strouhal number (frequency times pipe

diameter divided by the liquid superficial velocity) has been found to be inversely proportional to the Lockhart-Martinelli parameter. This implies that the frequency is directly proportional to the gas superficial velocity but that the effect of liquid superficial velocity is a minor effect. Data from the present experiments, when plotted in this matter shows the self-same trend.

Strouhal number is a dimensionless number given by:

$$St_L = \frac{f_w d}{V_{SL}} \tag{5.4}$$

Azzopardi (2004) showed that bubbly and slug flow regime frequency data could be correlated using Strouhal number and Lockhart-Martinelli parameter. Because of the analogous behavior of the flow structures between annular, slug and bubbly flows, Strouhal number and Lockhart-Martinelli parameter are utilized to correlate frequency data of the present study as shown in Figure 5.13 (a) for wave frequency and Figure 5.13 (b) for wave and drop frequencies respectively.

An empirical correlation for wave frequency in terms of Strouhal number was generated by curve-fitting based on the present data. The correlation shows that Strouhal number decays with Lockhart-Martinelli parameter. However, a better correlation was obtained when the liquid based Strouhal number was plotted against Lockhart-Martinelli parameter on a log-log chart as suggested by Azzopardi (2004). The data displayed in Figure 5.13 (a) shows a linear relationship with negative slope. The best fit obtained

followed a power law. The resulting correlation is given by the expression by Equation 5.5 as follows:

$$St_L = 0.4292 \quad X^{-0.908} \tag{5.5}$$

Where:

$$St = \frac{f_w d}{V_{SL}}, [-]; \quad X = \left[\frac{\rho_L v_{SL}^2}{\rho_G v_{SG}^2}\right]^{0.5}, [-]$$

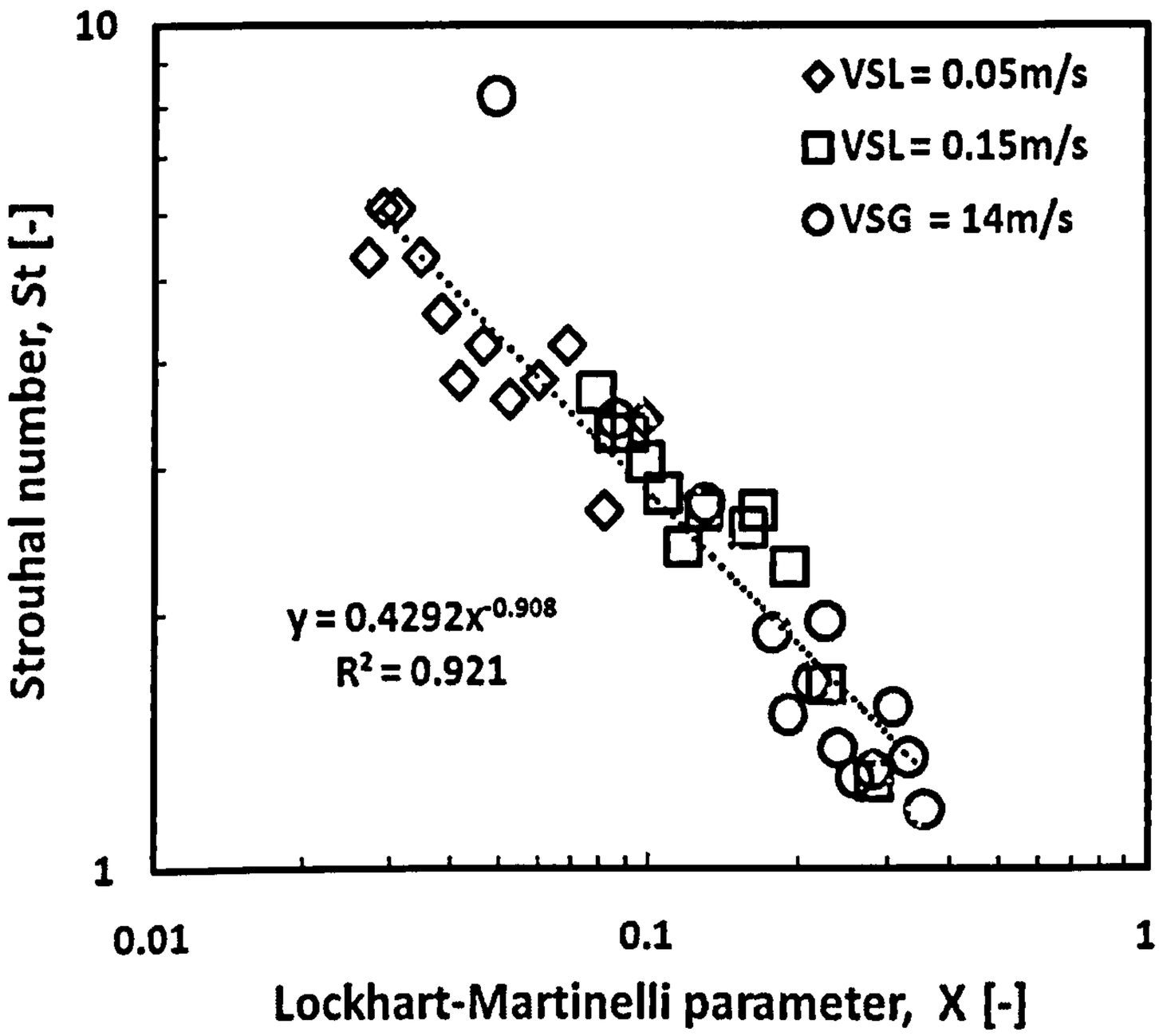

Figure 5.13 (a) : Relationship between the dimensionless wave frequency and the Lockhart-Martinelli parameter (the square root of the ratio of the superficial momentum fluxes of liquid and gas).

Correlating drop frequency data using the same approach as above produces a poor correlation, Figure 5.13 (b). The data shows a great deal of scatter which suggests the

inadequacy of the Strouhal number and Lockhart-Martinelli parameter in correlation drop frequency.

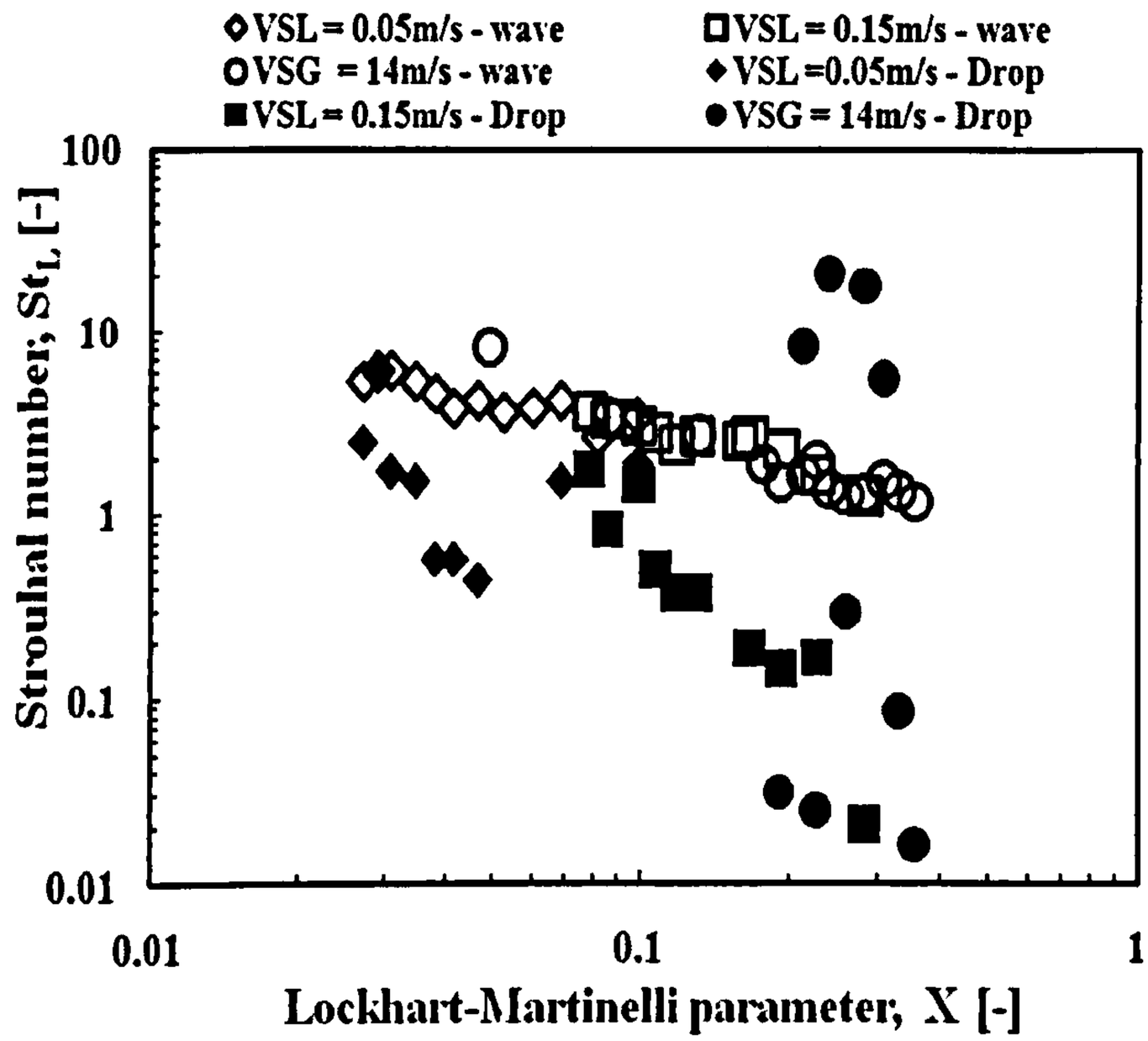

Figure 5.13 (b): Relationship between the dimensionless wave frequency and the Lockhart-Martinelli parameter (the square root of the ratio of the superficial momentum fluxes of liquid and gas).

The trend observed in Figure 5.13 (a) is similar to the trend reported by Kaji (2008) and Mantilla (2008) in Figure 5.14(a) and Figure 5.14(b) respectively. Both correlated wave frequency using liquid based Strouhal number. Kaji used same flow facility as used in this study. Kaji did not carry out drop size measurement.

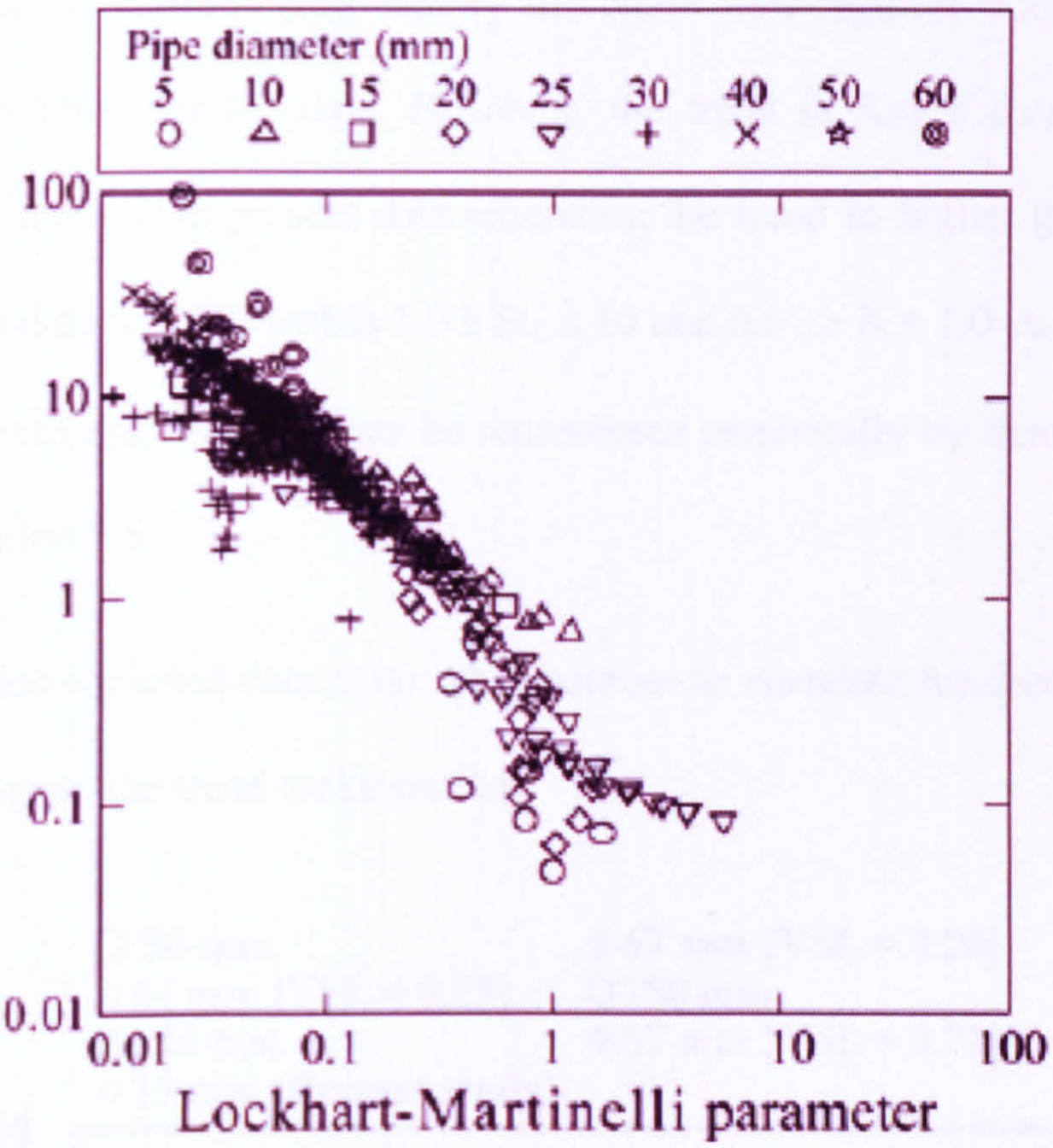

Figure 5.14 (a): Correlation of Strouhal number with Lockhart-Martinelli parameter, Kaji (2008).

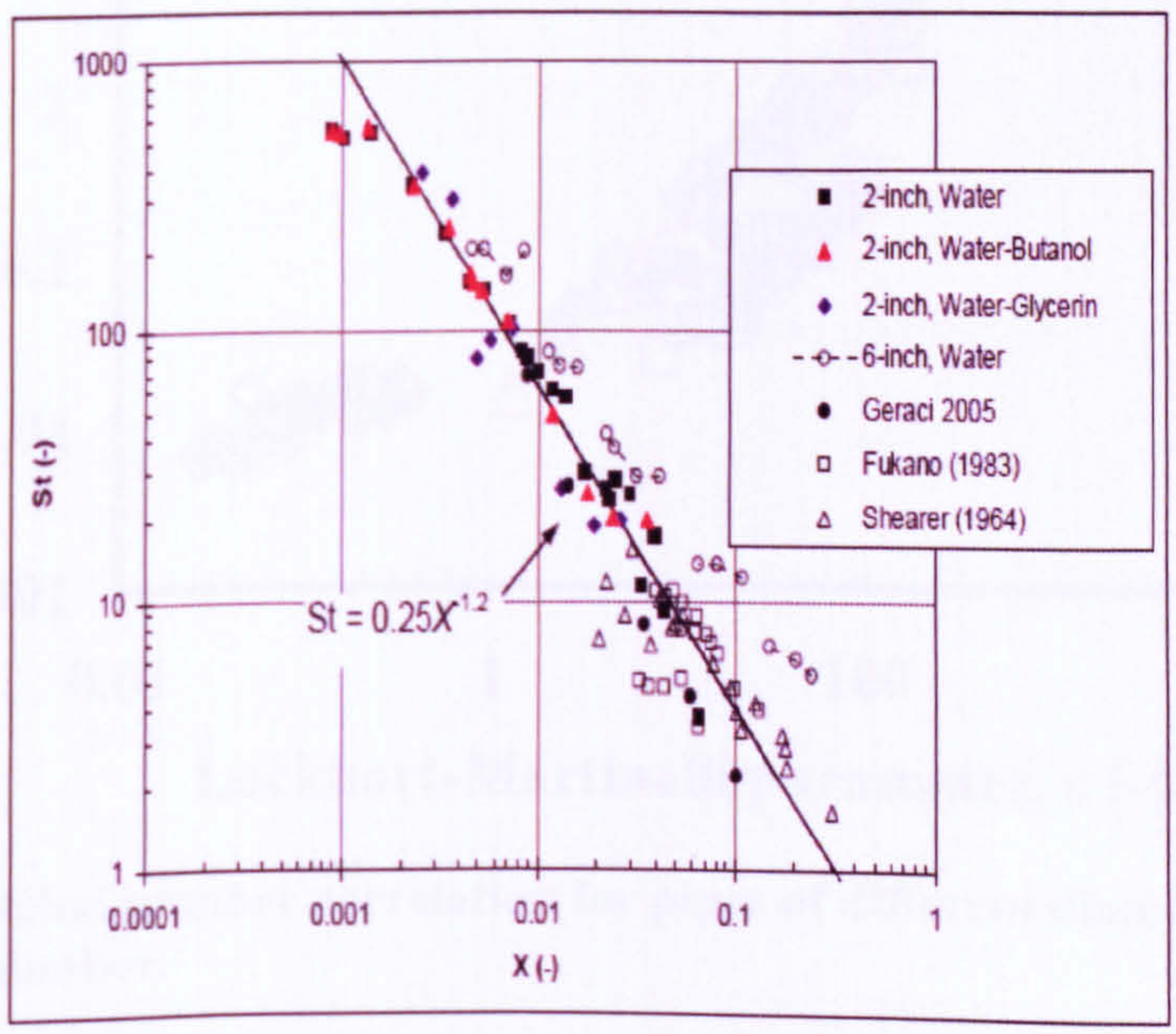

Figure 5.14 (b): Correlation of Strouhal number with Lockhart-Martinelli parameter, Mantilla (2008).

Kaji's data was mostly taken in slug, bubbly and churn flow regimes. Kaji did not give an empirical correlation for his data. However, the trend in Kaji's data and that of present study is similar with present data extending the trend to higher gas superficial velocities. Present data will fall within $1.0 \geq St_L \leq 10$ and $0.01 \geq X \leq 1.0$ on Kaji's line in Figure 5.14(a). Therefore, both data can be represented empirically by same Equation as proposed by Equation 5.5.

Mantilla (2008) also included data from other sources to correlate his data as shown in Figure 5.14 (b). Again, the trend looks similar.

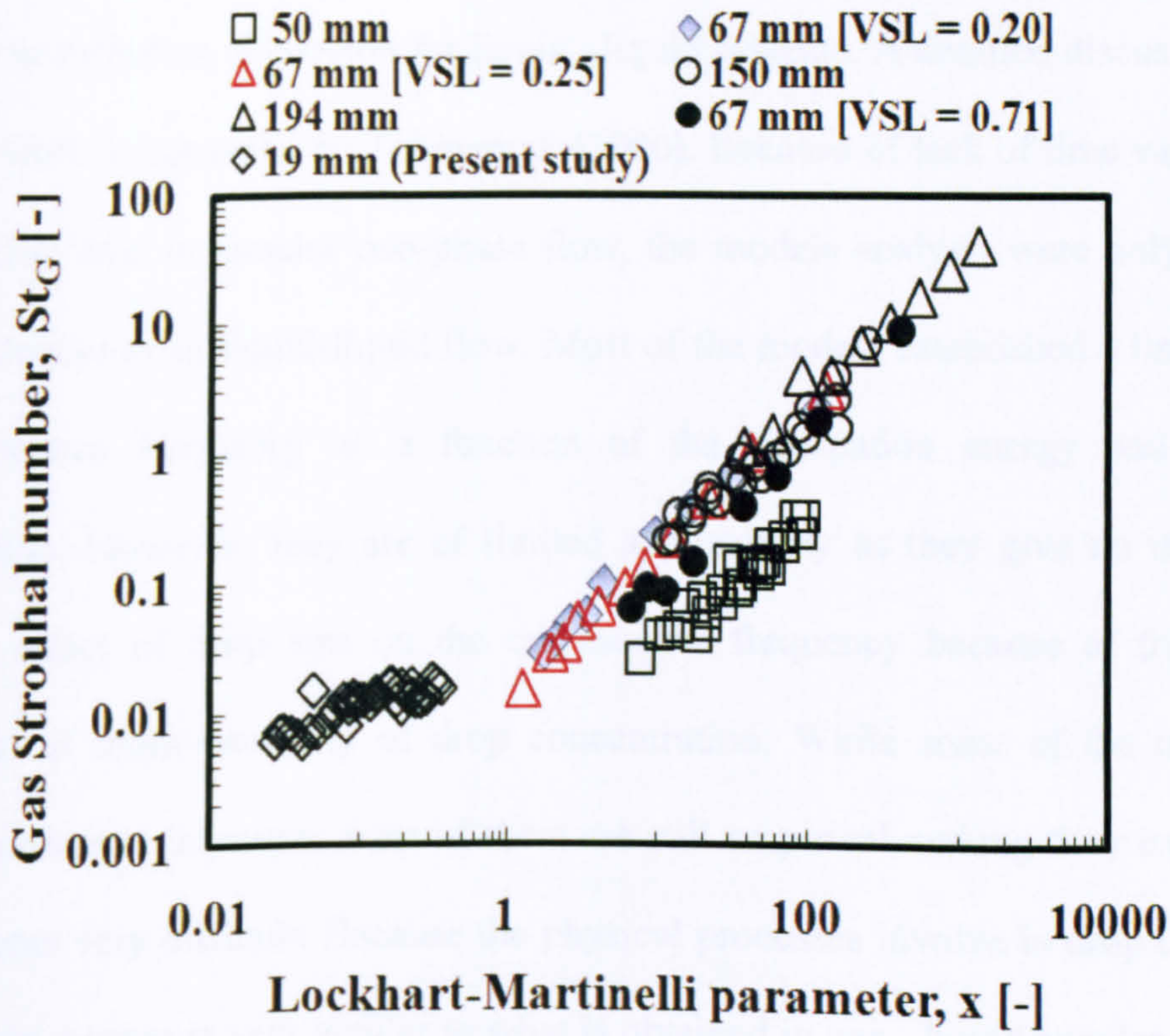

Figure 5.15: Strouhal number correlation for pipes of different diameter using gas based Strouhal number.

A different trend is observed when gas based Strouhal number is used to correlate frequency information as reported by Azzopardi et al. (2008) in Figure 5.15. This shows

Strouhal number to increase linearly with increase in Lockhart-Martinelli parameter. The present data agrees very well other data from different pipe diameter as shown in Figure 5.15.

5.5 Drop Collision Frequency

Liquid drops entrained in the gas core in annular two-phase flow are transported usually by turbulent or molecular diffusion. In general, drop collision occurs when the scale of turbulence exceeds the kolmogorov scale of turbulence which is observed in fully developed flow.

Several models have been proposed for estimating the coalescence rate and collision frequency in turbulent dispersion for liquid –liquid systems. A detailed discussion of the models is well documented by Tobin et al. (1990). Because of lack of time varying drop concentration data in annular two-phase flow, the models analysis were only based on collision frequency in liquid-liquid flow. Most of the models established a link between the coalescence frequency as a function of the dissipation energy and the drop concentration. However, they are of limited applicability as they give no information about the effect of drop size on the coalescence frequency because of the inherent assumption of mono-modality of drop concentration. While some of the models are purely mechanistic in nature, a lot of them are still empirical making their extension to other systems very difficult. Because the physical processes involve in drop collision in liquid–liquid system is very similar to what is obtained in gas - liquid annular two-phase flow same ideas and principles followed in their derivations will be extended to determine collision frequency in annular two-phase flow.

These models derive their names from collision theory on which they were built, namely constant efficiency, dynamic deformation, static deformation and kinetic theories. Thus the theories are summarized in the subsequent discussions.

The constant efficiency model was derived by considering the collision frequency between drops in a turbulent flow field in a manner analogous to that used to derive kinetic theory of gases, Delichatsios and Probstein, (1975). Writing the collision frequency as the product of the collision cross section and the root mean square relative velocity fluctuations. In order to facilitate the final expression of the model, assumption has to be made that a constant fraction of all collisions result in drop coalescence, the constant efficiency expression. From this view of coalescence the coalescence frequency may be written as the product of collision frequency and a coalescence efficiency or probability.

Based on dynamic and static deformation theories, two different models were derived. First, when the inertia of the colliding drops is neglected and the characteristic time of turbulent force fluctuations is much smaller than the drop deformation, the deformation of the drops may be determined an average turbulence force squeezing the drops. This average force given by the product of pressure fluctuations across the drop pair and the projected area of the drops is assumed positive because of the absence of turbulence between the contacting drops. The resulting model, referred to as the static deformation model, predicts an increase in the coalescence efficiency with increasing drop size. On the other hand if the drop shapes respond to every fluctuation in the field, their deformation is determined by the instantaneous force squeezing the drop pair. This gives rise to the model referred to as the dynamic deformation model, which predicts a

decrease in the coalescence probability with increasing drop size.

In violent collisions, the inertia of the drops is the governing factor and the effectiveness of the collision depends on the adequacy of the collision kinetic energy to accomplish film drainage work. By performing a dimensional analysis on this process one may arrive at the fourth coalescence expression, termed kinetic collision model. This model yields a drop size dependence of coalescence frequency similar to static deformation model, though it was obtained from a very different form of analysis.

The frequencies derived from the kinetic collision model and the static deformation model, which show very similar drop size dependence, predict the evolving transients best. These frequencies are in particular, able to track the drift in the peak of the drop size distribution and also at least qualitatively reproduce the bimodal feature of the spectra in their experiment study. The coalescence frequency expression derived from the dynamic deformation model predicts opposite trends in the displacement of the peak and fails to predict the bimodality in the experiment. The quantitative agreement is also poor. Interestingly, the coalescence frequency function obtained by assuming the coalescence efficiency to be a constant (collision frequency) predicts the transients satisfactorily although not as well as the frequencies from the kinetic collision and the static deformation models. This is explained from the fact that the latter models predict an efficiency of nearly unity for the larger drops. In other words, these models reduce to the constant efficiency model for the larger drops. These results show that the coalescence efficiency as well as the coalescence frequency is increasing functions of the drop sizes for the situations considered. The transient coalescence experiments

indicate that the coalescence frequency is an increasing function of the drop pair sizes.

Recently, a more pragmatic approach has been sought to model collision frequency in turbulent two-phase flow. Ceylan et al. (2003) derived a mechanistic model drops undergoing coalescence in a collision field , Figure 8. The authors utilized 1-D diffusivity Equations in radial coordinate with inclusion of eddy diffusion coefficient to describe the flow. The turbulent diffusion coefficient of the medium is related to the characteristics of flow and therefore, it may be stated in terms of the micro scale of the turbulence which is different for both turbulent and molecular diffusion. Empirical constant was introduced to facilitate description of turbulent coefficient in terms of scale of turbulence with a tacit assumption that drops are equally sized.

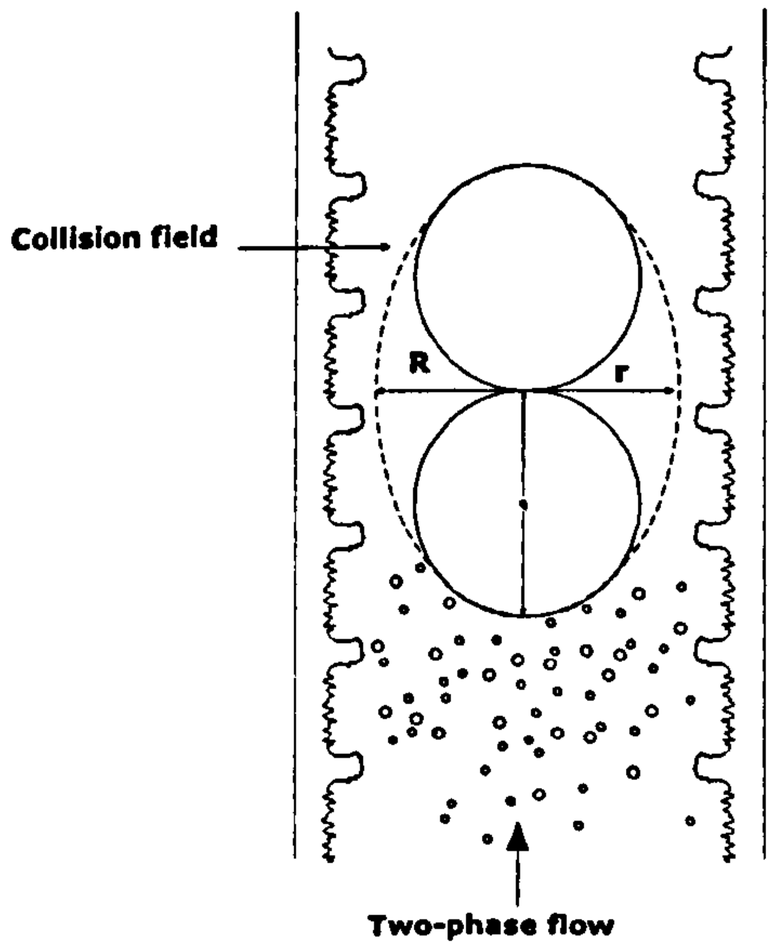

Figure 5.16: Collision field and coalescence of drops in annular two-phase flow.

The final Equation is time dependent, therefore can provide solution to transient drop size distribution in two-phase flow. For fully developed turbulent flow Ceylan proposed the following equation to determine collision frequency in turbulent dispersion:

$$\omega = 16\,\varphi_o\,\mu_R\,\alpha\left(\frac{\varepsilon_R}{a^2}\right)^{1/3} \tag{5.6}$$

Where:

ω = collision frequency, Hz

φ_o = drop concentration, -

μ_R = transport degree of particles by turbulent flow ($0 < \mu_R \leq 1.0$), -

α = empirical constant, -

a = drop size, m

ε_R = turbulent dissipation rate, m^2/S^3

The tuning parameter in Equation (5.6) is $\mu_R\alpha$ which was empirically determined to be 0.72. When this value is used in Equation (5.6), the value of collision frequency was over-estimated. However, the best match was achieved when the tuning parameter, $\mu_R\alpha$ = 0.1875. Substituting this value into Equation (5.6) produces expression below:

$$\omega = 3.0\,\varphi_o\left(\frac{\varepsilon_R}{a^2}\right)^{1/3} \tag{5.7}$$

The coefficient becomes 3.0 from original value of 11.52. Figure 5.17 presents the comparisons of results for the collision frequency model Equation (5.7) and the measured drop frequency. The drop measurement and the range of the prediction of the model. Good agreement is observed. The range of prediction of the improved model and that from the experiment also agrees very well.

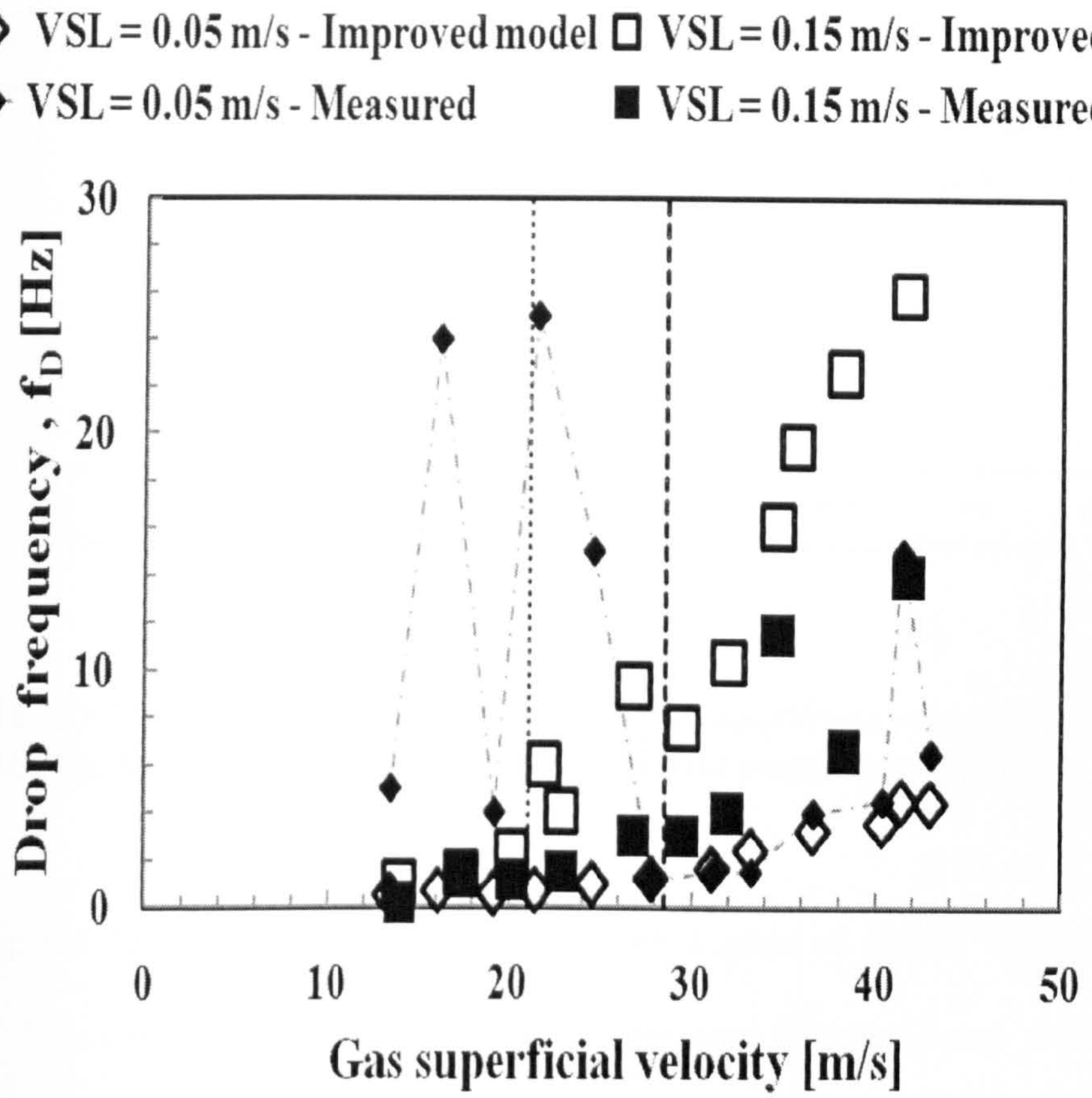

Figure 5.17: Comparison of experimental drop frequency with modal drop and wave frequency.

5.6 Wave velocity

Velocities of periodic structures in annular flow have been determined from analysis of time series data. In this study wave velocity was determined from cross-sectionally averaged, time-resolved void fraction. When any two signals from the probes are cross-correlated transit time and hence wave velocity can be obtained taking into account separation distance between the two probes. The separating distance between the sensors was 50mm in this study. Figure 5.18 (a) and Figure 5.18 (b) show how gas and liquid superficial velocities respectively. As can be seen wave velocity increases as gas and liquid superficial velocities increase.

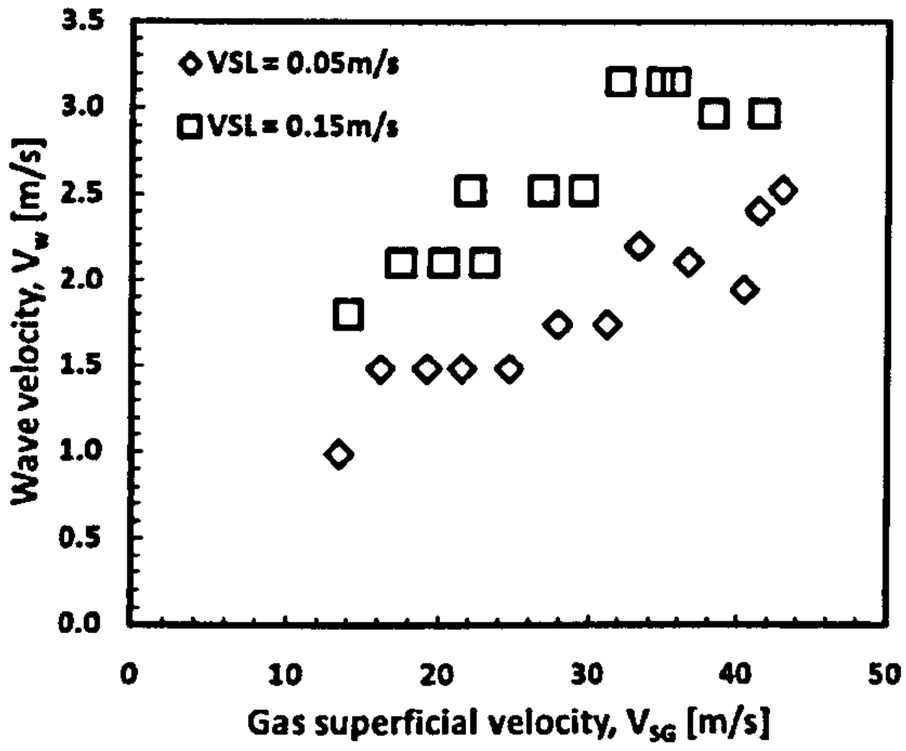

(a)

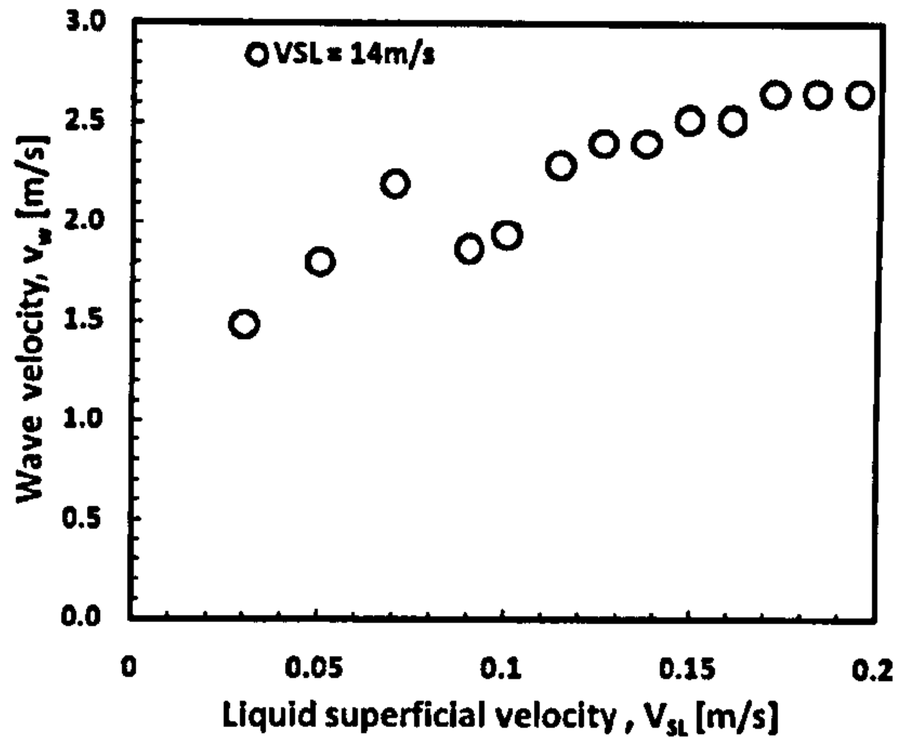

(b)

Figure 5.18 (a): Wave velocity variation with gas superficial velocity.
Figure 5.18 (b): Wave velocity variation with liquid superficial velocity.

It is observed that the wave velocity becomes higher as liquid superficial velocity increases. This can be as explained in terms of gas core density Figure 5.19. A lower gas density decreases the momentum and energy of the gas being transferred to the liquid film thus generating a lower velocity wave.

It has also been observed that wave velocity changes around the transition boundaries. While it is very obvious around V_{SG} = 30 m/s, the change in velocity gradient is not clear around V_{SG} = 21 m/s.

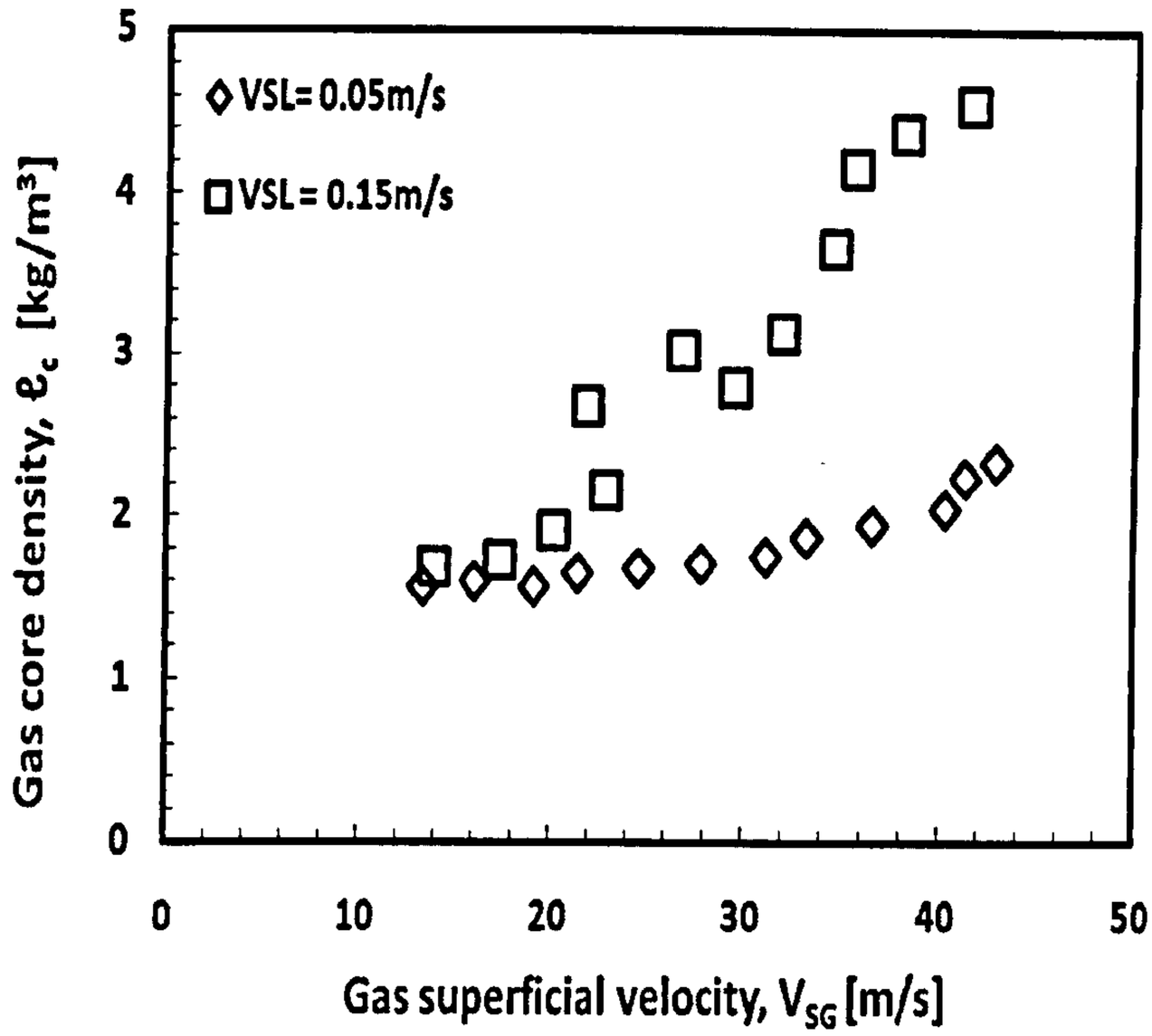

Figure 5.19: Effect of gas and liquid superficial velocities on gas core density.

5.7 Wave velocity prediction

Disturbance wave models have been used to predict the measured wave velocity. The popular Pearce et al. (1979) and Kumar et al. (2002) correlations have been used to predict disturbance or huge wave velocity for the inlet conditions tested. Pearce et al. (1979) wave velocity correlation is given by the following expression:

$$V_w = \frac{KV_F + V_{SG}\sqrt{\rho_G/\rho_L}}{K + \sqrt{\rho_G/\rho_L}} \tag{5.8}$$

Where:

$$V_F = \frac{D\,\dot{m}_L(1 - E_F)}{4\,\rho_L\,\delta_F} \tag{5.9}$$

Measured film velocity is expressed as:

$$V_{Fmeasured} = \frac{V_{SL}\ D\ (1 - E_F)}{4\ \delta_F} \tag{5.10}$$

Kumar et al. (2002) model is expressed by the following expression:

$$V_w = \frac{CV_{SG} + V_{SL}}{1 + C} \tag{5.11}$$

where:
$$C = \sqrt{\frac{\rho_G}{\rho_L}\frac{c_{L_{i/g}}}{c_{L_{i/l}}}} \tag{5.12}$$

Results obtained are shown in Figure 5.20 (a) and Figure 5.20 (b) for the two cases investigated.

Pearce (1979) model shows superiority to Kumar et al. (2002) in the first set of experimental campaign. Pearce (1979) model gives maximum relative error of +14.79 % and a minimum of -40.90 % for K = 0.30. Kumar's model on the other hand predicted the wave velocity with maximum relative error of +68.52% and a minimum of -23.92 % for the cases of V_{SL} = 0.05 m/s and V_{SL} = 0.15 m/s respectively.

In the case of V_{SG} = 14 m/s, Pearce (1979) predicted huge wave velocity within relative error range of +5 % with K = 0.65. It is not surprising that K is very high in this case. Pearce coefficient, K, is a function of wave amplitude and amplitude of huge wave being larger than that of regular disturbance wave. This is another proof that in the case of V_{SG} = 14 m/s the gas-liquid interface is dominated by huge wave.

Kumar model produces +79.13 % maximum relative error and +71.12 % minimum relative error in the case of V_{SG} = 14 m/s.

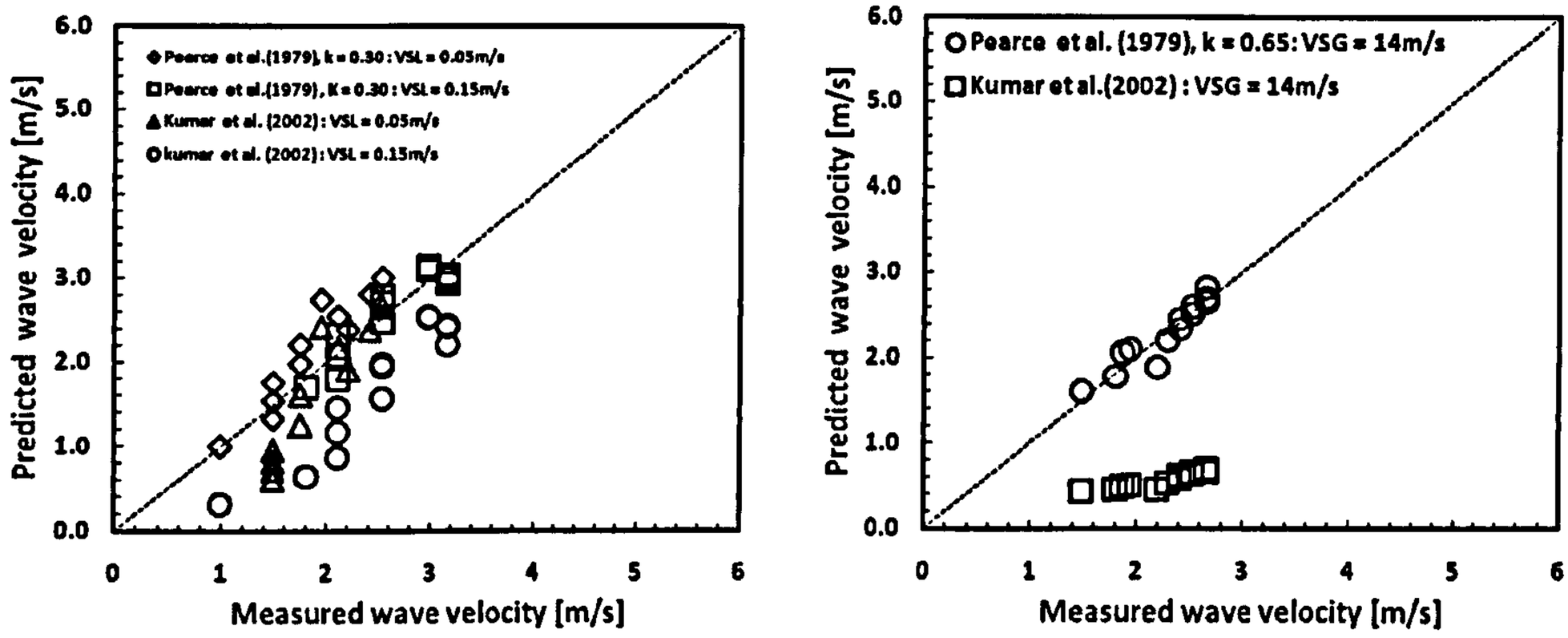

(a) **(b)**

Figure 5.20: (a) Prediction of wave velocity by various models.
Figure 5.20: (b) Prediction of wave velocity by various model V_{SG} = 14 m/s.

It can be concluded that K, the Pearce coefficient, is not only a function of pipe diameter but also a function of inlet condition. This is because it is a function of wave amplitude and wave amplitude is a function of gas and liquid superficial velocities.

5.8 Wave Spacing

Measured wave spacing is calculated by dividing measured wave velocity by measured wave frequency i.e.

$$\lambda_w = \frac{V_w}{f_w} \tag{5.13}$$

Wave spacing obtained from Equation (5.13) is plotted against gas superficial velocity as displayed in Figure 5.21 (a). The figure shows that disturbance wave spacing changes around transition boundaries where V_{SG} = 21 m/s, 30 m/s and 40 m/s (for V_{SL} = 0.05 m/s) respectively. Wave spacing transition for V_{SL} = 0.15 m/s at V_{SG} = 40 m/s is unclear.

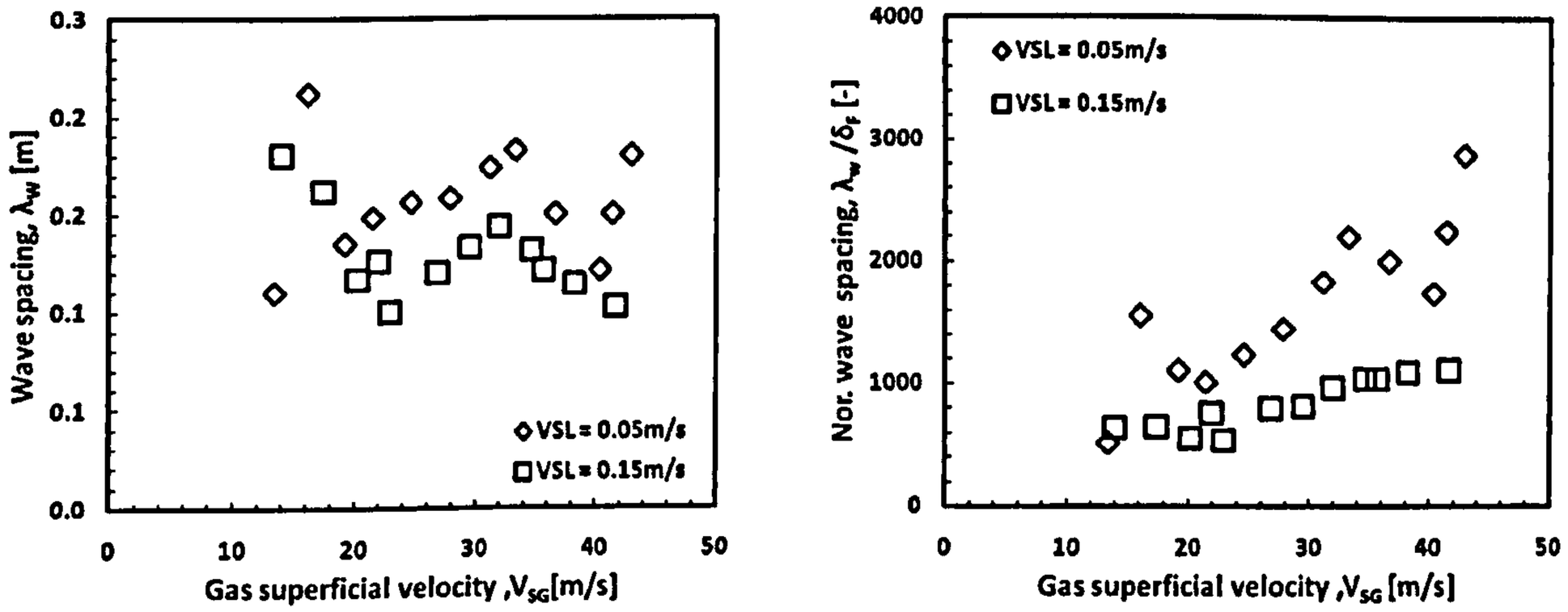

(a) (b)

Figure 5.21: (a) Wave spacing variation with gas superficial velocity.
Figure 5.21: (b) Dimensionless wave spacing variation with gas superficial velocity.

For the case of V_{SL} = 0.05 m/s and V_{SL} = 0.15 m/s in Figure 5.21 (a), wave spacing is indistinguishable before V_{SG} = 21m/s. After V_{SG} = 21m/s, wave spacing becomes higher as the superficial liquid velocity decreases. The reason responsible for this observation may be higher inertial and mass density possess by the liquid film when V_{SL} = 0.15 m/s. As a result

liquid film corresponding to V_{SL} = 0.15 m/s tend to resist the force exerted by the dispersed gas phase. This increase in resistance causes reduction in wave amplitude and hence wave spacing.

When wavelength is normalized by film thickness result shows that in transition boundaries are still very obvious and wavelength is seen to be higher for V_{SL} = 0.05 m/s.

In the case of V_{SG} = 14 m/s wavelength increases with increase in liquid superficial velocity Figure 5.22 (a). However, when the normalized wave spacing is plotted against liquid superficial velocity as in Figure 5.22 (b), the wave spacing is observed to decrease with increase in liquid superficial velocity Figure 5.22 (b)

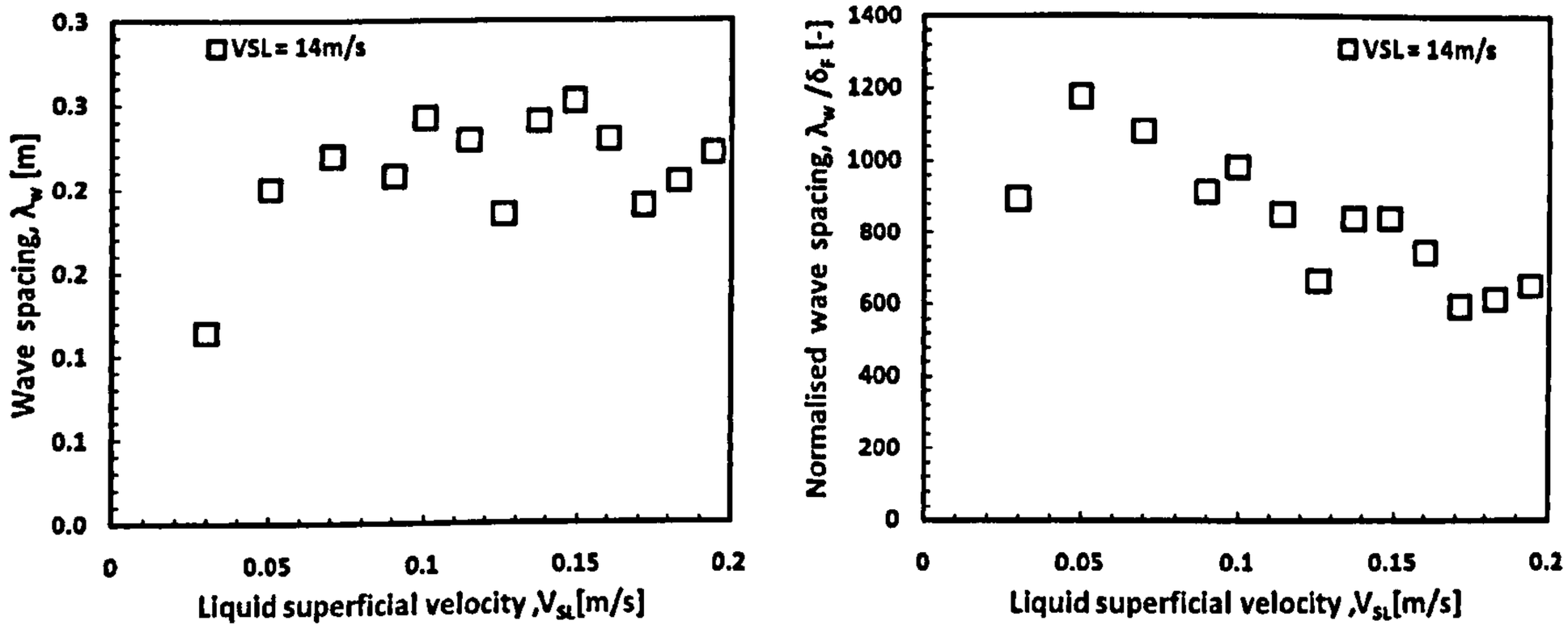

(a) **(b)**

Figure 5.22 (a) Wave spacing variation with liquid superficial velocity V_{SG} = 14 m/s. Figure 5.22 (b) Dimensionless wave spacing variation with liquid superficial velocity V_{SG} = 14m/s.

Wave spacing has been observed to be a revealing wave property according to this study. For instance when film thickness is normalized by wave spacing as shown in Figure 5.23, the various transition boundaries become readily visible. Again, when the wave amplitude is normalized by wave spacing the result is shown in Figure 5.24. The figure reveals a signature similar to the measured normalized drop size profile Figure 4.9 (a).

The similarity of Figure 4.9 (a) and Figure 5.24 shows that the proposed wave amplitude prediction (Chapter Six) is very reliable.

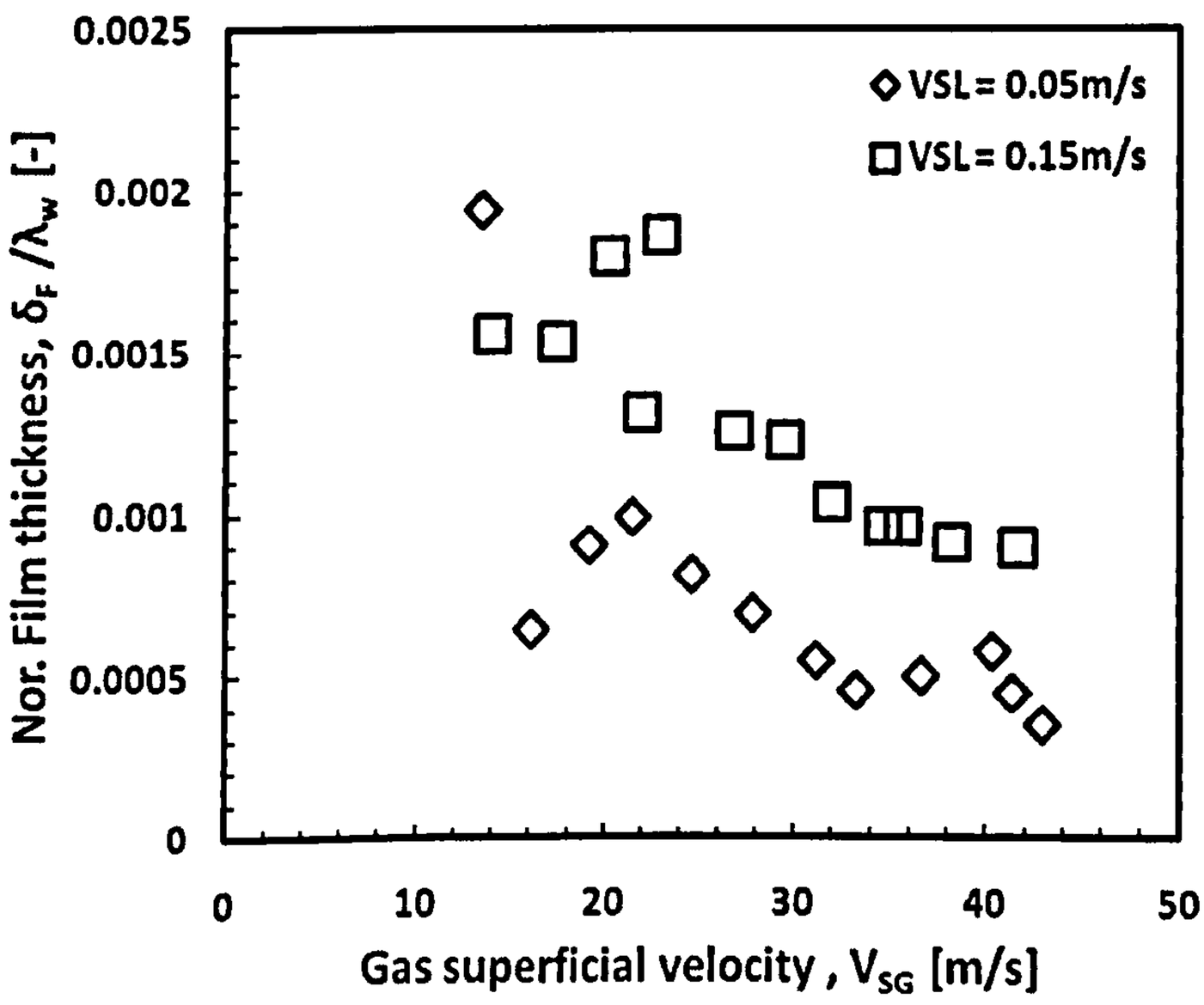

Figure 5.23: Normalized film thickness as a function gas superficial velocity.

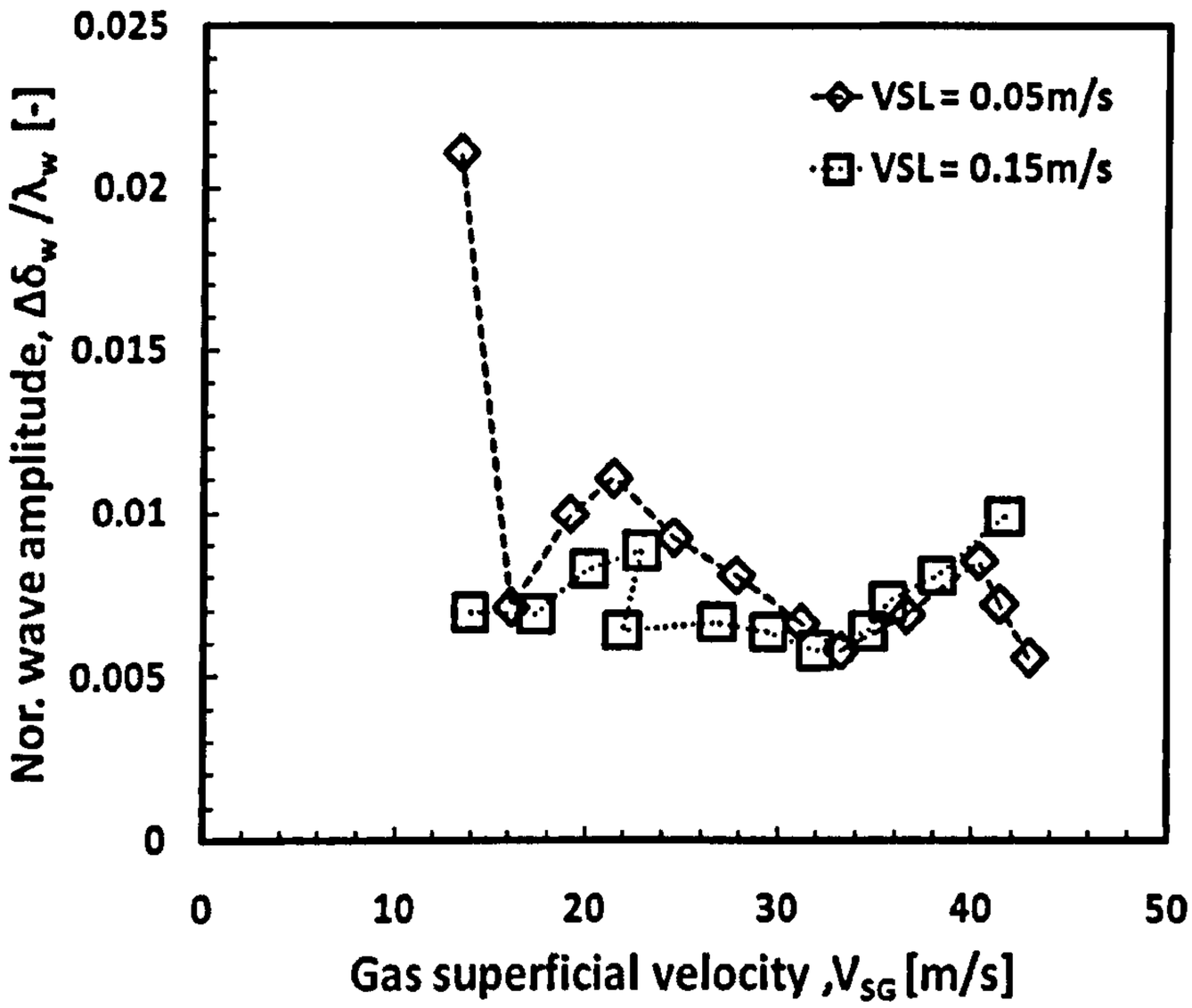

Figure 5.24: Normalized wave amplitude variation with gas superficial velocity.

5.9 Conclusions

From the results and discussions presented above the following conclusions can be drawn from dynamic measurements of wave properties:

1. Dynamic properties of the wave changes as wave identity changes. Wave properties change at transition boundaries within annular flow sub-regimes. Flow pattern transition within annular two-phase flow occurs at V_{SG} = 21 m/s, 30 m/s and 40 m/s respectively.

Wave frequency attains a maxima and then drops within wispy annular i.e. 0m/s > V_{SG} ≤ 21 m/s for V_{SL} = 0.05 m/s and 0 m/s > V_{SG} ≤ 30 m/s for the case of V_{SL} = 0.15 m/s.

2. The dominance of huge or disturbance wave depends on liquid superficial velocity when gas superficial velocity is maintained at a constant rate.

3. Wave frequency:

- is a strong function of gas superficial velocity
- increases with increase in gas superficial velocity
- increases with increase in liquid superficial velocity

4. Wave velocity:

- increases with increase in gas superficial velocity
- increases with decrease in liquid superficial velocity

5. Wave spacing:

- increases with increase in gas superficial velocity
- increases with decrease in liquid superficial velocity

6. Wave fluctuation with time is higher when compared with than drop concentration fluctuation with respect to time.

7. Drop frequency is directly proportional to the standard deviation of the film thickness.

8. Correlating wave and drop frequency using Strouhal number and Lockhart-Martinelli parameter give a good correlation for wave frequency. However, the correlating parameter proves inadequate to model drop frequency.

9. After gas superficial velocity, V_{SG} = 30 m/s, the dominating mechanism becomes ligament break-up as huge wave disappears. The liquid film becomes predominantly covered by disturbance wave.

10. At transition to co-current annular flow, gas superficial velocity, V_{SG} = 21 m/s, huge and disturbance waves co-exist. Disturbance wave dominates over huge waves.

11. Before gas superficial velocity , V_{SG} = 21 m/s, huge wave and ephemeral disturbance wave covered the liquid film interface , huge wave dominates over disturbance waves.

12. Drop collision frequency is directly proportional to drop size distribution.

13. At low drop concentration (usually at low gas velocity), drop frequency, in some cases, are seen to be higher than wave frequency, the controlling mechanism being ligament break-up. Meeting and merger of waves occur, wave bursts into droplet, and because the newly formed droplets are far apart coalescence hardly takes place suggesting why drop concentration is low under this condition.

Chapter 6

Wave Amplitude and Dynamics in Annular Two-Phase Flow

6.1 Introduction

Wave amplitude is defined as the difference between the wave peak height and wave base height. While the importance of studying the features of the waves was realized and suggested by many investigators, few studies focused on such aspects. The wave amplitude has not been satisfactorily predicted in the literature. This could be largely attributed to the complexity of the phenomena with a number of interrelated factors influencing the wave amplitude. Such factors include condensation, evaporation and the balance of forces that simultaneously influence the wave structure. Such forces are exerted by, for example, gravitational acceleration, pressure and interfacial shear stress exerted by the gas stream on the wave front and back and by the surface tension forces. The inter-dependence and coupling effects of these forces on the evolution of the wave shape are very complex.

Past work on wave amplitude modeling is usually based on cut-off criterion developed by DeJong (1999) defined as the sum of the average film thickness plus one standard deviation of the film thickness. Sawant et al. (2008) stated that accurate measurement of wave amplitude is not possible using the current conductance probe technique. This is because the probe has finite length in axial direction. The measured film thickness is an average over the probe width and the measured wave heights are lower than the actual wave

heights referring to the classical work of Hall Taylor (1966) and Martin(1983). However, Sawant et al. (2008) suggested this limitation should not affect the statistical characteristics

of disturbance waves such as frequency, velocity and wavelength but warned that the values of the measured amplitude presented in that study did not represent the absolute amplitude and therefore should only be used to study the trends in variation of disturbance wave amplitude with the change in boundary conditions. Next, we discuss modeling of wave amplitude in annular two-phase flow.

6.2 Interfacial shear stress dependent model

Ishii and Grolmes (1975) utilized the interfacial shear stress to estimate the wave amplitude. They assumed that interfacial shear stress at the top of the wave induces internal flow which is proportional to the velocity gradient in the liquid film as expressed by the shear flow model:

$$\tau_I = C_w \mu_L \frac{V_{LF}}{\Delta \delta_w} \tag{6.1}$$

Where:

C_w is a factor that accounts for the effect of the surface tension on the internal flow or the circulation and dissipation flow in the wave.

μ_L = liquid phase viscosity, kg/m-s

V_{LF} = liquid film velocity, m/s

$\Delta\delta_w$ = wave amplitude, m

Since the hydrodynamics inside the wave crest can be described in terms of viscous and surface tension force C_w is defined in terms of the liquid viscosity number, $N\mu$. It is the ratio of the viscous force induced by an internal flow to the surface tension force as given by the following expression:

$c_w = c_w(N_\mu)$ and;

$$N_\mu = \frac{\mu_L}{\left[\rho_L \sigma \left(\sqrt{\frac{\sigma}{g\Delta\rho}}\right)\right]^{1/2}} \qquad (6.2)$$

Ishii and Grolmes (1975) correlated the value of c_w based on data from several sources, as follows:

$$\frac{1}{3c_w} = 11.78\, N_\mu^{0.8} \quad \text{for} \quad N_\mu \leq \frac{1}{15} \qquad (6.3)$$

$$\frac{1}{3c_w} = 1.35 \quad \text{for} \quad N_\mu > \frac{1}{15} \qquad (6.4)$$

Measured film velocity, V_F is given by expression:

$$V_F = \frac{V_{SL}\, d(1 - E_F)}{4\delta_L} \qquad (6.5)$$

Since film thickness and entrained fraction measured from experiment and are time-resolved, it is possible from the Equation (6.5) to time-resolve film velocity because film

velocity is proportional to the entrained liquid fraction. From this film velocity distribution profile can be calculated, the result is presented in Figure 6.1 (b).

The Alves et al. (1991) mechanistic model for annular flow in vertical and off-vertical pipes is a 1-D two-fluid model. This annular flow model is formulated based on different flow geometry and different physical phenomena. The model enables detailed prediction of the annular flow- pattern characteristics, including the velocity distribution, liquid-film thickness, gas void fraction, and pressure gradient. Therefore, all other flow variables not measured directly in this study will be calculated utilizing based Alves. et al. (1991) models. The model expresses some of the flow parameters as follows in the next discussion.

Interfacial shear stress is expressed as:

$$\tau_i = f_I \frac{\rho c (v_c - v_F)^2}{2} \tag{6.6}$$

Where the interfacial friction factor is expressed in terms of a dimensionless parameter

I, being expressed as:

$$I = \frac{f_I}{f_{SC}} \tag{6.7}$$

Wallis (1969) correlation expressed interfacial friction factor, I as given below:

$$I = 1 + 300 \frac{\delta_F}{d} \tag{6.8}$$

Where:

$$d_F = 4\delta_F(d-\delta_F)/d \qquad (6.9)$$

d_F = hydraulic diameter of the liquid film, [m]

$$f_{SC} = 0.046\,\mathrm{Re}_{SC}^{-0.2}\ ;\quad \mathrm{Re}_C = \frac{\rho_C V_C d_C}{\mu_C}\ ;\ d_C = (d-2\delta_F)$$

$$\rho_C = \rho_G\alpha_C + \rho_L(1-\alpha_C);\qquad \mu_C = \mu_G\alpha_C + \mu_L(1-\alpha_C)$$

d= pipe diameter, [m]; δ_F = film thickness, [mm]; f_{SC} = gas core friction factor, [-]

ρ_C = gas core density, [kg/m^3]; μ_C =gas core viscosity, [kg/m-s]; α_C= gas core liquid hold-up, [-]

μ_G =gas phase viscosity; [kg/m-s]

Calculated interfacial stress and the film velocity are then plotted against V_{SG} as shown Figure 6.1(a) and Figure 6.1(b) respectively to establish a link between the two variable.

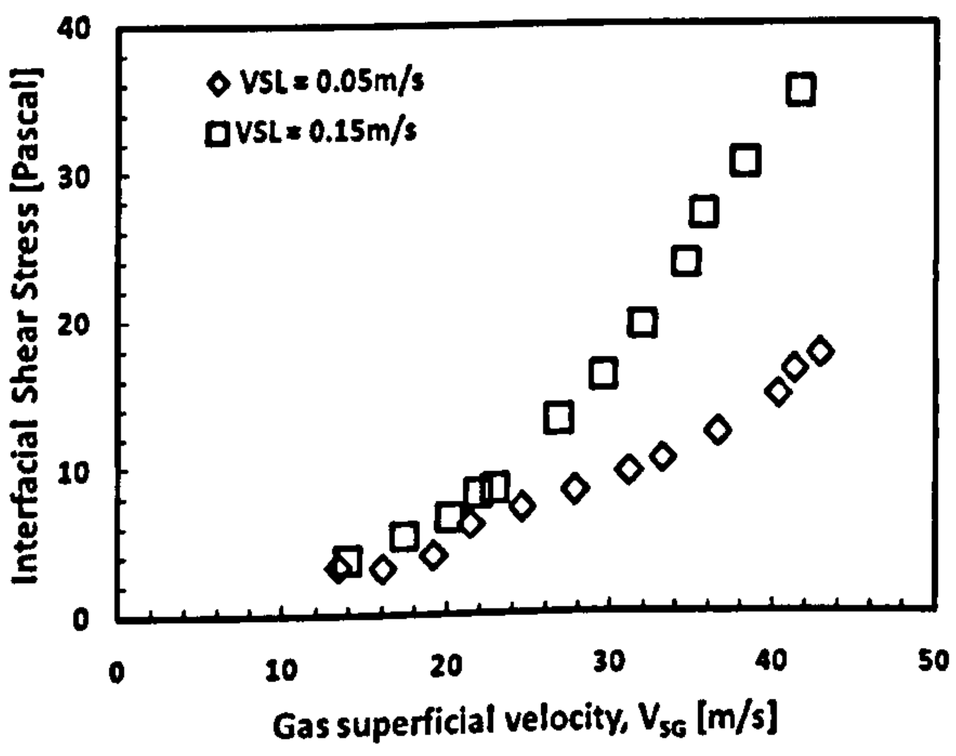

(a)

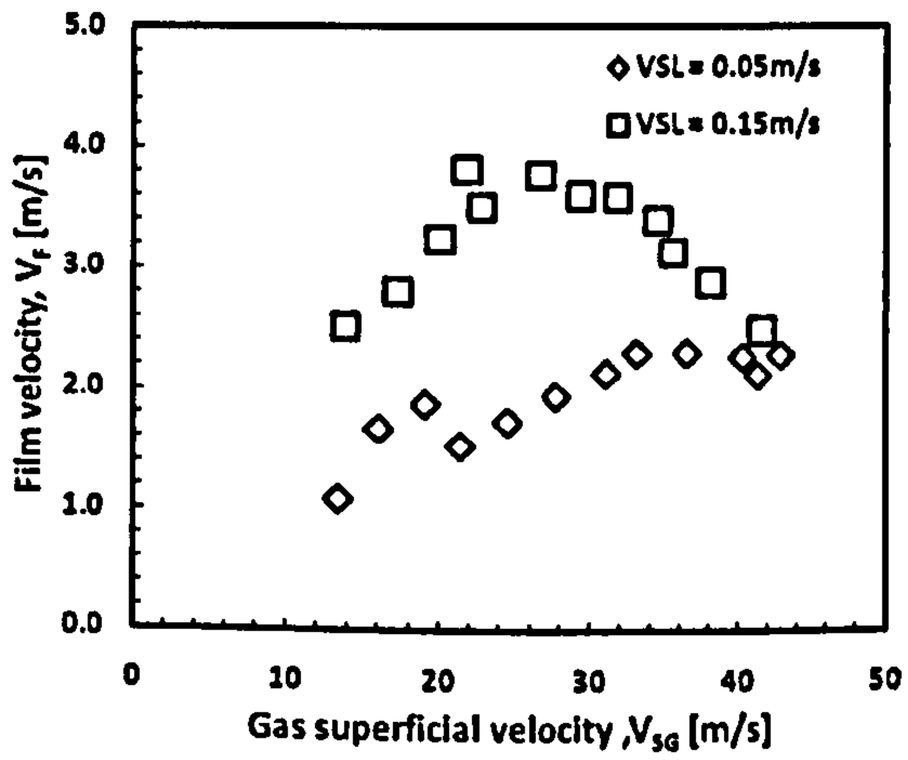

(b)

Figure 6.1 (a) Interfacial shear stress as a function of gas superficial velocity.
Figure 6.1 (b) Film velocity as a function of gas superficial velocity.

The physics to support what is happening in 6.1 (a) and 6.1(b) can be stated as follows. An increase in gas flow rate at constant liquid flow rate result in an increase in the interfacial velocity at the liquid-gas interface and hence an increase in interfacial shear stress. More momentum is transferred from the highly energetic gas core to the liquid film, resulting in an increase in the film velocity in the base area of the film. The increase in the interfacial shear stress increases in the interfacial friction factor. Pressure drop increases as interfacial friction factor increases.

Next, wave amplitude is calculated from Equation (6.1) utilizing calculated interfacial shear stress and the measured film velocity. Figures 6.2 (a) and 6.2 (b) are obtained when wave amplitude and normalized wave amplitude are plotted against gas superficial velocity.

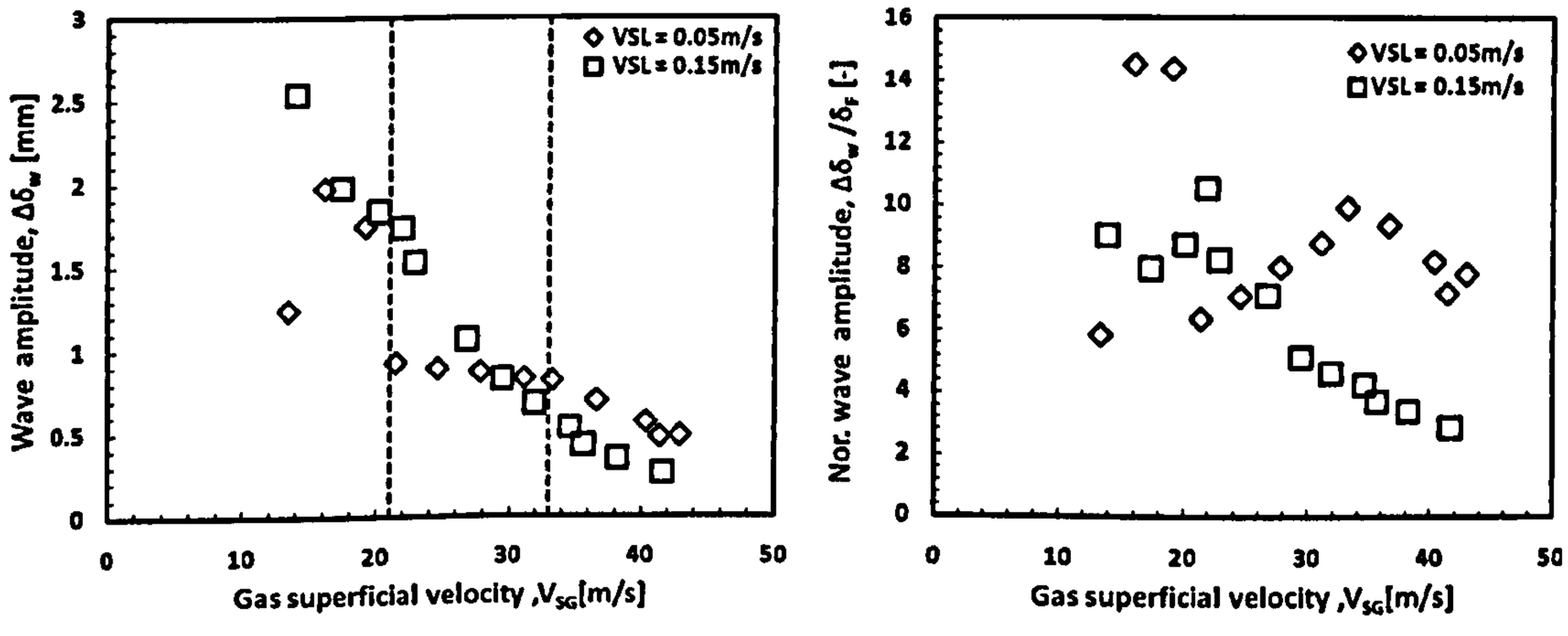

(c) **(d)**

Figure 6.2 (c) Effect of gas superficial velocity on wave amplitude.
Figure 6.2 (d) Effect of gas superficial velocity on dimensionless wave amplitude.

In annular flow, droplet size and velocity distribution is function of gas and liquid phase flow rates. Initially at low gas velocity, most of the liquid flow in the form liquid film and film thickness and disturbance wave amplitude are relatively large Sawant et al., (2008b).

Since the disturbance waves are the major source of droplets in annular flow (Ishii and Grolmes, 1975; Kataoka et al. 1983, Azzopardi et al. 2006), the droplet size distribution directly depends on the disturbance wave amplitude Sawant et al., (2009). This statement can be supported from the time-averaged film thickness from present experiments as can seen in Figure 6.3(a) and Figure 6.3 (c). The Figures show that disturbance wave amplitude reduces with increase in gas superficial velocity.

Figure 6.3 (b) and Figure 6.3 (d) are time resolved drop concentration signals produced from the disturbance wave. At lower gas superficial velocity V_{SG} = 13m/s the wave amplitude is highest Figure 6.3 (a). This corresponds to high amplitude drop concentration Figure 6.3 (b) and hence large drop size. Therefore, under low gas velocity condition, droplet size is relatively large. As the gas velocity increases, more liquid gets entrained into the gas core and liquid film flow rate gradually decreases resulting in decrease of disturbance wave amplitude Figure 6.3(c). Consequently the average size of droplets also decreases with the increase in gas velocity Figure 6.3 (d).

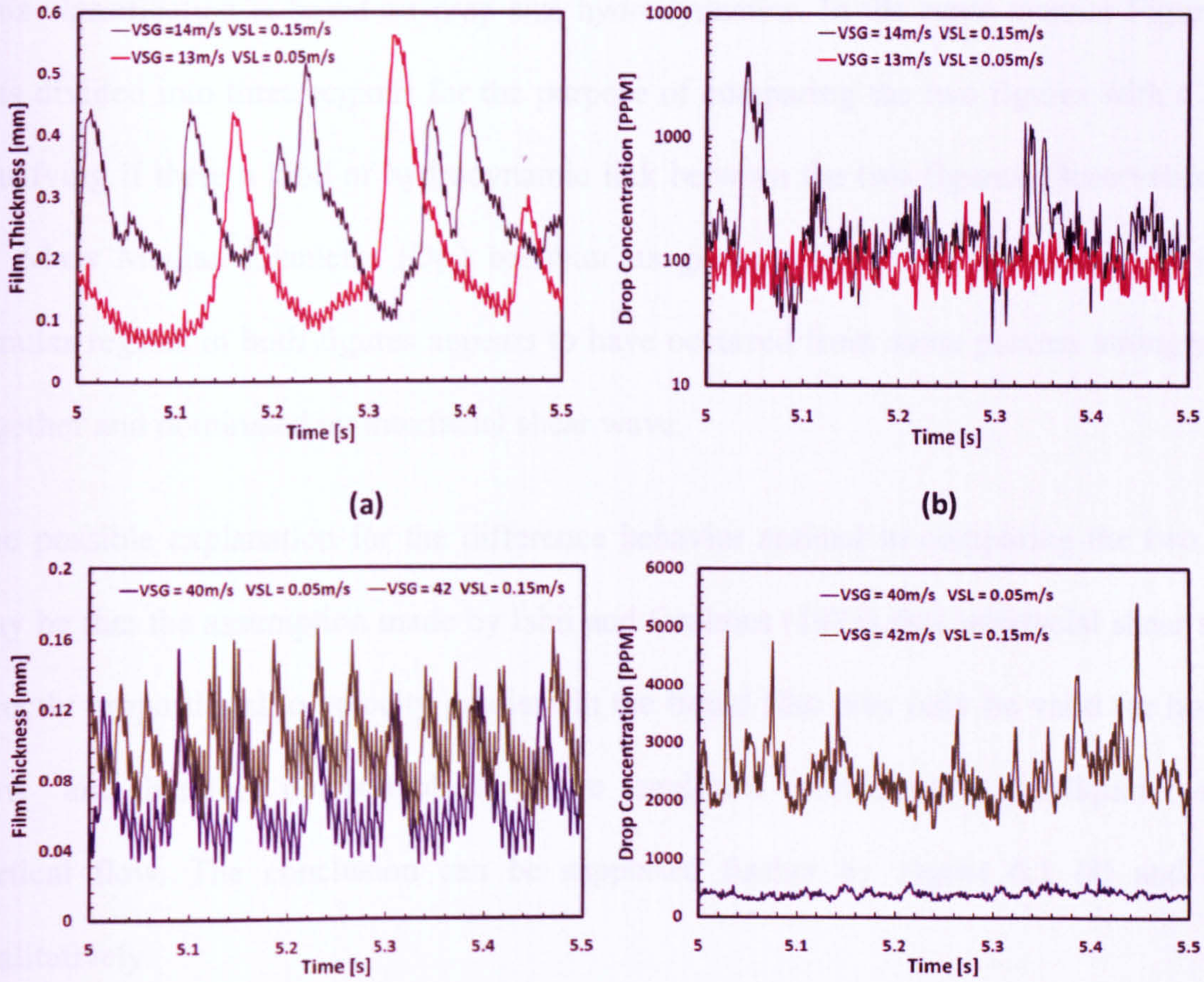

Figure 6.3 (a) Film thickness time-series at low gas superficial velocity.
Figure 6.3 (b) Drop concentration time-series at low gas superficial velocity.
Figure 6.3 (c) Film thickness time-series at high gas superficial velocity.
Figure 6.3 (d) Drop concentration time-series at high gas superficial velocity.

Since droplet size distribution directly depends on the disturbance wave amplitude Sawant et al., (2009) drop size (i.e.D_{50}) and wave amplitude profiles are expected to some common features.

Therefore, we divide the Figure 6.3(e) into three different regimes, namely:

1. Wispy annular regime (0 m/s ≥ V_{SG} ≤ 21 m/s),

2. Transition regime (21 m/s ≥ V_{SG} ≤ 30 m/s) and,

3. Mist flow regime (30 m/s ≥ V_{SG} ≤ 40 m/s).

This classification is based on drop size hydrodynamics. In the same manner Figure 6.3(f) was divided into three regions for the purpose of comparing the two figures with a view to clarifying if there a kind of hydrodynamic link between the two figures. Observation based on Mass Median Diameter (D_{50}) behavior as gas rate increases shows that only wispy annular regime in both figures appears to have occurred from same process strongly linked together and dominated by interfacial shear wave.

The possible explanation for the difference behavior noticed in comparing the two figures may be that the assumption made by Ishii and Grolmes (1975) that interfacial shear stress is directly proportional to velocity gradient in the liquid film may only be valid for horizontal flow and therefore not suitable for wave amplitude calculation in gas-liquid two-phase vertical flow. The conclusion can be supported further by Figure 6.1 (a) and 6.1 (b) qualitatively.

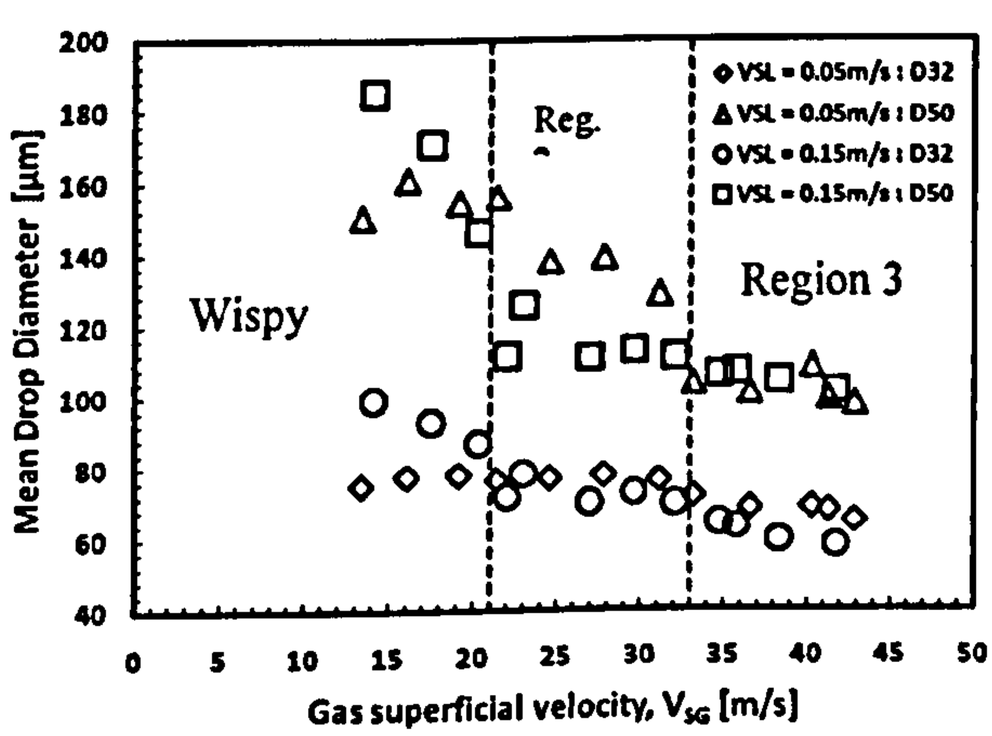

(e)

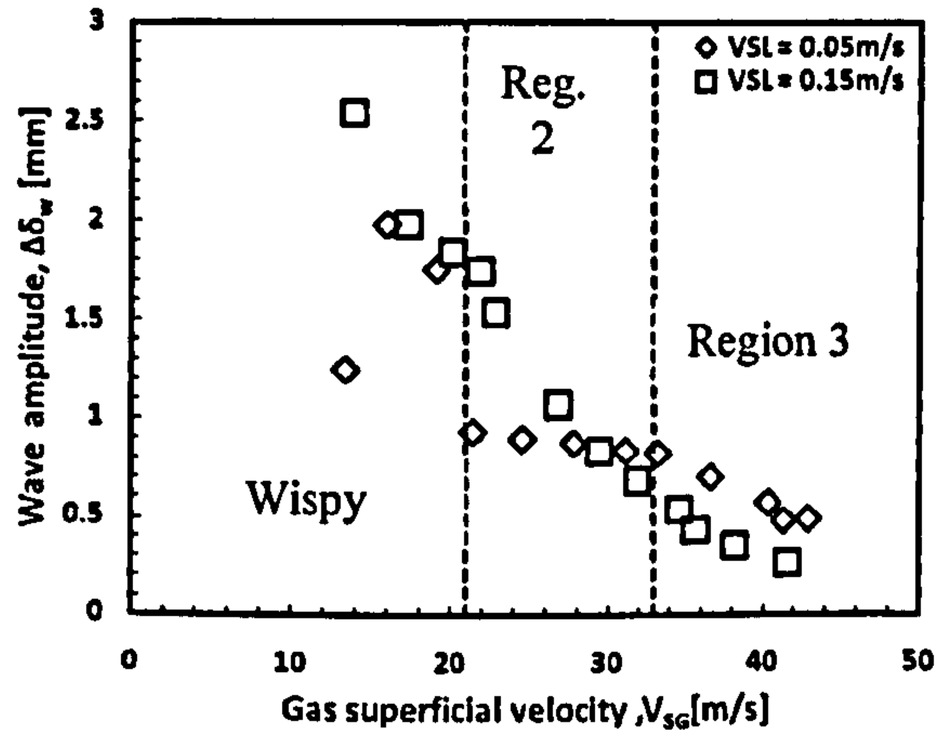

(f)

Figure 6.3: (e) Characteristic drop diameter as a function of gas superficial velocity.
Figure 6.3: (f) Dimensionless wave amplitude vs. gas superficial velocity.

6.3 Wall shear stress dependent model

At the next level of analysis, examination was based on the relationship between wall shear stress and the velocity gradient in the liquid film. Figures 6.4 (a) and 6.4(b) show that velocity gradient in the liquid film is directly proportional to the liquid film wall shear stress. Therefore, Ishii and Grolmes (1975) wave amplitude model was modified by replacing interfacial shear stress with wall shear stress in Equation (6.2) and utilize the new Equation (6.10) to calculate wave amplitude according to Equation (6.11).

$$\tau_{WF} = C_W \mu_L \frac{V_F}{\Delta \delta_W} \tag{6.10}$$

$$\Delta\delta_W = C_W \mu_L \frac{V_F}{\tau_{WF}} \tag{6.11}$$

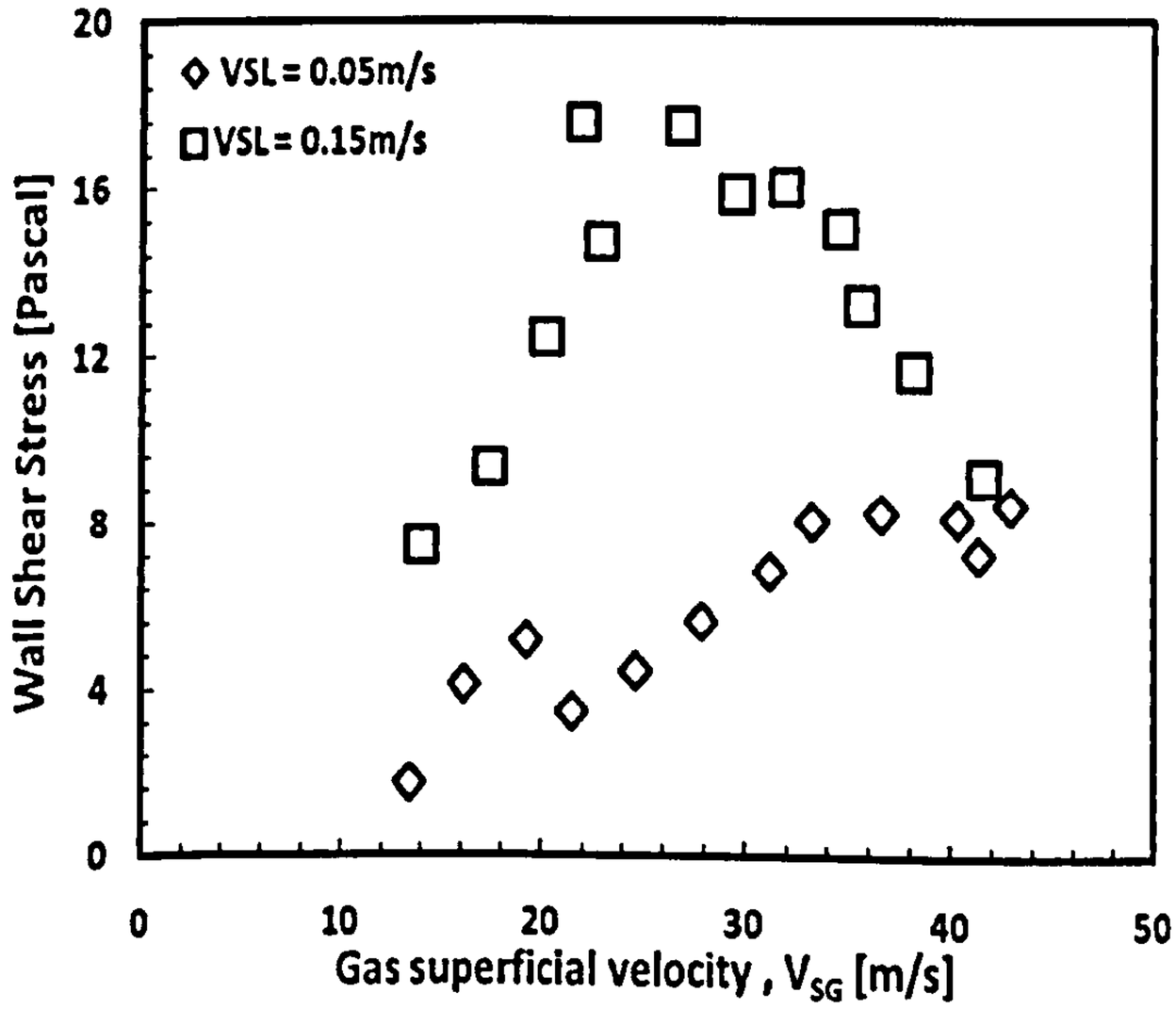

Figure 6.4(a): Wall shear stress profile

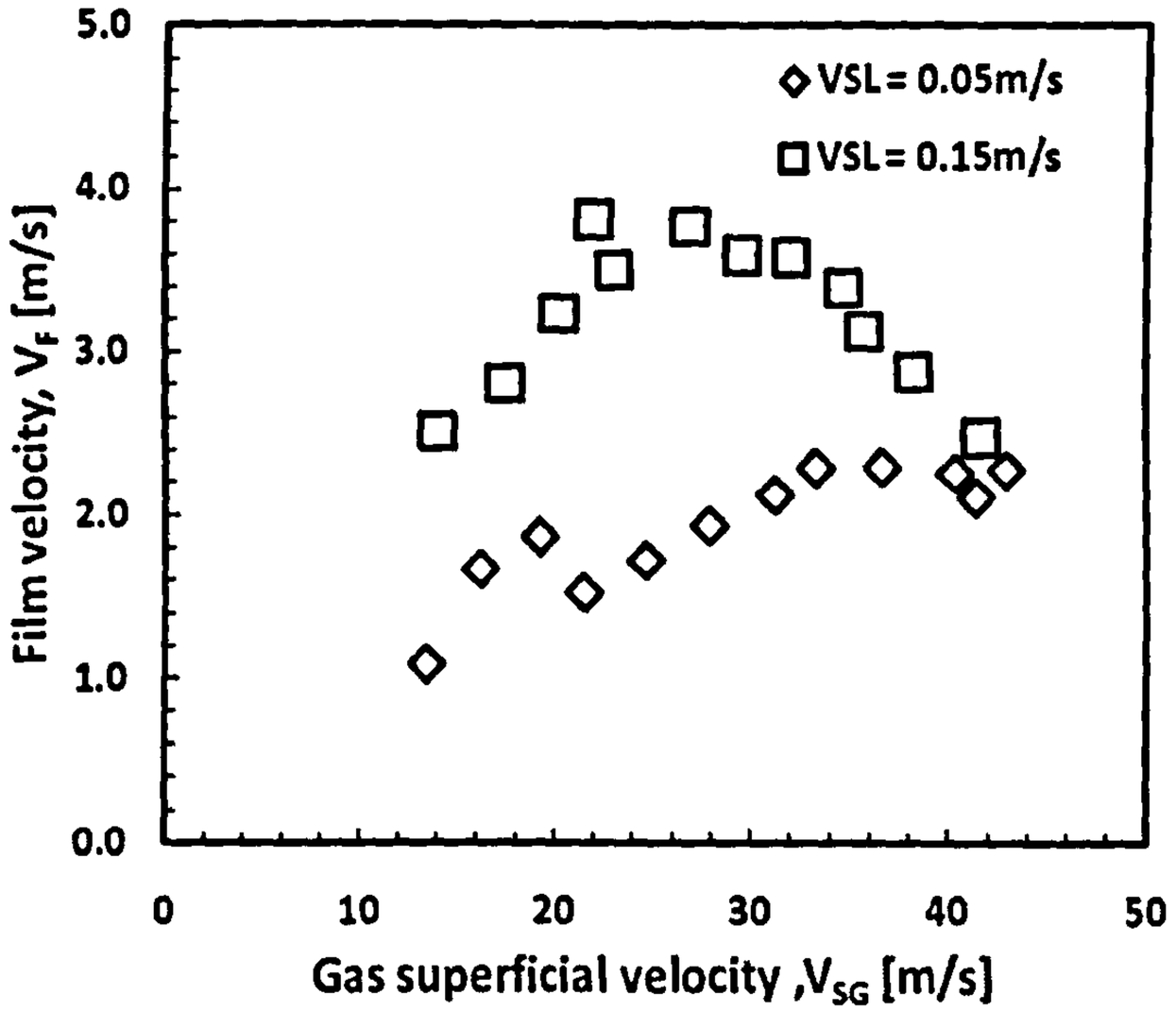

Figure 6.4(b): Film velocity profile.

Liquid film wall shear stress is calculated as follows:

$$\tau_{wF} = f_F \frac{\rho_L v_F^2}{2} \qquad (6.12)$$

Where:

$$f_F = 0.046\,\mathrm{Re}_F^{-0.2} \;; \quad \mathrm{Re}_F = \frac{\rho_L V_F d_F}{\mu_L} \;; \; d_F = 4\delta_F (d - \delta_F)/d$$

d_F = hydraulic diameter of the liquid film, [m]; δ_F = film thickness, [mm];

f_F = Liquid phase friction factor, [-]; d= pipe diameter, [m];

The new wave amplitude is plotted against superficial gas velocity as in Figure 6.5(a).Chaotic nature of the liquid film does not affect liquid film wall shear stress according to Figure 6.5(b) within gravity dominated regime where 0 m/s≥ V_{SG} ≤ 21 m/s. This is because wall shear stress unlike interfacial shear stress is not an interfacial phenomenon and

therefore does not expose to the turbulence and chaotic nature of the film. In the transition regime described by 21 m/s≥ V_{SG} ≤ 30 m/s, there is a strong link between the two Figure 6.5 (a) and Figure 6.5 (b). In the mist flow regime where V_{SG} > 30 m/s, good link is also observed.

In Figure 6.5 (c) and Figure 6.5 (d) where drop size and wave amplitude are normalized, the link between the two becomes obvious. It can be concluded that drop size distribution is strongly dependent on wave amplitude.

According to Figure 6.3 (b), wave amplitude for V_{SL} = 0.05 m/s and V_{SL} = 0.15 m/s both reduces as gas superficial velocity increases. Wispy annular regime is dominated by huge wave and dispersed phase is characterized by incomplete atomization.

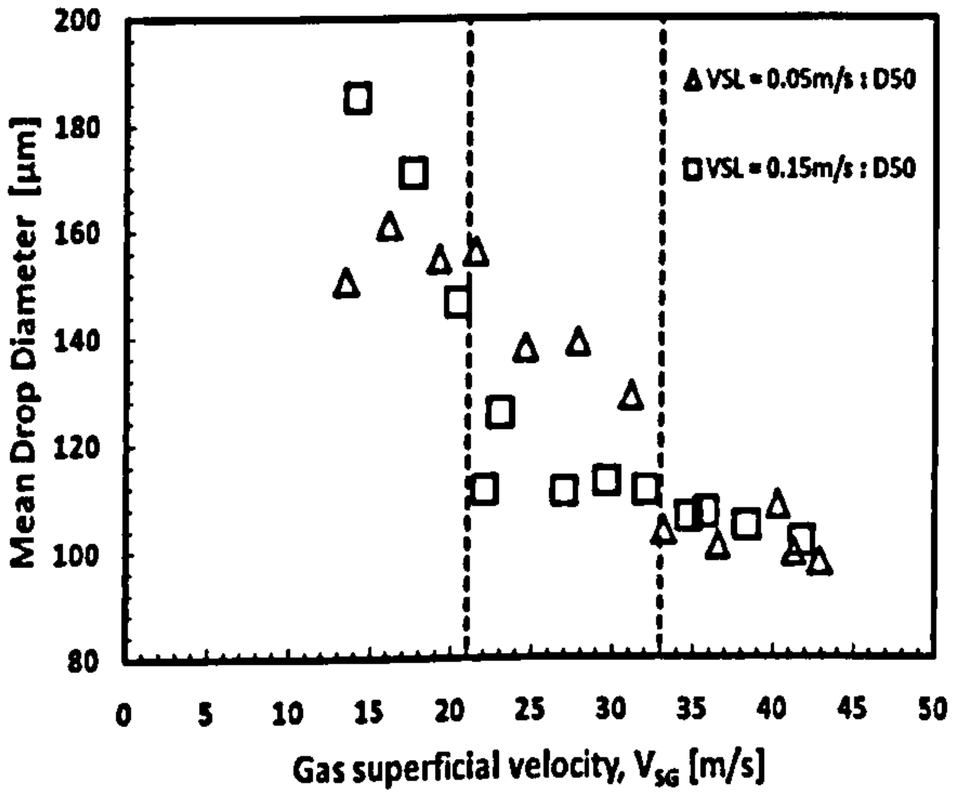

(a)

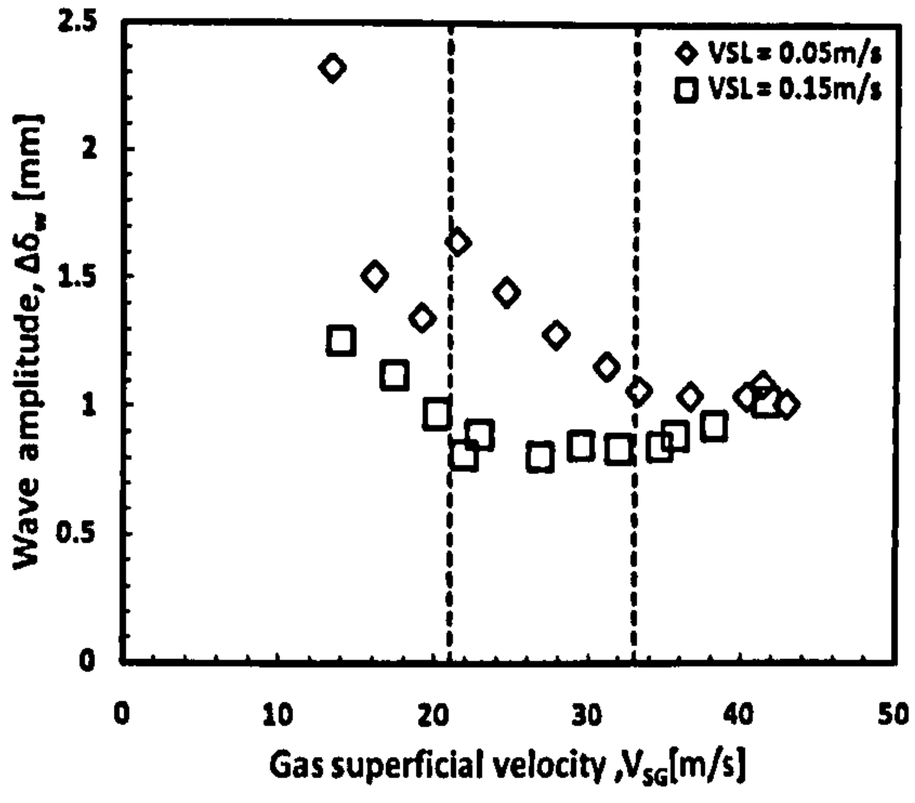

(b)

Figure 6.5: (a) Mean drop diameter vs. gas superficial velocity.
Figure 6.5: (b) Wave amplitude vs. gas superficial velocity.

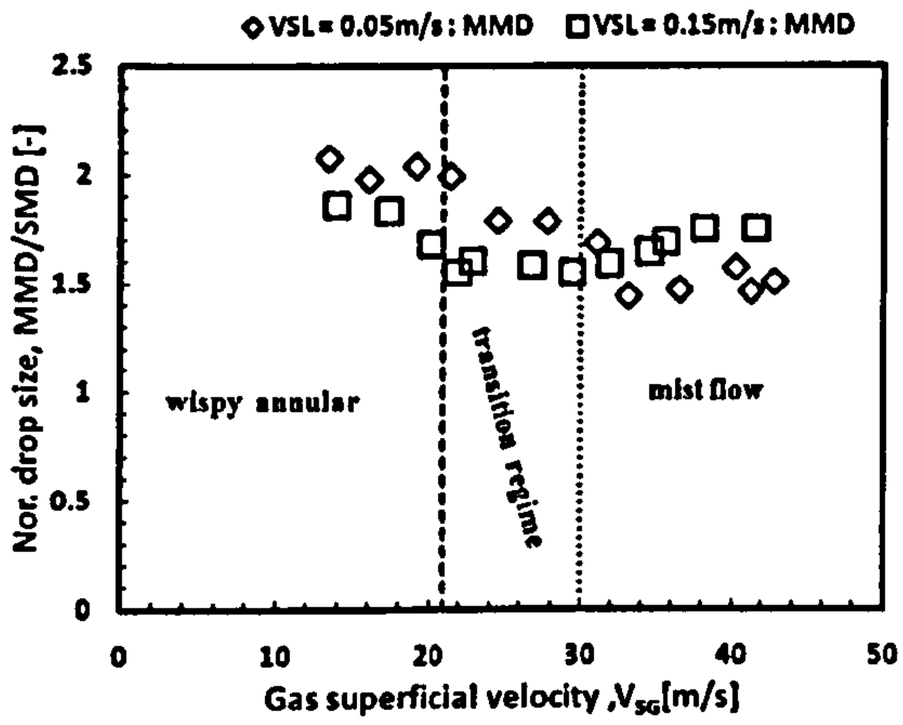

(c)

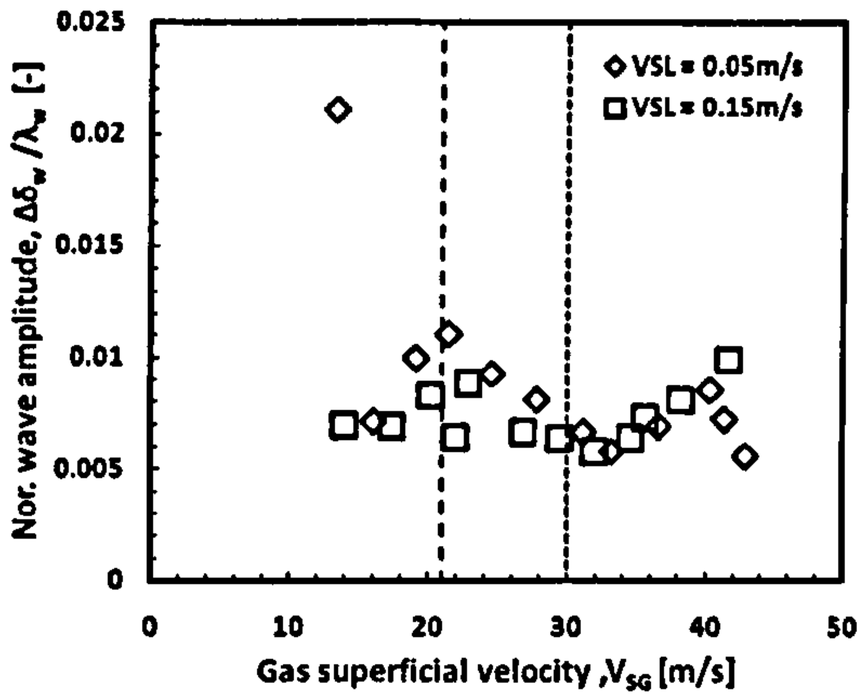

(d)

Figure 6.5: (c) Normalized drop size vs. gas superficial velocity.
Figure 6.5: (d) Normalized wave amplitude vs. gas superficial velocity.

Around V_{SG} = 21 m/s there is a transition from wispy annular to transition (wispy-mist annular) regime where film seems to have more stability. Disturbance wave and huge is believed to co-exist in this flow regime although disturbance wave appears to dominate.

In Wispy annular regime, indistinguishable values of D_{50} for V_{SL} = 0.05 m/s and V_{SL} = 0.15 m/s observed may be as a result of chaotic nature of the liquid film. In transition regime, while amplitude decreases with increase in gas superficial velocity for V_{SL} = 0.05 m/s, wave amplitude increases with increase in superficial gas velocity for V_{SL} = 0.15 m/s.

After the transition to mist flow at V_{SG} = 30 m/s, the wave changes from disturbance to pack of ring disturbance wave. Observations from high speed camera show that these waves are characterized by high amplitude, Mantilla (2008).

6.4 Averaged shear stresses dependent model

When arithmetic average value of interfacial and wall shear stresses is used in calculating wave amplitude and compared with drop size distribution Figure 6.6 (a). Calculated wave amplitude is presented in Figure 6.6 (b) as function of inlet conditions. Figure 6.6(b) does not replicate Figure 6.6(a) rather it seems to have averaged out the dominant effect of wall shear stress over interfacial shear stress after the transitions at V_{SG} = 21 m/s and 30 m/s respectively. However, an interesting feature observable is the similarities between this and D_{32} profile. It appears to relate directly to SMD than MMD.

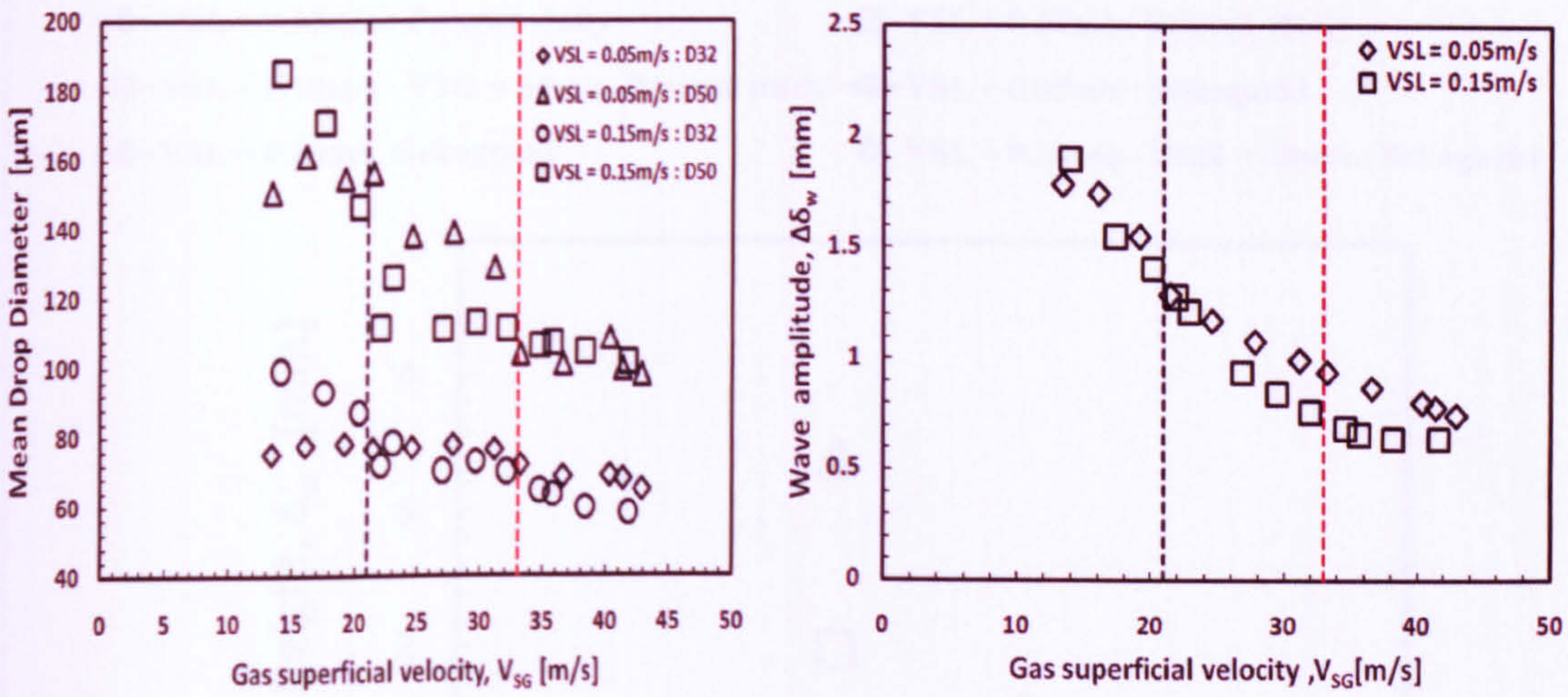

(a) (b)

Figure 6.6: (a) Mean drop size vs. gas superficial velocity.
Figure 6.6: (b) Wave amplitude vs. gas superficial velocity.

In conclusion, there is a strong indication that shear stresses should be included in the drop size model. This may be reason why the model prediction is poor as most existing models do not include shear stresses their formulations.

6.5 Validating wave amplitude model

Model calculation was compared with measurements of disturbance wave amplitude in vertical annular flow. The measurements were taken by Sekoguchi & Mori (1997); Sekoguchi et al. (1994); Sekoguchi & Takeishi (1989); Sekoguchi et al .(1985) in a 25.8mm tube as reported by Pols (1998) using Multiple Ring Electrode Probes (Super Multiple Point –Electrode Probes) at several axial positions along the tube measuring both the wave profile and the wave velocity. The intrusive probes are generally more accurate than non-intrusive flush mounted wall probes (Ceccio, 1991; Hewitt, 1978).

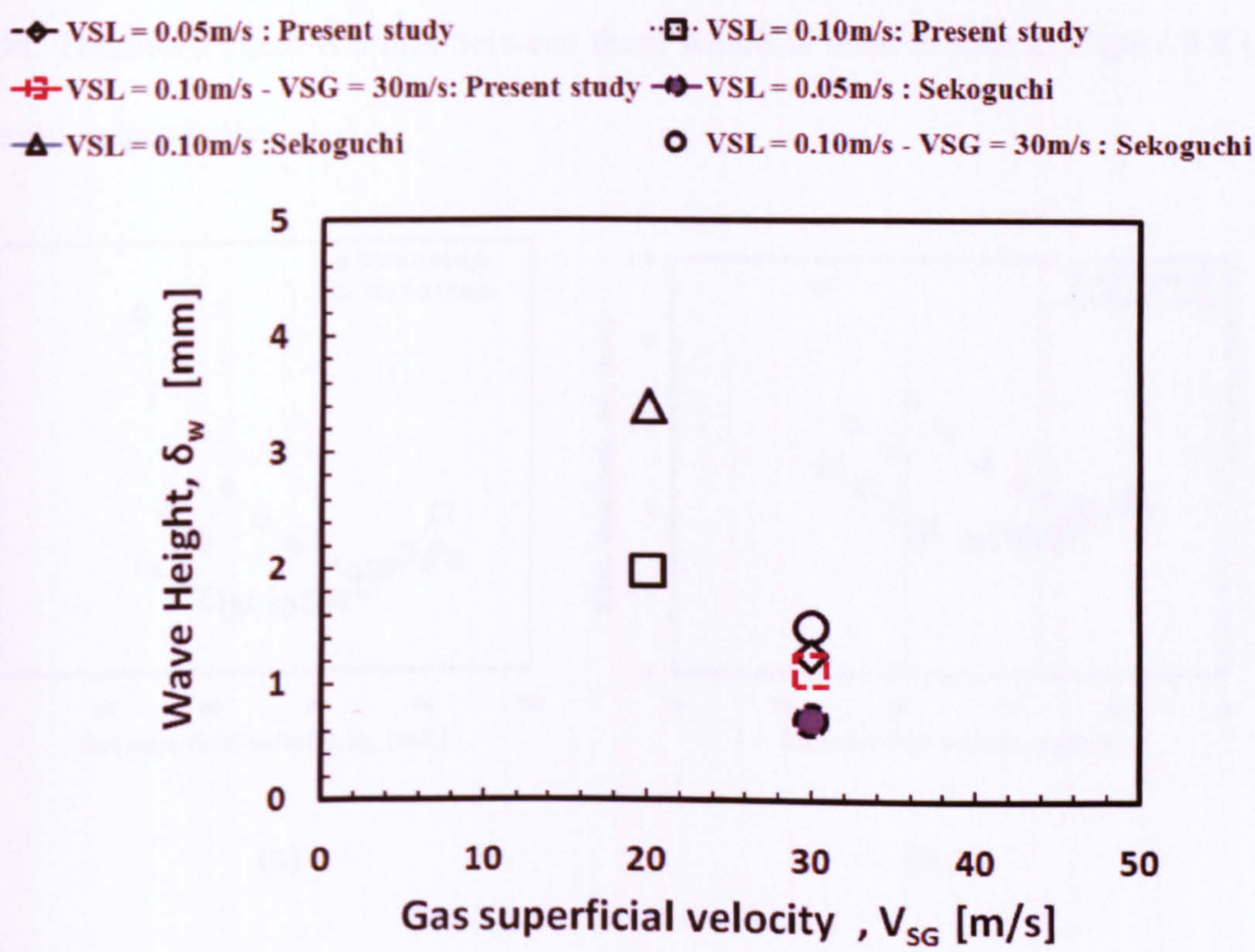

Figure 6.7: Comparison of measured wave height and the model prediction.

Wave height is determined by addition of average film thickness and wave amplitude calculated by the model. The results are compared with the data of Sekoguchi et al. as

presented in Figure 6.7.There is good agreement between the model prediction and measurements as shown in Figure 6.7.

6.6 Pressure drop and wave amplitude

Pressure drop and wave amplitude profile are compared to see if there is a relationship between them. Figures 6.8(a) and Figure 6.8(b) show that there is a strong relationship between pressure drop and wave amplitude. This is not surprising as entrained fraction is supposed to depend on wave amplitude. Pressure drop is directly dependent on entrained fraction. Therefore, there is a link between them which is what is seen in Figure 6.8 (a) and Figure (b) respectively.

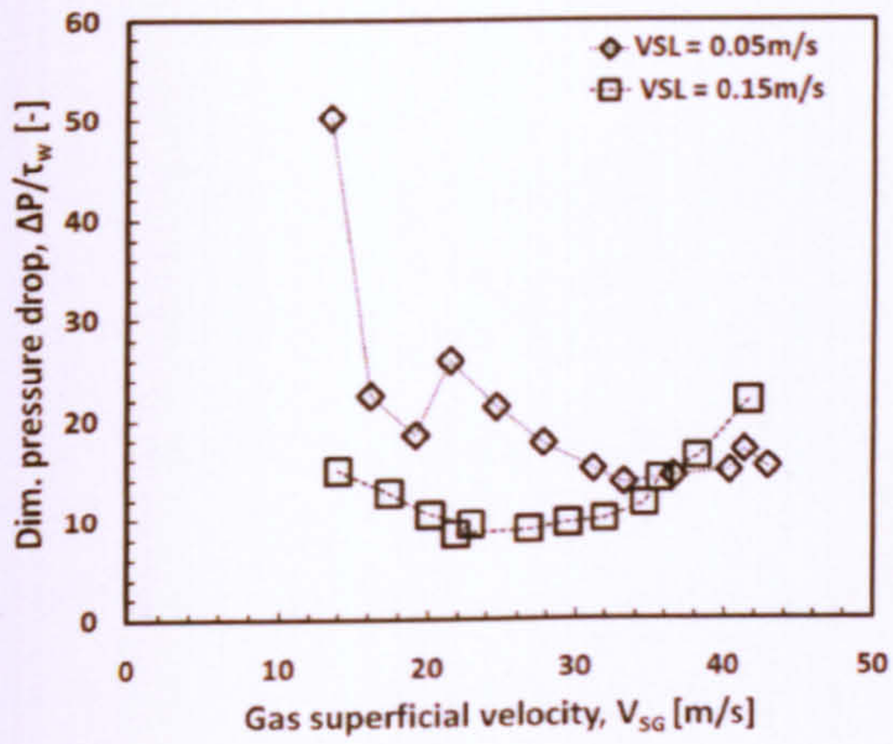

(a)

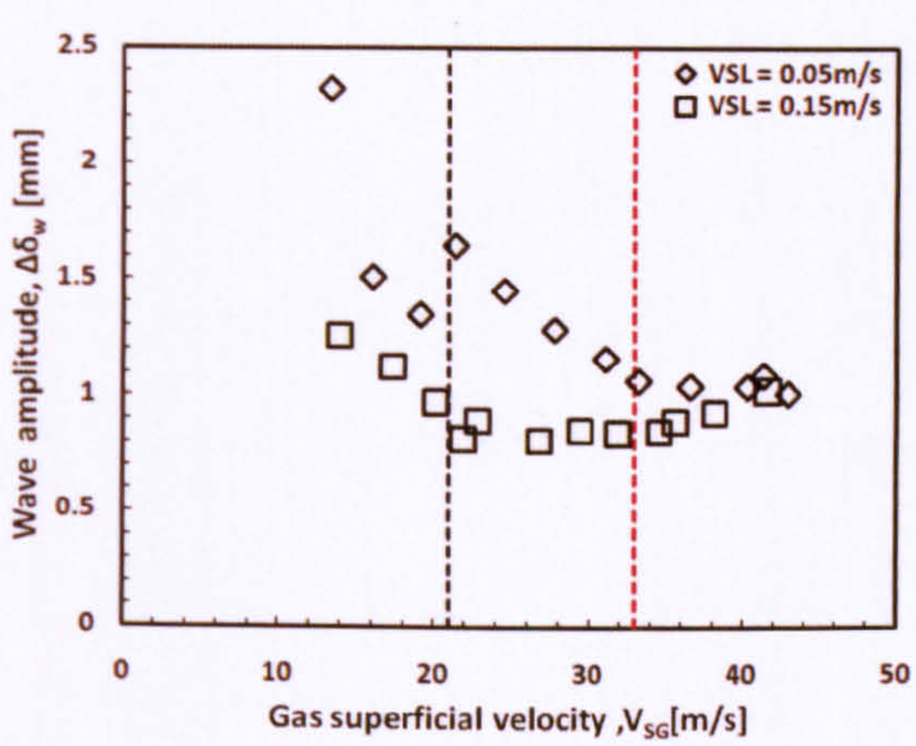

(b)

Figure 6.8: (a) Dimensionless pressure drop vs. gas superficial velocity.
Figure 6.8: (b) Wave amplitude vs. gas superficial velocity.

6.7 Conclusions

A new model to predict wave amplitude in vertical up-flow has been proposed. The proposed model is a modification of the existing correlation based on experimental findings. The model has demonstrated that wave amplitude is strongly dependent on wall shear stress. The predicted wave amplitude using the proposed model agrees reasonably well with the published data.

Chapter 7

Split of Gas-Liquid Two-Phase Flow at Vertical Dividing Junction

7.1 Introduction

Simultaneous flow of gas and liquid occurs over in a wide range of industrial equipment from large diameter pipes found in the oil and gas production industry to the micro-channels which might be employed to cool electronic components. In many arrangements it is necessary to divide the flow into two or more channel motivated by area restrictions or process requirements. Partial separation across T-junction is one of the mechanisms of separation which has been widely adopted in manifolds comprising gathering system in oil and gas production to reduce processing load on the main separator.

A junction can be defined as three connected pipes, Azzi et al. (2010). If one is an inlet and the other two are outlets, it is termed a dividing junction. The system with two inlets and one outlet is termed a combining junction. Though, for dividing junctions, the outlet pipes can be at any angle to the inlet, two geometries are commonly found. In that termed side arm junction one outlet is in-line with the inlet; the other outlet is perpendicular to these. In impacting junctions both outlets are perpendicular to the inlet. In the present work side arm dividing junctions are considered. The orientation of the pipes is also important. Junctions can be classified as horizontal or vertical depending on the orientation of the inlet pipe. The most important dimensions of a junction are the diameters of the pipes, D_1, D_2, D_3, where 1 refers to the inlet pipe, 2 to the straight

through continuation and 3 to the side arm. Azzopardi (1999) has noted that side arm junctions usually have $D_1 = D_2$.

The division of gas-liquid flows at a dividing junction depends on the resistance (pressure drops) in the two outlet pipes as well as the physical phenomena which affect the phase split. In practical applications, these resistances are caused by equipment downstream of the junction. In experimental studies, it is usual to place valves in the downstream lines. Altering the valve position changes the downstream resistance. In this way it is possible to go from zero take off through the side arm (infinite resistance in the side arm to 100% take off (infinite resistance in the straight-through pipe downstream of the junction).

Phase separation across T-junction is a secondary mechanism of separation process whose efficiency depends mainly on phase momentum, the existing flow pattern before the junction and the force of gravity Dionissios (2007). If satisfactory separation efficiency could be achieved; the device could be an excellent candidate for sub-sea application where minimum control system is required. The application of this separation principle in avoiding slugging at multiphase transportation system is very advantageous.

Works related to T-junction and its application has been reviewed in detail, Azzopardi et al. (1999). Recently, based on the Equation of mass, momentum and energy balance, Dionissios (2007) studied the dynamic separation of gas and liquid inside a T-junction with a horizontal run and a vertical branch. He proposed a mathematical model which

predicts phase distribution and pressure drop across T-junction of different orientations and pipe diameters taking into account the flow pattern before the junction.

The motivation for this work arises from the paucity of published data on separation of gas-high viscosity flows at vertical T-junction. For instance, the recent model proposed by Dionissios (2007) does not include flow after the junction as a parameter. The usual assumption is that flow pattern before and after is always the same. However, results from present study show that flow pattern often changes after leaving the junction. Therefore, this work provides new data from measurement carried out by increasing liquid phase viscosity in a systematic manner. The problem is approached by taking measurements of void fraction waves at each segment of the T-junction.

7.2 Experimental Facility

The Same experimental facility used by Mak et al. (2006) was used to carry out this experimental campaign. The difference in present work and that of Mak et al (2006) is in the test fluids. Mak et al. (2006) only tested with air/water whereas in the present study viscosities of the liquid phase were varied systematically from 1mP as s (water) to 36mPa s (glycerol solution). The flow diagram schematic is shown in Figure 7.1.

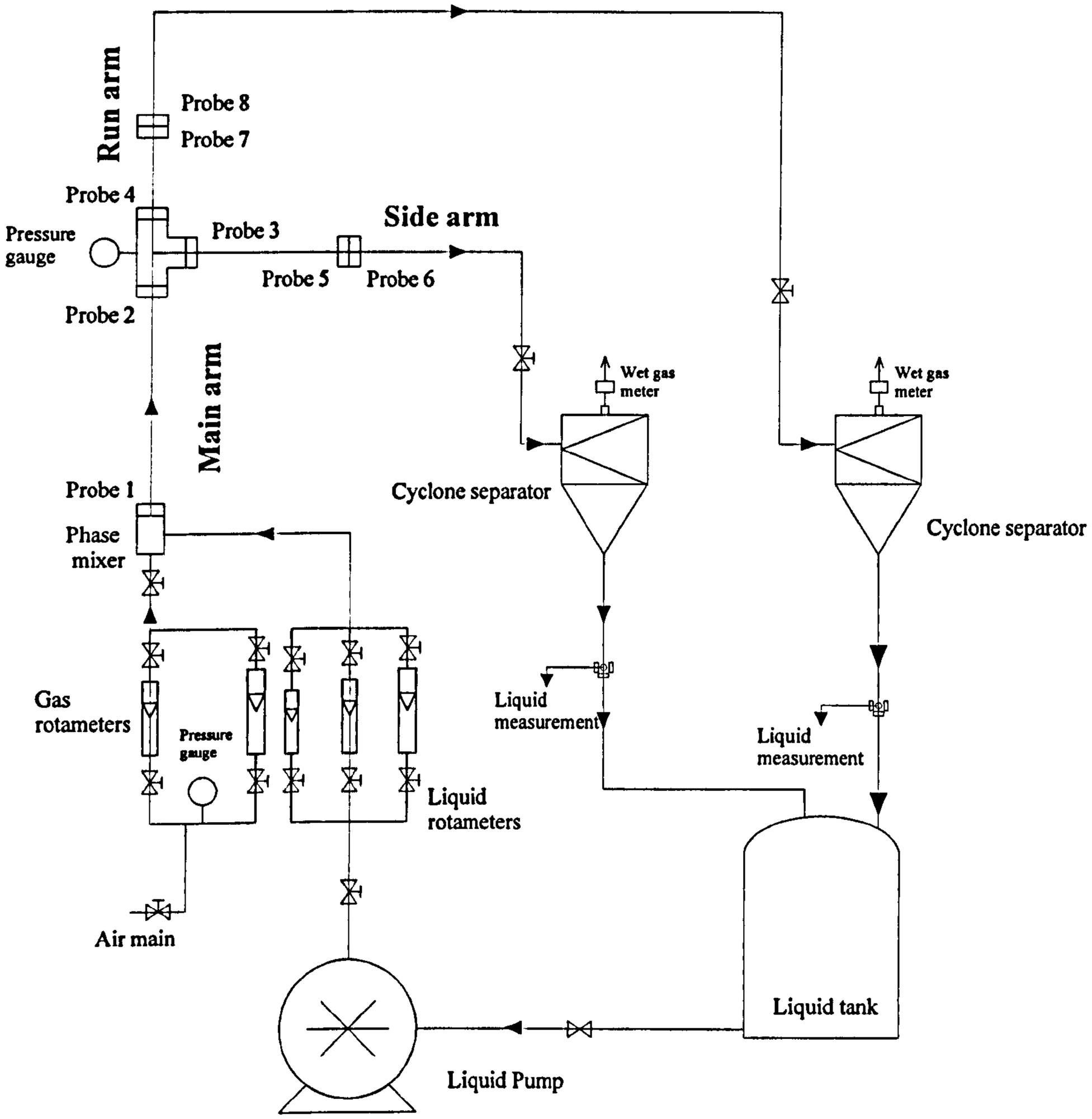

Figure 7.1: The flow diagram with t-junction test section.

Liquid glycerol solution carefully mixed to produce solution with varying dynamic liquid viscosity of 3.6, 6, 8, 10, 12, 18, 27 and 36 mPa s. The solution was then mixed with air at ambient temperature to form two-phase flow. Air was drawn from the compressed air main and supplied to the mixing unit where it combines with water /

glycerol solution drawn from a storage tank by means of a centrifugal pump. The mixing unit consisted of an annular section surrounding a porous wall. Water/glycerol solution enters the main pipe from the periphery to form a film on the wall whilst the air passes along the middle. Inflow of air and water/glycerol solution is controlled using separate banks of calibrated rotameters. Downstream of the mixer, the two phases flow vertically upward along a 1.3 m development length of stainless steel pipe of 5 mm diameter before entering the T-junction.

The test section pressure was measured 0.04 m upstream of the T-junction. The T-junction is smoothly machined inside a rectangular block of acrylic resin. The transparent block facilitates visualization while the flat external surface minimizes the distortion due to refraction. Beyond the T-junction, the two-phase flow stream in the run arm travels vertically upwards for 1.42 m, before flowing horizontally and vertically downwards to a separator consisting of a vertical cylinder of 100 mm diameter. The side arm consists of 1.06 m of straight horizontal pipe followed by a vertically downward pipe to an identical separator. The run and side arms are 5 mm in diameter and made of stainless steel.

The pressure and phase split at the T-junction is controlled using gate valves positioned at the inlet to each separator. After separation, the liquid is collected from the bottom of each separator and air passes out through a pipe at the top. The exit liquid could either be recycled or taken off to be measured. During measurements, water / glycerol solution was diverted into a measuring cylinder where the volumetric flow rate was measured for a sufficiently long time to minimize uncertainty of measurement.

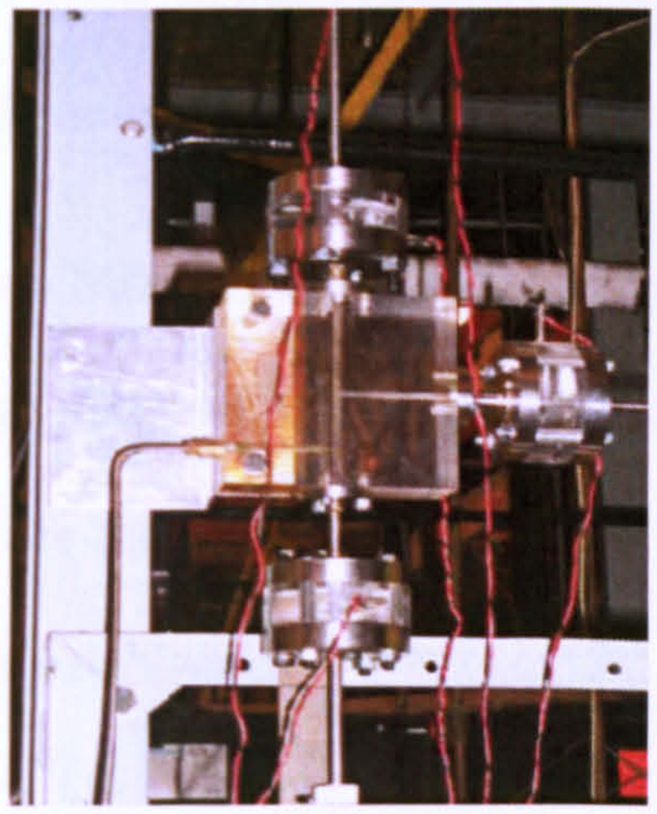

Figure 7.2: Picture of the T-junction with conductance probes (Probe 2, 3 and 4).

Air was metered at the top of a pipe using a calibrated wet gas flow meter which allowed the flow rates to be measured over a period of time. The liquid level in the separator vessels were kept constant to ensure accuracy.

Time varying, cross-section averaged void fractions were measured using eight identical conductance probes placed along the test section. The probes consist of two stainless steel ring electrodes mounted in acrylic resin housing. They were carefully manufactured so that the electrodes had the same diameter as the test section. A conductance probe is placed at 0.07 m after the mixer and three probes are situated in the main, run and side arms at 0.13 m from the junction. Two probes were placed close together at 1.1 m downstream of the junction on the run arm and two more were positioned 0.58 m away from the junction on the side arm. The probes around the T-junction are pictured in Figure 7.2.

The electronic circuitry employed for the conductance probe is similar to that of Fossa (1998) and Fossa and Guglielmini (1998). The conductance technique has been chosen

to measure void fraction because water is an electrical conductor, while air is essentially resistive. Glycerol in its raw form is not conductive. Sodium Chloride solution was added to the conductivity of the solution to that of water.

Andreussi et al. (1988) and Tsochatzidis et al. (1992) are some of the researchers to have used conductance probe successfully. In this technique, a cross-sectional averaged void fraction can be determined once the relationship between the electrical impedance and the phase distribution has been established.

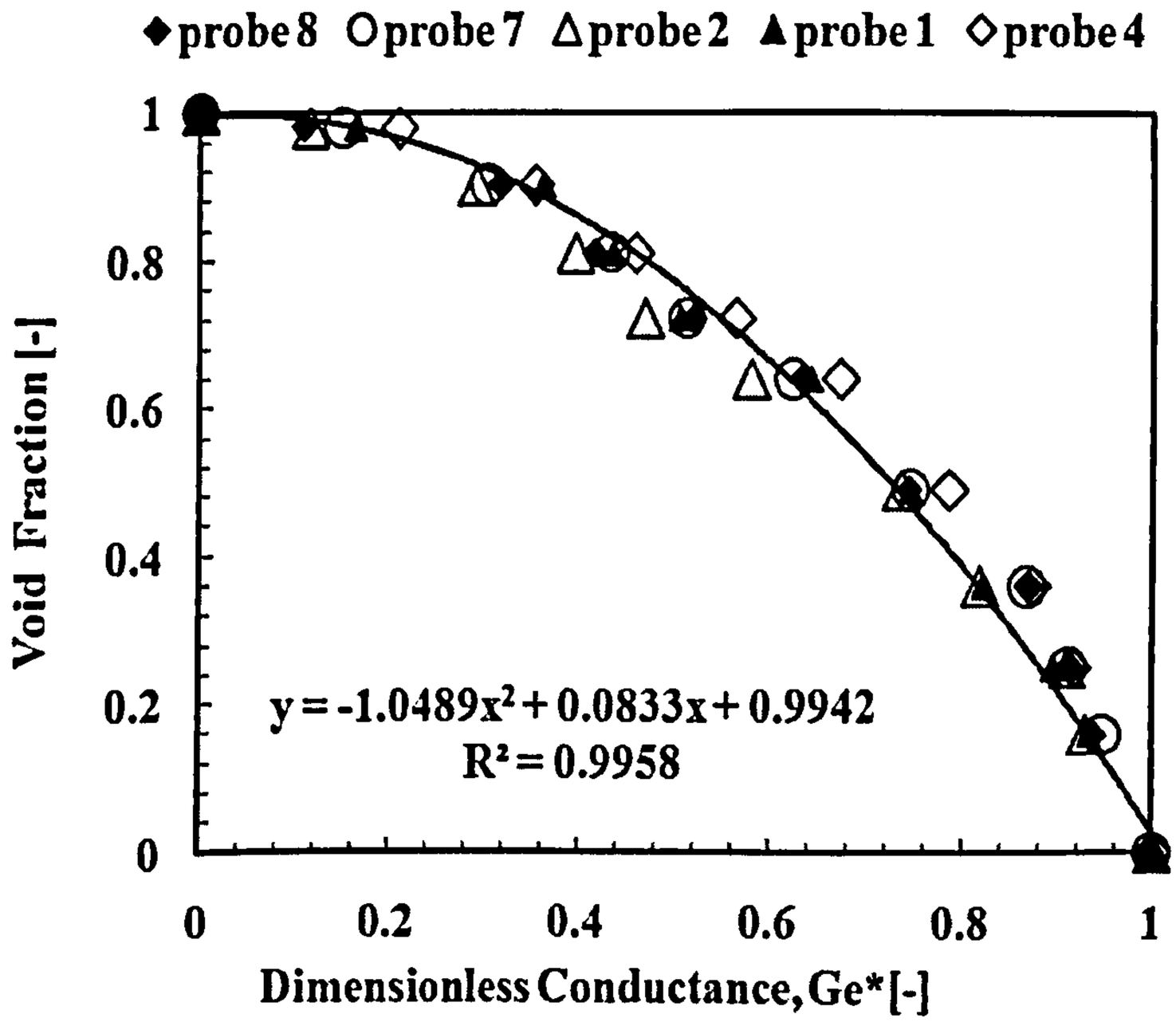

Figure 7.3: Calibration curves for the vertical conductance probes.

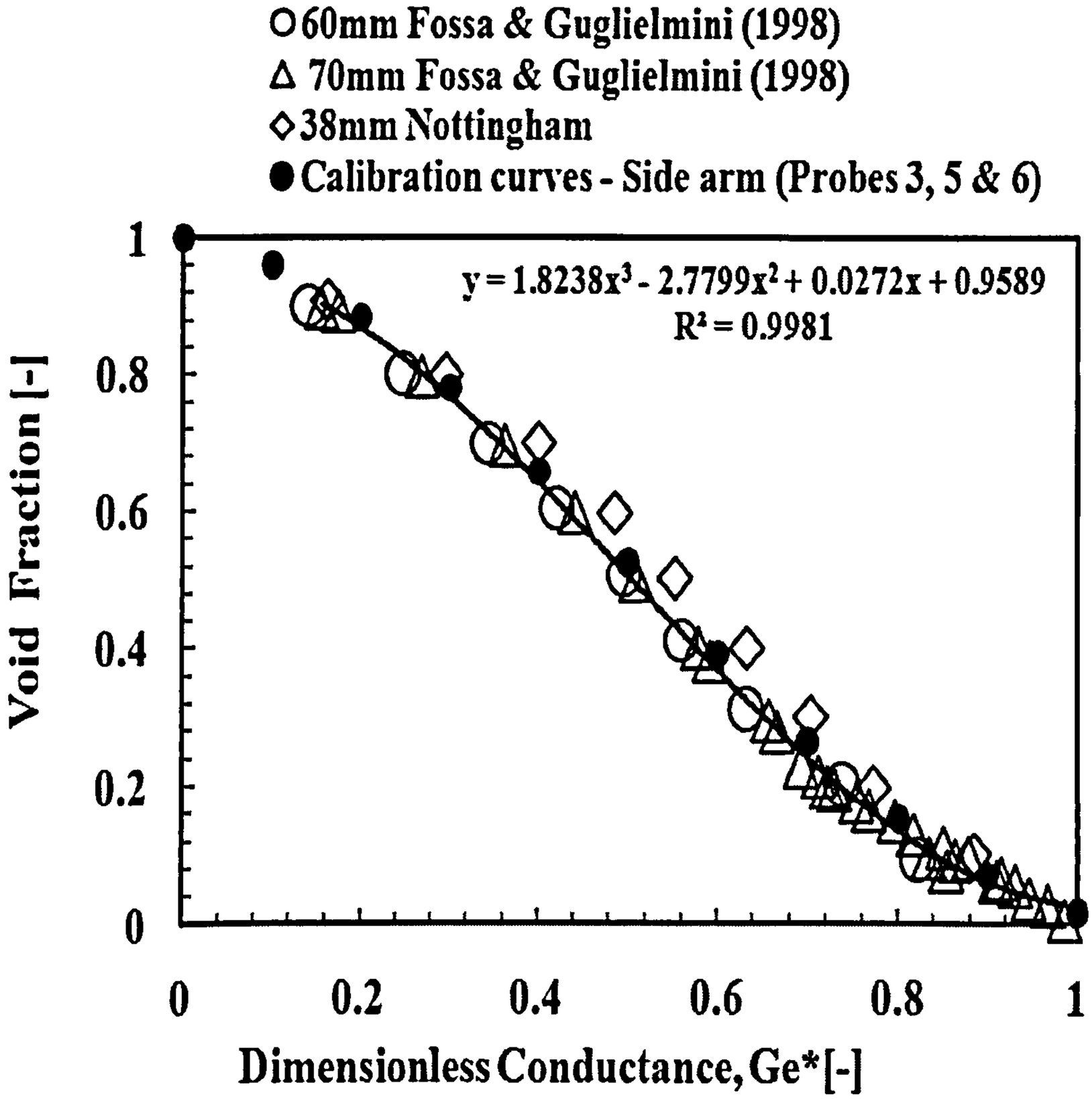

Figure 7.4: Calibration of the horizontal conductance probes.

For the ring conductance probes used in the present experiments, the distance between the electrode plates and width of each plate are 1.7 and 0.5 mm, respectively. This gives electrode spacing to pipe diameter ratio *(De/D)* of 0.34 and electrode width to pipe diameter ratio *(s/D)* of 0.1. The probes give a voltage output which is proportional to the resistance of the two-phase mixture. This response is converted to dimensionless conductance by referring to the value obtainable when the pipe is full of liquid. Different calibration relationships for void fraction were derived for the probes orientated horizontally and vertically in terms of dimensionless conductance. For the vertical

probes, the calibration which was undertaken by Omebere-Iyari et al. (2005) involved artificially creating instantaneous void fractions using plastic plugs with cylindrical rods of known diameters and relating this to the dimensionless conductance (Figure 7.3).

In the case of the horizontal probes, Mak et al. (2006) have compared test results for probes in a 38 mm diameter pipe with the work by Fossa and Guglielmini (1998) for 60 and 70 mm diameter tubes with similar aspect ratios (*De/D* and *s/D* ratios) to the 5 mm diameter probes.

This shows little differences in the relationship between void fraction and dimensionless conductance and the best fit line is applied for the present experiments as given in Figure 7.4.

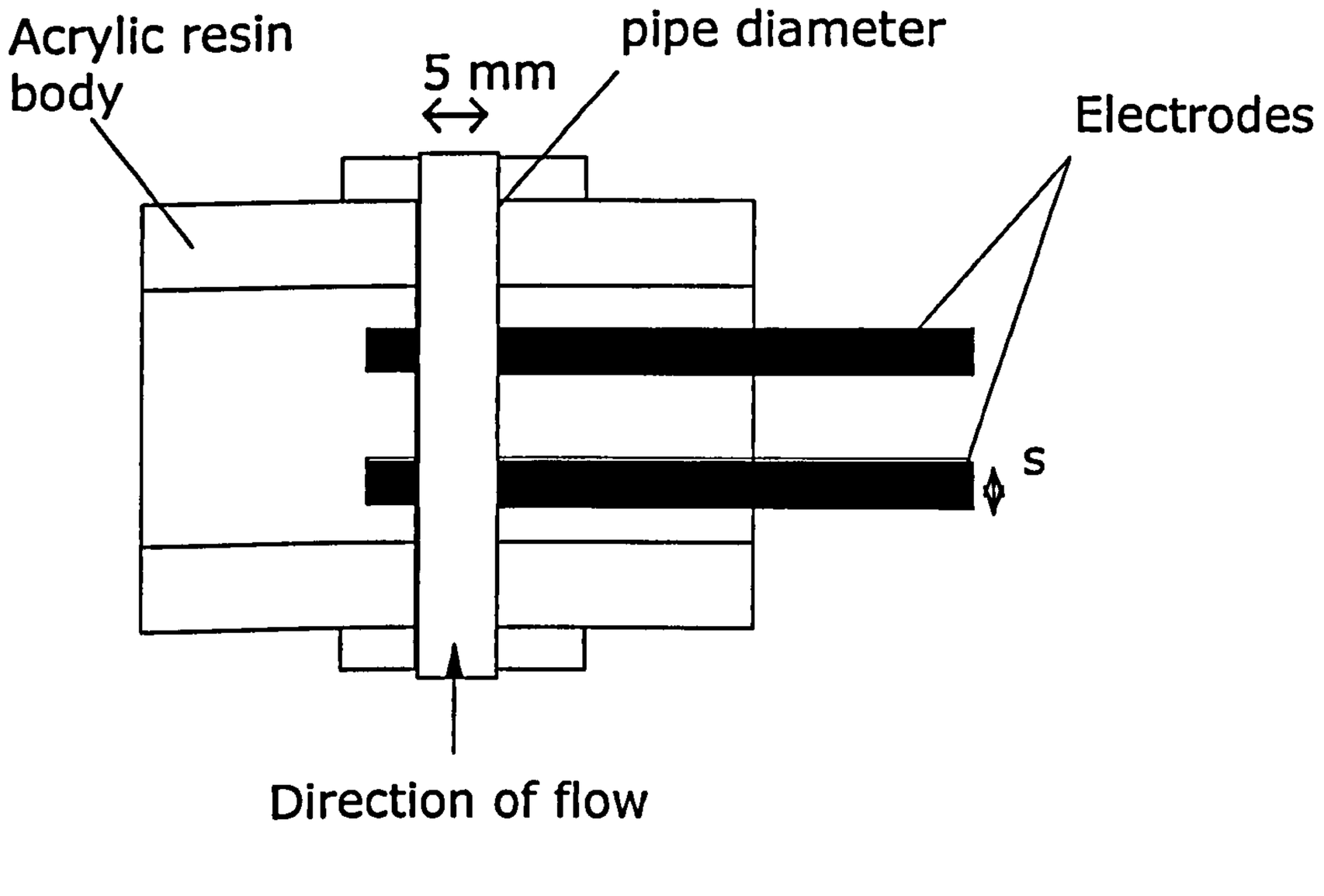

Figure 7.5: Cross sectional view of the ring type conductance probe.

Viscosities of the glycerol solutions were measured with Brookfield Dial Viscometer (Model LVT) while the sample conductivity was measured with cconductivity meter WTW model LF340.

7.3 Results

Liquid hold-up and phase split measured at each take-off are presented and discussed. For each test, the flow rates emerging from both the run and side arms out of the T-junction were recorded. The fractions of gas and liquid flows taken off through the side arm were calculated. Mass balances were carried out between the inlet and outlet flows. For gas and liquid, all reported data agree within ±5 %.

The results are considered in increasing levels of complexity. At the simplest level, the time series of cross sectionally averaged void fraction were examined. Firstly simple statistical measured were extracted.

7.3.1 Variation in time series – effect of liquid physical properties.

Time-resolved information can be examined at a number of levels. A great deal of information can be obtained by considering the time series of the cross-sectionally averaged void fraction. An example of this for the two liquids studied is shown in Figure 7.6. These are taken at gas superficial velocity of 3.2 m/s and a liquid superficial velocity of 0.12 m/s. In both cases the results show the characteristic alternate regions of higher and lower void fractions which epitomise slug flow. It is clearly seen that the void fraction in the liquid slug part is higher for the water than for the glycerol data for

flow leaving junction in the vertical run arm of the pipe. In the case of flow diverted to the side arm, the result shows characteristic alternate regions of high and low void fraction for water which is an indication of slug flow. An obvious uniform distribution of void fraction around a mean value is seen for glycerol which is strong indication of stratified flow. For flow approaching the junction, the time traces suggest a developing slug flow regime for water whereas the signature displays for glycerol shows regions of characteristic low void fraction with fairly regular peaks of higher void fraction probably representing clusters of bubbles.

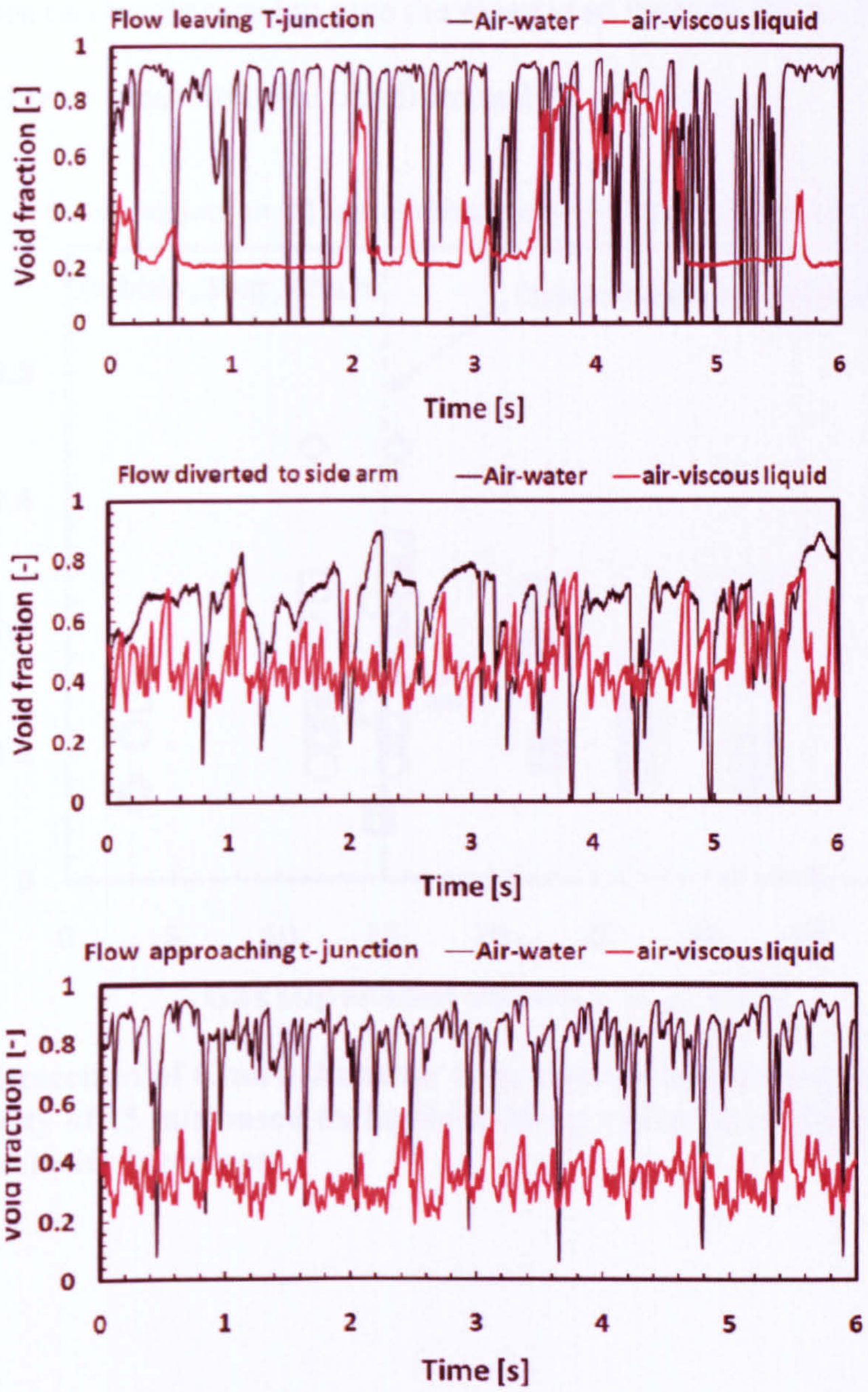

Figure 7.6: Time averaged void fraction for air/water and air-glycerol solution. Gas superficial velocity = 3.2 m/s, liquid superficial velocity = 0.12 m/s, Liquid viscosity = 36.0 mPa s, Gas Take Off = 0.68, Liquid Take Off = 0.68.

7.3.2 Flow Pattern transition

These time series can be averaged to give the mean void fraction. Mean liquid hold-up is then determined from mean void fraction from unity.

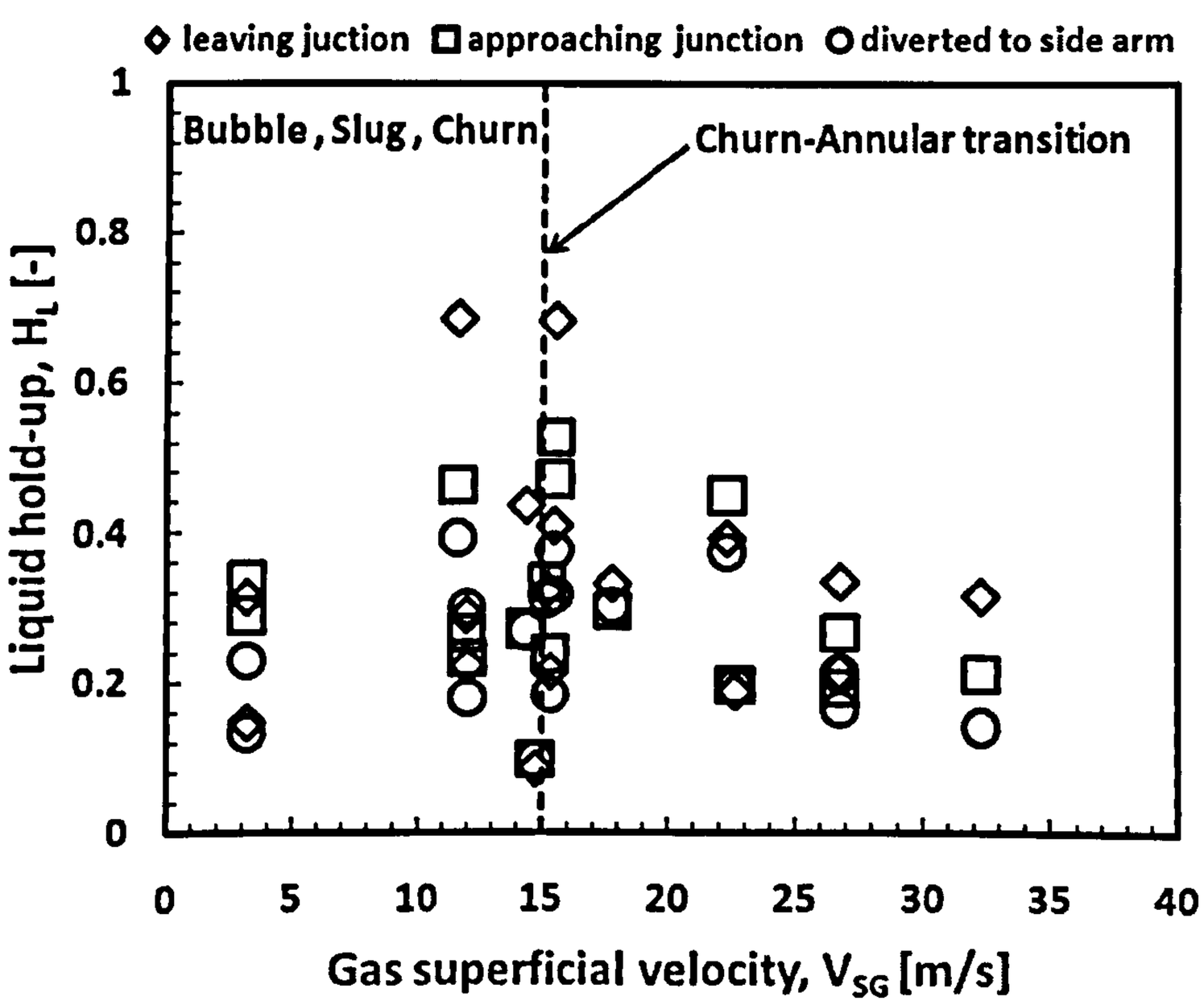

Figure 7.7 (a): Detection of Churn-Annular flow transition boundary at a gas superficial velocity of 15 m/s based on liquid hold-up variation within the system as gas superficial velocity increases.

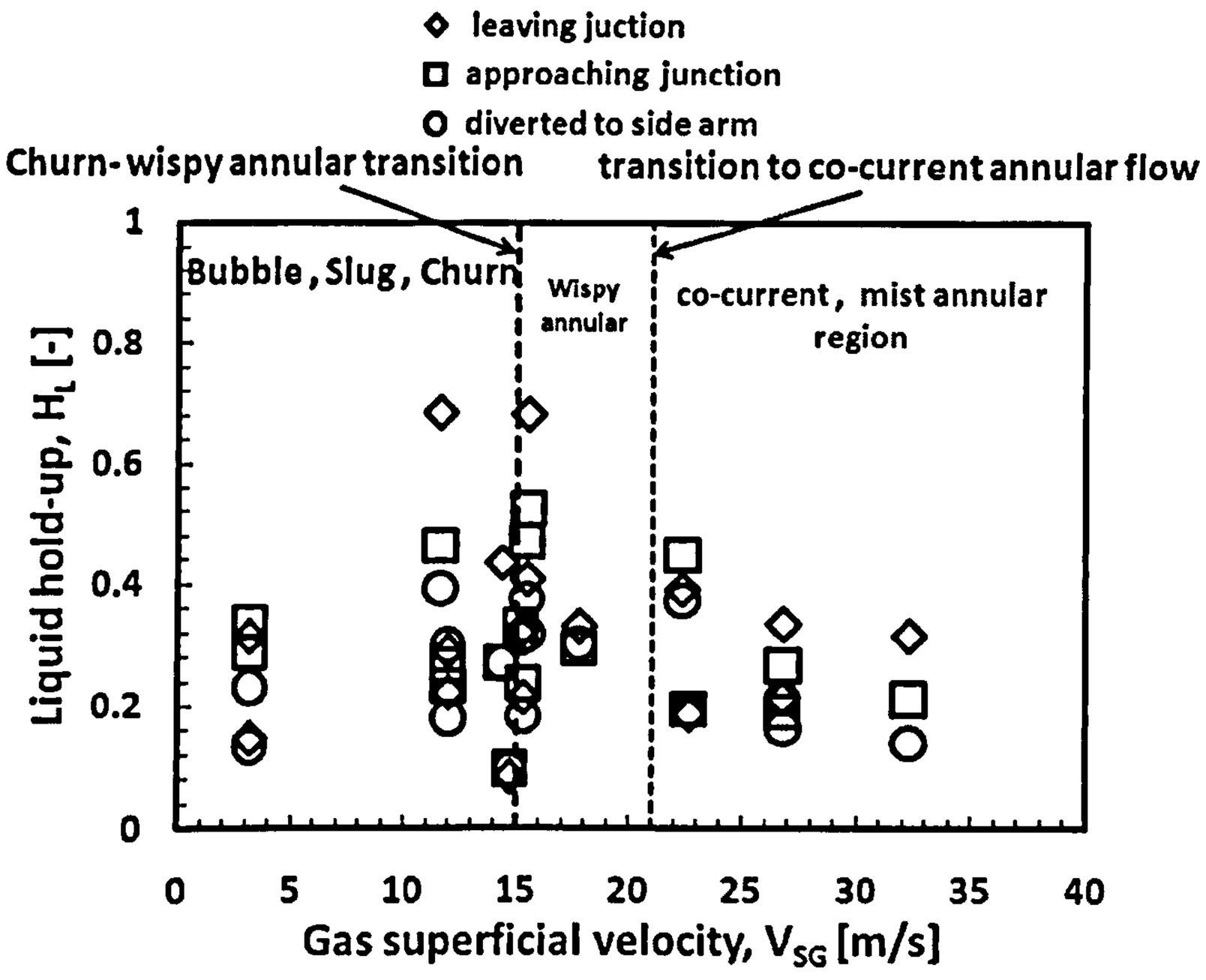

Figure 7.7 (b): Further analysis of the transitions within annular flow based on established information from drop size in chapter four.

This quantity is important to many engineering calculations particularly when pressure drop is involved as it is central to the gravitational component. Figure 7.7 shows how this parameter increases systematically with increasing gas superficial velocity within different segments of the junction.

Figure 7.7 (a) shows that liquid hold-up increases with gas superficial velocity towards a transitional gas superficial velocity of 15 m/s. This marks the beginning of annular flow considering the value of liquid hold-up. After the transition, the liquid hold-up decreases monotonically with increase in gas superficial velocity.

In Figure 7.7(b), transitions within annular flow are further examined based on the knowledge and depth of information available from drop size measurement in Chapter

Four. Thus, it has been established that co-current annular flow occurs at gas superficial velocity of 21 m/s based on subtle changes in the profiles of characteristic drop diameter (SMD) and entrained fraction. The evidences were further strengthened by the corresponding characteristic behaviours exhibited by disturbance wave properties around the transition. A lot of studies agree on this according to Table 4.2. It is equally observed in Table 4.2 that transition to co-current annular flow is independent on of pipe diameter, flow orientation and liquid superficial velocity. Based on these facts and figures, the transition seen in Figure 7.7 (a) can be thought of to be transition to wispy annular flow as indicated in Figure 7.7 (b). This transition marks the onset of atomization process of liquid film. However, this atomization is not complete due to the influence of huge waves. This regime continues until gas superficial velocity of 21 m/s where transition to co-current annular flow occurs as previously explained in Chapter Four. Because of the limitation of the pipe diameter drop size measurement was carried out on this facility.

Flow pattern prevailing in the main pipe is considered next. A strong theme in the modelling of two-phase flows is to use different models for each flow pattern. Therefore it is important to identify which flow pattern is present. In order to identify flow pattern at each inlet condition various operating points are plotted on vertical flow pattern map of Taitel et al. (1980) Figure 7.8. Very obviously, only two inlet conditions fall into slug flow regime i.e. V_{SG} = 3.2 m/s, V_{SL} = 0.1 and V_{SG} = 3.2 m/s, V_{SL} = 0.2 m/s respectively. This agrees vey well with visual observation during the experiment and the information from time series in Figure 7.6.

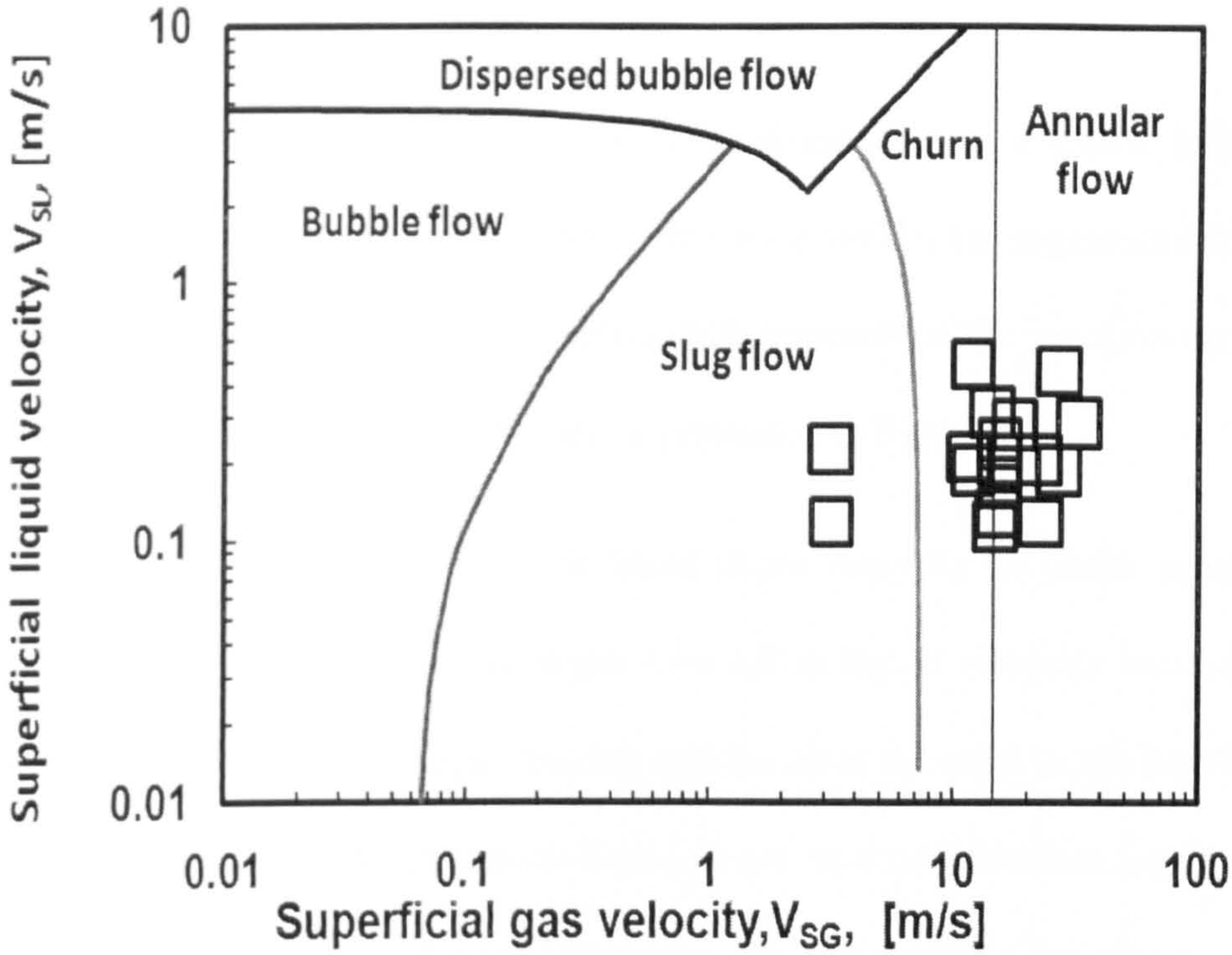

Figure 7.8: Representation of test conditions on the flow pattern map of Taitel et al. (1980). Churn -Annular transition boundary agrees with churn-annular transition observed in Figure 7.7 (a) and Figure 7.7 (b).

The good agreement between the present data and the flow map may be as a result of inclusion of fluid properties in the formulation of the transition models employed by Taitel et al. (1980). The experiment by Taitel et al. (1980) was conducted with fluid of similar physical properties as used in the present study. A pipe of internal diameters of 25 mm (five times the size of pipe diameter used in this study), 51 cm long, with air/water as fluid at 25^0C and at 1.0 Bar (10 N/cm^2) system pressure. Inlet conditions tested were also similar to the present study.

The most outstanding finding is the transition from churn to annular flow which occurs around superficial gas velocity of 15 m/s as in Figure 7.8 which tie in with the observation in Figure 7.7 (a).

7.3.3 Phase distribution

Temporally averaged void fraction/liquid hold-up distribution is a useful indicator of phase distribution of two-phase flow. Phase distribution within the segments of the pipes is examined by plotting liquid hold-up within each segment of the junction against gas fraction taken off at the side arm. The result is presented in Figure 7.9.

The trend observed shows strong effect of liquid phase viscosity on phase separation as liquid hold-up increases with increase in gas take off as liquid viscosity increases. This trend is similar for flow approaching, leaving and the flow diverted to the junction. The liquid hold-up increases with increase in liquid phase viscosity because liquid velocity of the viscous phase adjacent to the wall decreases and occupying more space across the cross section of the pipe.

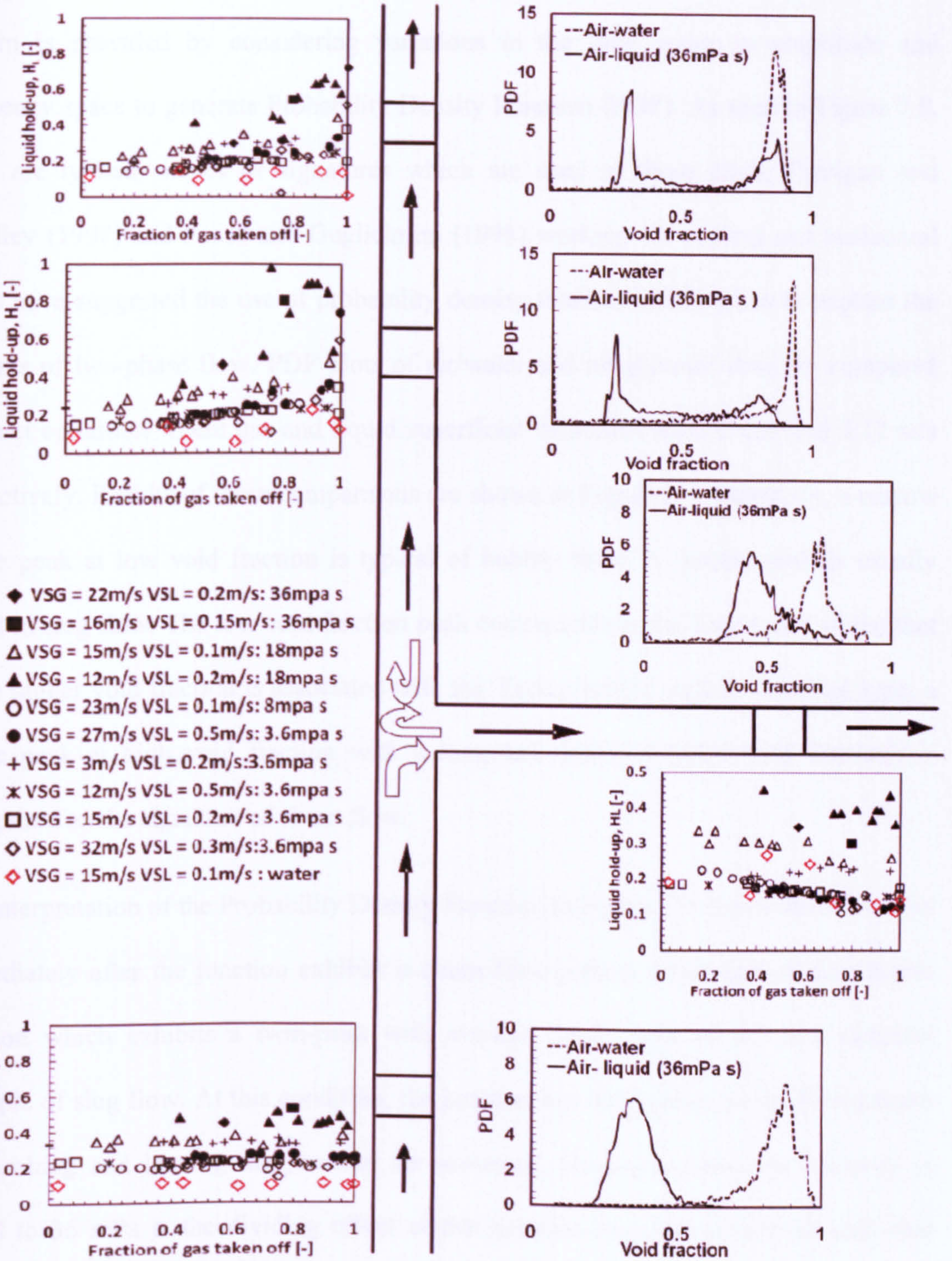

Figure 7.9: Comparison of air/water and air-viscous liquid data at the same flow conditions using liquid hold-up and PDF of void fraction. Gas superficial velocity = 3.2 m/s, liquid superficial velocity = 0.12 m/s. T-Junction Pressure = 1.4 bar. Gas Take Off = 0.68; Liquid Take Off = 0.68.

7.3.4 Flow pattern identification

Additional supporting detail to identify flow pattern along the three segments of the system is provided by considering variations in the time series in amplitude and frequency space to generate Probability Density Function (PDF). As seen in Figure 7.8, there are typical shapes or signatures which are seen in these plots. Costigan and Whalley (1997) and Fossa and Guglielmini (1998) working on vertical and horizontal flows have suggested the use of probability density function (PDF) plots to explain the features of two-phase flow. PDF plots of air/water and air-glycerol data are compared for inlet condition where gas and liquid superficial velocities are 3.2 m/s and 0.12 m/s respectively. Results of these comparisons are shown in Figure 7.9. Generally, a narrow single peak at low void fraction is typical of bubbly flow. A double peak is usually found in slug flow. The low void fraction peak corresponds to the liquid slug whilst that at the higher void fraction is associated with the Taylor bubble region. The third type, a single peak at high void fraction with a long tail down to lower void fractions is recognised as the signature of churn flow.

The interpretation of the Probability Density Function in Figure 7.9 shows air/water flow immediately after the junction exhibits a churn flow pattern while that of air-glycerol solution which exhibits a twin-peak with average liquid hold of 0.5 is a classical example of slug flow. At this condition, the junction has little effect on the flow pattern approaching and leaving the junction for air/water. However, when the viscosity is raised to 36 mPa s, the dividing effect of the junction becomes prominent such that churn flow before the junction becomes slug flow after the junction due to the splitting effect of the dividing junction on flow pattern. This is very important design information

as flow pattern after the junction is usually not considered as an important design parameter.

For air/water system, flow before and after the junction does not seem to change considerably. For instance, slug and annular flow approaching the junction emerge to be similar after leaving the junction. However, flow to the side arm is stratified with little effect of liquid viscosity on hold-up in both instances.

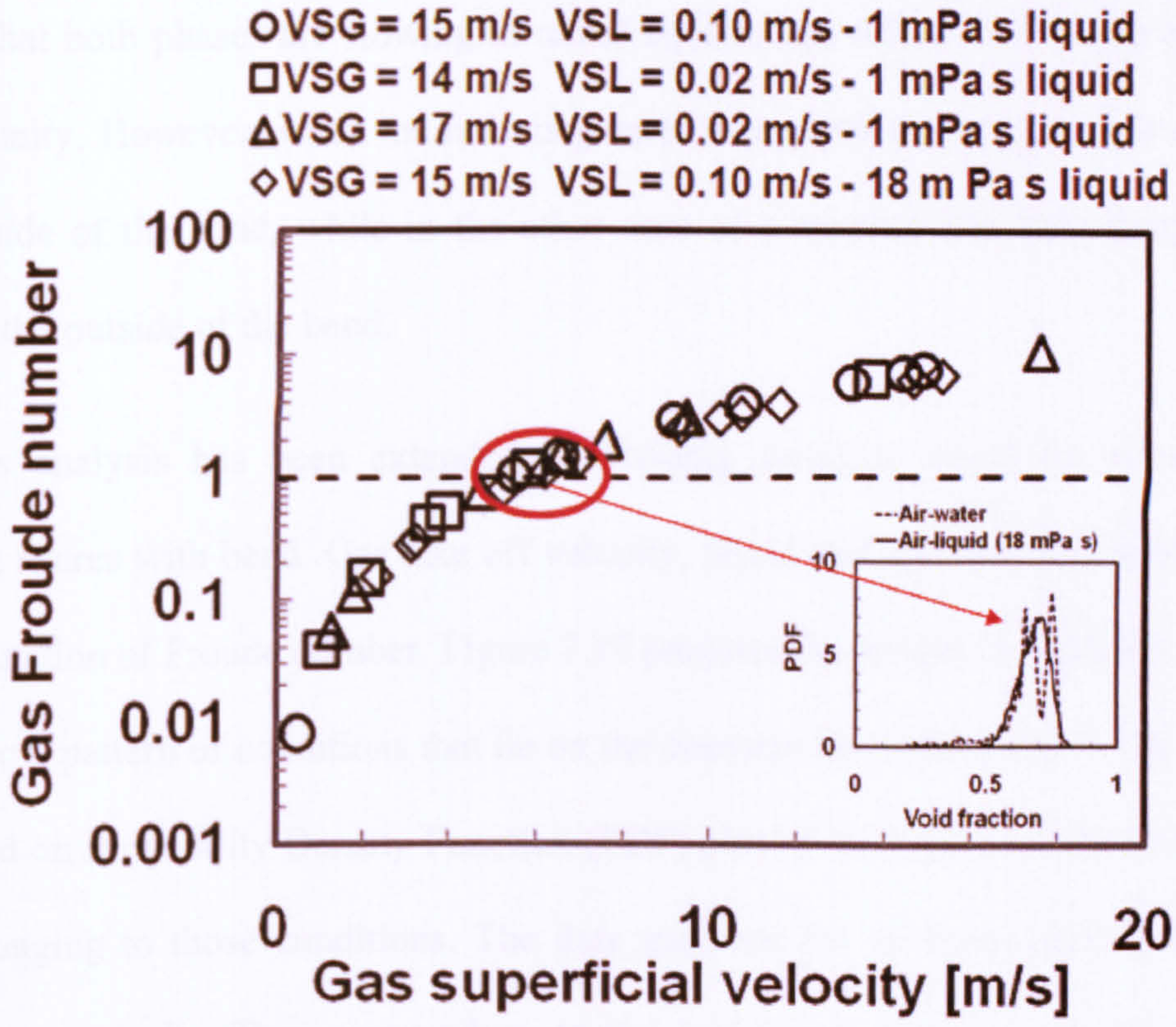

Figure 7.10: Use of Froude number to identifying flow pattern.

The phase split plot does not indicate flow pattern. Identifying flow pattern based on phase split can be misleading. In order to identify flow pattern additional information is required which can then be used in conjunction with phase split curve to determine prevailing flow pattern in the system. Therefore, analysis is taken another level of

complexity. At this level, the idea of Gardner and Neller (1969) is adopted to identify flow pattern based dynamic information acquired by the probes at every take off. Gardner and Neller (1969) has demonstrated the use of Froude number to identify flow pattern for the case of bubble/ slug flow upstream of a vertical bend. In the bend the gas can flow either on the outside or the inside of the bend depending on the balance between the centrifugal force tending to push the liquid phase to the outside and the gravity forcing it to the bottom. The authors expressed the competition between these two forces by Froude number (ratio of centrifugal to gravity force or V_{SG}^2/gD). It is claimed that both phases are flowing in radial equilibrium when the Froude number is equal to unity. However, when the ratio is greater than unity the gas phase is displaced to the inside of the bend, while in the other case of a number less than unity the gas moves to the outside of the bend.

Here, this analysis has been extended to dividing junction based on some similar features it shares with bend. Gas take off velocity, liquid and gas densities were used in the computation of Froude number. Figure 7.10 presents the results. It has been observed that the flow pattern of conditions that lie on the constant line where $Fr_G = 1$ is stratified flow based on Probability Density Function (PDF) plot of void fraction (insert in Figure 7.10) belonging to those conditions. The data used are for air/water and air-18 mPa s glycerol respectively. They were taken at the horizontal side arm of the junction. Therefore, the claim of Gardner and Neller is confirmed.

7.3.5 Phase Split

A Fortran 77 computer code based on several models developed by Azzopardi (1988) was used predicts phase. The computer code also incorporates other models for predicting entrained liquid fraction, liquid film thickness, gas momentum and liquid phase momentum respectively. Gas and liquid take offs are calculated by the following expressions:

$$G' = \frac{\dot{m}_3\, x_3}{\dot{m}_1 x_1} \tag{7.1}$$

$$L' = \frac{\dot{m}_3\,(1 - x_3)}{\dot{m}_1(1 - x_1)} \tag{7.2}$$

Where G' and L' are gas and liquid taken off respectively. $\dot{m}$ is the mass flow rate, kg/s. The quality, x, the ratio of gas mass flow rate to the total flow rate can be calculated from inlet condition using the following expression:

$$x = \frac{\rho_g\, V_{SG}}{(\rho_g V_{SG} + \rho_L V_{SL})} \tag{7.3}$$

In terms of entrained fraction, fraction of gas taken off, Equation (7.1) can be re-written as:

$$G' = \frac{1}{2\pi}\left[\frac{2\pi L'}{K(1-E)} - sin\left(\frac{2\pi L'}{K(1-E)}\right)\right]$$

(7.4)

E = entrained liquid fraction, [-]. K is a factor which accounts for the effects of the ratio of side arm to main pipe diameters given as:

$$k = 1.2\left(\frac{D_3}{D_1}\right)^{0.4} \tag{7.5}$$

The commonality between T-junction study and the previous study in Chapter Four is the entrained liquid fraction. However, entrained measurement could not be carried out on this facility because of the small pipe diameter.

Table 7.1 presents part of the output results generated by the computer programme. Govan et al (1988) model was used for entrained liquid fraction calculation while the equation of Willetts (1987) was used for calculation of film thickness for the inlet conditions within annular flow regime.

Table 7.1: Fluid properties at different viscosities

Mixture viscosity	Gas momentum	Film Momentum	Film thickness	Entrained fraction
[mPa s]	[N/M^2]	[N/M^2]	[mm]	[-]
1.00000	367.75000	645.99000	0.00257	0.00700
12.00000	449.51000	267.23000	0.00367	0.00000
18.00000	468.50000	240.18000	0.00388	0.00000
36.00000	505.26000	210.37000	0.00428	0.00000

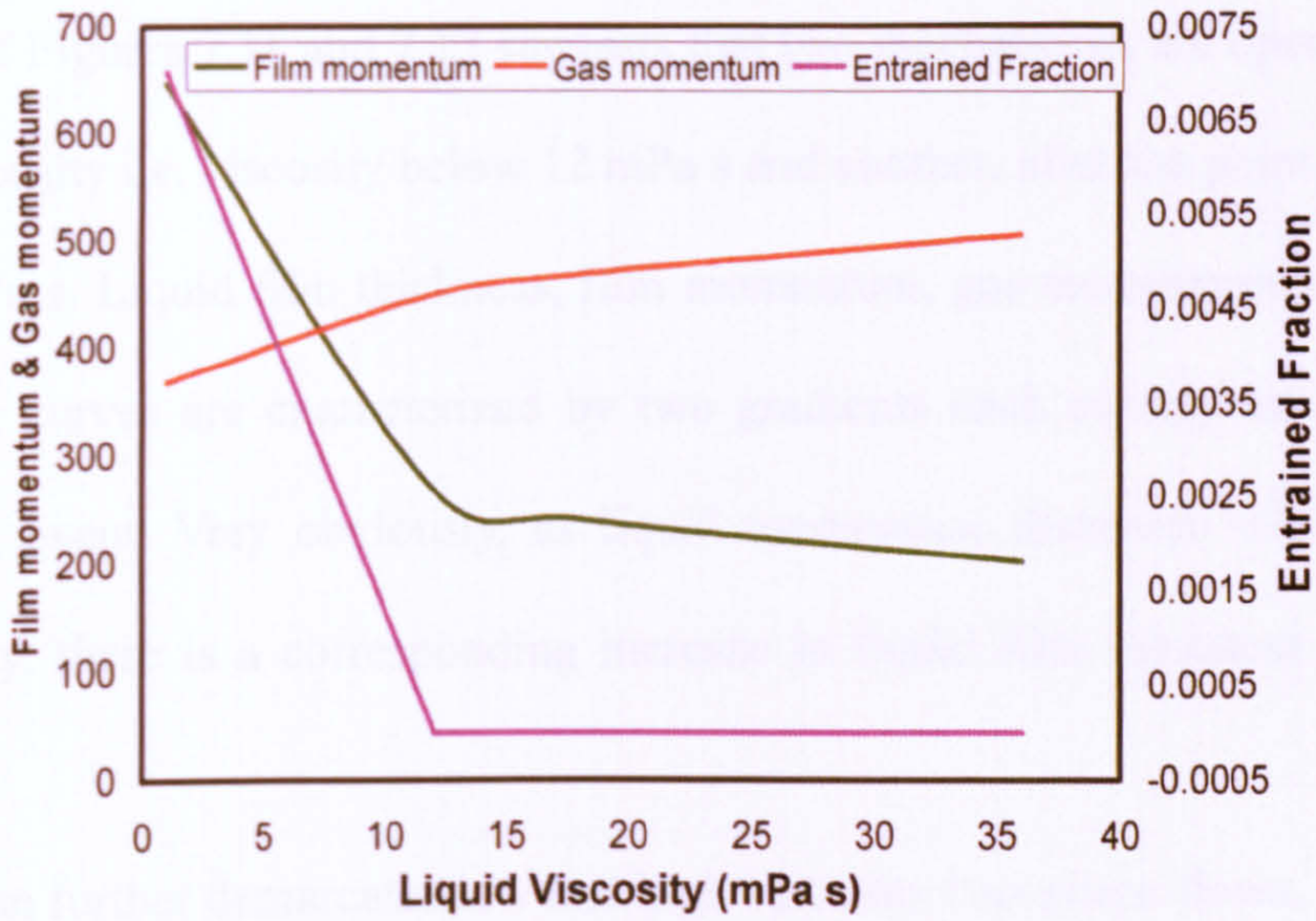

Figure 7.11: Variation of film momentum, gas momentum and entrained fraction with liquid viscosity. Gas superficial velocity = 15.2 m/s, liquid superficial velocity = 0.13m/s, liquid viscosities = 1.0, 12.0, 18.0 and 36.0 mPa s.

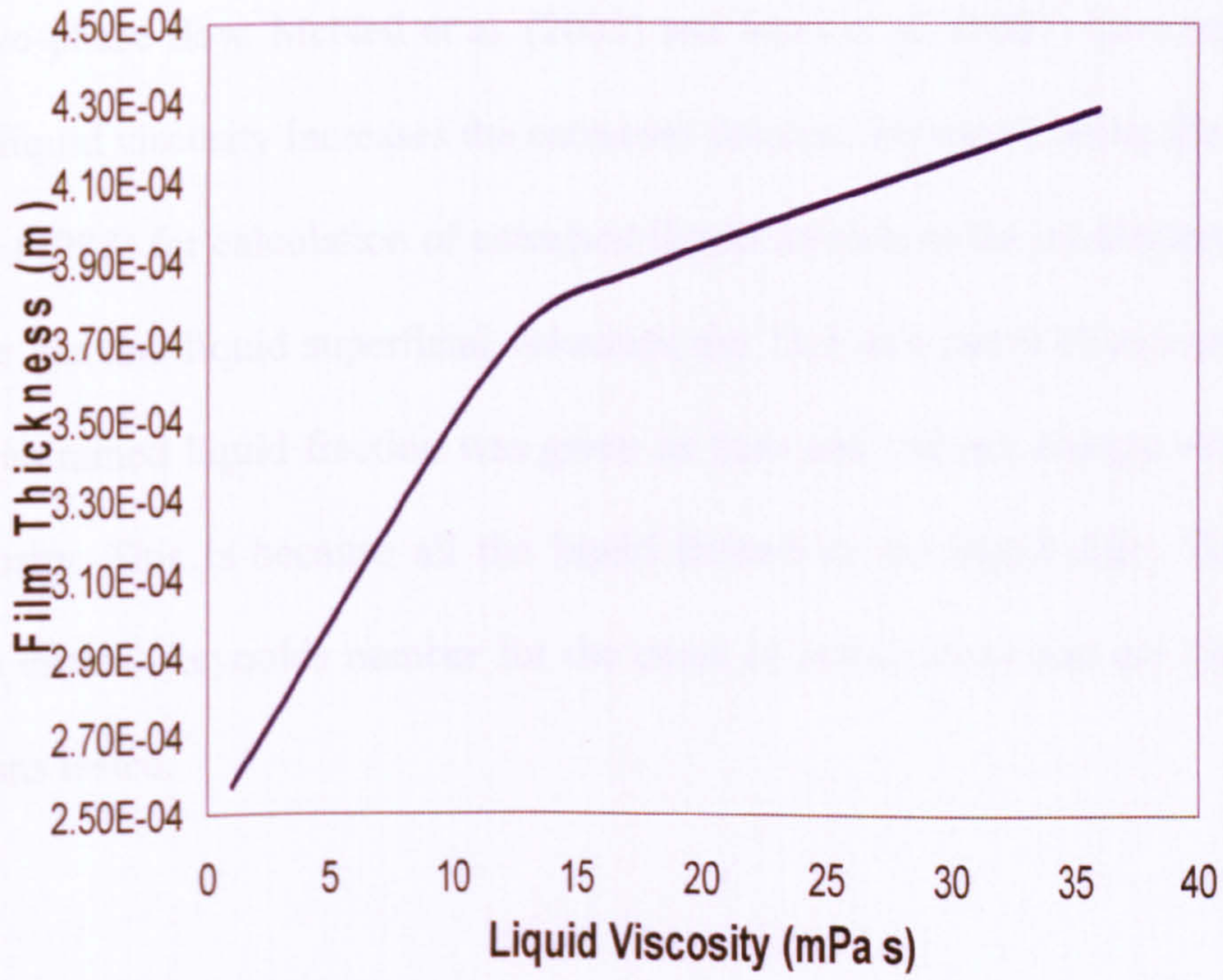

Figure 7.12: Variation of film thickness with liquid viscosity.

Film and gas momentum including entrained fraction are plotted in Figure 7.11 while variation of film thickness is plotted with increasing viscosity in Figure 7.12. Critical examination of Figures 7.11 and 7.12 suggests that two mechanisms are operating; one at low liquid viscosity i.e. viscosity below 12 mPa s and another, after the point of inflection beyond 12 mPa s. Liquid film thickness, film momentum, gas momentum and entrained liquid fraction curves are characterized by two gradients each corresponds to different mechanism or event. Very obviously, as liquid momentum decreases with increase in liquid viscosity, there is a corresponding increase in liquid film thickness as shown in Figure 7.11.

The observation further demarcates low and high viscosity two-phase flows. The possible explanation for this transition may probably be the change in the interfacial behaviour reported by Mori and Nakano (2001) and Kondo et al. (1999) between low and high viscosity two-phase flow. McNeil et al. (2003) and Mori et al. (2001) have reported that increase in liquid viscosity increases the entrained fraction. However, using the method of Govan et al (1988) for calculation of entrained liquid fraction at the conditions of present study where gas and liquid superficial velocities are 15.2 m/s and 0.13 m/s respectively. Calculated entrained liquid fraction was given as zero and did not change with increase liquid viscosity. This is because all the liquid flowed in the liquid film. This may be because the critical Reynolds number for the onset of atomization was not exceeded for the conditions tested.

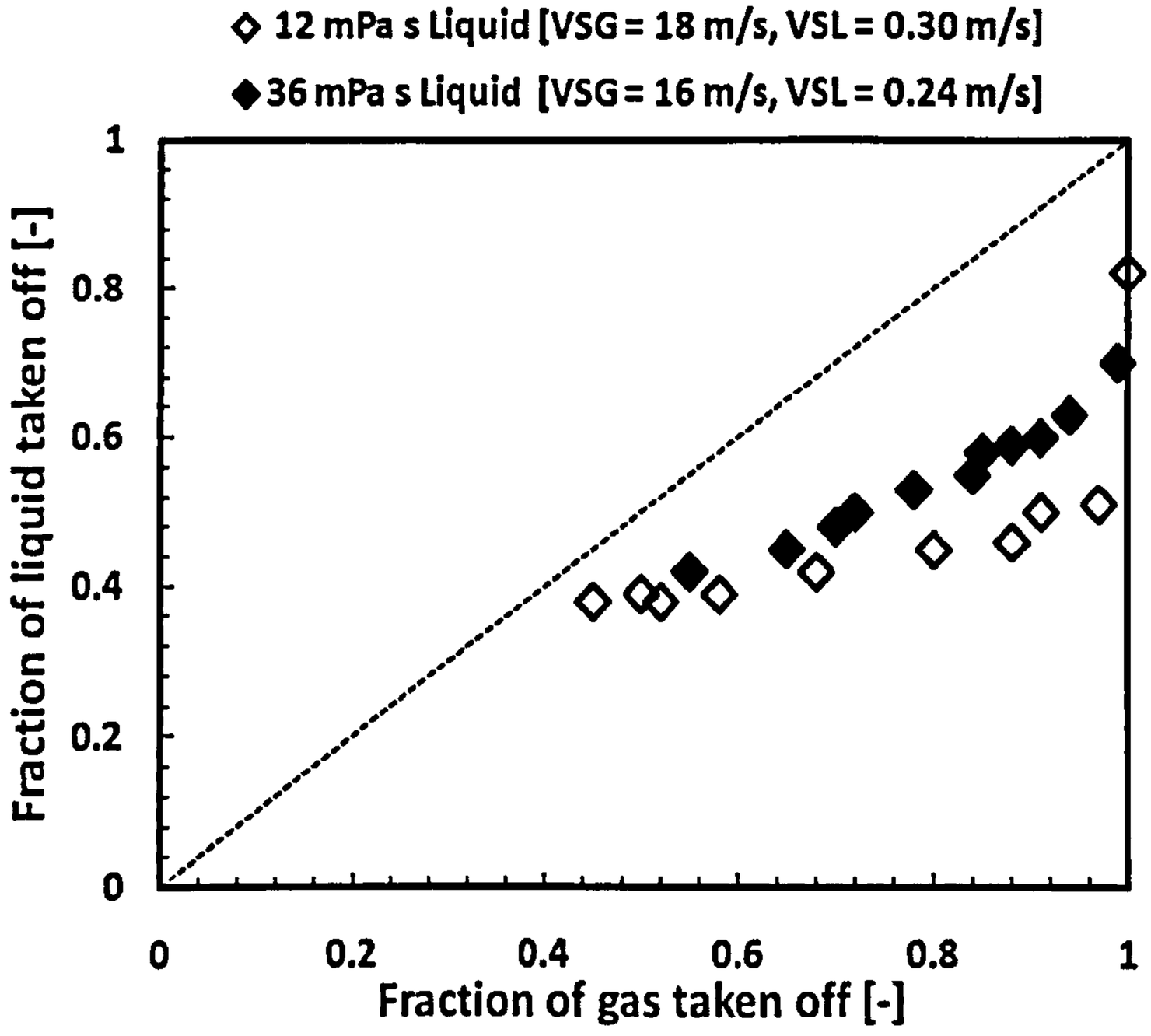

Figure 7.13: Effect of increase in liquid viscosity on phase split at similar conditions.

Next, effect of liquid viscosity on phase split is considered. Figure 7.13 shows that the phase split shift towards liquid dominated region as dynamic liquid phase viscosity increases when inlet conditions are held constant. This can be attributed to the lower liquid momentum at higher liquid viscosity. Low liquid momentum can promote film stop which could cause the liquid film to be easily taken off. Film stop occurs when liquid film is brought to a halt because of its low momentum flux due to pressure increase across the junction after a critical gas take off has been exceeded.

The effect of increase in the inlet gas flow rate was investigated by keeping the liquid superficial velocity constant as shown in Figure 7.14. More liquid is diverted to the side-arm as gas velocity increases. This trend agrees with the work of Azzopardi and

Memory (1989), which showed that a change in the gas inlet velocity had an effect on the liquid take off. Azzopardi and Memory used air/water as test fluid.

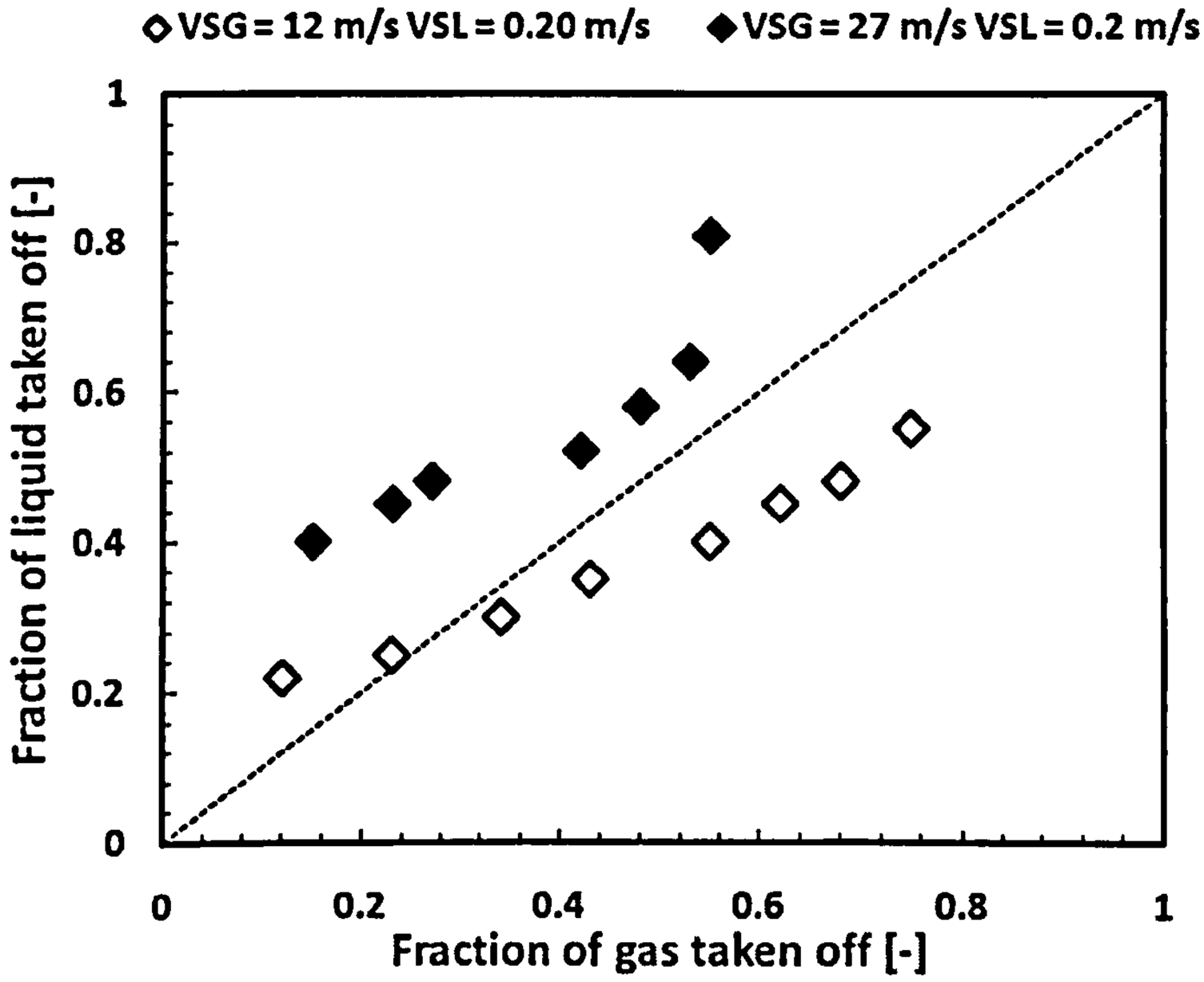

Figure 7.14: Effect of increase in gas superficial velocity on the phase split for liquid viscosity of 18.0mPa s. Fraction of gas taken off = 0.56 ; fraction of liquid taken off = 0.42.

At high gas superficial velocity of 27 m/s, liquid film is mostly transported as drops in the gas core. The drops could be re-deposited as film and can be taken off. Expansion of the core as gas velocity increases can push the liquid film towards the side arm as a result of pressure gradient created by re-circulation of liquid film or secondary flow close to the entrance of the junction.

More liquid was separated in the case of air/water at liquid and gas velocities of 0.02 m/s and 14 m/s, Figure 7.15 (a). Azzopardi (1988) attributed this high liquid take-off to be as a result of low liquid film momentum resulting from film stopping.

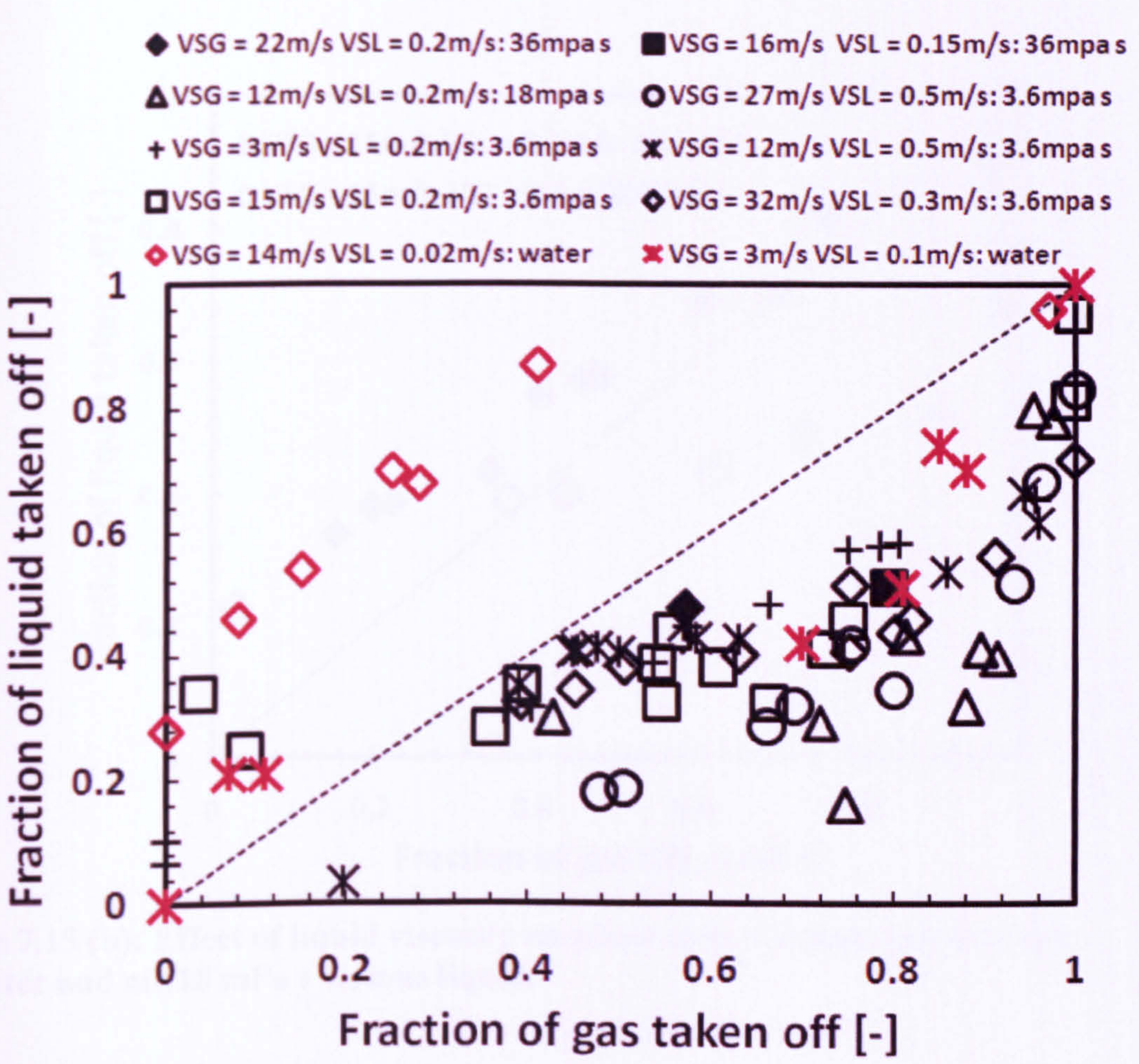

Figure 7.15 (a): Effect of liquid viscosity on phase split.

In Figures 7.15 (b) and 7.15 (c), the liquids that are more viscous than water according Table 7.1, are expected to have lower momentum compared to water. Therefore, for air-18 mPa s glycerol solution at V_{SG} = 15 m/s, V_{SL} = 0.1 m/s Figure 7.15 (b), and air/8 mPa s glycerol solution at V_{SG} = 23 m/s, V_{SL} = 0.1 m/s Figure 7.15 (c), more liquids are

partially separated due mainly to film stopping effect. At these conditions liquid entrainment is expected to high. Therefore, rate of drop deposition will be equally high. At these conditions, rate of atomization is very high as both conditions are in annular flow regime. It seems that the expansion of the gas core increases the mobility of the film around the wall and pushes it towards region of lower pressure in the side arm.

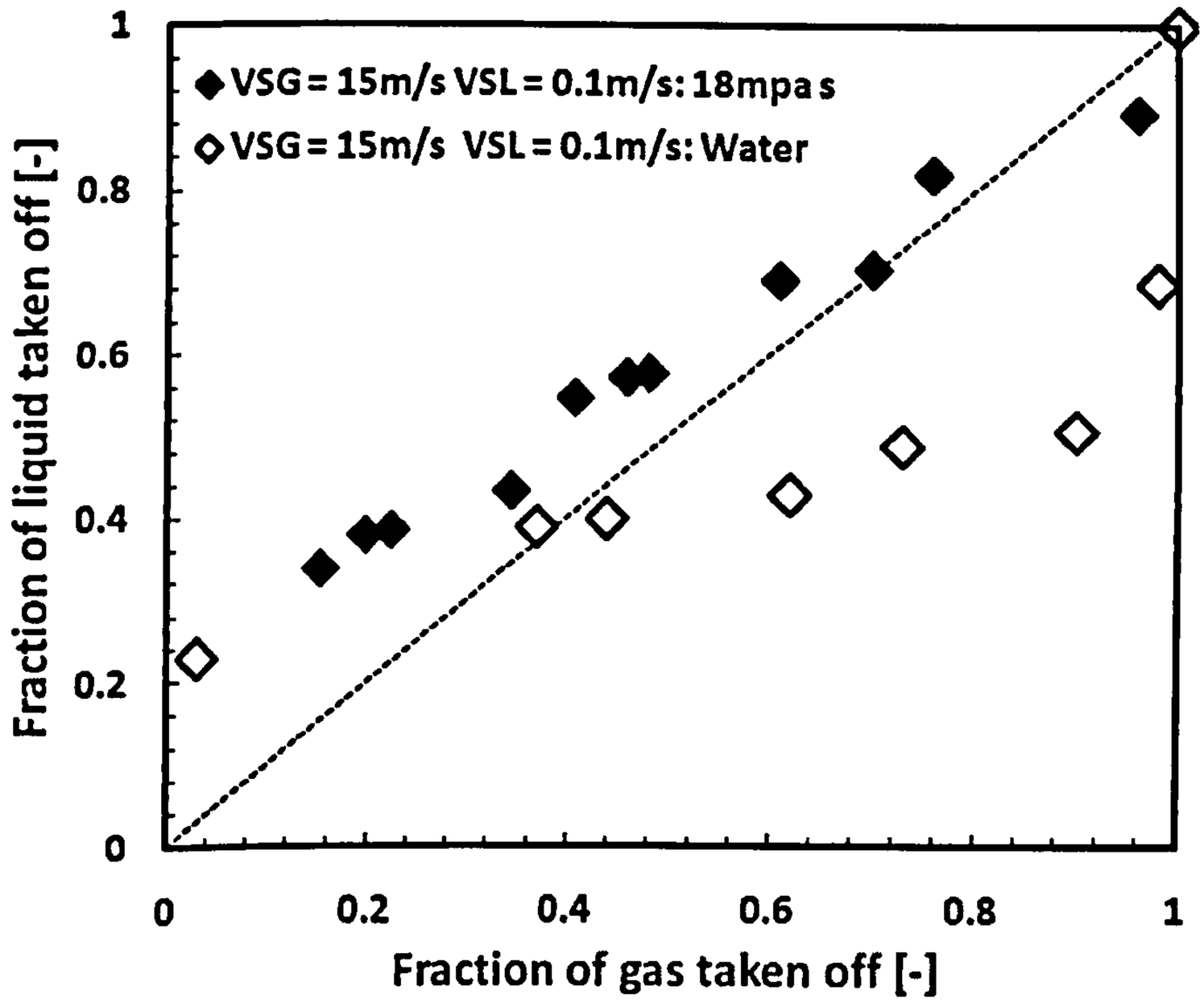

Figure 7.15 (b): Effect of liquid viscosity on phase split. Comparison between air/water and air/18 mPa s viscous liquid.

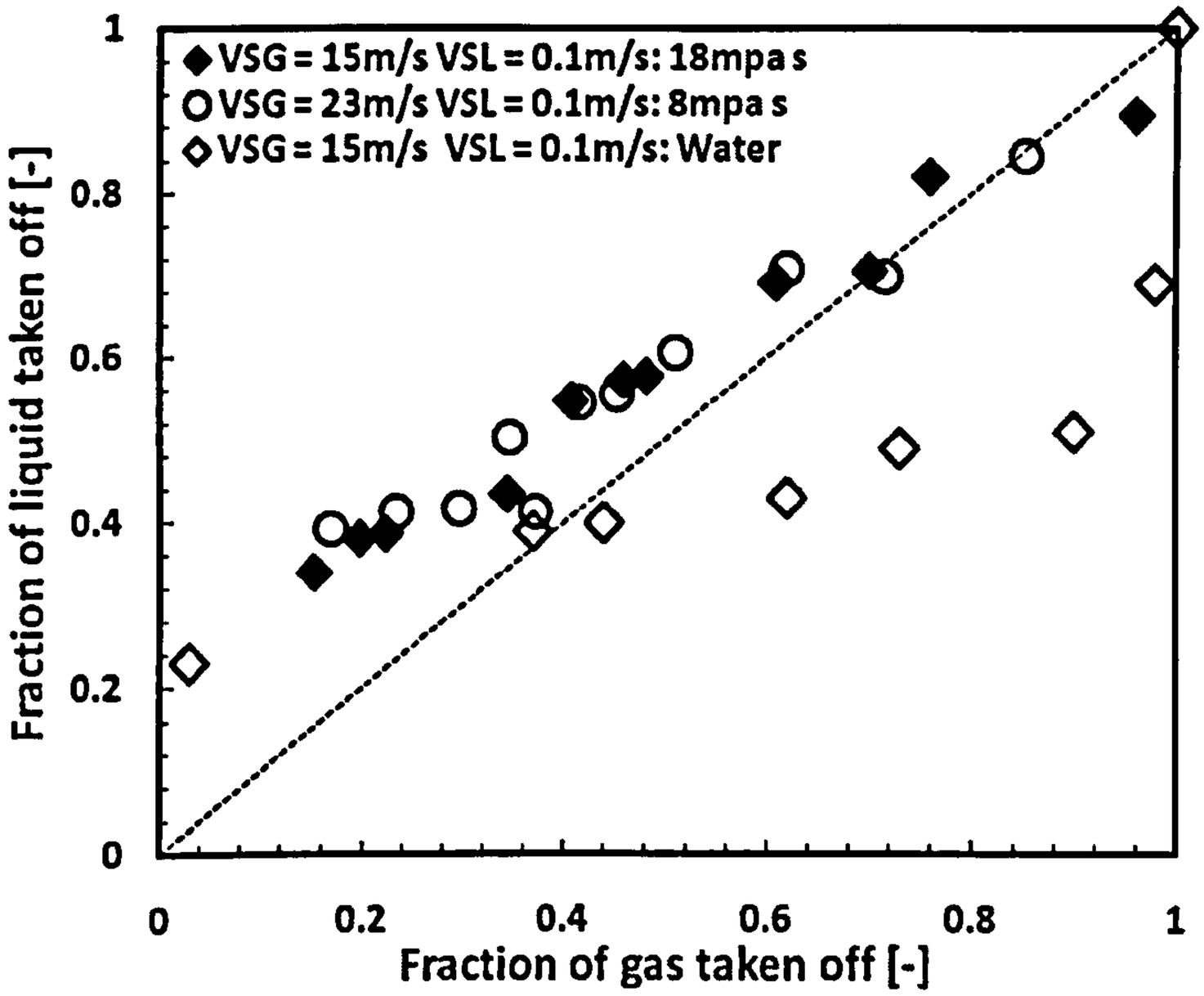

Figure 7.15(c): Effect of liquid viscosity on phase split. Comparison between air/water air/8 mPa s and air/18 mPa s viscous liquids.

Next, an explanation is sought for increase in liquid take off as liquid physical property changes based on the trend observed using the plot of liquid hold-up against gas take off Figure 7.11. The figure shows liquid hold-up increases with increasing gas taken-off. Critical examination of the plot however reveals that liquid viscosity only have significant effect on liquid hold-up when fraction of gas taken off exceeds a value of 0.40. After fraction of gas taken off of 0.40, liquid hold-up is seen to increase with increase in liquid viscosity as gas taken off increases. Because hold-up is high and liquid momentum is low, the liquid is easily taken off. This explains why more liquid are separated in Figure 7.15(b) and Figure 7.15 (c).

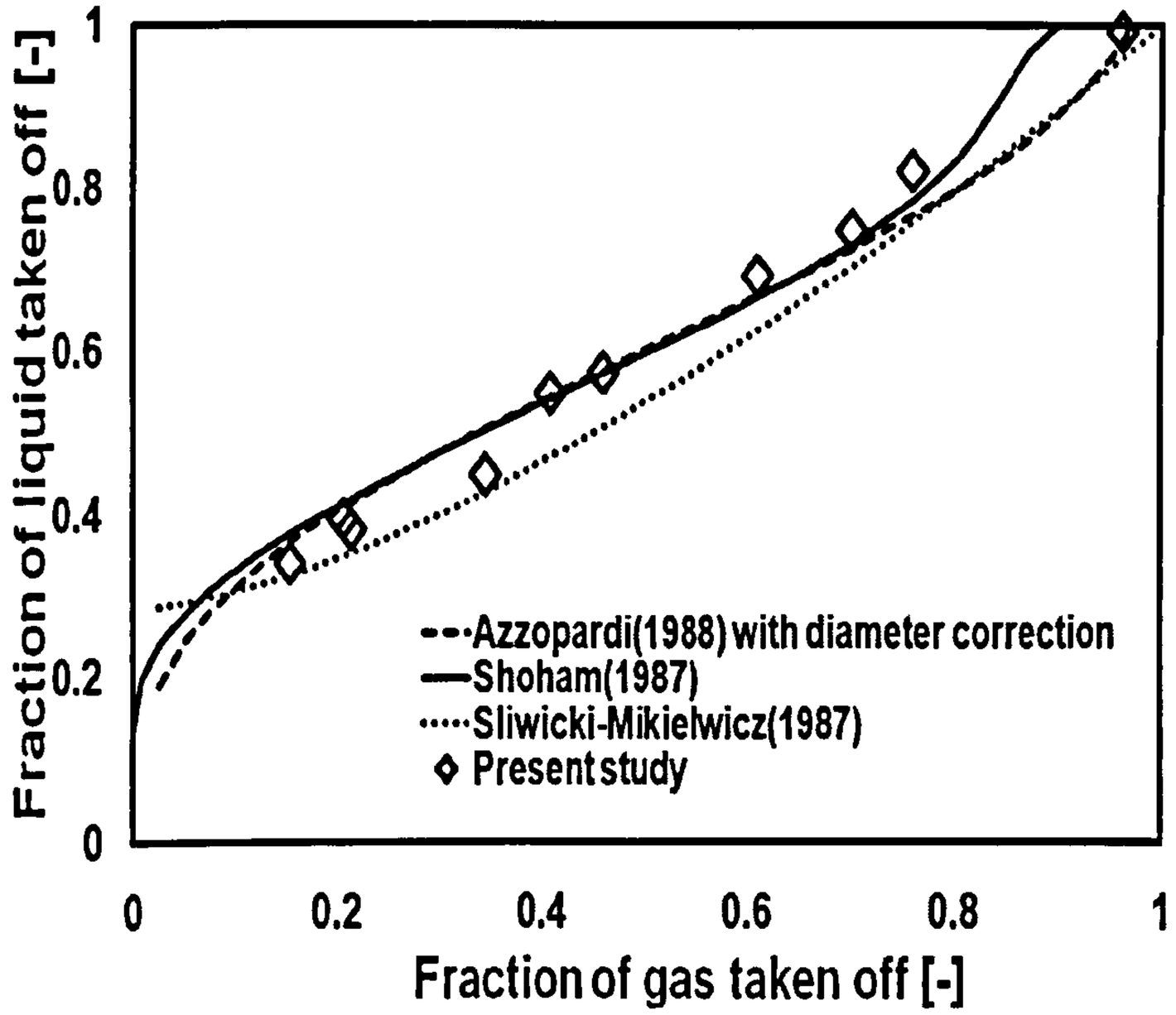

Figure 7.16: Comparisons with prediction models for the phase split at a T-junction. Gas superficial velocity = 15.2 m/s, liquid superficial velocity = 0.13 m/s, liquid viscosity = 18.0 mPa s.

The present data has been used to test the predictive ability of published models, Figure 7.16. The model of Azzopardi (1988), Shoham (1987) and Sliwicki-Mikielwicz (1987) are considered to predict the experiment phase split. Figure 7.11 shows the good agreement between the present data and the existing models. In the case of model of Azzopardi (1988), it was found that a better performance was obtained if flooding was not considered. Mak et al. (2006) provided justification for omitting that phenomenon. It was not seen in their air/water experiments carried out on the same facility as used in the present study. Flooding was also not observed in the pipe above the junction in the present experiments. Azzopardi (1988) assumes that the phenomenon of flooding causes entrained drops to deposit onto the wall film and hence fall back and be taken off. The over-prediction of the liquid taken off is explained by the absence of flooding. Better

predictions are obtained when the method of Azzopardi (1988) is modified to account for the non-existence of flooding.

The models by Shoham et al. (1987), Sliwicki and Mikielewicz (1987) also give excellent agreement as shown in Figure 7.16. Although the work of Shoham et al. (1987) was developed for a horizontal T-junction, it could be applied to vertical pipe arrangements because the model assumes the flow is a cylindrically symmetrical annular flow.

Where Shoham et al. (1987) under-predicted the liquid take off, the probable reason may be the dominance of centripetal forces suggested in their model which does not apply to this condition as liquid entrainment may not be significant. As the liquid superficial velocity is decreased, the void fraction is increased and it leads to decrease the film thickness. As the film thickness is decreased, the film velocity can then be increased. This leads to an increase in the centripetal forces.

7.3.6 Effect of physical properties

In the present study effect of fluid properties has been investigated using dimensional approach. Wallis (1969) proposed a dimensionless Archimedes number, N_{Ar}, Equation (7.6) for horizontal flow to include liquid viscosity, surface tension, fluid properties and gravitational acceleration parameters in one equation as follows:

$$N_{Ar} = \sigma\rho_L / [\mu_L^4 g(\rho_L - \rho_g)]^{0.5} \qquad (7.6)$$

White and Beardmore (1962) identified Morton number, M, as a property number which can be used to characterise gas-liquid two-phase flow structures. They proposed the following definition:

$$M = g\mu_L^4(\rho_L - \rho_G)/\rho_L^2\sigma^3 \qquad (7.7)$$

Where:

g is the gravity acceleration, μ is the viscosity, ρ is the density, and σ the surface tension.

Figure 7.16 shows dependence of liquid hold-up on liquid viscosity. Liquid hold-up decreases with Archimedes number and inverse Morton numbers respectively as liquid viscosity increases. Both Archimedes number and inverse Morton numbers show similar trend. This also explains dependence of gas and liquid take-offs on liquid viscosity. This agrees with findings reported by Hong et al. (1978). Therefore, based on Figure 7.9, it can be concluded that at low viscosity liquid hold-up is low and vice versa. Similarly, based on Figures 7.9 and 7.17 (a) , it can be implied that at high gas take off liquid hold-up is also high. Conclusively, division of two-phase flow at vertical dividing junction can be greatly influenced by liquid viscosity.

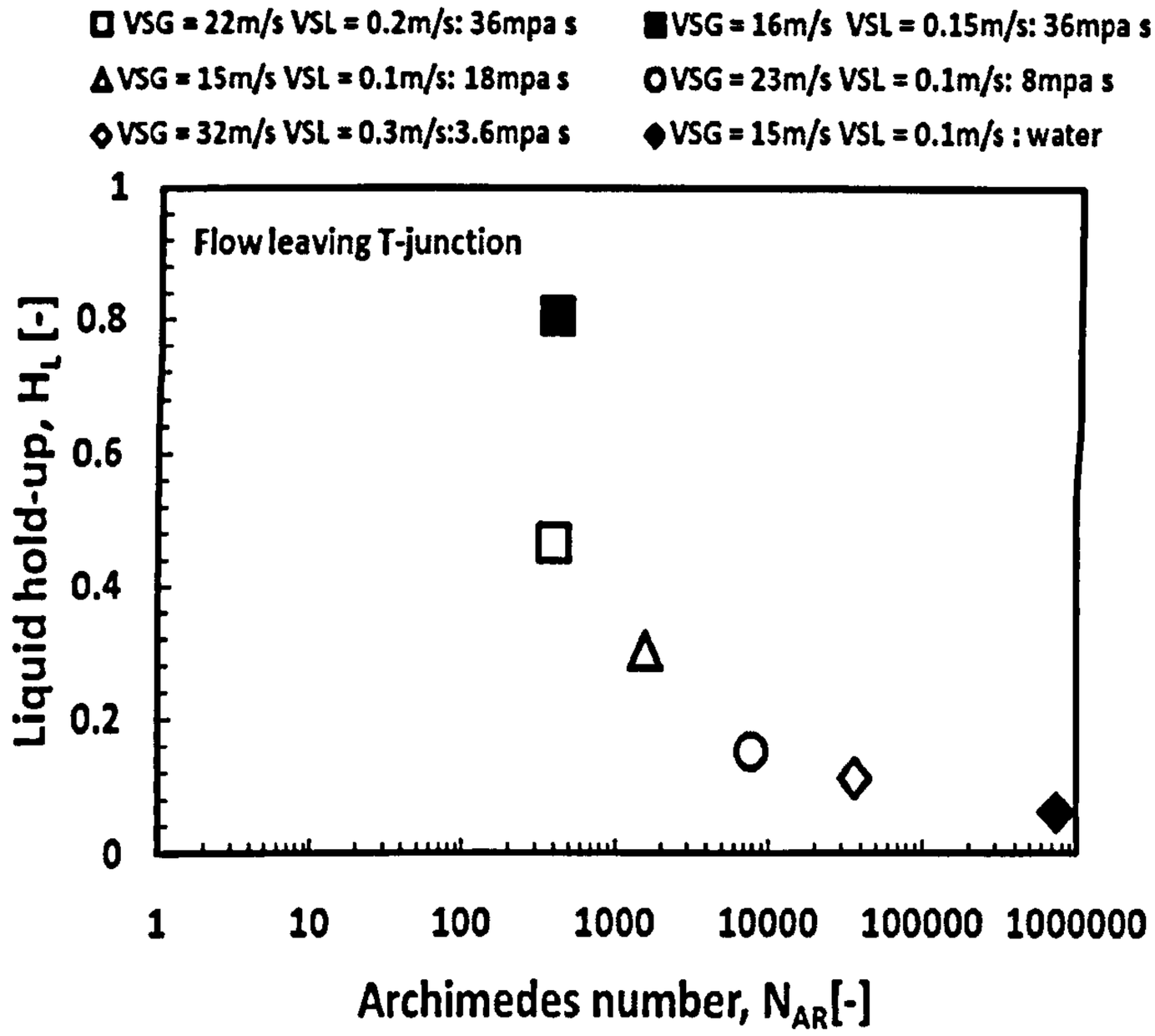

Figure 7.17 (a): Effect of physical property (Morton & Archimedes numbers) on liquid hold-up.

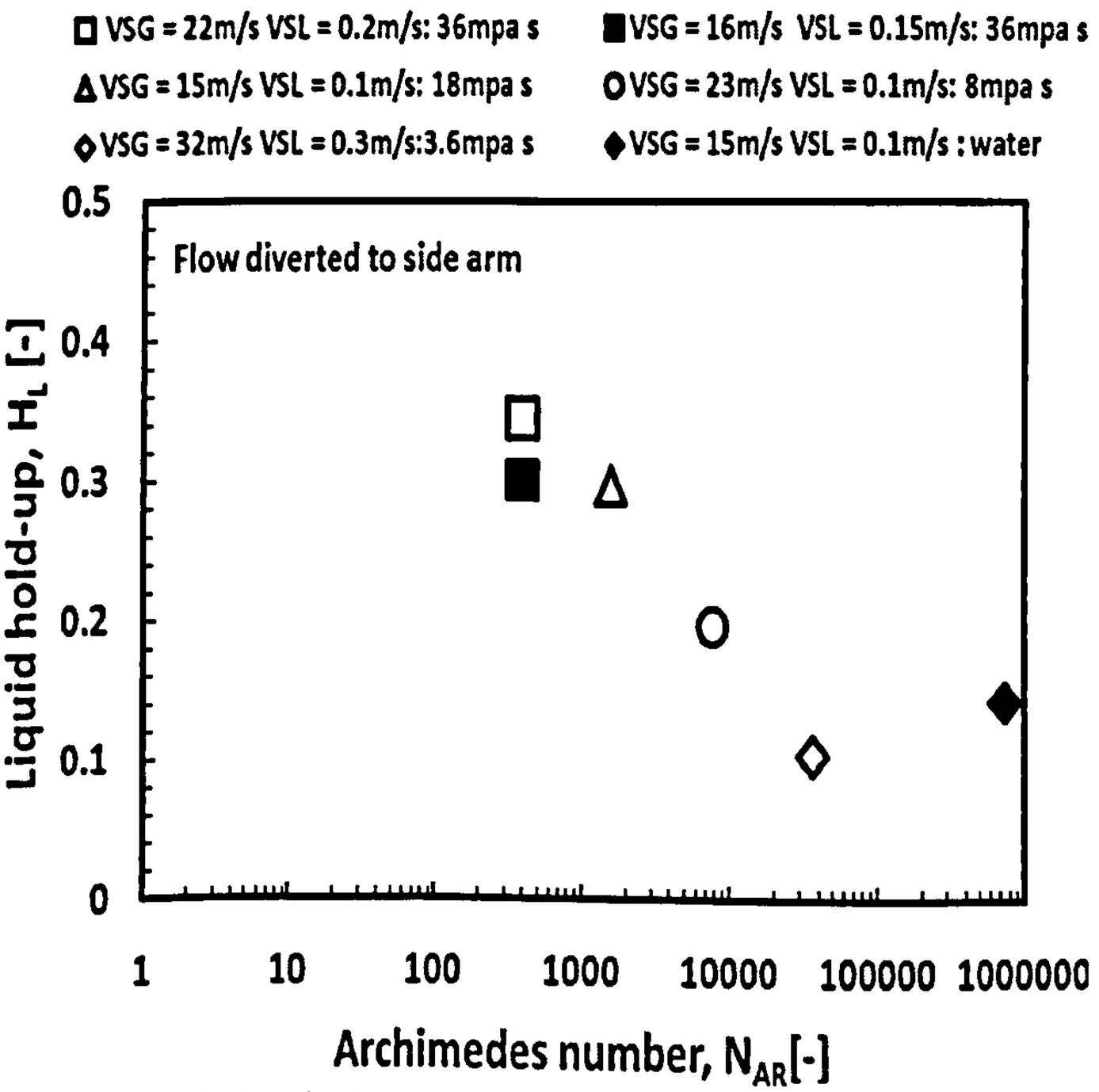

Figure 7.17 (b): Effect of physical property (Morton & Archimedes numbers) on liquid hold-up.

7.3.7 Structure frequency

At higher liquid viscosity, glycerol solution surface tension is lower than that of water Appendix C. Surface tension keeps flow structures within liquid film. When the value is low the coherence of the periodic structure is low and therefore more structures are released into the stream of the continuous phase. Structure frequency was estimated from PSD (discussed in Chapter Five) and plotted against mixture Reynolds number, defined by Equation (7.8), as shown in Figure 7.17.

$$\mathrm{Re}_M = \frac{\rho V_M d}{\mu_L}, [\text{-}] \qquad (7.8)$$

where $V_M = V_{SG}+V_{SL}$

Liquid based Strouhal number was used to correlate structure frequency and plotted against mixture Reynolds number. Poor correlation is observed Figure 7.18. This may be because Strouhal number does not include physical property in its formulation. However, it is clear that more structures are created at higher liquid viscosity as shown in the Figure 7.18.

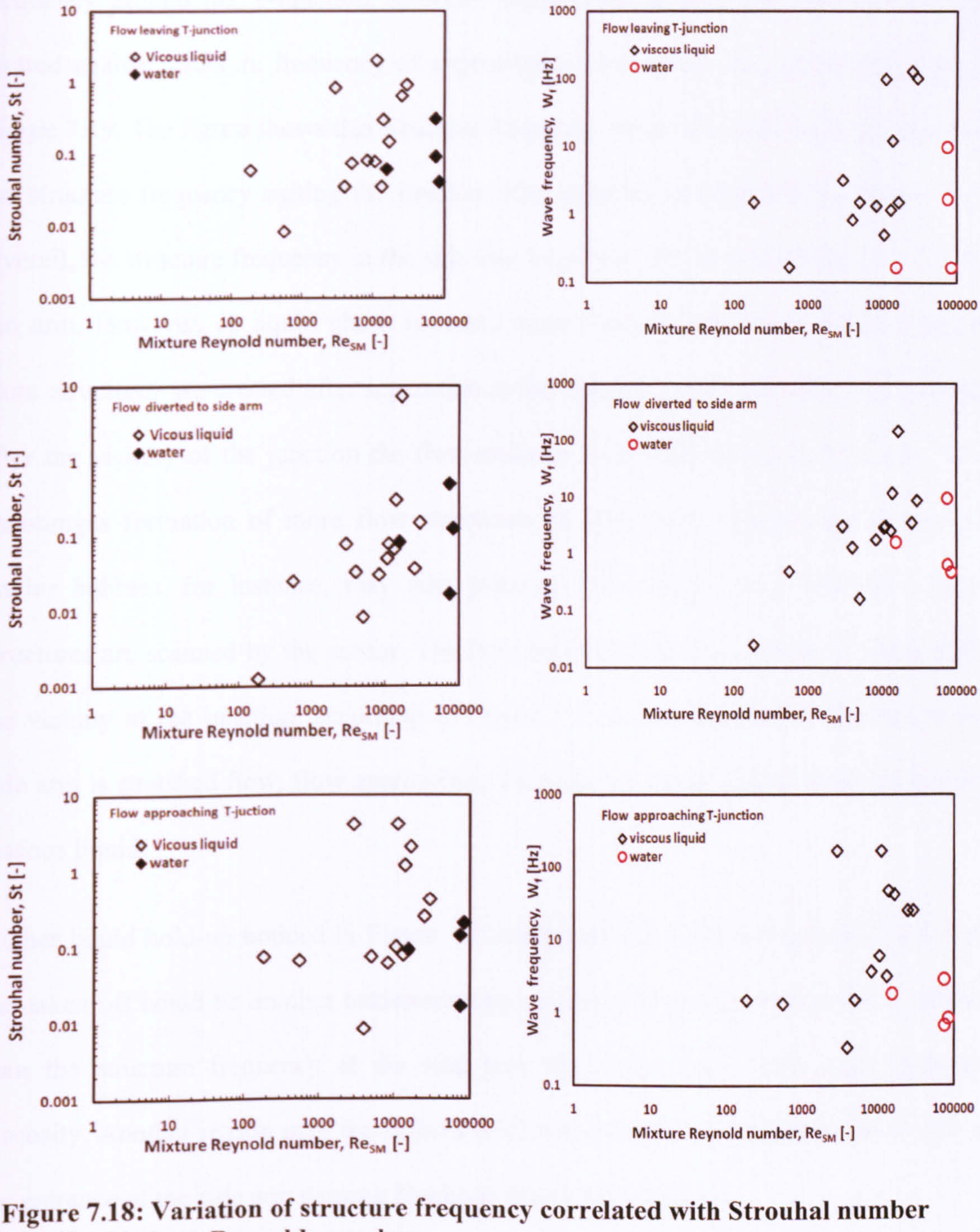

Figure 7.18: Variation of structure frequency correlated with Strouhal number with liquid phase Reynolds number.

In an attempt to investigate this further, frequency of structure approaching the junction is used as a yardstick to compare structure frequency at run arm and side arm

respectively. In order to study the distribution of the flow structure based on its frequency around the T-junction, structure frequencies at side arm and run arm are plotted against structure frequency of approaching flow before the junction as seen in Figure 7.19. The figure shows that structure frequency before the junction is greater than the structure frequency exiting the junction after splitting as indicated in Figure 7.19. Overall, the structure frequency in the side arm is greater than structure frequency on the run arm. However, as liquid phase becomes more viscous with lower surface tension more structures are created after separation at the junction to the run arm. Immediately after the vicinity of the junction the flow tends to re-develop along the run arm. This encourages formation of more flow structures. In slug flow, coalescence of smaller Taylor bubbles, for instance, may take place to form bigger one. Therefore, more structures are scanned by the sensor. The flow pattern observed in Probe 8, away from the vicinity of the junction, according to Figure 7.9 shows slug flow while that at the side arm is stratified flow, flow approaching the junction being bubbly flow for the air-viscous liquid.

Higher liquid hold-up noticed in Figure 7.9 when hold-up is plotted against fraction of gas taken off could be another testimony why structure frequency at Probe 8 is greater than the structure frequency at the side arm for liquid phase with same dynamic viscosity. Another reason may the influence of low pressure, re-circulation zone just at the entrance of the side arm causing blockage due to high hold-up.

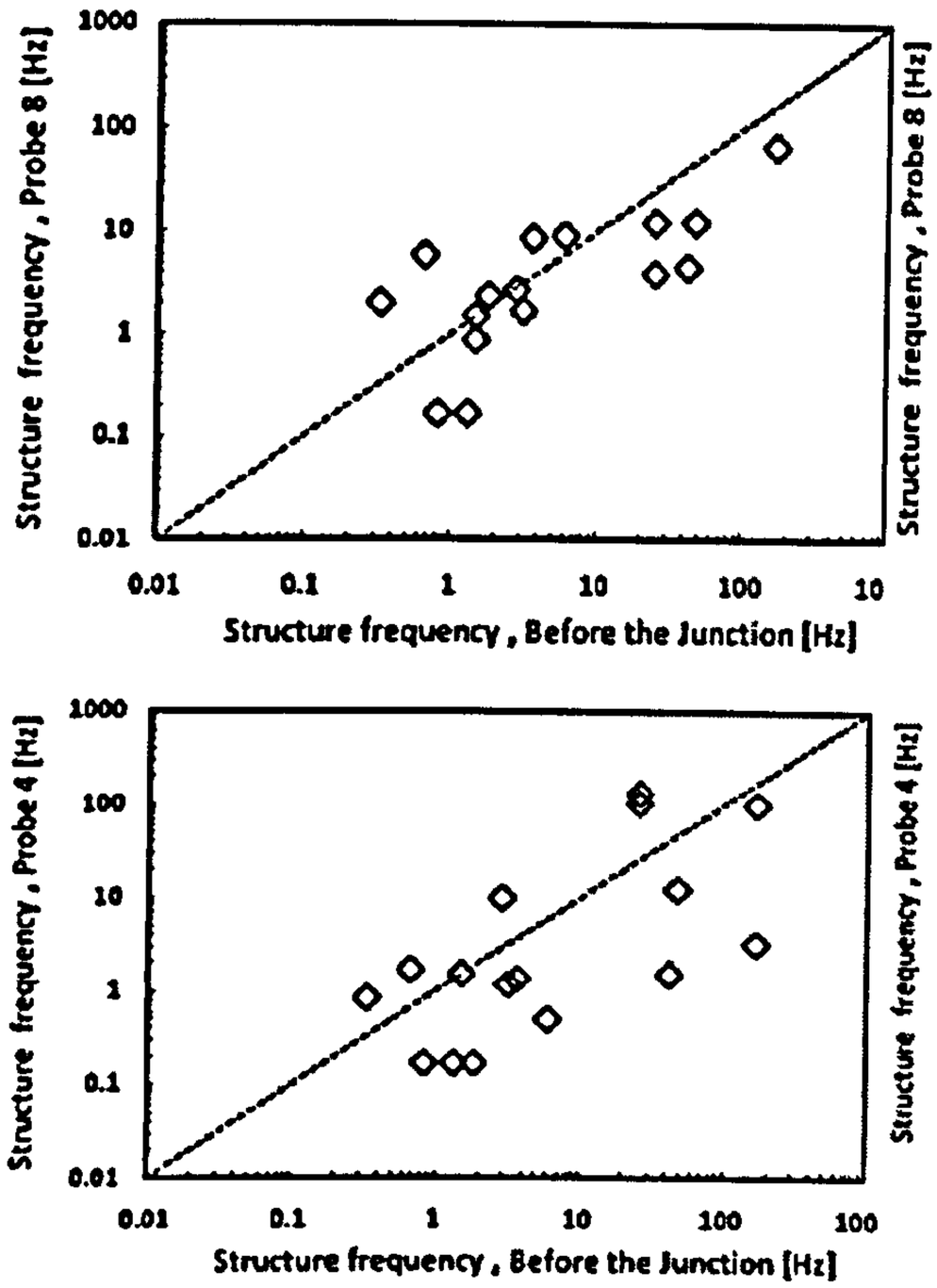

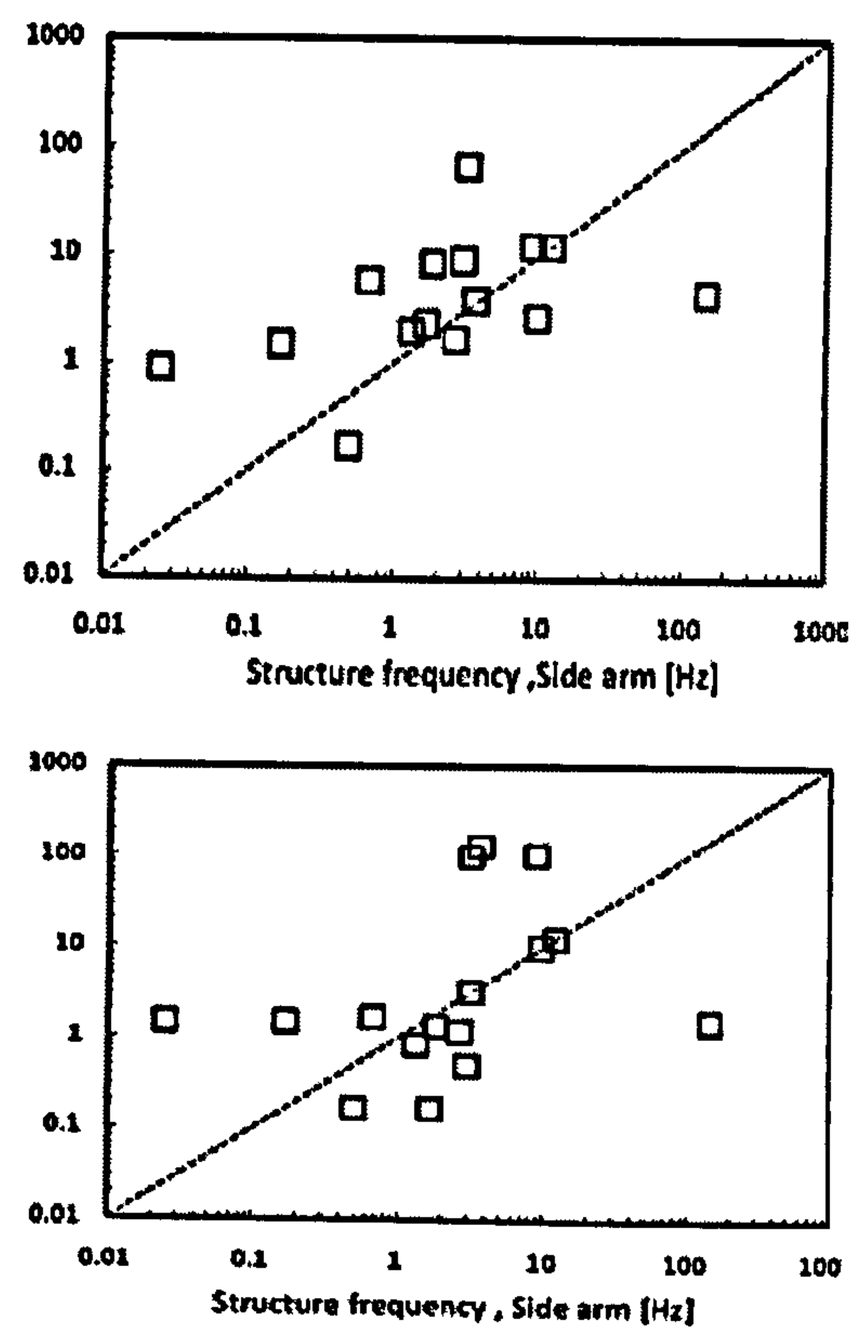

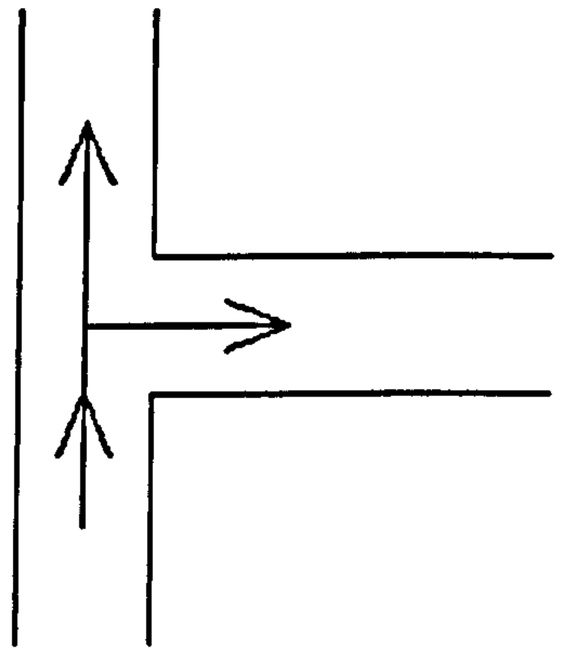

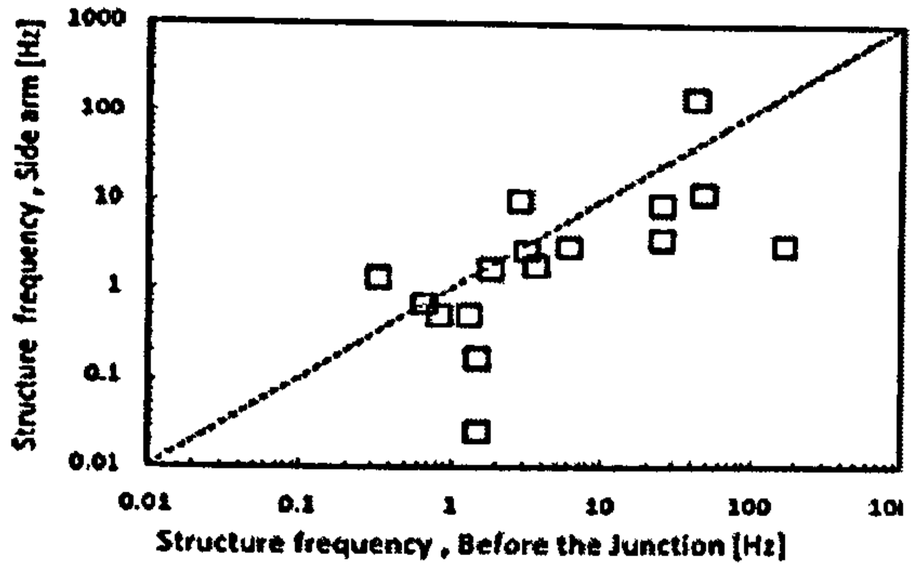

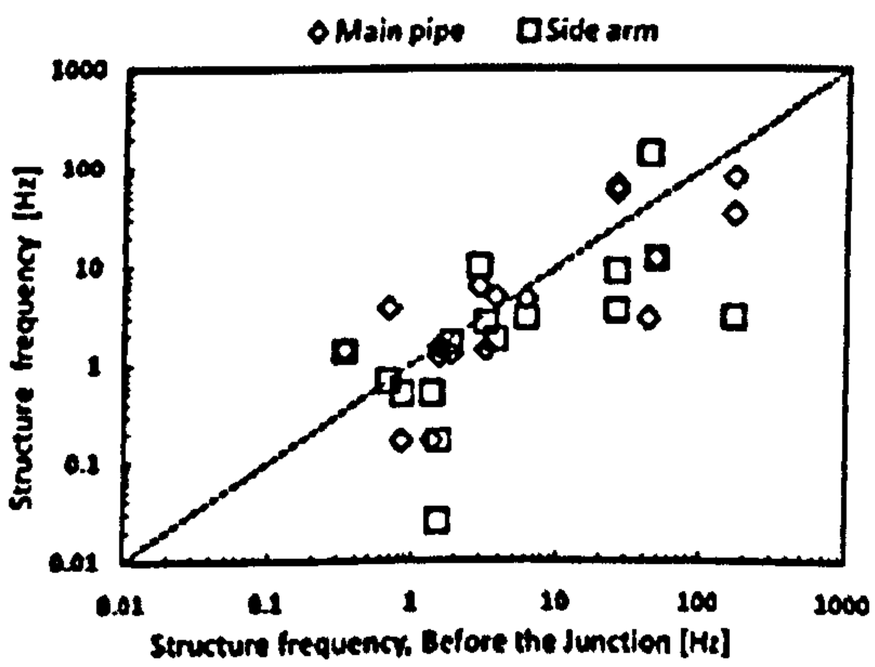

Figure 7.19: Variation of structure frequency correlated with Strouhal number with liquid phase Reynolds number.

It seems there appears to be a blockage of liquid around the entrance to the side arm caused by the recirculation of liquid. As a result, structures are carried straight on pass the junction to the run arm where flow re-develops after travelling certain distance. It seems flow structure development is enhanced at higher viscosity. All these explain the observation around Probe 8 in Figure 7.19 where the structure frequency at that location is observed to be greater than the frequency of the structure diverted to the side arm.

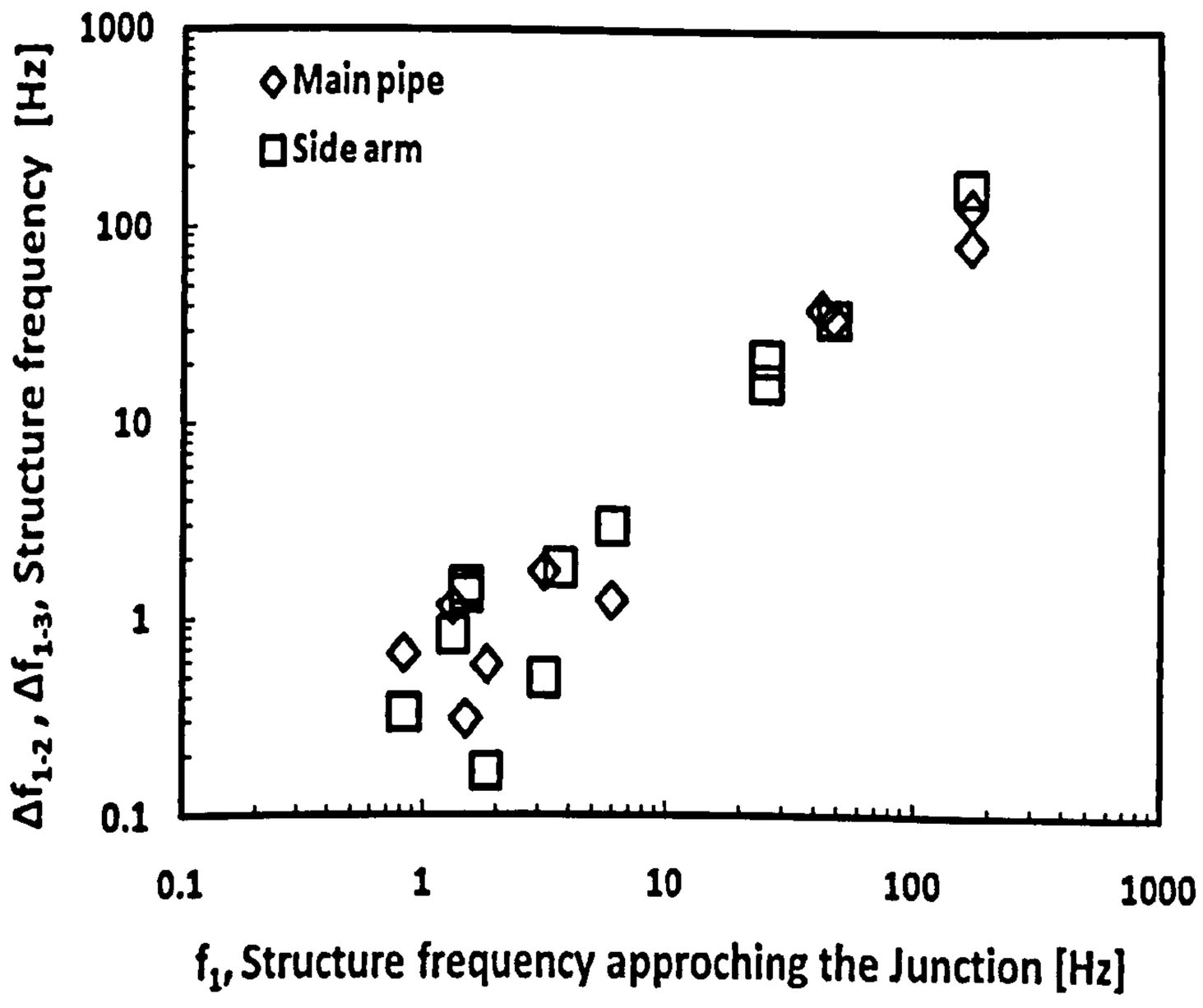

Figure 7.20: structure frequency at side arm and main pipe as a function of structure frequency approaching the junction.

The difference in structure frequency after flow split has been plotted against the frequency of structure approaching the junction in Figure 7.20. The figure shows an inevitably linear relationship. Therefore, the linearity provides another opportunity to examine the data further.

At the next level of analysis, the difference in structure frequency, that is the structure frequency of approaching flow towards the junction minus the structure frequency at the side arm and run arm respectively, after flow division has occurred are plotted in Figure 7.21.

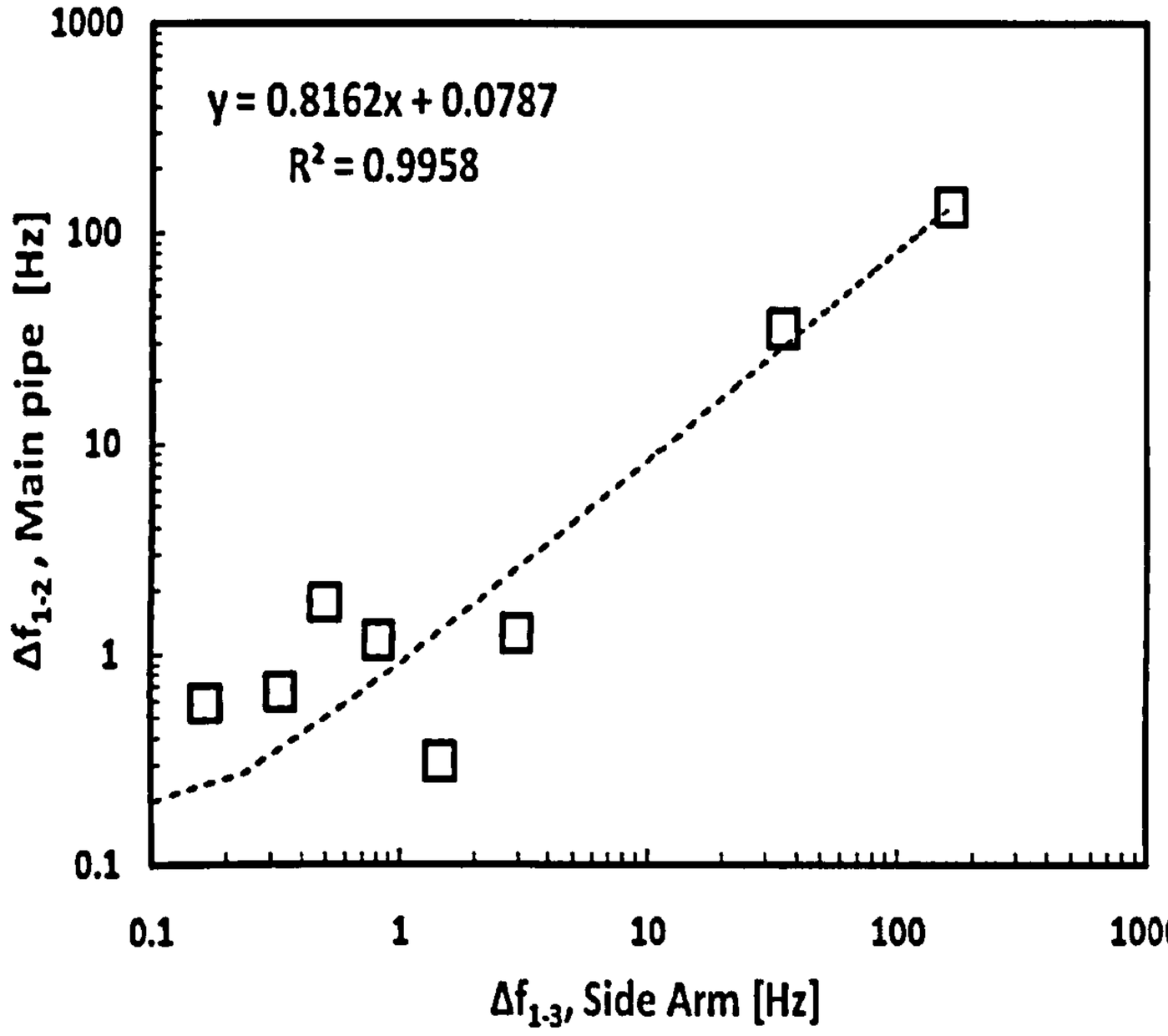

Figure 7.21: Difference in structure frequency approaching the junction and structure frequency after separation at run arm plotted as function of difference in structure frequency approaching the junction and structure frequency after separation at the side arm.

The relationship also produces a linear behaviour with a straight line with a gradient of approximately 0.82. The relationship can be expressed mathematically as follows:

$$\frac{f_1 - f_2}{f_1 - f_3} = 0.82$$

..... (7.9)

For instance, f_3, slug frequency, based on the experimental data obtained for different pipe diameters in horizontal flow, according to Azzi et al. 2010 , can be estimated by:

$$f_{slug} = \frac{0.0039}{d} V_{SL} \sqrt{\frac{\rho_L}{\rho_G}} \qquad (7.10)$$

Substituting for side arm pipe diameter, d = 0.005m, in Equation (7.10) yields f_3 , slug frequency on the side arm:

$$f_3 = 0.78\, V_{SL} \sqrt{\frac{\rho_L}{\rho_G}} \qquad (7.11)$$

Structure frequency in the run arm can be estimated using Equation (3.4) such that:

$$f_2 = 0.009\, V_{SG} \sqrt{\frac{\rho_L}{\rho_G}} \qquad (7.12)$$

Therefore, frequency of the approaching structure, f_1 , can be estimated by substituting f_2 and f_3 respectively in Equation (7.4) as follows:

$$f_1 = 0.05\, V_{SG} \sqrt{\frac{\rho_L}{\rho_G}} + 3.55 V_{SL} \sqrt{\frac{\rho_L}{\rho_G}} \qquad (7.13)$$

Equation (7.13) is advantageous because frequency of approaching slug can be computed if inlet conditions are specified.

7.4 Conclusions

From the results and discussions presented above the following conclusions can be drawn:

1. This work has demonstrated that flow pattern approaching the T-junction does change after leaving the junction along the main pipe as the viscosity of liquid phase increases. It is therefore, important to include flow pattern after the junction as one of the parameters for design.

2. Change in liquid viscosity does not have a significant effect on flow pattern in the horizontal side-arm.

3. In some cases tested, at superficial liquid velocity, V_{SL}= 0.1m/s and gas superficial velocities of V_{SG} = 15 m/s for air/water, V_{SG} = 23 m/s for air-8 mPa s viscous liquid and V_{SG} = 15 m/s for air-18 mPa s viscous liquid , an increase in liquid viscosity leads to more liquid take off at the horizontal side arm.

4. An increase in the gas superficial velocity at a fixed liquid superficial velocity constant causes more diversion of the liquid into the sidearm.

5. Churn-annular transition occurs at a gas superficial velocity of 15 m/s.

6. Liquid viscosity does not affect significantly liquid hold-up until fraction of gas taken off exceeds 0.40.

7. Thicker film or viscous liquid displays lower momentum and can be easily taken off.

Chapter 8

Conclusions and Recommendations

8.1 Conclusions

Periodic structures in vertical gas-liquid two-phase flow have been identified as void waves in bubbly flow, liquid slugs and or Taylor bubbles in slug flow, huge waves in churn flow, disturbance waves in annular flow and wisps in wispy-annular flow. In order to obtain detailed information on characteristics and behaviour of these periodic structures, a series of experimental campaigns were carried out starting from simple pipe flow arrangements through to complex pipe geometry employing pipes of different diameters (5mm and 19mm internal diameters).

Experimental programmes were carefully controlled to minimise measurement uncertainties to obtained good quality data. Results were extensively analysed leading to the following accomplishments:

A. Dynamic drop size measurement in vertical annular two-phase flow.

This thesis has advanced knowledge in annular flow two-phase flow by making the following novel contributions:

1. In the history of drop size measurements, new, time-resolved drop size and concentration data are reported for the first time. They have been obtained simultaneously with film thickness and pressure drop information by synchronizing the various acquisition systems. All these parameters show fluctuations with time. Some, such as film thickness, are more obviously periodic than others.

2. The time averaged values are in agreement with prior data.

3. Drop frequency has been estimated from fluctuations of drop concentration with time using Power Spectrum Density (PSD) of auto-covariance function.

4. Interrelationship of drop concentration fluctuation and wave frequency has been reported. Wave fluctuations are higher than drop concentration fluctuations.

5. Transition boundaries within annular flow have been elucidated by careful analysis of the drop size and entrained fraction data. Interestingly, all instrumentation employed picked up these transitions:

(i) Tra nsition to annular flow occurs when gas superficial velocity exceeds V_{SG} = 21m/s with maximum entrained fraction, E_F = 0.05. This value agrees with published data.

(ii) Wisps were seen in the region identified as churn area by published transition models. This occurs below V_{SG} = 21m/s. This is supported by video footage of flow recorded during the experiments. Transition boundaries in the Hewitt & Roberts (1969) flow map has been modified to reflect this observation. Characteristic wave features show that huge wave dominates the gas-liquid interface before transition to annular flow at V_{SG} = 21 m/s.

(iii) Transition to mist annular flow occurs at V_{SG} = 30 m/s. Normalized drop size shows that droplets shedding from disturbance wave are controlled by liquid superficial velocity. The higher the liquid velocity, the higher the drop size. After

V_{SG} = 30 m/s, huge wave disappears, liquid film surface being covered by disturbance waves. The transition is characterized by entrained fraction, $E_F = 0.20$.

6. Considering MMD (D_{50}), thinner film produces bigger drops only at this boundary condition: 21 m/s ≥ V_{SG} ≤ 30 m/s

7. Before VSG = 21 m/s, and after V_{SG} = 30 m/s, thicker film produces bigger droplets.

8. In terms of SMD (D_{32}), thicker film produces bigger drop up to V_{SG} = 21 m/s. After V_{SG} = 21m/s, thinner film produces bigger drop.

9. Entrained fraction depends on gas and liquid superficial velocities. Entrainment of liquid droplets into the gas core of annular flow is a diffuse flow phenomenon and not a piston-like displacement. This is evident by the nature of entrained fraction- gas superficial velocity plot.

10. Below V_{SG} = 21 m/s, both entrained fraction and entrained mass flux are indistinguishable. After V_{SG} = 21 m/s, both entrained fraction and entrained mass flux are higher the higher the liquid superficial velocity.

11. Below entrained fraction of 0.05 (E_F = 0.05) and $V_{SG} \leq 21$ m/s droplet flow is inertial-driven and gravity appears to have significant effect on entrained fraction. The flow is chaotic and huge waves dominate the gas-liquid interface. Drop size or MMD is large under gravity-dominated flow. Effects of gravity diminishes after entrained fraction exceeds 0.05(i.e. $E_F > 0.05$).After E_F = 0.05 pressure drops uniformly with entrained fraction until a minimum is reached where $E_F = 0.20$, V_{SG} = 30 m/s.

12. Pressure drop recovers after $E_F = 0.20$, increases with increase entrained fraction as gas superficial velocity increases. Mist flow occurs as a result of complete atomization of liquid film.

13. In mist flow regime droplet size do not change significantly with increase gas superficial velocity. After this transition normalized pressure drop increases with entrained fraction as gas superficial velocity increases.

14. Examination of the time series in amplitude and frequency space reveals interesting features. From the probability density function of mass median diameter, it is seen that there are distinct regions of large and smaller mean drop sizes are evident are visible at lower gas superficial velocities but that there is not this feature at higher gas velocities. PDF of MMD indicates multi-modal distributions before $V_{SG} = 30$ m/s. After $V_{SG} = 30$ m/s, PDF changes to mono-modal distribution.

15. For gas producer the best operating practice would be to produce natural gas within the transition region with the following boundary conditions:

$$21 \text{ m/s} \geq V_{SG} \leq 30 \text{ m/s}$$

$$0.05 \geq E_F \leq 0.20$$

This region is characterized by minimum entrained fraction and pressure drop which means less shut-downs and more revenue.

B. Wave dynamics in vertical annular two-phase flow

From the results and discussions presented the following conclusions can be drawn from dynamic measurements of wave properties:

1. Dynamic properties of the wave changes as wave identity changes. Wave properties changes at transition boundaries within annular flow sub-regimes. Flow pattern transition within annular two-phase flow occurs at V_{SG} = 21 m/s, 30 m/s and 40 m/s respectively. Wave frequency attains a maxima and then drops within wispy annular i.e. 0 m/s > V_{SG} ≤ 21 m/s for V_{SL} = 0.05 m/s and 0 m/s > V_{SG} ≤ 30 m/s for the case of V_{SL} = 0.15 m/s.

2. The dominance of huge or disturbance wave depends on liquid superficial velocity when gas superficial velocity is maintained at a constant rate.

3. Wave frequency:

- is a strong function of gas superficial velocity
- increases with increase in gas superficial velocity
- is higher the higher the liquid superficial velocity

4. Wave velocity:

- increases with increase in gas superficial velocity
- is higher the higher the liquid superficial velocity

5. Wave spacing:

- increases with increase in gas superficial velocity
- is higher the lower the liquid superficial velocity

C. Effect of liquid viscosity on periodic structures in two-phase gas-liquid flow.

Since most published data were acquired from experiments using air and water as test fluids, this thesis has contributed to the existing knowledge and distinguished itself by demonstrating effect of liquid viscosity on periodic flow structures in two-phase gas-liquid flow in the following ways:

13. Void fraction decreases with increase in liquid viscosity.

14. Structure frequency increases with increased liquid viscosity.

15. Liquid viscosity and surface tension causes shift to transition boundary.

16. Higher viscosity liquid phase induces higher slippage between gas and liquid phase in two-phase gas-liquid flow.

17. Flow distribution coefficient, C_o, has a strong dependence on liquid viscosity.

18. Structure velocity is strongly dependent on viscosity and surface tension.

19. Flow structure travels faster at the centre-line in medium of higher viscosity and lower surface tension.

20. Structures are held together by surface tension forces. Lower surface tension fluid tends to produce more periodic structures than their higher surface tension counterparts. Hence, fluid with lower surface tension has higher structure frequency and lower drift velocity.

21. Flow pattern transitions form slug to churn and churn annular flow are clearly identified on the structure velocity versus mixture velocity plot.

D. Split of gas-liquid two-phase flow at vertical T-junction

From the results and discussions presented above the following conclusions can be drawn:

1. This work has demonstrated that flow pattern approaching the T-junction does change after leaving the junction along the main pipe as the viscosity of liquid phase increases. It is therefore, important to include flow pattern after the junction as one of the parameters for design.

2. Change in liquid viscosity does not have a significant effect on flow pattern in the horizontal side-arm.

3. In some cases tested, at superficial liquid velocity, V_{SL}= 0.1 m/s and gas superficial velocities of V_{SG} = 15 m/s for air/water, V_{SG} = 23 m/s for air/8mPa s viscous liquid and V_{SG} = 15 m/s for air/18 mPa s viscous liquid , an increase in liquid viscosity leads to more liquid being diverted to the side arm.

4. An increase in the gas superficial velocity at constant liquid superficial velocity constant leads to more diversion of the liquid into the sidearm.

5. This work in addition to the present methods has uncovered another diagnostic criterion for churn annular flow transition when V_{SG} = 15 m/s.

6. Liquid viscosity does not affect liquid hold-up until after fraction of gas taken off exceeds 0.40. Thicker film or viscous liquid displays lower momentum and can be easily taken off.

7. PDF plot of void fraction has successfully captured the effect of liquid viscosity on phase distribution.

8. Archimedes and Morton numbers have demonstrated ability to track effect of liquid viscosity on phase distribution.

8.2 Recommendations for future works

The following recommendations for further works are suggested to advance further on the milestone achievement of this thesis:

1. This study has shown that predictive abilities of the existing drop size and entrained fraction correlations are limited. Therefore, a mechanistic model with a sound physical basis is advocated.

2. Inclusion of shear stresses in the formulation of future drop size model is inevitably necessary going by findings of this thesis.

3. Expansion of experimental matrix to cover and extend present matrix using air and more viscous liquids on the existing facility and bigger diameter pipes (67 mm and 127 mm) to investigate effects of liquid properties (viscosity and surface tension) on droplet creation and dispersion in the gas core is strongly recommended.

4. The assumption that centre-line drop velocity approximately equals gas phase superficial velocity is clearly an identified source of error in conversion of drop concentration to entrained fraction. In order to have more confidence in drop

velocity value, it is recommended that cross-correlation of two drop concentration signals from Spraytec be carried out to yield true and representative drop velocity which can be used in the conversion with a view to improving the accuracy of the entrained fraction obtained from drop concentration.

5. More experimental activities should be focussed on investigation of liquid viscosity on flow distribution parameters and the coefficient of drift velocity by testing with liquid of higher viscosity than used in this study.

6. More works need to be carried out to extend *finding s of this work by expanding* experimental matrix in slug flow regime using liquid of higher viscosity to track changes to flow pattern leaving the T-junction.

References

Adechy D., Issa R.I. , 2004. Modelling of annular flow through pipes and T-junctions. Computers and Fluids, 33(2): 289-313.

Andreussi, P., Di Donfrancesco, A., Messia, M., 1988. An impedance method for the measurement of liquid hold-up in two-phase flow. International Journal of Multiphase Flow 14, 777–785.

Andreussi, P., J. C. Asali and T. J. Hanratty , 1985. Initiation of Roll Waves in Gas-Liquid Flows. AIChE Journal 31(1): 119-126.

Andritsos, N., 1986. Effect of Pipe Diameter and Liquid Viscosity on Horizontal Stratified Flow. Ph.D. Dissertation. University of Illinois at Urbana-Champaign.

Al-Sarkhi, A. & Hanratty, 2002. T.J. Effect of pipe diameter on the drop size in a horizontal annular gas-liquid flow. Int. J. Multiphase Flow, Vol. 28, 1617-1629

Alves, N. I., E. F. Caetano, K. Minami and O. Shoham., 1991. Modeling Annular Flow Behavior for Gas Wells. SPE Prod. Eng., pp.435-440.

Asali, J.C., Leman, G.W., Hanratty, T.J., 1985. Entrainment measurement and their use in design equations. PCH Physicochem. Hydrodyn. 6, 207–221

Azzi, A., Al-Attiyah, A., Liu Qi, W. Cheema, Azzopardi, B.J., 2010.Gas-liquid two-phase flow division at a micro-T-junction. Chem. Eng Sc., 65, 3986 - 3993

Azzopardi B.J., Hernandez Perez V., Kaji R., Da Silva M.J., Byers M., and Hample U., 2008. Wire mesh sensor studies in a vertical pipe. HEAT 2008, Fifth International Conference on Transport Phenomena in Multiphase Systems, Bialystok, Poland.

Azzopardi, B.J., 2006. Gas-Liquid Flows. Begell House Inc., New York.

Azzopardi, B.J., 2004.Bubbles, drops and waves - differences or underlying commonality. 42nd European Two-Phase Flow Group Meeting, Genoa, 23-25 June.

Azzopardi, B.J., Colman, D.A., Nicholson, D., 2002. Plant application of a T-junction as a partial phase separator. Chemical Engineering Research and Design, Vol. 80, 87-96 .

Azzopardi, B.J., 1999. Phase separation at T-junction. Multiphase Science and Technology, Vol. 11, 223-329.

Azzopardi, B. J., 1997. Drops in Annular Two-Phase Flow. International Journal of Multiphase Flow 23, Suppl.: 1-53.

Azzopardi, B.J., Teixeira, J.C.F., 1994 a. Detailed measurements of vertical annular two phase flow - Part I: drop velocities and sizes. J. Fluids Eng., Vol. 116, 792-795.

Azzopardi, B.J., Teixeira, J.C.F., 1994 b. Detailed Measurements of Vertical Annular Two-Phase Flow – Part II: Gas Core Turbulence. Journal of Fluid Engineering. Vol. 116, pp 796-800.

Azzopardi, B.J., 1994 c. The split of vertical annular flow at a large diameter T-junction. International Journal of Multiphase Flow 20, 1071–1083.

Azzopardi, B.J., Piearcey, A., Jepson, D.M., 1991. Drop Size Measurements for Annular two-phase flow in a 20mm diameter vertical tube. Experiments in Fluids Vol.11, pp. 191 -197.

Azzopardi, B.J., Memory, S.B, 1989. The split of two-phase flow at a horizontal T-annular and stratified flow. 4th Int. Conf. on Multi-phase Flow, Nice, France, 19-21 June (Pub. BHRA) .

Azzopardi, B.J., 1988. Measurements and observations of the split of annular flow at a vertical T-Junction. International Journal of Multiphase Flow, Vol. 14, 701-710.

Azzopardi, B.J., 1987. Dividing two-phase flow at a junction part I: annular flow at a vertical T. Third International Conference on Multiphase Flow, The Hague, Netherlands, 18–20 May.

Azzopardi, B. J., 1986. Disturbance Wave Frequencies, Velocities and Spacing in Vertical Annular Two-Phase Flow. Nuclear Engineering and Design 92(2): 121-133.

Azzopardi, B.J., Whalley, P.B., 1982. The effect of flow patterns on two-phase flow in a T-junction. International Journal of Multiphase Flow 8, 491–507.

Azzopardi, B.J., Whalley P.B., 1980 a. Artificial Waves in Annular two-phase flow. Basic Mechanisms in Two-Phase Flow and Heat Transfer proceeding, The America Soc.of Mech.Eng., Chicago, Nov. 16 -21, pp.1–8.

Azzopardi, B.J., Freeman, G., King, D.J., 1980 b. Drop sizes and deposition in annular two phase flow. UKAEA Report AERE R9634.

Baker, O.,1954. Design of Pipelines for Simultaneous Flow of Oil and Gas. Oil and Gas Journal, 53,185.

Bankoff, S.G., 1960. A variable density single fluid model for two phase flow with particular reference to steam water flow. Trans. ASME, J. Heat Transfer 82, 265–272.

Barbosa, J.R., Hewitt, G.F., Konig, G., Richardson, S.M., 2002.Liquid Entrainment, Droplet Concentration and Pressure Gradient at the Onset of Annular Flow in a Vertical Pipe. Int. J. Multiphase Flow, Vol. 28, pp.943–961.

Barnea, D., 1986. Transition from Annular Flow and from Dispersed Bubble Flow-Unified Models for the Whole Range of Pipe Inclinations. I nternational Journal of Multiphase Flow, 12 (5), 733-744 .

Belfroid, S.P.C., Schiferli, W., Alberts, G.J.N., Veeken, C.A.M., Biezen, E., 2008. Prediction Onset and Dynamic Behavior of Liquid Loading Gas Wells. Paper SPE 115567, ATCE, Denver, Colorado, USA.

Bendiksen, K. H., 1984. An Experimental Investigation of the Motion of Long Bubbles in Inclined Tubes. International Journal of Multiphase Flow, 4, 467-483.

Bennett, A.W., Hewitt, G.F., Kearsey, H.A., Keeys, R.K.F., Lacey, P.N.C., 1965. Flow visualization studies of boiling at high pressure. Proc. Inst. Mech. Eng. 180 (Part 3C), 1–11.

Bonizzi M., Issa, R. I. ,2003. A Model for Simulating Gas Bubble Entrainment in Two-Phase Horizontal Slug Flow. International Journal of Multiphase Flow, 29, 1685

Brown, K. E., 1977. The Technology of Artificial Lift Methods, PennWell Publishing Co., Tulsa, OK. 1.

Bruno, K. , M. J. McCready , 1988. Origin of Roll Waves in Horizontal Gas-Liquid Flows. AIChE Journal 34(9): 1431-1440.

Caetano, E.F., Shoham, O., Brill, J.P., 1992. Upward Vertical Two-Phase Flow through an Annulus. Part II. Modeling Bubble, Slug, and Annular Flow. Proc., Fourth BHRA Intl. Conference on Multiphase Flow, Nice, France .1989. ASME J.Energy Resources Technology, 114, 13.

Ceccio, S.L., 1991. Electrical Impedance Techniques for the Measurement of Multiphase Flows. Experimental Techniques in Multiphase Flows. ASME.

Ceylan, S., Kelbaliyev, G., Ceylan, S., 2003. Estimation of the Maximum Stable Drop Sizes, Coalescence Frequencies and the Drop Size Distributions in Isotropic Turbulent Dispersions. Colloids and Surfaces A: Physicochem. Eng. Aspects 212, pp. 285 – 295.

Chopra, A. K. ,1982. Characterization and Modeling of Annular Two-Phase Flows. Ph.D. Dissertation. University of Houston.

Coddington, P., Macian, R., 2002. A study of the performance of void fraction correlations used in the context of drift-flux two-phase flow models. Nucl. Eng. Design 215, 199–216.

Collins, R., de Moraecs, F.F., Davidson, J.F., Harrison, D., 1978. The motion of large bubbles rising through liquid flowing in a tube. J. Fluid Mech. 89, 497–514.

Corcoran, T.E., Hitron, R., Humphrey, W., Chigier, N., 2000.Optical Measurement of Nebulizer Sprays: A Quantitative Comparison of Diffraction, Phase Doppler Interferometry, and Time of Flight techniques. Journal of Aerosol Sci., Vol.31, pp.35–50.

Costigan, G., Whalley, P.B., 1997. Slug flow regime identification from dynamic void fraction measurements in vertical air/water flows. International Journal of Multiphase Flow 23, 263–282.

Das, G., Das, P.K., Azzopardi, B.J., 2005. The split of stratified gas–liquid flow at a small diameter T-junction. International Journal of Multiphase Flow 31, 514–528.

Davies , R. M., Taylor, G. I., 1950. The mechanics of large bubbles rising through Extended liquids and through liquids in tubes. Proc Roy. Soc., 200A, 375-390.

DeJong, P., 1999. An investigation of film structure and pressure drop in microgravity annular flow. M.Sc. Thesis, University of Saskatchewan, Canada.

Delichatsios and 'Probstein,. R. F., 1975. Coagulation in turbulent flow: theory and experiment. J. Colloid InterfLee sci. 51, 394-405.

Dionissios P.M., 2007. T-junction separation modelling in gas-liquid two-phase flow. Chemical Engineering and Processing, Vol. 46, 150-158.

Dressler, R. F. , 1949. Mathematical solution of the problem of roll waves in inclined open channels. Communications on Pure and Applied Mathematics 2: 149-194.

Dukler, A. E.,1960. Fluid Mechanics and Heat Transfer in Vertically Falling-Film Systems. Chem Eng. Prog. Symposium Series, 56, No 30, 1.

Dumouchel, C., Yongyingsakthavorn, P., Cousin J., 2009. Light Multiple Scattering Correction of Laser-Diffraction Spray Drop-Size Distribution Measurements. Int. J. Multiphase Flow, Vol.35, 277-287.

Ferré D.,1979. Ecoulements diphasiques a poches en conduite horizontale Rev. Inst. Fr. Pet., 34, 113-142.

Fernandes, R. C., Semiat, R., and Dukler A.E., 1983: Hydrodynamic Model for Gas-Liquid Slug Flow in Vertical Tubes AIChE Journal, 29 (6), 981-989

Fore, L.B., Dukler, A.E., 1995. The distribution of drop size and velocity in gas -liquid annular Flow. Int. J.Multiphase Flow, 21, 137-149.

Fossa, M., 1998. Design and performance of a conductance probe for measuring liquid fraction in two-phase gas–liquid flow. Flow Measurement and Instrumentation 9, 103–109.

Fossa, M., Guglielmini G. ,1998. Dynamic void fraction measurements in horizontal ducts with sudden area contraction.' International Journal of Heat Transfer, Vol. 14, 3807-3815.

Fukano, T., T. Morimoto, K. Sekoguchi A. Ousaka ,1983. Air/water Annular Two-Phase Flow in a Horizontal Tube. 2nd Report, Circumferential Variations of Film Thickness Parameters. Bulletin of the JSME 26(218): 1387-1395.

Gardner, G.C., Neller, P.H., 1969. Phase Distribution in Flow of an Air/Water Mixture Rounds and Past Obstructions at the Wall of 76 mm Bore Tube. Proc. Inst. Mech. Engrs., 184, 36.

Geraci, G., 2005.Gas-Liquid Flows in Inclined Pipes and Venturis. PhD Dissertation, Chem. Eng. Dept. University of Nottingham.

Griffith, P., Wallis, G. B . 1 96 1 . Two-phase slug flow. J. Heat Transfer 83: 307-20.

Govan, A.H., 1988. A note on statistical methods for comparing measured and calculated values. UKAEA Report AERE-M 3621.

Govier, G. W., Aziz, K., 1972. The Flow of Complex Mixtures in Pipes. Van Nostrand Reinhold Co., New York, NY.

Hagedorn, A.R., Brown, K.E., 1964. The Effects of Viscosity in Two-Phase Vertical Flow, ''JPT, Feb.

Hale C. P., 1994. Modelling the slug flow regime. Technical Report, MPS/62, WASP/16, Department of Chemical Engineering, Imperial College of Science, Technology & Medicine, London, UK.

Hall Taylor, N.S., Hewitt, G.F., Lacey, P.M.C., 1963. The Motion and Frequency of Large Disturbance Waves in Annular Two-Phase Flow of Air/water Mixtures. Chem. Eng. Sc., Vol. 18. pp. 537 – 552.

Hall Taylor, N.S., Nedderman, R.M, 1968. The coalescence of disturbance waves in annular two-phase flow. Chem. Eng. Sci. Vol. 23, 551-564.

Hall Taylor, N.S., 1966. Interfacial wave phenomena in vertical annular two-phase flow. Ph.D. Thesis. Trinity College, Cambridge.

Han, H., Z. Zhu , K. Gabriel , 2006. A Study on the Effect of Gas Flow Rate on the Wave Characteristics in Two-Phase Gas-Liquid Annular Flow. Nuclear Engineering and Design 236(24): 2580-2588.

Hanratty, T. J., A. Hershman , 1961. Initiation of Roll Waves. AIChE Journal: 488-497.

Hanratty, T. J., Asali, J.C., 1983. Entrainment Measurements and Their Use in Design Equations. Report forDesign Inst. For Multiphase Flow, U.of Illinois, Urbana, Illinois.

Harmathy, T. Z., 1960. Velocity of Large Drops and Bubbles in Media of Infinite or Restricted Extent. AIChE J., 6, p. 281.

Hassan , A.R, Kabir, C.S., 1988. A Study of Multiphase Flow Behaviour in Vertical Wells. SPEPE , 263, Trans., AIME, 285.

Henstock, W.H., Hanratty, T.J., 1976. The interfacial drag and height of the wall layer in annular flows. *AIChE J.* 22 6, pp. 990–1000.

Hewitt, G.F., 1961. Analysis of Annular Two-Phase Flow: Application of Dukler Analysis to Vertical Upwards Flow in a Tube. AERE-R 3680.

Hewitt, G.F., 1978. Measurements of two-phase flow parameters. Academic Press, London.

Hewitt, G.F., Hall-Taylor, N.S., 1970. Annular Two-Phase Flow. Pergamon Press, Oxford.

Hewitt, G.F., Roberts, D.N., 1969. Study of Two-phase Flow Pattern by Simultaneous X-Ray and Flash Photography. UKAEA, Report AERE-M2159.

Hills, J.H., 1997. The critical liquid flow rates for wave and droplet formation in annular gas–liquid flow. Exp. Heat Transfer Fluid Mech. Thermodyn. Ed. ETS 2, 1241–1247

Hinze, J. O. 1955. Fundamentals of the Hydrodynamic Mechanism of Splitting in Dispersion Processes. AIChE J.1, 289.

Hong, K.C.,1978. Two-phase flow splitting at an impacting tee. J. Pet. Technology, 290-296.

Ilobi, M. I., Ikoku, C. U., 1981, Minimum Gas Flow Rate for Continuous Liquid Removal in Gas Wells. Paper SPE 10170 presented at SPE Annual Technical Conference and Exhibition, San Antonio, TX, October 4–7.

Ishii, M., Grolmes, M.A., 1975. Inception criteria for droplet entrainment in two-phase concurrent film flow.''American Institute of Chemical Engineers Journal, Vol. 21, 308-318.

Ishii, M. ,K. Mishima ,1989. Droplet Entrainment Correlation in Annular Two-Phase Flow 3. of Heat International Journal and Mass Transfer 2(10): 1835-1846.

Issa R.I., Bonizzi M., Barbeau S., 2006. Improved closure models for gas entrainment and interfacial shear for slug flow modeling in horizontal pipes. Int. J. Multiphase Flow, 2006, Vol: 32, pp: 1287-1293.

Jayanti, S., G. F. Hewitt, S. P. White ,1990. Time-dependent behaviour of the liquid film in horizontal annular flow. International Journal of Multiphase Flow 16(6): 1097-1116.

Johnson, G. W., Nossen J, Bertelsen A. F. , 2005. A Comparison between Experimental and Continuous Theoretical Roll Waves in Horizontal and Slightly Inclined Pipes at High Pressure. BHR Group 2005 Multiphase Production.

Kaji, R., 2008. Characteristics of Two-Phase Structures and Transitions in Vertical Up-flow. PhD Thesis, Chem. Eng. Dept. University of Nottingham.

Kataoka, I., Ishii, M., Mishima, K., 1983. Generation and size distribution of droplet in annular two-phase flow. Journal of Fluids Engineering Transactions of the ASME 105 (2), 230–238.

Kondo,Y., Mori, K., Yagishita, T., Nakabo, A. 1999. Effects of liquid viscosity on wave behaviour in gas-liquid two-phase flow. In: Proc. 5th ASME/JSME Joint Thermal.

Kumar, R., M. Gottmann , K. R. Sridhar ., 2002. Film Thickness and Wave Velocity Mesaurements in a Vertical Duct. Transactions of the ASME 124(September): 634-642.

Kuru, W. C., Sangalli M., Uphold D.D., McCready M.J., 1995. Linear Stability of Stratified Channel Flow. International Journal of Multiphase Flow 21(5): 733-753.

Lin, P.-Y. , 1985. Flow Regime Transitions in Horizontal Gas-Liquid Flow. Ph.D. Dissertation. University of Illinois at Urbana-Champaign.

Lee, J.K., Lee, S.Y., 2001. Dividing two-phase annular flow within a small vertical rectangular channel with a horizontal branch. Proceedings of the Third International Conference on Compact Heat Exchangers and Enhancement Technology for the Process Industries, Davos, Switzerland, July 1–6.

Lee, J.K., Lee, S.Y., 2004. Assessment of models for dividing two-phase flow at small T-junctions. Fifth International Conference on Multiphase Flow, Yokohama, Japan, May 30–June 4.

Lin, P. Y., and Hanratty, T. J., 1986. Prediction of the Initiation of Slugs with Linear Stability Theory. Int. J. Multiphase Flow, 12, 79–98.

Mak, C.Y., Omebere-Iyari, N.K., Azzopardi, B.J.,2006. The Split of vertical two-phase flow at a small diameter T-junction. Chem. Eng.Sci., 61, 6261-6272.

Mandhane, J. M., Gregory, G.A, Aziz, K., 1974. Flow Pattern Map for Gas-Liquid Flow in Horizontal Pipes. Int. J. Multiphase Flow, 1, 537-553.

Mandil, C, 2002 Environmental and Technical Issues Associated with Non-Conventional Oil. International Energy Agency (IEA) Conf. on Non-Conventional Oil, Calgary, Canada, Nov. 25 – 26.

Mantilla I., 2008.Mechanistic Modeling of Liquid Entrainment in Gas in Horizontal Pipes. PhD Thesis, Petroleum Engr. Dept. University of Tulsa, Ok, USA.

Martin, C. J., Azzopardi B.J., 1984. Wave in Vertical Annular Flow. *PCH,* Physico Chemical Hydrodynamics 6 (1-2): 257-265.

Martin, C.J., 1983. Annular two-phase flow. D.Phil. Thesis, University of Oxford.

McGillivray, R.M., Gabriel, K.S., 2002. Annular flow film characteristics in variable gravity. Ann. N.Y. Acad. Sci., Vol. 974, 306-315.

McNeil, D.A., Stuart, A.D.,2003. The effects of a highly viscous liquid phase on vertically upward two-phase flow in a pipe. International Journal of Multiphase Flow, Vol. 29, 1523-1549.

Miya, M., Woodmansee D. E , Hanratty T. J, 1971. A Model for Roll Waves in Gas-Liquid Flow. Chemical Engineering Science 26: 1915-1931.

Moalem Maron, D., Dukler,A.E., 1984. Flooding and upward filmflow in vertical tubes II: Speculations on film flow mechanisms. International Journal of Multiphase Flow 10, 599.

Mori, K. , Nakano, K., 2001. Effects of liquid viscosity on inception of disturbance waves behavior in gas-liquid two-phase flow. Experimental Heat Transfer, Fluid Mechanics and Thermodynamics, Thessaloniki, 1829-1834.

Nan Da Hlaing, Anuvat Sirivat, Kitipat Siemanond , James O. Wilkes, 2007. Vertical two-phase flow regimes and pressure gradients :Effect of Viscosity. Ex perimental Thermal and Fluid Science, 31, 567 – 577.

Nicklin, D.J., Wilkes, J.O. , Davidson, J.F. ,1962. Two-phase flow in vertical tubes. Transaction of the Institution of Chemical Engineers, vol. 40, pp 61-68.

Oliemans, R. V. A., B. F. M. Pots , N. Trompe, 1986. Modeling of Annular Dispersed Two-Phase Flow in Vertical Pipes. International Journal of Multiphase Flow 12(5), pp. 711-732.

Omebere-Iyari, N.K., Azzopardi, B.J. ,2006. A study of flow patterns for gas/liquid flow in small diameter tubes."Chemical Engineering Research and Design, Vol. 85, 180-192.

Omebere-Iyari, N.K., Azzopardi, B.J., Akinmade, A.A., 2005. Flow patterns for gas-liquid flow in small diameter tubes. Ninth UK National Heat Transfer Conference, Manchester, UK, 5–6 September.

Oranje L. , 1973. Condensate Behaviour in Gas Pipelines is Predictable. Oil & Gas Journal, 32: 39-44.

Paleev, I. I. , B. S. Filippovich, 1966. Phenomena of Liquid Transfer in Two-Phase Dispersed Annular Flow. International Journal of Heat and Mass Transfer, Vol.9, pp.1089 – 1093.

Pan, L., T. J. Hanratty, 2002. Correlation of Entrainment for Annular Flow in Vertical Pipes. International Journal of Multiphase Flow, vol. 28, pp. 363 - 384.

Paras, S. V., A. J. Karabelas, 1991. Droplet Entrainment and Deposition in Horizontal Annular Flow. International Journal of Multiphase Flow 17(4): 455-468.

Paras, S. V., N. A. Vlachos , A. J. Karabelas 1994. Liquid Layer Characteristics in Stratified-Atomization Flow. International Journal of Multiphase Flow 20(5): 939-956.

Pearce, D.L., 1979. Film waves in horizontal annular flow: space time correlator experiments. Central Electricity Research Laboratories Report RD/L/N/111/79.

Petalas N., Aziz K., 1998 . A mechanistic model for multiphase flow in pipes. 49th Annual Technical Meeting of Petroleum Society of the Canadian Institute of Mining, Metallurgy & Petroleum. Paper 98-39, Calgary, Alberta June 8-10, Canada.

Pickering, P.F., Hewitt, G.F., Watson, M.J., Hale, C.P., 2001. The Prediction of Flows in Production Risers – Truth or Myth?., FEESA Ltd., Camberley, Surrey, UK.

Pinto, A. M. F. R., , Campos, J. B. L. M., 1996. Coalescence of Two Gas Slugs Rising in a Vertical Column of Liquid. Chemical Engineering Science, 51 (1), 45-54.

Pols, R. M. , 1998. Waves in separated two-phase flow. Ph.D Thesis. The University of Nottingham , UK.

Ros , N.C.J.,1961. Simultaneous Flow of Gas and Liquid as Encountered in Well Tubing. JPT, Oct.

Rosin, P ., Rammler, E., 1933. Laws Governing the Fitness of Powdered Coal. Journal of the Inst. Of Fuel, Vol.7, pp.29-36.

Sawant, P.H., Ishii, M., Mori, M., 2008a. Droplet entrainment correlation in vertical upward co-current annular two-phase flow. Nucl. Eng. Des. 238 (6), 1342–1352.

Sawant, P.H., Ishii, M., Mori, M., 2008b. Properties of disturbance waves in vertical annular flow. Nucl. Eng. Des. 238 (12), 3528–3541.

Sawant, P.H., Ishii, M., Mori, M., 2009. Prediction of Amount of Entrained Droplets in Vertical Annular Two-phase Flow. Int. J. Heat Fluid Flow.

Schmidt, J., Giesbrecht, H. , Van der Geld, C.W.M., 2008. Phase and velocity distribution in vertically up-ward high-viscosity two-phase flow. Int. J. Multiphase Flow, 34, 363 – 374.

Sekoguchi, K., Mori, K., 1997. New development of experimental study on interfacial structure in gas–liquid two-phase flow. In: Giot, M., Mayinger, F., Celata, G.-P. (Eds.), Experimental Heat Transfer, Fluid Mechanics and Thermodynamics. Edizione ETS 2, pp. 1177–1188.

Sekoguchi, K., Mori, K., Tsujino, H., Ikeshita, M., and Kaji, M., 1994. Wave Venation in gas-liquid two-phase flow. First report, time-spatial map of wave behavour and its characterisations.

Sekoguchi, K., Ueno, T., Tanaka, O., 1985. An investigation of the flow Characteristics in the disturbance wave region of annular flow: 2nd report, on correlation of principal flow parameters. Trans. JSME Series B 51, 1798–1806.

Sekoguchi, K., Takeishi, M., 1989. Interfacial Structures in Upward Huge Wave Flow and Annular Flow Regimes. Int. J. Multiphase Flow, Vol. 15, pp.295-305.

Shoham O. , 2006 . Mechanistic Modelling of Gas-Liquid Two-Phase Flow in Pipes. ,SPE Book, U. of Tulsa, Oklahoma, USA.

Shoham, O., Brill, J.P., Taitel, Y., 1987. Two-phase flow splitting in a teejunction—experimental and modelling. Chemical Engineering Science 42, 2667–2676.

Simmons, M.J.H. , Hanratty, T.J., 2001. Droplet size measurements in horizontal annular gas-liquid flows. Int. J. Multiphase Flow, Vol. 27, 861-883.

Sleicher, C.A., 1962. Maximum stable drop size in turbulent flow. American Institute of Chemical Engineers Journal 8 (4), 471–477.

Sliwicki, E., Mikielewicz, J., 1988. Analysis of an annular-mist flow model in a T-junction. International Journal of Multiphase Flow 14, 321–331.

Soleimani, A., Hanratty, T. J. ,2003. Critical Liquid Flows for the Transition from the Pseudo-Slug and Stratified Patterns to Slug Flow. Int. J. Multiphase Flow, 29, 51-67.

Stacey, T., Azzopardi, B.J., Conte, G., 2000. The split of annular two-phase flow at a small diameter T-junction. International Journal of Multiphase Flow 26, 845–856.

Strand, B, Djuve, S.M. ,2000. Pipeline Transport of Oil with Strongly Temperature Dependent Viscosity. BHR Group Multiphase Technology, pp.17-33.

Taitel, Y., Barnea, D., Dukler, A. E., 1980. Modeling Flow Pattern Transitions for Steady State Upward Gas-Liquid Flow in Vertical Tubes. AIChE. J., 26, pp. 345–354.

Taitel, Y., and Barnea, D. ,1990. Two-Phase Slug Flow. Advances in Heat Transfer, 20, 83-132.

Taylor, G.I., 1961. Deposition of a viscous fluid on the wall of a tube. J. Fluid Mech., Vol 10, pp. 161-165 .

Théron B.,1989. Ecoulements diphasiques instationnaires en conduite horizontale. *PhD thesis*, Institut National Polytechnique de Toulouse, France.

Tobin, T., Muralidhar, R., Ramkarishna, D., 1990. Determination of Coalescence Frequencies in Liquid – Liquid Dispersions: Effects of Drop Size Dependence. Chem. Eng. Sci. Vol. 45, No. 12, 3491 – 3504.

Tsochatzidis, N.A., Karapantsios, *T.D., Vostoglou, M.V.,* Karabelas, A.J., 1992. A conductance probe for measuring liquid fraction in pipes *and packed beds. Int. J.* Multiphase Flow 18, 653–667.

Turner, R.G., Hubbard, M.G., Dukler, A.E., 1969.Analysis and Prediction of Minimum Flow Rate for Continous Removal of Liquid from Gas Wells. Journal of Petroleum Technology, pp.1475- 1482.

Uphold, D. D. , 1997. Linear Stability of Multifluid Flows. Ph.D. Dissertation. Department of Chemical Engineering. University of Notre Dame.

van Hout, R.,Barnea, D., Shemer, L. , 2002. Experimental investigation of the velocity field induced by a Taylor bubble rising in stagnant water. International Journal of Multiphase Flow vol. 28, pp 579-596.

van't Westende, J.M.C., Kemp, H.K., Belt, R.J., Portela, L.M., Mudde, R.F., Oliemans, R.V.A., 2007. On the Role of Droplets in Cocurrent Annular and Churn-Annular Flow. Int. J. Multiphase Flow, Vol. 33, pp.595–615.

Wallis, G. B., 1969. One-dimensional Two-phase Flow. McGraw-Hill, New York.

Wang L., Wu Y., Zheng Z., Guo J., Tang C., 2008. Oil-Water Two-Phase Flow Inside T-junction. Journal of Hydrodynamics, 20(2), 147-153.

Watson, M. ,1989. Wavy Stratified Flow and the Transition to Slug Flow. Proceedings of the 4th International Conference in Multi-phase Flows, Nice, France.

Weber, M.E., 1981. Drift in intermittent two-phase flow in horizontal pipes, Canadian J. chem. Eng 59 (1981), pp. 398–399.

Weihong Meng, Xuanzheng T. Chen, Gene E. Kouba, Cem Sarica, James P. Brill, 2001.Experimental Study of Low-Liquid-Loading Gas-Liquid Flow in Near-Horizontal Pipes. SPE Production & Facilities (November), pp.240-249.

Whalley, P. B., Hewitt, G. F., 1978. The Correlation of Liquid Entrainment Fraction and Entrainment Rate in Annular Two-Phase Flow. UKAEA Report, AERE-R9187, Harwell.

White, E.R. , Beardmore, R.H., 1962. The velocity of rise of single cylindrical air bubbles through liquids in vertical tubes. Chem Eng Sci, 17: 351.

Wilkes, N.S., Azzopardi, B.J. , Thompson, C.P., 1983. Wave coalescence and entrainment in vertical annular two-phase flow. Int. J. Multiphase Flow, Vol. 9, 383-398

.

Willets, I.P., 1987. Non-aqueous annular two-phase flow. *Ph. D. Thesis*, University of Oxford, UK.

Woldesemayat, M.A., Ghajar, A J., 2007. Comparison of void fraction correlations for different flow patterns in horizontal and upward inclined pipes. International Journal of Multiphase Flow, 33, 347–370

Wolf, A., Jayanti, S., Hewitt, G. F., 2001. Flow development in vertical annular flow", Chemical Engineering Science, Vol. 56, pp. 3221-3235.

Woodmansee, D. E. ,1968 . Atomization from a Flowing Horizontal Water Film by a Parallel Air Flow. Ph.D. Dissertation. University of Illinois at Urbana-Champaign.

Woodmansee, D.E., Harrantty, T.J., 1969. Mechanisms for the removal of droplets from a liquid surface by a parallel air flow. Chem. Eng. Sci., Vol.24, pp. 299-307.

Wren, E., Baker, G., Azzopardi, B.J., Jones, R., 2005. Slug flow in small diameter pipes and T-junctions. Experimental Thermal and Fluid Science, 29, 893–899.

Xiaodong Z., 2005. Mechanistic-based models for slug flow in vertical pipes. PhD Thesis.Texas Technology University.

Yao, S.C., Sylvester, N.D., 1987. A Mechanistic Model for Two-Phase Annular Mist Flow in Vertical Pipes. AIChE J., 33, 1008.

Zabaras, G., Dukler, A.E., Moalem-Maron, D., 1986. Vertical Upward Co-current Gas–Liquid Annular Flow. AIChE J., Vol.32, pp.829–843.

Zaidi, S.H., Altunbas, A., Azzopardi, B.J., 1998. A Comparative Study of Phase Doppler and Laser Diffraction Techniques to Investigate Drop Sizes in Annular Two-Phase Flow. Chem. Eng. J., Vol. 71, pp.135 – 143.

Zhang, H.Q., Wang, Q., Sarica, C., Brill, J.P., 2003. A Unified Mechanistic Model for Slug Liquid Hold up and Transition between Slug and Dispersed Bubble Flows. Int. J. Multiphase Flow, Vol.29,pp. 97-107.

Zhou, D., Yuan, H., 2009. New Model for Gas Well Loading Prediction. Paper SPE 120580, SPE Production and Operation Symposium, Oklahoma, USA.

Zuber, N. , Findlay, J. A. ,1965. Average Volumetric Concentration in Two-Phase Flow Systems. J. Heat Transfer, Trans. ASME, 87, 453-468 .

Zukoski,E.E. , 1966. Influence of Viscosity , Surface Tension, and inclination angle on motion of long bubbles in closed tubes. J. Fluid Mech., 25(4), 821-837.

Nomenclature

A_F	Area of the liquid film	m^2
A_C	Area of the liquid film	m^2
A_P	Area of the pipe	m^2
B	Flow distribution coefficient, used in Eqt. 2.25	-
C	Volumetric drop concentration	-
C_F	Film friction factor constant, used in Eqt.2.48	-
C_I	Drift velocity coefficient	-
C_o	Flow distribution coefficient	-
C_w	Factor that accounts for the effect of surface tension on the internal flow, used in Eqt. 6.1	-
D, d, d_p	Pipe diameter	m
D_{50}	Mass Median Diameter	μm
D_{32}	Sauter Mean Diameter	μm
d_F	Liquid film hydraulic diameter	m
d_{max}	Maximum stable diameter of dispersed bubble	m
d_{CB}	Critical bubble diameter	m
d_{CD}	Critical bubble diameter above bubbles start to coalesce and deform	m
D_f	Drop frequency	Hz
dL	Differential length, used in Eqt.2.32	m
dP	Differential pressure, used in Eqt. 2.33	Pa
d_C	Gas core diameter, used in Eqt.2.36	m
E_0	Eotvos number	-
E_{Max}	Maximum entrained fraction	-
E_F	Entrained fraction	-
f_I	Interfacial friction factor, used in Eqt.2.5	-
f_F	Film friction factor	-
f_F	Liquid phase friction factor , used in Eqt.6.12	-
Fr_L	Liquid Froude number	-
Fr_c	Critical Froude number, used in Eqt.2.14	-
Fr_M	Mixture Froude number	-
f_W	Wave frequency, used in Eqt.5.10	Hz
f_{SC}	Gas core friction factor	-
f_E	Entrained fraction	-
g	Acceleration due to gravity	m/s^2
I	Interfacial friction factor	-
K	Pearce Coefficient constant, used in Eqt.5.5	-
M	Morton number	-
M_{LE}	Total liquid mass flux	$kg/m\text{-}s^2$
N_f	Inverse velocity number	-
n	Exponent, used in Eqt. 2.27	-
N_μ	Liquid viscosity number	-
N_{Ar}	Archimedes number	-
P_{atm}	Atmospheric pressure, used in Eqt.3.6	Bar

q_F	Volumetric liquid flow rate in the film, used in Eqt.2.37	m^3/s
q_L	Volumetric liquid flow rate, used in Eqt.2.37	m^3/s
q_G	Volumetric gas flow rate, used in Eqt. 2.39	m^3/s
Rxx	Auto-covariance function, used in Eqt. 5.1	
Re_S	Slug Reynolds number	-
Re	Reynolds number	-
Re_C	Core Reynolds number	
Re_{SC}	Superficial core Reynolds number	-
Re_F	Film Reynolds number	-
Re_L	Liquid Reynolds number, used in Eqt. 2.60	-
Re_{LMin}	Minimum liquid Reynolds number, used in Eqt.2.61	-
S	Slip velocity ratio	-
S_L	Annular liquid film perimeter, used in Eqt. 2.32	m
St	Strouhal number, used in Eqt. 3.1	-
St_L	Liquid based Strouhal number, used in Eqt. 5.4	-
S_I	Interfacial annular parameter, used in Eqt. 2.33	m
T	Sampling time	s
V	superficial velocity	m/s
V_{TB}	Taylor bubble velocity, used in Eqt. 2.1, 2.3, 2.3	m/s
V_T	Structure velocity	m/s
V_{SG}	Superficial gas velocity	m/s
V_{SL}	Superficial liquid velocity	m/s
V_{Drift}	Drift velocity, used in Eqt.3.5	m/s
V_{SC}	Superficial core velocity, used in Eqt.2.40	m/s
V_M	Superficial mixture velocity	m/s
V_T	Translational velocity	m/s
V_C	Core velocity	m/s
V_G	Gas velocity	m/s
V_D	Drop velocity	m/s
V_F	Film velocity, used in Eqt. 2.38	m/s
V_{LF}	Liquid film velocity	m/s
V_{Gcr}	Critical gas velocity at the onset of atomization	m/s
V_w	Wave velocity	m/s
$w(k\Delta\tau)$	Windowing function	
We	Weber number	-
We_{cr}	Critical Weber number, used in Eqt. 2.60	-
X	Lockhart-Martinelli parameter, used in Eqt. 3.2	-

Greek Letters

ρ	Density	Kg/m^3
ϵ	Rate of energy dissipation per unit mass	m^2/s^3
ε_g	Cross sectional average void fraction	-
μ	Viscosity	Kg/m-s or mPa s
μ_G	Gas phase viscosity	Kg/m-s
μ_L	Liquid phase viscosity	Kg/m-s
μ_C	Gas core viscosity	Kg/m-s
β	Pipe inclination from horizontal	degrees
Δ	delta/difference	
ρ_L	Liquid phase density	Kg/m^3
ρ_G	Gas phase density	Kg/m^3
ρ_C	Core density	Kg/m^3
λ_w	Wave spacing, used in Eqt. 5.10	m
ΔP	Pressure drop	Pa/m
δ_L	Film thickness, used in Eqt. 2.35	m
δ_F	Film thickness	m
$\Delta\delta_W$	Wave amplitude	m
σ	Surface tension	N/m
$\emptyset$	Dimensionless constant, used in Eqt. 2.52	-
τ_{WL}	Wall shear stress	Pascal
τ_I	Interfacial shear stress	Pascal
π	3.1415926	
$\Delta\delta_w$	Wave amplitude	m
α_C	Core void fraction, used in Eqt. 2.42	-
α_T	Total void fraction, used in Eqt. 2.44	-

Subscripts

Ar	Archimedes
F	Film
L	Liquid
G	Gas
C	Core
M	Mixture
S	slug
SG	Superficial gas
SL	Superficial liquid
Max	Maximum
CD	Critical bubble diameter
CB	Critical bubble diameter
f	Frequency

APPENDIX A

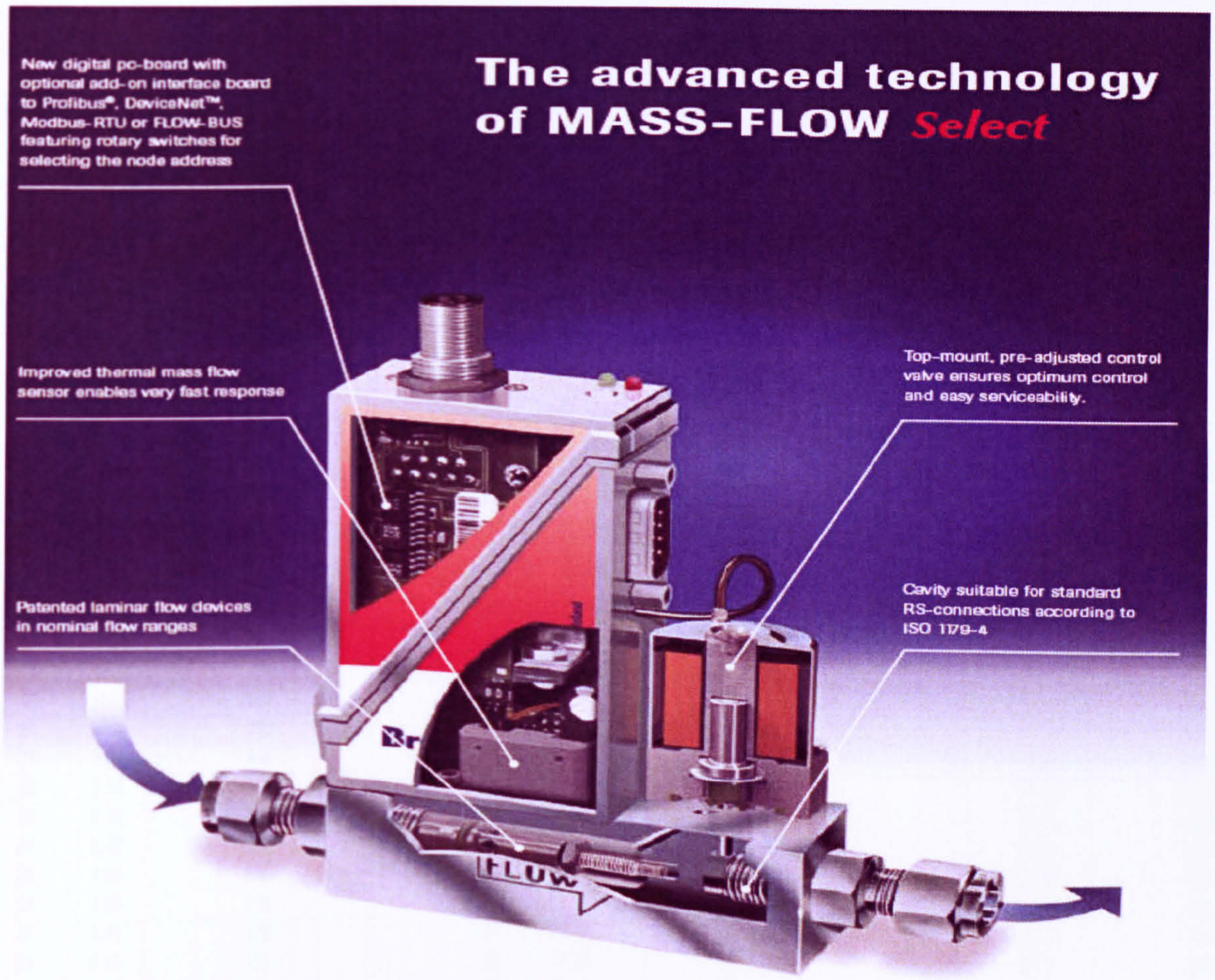

Cross sectional view of advance technology of gas mass flow controller (source: Bronkhorst, UK)

APPENDIX B

Spraytec vignetting distance for various lens applications

Spraytec Vignetting distance								
100mm lens			200mm lens			450mm lens		
Detector	Size	Working Distance [mm]	Detector	Size	Working Distance [mm]	Detector	Size	Working Distance [mm]
0	227.71	11760	0	455.42	23520	0	1024.69	52920
1	189.71	9797	1	379.41	19595	1	853.68	44088
2	162.29	8382	2	324.58	16763	2	730.31	37717
3	138.99	7178	3	277.99	14356	3	625.47	32302
4	118.97	6144	4	237.94	12288	4	535.36	27648
5	101.73	5254	5	203.45	10507	5	457.77	23641
6	87.19	4503	6	174.39	9006	6	392.37	20264
7	74.67	3856	7	149.34	7713	7	336.02	17354
8	63.96	3303	8	127.91	6606	8	287.80	14863
9	54.78	2829	9	109.57	5659	9	246.53	12732
10	46.95	2425	10	93.90	4849	10	211.28	10911
11	40.22	2077	11	80.45	4155	11	181.01	9348
12	34.47	1780	12	68.94	3560	12	155.12	8011
13	29.55	1526	13	59.11	3053	13	132.99	6868
14	25.33	1308	14	50.66	2616	14	113.98	5886
15	21.71	1121	15	43.41	2242	15	97.68	5044
16	18.60	961	16	37.20	1921	16	83.70	4323
17	15.94	823	17	31.89	1647	17	71.75	3705
18	13.67	706	18	27.33	1412	18	61.50	3176
19	11.71	605	19	23.43	1210	19	52.71	2722
20	10.04	519	20	20.08	1037	20	45.18	2333
21	8.61	444	21	17.21	889	21	38.73	2000
22	7.38	381	22	14.76	762	22	33.20	1715
23	6.32	327	23	12.65	653	23	28.46	1470
24	5.42	280	24	10.84	560	24	24.40	1260
25	4.65	240	25	9.29	480	25	20.91	1080
26	3.98	206	26	7.97	411	26	17.93	926
27	3.41	176	27	6.83	353	27	15.37	794
28	2.93	151	28	5.85	302	28	13.17	680
29	2.51	130	29	5.02	259	29	11.29	583
30	2.15	111	30	4.30	222	30	9.68	500
31	1.84	95	31	3.69	191	31	8.30	429

(source: Malvern Instruments, UK)

APPENDIX C

Glycerol surface tension	64.0 m N/ m at 20°C
Temperature Coefficient	-0.0598 m N/ m K

A. Physical Properties of Air and Water at test conditions

Equilibrium / steady state temperature	20°C
T-Junction pressure	1.4Bara
Surface tension (N/m)	0.073
Gas density (kg/m^3)	1.40
Liquid density (kg/m^3)	998.0
Gas Viscosity (Pa s)	1.8E-05 (0.018 c P)
Liquid viscosity (Pa s)	1.0E-03 (1.0 c P)

B .Physical Properties of Air and Glycerol-Water mixture at test conditions

Equilibrium / steady state temperature	31°C
T-Junction pressure	1.4Bara
Surface tension (N/m)	0.04582
Gas density (kg/m^3)	1.40
Liquid density (kg/m^3)	1261.0
Gas Viscosity (Pa s)	1.8E-05 (0.018 c P)
Liquid viscosity (Pa s)	1.2E-02 (12 c P)

C. Physical Properties of Air and Glycerol-Water mixture at test conditions

Equilibrium / steady state temperature	40°C
T-Junction pressure	1.4Bara
Surface tension (N/m)	0.04528
Gas density (kg/m^3)	1.40
Liquid density (kg/m^3)	1261.0
Gas Viscosity (Pa s)	1.8E-05 (0.018 c P)
Liquid viscosity (Pa s)	1.8E-02 (18.0 c P)

D .Physical Properties of Air and Glycerol-Water mixture at test conditions

Equilibrium / steady state temperature	35°C
T-Junction pressure	1.4Bara
Surface tension (N/m)	0.04558
Gas density (kg/m^3)	1.40
Liquid density (kg/m^3)	1261.0
Gas Viscosity (Pa s)	1.8E-05 (0.018 c P)
Liquid viscosity (Pa s)	3.6E-02 (36.0 c P)

E Physical Properties of Air and Glycerol-Water mixture (3.6 mPa s) at test conditions

Equilibrium/steady state temperature	21°C
T-junction pressure (Bara)	1.4
Surface tension (N/m)	0.071
Gas density (kg/m^3)	1.40
Liquid density (kg/m^3)	1097.0
Gas Viscosity (Pa s)	1.8E-05 (0.018 mPa s)
Liquid viscosity (Pa s)	3.60E-03 (3.6 mPa s)

APPENDIX D

Tabulated Drop Size Data

V_{SG}	V_{SL}	Void Fraction	Film Thickness	Film Hold-up	Pressure Drop	SMD (D_{32})	MMD (D_{50})	Drop Con.	Drop Conc. (PPM)	Entrained Fraction (E_F)
[m/s]	[m/s]	[-]	[mm]	[-]	[Pa/m]	[µm]	[µm]	C [%]	[-]	[-]
42.9011	0.0500	0.9869	0.0624	0.0131	6718.46	65.02	97.90	0.047023	470.23	0.4035
41.3499	0.0500	0.9860	0.0667	0.0140	6518.46	68.06	99.62	0.049484	494.84	0.4092
40.3161	0.0500	0.9854	0.0696	0.0146	6381.50	69.00	108.47	0.042306	423.06	0.3411
36.5874	0.0500	0.9843	0.0749	0.0157	6256.90	68.70	101.03	0.038222	382.22	0.2797
33.2238	0.0500	0.9826	0.0830	0.0174	5858.89	71.99	103.83	0.030547	305.47	0.2030
31.1410	0.0500	0.9801	0.0950	0.0199	5481.64	76.50	128.81	0.024752	247.52	0.1542
27.8176	0.0500	0.9771	0.1094	0.0229	5231.12	77.87	139.06	0.020313	203.13	0.1130
24.5847	0.0500	0.9735	0.1267	0.0265	4955.99	77.09	138.02	0.017526	175.26	0.0862
21.4446	0.0500	0.9693	0.1470	0.0307	4732.68	77.57	154.55	0.014527	145.27	0.0623
19.1663	0.0500	0.9745	0.1219	0.0255	5047.62	76.72	156.26	0.012099	120.99	0.0464
16.0963	0.0500	0.9715	0.1364	0.0285	4870.68	78.20	154.74	0.015245	152.45	0.0491
13.4136	0.0500	0.9555	0.2138	0.0445	4617.45	77.71	161.26	0.012032	120.32	0.0323
41.6249	0.1500	0.9808	0.0916	0.0192	10507.48	58.14	101.74	0.246087	2460.87	0.6829
38.2017	0.1500	0.9782	0.1041	0.0218	10075.07	59.77	104.68	0.228190	2281.90	0.5811
35.6549	0.1500	0.9756	0.1166	0.0244	9760.72	63.39	107.20	0.206408	2064.08	0.4906
34.6018	0.1500	0.9736	0.1262	0.0264	9218.08	64.61	106.37	0.174402	1744.02	0.4023
31.9401	0.1500	0.9690	0.1484	0.0310	8489.04	69.97	111.28	0.121929	1219.29	0.2596
29.4945	0.1500	0.9660	0.1629	0.0340	8046.42	72.95	113.01	0.093866	938.66	0.1846
26.8132	0.1500	0.9685	0.1508	0.0315	8311.12	70.25	111.16	0.116874	1168.74	0.2089
21.9189	0.1500	0.9654	0.1658	0.0346	7925.56	72.02	111.66	0.082051	820.51	0.1199
22.8756	0.1500	0.9611	0.1866	0.0389	7414.69	78.50	125.92	0.060173	601.73	0.0918
20.1558	0.1500	0.9562	0.2104	0.0438	6860.02	87.19	146.57	0.040796	407.96	0.0548
17.3860	0.1500	0.9484	0.2483	0.0516	6262.63	93.18	171.04	0.029275	292.75	0.0339
13.9613	0.1500	0.9417	0.2811	0.0583	5887.81	99.31	185.17	0.024657	246.57	0.0229
15.7700	0.0300	0.9733	0.1277	0.0267	3188.13	11.62	63.59	0.000569	5.69	0.0030
15.0200	0.0500	0.9645	0.1701	0.0355	3582.94	30.58	150.11	0.003408	34.08	0.0102
13.8200	0.0700	0.9578	0.2026	0.0422	3548.82	76.88	232.13	0.017256	172.56	0.0341
13.1300	0.0900	0.9528	0.2269	0.0472	3648.39	70.9	233.01	0.014960	149.6	0.0218
13.5100	0.1000	0.9488	0.2464	0.0512	4034.87	104.97	222.91	0.019677	196.77	0.0266
13.8800	0.1143	0.9443	0.2684	0.0557	4325.83	86.64	222.59	0.015188	151.88	0.0184
14.3300	0.1257	0.9425	0.2772	0.0575	4386.98	83.06	236.5	0.013223	132.23	0.0151
14.7800	0.1371	0.9408	0.2855	0.0592	4121.73	99.7	235.31	0.015207	152.07	0.0164
14.7800	0.1486	0.938	0.2992	0.0620	3429.78	97.69	225.11	0.015954	159.54	0.0159
14.6400	0.1600	0.9365	0.3066	0.0635	3461.51	103.65	209.67	0.018796	187.96	0.0172
14.3300	0.1714	0.9342	0.3179	0.0658	2497.41	107.16	199.55	0.019185	191.85	0.0160
14.2600	0.1829	0.9316	0.3307	0.0684	2467.88	106.38	200.4	0.020818	208.18	0.0162
14.0800	0.1943	0.9303	0.3371	0.0697	2268.72	121.02	241.72	0.095606	956.06	0.0693

APPENDIX E

Tabulated Film and Wave Data

VSG [m/s]	VSL [m/s]	Film Thickness [mm]	STDEV [mm]
42.9011	0.0500	0.0627	0.0226
41.3499	0.0500	0.0665	0.0214
40.3161	0.0500	0.0694	0.0226
36.5874	0.0500	0.0747	0.0245
33.2238	0.0500	0.0827	0.0342
31.1410	0.0500	0.0946	0.0422
27.8176	0.0500	0.1097	0.0483
24.5847	0.0500	0.1270	0.0579
21.4446	0.0500	0.1470	0.0579
19.1663	0.0500	0.1221	0.0535
16.0963	0.0500	0.1364	0.0997
13.4136	0.0500	0.2139	0.0997
41.6249	0.1500	0.0913	0.0289
38.2017	0.1500	0.1037	0.0244
35.6549	0.1500	0.1168	0.0289
34.6018	0.1500	0.1261	0.0321
31.9401	0.1500	0.1487	0.0374
29.4945	0.1500	0.1632	0.0422
26.8132	0.1500	0.1509	0.0380
21.9189	0.1500	0.1660	0.0590
22.8756	0.1500	0.1867	0.0501
20.1558	0.1500	0.2108	0.0590
17.3860	0.1500	0.2484	0.0768
13.9613	0.1500	0.2813	0.0908
15.7700	0.0300	0.1275	
15.0200	0.0500	0.1703	
13.8200	0.0700	0.2026	
13.1300	0.0900	0.2271	0.0793
13.5100	0.1000	0.2464	0.0843
13.8800	0.1143	0.2689	0.0856
14.3300	0.1257	0.2775	0.0919
14.7800	0.1371	0.2855	0.0898
14.7800	0.1486	0.2995	
14.6400	0.1600	0.3066	0.0907
14.3300	0.1714	0.3186	0.0936
14.2600	0.1829	0.3313	
14.0800	0.1943	0.3372	0.0996

APPENDIX F

Tabulated Wave Data

VSG [m/s]	VSL [m/s]	VM [m/s]	Void Fraction [-]	Film Thickness [mm]	Film Hold-up [-]	Pressure Drop [Pa/m]	Measured wave Velocity [m/s]
42.9011	0.0500	42.9511	0.9869	0.0627	0.0131	6718.4600	2.5250
41.3499	0.0500	41.3999	0.9860	0.0665	0.0140	6518.4600	2.4047
40.3161	0.0500	40.3661	0.9854	0.0694	0.0146	6381.5000	1.9423
36.5874	0.0500	36.6374	0.9843	0.0747	0.0157	6256.9000	2.1041
33.2238	0.0500	33.2738	0.9826	0.0827	0.0174	5858.8900	2.1956
31.1410	0.0500	31.1910	0.9801	0.0946	0.0199	5481.6400	1.7413
27.8176	0.0500	27.8676	0.9771	0.1097	0.0229	5231.1200	1.7413
24.5847	0.0500	24.6347	0.9735	0.1270	0.0265	4955.9900	1.4853
21.4446	0.0500	21.4946	0.9693	0.1470	0.0307	4732.6800	1.4853
19.1663	0.0500	19.2163	0.9745	0.1221	0.0255	5047.6200	1.4853
16.0963	0.0500	16.1463	0.9715	0.1364	0.0285	4870.6800	1.4853
13.4136	0.0500	13.4636	0.9555	0.2139	0.0445	4617.4500	0.9901
41.6249	0.1500	41.7749	0.9808	0.0913	0.0192	10507.4800	2.9706
38.2017	0.1500	38.3517	0.9782	0.1037	0.0218	10075.0700	2.9706
35.6549	0.1500	35.8049	0.9756	0.1168	0.0244	9760.7200	3.1563
34.6018	0.1500	34.7518	0.9736	0.1261	0.0264	9218.0800	3.1563
31.9401	0.1500	32.0901	0.9690	0.1487	0.0310	8489.0400	3.1563
29.4945	0.1500	29.6445	0.9660	0.1632	0.0340	8046.4200	2.5250
26.8132	0.1500	26.9632	0.9685	0.1509	0.0315	8311.1200	2.5250
21.9189	0.1500	22.0689	0.9654	0.1660	0.0346	7925.5600	2.5250
22.8756	0.1500	23.0256	0.9611	0.1867	0.0389	7414.6900	2.1041
20.1558	0.1500	20.3058	0.9562	0.2108	0.0438	6860.0200	2.1041
17.3860	0.1500	17.5360	0.9484	0.2484	0.0516	6262.6300	2.1041
13.9613	0.1500	14.1113	0.9417	0.2813	0.0583	5887.8100	1.8036
15.7700	0.0300	15.8000	0.9733	0.1275	0.0267	3188.1300	1.4853
15.0200	0.0500	15.0700	0.9645	0.1703	0.0355	3582.9400	1.8036
13.8200	0.0700	13.8900	0.9578	0.2026	0.0422	3548.8200	2.1957
13.1300	0.0900	13.2200	0.9528	0.2271	0.0472	3648.3900	1.8700
13.5100	0.1000	13.6100	0.9488	0.2464	0.0512	4034.8700	1.9400
13.8800	0.1143	13.9943	0.9443	0.2689	0.0557	4325.8300	2.2900
14.3300	0.1257	14.4557	0.9425	0.2775	0.0575	4386.9800	2.4048
14.7800	0.1371	14.9171	0.9408	0.2855	0.0592	4121.7300	2.4047
14.7800	0.1486	14.9286	0.9380	0.2995	0.0620	3429.7800	2.5250
14.6400	0.1600	14.8000	0.9365	0.3066	0.0635	3461.5100	2.5250
14.3300	0.1714	14.5014	0.9342	0.3186	0.0658	2497.4100	2.6579
14.2600	0.1829	14.4429	0.9316	0.3313	0.0684	2467.8800	2.6579
14.0800	0.1943	14.2743	0.9303	0.3372	0.0697	2268.7200	2.6579

APPENDIX G

Tabulated Measured Wave Properties

VSG [m/s]	VSL [m/s]	Measured Wave Velocity [m/s]	Measured Wave Frequency [Hz]	Measured Wave spacing [m]
42.9011	0.0500	2.5250	14.0000	0.1804
41.3499	0.0500	2.4047	16.0000	0.1503
40.3161	0.0500	1.9423	16.0000	0.1214
36.5874	0.0500	2.1041	14.0000	0.1503
33.2238	0.0500	2.1956	12.0000	0.1830
31.1410	0.0500	1.7413	10.0000	0.1741
27.8176	0.0500	1.7413	11.0000	0.1583
24.5847	0.0500	1.4853	9.5000	0.1563
21.4446	0.0500	1.4853	10.0000	0.1485
19.1663	0.0500	1.4853	11.0000	0.1350
16.0963	0.0500	1.4853	7.0000	0.2122
13.4136	0.0500	0.9901	9.0000	0.1100
41.6249	0.1500	2.9706	29.0000	0.1024
38.2017	0.1500	2.9706	26.0000	0.1143
35.6549	0.1500	3.1563	26.0000	0.1214
34.6018	0.1500	3.1563	24.0000	0.1315
31.9401	0.1500	3.1563	22.0000	0.1435
29.4945	0.1500	2.5250	19.0000	0.1329
26.8132	0.1500	2.5250	21.0000	0.1202
21.9189	0.1500	2.5250	20.0000	0.1263
22.8756	0.1500	2.1041	21.0000	0.1002
20.1558	0.1500	2.1041	18.0000	0.1169
17.3860	0.1500	2.1041	13.0000	0.1619
13.9613	0.1500	1.8036	10.0000	0.1804
15.7700	0.0300	1.4853	13.0000	0.1143
15.0200	0.0500	1.8036	9.0000	0.2004
13.8200	0.0700	2.1957	10.0000	0.2196
13.1300	0.0900	1.8700	9.0000	0.2078
13.5100	0.1000	1.9400	8.0000	0.2425
13.8800	0.1143	2.2900	10.0000	0.2290
14.3300	0.1257	2.4048	13.0000	0.1850
14.7800	0.1371	2.4047	10.0000	0.2405
14.7800	0.1486	2.5250	10.0000	0.2525
14.6400	0.1600	2.5250	11.0000	0.2295
14.3300	0.1714	2.6579	14.0000	0.1899
14.2600	0.1829	2.6579	13.0000	0.2045
14.0800	0.1943	2.6579	12.0000	0.2215

APPENDIX H

Tabulated Measured Wave and Drop Frequency

VSG [m/s]	VSL [m/s]	Measured Drop Frequency [HZ]	Measured wave Frequency [Hz]
42.9011	0.0500	6.5000	14.0000
41.3499	0.0500	15.0000	16.0000
40.3161	0.0500	4.5000	16.0000
36.5874	0.0500	4.0000	14.0000
33.2238	0.0500	1.5000	12.0000
31.1410	0.0500	1.5000	10.0000
27.8176	0.0500	1.1600	11.0000
24.5847	0.0500		9.5000
21.4446	0.0500		10.0000
19.1663	0.0500	4.0000	11.0000
16.0963	0.0500		7.0000
13.4136	0.0500	5.0000	9.0000
41.6249	0.1500	14.0000	29.0000
38.2017	0.1500	6.6600	26.0000
35.6549	0.1500		26.0000
34.6018	0.1500	11.5000	24.0000
31.9401	0.1500	4.0000	22.0000
29.4945	0.1500	3.0000	19.0000
26.8132	0.1500	3.0000	21.0000
21.9189	0.1500		20.0000
22.8756	0.1500	1.5000	21.0000
20.1558	0.1500	1.1600	18.0000
17.3860	0.1500	1.3300	13.0000
13.9613	0.1500	0.1660	10.0000
15.7700	0.0300		13.0000
15.0200	0.0500		9.0000
13.8200	0.0700		10.0000
13.1300	0.0900		9.0000
13.5100	0.1000	0.1660	8.0000
13.8800	0.1143	50.3300	10.0000
14.3300	0.1257	0.1660	13.0000
14.7800	0.1371	150.1600	10.0000
14.7800	0.1486	2.3330	10.0000
14.6400	0.1600	150.5000	11.0000
14.3300	0.1714	50.1600	14.0000
14.2600	0.1829	0.8333	13.0000
14.0800	0.1943	0.1660	12.0000